

VIDYA REPORT NO. 37
FINAL TECHNICAL REPORT, PHASE II

EFFECTS OF SUPERSONIC AND HYPERSONIC AIRCRAFT SPEED UPON AERIAL PHOTOGRAPHY

This Report Covers the Period of April 26, 1960, to January 26, 1961
CONTRACT NO. DA-44-009-ENG-3990 PROJECT NO. 8-35-12-420

placed by

U. S. ARMY ENGINEER
GEODESY, INTELLIGENCE AND MAPPING
RESEARCH AND DEVELOPMENT AGENCY
FORT BELVOIR, VIRGINIA



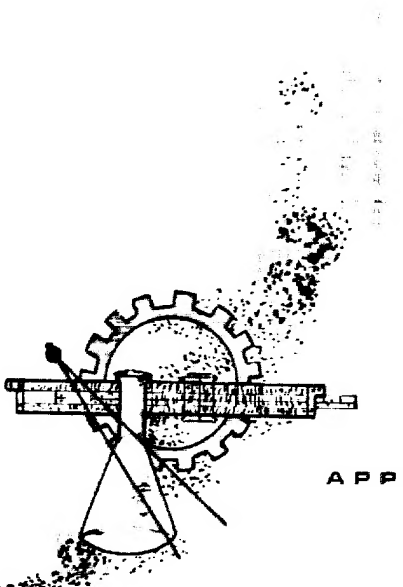
V I D Y A

RESEARCH AND DEVELOPMENT

2626 HANOVER ST., PALO ALTO, CALIFORNIA



The word Vidya, taken from the Vedanta philosophy of the Hindus, means knowledge. The symbol used to denote the Vidya organization is the letter "V" from Sanskrit, the ancient language of India.



APPLIED MECHANICS . . . PHYSICS . . . ANALYSES

Approved For Release 2000/04/12 : CIA-RDP67B00657R000300070001-0

AD Accession No.
Vidya, Inc., 2626 Hanover Street, Palo Alto, California
EFFECTS OF SUPERSONIC AND HYPERSONIC AIRCRAFT SPEED UPON AERIAL PHOTOGRAPHY - FINAL REPORT, PHASE II - Jack N. Nielsen, Frederick K. Goodwin, Alvin H. Sacks, Morris W. Rubesin, Jack A. Burnell. Vidya Report No. 37, January 1961, approx. 410 pages including 59 figures and 2 tables.

Prepared for U. S. Army Engineer Geodesy, Intelligence and Mapping Research and Development Agency, Port Belvoir, Virginia under Contract No. DA-44-009 ENG-3990, Project No. 8-35-12-420.

Analyses have been made of certain environmental influences known to affect the quality of aerial photography at supersonic and hypersonic speeds. This Phase II investigation extends the Phase I study (Vidya Report 17) to Mach numbers of about 35 and to satellite altitudes. The present study is divided into nine parts as listed below:

Part I.- Summary report; Part II.- Selection of Hypersonic Configurations; Part III.- Aerodynamic Flow Field Outside the Boundary Layer; Part IV.- Determination of Boundary-Layer Characteristics; Part V.- Thermal Characteristics of the Camera Window; Part VI.- Luminosity and Contrast; Part VII.- Optical Resolution; Part VIII.- Refraction and Metric Distortion; Part IX.- Mapping and Reconnaissance from Hypersonic Vehicles.

This report, the Final Technical Report under Phase II, contains all of the information presented in Vidya Reports Nos. 24 and 28, the two interim reports of this phase, and the additional work required to complete the study.

AD Accession No.
Vidya, Inc., 2626 Hanover Street, Palo Alto, California
EFFECTS OF SUPERSONIC AND HYPERSONIC AIRCRAFT SPEED UPON AERIAL PHOTOGRAPHY - FINAL REPORT, PHASE II - Jack N. Nielsen, Frederick K. Goodwin, Alvin H. Sacks, Morris W. Rubesin, Jack A. Burnell. Vidya Report No. 37, January 1961, approx. 410 pages including 59 figures and 2 tables.

Prepared for U. S. Army Engineer Geodesy, Intelligence and Mapping Research and Development Agency, Port Belvoir, Virginia under Contract No. DA-44-009 ENG-3990, Project No. 8-35-12-420.

Analyses have been made of certain environmental influences known to affect the quality of aerial photography at supersonic and hypersonic speeds. This Phase II investigation extends the Phase I study (Vidya Report 17) to Mach numbers of about 35 and to satellite altitudes. The present study is divided into nine parts as listed below:

Part I.- Summary report; Part II.- Selection of Hypersonic Configurations; Part III.- Aerodynamic Flow Field Outside the Boundary Layer; Part IV.- Determination of Boundary-Layer Characteristics; Part V.- Thermal Characteristics of the Camera Window; Part VI.- Luminosity and Contrast; Part VII.- Optical Resolution; Part VIII.- Refraction and Metric Distortion; Part IX.- Mapping and Reconnaissance from Hypersonic Vehicles.

This report, the Final Technical Report under Phase II, contains all of the information presented in Vidya Reports Nos. 24 and 28, the two interim reports of this phase, and the additional work required to complete the study.

1. Aerial photographs - Mathematical analysis.
2. Aerial photography - Mathematical analysis.
3. Aerial photography - Theoretical corrections.
4. Light-refraction.
5. Light-scattering.
6. Boundary layer - heating.
7. Hypersonic flow-analysis.
8. Contract No. DA-44-009-ENG-3990.
9. Project No. 8-35-12-420.

AD Accession No.
Vidya, Inc., 2626 Hanover Street, Palo Alto, California
EFFECTS OF SUPERSONIC AND HYPERSONIC AIRCRAFT SPEED UPON AERIAL PHOTOGRAPHY - FINAL REPORT, PHASE II - Jack N. Nielsen, Frederick K. Goodwin, Alvin H. Sacks, Morris W. Rubesin, Jack A. Burnell. Vidya Report No. 37, January 1961, approx. 410 pages including 59 figures and 2 tables.

Prepared for U. S. Army Engineer Geodesy, Intelligence and Mapping Research and Development Agency, Port Belvoir, Virginia under Contract No. DA-44-009 ENG-3990, Project No. 8-35-12-420.

Analyses have been made of certain environmental influences known to affect the quality of aerial photography at supersonic and hypersonic speeds. This Phase II investigation extends the Phase I study (Vidya Report 17) to Mach numbers of about 35 and to satellite altitudes. The present study is divided into nine parts as listed below:

Part I.- Summary report; Part II.- Selection of Hypersonic Configurations; Part III.- Aerodynamic Flow Field Outside the Boundary Layer; Part IV.- Determination of Boundary-Layer Characteristics; Part V.- Thermal Characteristics of the Camera Window; Part VI.- Luminosity and Contrast; Part VII.- Optical Resolution; Part VIII.- Refraction and Metric Distortion; Part IX.- Mapping and Reconnaissance from Hypersonic Vehicles.

This report, the Final Technical Report under Phase II, contains all of the information presented in Vidya Reports Nos. 24 and 28, the two interim reports of this phase, and the additional work required to complete the study.

1. Aerial photographs - Mathematical analysis.
2. Aerial photography - Mathematical analysis.
3. Aerial photography - Theoretical corrections.
4. Light-refraction.
5. Light-scattering.
6. Boundary layer - heating.
7. Hypersonic flow-analysis.
8. Contract No. DA-44-009-ENG-3990.
9. Project No. 8-35-12-420.

AD Accession No.
Vidya, Inc., 2626 Hanover Street, Palo Alto, California
EFFECTS OF SUPERSONIC AND HYPERSONIC AIRCRAFT SPEED UPON AERIAL PHOTOGRAPHY - FINAL REPORT, PHASE II - Jack N. Nielsen, Frederick K. Goodwin, Alvin H. Sacks, Morris W. Rubesin, Jack A. Burnell. Vidya Report No. 37, January 1961, approx. 410 pages including 59 figures and 2 tables.

Prepared for U. S. Army Engineer Geodesy, Intelligence and Mapping Research and Development Agency, Port Belvoir, Virginia under Contract No. DA-44-009 ENG-3990, Project No. 8-35-12-420.

Analyses have been made of certain environmental influences known to affect the quality of aerial photography at supersonic and hypersonic speeds. This Phase II investigation extends the Phase I study (Vidya Report 17) to Mach numbers of about 35 and to satellite altitudes. The present study is divided into nine parts as listed below:

Part I.- Summary report; Part II.- Selection of Hypersonic Configurations; Part III.- Aerodynamic Flow Field Outside the Boundary Layer; Part IV.- Determination of Boundary-Layer Characteristics; Part V.- Thermal Characteristics of the Camera Window; Part VI.- Luminosity and Contrast; Part VII.- Optical Resolution; Part VIII.- Refraction and Metric Distortion; Part IX.- Mapping and Reconnaissance from Hypersonic Vehicles.

This report, the Final Technical Report under Phase II, contains all of the information presented in Vidya Reports Nos. 24 and 28, the two interim reports of this phase, and the additional work required to complete the study.

1. Aerial photographs - Mathematical analysis.
2. Aerial photography - Mathematical analysis.
3. Aerial photography - Theoretical corrections.
4. Light-refraction.
5. Light-scattering.
6. Boundary layer - heating.
7. Hypersonic flow-analysis.
8. Contract No. DA-44-009-ENG-3990.
9. Project No. 8-35-12-420.

AD Accession No.
Vidya, Inc., 2626 Hanover Street, Palo Alto, California
EFFECTS OF SUPERSONIC AND HYPERSONIC AIRCRAFT SPEED UPON AERIAL PHOTOGRAPHY - FINAL REPORT, PHASE II - Jack N. Nielsen, Frederick K. Goodwin, Alvin H. Sacks, Morris W. Rubesin, Jack A. Burnell. Vidya Report No. 37, January 1961, approx. 410 pages including 59 figures and 2 tables.

Prepared for U. S. Army Engineer Geodesy, Intelligence and Mapping Research and Development Agency, Port Belvoir, Virginia under Contract No. DA-44-009 ENG-3990, Project No. 8-35-12-420.

Analyses have been made of certain environmental influences known to affect the quality of aerial photography at supersonic and hypersonic speeds. This Phase II investigation extends the Phase I study (Vidya Report 17) to Mach numbers of about 35 and to satellite altitudes. The present study is divided into nine parts as listed below:

Part I.- Summary report; Part II.- Selection of Hypersonic Configurations; Part III.- Aerodynamic Flow Field Outside the Boundary Layer; Part IV.- Determination of Boundary-Layer Characteristics; Part V.- Thermal Characteristics of the Camera Window; Part VI.- Luminosity and Contrast; Part VII.- Optical Resolution; Part VIII.- Refraction and Metric Distortion; Part IX.- Mapping and Reconnaissance from Hypersonic Vehicles.

This report, the Final Technical Report under Phase II, contains all of the information presented in Vidya Reports Nos. 24 and 28, the two interim reports of this phase, and the additional work required to complete the study.

Approved For Release 2000/04/12 : CIA-RDP67B00657R000300070001-0

AD Accession No.
Vidya, Inc., 2626 Hanover Street, Palo Alto, California
EFFECTS OF SUPERSONIC AND HYPERSONIC AIRCRAFT SPEED UPON AERIAL PHOTOGRAPHY - FINAL REPORT, PHASE II - Jack N. Nielsen, Frederick K. Goodwin, Alvin H. Sacks, Morris W. Rubesin, Jack A. Burnell. Vidya Report No. 37, January 1961, approx. 410 pages including 59 figures and 2 tables.

Prepared for U. S. Army Engineer Geodesy, Intelligence and Mapping Research and Development Agency, Port Belvoir, Virginia under Contract No. DA-44-009 ENG-3990, Project No. 8-35-12-420.

Analyses have been made of certain environmental influences known to affect the quality of aerial photography at supersonic and hypersonic speeds. This Phase II investigation extends the Phase I study (Vidya Report 17) to Mach numbers of about 35 and to satellite altitudes. The present study is divided into nine parts as listed below:

Part I.- Summary report; Part II.- Selection of Hypersonic Configurations; Part III.- Aerodynamic Flow Field Outside the Boundary Layer; Part IV.- Determination of Boundary-Layer Characteristics; Part V.- Thermal Characteristics of the Camera Window; Part VI.- Luminosity and Contrast; Part VII.- Optical Resolution; Part VIII.- Refraction and Metric Distortion; Part IX.- Mapping and Reconnaissance from Hypersonic Vehicles.

This report, the Final Technical Report under Phase II, contains all of the information presented in Vidya Reports Nos. 24 and 28, the two interim reports of this phase, and the additional work required to complete the study.

1. Aerial photographs - Mathematical analysis.
2. Aerial photography - Mathematical analysis.
3. Aerial photography - Theoretical corrections.
4. Light-refraction.
5. Light-scattering.
6. Boundary layer - heating.
7. Hypersonic flow-analysis.
8. Contract No. DA-44-009-ENG-3990.
9. Project No. 8-35-12-420.

AD Accession No.
Vidya, Inc., 2626 Hanover Street, Palo Alto, California
EFFECTS OF SUPERSONIC AND HYPERSONIC AIRCRAFT SPEED UPON AERIAL PHOTOGRAPHY - FINAL REPORT, PHASE II - Jack N. Nielsen, Frederick K. Goodwin, Alvin H. Sacks, Morris W. Rubesin, Jack A. Burnell. Vidya Report No. 37, January 1961, approx. 410 pages including 59 figures and 2 tables.

Prepared for U. S. Army Engineer Geodesy, Intelligence and Mapping Research and Development Agency, Port Belvoir, Virginia under Contract No. DA-44-009 ENG-3990, Project No. 8-35-12-420.

Analyses have been made of certain environmental influences known to affect the quality of aerial photography at supersonic and hypersonic speeds. This Phase II investigation extends the Phase I study (Vidya Report 17) to Mach numbers of about 35 and to satellite altitudes. The present study is divided into nine parts as listed below:

Part I.- Summary report; Part II.- Selection of Hypersonic Configurations; Part III.- Aerodynamic Flow Field Outside the Boundary Layer; Part IV.- Determination of Boundary-Layer Characteristics; Part V.- Thermal Characteristics of the Camera Window; Part VI.- Luminosity and Contrast; Part VII.- Optical Resolution; Part VIII.- Refraction and Metric Distortion; Part IX.- Mapping and Reconnaissance from Hypersonic Vehicles.

This report, the Final Technical Report under Phase II, contains all of the information presented in Vidya Reports Nos. 24 and 28, the two interim reports of this phase, and the additional work required to complete the study.

1. Aerial photographs - Mathematical analysis.
2. Aerial photography - Mathematical analysis.
3. Aerial photography - Theoretical corrections.
4. Light-refraction.
5. Light-scattering.
6. Boundary layer - heating.
7. Hypersonic flow-analysis.
8. Contract No. DA-44-009-ENG-3990.
9. Project No. 8-35-12-420.

AD Accession No.
Vidya, Inc., 2626 Hanover Street, Palo Alto, California
EFFECTS OF SUPERSONIC AND HYPERSONIC AIRCRAFT SPEED UPON AERIAL PHOTOGRAPHY - FINAL REPORT, PHASE II - Jack N. Nielsen, Frederick K. Goodwin, Alvin H. Sacks, Morris W. Rubesin, Jack A. Burnell. Vidya Report No. 37, January 1961, approx. 410 pages including 59 figures and 2 tables.

Prepared for U. S. Army Engineer Geodesy, Intelligence and Mapping Research and Development Agency, Port Belvoir, Virginia under Contract No. DA-44-009 ENG-3990, Project No. 8-35-12-420.

Analyses have been made of certain environmental influences known to affect the quality of aerial photography at supersonic and hypersonic speeds. This Phase II investigation extends the Phase I study (Vidya Report 17) to Mach numbers of about 35 and to satellite altitudes. The present study is divided into nine parts as listed below:

Part I.- Summary report; Part II.- Selection of Hypersonic Configurations; Part III.- Aerodynamic Flow Field Outside the Boundary Layer; Part IV.- Determination of Boundary-Layer Characteristics; Part V.- Thermal Characteristics of the Camera Window; Part VI.- Luminosity and Contrast; Part VII.- Optical Resolution; Part VIII.- Refraction and Metric Distortion; Part IX.- Mapping and Reconnaissance from Hypersonic Vehicles.

This report, the Final Technical Report under Phase II, contains all of the information presented in Vidya Reports Nos. 24 and 28, the two interim reports of this phase, and the additional work required to complete the study.

AD Accession No.
Vidya, Inc., 2626 Hanover Street, Palo Alto, California
EFFECTS OF SUPERSONIC AND HYPERSONIC AIRCRAFT SPEED UPON AERIAL PHOTOGRAPHY - FINAL REPORT, PHASE II - Jack N. Nielsen, Frederick K. Goodwin, Alvin H. Sacks, Morris W. Rubesin, Jack A. Burnell. Vidya Report No. 37, January 1961, approx. 410 pages including 59 figures and 2 tables.

Prepared for U. S. Army Engineer Geodesy, Intelligence and Mapping Research and Development Agency, Port Belvoir, Virginia under Contract No. DA-44-009 ENG-3990, Project No. 8-35-12-420.

Analyses have been made of certain environmental influences known to affect the quality of aerial photography at supersonic and hypersonic speeds. This Phase II investigation extends the Phase I study (Vidya Report 17) to Mach numbers of about 35 and to satellite altitudes. The present study is divided into nine parts as listed below:

Part I.- Summary report; Part II.- Selection of Hypersonic Configurations; Part III.- Aerodynamic Flow Field Outside the Boundary Layer; Part IV.- Determination of Boundary-Layer Characteristics; Part V.- Thermal Characteristics of the Camera Window; Part VI.- Luminosity and Contrast; Part VII.- Optical Resolution; Part VIII.- Refraction and Metric Distortion; Part IX.- Mapping and Reconnaissance from Hypersonic Vehicles.

This report, the Final Technical Report under Phase II, contains all of the information presented in Vidya Reports Nos. 24 and 28, the two interim reports of this phase, and the additional work required to complete the study.

1. Aerial photographs - Mathematical analysis.
2. Aerial photography - Mathematical analysis.
3. Aerial photography - Theoretical corrections.
4. Light-refraction.
5. Light-scattering.
6. Boundary layer - heating.
7. Hypersonic flow-analysis.
8. Contract No. DA-44-009-ENG-3990.
9. Project No. 8-35-12-420.

Approved For Release 2000/04/12 : CIA-RDP67B00657R000300070001-0

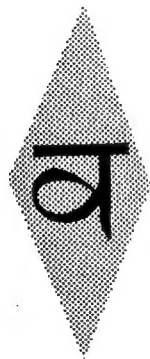
VIDYA REPORT NO. 37
FINAL TECHNICAL REPORT, PHASE II

EFFECTS OF SUPERSONIC AND HYPERSONIC AIRCRAFT SPEED
UPON AERIAL PHOTOGRAPHY

This Report Covers the Period of April 26, 1960 to January 26, 1961
CONTRACT NO. DA-44-009-ENG-3990 PROJECT NO. 8-35-12-420
VIDYA PROJECT NO. 58/C

placed by

U. S. ARMY ENGINEER
GEODESY, INTELLIGENCE AND MAPPING
RESEARCH AND DEVELOPMENT AGENCY
FORT BELVOIR, VIRGINIA



VIDYA, INC.

A DIVISION OF

Itek

CORPORATION

2626 HANOVER STREET • PALO ALTO, CALIFORNIA

TEL: DAVENPORT 1-2455 TWX: PAL AL 82

PREFACE

The present report is the final technical report of Phase II of an investigation carried out for the U. S. Army Geodesy, Intelligence and Mapping Research and Development Agency, Ft. Belvoir, Virginia, under Contract No. DA-44-009 ENG-3990, Project No. 8-35-12-420. A final technical report for Phase I was issued as VIDYA Report No. 17, covering the period of May 26, 1959 to April 28, 1960.

Phase II of the present investigation represents an extension of the studies made in Phase I to higher speeds and altitudes and investigates, further, certain problem areas which were found to be significant in Phase I. The same general format is retained in this report as in previous reports.

The following authors of the present report are also the principal investigators:

Jack A. Burnell

Frederick K. Goodwin

Jack N. Nielsen

Morris W. Rubesin

Alvin H. Sacks

The technical advice of Mr. Thomas Leighton of Information Technology Laboratories, Palo Alto Division, on optical questions is gratefully acknowledged.

TABLE OF CONTENTS

	Page
TITLE PAGE	1
PREFACE	2
TABLE OF CONTENTS	3
SUMMARY	7
 PART I: - SUMMARY REPORT	 I-1
INTRODUCTION	I-1
OVERALL INVESTIGATION AND DISCUSSION	I-3
Part I	I-3
Part II	I-3
Part III	I-5
Part IV	I-8
Part V	I-11
Part VI	I-12
Part VII	I-14
Part VIII	I-15
Part IX	I-17
CONCLUSIONS	I-18
RECOMMENDATIONS	I-20
REFERENCES	I-22
 PART II: - SELECTION OF HYPERSONIC CONFIGURATIONS	 II-1
INTRODUCTION	II-1
SYMBOLS	II-3
INVESTIGATION	II-5
Hemispherically Blunted Circular Cone	II-6
Thick Triangular Wing with Cylindrical Leading Edge	II-11
CONCLUSIONS	II-15
REFERENCES	II-17
FIGURES	Following
 PART III: - DETERMINATION OF FLOW FIELD OUTSIDE THE BOUNDARY LAYER	 III-1
INTRODUCTION	III-1
SYMBOLS	III-4
INVESTIGATION	III-7
Flow Field Around a Blunt Cone	III-10
Conditions at the Edge of the Boundary Layer	III-10
Determination of Boundary Layer Type	III-12
Shock Layer Thickness and Shock Layer Slope	III-17
Conditions Just Inside the Shock Wave	III-20
Temperature and Density Distributions Between the Edge of the Boundary Layer and the Shock Wave	III-22

Flow Field Around a Blunt Swept Wing	III-24
<u>Conditions at the Edge of the Boundary Layer</u>	III-24
<u>Determination of Boundary Layer Type</u>	III-27
<u>Shock Layer Thickness and Shock Wave Shape</u>	III-28
<u>Conditions Just Inside the Shock Wave</u>	III-29
<u>Temperature and Density Distributions Between the Edge of the Boundary Layer and the Shock Wave</u>	III-29
RESULTS AND DISCUSSION	III-30
CONCLUSIONS	III-33
APPENDIX IIIA: - COMPARISON OF SEVERAL METHODS FOR CALCULATING SURFACE PRESSURE DISTRIBUTIONS ON BLUNT CONES	III-35
REFERENCES	III-39
FIGURES	Following
PART IV: - DETERMINATION OF BOUNDARY-LAYER CHARACTERISTICS	
INTRODUCTION	IV-1
SYMBOLS	IV-1
INVESTIGATION	IV-4
Derivation of Basic Equations for a Flat Plate	IV-6
Momentum Thickness on Hypersonic Configurations	IV-8
Boundary Layer Thickness on Hypersonic Configurations	IV-15
Calculative Method	IV-16
<u>Calculation of Momentum Thickness</u>	IV-17
<u>Calculation of η_s</u>	IV-18
<u>Calculation of Boundary Layer Thickness and Boundary Layer Profiles</u>	IV-21
<u>Calculation of Boundary Layer Mass Flow</u>	IV-21
RESULTS AND DISCUSSION	IV-25
CONCLUSIONS	IV-26
APPENDIX IVA: - NUMERICAL EXAMPLE OF THE DETERMINATION OF THE BOUNDARY LAYER CHARACTERISTICS	IV-30
REFERENCES	IV-32
TABLE	IV-36
FIGURES	Following
PART V: - THERMAL CHARACTERISTICS OF THE CAMERA WINDOW	
INTRODUCTION	V-1
SYMBOLS	V-1
INVESTIGATION	V-3
Method of Solution for Blunt Cone	V-5
Method of Solution for Blunt Wing	V-11
Camera Window Temperatures	V-14
RESULTS AND DISCUSSION	V-15
CONCLUSIONS	V-17
	V-20

APPENDIX VA: - DERIVATION OF INTEGRAL TYPE EQUATIONS FOR EVALUATING CONVECTIVE HEAT TRANSFER USING REFERENCE ENTHALPY TECHNIQUES	V-22
Solution of Energy Integral Equations	V-28
APPENDIX VB: - CONVECTIVE HEAT TRANSFER RATE AT STAGNATION POINT	V-37
APPENDIX VC: - CALCULATIVE EXAMPLE FOR CONVECTIVE HEAT TRANSFER RATE TO CAMERA WINDOW ON BLUNT CONE	V-38
REFERENCES	V-48
FIGURES	Following
 PART VI: - LUMINOSITY AND CONTRAST	 VI-1
INTRODUCTION	VI-1
SYMBOLS	VI-3
GENERAL DESCRIPTION OF PROBLEM	VI-5
EFFECT OF ATMOSPHERE ON BRIGHTNESS AND CONTRAST	VI-8
Attenuation of Brightness by Rayleigh Scattering	VI-8
Increase in Brightness Due to Air Light	VI-10
Contrast for Downward Viewing from Camera	
Objective; Brightness	VI-13
EFFECT OF LUMINOUS LAYER ON BRIGHTNESS AND CONTRAST	VI-17
Increase in Brightness Due to the Luminous Layer	VI-17
Contrast for Downward Viewing from Camera	
Objective Including Effect of Luminous Layer	VI-21
RESULTS AND DISCUSSION	VI-25
CONCLUSIONS	VI-29
RECOMMENDATIONS	VI-30
APPENDIX VIA: - RELATIONSHIPS BETWEEN FLUX, INTENSITY, AND BRIGHTNESS	VI-31
APPENDIX VIB: - ATTENUATION OF IMAGE BRIGHTNESS BY RAYLEIGH SCATTERING	VI-34
APPENDIX VIC: - CONVERSION OF ABSORPTION COEFFICIENT DATA TO BRIGHTNESS	VI-37
APPENDIX VID: - DETERMINATION OF GROUND BRIGHTNESS	VI-40
REFERENCES	VI-43
TABLE	VI-44
FIGURES	Following
 PART VII: - OPTICAL RESOLUTION	 VII-1
INTRODUCTION	VII-1
INVESTIGATION	VII-3
DISCUSSION AND CONCLUSIONS	VII-9
RECOMMENDATIONS	VII-10
REFERENCES	VII-11

PART VIII: - REFRACTION AND METRIC DISTORTION	VIII-1
INTRODUCTION	VIII-1
SYMBOLS	VIII-4
INVESTIGATION	VIII-6
Ground Displacement Caused by Camera	
Window Curvature	VIII-6
Ground Displacement Caused by Refraction	
by the Boundary Layer	VIII-8
Ground Displacement Caused by Refraction by	
the Flow Field Between the Boundary Layer	
and the Bow Shock Wave	VIII-10
Ground Displacement Caused by Refraction by	
the Shock Wave	VIII-12
Ground Displacement Caused by Refraction by	
the Atmosphere	VIII-12
RESULTS AND DISCUSSION	VIII-18
CONCLUSIONS	VIII-19
RECOMMENDATIONS	VIII-20
APPENDIX VIIIA: - EFFECT OF TEMPERATURE ON THE	
SPECIFIC REFRACTIVITY OF AIR	VIII-21
REFERENCES	VIII-23
FIGURES	Following
PART IX: - MAPPING AND RECONNAISSANCE FROM HYPERSONIC	
VEHICLES	
INTRODUCTION	IX-1
SYMBOLS	IX-1
DISCUSSION	IX-3
Corridors of Continuous Flight	IX-4
External Window Temperature	IX-5
Window Temperature Differences	IX-6
Luminosity and Contrast	IX-7
Refraction Errors	IX-12
Loss of Resolution Due to Turbulent	
Boundary Layers	IX-15
CONCLUSIONS	IX-15
RECOMMENDATIONS	IX-17
FIGURES	Following

SUMMARY

This is the final technical report, Phase II, of a study of the effects of the environment on aerial photography taken at supersonic and hypersonic speeds. In particular, this phase of the study considers aerial mapping and reconnaissance up to satellite speeds and altitudes. The present phase is divided into nine parts as listed below:

- Part I Summary Report
- Part II Selection of Hypersonic Configurations
- Part III Aerodynamic Flow Field Outside the Boundary Layer
- Part IV Determination of Boundary Layer Characteristics
- Part V Thermal Characteristics of the Camera Window
- Part VI Luminosity and Contrast
- Part VII Optical Resolution
- Part VIII Refraction and Metric Distortion
- Part IX Mapping and Reconnaissance from Hypersonic Vehicles

This report completes the investigation carried out under the present contract, DA-44-009 ENG-3990, Project No. 8-35-12-420.

PART I: SUMMARY REPORT

INTRODUCTION

The purpose of this summary report is to furnish a concise view of the Phase II investigation.

The present investigation of aerial photography from high-speed aircraft is sponsored by the Geodesy, Intelligence and Mapping Development Agency (GIMRADA) of Fort Belvoir, Virginia, and has progressed through Phase I (Ref. 1) and Phase II. Phase I covered the supersonic Mach number range up to about a Mach number of 5 and the altitude range from sea level to 100,000 feet. The photographic problems of refraction, luminosity, scattering of light by turbulent boundary layers, aerodynamic heating of the camera window, and effects of window heating on optical quality were all investigated. The Phase II investigation extends these general studies to higher Mach numbers and altitudes so that an overall view of the flight spectrum is obtained. Also, special aspects of the above subject needing further emphasis are included in the Phase II study.

The special subjects being investigated in the Phase II study include consideration of real-gas effects, that is, departures of air from an ideal gas, as they affect refraction, aerodynamic heating of the camera window, and camera window temperatures. In addition, the real-gas

effect of air luminosity is more extensively studied than it was in the Phase I investigation. In addition to these changes, two hypersonic configurations are being investigated with respect to deleterious effects on aerial photography in order to determine those areas in the flight spectrum suitable for reconnaissance and mapping at the higher Mach numbers and altitudes.

The present report is divided into nine sections which correspond to the sub-tasks of the investigation. The parts are as follows:

- Part I Summary Report
- Part II Selection of Hypersonic Configurations
- Part III Aerodynamic Flow Field Outside the Boundary Layer
- Part IV Determination of Boundary-Layer Characteristics
- Part V Thermal Characteristics of the Camera Window
- Part VI Luminosity and Contrast
- Part VII Optical Resolution
- Part VIII Refraction and Metric Distortion
- Part IX Mapping and Reconnaissance from Hypersonic Vehicles

Parts II, III, IV, and V are basically combined aerodynamic-thermodynamic analyses required as basic inputs to the mapping and reconnaissance studies of Parts VI, VII, VIII, and IX.

OVERALL INVESTIGATION AND DISCUSSION

In the following paragraphs, each part of the investigation is described, particularly as it fits into the overall investigation.

Part I

The purpose of the present summary report is simply to give an overall view of the status of the present investigation without necessitating a detailed study of its various parts. It summarizes important findings and makes general recommendations.

Part II

The principal objective of Part II is to make a rational selection of several hypersonic configurations which can be used in the present study. While an attempt is made to reach conclusions which are independent of configurations, nevertheless, it is necessary to make calculations for specific configurations if any quantitative insight into the effects of hypersonic speed on aerial photography is to be obtained. For this purpose, it was decided to select two configurations which might be representative of winged and nonwinged hypersonic configurations. In Phase I, a sharp cone was chosen as representative of aircraft nose shapes for Mach numbers less than 5. For Phase II, which considers much higher Mach numbers, a sharp conical nose would burn because of aerodynamic heating.

Accordingly, a very blunt cone was chosen as representative of a nonwinged hypersonic configuration or the nose section of a winged configuration. For a winged hypersonic configuration, a swept-wing glider of a large leading-edge radius was chosen.

In Part II, an analysis is made to determine the area in the Mach number, altitude diagram wherein the foregoing configurations can operate continuously. For a given flight speed, the upper altitude limit is determined by the requirement that the aerodynamic lift plus the centrifugal force due to motion about the earth equals the weight. Above this altitude, the vehicle speed would not be sufficient to sustain flight. The lower limit is represented by the lowest altitude at which the vehicle can fly at the given air speed without exceeding its allowable temperature limits. The area between these limits is termed the corridor of continuous flight. The actual extent of the corridor depends on certain vehicle characteristics, as discussed in Part II. For the configurations selected for the present study, a range of Mach numbers at each altitude is specified as a region of practical interest in which to investigate aerial photography.

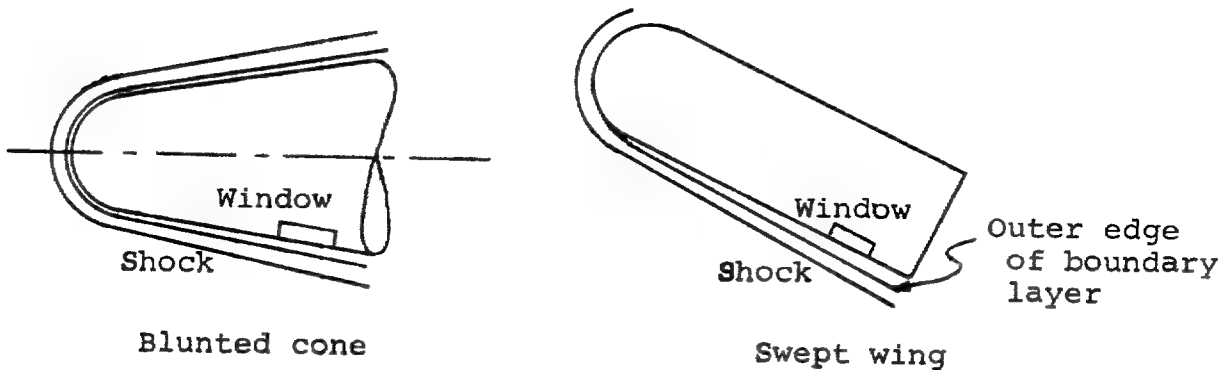
Part III

A knowledge of the aerodynamic flow field external to the boundary layer is necessary for the following calculations:

1. Thermal characteristics of camera window.
2. Effects of luminosity of flow external to boundary layer on aerial photography.
3. Effect of turbulence on resolution.
4. Refraction errors due to flow external to boundary layer.

The determination of the aerodynamic flow field about cones traveling at Mach numbers below 5, which were treated in Phase I, was a simple task because the air behaves as an ideal gas, and the supersonic flow about cones for such a gas has been tabulated. However, for the range of Mach numbers above 5, air can depart markedly from an ideal gas. Furthermore, aerodynamic heating requires the use of blunt configurations which complicates the calculation of the aerodynamic flow field which is of the mixed (i.e., supersonic and subsonic) type. Methods exist and others are developed in Part III for calculating the flow characteristics behind the shock wave and at the edge of the boundary layer for the present configurations for the real-gas effects exhibited by air. In Part III, attention is paid to the flow external to the boundary layer because this flow must be determined before the boundary-layer flow is calculated. Furthermore, the boundary-layer flow requires quite different calculative techniques for its determination.

The flow considered in Part III corresponds roughly to that in the following sketch:



The general shape of the shock wave is established, together with its standoff distance from the window. The pressure coefficient at the surface of the blunt cone is calculated by several methods and compared with available experiment. Methods are presented for calculating the conditions of the air at the outer edge of the boundary layer.

Methods are given for estimating the temperature and velocity profiles between the shock wave and the boundary layer and for predicting the position of boundary-layer transition on the aerodynamic configurations. It appears that turbulent flow is probable on the wing at 100,000 feet and also possibly on the cone.

The numerical results of this report differ somewhat for 250,000 feet altitude from those for the first interim report for two reasons. First, a mistake in sign was found in

Reference 3 of Part III which influenced the numerical results. This error has been rectified. Also, the former calculations were made for the 1956 ARDC atmosphere, whereas the results of the present report are for the 1959 ARDC atmosphere. There are slight differences between the 1956 and 1959 ARDC atmospheres starting at about 186,000 feet altitude. At 250,000 feet altitude, the following differences occur:

<u>Atmosphere</u>	<u>Pressure (lbs/ft²)</u>	<u>Density (slugs/ft³)</u>	<u>Temperature °R</u>
1956 ARDC	4.864×10^{-2}	7.996×10^{-8}	345.3
1959 ARDC	4.364×10^{-2}	7.748×10^{-8}	328.2

At much higher altitudes, the 1959 ARDC atmosphere is denser than the 1956 atmosphere.

One point should be borne in mind concerning Part III. The flow-field calculations have been made on the basis of the best analytical results known to Vidya at the present time. However, it must be remembered that the analysis is a first approximation to the flow field which will occur in flight. This is so because hypersonic data are not available from flight or the wind tunnel to check the validity of the assumptions which must be made to obtain quantitative results. As hypersonic data become available, particularly from flight-test programs, it will be possible to improve the flow-field calculative methods. These general remarks apply also to Parts IV and V.

Part IV

The purpose of Part IV is to develop methods for calculating the details of the flow in the boundary layer. Such information is required for calculating the following quantities:

1. Effects of luminosity of air in the boundary layer on aerial photography.
2. Effect of turbulence on resolution.

The boundary-layer characteristics which must be calculated include:

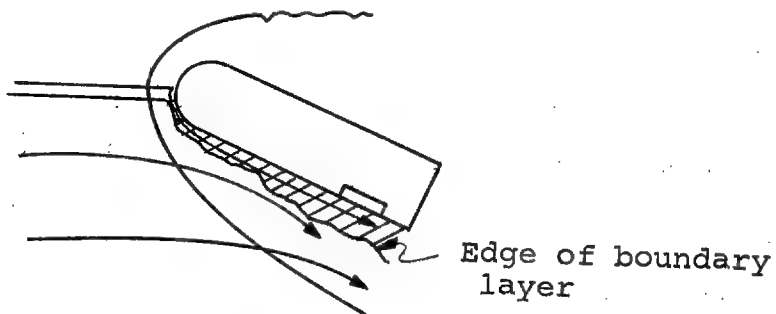
1. Boundary-layer thickness.
2. The following boundary-layer profiles:
 - a. Temperature
 - b. Velocity
 - c. Density

Whether the boundary layer at the window is laminar or turbulent is determined by methods considered in Part III.

There are several circumstances which make calculation of the boundary-layer flow different from its calculation in the Phase I study. In the first place, the configurations are now blunt rather than sharp cones so that the boundary layer is not at uniform pressure along its entire extent. Generally, both the surface pressure and temperature will be variable from the nose to the windows for the present configurations. Also, the temperatures within the boundary layer are sufficiently large in certain cases of interest that the air no longer acts as a perfect gas, and real-gas effects have to be included in the

boundary-layer analysis. Because a general theory of boundary layers with real-gas effects is not available in the literature, special calculative methods have been devised. Actually, the calculative methods developed for this part are based on analysis presented in Part V.

One of the principal assumptions in the analysis of Parts III, IV, and V is that all the air in the boundary layer came through the part of the bow shock which is essentially normal to the free-stream direction, as shown in the following sketch.



To check this assumption we must know the mass flow in the boundary layer at the camera location. The thickness of free-stream flow to provide this mass flow can then be determined. From the shape of the bow shock nose, it can be estimated whether this mass flow could have come through an essentially normal part of the bow shock. Such estimates have been made, and it is found that the assumption is valid up to 200,000 feet altitude. Above 200,000 feet the assumption breaks down gradually so that the results for 250,000 feet contain some errors due to this source.

Another implicit assumption in the foregoing sketch is that the boundary layer thickness is small compared to the stand-off distance of the shock from the lower surface. It turns out that this assumption is valid up to 200,000 feet also and breaks down progressively above this altitude. However, this assumption can be easily modified by measuring the shock stand-off distance from the outer edge of the boundary layer rather than the wing surface. This adjustment was made in calculating the path length of luminous air in Part VI. It probably should also be mentioned that the art of calculating boundary layers with real-gas effects is not highly developed, and that the calculative methods of Parts IV and V must be considered as preliminary.

In the first interim report, attention was directed to the problem of whether local "hot spots" existed in the boundary layer. It was found that under conditions of the worst aero-dynamic heating the peak temperatures occur at the outer edge of the boundary layer - not within it.

In Part IV of this report, approximate calculative methods are presented for calculating all the boundary-layer quantities mentioned previously. A sample calculation based on these methods is also presented.

Part V

The principal purposes of Part V are to determine the effects of aerodynamic heating on the camera window inner and outer temperatures, as well as the heat transfer into the camera cavity. Such information is basic to an evaluation of refraction errors, luminosity effects, and resolution losses.

In Phase I, a method was developed for calculating heat transfer to windows mounted on the surface of pointed cones. In that method, account was taken of the effect on the heat transfer of variation through the boundary layer of the physical properties of air such as viscosity, thermal conductivity, density, etc., which vary with temperature. In Phase I, the surface temperature of the pointed cones was assumed to be uniform, as well as the pressure distribution.

In the present phase, the configurations in question are blunted cones (assumed three-dimensional) and blunt wings (assumed two-dimensional), rather than pointed cones. The pressure distributions on the configurations are thus non-uniform. Also, the surface temperature between the stagnation point and the window is allowed to vary. It is essential that the analysis take account of real-gas effects on heat transfer as they are important for hypersonic speeds. The effects of dissociation and ionization on the physical properties of air are also important. The analysis presented in Part V takes into account all the above effects and is applicable to both

laminar and turbulent flow. Calculation of heat-transfer rates and surface temperature distribution requires an iterative calculation since local surface temperature depends on local heat-transfer coefficient and conversely. A sample calculation is included in Part V on the assumption of a surface at radiation equilibrium with its surroundings.

In the analysis a method has been devised for calculating the heat transfer based on the assumption that the air at the outer edge of the boundary layer goes through a section of the bow wave which is essentially normal to the free stream. This assumption was discussed previously under Part IV. The analysis also yields calculative material which is used as a basis of the analysis of Part IV. The calculative method has been applied to a range of speeds and altitudes for the example configurations to obtain the necessary information for mapping and reconnaissance studies.

Part VI

This part has three purposes:

1. Development of a rational criterion for assessing the effects of air luminosity on aerial photography.
2. Determination of luminosity boundaries in the Mach number, altitude diagram which delineate those regimes wherein the effects of luminosity are deleterious for the example configurations of Part II.

3. Investigation of methods for alleviating the deleterious effects of luminosity on aerial photography.

In Phase I, a rough criterion was advanced that the film illumination at the center (i.e., on the optical axis) due to luminosity does not exceed one-fifth that due to the average illumination without luminosity. In this phase, the criterion is refined to include its dependence on the contrast of the object being photographed against its background, the wavelength of the light used, and the ratio of sky brightness to the brightness of the background.

The reduction in inherent contrast of the ground object against its background is determined for a Rayleigh atmosphere as a function of altitude, nadir angle, and wavelength. A method is advanced for evaluating the contrast reduction through the luminous layer of air, the thermodynamic condition of which is determined in Parts III and IV. The method for calculating the brightness of the luminous layer utilizes calculated absorption coefficients for air. Since Phase I, more extensive tables of this quantity have become available; in particular, the absorption coefficients are available for lower densities by five order of magnitude than formerly.

Detailed calculations of the luminous boundaries in the Mach number, altitude diagram have been made for the example configurations to delineate the regime wherein luminosity has an adverse effect on aerial photography at hypersonic speeds. This information is utilized in the study of Part IX.

No deleterious effects were found for the nonwinged vehicle as far as degradation of contrast due to luminosity is concerned. Large deleterious effects were found for the winged vehicle for 0.4 microns, but small effects for 0.7 microns. The difference can generally be ascribed to the large angle of attack of the impact surface on which the window is mounted for the winged vehicle.

Part VII

In Phase I, wind-tunnel data were applied to the prediction of the loss of resolution in flight caused by turbulent boundary layers. The method employed is semi-empirical, and its applicability to flight is questionable because the boundary layer in flight is cooled rather than adiabatic as in the wind tunnel. To adapt the wind-tunnel results to flight requires removing the empiricism from the wind-tunnel results so that their application to flight can be rationally evaluated. The same rational analysis of light scattering by turbulence should solve the problem of rational correlation of the data and application of wind-tunnel results to flight.

A rational approach to the problem has been advanced by Liepmann in Reference 4. This analysis has been reexamined to try to apply it to highly cooled boundary layers. A local similarity assumption has been suggested for this purpose.

No calculations have been made to determine the loss of resolution due to turbulent boundary layers because the boundary layers have been almost all laminar in the present study.

Part VIII

The principal purpose of Part VIII is to extend the refraction calculation methods of Phase I to hypersonic configurations, and to investigate the variation of refractive errors with altitude and Mach number in the extended range of Phase II.

An investigation was undertaken to see how the assumed variation of atmospheric density with altitude affects the calculated ground displacement due to refraction. The theory of Phase I based on an exponential atmosphere is compared with ground displacement calculated by numerical integration for an ARDC atmosphere. The numerical integration yields a more accurate solution for ground displacements and can be used in full generality.

Another area of potential importance is the role real-gas effects can play in increasing refraction errors due to the near flow field. At least two phenomena appear to be of significance. First, because of real-gas effects of dissociation or ionization, the index of refraction of the air may be changed from its usual room-temperature value. An investigation of dissociation reveals significant increases in the

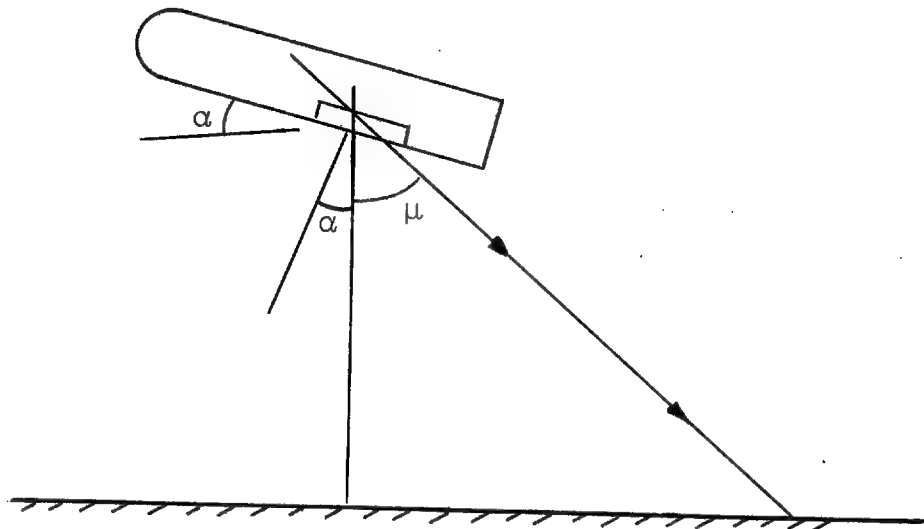
specific refractivity due to this phenomenon. Second, with dissociation and ionization of the air, the air densities of the near flow field can be significantly greater than for an ideal gas, thereby increasing the refractive errors.

Systematic calculations of the refractive errors in the vertical plane of symmetry have been made for the configurations described in Part II. These calculations give insight into the relative importance of the following sources of refractive errors:

1. Atmospheric refraction (far flow field)
2. Boundary layer
3. Flow field between boundary layer and bow wave
4. Bow wave
5. Temperature-induced curvature to the camera window

Near flow field

As it turns out, items 2, 3, and 4 are not important for altitudes well above 100,000 feet. Items 1 and 5 are the significant ones. The temperature-induced lens effect of the window increases with aerodynamic heating. For the blunt swept wing it can be very large; a 40-foot ground displacement for the examples calculated. At high angle of attack with a flush window, the incidence of the light rays to the window can be very large for rearward vision.



The angle of incidence in this case is the sum $\alpha + \mu$. For an angle of attack of 45° and a nadir angle of 45° , we have grazing incidence.

Part IX

The principal purpose of this section is to examine the suitability of various configurations for mapping and reconnaissance. The two configurations of Part II are used and the corridors of continuous flight are determined in the Mach number - altitude diagram. These corridors are regions in the diagram where the vehicles must operate if they are to be able to generate enough lift to sustain flight and withstand the structural temperatures due to aerodynamic heating. From the standpoint of mapping and reconnaissance we are interested to know the limiting lines in the diagram with respect to the following parameters:

- (1) Window temperature, T_o
- (2) Window temperature gradients, ΔT
- (3) Contrast reduction due to luminosity
- (4) Refraction errors (metric distortion)
- (5) Resolution loss due to turbulent boundary layers

Both configurations have been examined in connection with these five points. The results for the configurations are summarized in the Conclusions section.

CONCLUSIONS

1. An analysis taking into account real-gas effects has been developed for estimating the temperatures of the windows mounted in hypersonic configurations. It was found that within the corridors of continuous flight the window external temperatures did not exceed those which can be withstood by quartz glass.

2. While no serious loss of contrast due to air luminosity is found for the nonwinged vehicle, serious loss of contrast is encountered for the winged vehicle at low wave lengths (0.4μ). Increases in angle of attack will further increase the luminosity for the winged vehicle.

3. The general methods for calculating the flow field with real-gas effects as developed herein are valid to altitudes of 200,000 feet. Above this altitude, the boundary layer becomes nearly as thick as the calculated flow field. Also, the boundary

layer air does not come through a normal point of the bow shock wave. The analysis is grossly complicated by the second effect.

5. A method has been suggested for correlating wind tunnel data on light scattering by turbulent boundary layers which takes account of large density changes through the boundary layer.

6. The significant refraction errors at high altitudes are due to the atmosphere and to the lens effect of the window induced by aerodynamic heating. The ground displacements due to the vehicle flow field are small because of the low air densities at high altitudes. For rearward looking rays from the blunt wing at high angles of attack very large ground displacements due to the lens effect of the window can occur.

7. A precise numerical evaluation of the ground displacements due to atmospheric refraction using the 1959 ARDC atmosphere has been made.

8. Increases in the specific refractivity of air of 20 percent can occur because of dissociation of air caused by high temperatures.

9. The nonwinged vehicle investigated seems suitable for mapping and reconnaissance for several reasons.

- (a) The maximum window temperature of 1200°R is well within the capabilities of quartz windows.
- (b) The maximum temperature difference across a quartz glass window of 1/2-inch thickness is about 80°F .

- (c) No severe effects of air luminosity on aerial photography are found.
- (d) Aside from atmospheric refraction, the greatest refractive error is due to the lens effect of the window induced by aerodynamic heating. The net ground displacement is a maximum of 6 feet.
- (e) Because the boundary layer is laminar for altitudes above 100,000 feet, the loss of resolution due to turbulent boundary layers does not appear to be important.

10. The winged configuration exhibits the same general effects as the nonwinged vehicle but generally to a greater degree. At 45° rearward nadir angle ground displacements of 40 feet occur. This value will increase rapidly with increases in angle of attack. At a wave length of 0.4 microns there are large reductions in image contrast due to luminosity of the air. At a wave length of 0.7 microns this deleterious effect has almost entirely disappeared.

RECOMMENDATIONS

1. The present investigation could be usefully extended to infra-red photography and radar photography.
2. Work should be started toward an understanding of radiation heat transfer, structural failure due to thermal shock, and contrast reduction in "hot" glass windows. Experimental data in these areas are required.

3. The study of the winged configuration needs extending to investigate the importance of angle of attack and to extend the luminosity calculations.

4. Methods should be developed for calculating flow fields around hypersonic configurations when the boundary layer does not come through a normal part of the bow wave and when the boundary layer is as thick as the shock stand-off distance.

5. It is recommended that the suggestion made herein for correlation of wind tunnel data on loss of resolution due to turbulent boundary layers be attempted. If successful, it should be applied to predictions of resolution losses in flight since it considers large changes in density through the boundary layer.

6. A flight test program to obtain loss of resolution due to turbulent boundary layers is needed. The flight test program must be carefully planned so that it will yield data which can be compared with existing wind tunnel data.

7. Methods of mounting the viewing window should be investigated with an aim of minimizing the lens effect induced in the window by aerodynamic heating.

REFERENCES

1. Nielsen, Jack N., et al: Effect of Supersonic and Hyper-
sonic Aircraft Speed Upon Aerial Photography. Final
Report, Phase I, Vidya Report No. 17, April 1960.
2. Nielsen, Jack N., et al: Effect of Supersonic and Hyper-
sonic Aircraft Speed Upon Aerial Photography. First
Interim Report, Phase II, Vidya Report No. 24, July 1960.
3. Nielsen, Jack N., et al: Effect of Supersonic and Hyper-
sonic Aircraft Speed Upon Aerial Photography. Second
Interim Report, Phase II, Vidya Report No. 28, October
1960.
4. Liepmann, H. W.: Deflection and Diffusion of a Light Ray
Passing Through a Turbulent Boundary Layer. Report No.
SM-14397, Douglas Aircraft Co., May 1952.

PART II: SELECTION OF HYPERSONIC CONFIGURATIONS

INTRODUCTION

A realistic examination of the effects of supersonic and hypersonic speeds on aerial photography cannot be made without some notions of the configurations typical of vehicles operating in the speed and altitude range under consideration. In Reference 1 (the Phase I study of this contract), where the Mach number range was between 1.0 and 5.0, a sharp cone was chosen as a typical configuration. This was thought to be representative of the nose configuration of current manned aircraft and drones. Given this simple shape, the cone angle, and the camera window location, calculations of the temperatures and densities in the flow field surrounding the vehicle, in the boundary layer on the vehicle surface, and across the camera window could be made for a particular flight altitude and flight Mach number. The results of these calculations could then be used to determine the metric distortion and loss of resolution to be expected in photographs taken at these flight conditions.

In the present investigation, which is an extension of the flight regime of Reference 1 to higher altitudes and Mach numbers, the same details of the flow field surrounding the vehicle must be known. Hence, typical configurations must again be specified in order to develop the required aerodynamic,

thermodynamic, and optical calculative methods. At Mach numbers above 5.0, the so-called hypersonic speed range, the sharp cone does not serve as a realistic model since structurally it would not be able to withstand the extremely high temperatures which occur because of aerodynamic heating.

It is, therefore, the purpose of this part of the present report to select configurations and their dimensions which are thought to be representative of vehicles which will operate at these high Mach numbers and altitudes. These models will then be used, in the succeeding parts of this report, in developing the methods for determining the effects of hypersonic speeds on aerial photography. In addition, a comparison will be made between the temperatures to be expected on the vehicles and trajectories which they might fly in order to specify Mach numbers and altitudes for the calculations of the following parts of this report. It should be borne in mind that the results of the present report will not be applicable solely to the specific configurations. Every effort will be made to generalize the conclusions to ranges of configurations and to discover design principles which will minimize undesirable configuration effects.

SYMBOLS

a_∞	speed of sound in atmosphere at flight altitude, ft/sec
A	reference area, sq ft
c	chord length of wing, ft
C_D	drag coefficient
C_L	lift coefficient
g	acceleration due to gravity, taken as 32.2 ft/sec ²
h_∞	flight altitude above sea level, ft
L	lift, lbs
L_W	distance of camera window from shoulder, ft
M_∞	flight Mach number
$P(\alpha, \Lambda)$	defined by Equation (II-7)
q_{conv}	convective heat-transfer rate, BTU/sq ft-sec
q_{rad}	radiation heat-transfer rate, BTU/sq ft-sec
r	distance from center of earth to vehicle, taken as earth radius, 20,926,428 ft
R	nose or leading-edge radius, ft
T_{le}	radiation equilibrium temperature along stagnation line of leading edge, °R unless specified otherwise
T_s	radiation equilibrium temperature at stagnation point of hemispherical nose, °R unless specified otherwise
T_∞	free-stream temperature, °R
V_∞	flight velocity, ft/sec
W	weight, lbs
α	angle of attack, deg
γ	ratio of specific heats, 1.4 for low-temperature air

ϵ emissivity of vehicle surface at stagnation point
(≈ 0.8)

θ_c cone semiapex angle, deg

λ quantity defined by Equation (II-8)

Λ angle of sweep, deg

ρ_0 sea-level mass density, (0.002378 slug/ft³)

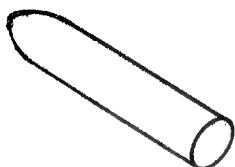
ρ_∞ free-stream mass density, slugs/ft³

σ Stefan-Boltzmann constant, 0.481×10^{-12}

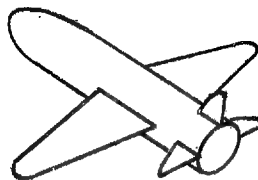
ϕ_s angle defined by Equation (II-9)

INVESTIGATION

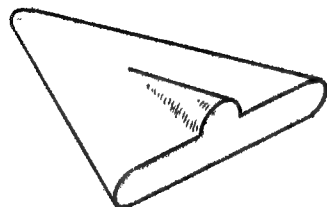
Vehicles which are to operate at Mach numbers in excess of 5.0 and altitudes above 100,000 feet can be divided into three groups for purposes of classification. These are shown in the following sketch:



Wingless Missile



Winged Missile



Glider

The first is a wingless missile. The entire vehicle or only the nose cone could be used for photographic purpose. The second is a winged lifting vehicle which could be used for hypersonic reconnaissance or mapping purposes, and the third is an all-wing vehicle designed to operate as a reentry glider. A camera could be mounted in the lower surface.

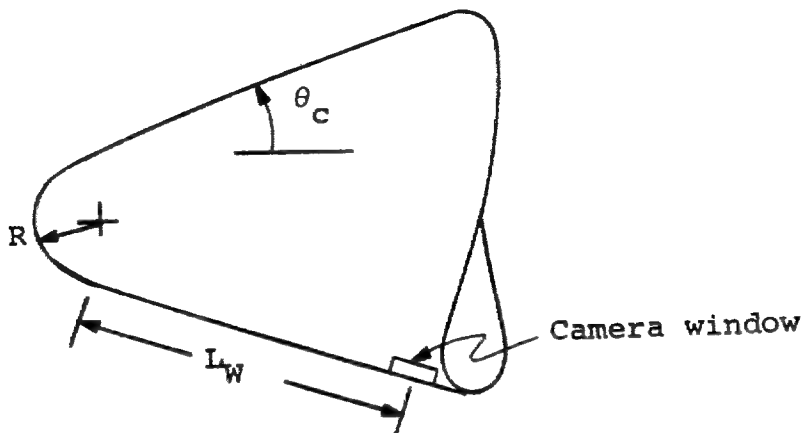
The flow fields surrounding the noses of the first two vehicles are identical for the same flight conditions and nose shapes. If the camera is placed in the nose, the same analysis of the aerodynamic and thermodynamic effects would apply to both. A nose cone, therefore, will be one configuration studied. Specifically, we will study a hemispherically blunted circular cone.

Another generic type of vehicle is that shown on the right in the preceding sketch. Let this glider be considered to be a thick triangular wing with a cylindrical leading edge and a hemispherically blunted nose. Photography taken from a configuration of this type will also be studied.

Let us now describe these two configurations in more detail.

Hemispherically Blunted Circular Cone

For this configuration let us assume the following general shape:



The blunt nose, which is a segment of a hemisphere, has a radius, R . The afterbody is a truncated cone of semiaxial angle, θ_c , and the camera window is mounted a distance, L_W , back along the surface of the cone from the tangent point (the point where the hemisphere and the cone join).

To specify the geometry of the configuration so that the necessary calculations can be made, consider Figure II-1(a).

Let the window be located 6 feet behind the tangent point ($L_W = 6$ ft) and, in order to have sufficient room in the cone for mounting an optical system, let us assume the diameter at the camera location is approximately 3 feet. Let the nose radius be 1.0 foot. Since

$$\text{Base diameter} = 2(R \cos \theta_c + L_W \sin \theta_c)$$

we have the following set of parameters specifying the geometry which yields approximately a 3-foot base diameter

$$L_W = 6.0 \text{ ft}$$

$$R = 1.0 \text{ ft}$$

$$\theta_c = 5.0^\circ$$

The Mach number range through which a vehicle of this type could operate will probably be determined by the temperature limitation of the material used for the vehicle nose. Since for photographic purposes it will probably not be possible to use an ablative nose, the flight corridor will have to be chosen so that the maximum temperature, which occurs at the stagnation point of the nose, does not exceed that which is allowable for the material before melting occurs.

If the nose of the vehicle is not cooled by artificial means, it will come to radiation equilibrium temperature. The maximum value of this temperature will occur at the stagnation point and may be found by equating the radiation cooling

rate to the convective heating rate. The radiation cooling rate is the rate at which heat is radiated away from the vehicle, and the convective heating rate is the rate at which the vehicle is heated by convection from the surrounding air. These two rates are as follows from References 2 and 3:

$$q_{\text{rad}} = \epsilon \sigma T_s^4 \quad (\text{II-1})$$

$$q_{\text{conv}} = \frac{17,600}{\sqrt{R}} \left(\frac{p_\infty}{p_0} \right)^{1/2} \frac{v_\infty^3}{(gr)^{3/2}} \quad (\text{II-2})$$

From Reference 4 we have the following relation between velocity and Mach number:

$$v_\infty = M_\infty a_\infty \approx 49 M_\infty \sqrt{T_\infty} \quad (\text{II-3})$$

Equations (II-1) and (II-2) can now be equated and the following expression obtained relating the radiation equilibrium temperature at the stagnation point to the free-stream conditions

$$(T_s)^4 = \frac{17,600 (49)^3 M_\infty^3}{\epsilon \sigma \sqrt{R} (gr)^{3/2}} \left(\frac{p_\infty}{p_0} \right)^{1/2} (T_\infty)^{3/2} \quad (\text{II-4})$$

Thus, for a given set of flight conditions, we are able to calculate the radiation equilibrium temperature at the stagnation point of the hemispherically blunted cone.

Since we are interested in defining a corridor through which a vehicle of this type can operate without the stagnation point temperature becoming too high, let us take the

configuration of Figure II-1(a) and calculate, for specific values of T_s , the combinations of Mach number and altitudes at which these temperatures occur. Current materials will withstand temperatures of approximately 2000° F (2460° R) so calculations are made for this temperature. To bracket this value, temperatures of 1500° F and 3000° F are also used. Equation (II-4) is used for the calculations by assuming an altitude, using Reference 5 to obtain the density ratio and temperature for this altitude, and, thus, computing the Mach number. The results of these calculations are shown in Figure II-2 for the dimensions of the hemispherically blunted cone specified earlier.

Superimposed on these constant temperature lines are three trajectories which a vehicle with a nose of this type might follow. As can be seen from Figure II-2, for a good portion of the flights, the temperature greatly exceeds the 2000° F limit of current materials. This is particularly true for the heavier vehicles ($W/C_D A = 32.2$ lbs/sq ft) since temperatures in these cases exceed 3000° F. For the lighter vehicle ($W/C_D A = 3.22$ lbs/sq ft), the temperatures are somewhat lower. Consequently, if the temperature at the stagnation point of the vehicle is to be the critical one, it will be necessary to use a very light vehicle unless an ablative or heat-sink nose can be used or large amounts of artificial cooling can be applied.

In Figure II-2, the temperature curves can be thought of as the lower limits of the corridors of continuous flight, the actual curve depending on the structural temperature limit the airframe can withstand. The trajectory curves can be thought of as the upper limits of the corridors of continuous flight for the particular vehicle parameters indicated. It is seen that for a nonlifting vehicle with $W/C_D A = 3.22$ and for a structural temperature limit of 2000° F, the corridor closes at a Mach number of about 10. To raise the trajectory curve so that the corridor goes to higher Mach numbers, we can further reduce $W/C_D A$, increase the nose radius R , increase the structural temperature limit, or provide lift to the vehicle carrying the camera. Approaches such as these to extend the range in the Mach number, altitude diagram that would be useful for mapping and reconnaissance will be considered in Part IX when all the factors have been studied and calculated.

In order to perform the calculations in the succeeding sections of this report for this configuration, a range of Mach numbers and altitudes at which a vehicle of this type might operate must be chosen. From Figure II-2, the following range was selected:

<u>Altitude, h_∞, ft</u>	<u>Mach number, M_∞</u>
100,000	5 to 9
150,000	5 to 11
200,000	7 to 16
250,000	10 to 26
300,000	16 to 32
350,000	22 to 32
400,000	28 to 32

Thick Triangular Wing With Cylindrical
Leading Edge

Let us now examine the second generic type of hypersonic configuration, the thick triangular wing with a cylindrical leading edge and a hemispherically blunted nose. The general shape shown in Figure II-1(b) will be assumed for this configuration. The leading edge has a radius, R , which is everywhere normal to the leading edge. The wing is 2 radii thick and is swept back at an angle, Λ . It flies at an angle of attack, α , and has the camera window located in the plane of symmetry at a distance, L_W , behind the tangent point on the lower surface of the wing. Let us specify the following values of the above-mentioned quantities:

$$\begin{aligned}
 \Lambda &= 70^\circ \\
 \alpha &= 20^\circ \\
 R &= 1.0 \text{ ft} \\
 L_W &= 6.0 \text{ ft} \\
 C &= 10.0 \text{ ft}
 \end{aligned}$$

The Mach number, altitude range through which a vehicle of this type could operate will again probably be determined by the temperature which the structure can withstand. The hottest point will be the stagnation point of the nose of this wing. Here, the radiation equilibrium temperature will be the same as for the blunt cone of the preceding section since R is the same. Another temperature of interest on the wing is the radiation equilibrium temperature along the stagnation line of the leading edge. This temperature can be determined by equating the radiation cooling rate and the convective heating rate given in Reference 2. These equations are

$$q_{\text{rad}} = \epsilon \sigma T_{le}^4 \quad (\text{II-5})$$

and

$$q_{\text{conv}} = \frac{13,200}{\sqrt{R}} \left(\frac{p_{\infty}}{p_0} \right)^{\frac{1}{2}} \frac{v_{\infty}^3}{(gr)^{3/2}} P(\alpha, \Lambda) \quad (\text{II-6})$$

where

$$P(\alpha, \Lambda) = \lambda^{\frac{1}{2}} (1 - 0.16 \cos^2 \alpha \sin^2 \Lambda) \left\{ \frac{\left[1 - \cos^2 \alpha \sin^2 \Lambda + \frac{2}{(\gamma-1)M_{\infty}^2} \right] \left(\lambda^2 + \frac{1}{\gamma M_{\infty}^2} \right)}{1 - 0.62 \cos^2 \alpha \sin^2 \Lambda} \right\}^{\frac{1}{4}} \quad (\text{II-7})$$

$$\lambda = \sin \alpha \sin \phi_s + \cos \alpha \cos \Lambda \cos \phi_s \quad (\text{II-8})$$

$$\tan \phi_s = \frac{\tan \alpha}{\cos \Lambda} \quad (\text{II-9})$$

The following expression is obtained from Equations (II-3), (II-5), and (II-6):

$$T_{le}^4 = \frac{13,200 (49)^3 M_{\infty}^3 P(\alpha, \Lambda)}{\epsilon \sigma \sqrt{R} (gr)^{3/2}} \left(\frac{p_{\infty}}{p_0} \right)^{1/2} \left(T_{\infty} \right)^{3/2} \quad (II-10)$$

This equation is evaluated in the same manner as Equation (II-4). This has been done for the same temperatures as were used in Figure II-2, that is, 1500° F, 2000° F, and 3000° F, and the results are plotted in Figure II-3. A comparison of these curves for the leading-edge temperature with those for the temperature at the stagnation point of the nose (Fig. II-2) indicates that, at a given altitude and speed, the leading edge is cooler than the stagnation point.

Superimposed on the temperature curves of Figure II-3 is an equilibrium glide trajectory. This type of a trajectory would be typical of this type of a vehicle and satisfies the condition that the weight of the vehicle be equal to the aerodynamic lift plus the centrifugal force.

$$W = L + \frac{W}{g} \frac{V_{\infty}^2}{r} \quad (II-11)$$

The lift coefficient is defined as

$$C_L = \frac{L}{(1/2) \rho_{\infty} V_{\infty}^2 A} \quad (II-12)$$

Equations (II-3) and (II-12) will allow Equation (II-11) to be rewritten in the following form:

$$M_{\infty}^2 = \frac{1}{(49)^2 T_{\infty} \left[\frac{\rho_{\infty}}{2(w/C_L A)} + \frac{1}{gr} \right]} \quad (II-13)$$

In order to solve this equation for the trajectory by assuming an altitude, obtaining ρ_{∞} and T_{∞} from Reference 5, and solving for M_{∞} , the parameter $w/C_L A$ must be specified. The lift coefficient, C_L , can be obtained again using Reference 2. Thus,

$$C_L = 2 \left[\sin^2 \alpha \cos \alpha - \frac{2R}{C} \sin \alpha \left(\frac{1}{3} \sin^2 \alpha + \frac{2}{3} \sin \alpha \cos \alpha \cos \Lambda + \frac{4}{3} \cos^2 \alpha \cos^2 \Lambda \right) \right] \quad (II-14)$$

For the configuration and angle of attack considered here, we find

$$C_L = 0.186$$

Let us assume a weight-to-area ratio (wing loading) of

$$\frac{w}{A} = 20 \text{ lbs/sq ft}$$

Now if we assume various altitudes and solve Equation (II-13) for the corresponding Mach numbers, we obtain the trajectory shown in Figure II-3.

A comparison of this trajectory with the temperature curves of Figures II-2 and II-3 led to the selection of the following Mach number, altitude range to be used for the

winged vehicle in the following parts of the report:

<u>Altitude, h_{∞}, ft</u>	<u>Mach number, M_{∞}</u>
100,000	5 to 12
150,000	6 to 16
200,000	10 to 22
250,000	14 to 32
300,000	24 to 32
350,000	24 to 32
400,000	24 to 32

CONCLUSIONS

The following two configurations were chosen as representative of future hypersonic vehicles:

1. Circular cone with a hemispherically blunted nose
2. Thick triangular wing with a cylindrical leading edge and hemispherically blunted nose

The following dimensions were chosen for the calculations of the following parts of the report:

1. Circular cone

$$\theta_c = 5^\circ$$

$$R = 1.0 \text{ ft}$$

$$L_w = 6.0 \text{ ft}$$

2. Thick wing

$$R = 1.0 \text{ ft}$$

$$L_w = 6.0 \text{ ft}$$

$$\Lambda = 70^\circ$$

$$\alpha = 20^\circ$$

The following flight conditions were chosen as typical:

1. Circular cone

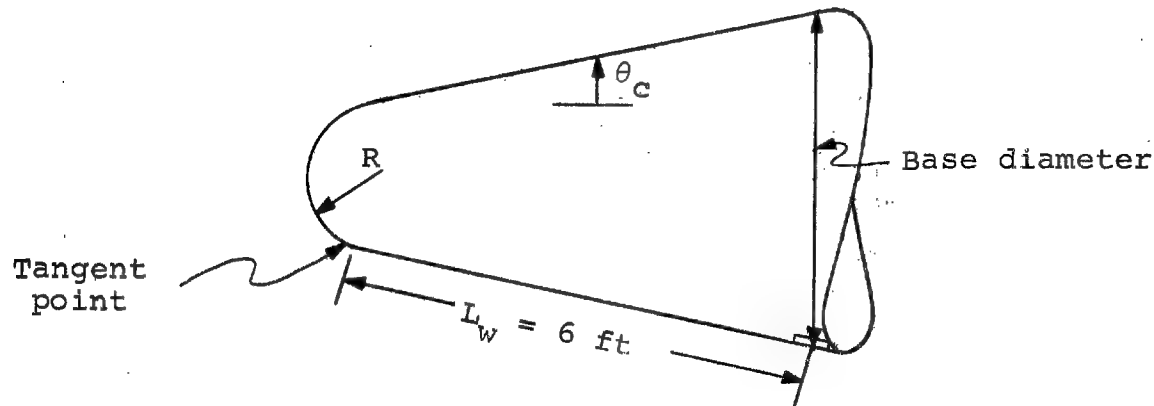
<u>h_{∞}, ft</u>	<u>M_{∞}</u>
100,000	5 to 9
150,000	5 to 11
200,000	7 to 16
250,000	10 to 26
300,000	16 to 32
350,000	22 to 32
400,000	28 to 32

2. Thick wing

<u>h_{∞}, ft</u>	<u>M_{∞}</u>
100,000	5 to 12
150,000	6 to 16
200,000	10 to 22
250,000	14 to 32
300,000	24 to 32
350,000	24 to 32
400,000	24 to 32

REFERENCES

1. Nielsen, Jack N., Goodwin, Frederick K., Sacks, Alvin H., Rubesin, Morris W., Ragent, Boris, and Noble, Charles E.: Effects of Supersonic and Hypersonic Aircraft Speed Upon Aerial Photography. Final Technical Report, Phase I, VIDYA Report No. 17, March 1960.
2. Rubesin, Morris W.: The Influence of Aerodynamic Heating on the Structural Design of Aircraft. AGARD Report 207, 1958.
3. Chapman, Dean R.: An Approximate Analytical Method for Studying Entry into Planetary Atmospheres. NASA TR R-11, 1959.
4. Ames Research Staff: Equations, Tables, and Charts for Compressible Flow. NACA Rep. 1135, 1953.
5. Minzner, R. A., Champion, K. S. W., and Pond, H. L.: The ARDC Model Atmosphere, 1959. Air Force Surveys in Geophysics No. 115, A. F. Cambridge Res. Center, TR-59-267, Aug. 1959.

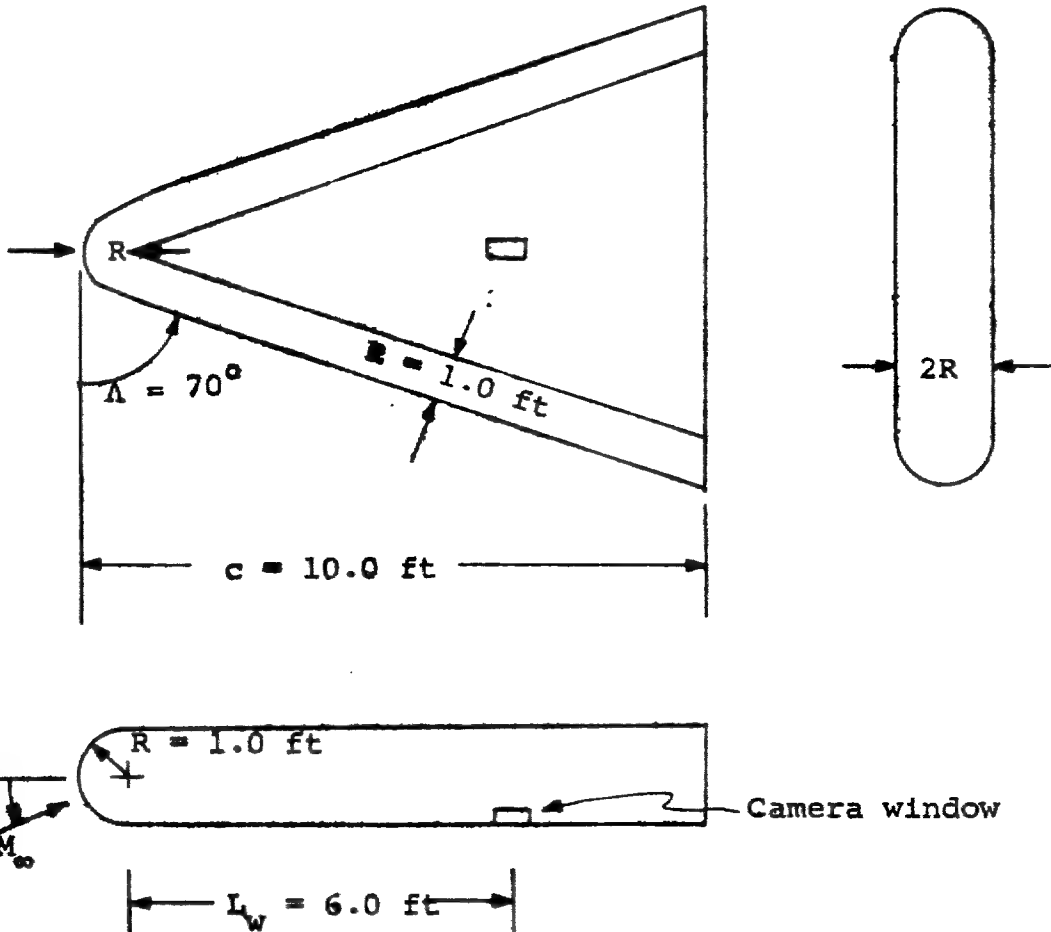


$$R = 1.0 \text{ ft}, \theta_c = 5^\circ$$

$$\begin{aligned} \text{Base diameter} &= 2(R \cos \theta_c + L_w \sin \theta_c) \\ &= 2(\cos 5^\circ + 6.0 \sin 5^\circ) \\ &= 3.04 \text{ ft} \end{aligned}$$

(a) Hemispherically blunted circular cone.

Figure III-1.- Geometry of hypersonic configurations to be studied



(b) Thick triangular wing with cylindrical leading edge.

Figure II-1-- (Concluded).

Approved For Release 2000/04/12 : CIA-RDP67B00657R000300070001-0

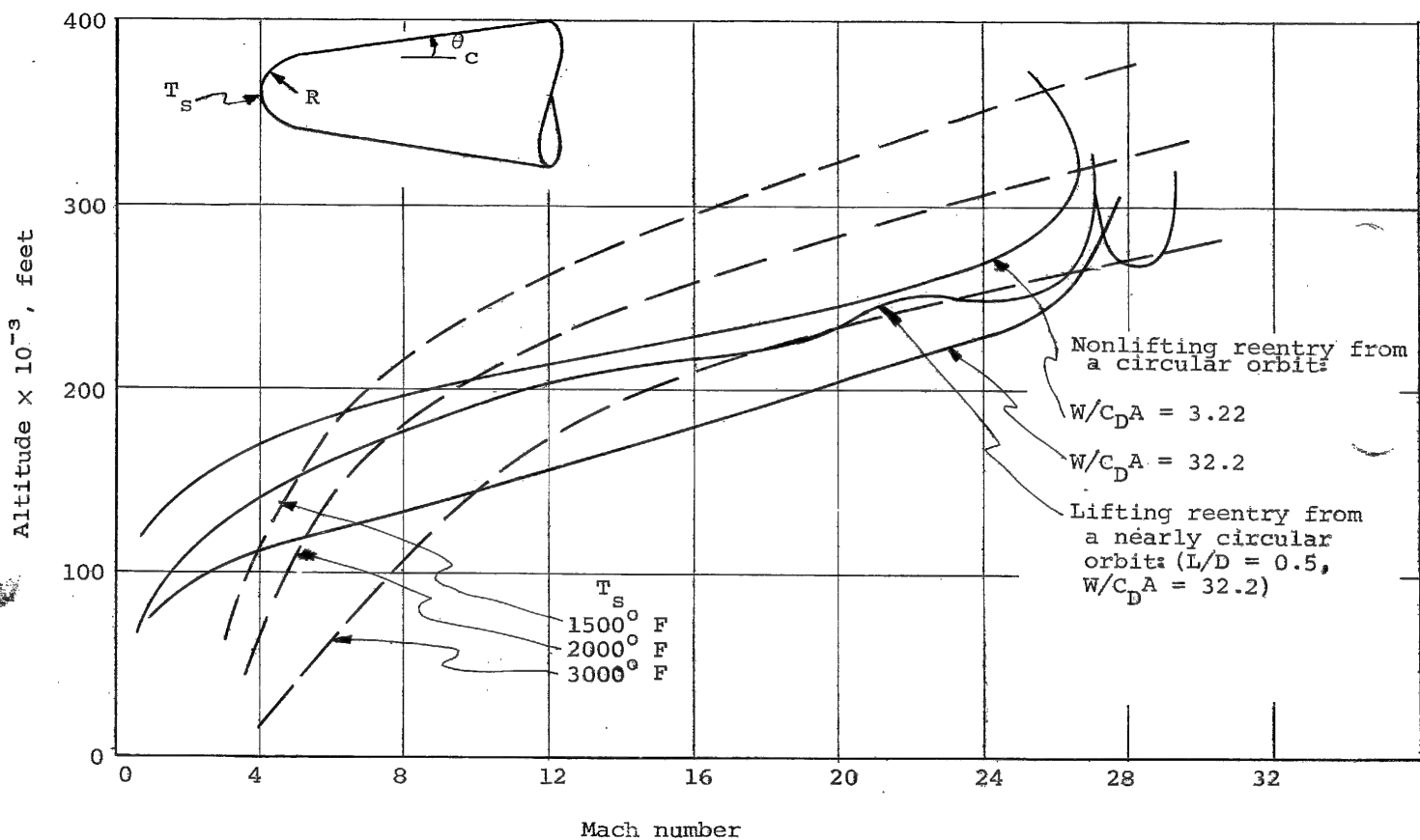


Figure II-2.- Radiation equilibrium temperature at the stagnation point of a hemispherically blunted cone ($R = 1.0$ ft, $\theta_c = 5^\circ$),

Approved For Release 2000/04/12 : CIA-RDP67B00657R000300070001-0

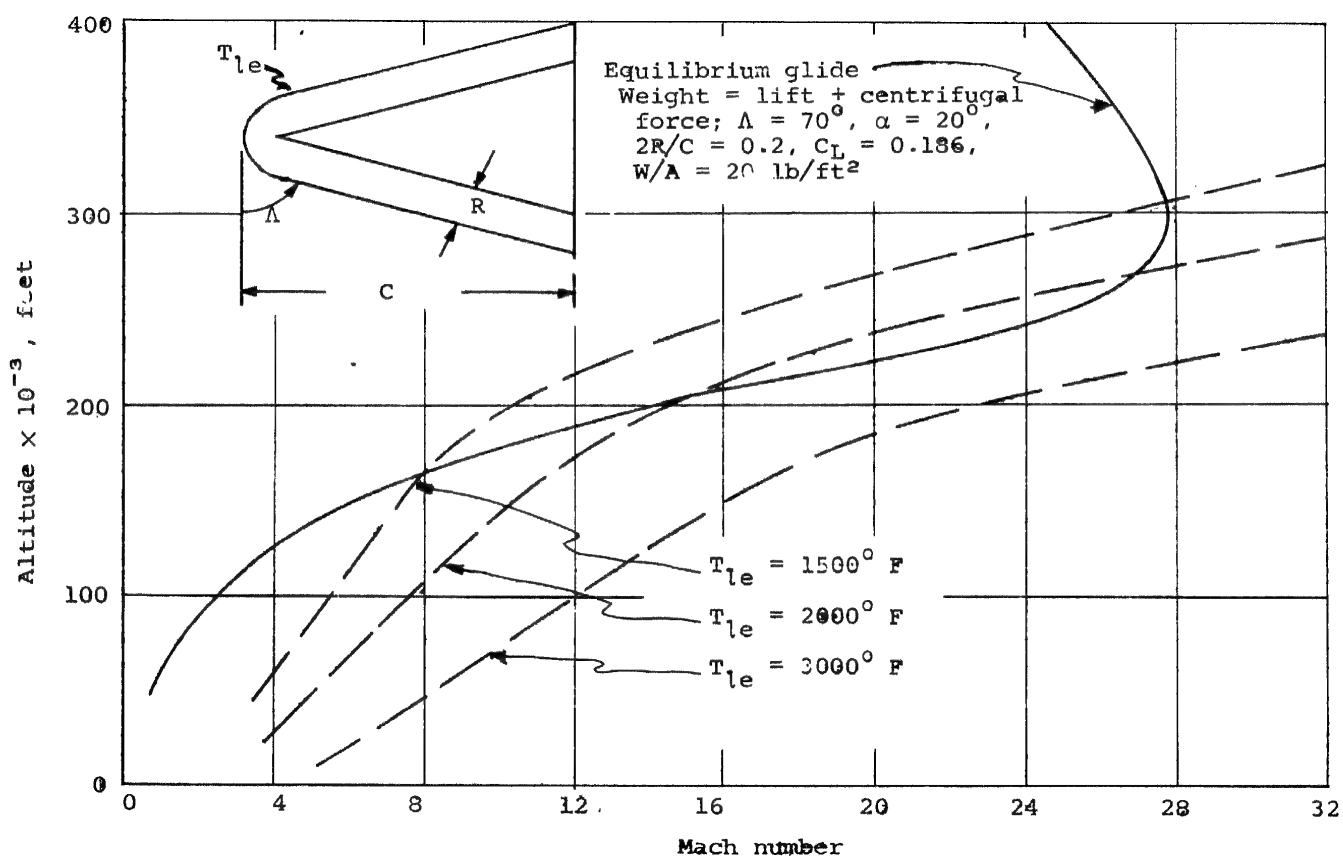


Figure III-3.- Radiation equilibrium temperature at the stagnation line of the leading edge ($R = 1.0$ ft, $\Lambda = 70^{\circ}$, $\alpha = 20^{\circ}$).

PART III: DETERMINATION OF FLOW FIELD
OUTSIDE THE BOUNDARY LAYER

INTRODUCTION

The photographic problems of optical resolution, loss of contrast, refraction, and metric distortion which are likely to be encountered in aerial reconnaissance from hypersonic vehicles are dependent upon the variations in density, temperature, and turbulence level of the intervening air between the camera objective and the ground object being photographed. Therefore, before any calculations can be made of the optical quality of the photograph to be obtained at given flight conditions, one must first calculate the characteristics of the aerodynamic flow field surrounding the photographing vehicle. This part of the report and the succeeding part are concerned with this task.

At extremely high altitudes, where the vehicle would be at nearly orbital velocity, the aerodynamic effects are negligible because of the virtual absence of air. As the vehicle descends into the atmosphere, however, it gradually becomes subjected to the increasing effects of the air impinging upon it, first as individual particles (the so-called free-molecule flow) and finally as a continuous fluid (the so-called continuum flow). In the latter flow regime, a well-defined shock wave has been established around the vehicle,

and the aerodynamic flow field is confined within that shock wave. At intermediate altitudes between the free-molecule regime and the continuum-flow regime, where the mean free path of the air is comparable to the shock standoff distance, the very mechanism involved in the formation of a shock wave is not at all clear, and the methods of analysis for determining the flow field are nonexistent at the present time. It was shown in Reference 1 that the cutoff altitude for using continuum analysis is of the order of 300,000 feet. Therefore, the aerodynamic flow field analysis of the present study will be confined to altitudes of 250,000 feet and below.

Since we shall be concerned here with the continuum-flow or aerodynamic regime, we shall divide the flow field into two general regions; that between the shock wave and the outer edge of the boundary layer (the inviscid region), and that inside the boundary layer¹. This part of the report will deal with the former region, which must be calculated first, and the details of the boundary layer itself will be the subject of Part IV. It should be pointed out that such a division of regions within the shock layer again implies some restriction of altitude, since at the more extreme altitudes the velocity

¹The existence of a distinct boundary layer actually becomes questionable at extreme altitudes even in the continuum-flow regime and one should treat the entire region within the shock layer as a single region of viscous flow if exact results are required.

at the body surface will not be zero relative to it (i.e., there will be "slip flow"). However, it must be borne in mind that as the aerodynamic flow field becomes ill-defined at the more extreme altitudes, the aerodynamics also becomes less important as a factor in determining the overall performance of the optical system for aerial reconnaissance and mapping.

SYMBOLS

a speed of sound, ft/sec

c_p specific heat at constant pressure, $\text{ft}^2/\text{sec}^2 \cdot {}^{\circ}\text{R}$

c_v specific heat at constant volume, $\text{ft}^2/\text{sec}^2 \cdot {}^{\circ}\text{R}$

c_D Newtonian drag coefficient of a circular cylinder normal to the stream ($c_D = 1.2$)

c_p pressure coefficient, $(p - p_\infty) / (\frac{1}{2} \rho_\infty V_\infty^2)$

c_γ constant (see Fig. III-3)

d thickness of blunt delta wing, ft ($d = 2R$)

e internal energy, ft^2/sec^2

h_∞ altitude of vehicle, ft

i enthalpy, ft^2/sec^2

L_w distance from shoulder to camera window, ft

M Mach number

p static pressure, lb/ft^2

r local radius of shock wave for blunt cone at zero angle of attack measured normal to axis of symmetry, ft

R nose radius, ft

R_w radius of blunt cone at camera window, ft

Re_{tr} transition Reynolds number, $\frac{\rho_0 V_0 S_{tr}}{\mu_0}$

$Re_{a,x}$ Reynolds number, $\frac{\rho_a V_a x}{\mu_a}$

$Re_{0,w}$ local Reynolds number at camera window, $\frac{\rho_0 V_0 S_w}{\mu_0}$

R' low temperature universal gas constant = 1,724 $\text{ft}^2/\text{sec}^2 \cdot {}^{\circ}\text{R}$

s distance measured along wing or body surface in plane symmetry from zero angle of attack stagnation point, ft

T temperature, $^{\circ}$ R

V velocity, ft/sec

$V_{\infty N}$ component of free stream velocity normal to shock wave, ft/sec

x axial distance from nose, ft

y distance outward from vehicle surface in direction normal to surface, ft

z compressibility factor

α local angle of attack of body or wing surfaces, radians

γ ratio of specific heat, c_p/c_v

δ boundary layer thickness, ft

δ^* boundary layer displacement thickness, ft

Δ_c shock-layer thickness at camera window on blunt cone, ft

Δ_o shock standoff distance at stagnation point, ft

Δ_w shock-layer thickness at camera window on blunt delta wing, ft

ϵ local slope of shock wave relative to free stream, radians

θ_c half angle of blunt cone (5° in present study)

Λ sweepback angle of blunt delta wing (70° in present study)

μ viscosity, lb-sec/ft²

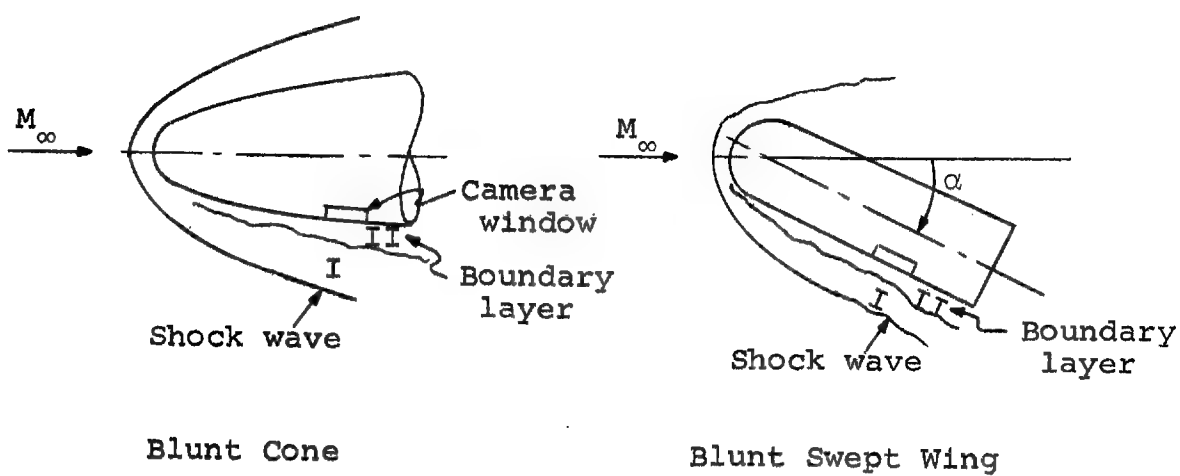
ρ mass density of gas, slugs/ft³

Subscripts

- α conditions on a wedge of half angle α at zero angle of attack in inviscid flow
- δ outer edge of boundary layer
- s stagnation
- sw immediately behind shock wave
- tr transition
- w camera window or body or wing surface
- ∞ free stream

INVESTIGATION

Since the aerial camera will be mounted in the lower surface of the mapping or reconnaissance vehicle, the aerodynamic flow field will be calculated only for the high-pressure side of a lifting vehicle. Thus, the aerodynamic flow fields to be considered for the two generic types of hypersonic configuration selected in Part II are illustrated in the following sketch:



In order to calculate optical errors caused by the aerodynamic flow fields surrounding the camera window of these vehicles, one must determine the local pressures, densities, and temperatures throughout regions I and II (i.e., throughout the shock layer). The pressure distribution over the body surface is required for the determination of the boundary-

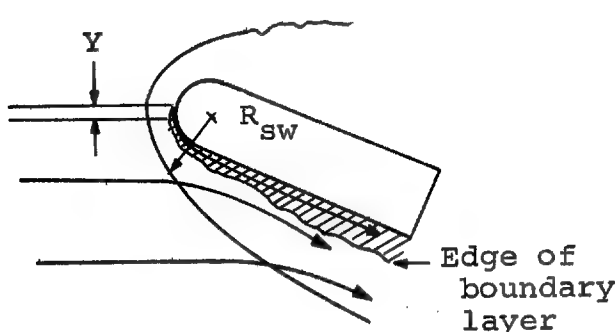
layer growth and of the heat transfer to the window. The local densities and temperatures enter directly into the calculation of refraction errors and the determination of luminosity boundaries in the Mach number, altitude diagram. The detailed characteristics of the boundary layer, and, in particular, whether it is laminar or turbulent over the camera window, will determine the severity of aerodynamically-induced losses of optical resolution.

The precise calculation of the inviscid flow field (region I) on the blunt cone involves a very laborious numerical calculation for each flight condition, even for the case of zero angle of attack. At the present time there is no method available for computing the inviscid flow field, precisely, on the blunt swept wing. Since, for the present investigation, precise calculations are probably unnecessary, we shall use approximate methods and calculate the flow fields about both configurations in the following steps:

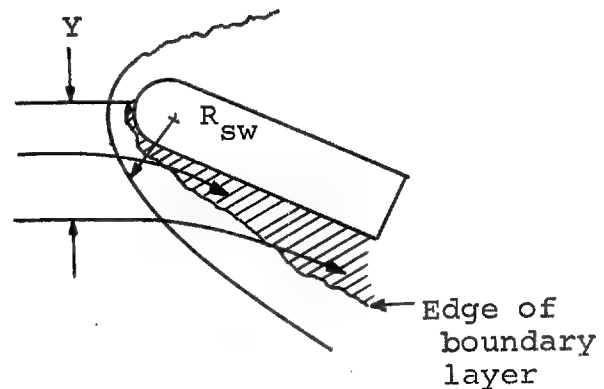
1. Determine the conditions at the edge of the boundary layer.
2. Determine the type of boundary layer, that is, laminar or turbulent, at the camera window.
3. Determine the shock layer thickness and the shock wave slope at the camera window location.
4. Determine the conditions behind the shock wave at the window location.

5. Determine the density and temperature distributions between the edge of the boundary layer and the shock wave at the window location.

The procedure to be described implies the assumption that all of the air contained in the boundary layer has passed through a normal shock wave. This in turn implies that the boundary layer is very thin so that the edge of the boundary layer is essentially a streamline. Consider, for example, the flow in the vertical plane of symmetry for two cases, as shown in the following sketch:



Case (a)



Case (b)

Let Y represent the cross section of free-stream air particles which end up in the boundary layer. In case (a), the boundary layer is very thin and all the air in Y has passed through a normal shock. In case (b), however, the boundary

layer is so thick (i.e., Y is so large) that much of the air in Y passes through an oblique shock. In this case, the previously mentioned assumption would not be valid. On the other hand, if the curvature of the shock were very small, then the normal shock wave would extend out to Y and again the assumption would be valid, despite the relatively thick boundary layer. It thus becomes clear that the requirement for the analysis of this part of the report to be valid is that the boundary-layer displacement thickness δ^* should be much smaller than the radius of curvature of the shock wave. The assumption made in the analysis can thus be written as

$$\frac{\delta^*}{R_{sw}} \ll 1$$

The validity of this assumption must await the numerical results of Part IV.

The methods for obtaining the previously mentioned quantities will now be described, first for the blunt cone and then for the blunt swept wing.

Flow Field Around a Blunt Cone

Conditions at the Edge of the Boundary Layer.-

In order to determine conditions at the edge of the boundary layer on the blunt cone, including real gas effects, by means of thermodynamic charts, two coordinates are required

to define the proper location on the chart. Specifically, if we know the enthalpy and pressure, the chart yields all the corresponding gas properties. For this purpose, we shall make use of the condition that the total enthalpy is conserved along the stagnation streamline through the normal shock wave. Thus²

$$i_s = c_p T_\infty + \frac{V_\infty^2}{2} = 6006 T_\infty + \frac{a_\infty^2 M_\infty^2}{2} \quad (\text{III-1})$$

The flow from the stagnation point rearward along the edge of the boundary layer is then assumed to be isentropic, so that all the gas properties along the edge of the boundary layer can be determined with thermodynamic charts by moving along an isentrope (which is determined by the stagnation enthalpy i_s and the stagnation pressure p_s) to the local pressure at the desired point. Thus, to determine conditions at the edge of the boundary layer at the location of the camera window, we must have the static pressures at the stagnation point and at the window.

In order to obtain a reliable determination of the two pressures mentioned, that at the stagnation point and that at the point of interest, the camera window, an investigation has been made to determine which of a number of available methods best predicts the pressure distribution over the blunt cone. The results of that investigation are presented in Appendix IIIA and it was found that Newtonian impact

²The free-stream conditions are obtained from Reference 2 for the specified flight altitude.

theory gave good agreement with experiment over a fairly wide range of Reynolds numbers and Mach numbers. Consequently, this method will be used for the blunt cone and the two pressures we desire are

$$p_s = C_{p_s} \left(\frac{1}{2} \rho_\infty V_\infty^2 \right) + p_\infty \quad (\text{III-2})$$

and

$$p_5 = C_{p_s} \left(\frac{1}{2} \rho_\infty V_\infty^2 \right) \sin^2 \theta_c + p_\infty \quad (\text{III-3})$$

where C_{p_s} is the pressure coefficient at the stagnation point. This quantity is determined in Appendix IIIA and is plotted in Figure III-1 as a function of flight Mach number.

These three quantities are then used in conjunction with a Mollier chart of the thermodynamic properties of air in chemical equilibrium (e.g. Ref. 3 or 4) to determine the remainder of the gas properties at the edge of the boundary layer at the camera window. The point determined by p_s and i_s is found on the chart. The air is then allowed to expand isentropically (constant entropy) to the point determined by p_5 . This point then specifies the other gas properties at the edge of the boundary layer at the camera window.

Determination of Boundary Layer Type.-

In Ref. 5, it was found possible to correlate a large mass of data pertaining to natural transition from laminar

to turbulent flows on aerodynamically smooth, sharp-nose cones at zero angle of attack. By this means, the longest probable run of a laminar boundary layer could be reasonably predicted for a configuration suitable for the Mach number range from 1 to 5. Furthermore, the stagnation enthalpies are sufficiently low in that regime so that only a moderate amount of cooling is required to maintain acceptable temperatures of the cone surface. Thus, the correlation was found to apply to cooled cones as well.

For the present study, we are concerned with a somewhat different problem. In particular, the flight regime above Mach 5 entails very high stagnation enthalpies and, consequently, very high recovery temperatures at the vehicle surface. This means, first of all, that the vehicle must have a rather blunt nose, as discussed in Part II. (This of course introduces a pressure gradient along the body surface.) Second, if the skin temperatures are to be maintained at permissible levels, then a large amount of cooling must be applied. Even though this cooling may take place naturally through radiation, it nevertheless leads to a very low ratio of wall temperature to temperature at the edge of the boundary layer. Thus, we have the "highly cooled" case, and the data correlation of Ref. 5 is not applicable, even for sharp cones.

The effects of bluntness and extreme cooling on boundary-layer transition have both been investigated by numerous

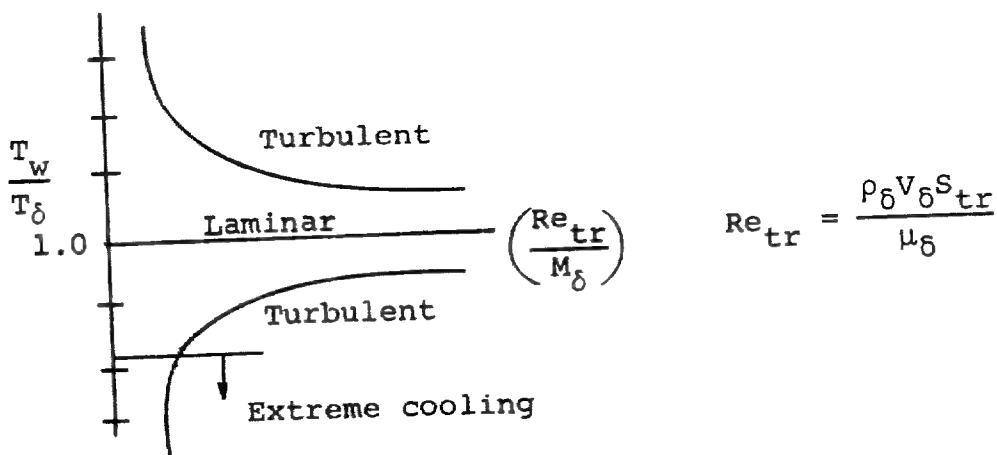
authors over the past several years, largely because of the interest in practical hypersonic vehicles. (See e.g. Refs. 6-10.) However, data in the highly cooled regime are rather difficult to obtain in the wind tunnel, because the low stagnation enthalpies obtaining therein require that rather sophisticated techniques be employed for cooling the model in order to reach low ratios of surface to stagnation temperature. On the other hand, the shock tube, in which higher stagnation enthalpies can be readily obtained, is limited in Mach number range. Consequently, only scattered data have been obtained on the combined effects of bluntness and extreme cooling, and no real attempt has been made to correlate the limited available data.

As a result of the above-mentioned research, however, one basic finding stands out. It has been clearly demonstrated (e.g. Ref. 7) that boundary-layer transition is generally delayed by moderate amounts of cooling (as predicted by stability theory), but that if further cooling is applied transition moves forward again. This phenomenon is generally referred to as "transition reversal" and is not well understood. A similar reversal appears to be present in the effect of bluntness on transition. That is, a small amount of blunting delays transition, but further blunting finally reverses the trend and moves transition forward. There is a certain qualitative consistency in the limited data available, and it

seems to lend some credence to the explanation proposed by van Driest (Ref. 11) for the cause of the transition reversal. van Driest's hypothesis is that as the stabilized boundary layer is cooled further, it becomes thinner ahead of and behind a given small roughness element until the roughness element is sufficiently large compared with the boundary-layer thickness to precipitate transition. This is particularly well illustrated by the data of Reference 7 which are reproduced in Figure III-2 for a spherically blunted cone. The transition reversal is clearly indicated by the upper two curves, which show opposite trends for the effect of cooling on transition, depending upon the level of cooling applied. For larger amounts of cooling the lower three curves are of particular interest in regard to van Driest's argument, which appears to be substantiated by the following two observations. First, for small roughnesses, the wall temperature ratio must be reduced to a low level independent of Reynolds number, to induce transition. Second, as the roughness size is increased, the wall temperature ratio for transition increases. That is, the smoother the surface finish, the more the boundary-layer thickness must be reduced to cause transition.

For the flight regimes and configurations of the present study (see Part II), the wall temperatures are even lower than those of Reference 7 compared with the temperatures at the

edge of the boundary layer. Fortunately, however, they fall into a range which has been covered experimentally in a shock tube (Ref. 12) for a blunt cylinder. In this region of extreme cooling, it appears that the transition Reynolds number is relatively insensitive to the exact amount of cooling. In other words, it would appear that in the final analysis, the effect of cooling on transition can be represented as shown in the following sketch.



The upper branch of the curve ($\frac{T_w}{T_{\delta}} > 1$) has been well defined by the data correlation of Ref. 5, and it appears that all cases considered in the present study fall in the region of extreme cooling indicated in the sketch. The data of Ref. 12 (which extends the data of Ref. 7 to larger amounts of cooling) show a relatively constant transition Reynolds number Re_{tr} of 0.5×10^6 for this regime, and this figure will be

used here to determine whether the boundary layer over the camera window is laminar or turbulent. It should be pointed out that the transition data of both Refs. 7 and 12 are restricted to the Mach number range between about two and three, and that the transition Reynolds number would be expected to increase with flight Mach number, on the basis of the correlation of Ref. 5. However, data are not presently available for highly cooled blunt bodies at high Mach numbers, so the transition Reynolds number obtained in Reference 12

$$Re_{tr} = 0.5 \times 10^6$$

will be assumed for the entire Mach number range of the present study. This is believed to be a conservative assumption.

Thus, if the Reynolds number at the camera window based on conditions at the edge of the boundary layer and the distance along the surface of the cone to the window is less than 0.5×10^6 , the boundary layer over the camera window is considered to be laminar. If this Reynolds number is greater than 0.5×10^6 , the boundary layer over the window is considered turbulent.

Shock Layer Thickness and Shock Wave Slope.-

In reference 13, Feldman presented numerical calculations to determine the inviscid flow field (i.e., the flow in region I) surrounding a hemispherically blunted cylinder

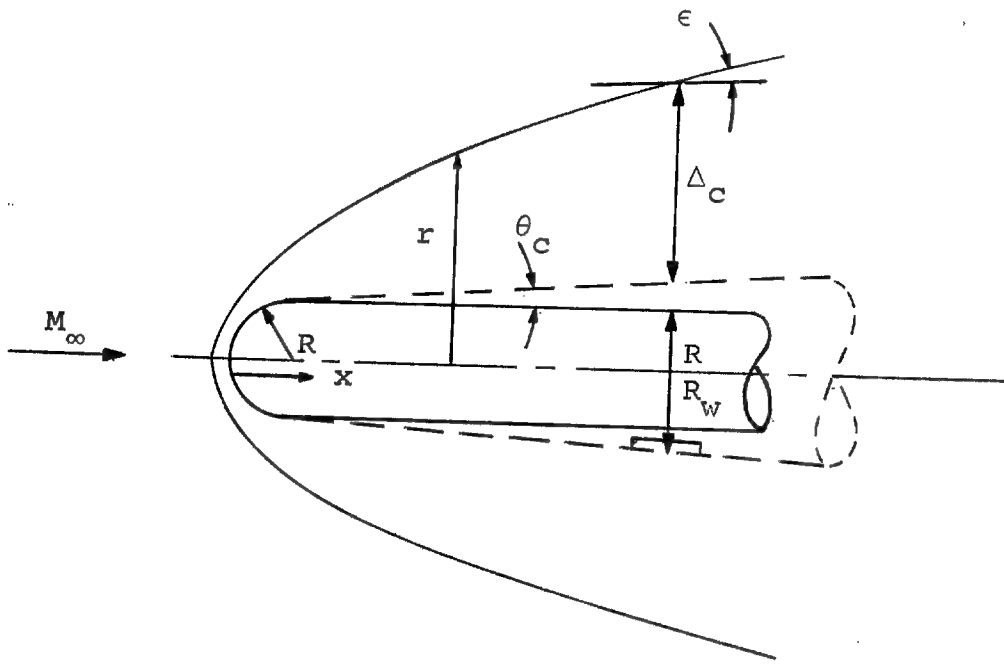
flying through a real gas at hypersonic speeds. As a result of those calculations, it was found that the density is low in the neighborhood of the body as compared with regions closer to the shock. Therefore, Feldman reasoned that the shock-wave shape should not be affected by a certain amount of change in the body shape, and he demonstrated by numerical calculations that such was in fact the case. Thus, for small cone angles, as in the present blunt cone configuration ($\theta_c = 5^\circ$), the shock-wave shape should be satisfactorily predicted by the second-order blast-wave theory formula of Lees and Kubota (Ref. 14) for blunt cylinders ($\theta_c = 0$). That is,³

$$\frac{r}{R} = 1.104 \left(\frac{x}{R} \right)^{\frac{1}{2}} \left(1 + 0.81 \frac{x/R}{M_\infty^2} \right) \quad (\text{III-4})$$

where R is the radius of the blunt cylinder, x is measured from the nose along the axis of symmetry, and r is the local radius of the shock wave measured normal to the x -axis. It should be pointed out that this equation will not predict the shock shape around the nose but only applies downstream.

³Feldman (Ref. 13) actually found very good agreement between this formula and his numerical calculations which include real-gas effects.

The shock-layer thickness at the camera window for the blunt cone configuration of the present investigation (see sketch)



is therefore given by

$$\Delta_c = r_w - R_w \quad (III-5)$$

where R_w is the radius of the cone at the location of the camera window and r_w is the corresponding value of r . The body radius R_w is given by

$$R_w = R \cos \theta_c + L_w \sin \theta_c \quad (III-6)$$

and the distance x_w from the nose to the camera window station is

$$x_w = L_w \cos \theta_c + R (1 - \sin \theta_c) \quad (III-7)$$

Using these definitions, the shock layer thickness at the camera window is

$$\Delta_c = 1.104 (x_w R)^{\frac{1}{2}} \left(1 + 0.81 \frac{x_w}{R M_\infty^2} \right) - R_w \quad (\text{III-8})$$

It can be seen in the preceding sketch that the shock wave slope is given by the rate of change of r with x . That is

$$\tan \epsilon = \frac{d(r/R)}{d(x/R)} \quad (\text{III-9})$$

The shock wave slope at the camera window location is therefore obtained by differentiating Equation (III-4) and evaluating this derivative at $x = x_w$. Thus,

$$\tan \epsilon = \frac{1.104}{2(x_w/R)^{\frac{1}{2}}} \left(1 + 0.81 \frac{x_w}{R M_\infty^2} \right) + \frac{1.104(0.81)}{M_\infty^2} \left(\frac{x_w}{R} \right)^{\frac{1}{2}} \quad (\text{III-10})$$

Conditions Just Inside the Shock Wave.-

The calculation of conditions immediately behind an oblique shock wave of known angle for a real gas in thermodynamic equilibrium is straightforward, although laborious, and involves a simultaneous (graphical) solution of the equations of continuity, momentum, energy, and state across the shock wave. Such calculations have been carried out in Reference 3 for altitudes up to 250,000 feet over a range of shock-wave angles using the atmosphere of Reference 15. Thus, having determined the inclination of the shock wave

relative to the free stream for each flight condition (in the preceding section), we shall use the method of Reference 3 and the atmosphere of Reference 2 to determine conditions just behind the shock wave for the present study.

The equations to be solved (taken from Ref. 3) are the following

$$\left(\frac{c_p}{R'} - 1 \right) \frac{T_\infty}{T_0} - \frac{e_{sw}}{R' T_{sw}} \left(\frac{T_{sw}}{T_0} \right) + \frac{1}{2} \left(\frac{p_\infty}{p_0} + \frac{p_{sw}}{p_0} \right) \left(\frac{\rho_0}{\rho_\infty} - \frac{\rho_0}{\rho_{sw}} \right) = 0 \quad (\text{III-11})$$

$$V_{\infty N}^2 - \left[R' T_0 \left(\frac{\rho_{sw}}{\rho_0} \right) \left(\frac{\rho_0}{\rho_\infty} \right) \left(\frac{p_{sw}}{p_0} - \frac{p_\infty}{p_0} \right) \right] / \left(\frac{\rho_{sw}}{\rho_0} - \frac{\rho_\infty}{\rho_0} \right) = 0 \quad (\text{III-12})$$

where

$$c_p = 6,006 \text{ ft}^2/\text{sec}^2 - ^0\text{R}$$

$$R' = 1,724 \text{ ft}^2/\text{sec}^2 - ^0\text{R}$$

$$T_0 = 491.69 \text{ } ^0\text{R}$$

$$\frac{e_{sw}}{R' T_{sw}} = \frac{i_{sw}}{R' T_{sw}} - z_{sw}$$

$$\rho_0 = 2.498 \times 10^{-3} \text{ slugs}/\text{ft}^3$$

$$p_0 = 2,117 \text{ lb}/\text{ft}^2$$

$$V_{\infty N} = a_\infty M_\infty \sin \epsilon$$

The method of solution of the two equations is to:

1. Assume a value of T_{sw} and find the set of values of p_{sw} , ρ_{sw} and e_{sw} (from Ref. 3, 4 or 16) for this temperature which satisfy Equation (III-11).

2. Use these values in Equation (III-12) and determine the value of the left-hand side.

3. Repeat steps 1 and 2 until a plot of the value of the left-hand side of Equation (III-12) against T_{sw} goes through zero. The value of T_{sw} at this zero point on the plot is the correct value of T_{sw} , the temperature behind the shock wave.

4. From step 1 and the repetitions of this step, a plot of p_{sw} and ρ_{sw} against T_{sw} can be constructed and the values of these two quantities for the correct value of T_{sw} from step 3 determined.

Temperature and Density Distributions Between the Edge of the Boundary Layer and the Shock Wave.-

As previously mentioned, the detailed calculation of the fluid properties in the inviscid region between the boundary layer and the shock wave of the blunt cone is a very laborious and time-consuming process involving the numerical method of characteristics. This means that each flight condition must be treated separately, and such an undertaking is clearly beyond the scope of the present contract. However, in order to make meaningful calculations of the optical effects of such flow fields on aerial photography obtained at hypersonic speeds, reliable estimates of the density and temperature distribution

through the inviscid region of the shock layer are required. Toward this end, we shall avail ourselves of the detailed calculations made by Feldman in Reference 13 for the density and temperature fields surrounding some blunt vehicles at hypersonic speeds.

The results of Reference 13, in which calculations were made at various axial positions along a hemispherically blunted cylinder, indicated that beyond two to three nose radii downstream, the density remains essentially constant with radial distance over the inner portions of the inviscid region, and that the maximum radial density gradient occurs just inside the shock wave. On this basis, we shall assume for the present study that the density distribution from the edge of the boundary layer to just inside the shock wave can be represented by a parabola, with zero slope at the edge of the boundary layer. Thus, we shall assume the density distribution to be

$$\rho = \rho_\delta + (\rho_{sw} - \rho_\delta) \left(\frac{r - R_w - \delta}{\Delta_c - \delta} \right)^2, \quad r \geq R_w \quad (\text{III-13})$$

where δ is the boundary layer thickness.

For the temperature distribution, a still simpler assumption appears to be warranted; namely a linear temperature distribution. Thus, the temperatures between the shock wave and the boundary layer are taken to be distributed as follows:

$$T = T_\delta + (T_{sw} - T_\delta) \left(\frac{r - R_w - \delta}{\Delta_c} \right), \quad r \geq R_w \quad (\text{III-14})$$

Thus, the density and temperature distributions through the inviscid region of the shock layer surrounding the blunt cone are represented by Equations (III-13) and (III-14), where the constants appearing in those expressions have been determined for each flight condition as explained in the foregoing sections.

Flow Field Around a Blunt Swept Wing

Conditions at the Edge of the Boundary Layer.-

For the blunt swept wing at 20° angle of attack, the induced pressures caused by the blast wave from the blunt leading edge are likely to be significant, and Newtonian impact theory is not satisfactory. For this configuration, the semi-empirical method developed by Creager (Refs. 17 and 18) and extended by Rubesin (Ref. 19) to flight conditions⁴ has been selected for the present calculations. For the case

⁴It should be pointed out that agreement with wind-tunnel data does not guarantee agreement with flight data under conditions of high stagnation enthalpies, as desired for the present study. However, such flight data are not available.

of a laminar boundary layer, the resulting expression for the pressures along the lower surface of the blunt swept wing at angle of attack α is

$$\left(\frac{p_0}{p_\alpha} \right)_{\text{lam}} = 1 + \left(0.166 + 0.86 \frac{i_w}{V_\alpha^2} \right) \frac{\gamma_\alpha}{\sqrt{\gamma_\alpha - 1}} \frac{V_\alpha^3}{(i_\alpha)^{3/2}} \frac{(T_\alpha/T_w)^{1/4}}{\sqrt{Re_{\alpha,x}}} + \frac{C_\gamma}{\gamma_s} \left(\frac{C_D}{2} \right)^{2/3} \frac{\cos^{4/3} \Lambda}{\tan^2 \alpha} \left(\frac{x}{d} \right)^{-2/3} \quad (\text{III-15})$$

where the subscript w refers to conditions at the wall or wing surface and the subscript α refers to conditions on a sharp wedge of half angle α at zero angle of attack in an inviscid flow. These latter quantities are approximated by

$$\left. \begin{aligned} p_\alpha &= C_{p_s} \left(\frac{1}{2} \rho_\infty V_\infty^2 \right) \sin^2 \alpha \\ V_\alpha &= V_\infty (\cos \alpha)^{1/3} \\ i_\alpha &= i_\infty + \frac{V_\infty^2}{2} \left[1 - (\cos \alpha)^{2/3} \right] \end{aligned} \right\} \quad (\text{III-16})$$

The second term on the right-hand side of Equation (III-15) represents the pressure rise induced by the boundary-layer growth, and the third term represents the pressure rise due to the blast wave off the leading edge. Several physical assumptions are implied in these equations. First, it is assumed that the pressure rise due to boundary-layer growth on the wing can be represented by the pressure corresponding to a boundary layer growing on a wedge with a sharp leading

edge that is at the same angle to the stream as the wing. Thus, the pressure field due to the blunt leading edge and the angle of sweep are not considered in the boundary-layer growth. Second, it is assumed that pressure rise due to the blunt leading edge is produced by a flow that remains in the chordwise direction. Since the flow remains in the chordwise direction in both of the above assumptions, Equation (III-15) may be considered as a representation of "strip theory."

It should be mentioned that Equation (III-15) was actually developed for predicting the pressures over the entire lower surface of a swept blunt wing and that recourse was had to simple sweep theory which would not be expected to be applicable in the plane of symmetry of the wing where the camera window is to be placed. However, Creager's results show reasonable agreement with wind-tunnel data even along the centerline of the wing.

The value of γ_s in the preceding equations is determined by the stagnation conditions, p_s and i_s , which are determined in the same manner as for the blunt cone (Eqs. (III-1) and (III-2)). The wall enthalpy, i_w , is determined with the aid of a Mollier chart (Ref. 3 or 4) using the specified wall temperature, T_w , and the inviscid wedge pressure, p_a .

The Reynolds number, $Re_{\alpha,x}$, in Equation (III-15) is defined as

$$Re_{\alpha,x} = \frac{\rho_{\alpha} V_{\alpha} x}{\mu_{\alpha}} \quad (III-17)$$

where

$$\mu_{\alpha} = 2.27 \times 10^{-8} \frac{T_{\alpha}^{3/2}}{T_{\alpha} + 199}$$

The subscript α conditions not calculated in Equation (III-16) are also found with the aid of a Mollier chart using p_{α} and i_{α} to locate the point on the chart.

The quantity C_D is the Newtonian drag coefficient of the leading edge for zero α and zero sweep ($C_D = 1.2$). The quantity C_{γ} is given in Figure III-3 as a function of γ_s .

With p_s , i_s and p_{α} determined, the procedure for determining the remaining conditions at the edge of the boundary layer is identical to that described for the blunt cone.

Determination of Boundary Layer Type.-

The general comments made regarding the effects of leading edge blunting and surface cooling on boundary layer transition on the blunt cone presumably apply to the blunt swept wing configuration although data are not currently available for the latter. Consequently, the Reynolds number

of transition to be used here in determining whether the boundary layer over the camera window on the wing is laminar or turbulent will again be

$$Re_{tr} = 0.5 \times 10^6$$

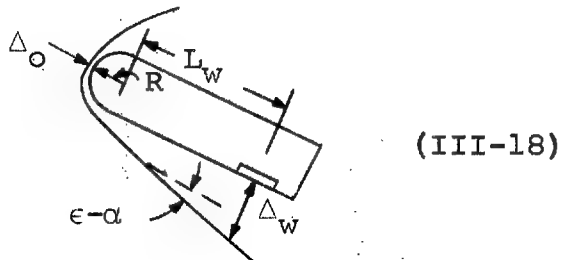
That is, if the Reynolds number at the camera window based on conditions at the edge of the boundary layer and the length of run along the surface of the wing to the window is less than 0.5×10^6 the boundary layer is assumed to be laminar. If it is greater than 0.5×10^6 , the boundary layer is considered turbulent.

Shock Layer Thickness and Shock Wave Shape.-

For the blunt swept wing at angle of attack, no analytical method actually exists at the present time for predicting the shock-wave shape around the wing. However, this problem has been considered in Reference 1 which deals with a configuration and flight conditions not too different from those of the present investigation. On the basis of experimental data obtained on both blunt and sharp delta wings of 78° sweep at high angles of attack for a Mach number of 5.8, it was concluded in Reference 1 that the angle between the shock wave and the lower wing surface is given quite well by a tangent-cone analysis and that, above a Mach number of 10, this angle remains essentially constant at a value of about $2\frac{1}{2}^\circ$.

For the configuration treated here, this angle is given in Figure III-4 as a function of M_∞ . Furthermore, it was found that the shock standoff distance at the stagnation point is of the order of 6 percent of the nose radius, accounting for real-gas effects at hypersonic Mach numbers. Therefore, for the present analysis, the shock wave over the lower wing surface is taken to be (see sketch)

$$\begin{aligned}\Delta_w &\approx \Delta_o + L_w(\epsilon - \alpha) \\ &\approx 0.06R + L_w(\epsilon - \alpha)\end{aligned}$$



Conditions Just Inside the Shock Wave.-

To determine the gas properties just inside the shock wave at the camera window location, the same equations (Eqs. (III-11) and (III-12)) are solved as were solved in the case of the blunt cone. The method of solution is the same as that presented there.

Temperature and Density Distributions Between the Edge of the Boundary Layer and the Shock Wave.-

The same type of density distribution (parabolic) and temperature distribution (linear) between the shock wave and boundary layer will be assumed for the blunt swept wing as for the cone. The equations are

$$\rho = \rho_\delta + (\rho_{sw} - \rho_\delta) \left(\frac{y - \alpha}{\Delta_w} \right)^2 \quad (III-19)$$

and

$$T = T_\delta + (T_{sw} - T_\delta) \left(\frac{y-\delta}{\Delta_w} \right) \quad (III-20)$$

where Δ_w is given by Equation (III-18) and y is the distance outward normal to the camera window. Thus, at $y = \delta$, $T = T_\delta$ and $\rho = \rho_\delta$, and at $y = \Delta_w$, $T = T_{sw}$ and $\rho = \rho_{sw}$.

RESULTS AND DISCUSSION

Calculations have been carried out in accordance with the foregoing analysis to determine the flow fields surrounding the camera window on both the blunt cone and the blunt swept wing at altitudes of 100,000; 150,000; 200,000; and 250,000 feet. The results for the blunt cone are presented in Figures III-5 to III-9, in the order in which the analysis has been presented above. Thus, the δ conditions are presented in Figure III-5, the Reynolds number for determining transition in Figure III-6, the shock wave location and slope in Figures III-7 and III-8, and conditions just behind the shock wave in Figure III-9.

Perhaps the first significant result to be noted is shown in Figure III-6 by the calculated Reynolds number $Re_{\delta,w}$ at the camera window. Evidently, the Reynolds number remains well below that for boundary-layer transition (0.5×10^6) except at the lowest altitude of 100,000 feet. But even at

100,000 feet the Reynolds number does not exceed 10^6 and drops off rapidly as the flight Mach number is increased. Therefore, it appears that the assumption of laminar flow over the camera window of the blunt cone is not unreasonable for the entire flight spectrum of the present study.

It can be seen from Figures III-5(b) and III-9(b) that the densities just inside the shock wave are of the order of ten times those at the edge of the boundary layer. Similarly, as shown in Figures III-5(c) and III-9(c), the pressures just inside the shock wave are several times those at the edge of the boundary layer. The temperatures (Figs. III-5(a) and III-9(a)) are correspondingly lower behind the shock, and the increase in T_0 with flight Mach number is evidently quite nonlinear. Similar nonlinear rises in temperature, possibly related to the completion of oxygen dissociation prior to the onset of nitrogen dissociation, have been observed in Reference 3. As expected, the local densities, pressures, and temperatures all increase with increasing flight Mach number.

The decrease of both shock layer thickness and shock wave slope with flight Mach number are shown in Figures III-7 and III-8, and Figure III-5(e) indicates that the Mach number M_0 at the edge of the boundary layer remains almost constant at a value of about 3, independent of both flight Mach number and altitude.

The calculated results for the blunt swept wing at 20° angle of attack are presented in Figures III-10 through III-13 and it can be seen that, in general, the remarks just made for the blunt cone calculations also apply to the blunt swept wing. The densities just behind the shock wave at the camera location are again of the order of ten times those at the edge of the boundary layer (Fig. III-10(b) compared with Fig. III-13(b)); the pressure does not change much between the shock wave and the boundary layer (Fig. III-10(c) and Fig. III-13(c)); and the temperature at the edge of the boundary layer is higher than that behind the shock wave by about a factor of two (Fig. III-10(a) and Fig. III-13(a)).

The shock layer thickness (Fig. III-12) and the shock wave slope (Fig. III-4 which is taken from Ref. 1) both decrease with increasing flight Mach number. The Mach number at the edge of the boundary layer (Fig. III-10(e)) remains essentially constant at a value of 2.0 for all flight altitudes and Mach numbers.

Figure III-11 shows the calculated value of the Reynolds number at the edge of the boundary layer at the window location. As can be seen, the value remains below the value required for boundary layer transition (0.5×10^6) except at an altitude of 100,000 feet where $Re_{\delta, w}$ remains almost constant at a value of 1.5×10^6 . Thus, on the basis of this Reynolds number of transition, the boundary layer over the window is

turbulent at a flight altitude of 100,000 feet for all of the flight Mach numbers considered.

One other fact is of interest and should be pointed out. The expression for the pressure at the edge of the boundary layer on the blunt swept wing (Eq. (III-15)) is a function of the wall temperature of the vehicle, T_w . Calculations were made for a range of T_w from 0° F to 2000° F and it was found that this temperature only affected the conditions at the edge of the boundary layer by a very small percentage. In fact, the scales to which the results are plotted in Figure III-10 will not permit the difference to be seen.

CONCLUSIONS

In this part of the report, methods have been presented which allow approximate calculations to be made of the flow fields between the edge of the boundary layer and the shock wave on a blunt cone at small angles of attack and a blunt swept wing at angle of attack. These methods will yield sufficient information to calculate the quantities to be considered in the following parts of the report.

The type of boundary layer over the camera window, that is, laminar or turbulent, is determined on the basis of a transition Reynolds number of 0.5×10^6 based on conditions at the edge of the boundary layer and the length of run measured along the surface of the vehicle. Using this criterion it was found that for all of the altitudes and Mach numbers

considered, the boundary layer at the window was laminar except at 100,000 feet. Here it was turbulent on the wing and cone at nearly all of the Mach numbers considered.

The state of aerodynamic art with respect to the calculation of hypersonic flow fields is still in its infancy. As progress is made, it will be possible to improve the accuracy of the foregoing calculation techniques.

APPENDIX IIIA

COMPARISON OF SEVERAL METHODS FOR CALCULATING
SURFACE PRESSURE DISTRIBUTIONS ON BLUNT CONES

For calculating the surface pressure distribution on blunt cones, several methods are available, so we must make a comparison of those methods with experimental data in order to select the one most appropriate to the chosen configuration and flight conditions. In all of the methods to be considered, Newtonian impact theory is used to predict the surface pressures ahead of the sonic point (i.e., in the subsonic region). Downstream of the sonic point, (in the supersonic region) the following methods might be considered (see Refs. 20 and 21):

1. Newtonian impact theory
2. Newtonian impact theory including centrifugal forces
3. Tangent-cone theory
4. Hypersonic small-disturbance theory
5. Prandtl-Meyer expansion

Two of the above methods can be eliminated at once for the case of the hemispherically blunted cone. Method 2 (Newtonian theory with centrifugal force) is not applicable because of the discontinuity of the curvature, and hence of the pressures, at the shoulder. Method 4 (hypersonic small-disturbance theory) is not applicable because the body shape

is not of the required form

$$\frac{R}{L} = k \left(\frac{x}{L} \right)^m \quad \text{where } \frac{1}{2} \leq m \leq 1$$

Therefore, only methods 1, 3, and 5 are applicable to the configuration of interest here. However, as a matter of general interest, a comparison of all five methods has been made for a special body to which all the methods are applicable. This comparison is shown in Figure III-14 for a free stream Mach number of 7.7. It can be seen that all of the methods give reasonable results with the exception of the Prandtl-Meyer expansion⁵ which predicts excessively high pressure coefficients. On the basis of these results, the Prandtl-Meyer expansion method (method 5) will also be eliminated from the present analysis. Thus, we are left with only two methods to choose from: Newtonian impact theory and the tangent-cone theory.

According to Newtonian impact theory, each elemental mass of air loses its normal component of momentum upon striking the body surface from the direction of the free stream. This theory results in the following expression for the pressure coefficient:

$$c_p = \frac{p - p_\infty}{(1/2) \rho_\infty V_\infty^2} = c_{p_s} \sin^2 \alpha \quad (\text{IIIA-1})$$

⁵The Prandtl-Meyer pressures were actually matched at a point which assured no discontinuity of pressure gradient. However, this point is very close to the sonic point.

where α is the local angle of attack of the body surface and C_{p_s} is the stagnation pressure coefficient. Since the shock wave in the vicinity of the stagnation point is a normal shock wave ($\alpha = 90^\circ$), C_{p_s} is obtained from the normal shock relations. In fact, it can be shown from these shock relations that the limiting value of C_{p_s} for very high Mach numbers is given by⁶

$$M_{\infty}^{\lim_{\infty}} (C_{p_s}) = \frac{[(\gamma+1)/2]^{\gamma/\gamma-1} [(\gamma+1)/2\gamma]^{1/\gamma-1}}{\gamma/2} \quad (\text{IIIA-2})$$

where γ is the ratio of specific heats. The variation of C_{p_s} with free-stream Mach number is shown in Figure III-1 for $\gamma = 1.4$ and it can be seen that C_{p_s} is nearly constant over the range of Mach numbers to be considered in the present investigation.

According to the tangent-cone theory, the surface pressures aft of the sonic point are the same as those on a semi-infinite circular cone at zero yaw having a half angle equal to the local angle of attack of the actual body surface. The local pressure coefficients in this method are found from the Taylor-Maccoll solution, graphs of which appear in Reference 22.

A direct comparison of the surface pressures on a hemispherically blunted cone of 5° half angle as calculated by

⁶This equation is valid only if γ is the same on either side of the shock wave. However, calculations including real-gas effects through the shock wave indicate that the effect of changes in γ across the shock are small.

Newtonian impact theory and by the tangent-cone theory has indicated little difference between the two methods. (This is also seen in Fig. III-14.) Furthermore, a comparison of Newtonian theory with available experiment for hemispherically blunted cones of 10° and 20° half angle is shown in Figure III-15 over a range of Reynolds numbers and Mach numbers, and the agreement is seen to be quite satisfactory. Therefore, Newtonian theory was selected for predicting the surface pressures on the blunt cone for this investigation.

REFERENCES

1. Breene, R.G., Bortner, M., Carlson, W.O., Long, M., Ness, N., and Ridyard, H.W.: Electromagnetic Effects Associated with Hypersonic Vehicles. Aerosciences Laboratory Missile and Space Vehicle Department, General Electric Company. Final Report, May 15, 1959.
2. Minzner, R.A., Champion, K.S.W., and Pond, H.L.: The ARDC Model Atmosphere, 1959. Air Force Surveys in Geophysics No. 115, A. F. Cambridge Res. Center, TR-59-267, Aug. 1959.
3. Feldman, Saul: Hypersonic Gas Dynamic Charts for Equilibrium Air. Avco Research Laboratory, Avco Mfg. Corp., Jan. 1957.
4. Moeckel, W.E. and Weston, K.C.: Composition and Thermo-dynamic Properties of Air in Chemical Equilibrium. NACA TN 4265, 1958.
5. Nielsen, J.N., Goodwin, F.K., et al: Effects of Supersonic and Hypersonic Aircraft Speed Upon Aerial Photography. Final Technical Report, Phase I. Vidya Report No. 17, April 1960.
6. Brinich, Paul F., and Sands, Norman: Effect of Bluntness on Transition for a Cone and a Hollow Cylinder at Mach 3.1. NACA TN 3979, 1957.
7. Jack, John R., Wisniewski, Richard J., and Diaconis, N.S.: Effects of Extreme Surface Cooling on Boundary-Layer Transition. NACA TN 4094, 1957.
8. Diaconis, N.S., Wisniewski, Richard J., and Jack, John R.: Heat Transfer and Boundary-Layer Transition on Two Blunt Bodies at Mach Number 3.12. NACA TN 4099, 1957.
9. Jack, John R.: Effect of Favorable Pressure Gradients on Transition for Several Bodies of Revolution at Mach 3.12. NACA TN 4313, 1958.
10. Rogers, Ruth H.: The Effect of Tip Bluntness on Boundary-Layer Transition on a 15° Included Angle Cone at $M = 3.12$ and 3.81. RAE Tech. Note No. Aero. 2645, Aug. 1959.
11. van Driest, E.R., and Boison, J.C.: Experiments on Boundary-Layer Transition at Supersonic Speeds. Jour. Aero. Sci., vol. 24, no. 12, Dec. 1957.

12. Stetson, Kenneth F.: Boundary-Layer Transition on Blunt Bodies with Highly Cooled Boundary Layers, *Jour. Aero-/Space Sci.*, vol. 27, no. 2, Feb. 1960.
13. Feldman, Saul: Numerical Comparison Between Exact and Approximate Theories of Hypersonic Inviscid Flow Past Slender Blunt-Nosed Bodies. *Jet Propulsion*, Vol. 30, No. 5, May 1960.
14. Lees, L. and Kubota, T.: Inviscid Hypersonic Flow Over Blunt-Nosed Slender Bodies. *Journal of the Aeronautical Sciences*, Vol. 24, No. 3, March 1957.
15. Minzner, R.A. and Ripley, W.S.: The ARDC Model Atmosphere, 1956. A. F. Survey in Geophysics, No. 86, A. F. Cambridge Res. Center, TN 56-204, December 1956.
16. Hilsenrath, Joseph, and Beckett, Charles W.: Tables of Thermodynamic Properties of Argon-Free Air to 15,000°K. AEDC TN 56-12, Arnold Eng. Dev. Center, Sept. 1956.
17. Creager, Marcus O.: The Effect of Leading-Edge Sweep and Surface Inclination on the Hypersonic Flow Field over a Blunt Flat Plate. NASA Memo 12-26-58A, 1959.
18. Creager, Marcus O.: Surface Pressure Distribution at Hypersonic Speeds for Blunt Delta Wings at Angle of Attack. NASA Memo 5-12-59A, 1959.
19. Rubesin, Morris W.: A Preliminary Examination of Improved Methods for Calculating Heat Transfer to Reentry Vehicles Shaped as Delta Wings with Blunt Leading Edges. *Vidya* Rep. No. 9, Jan. 1959.
20. Hayes, Wallace D. and Probstein, Ronald F.: Hypersonic Flow Theory. Academic Press, New York, 1959.
21. Kubota, T.: Inviscid Hypersonic Flow over Blunt-Nosed Slender Bodies. GALCIT Publication No. 417.
22. Ames Research Staff: Equations, Tables, and Charts for Compressible Flow. NACA Rep. 1135, 1953.

Approved For Release 2000/04/12 : CIA-RDP67B00657R000300070001-0

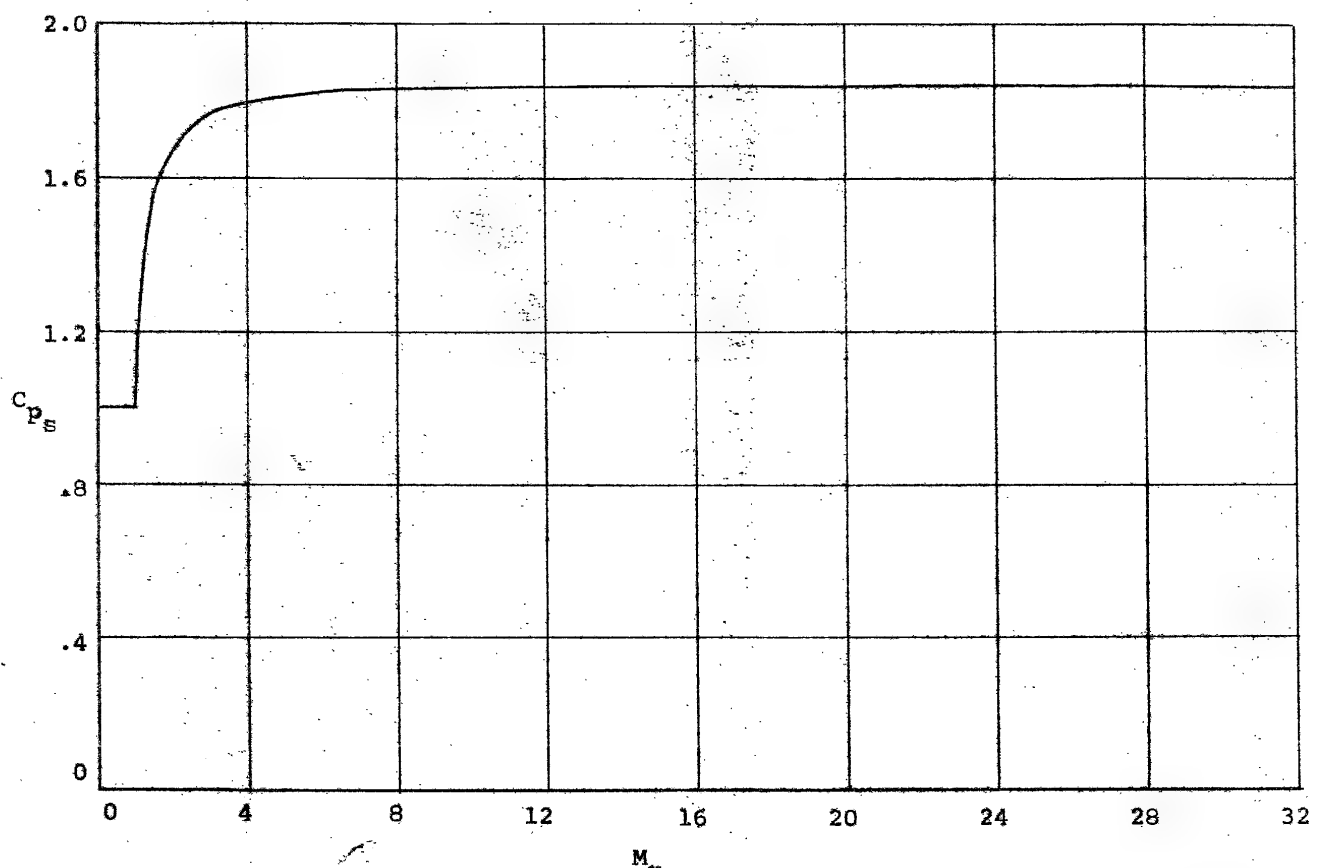


Figure III-1.- variation of stagnation pressure coefficient with flight Mach number for $\gamma = 1.4$.

Approved For Release 2000/04/12 : CIA-RDP67B00657R000300070001-0

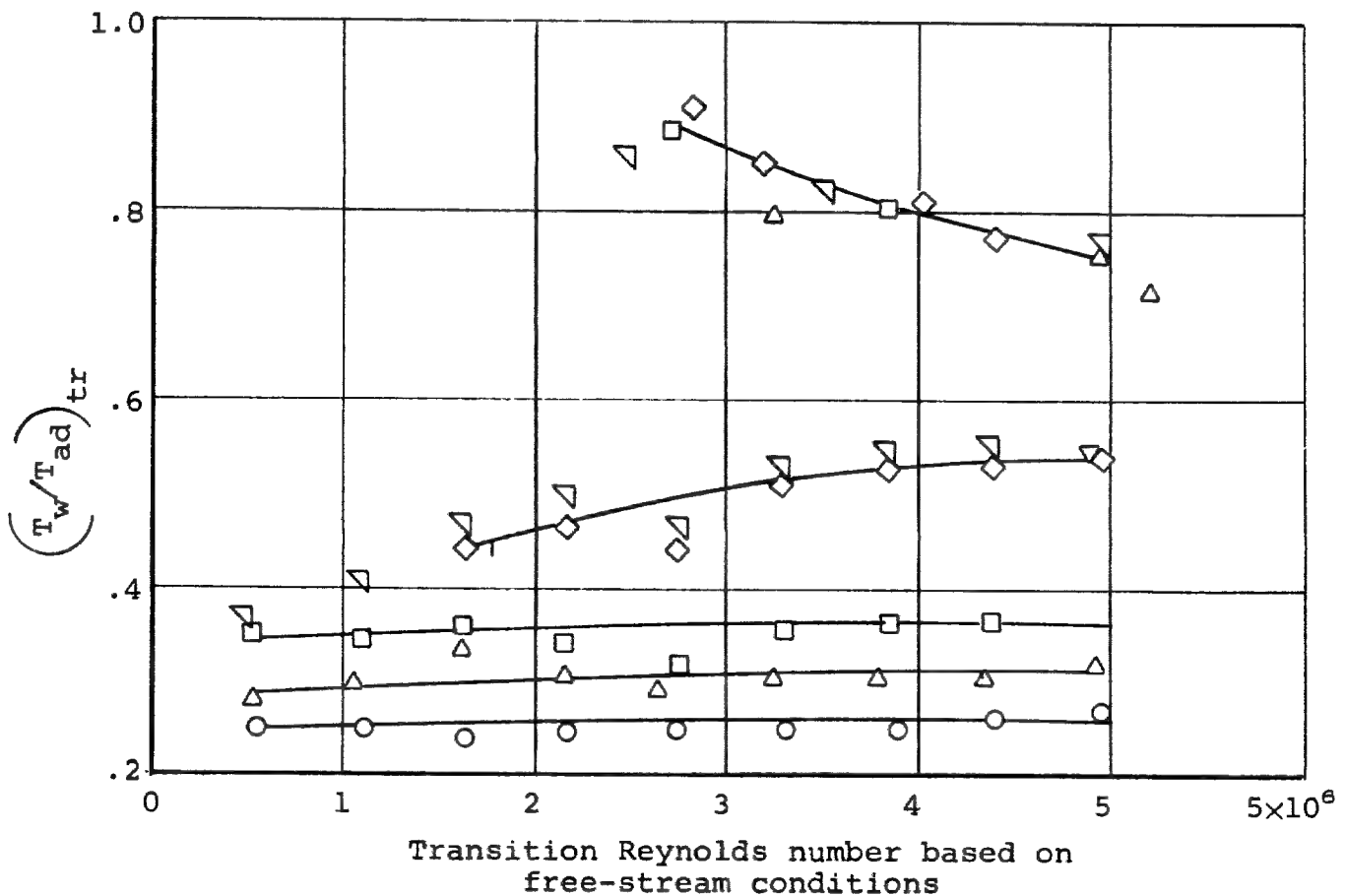
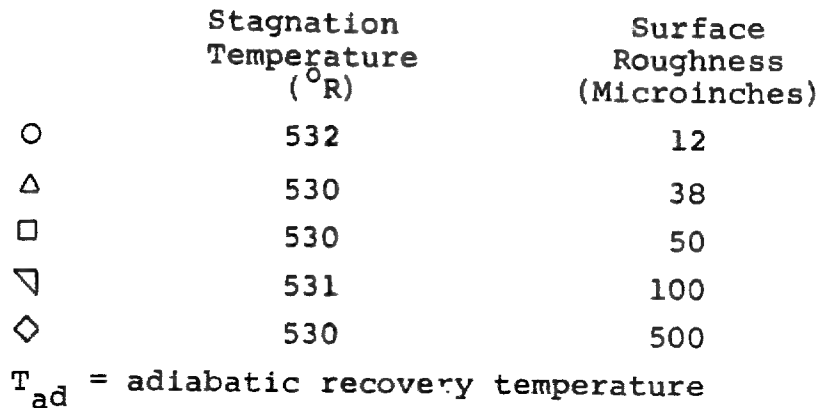


Figure III-2.- Effect of cooling and roughness on boundary-layer transition. Spherically blunted cone, $M_\infty = 3.12$. (Data of Ref. 7)

Approved For Release 2000/04/12 : CIA-RDP67B00657R000300070001-0

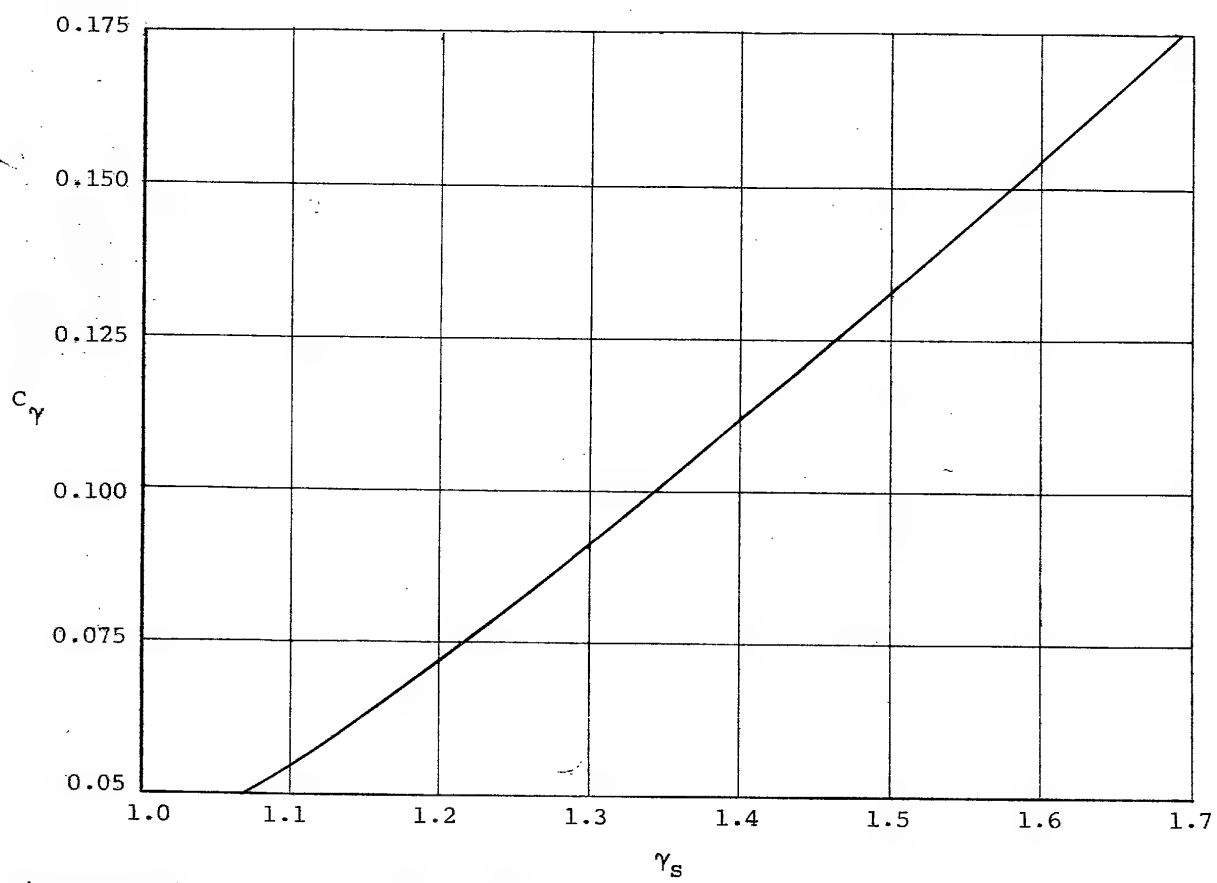


Figure III-3.- C_γ as a function of γ_s .

Approved For Release 2000/04/12 : CIA-RDP67B00657R000300070001-0

Approved For Release 2000/04/12 : CIA-RDP67B00657R000300070001-0

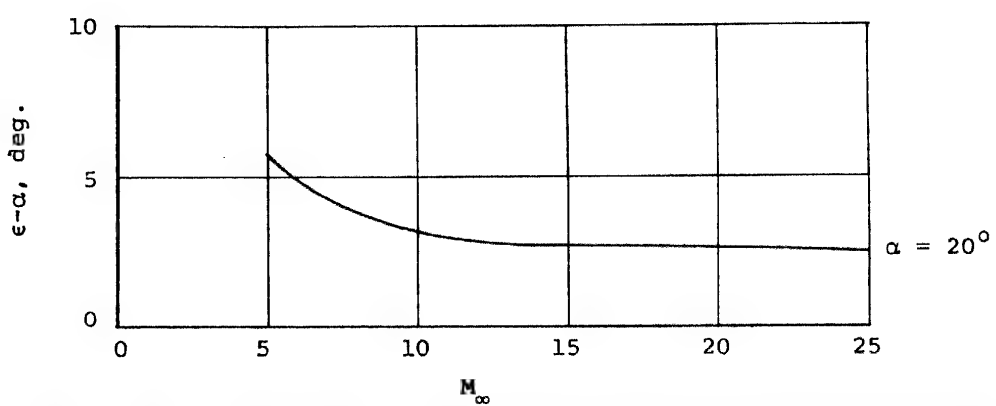
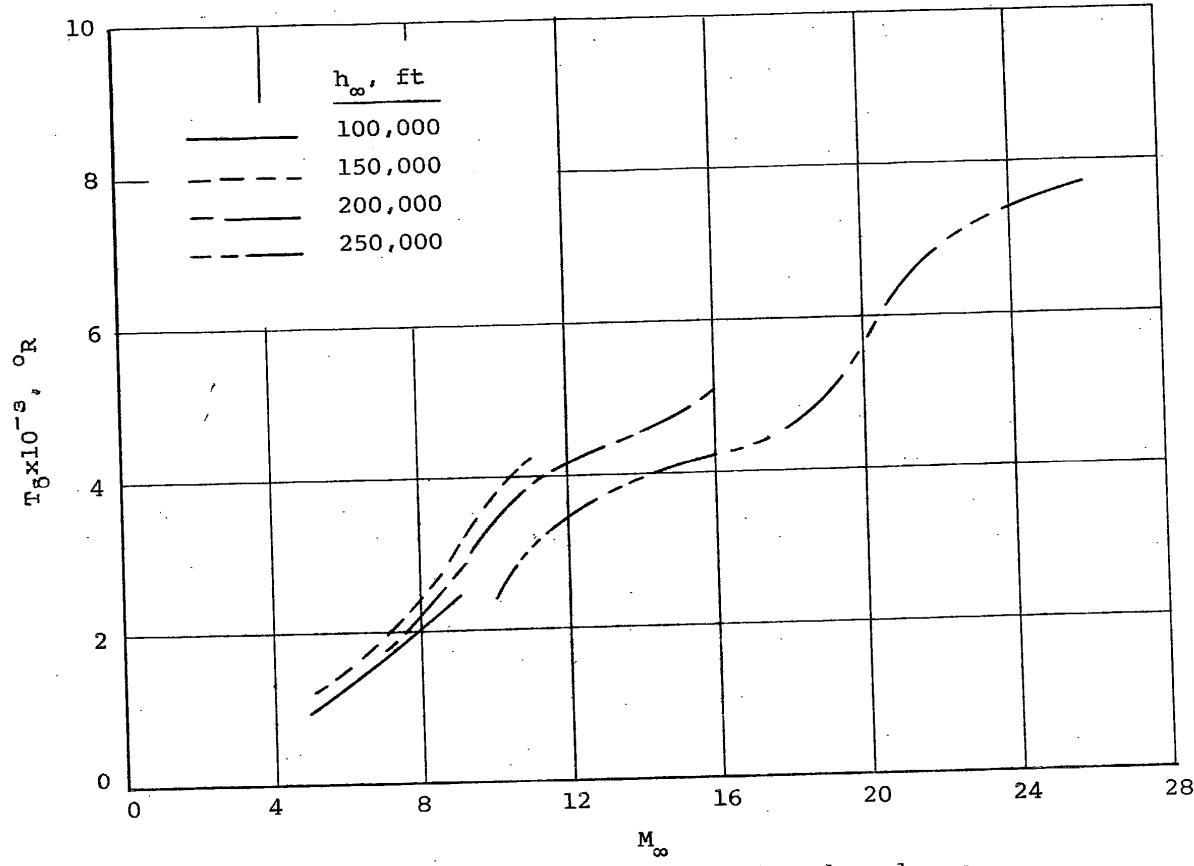


Figure III-4.- Shock wave slope relative to blunt swept wing surface

Approved For Release 2000/04/12 : CIA-RDP67B00657R000300070001-0

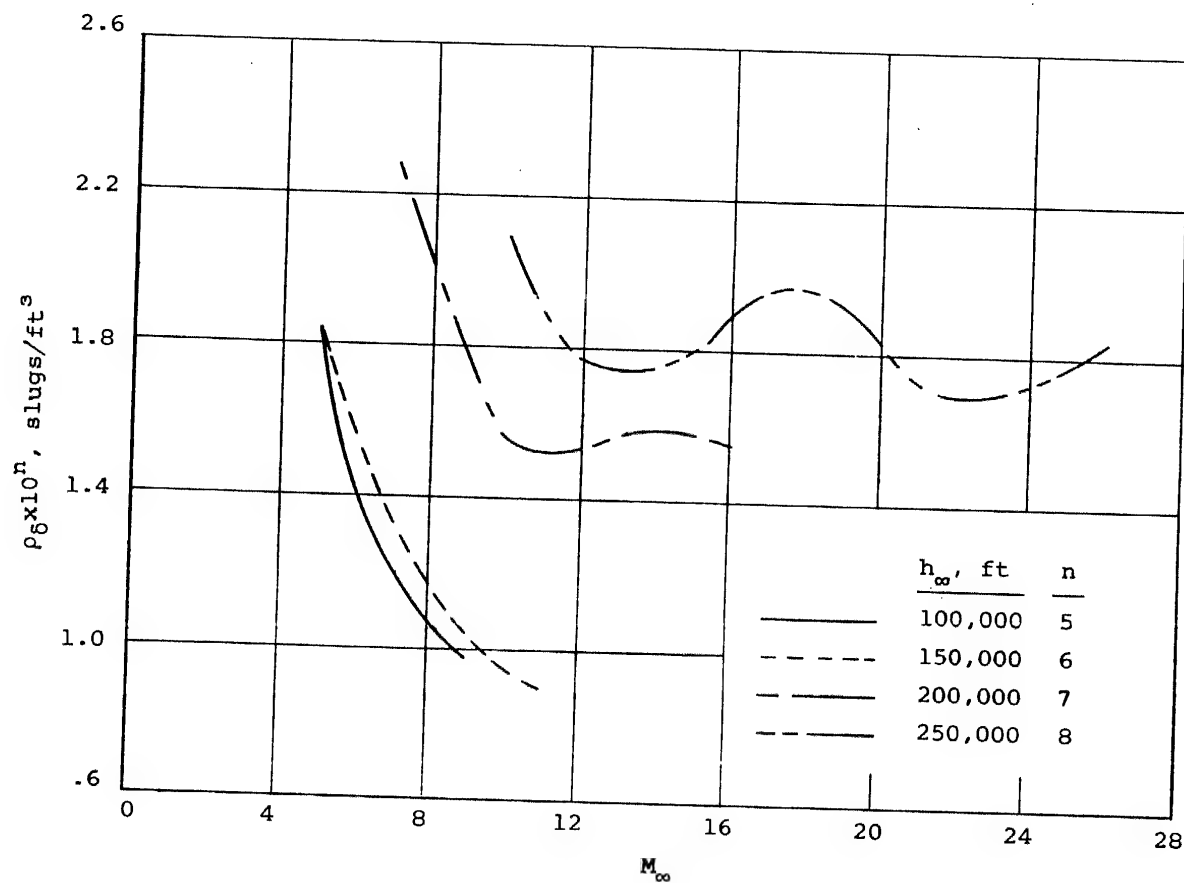
Approved For Release 2000/04/12 : CIA-RDP67B00657R000300070001-0



(a) Temperature at edge of boundary layer

Figure III-5.- Gas properties at the edge of the boundary layer (6.0 feet behind the shoulder) of a blunt cone ($\theta_c = 5.0^{\circ}$, $R = 1.0$ ft).

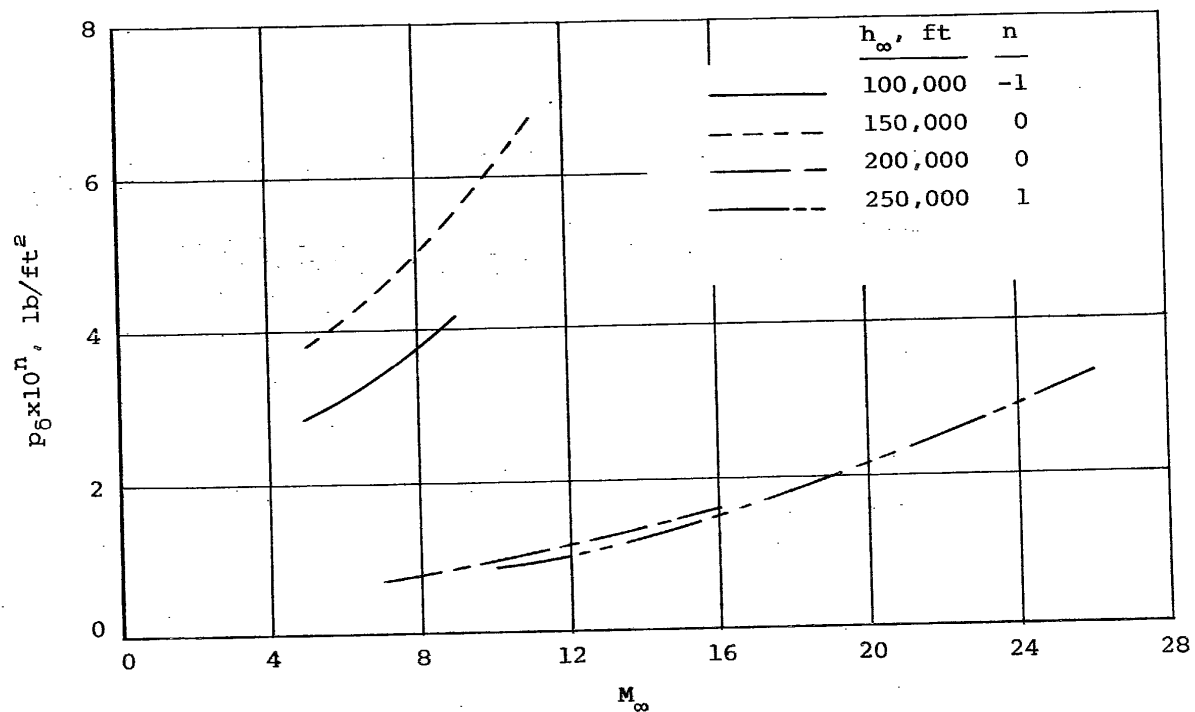
Approved For Release 2000/04/12 : CIA-RDP67B00657R000300070001-0



(b) Density at edge of boundary layer

Figure III-5.- Continued.

Approved For Release 2000/04/12 : CIA-RDP67B00657R000300070001-0

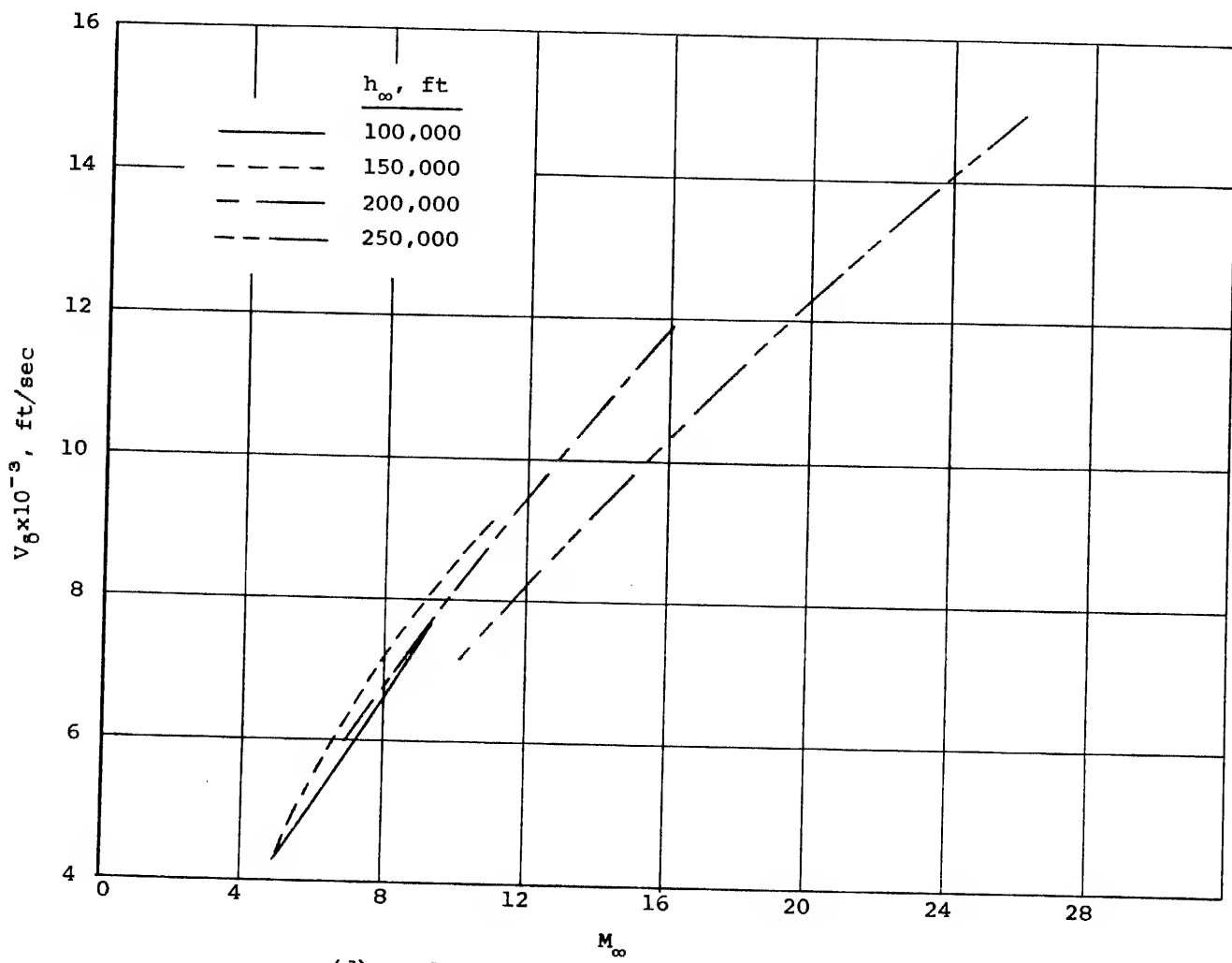


(c) Pressure at edge of boundary layer

Figure III-5.- Continued.

Approved For Release 2000/04/12 : CIA-RDP67B00657R000300070001-0

Approved For Release 2000/04/12 : CIA-RDP67B00657R000300070001-0



(d) Velocity at edge of boundary layer

Figure III-5.- Continued.

Approved For Release 2000/04/12 : CIA-RDP67B00657R000300070001-0

Approved For Release 2000/04/12 : CIA-RDP67B00657R000300070001-0

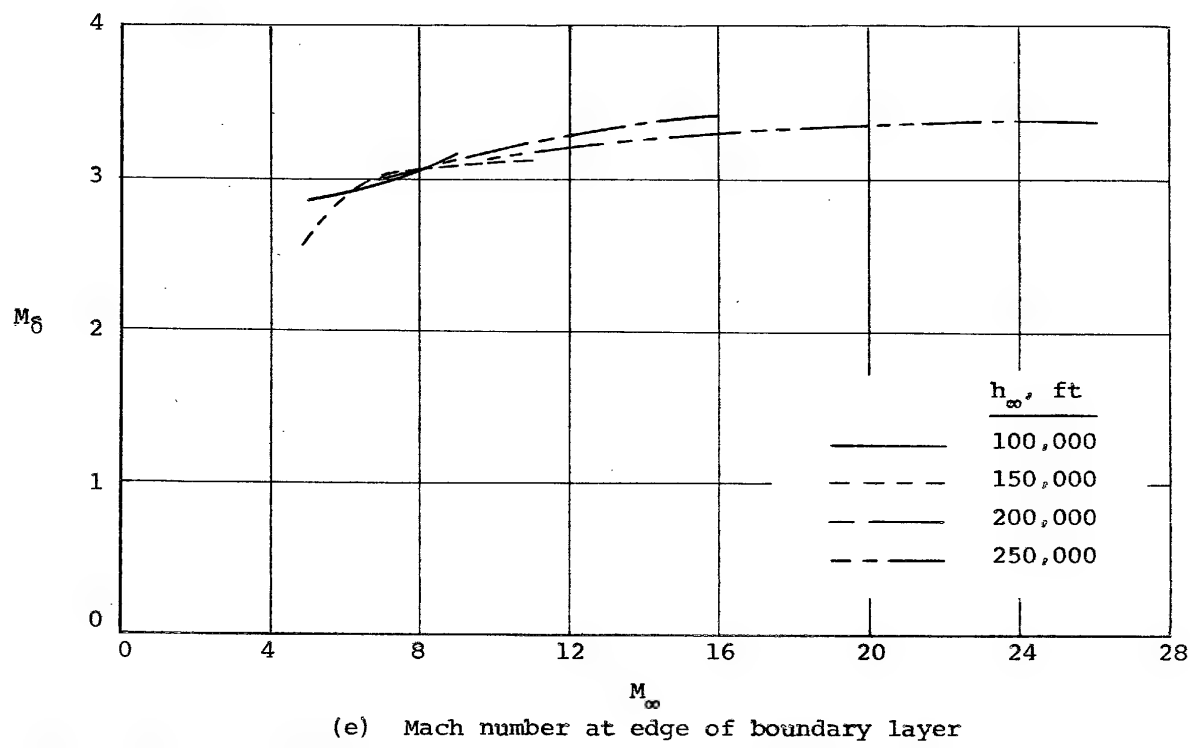


Figure III-5.- Concluded.

Approved For Release 2000/04/12 : CIA-RDP67B00657R000300070001-0

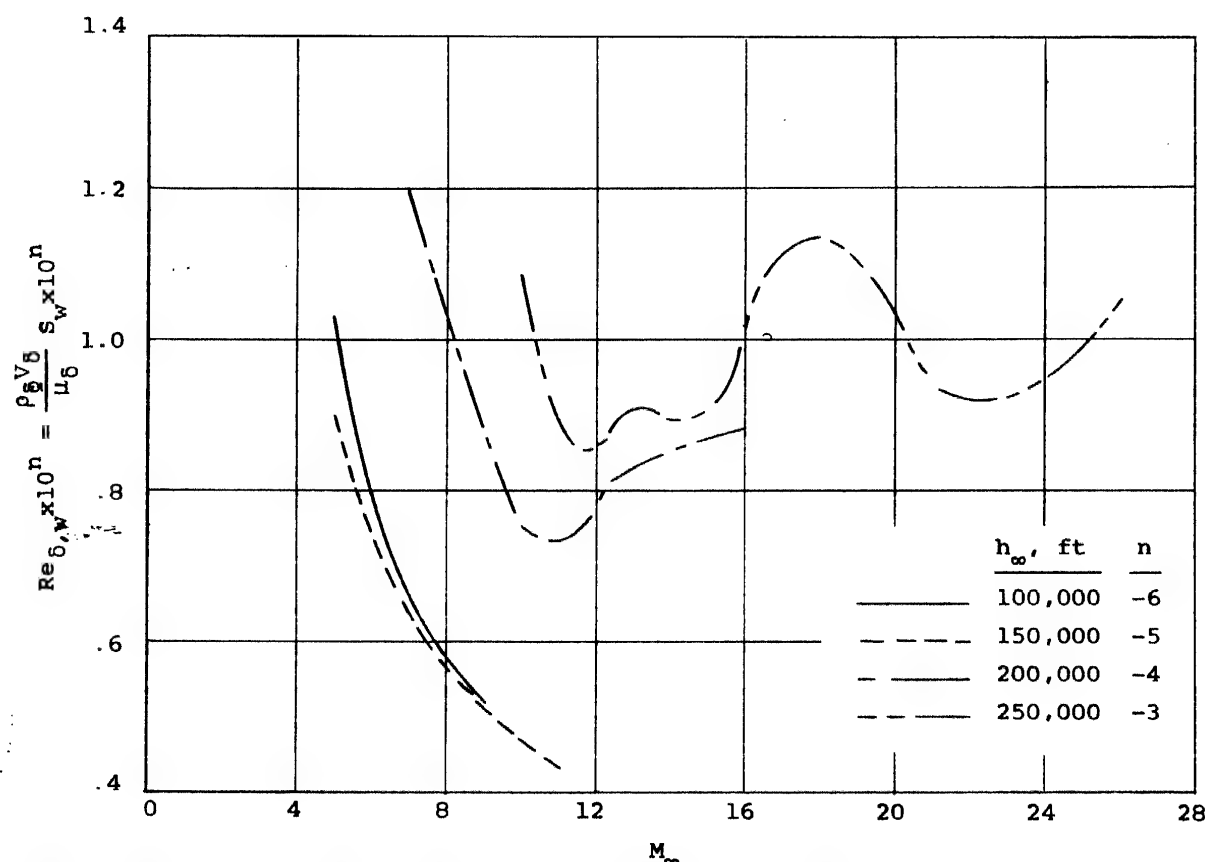


Figure III-6.- Reynolds number at the edge of the boundary layer (6.0 feet behind the shoulder) of a blunt cone ($\theta_c = 5.0^\circ$, $R = 1.0$ ft).

Approved For Release 2000/04/12 : CIA-RDP67B00657R000300070001-0

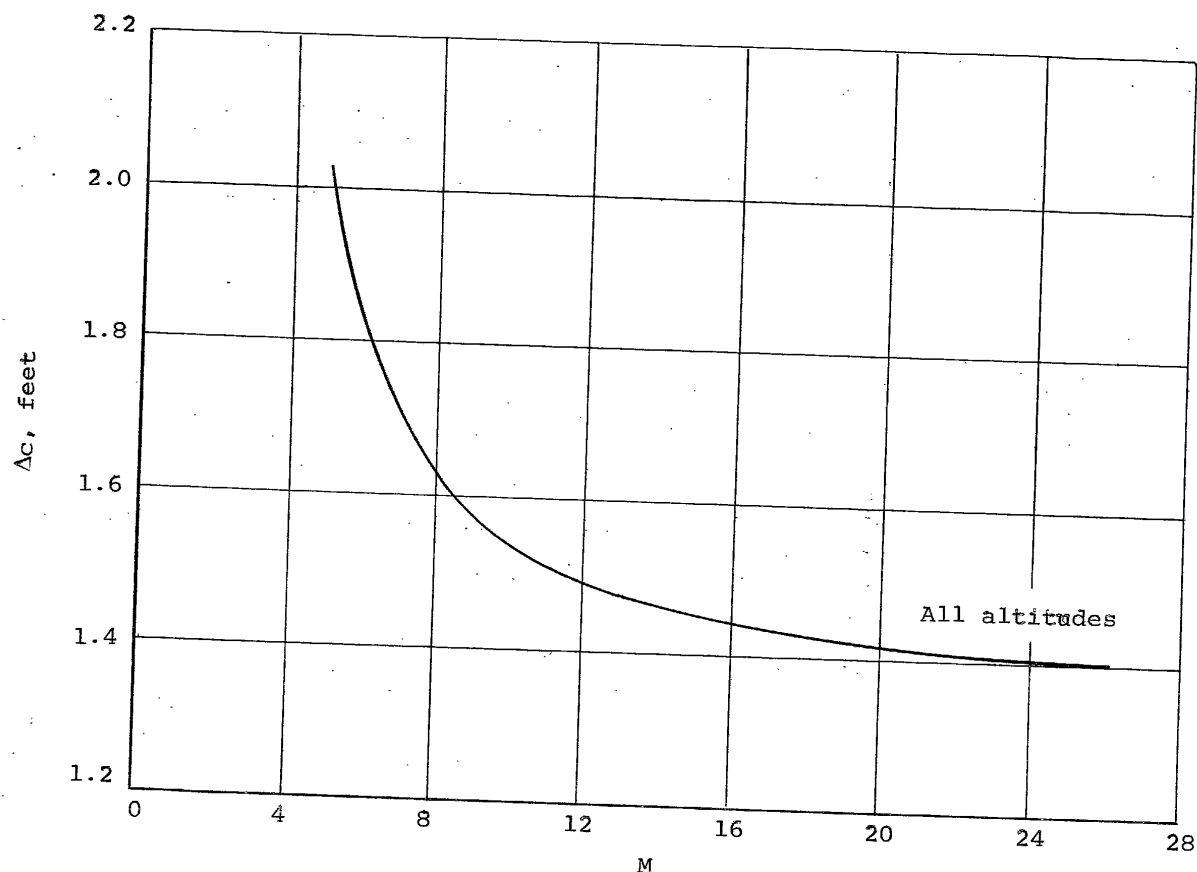


Figure III-7.- Shock layer thickness at the camera window 6.0 feet behind the shoulder of a blunt cone ($\theta_c = 5.0^\circ$, $R = 1.0$ ft).

Approved For Release 2000/04/12 : CIA-RDP67B00657R000300070001-0

Approved For Release 2000/04/12 : CIA-RDP67B00657R000300070001-0

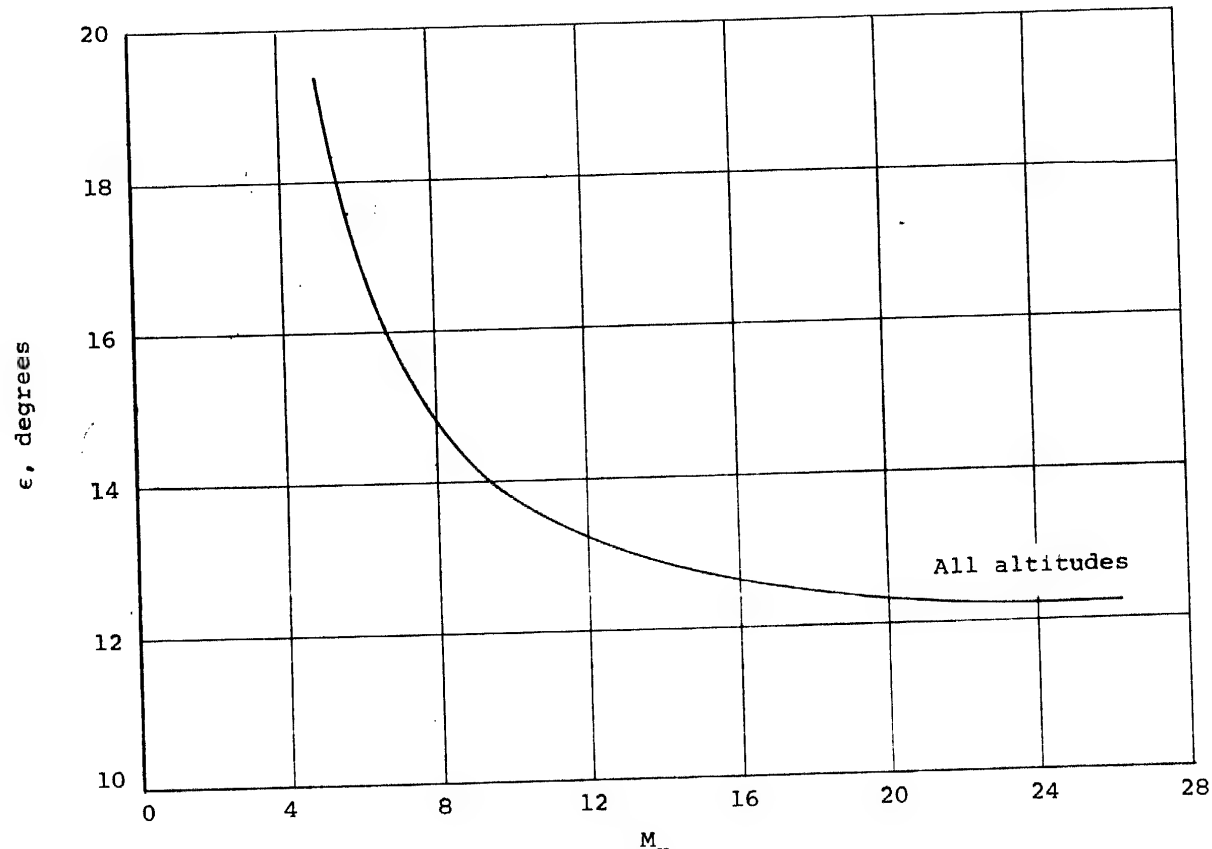
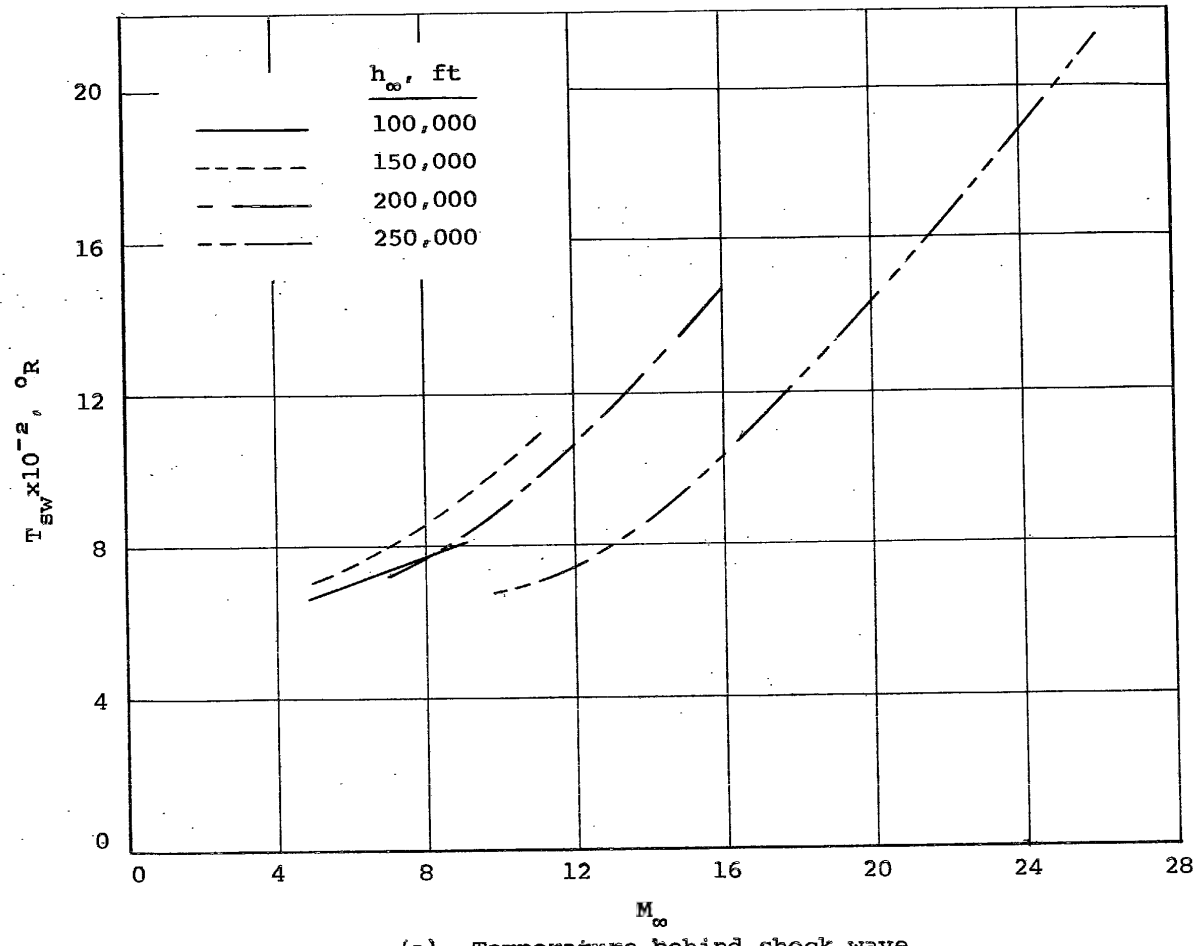


Figure III-8.- Shock wave slope, relative to the free stream direction, at the camera window 6.0 feet behind the shoulder of a blunt cone ($\theta_c = 5.0^\circ$, $R = 1.0$ ft).

Approved For Release 2000/04/12 : CIA-RDP67B00657R000300070001-0

Approved For Release 2000/04/12 : CIA-RDP67B00657R000300070001-0

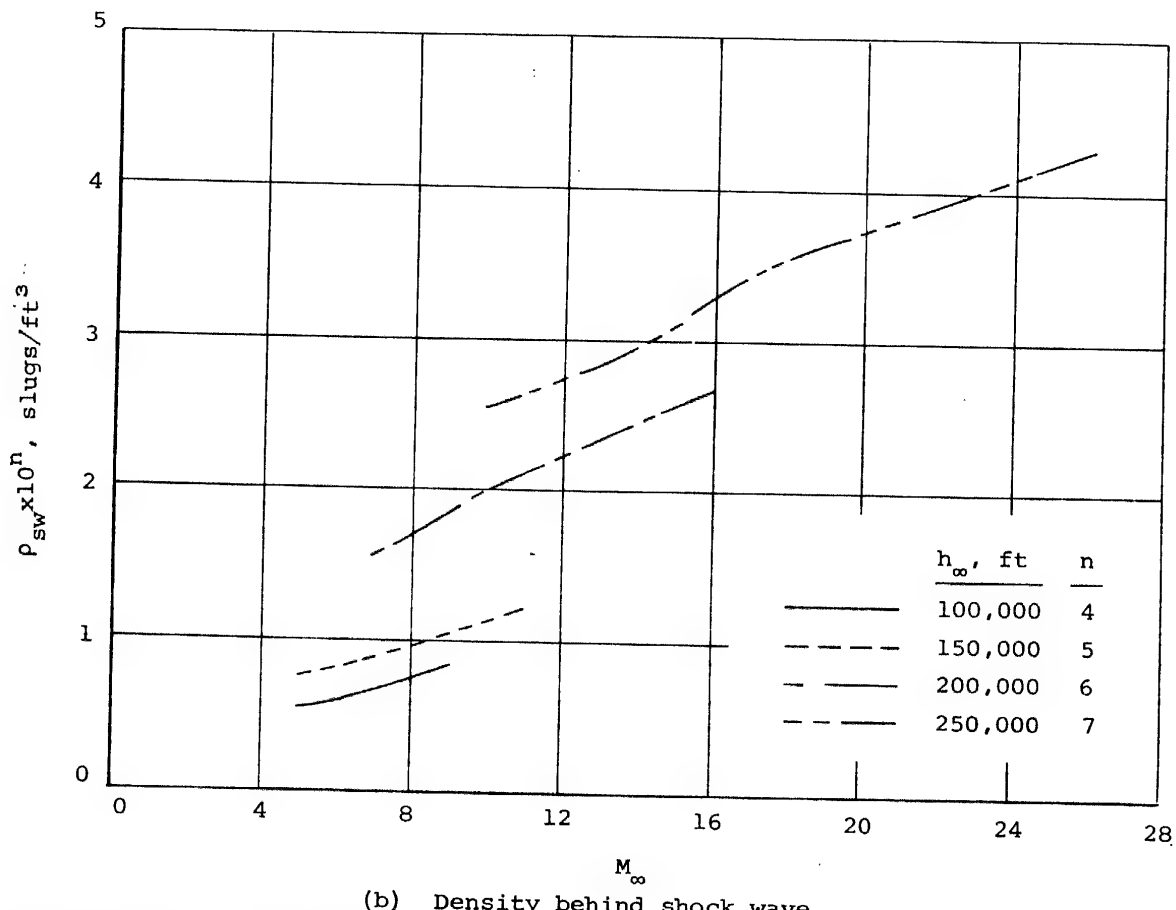


(a) Temperature behind shock wave

Figure III-9.- Gas properties behind the shock wave (6.0 feet behind the shoulder) of a blunt cone ($\theta_c = 5.0^\circ$, $R = 1.0$ ft).

Approved For Release 2000/04/12 : CIA-RDP67B00657R000300070001-0

Approved For Release 2000/04/12 : CIA-RDP67B00657R000300070001-0

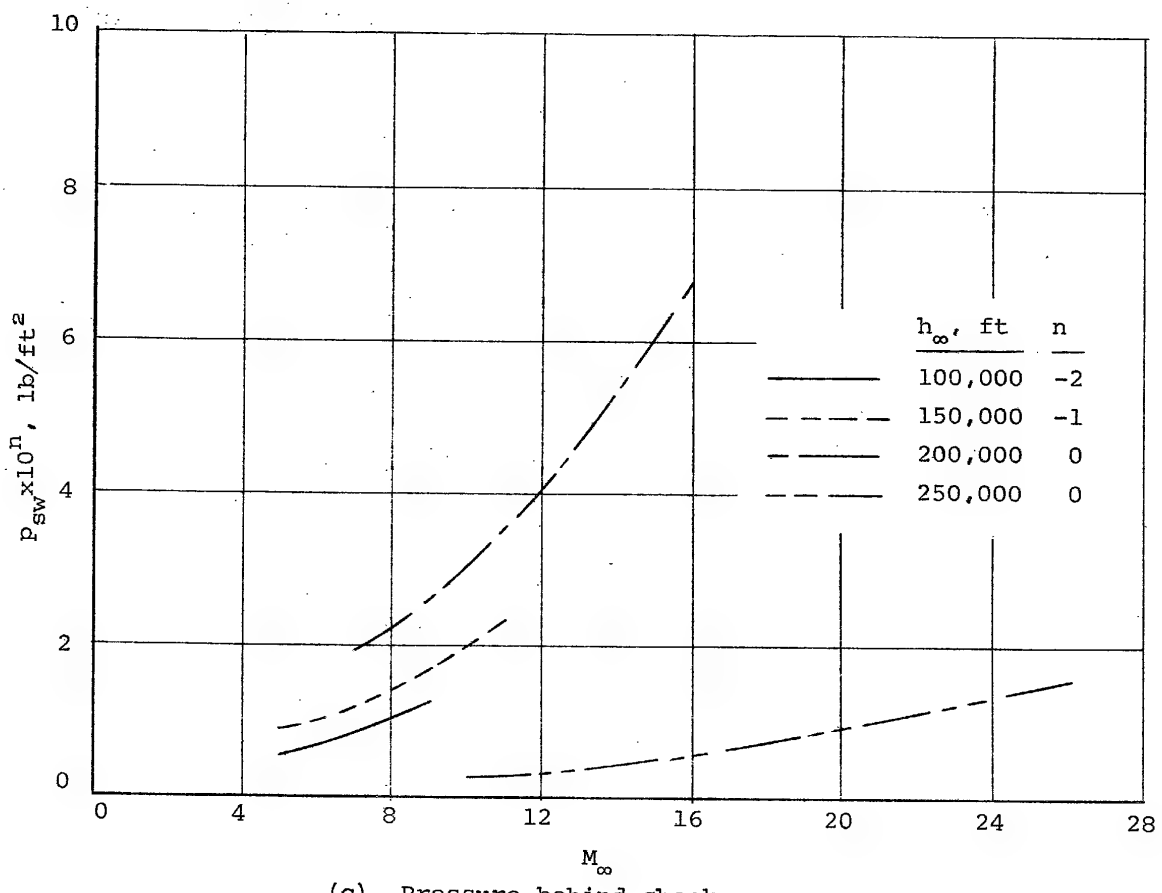


(b) Density behind shock wave

Figure III-9.- Continued.

Approved For Release 2000/04/12 : CIA-RDP67B00657R000300070001-0

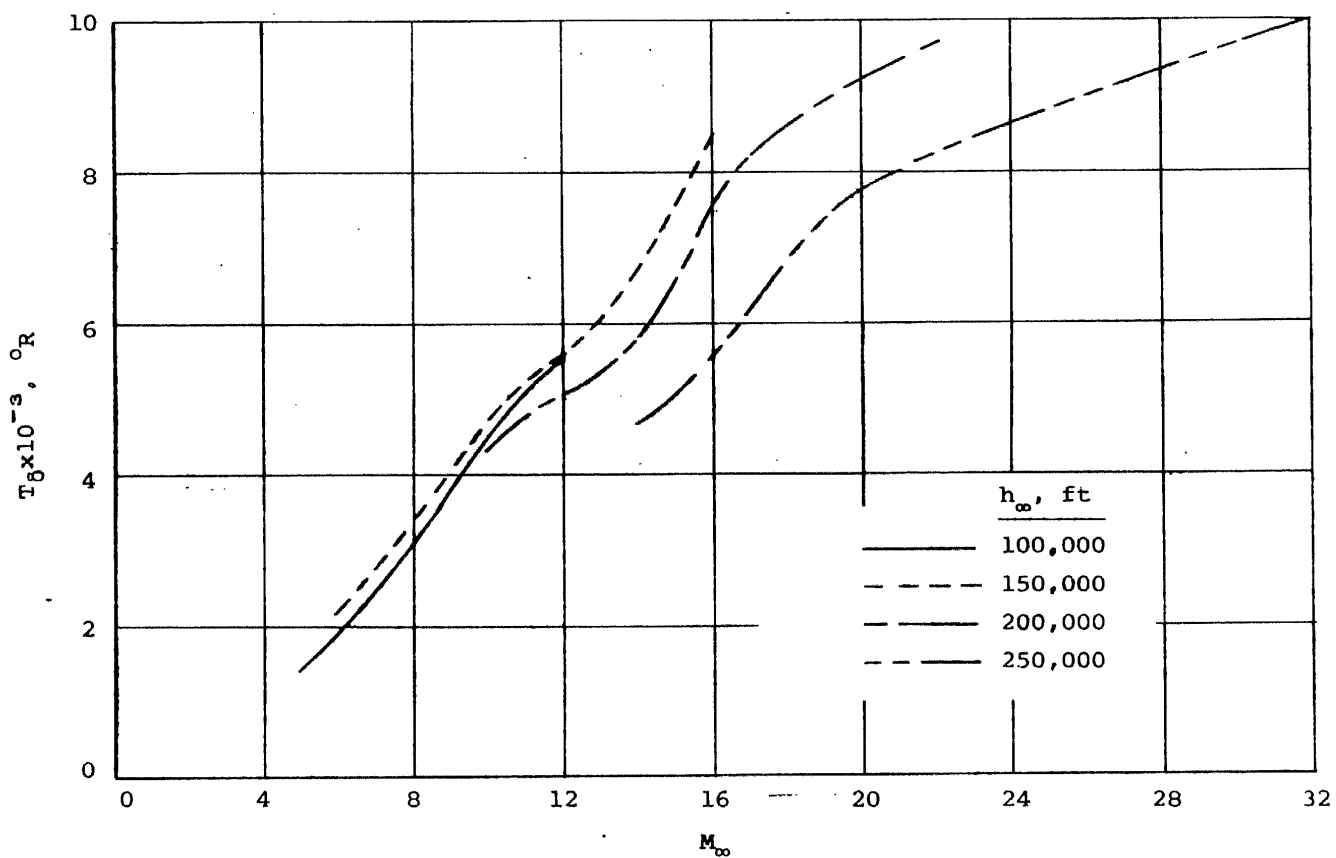
Approved For Release 2000/04/12 : CIA-RDP67B00657R000300070001-0



(c) Pressure behind shock wave

Figure III-9.- Concluded.

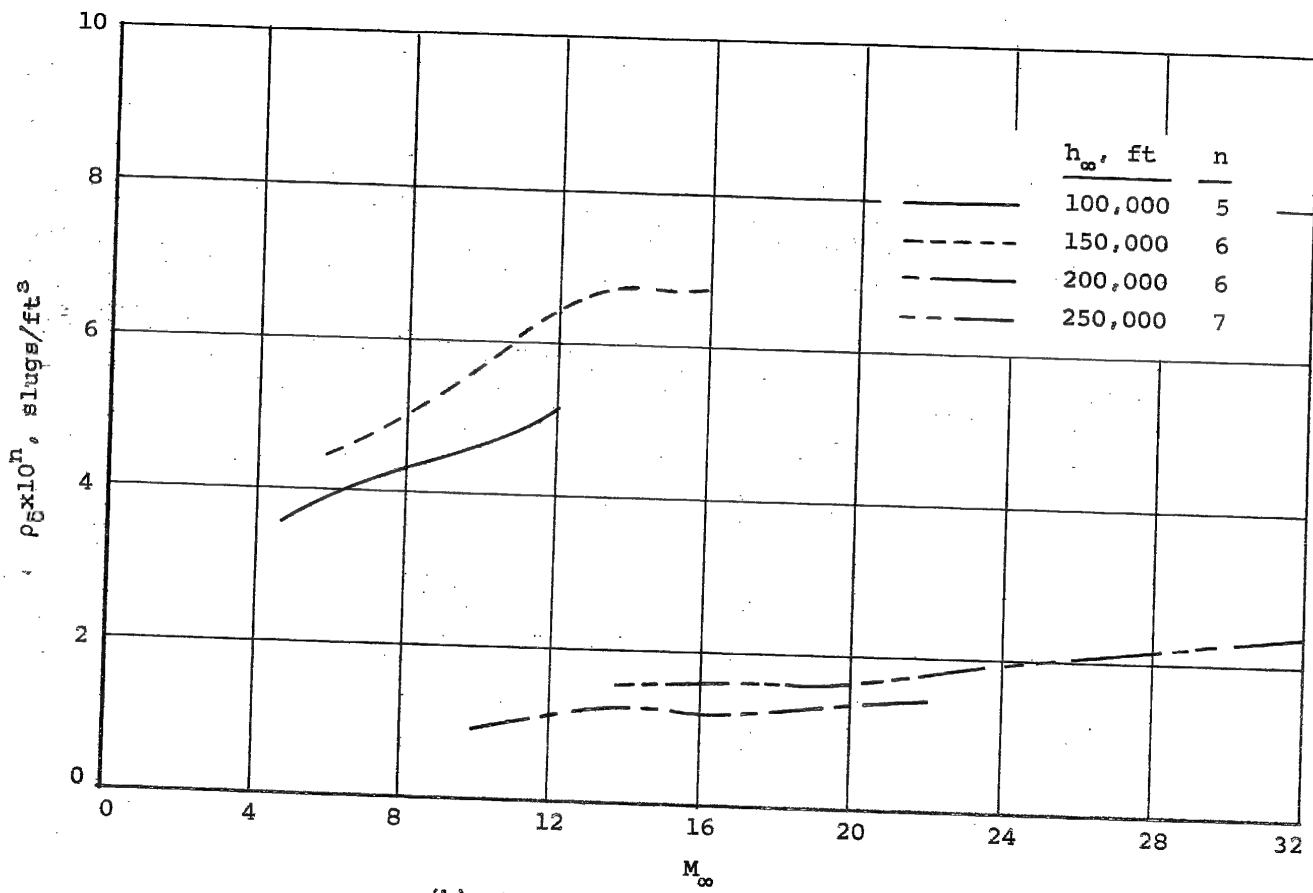
Approved For Release 2000/04/12 : CIA-RDP67B00657R000300070001-0



(a) Temperature at edge of boundary layer

Figure III-10.- Gas properties at the edge of the boundary layer (6.0 feet behind the shoulder) on the lower surface of a blunt swept wing ($\alpha = 20^\circ$, $R = 1.0$ ft, $T_w = 0^\circ F$ to $2000^\circ F$, $\Lambda = 70^\circ$).

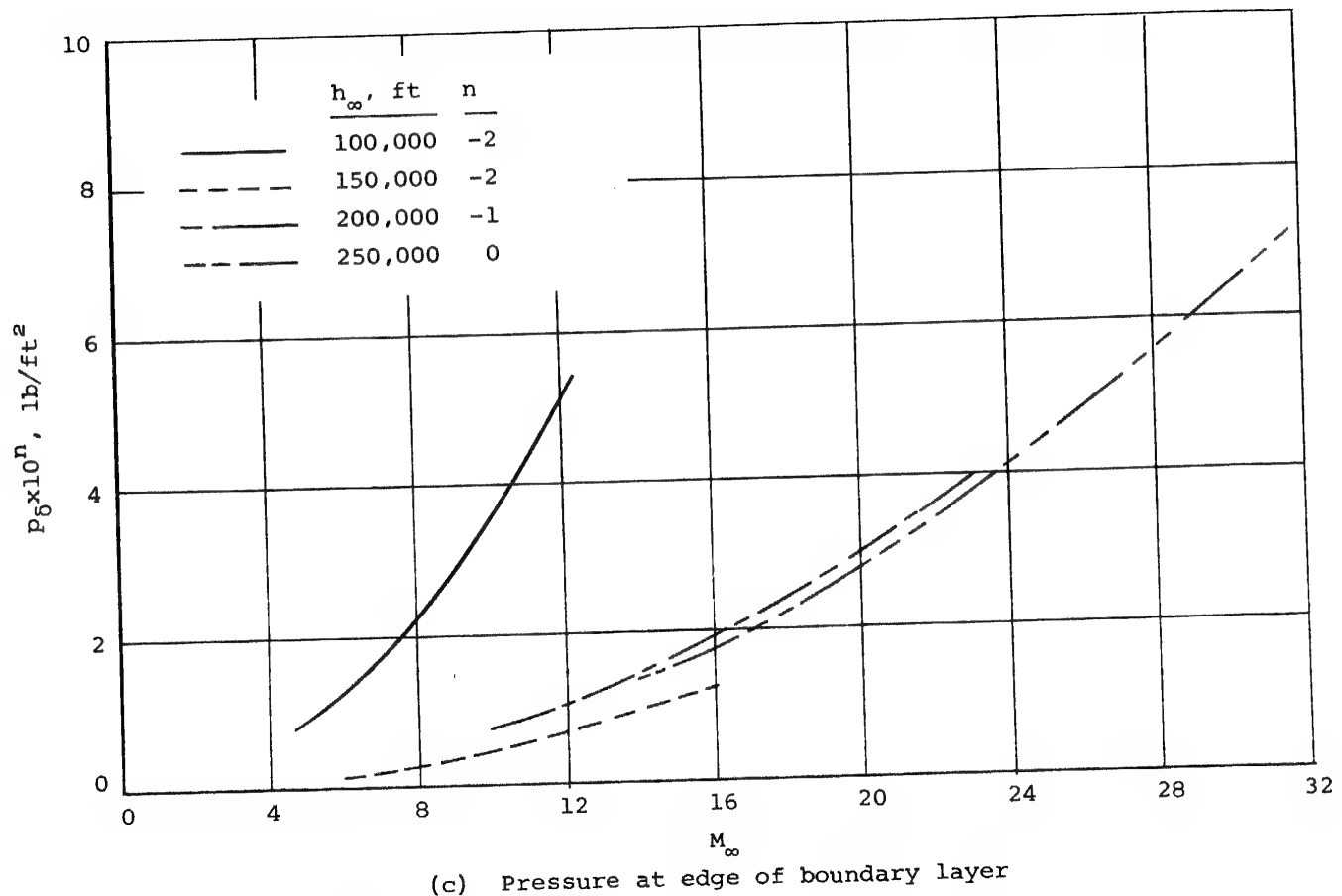
Approved For Release 2000/04/12 : CIA-RDP67B00657R000300070001-0



(b) Density at edge of boundary layer

Figure III-10.- Continued.

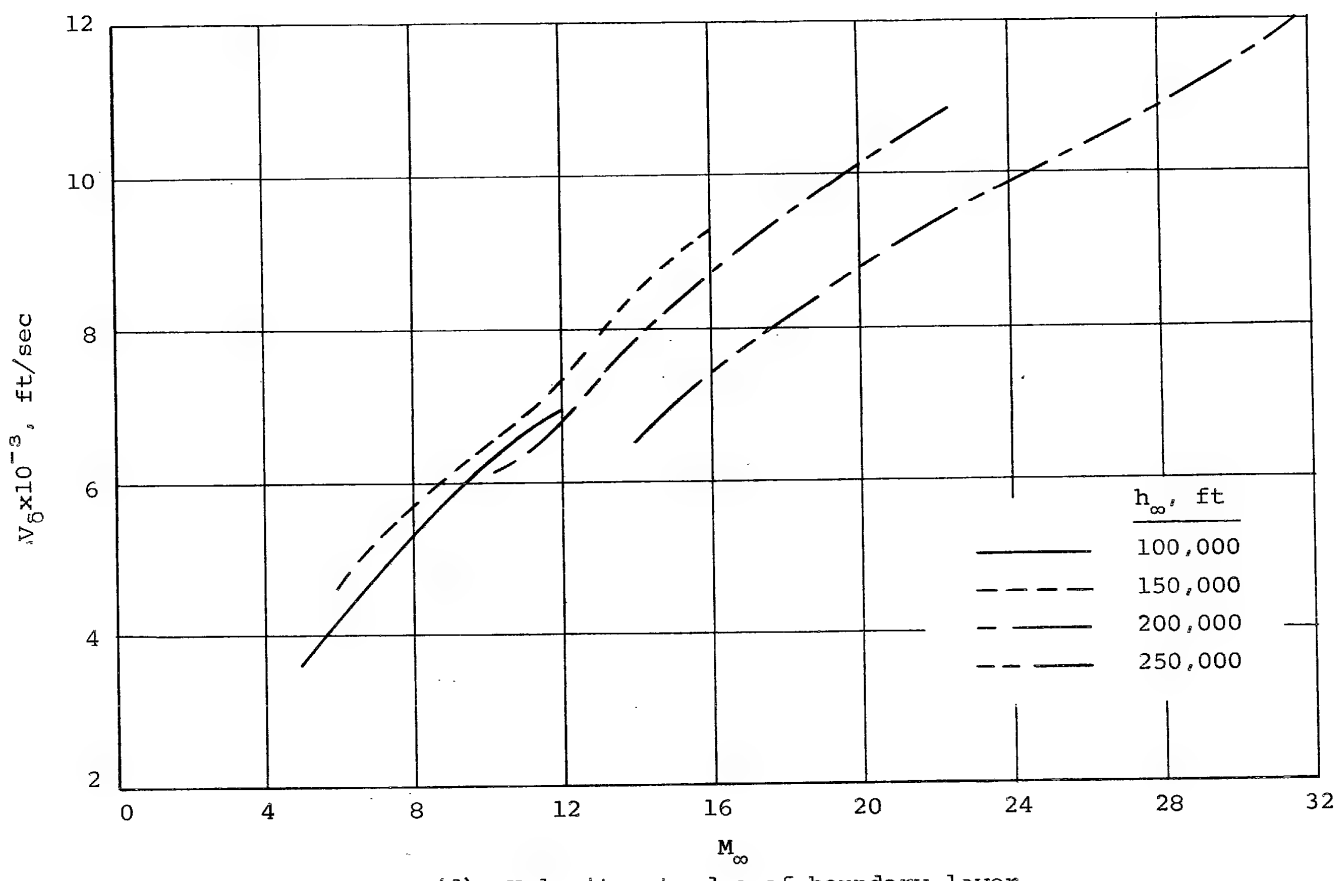
Approved For Release 2000/04/12 : CIA-RDP67B00657R000300070001-0



(c) Pressure at edge of boundary layer

Figure III-10.- Continued.

Approved For Release 2000/04/12 : CIA-RDP67B00657R000300070001-0

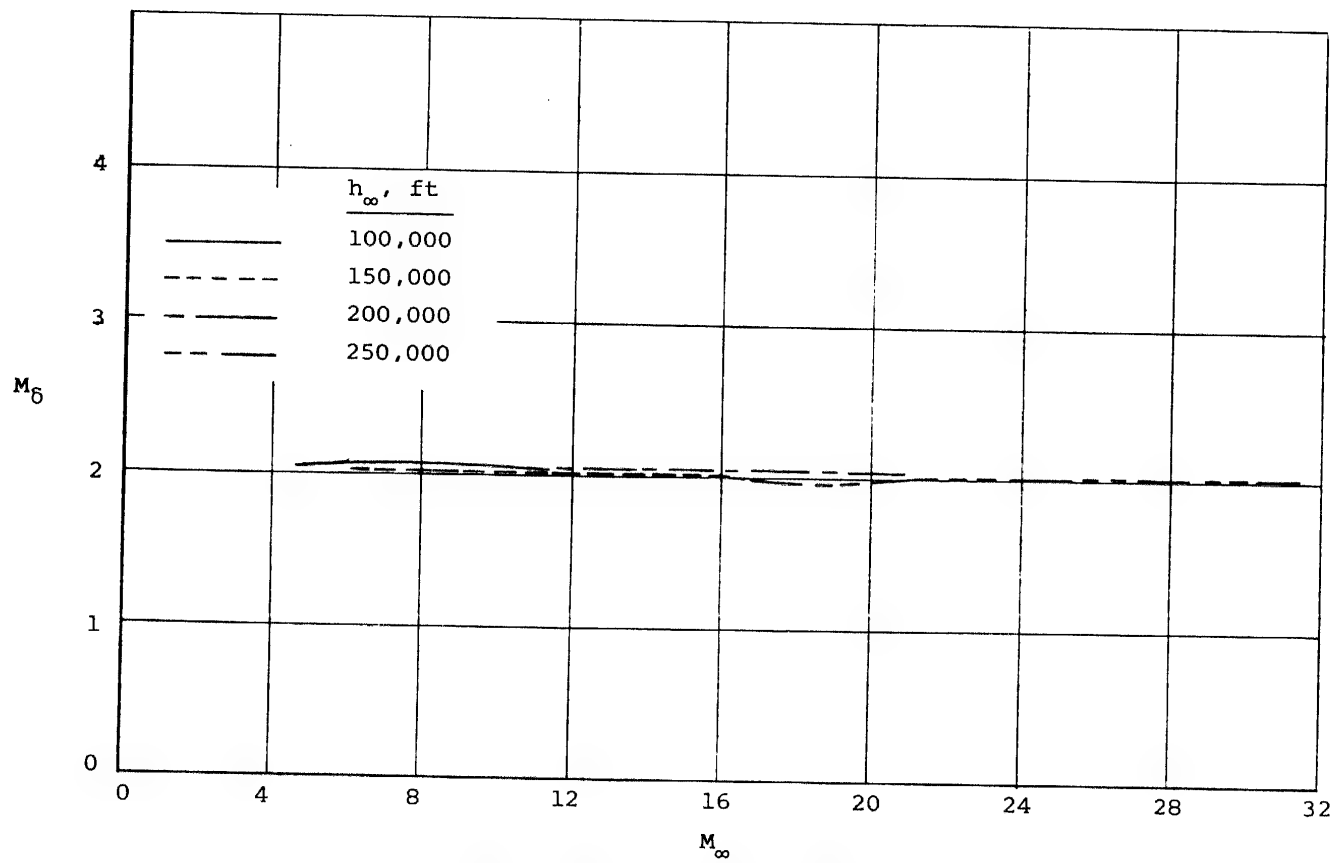


(d) velocity at edge of boundary layer

Figure III-10.- Continued.

Approved For Release 2000/04/12 : CIA-RDP67B00657R000300070001-0

Approved For Release 2000/04/12 : CIA-RDP67B00657R000300070001-0



(e) Mach number at edge of boundary layer

Figure III-10.- Concluded.

Approved For Release 2000/04/12 : CIA-RDP67B00657R000300070001-0

Approved For Release 2000/04/12 : CIA-RDP67B00657R000300070001-0

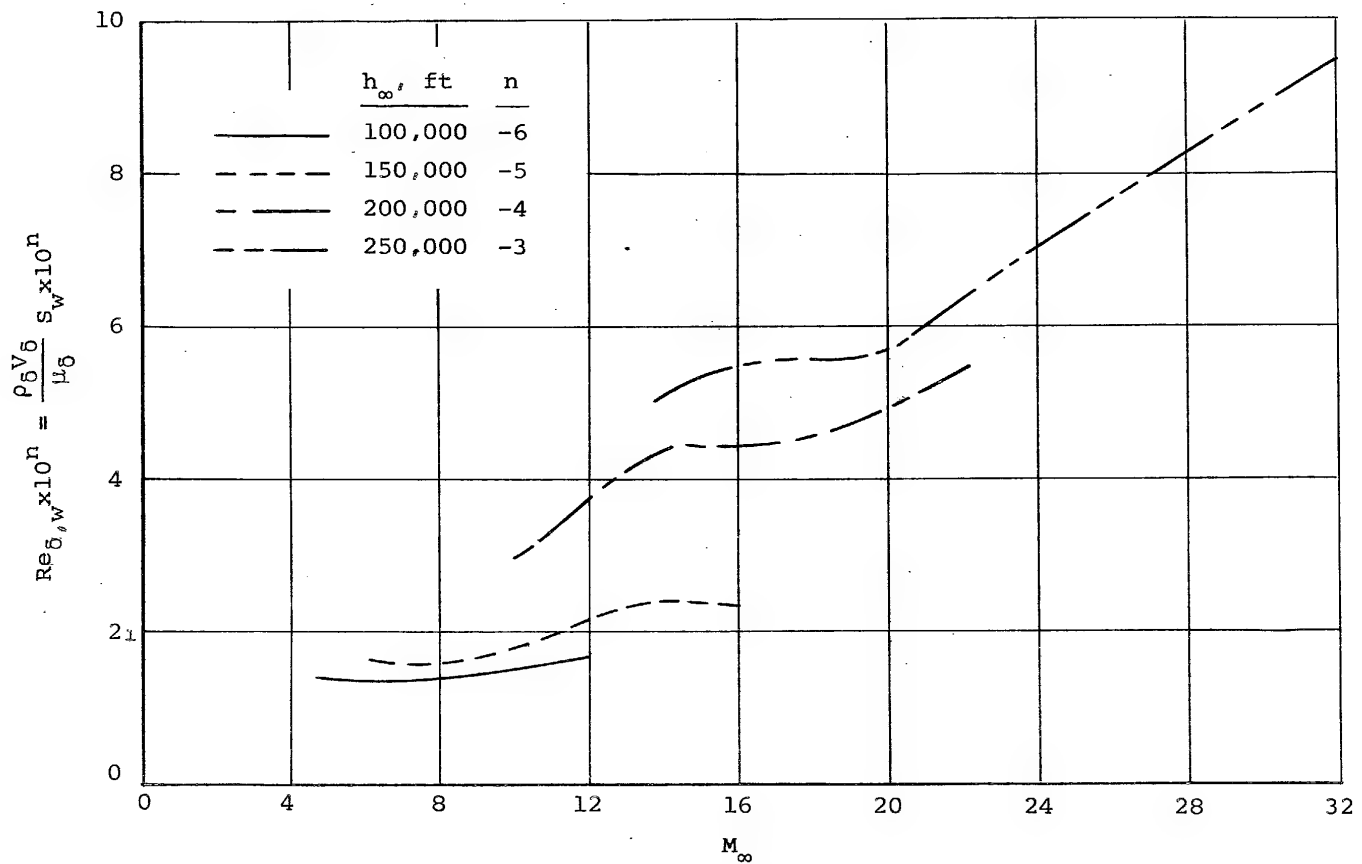


Figure III-11.- Reynolds number at the edge of the boundary layer (6.0 feet behind the shoulder) on the lower surface of a blunt swept wing ($\alpha = 20^\circ$, $R = 1.0$ ft, $T_w = 0^\circ F$ to $2000^\circ F$, $\Lambda = 70^\circ$).

Approved For Release 2000/04/12 : CIA-RDP67B00657R000300070001-0

Approved For Release 2000/04/12 : CIA-RDP67B00657R000300070001-0

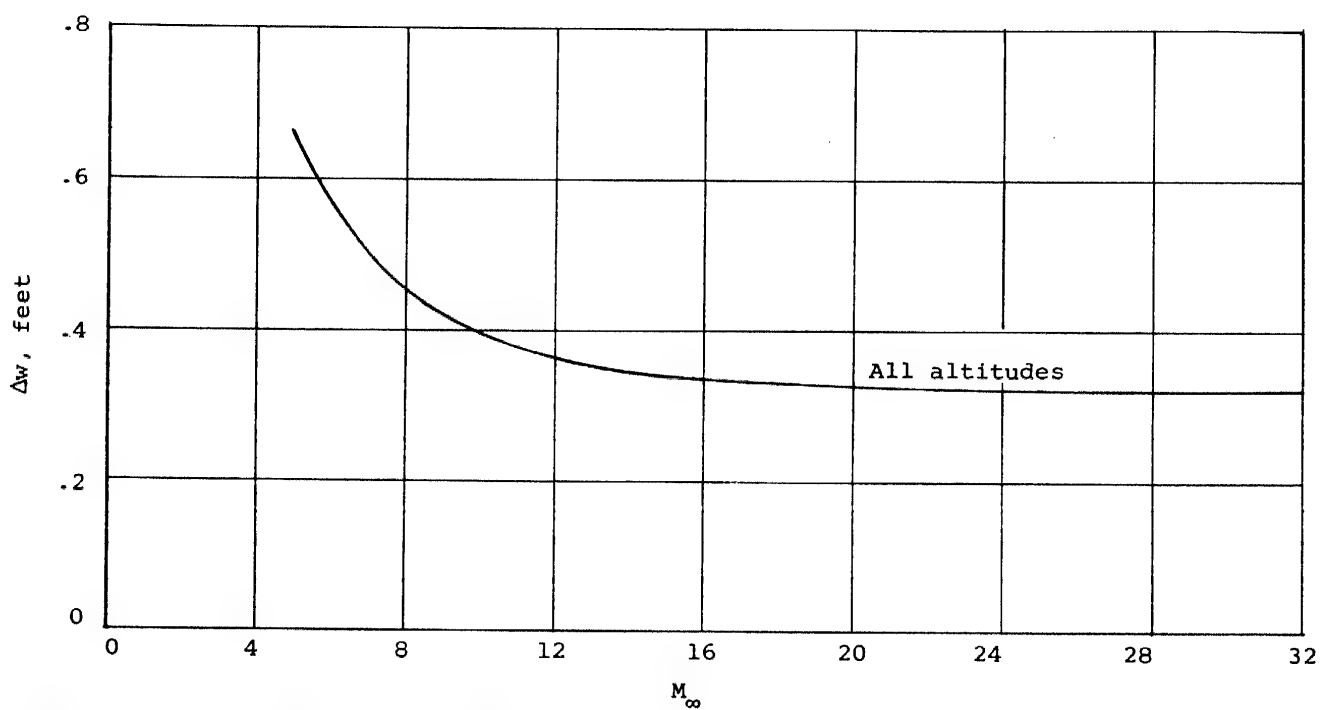
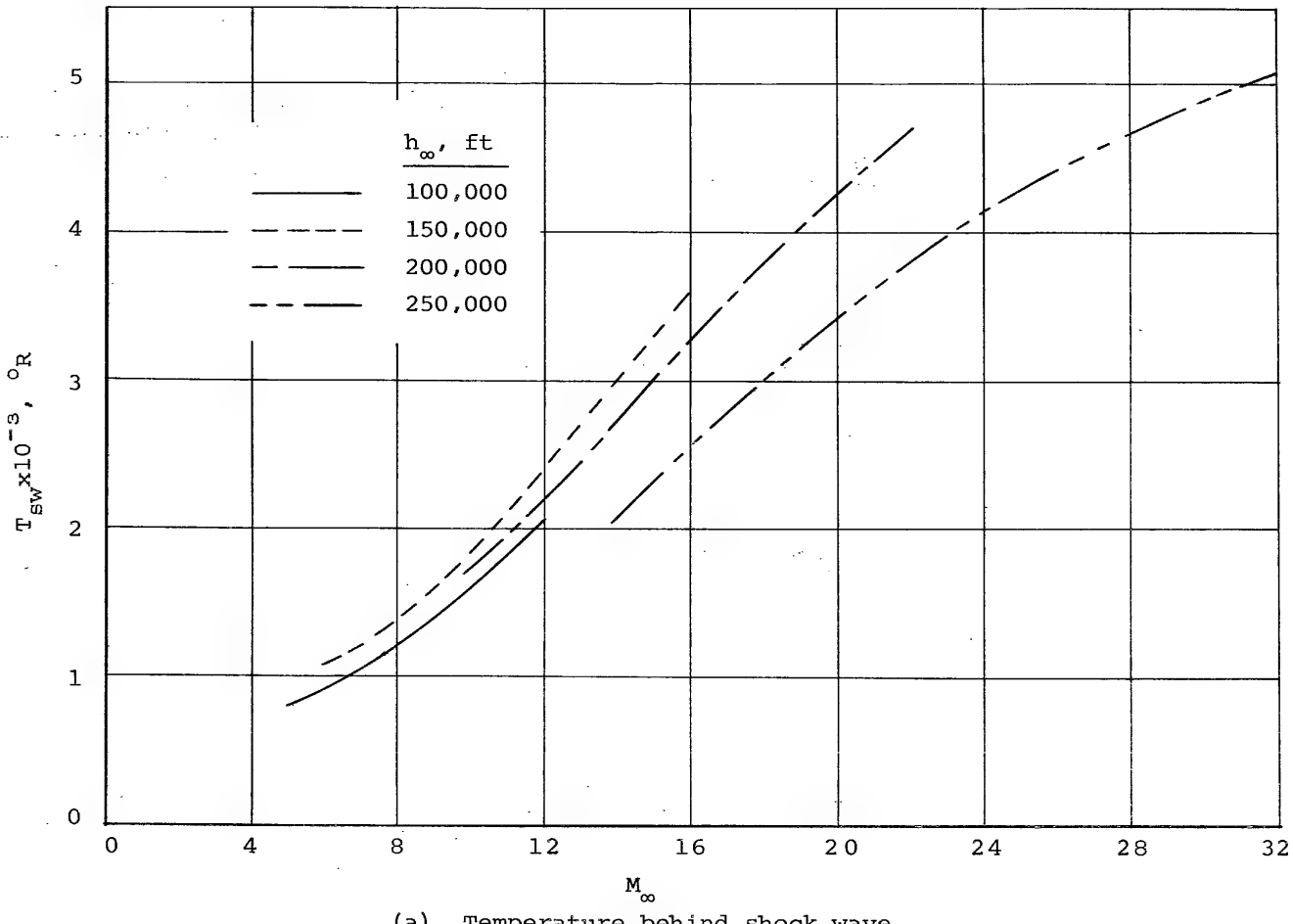


Figure III-12.- Shock layer thickness at the camera window 6.0 feet behind the shoulder on the lower surface of a blunt swept wing. ($\alpha = 20^\circ$, $R = 1.0$ ft)

Approved For Release 2000/04/12 : CIA-RDP67B00657R000300070001-0

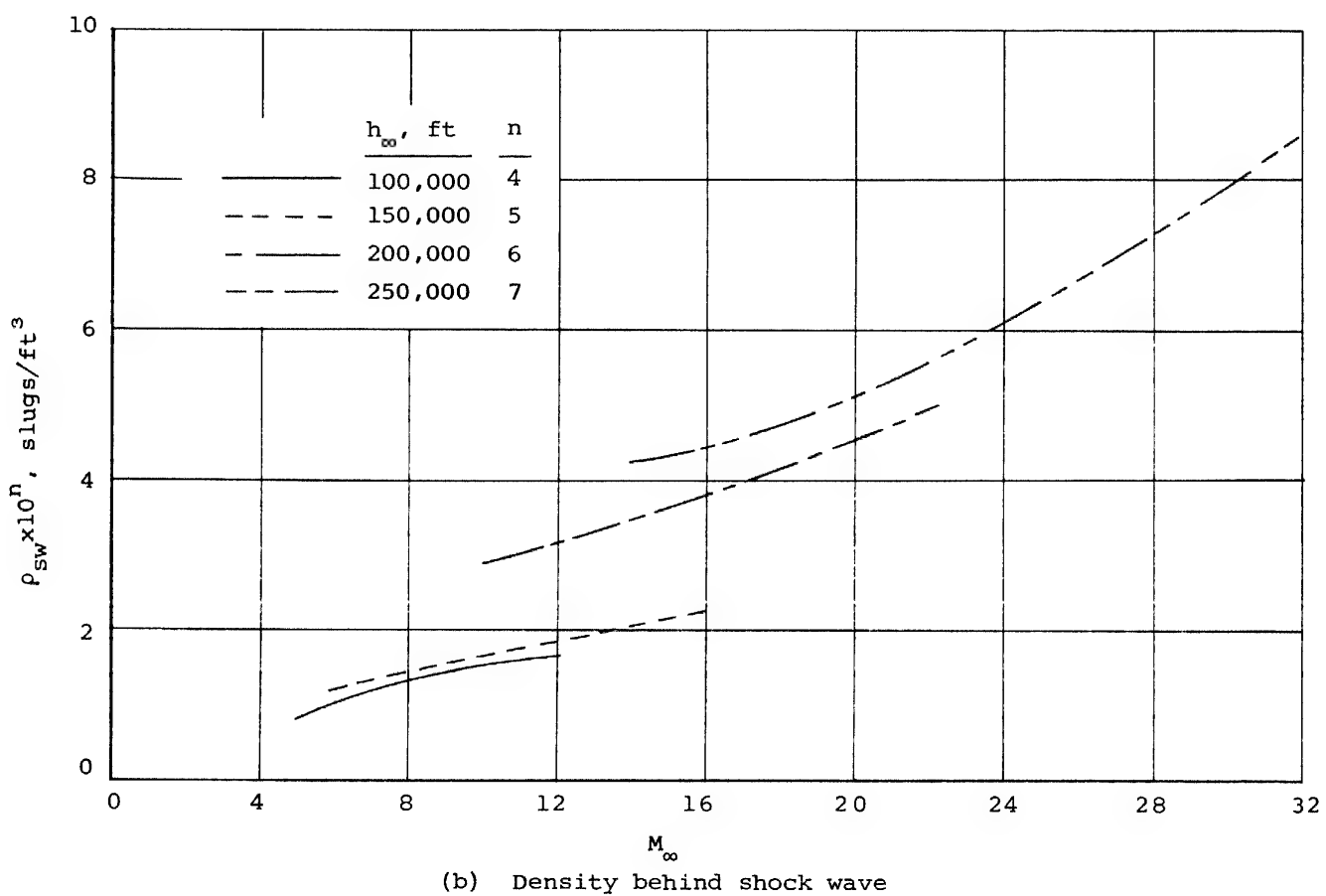
Approved For Release 2000/04/12 : CIA-RDP67B00657R000300070001-0



(a) Temperature behind shock wave

Figure III-13.- Gas properties behind the shock wave (6.0 feet behind the shoulder) on the lower surface of a blunt swept wing. ($\alpha = 20^{\circ}$, $R = 1.0$ ft, $\Lambda = 70^{\circ}$).

Approved For Release 2000/04/12 : CIA-RDP67B00657R000300070001-0



(b) Density behind shock wave

Figure III-13.- Continued.

Approved For Release 2000/04/12 : CIA-RDP67B00657R000300070001-0

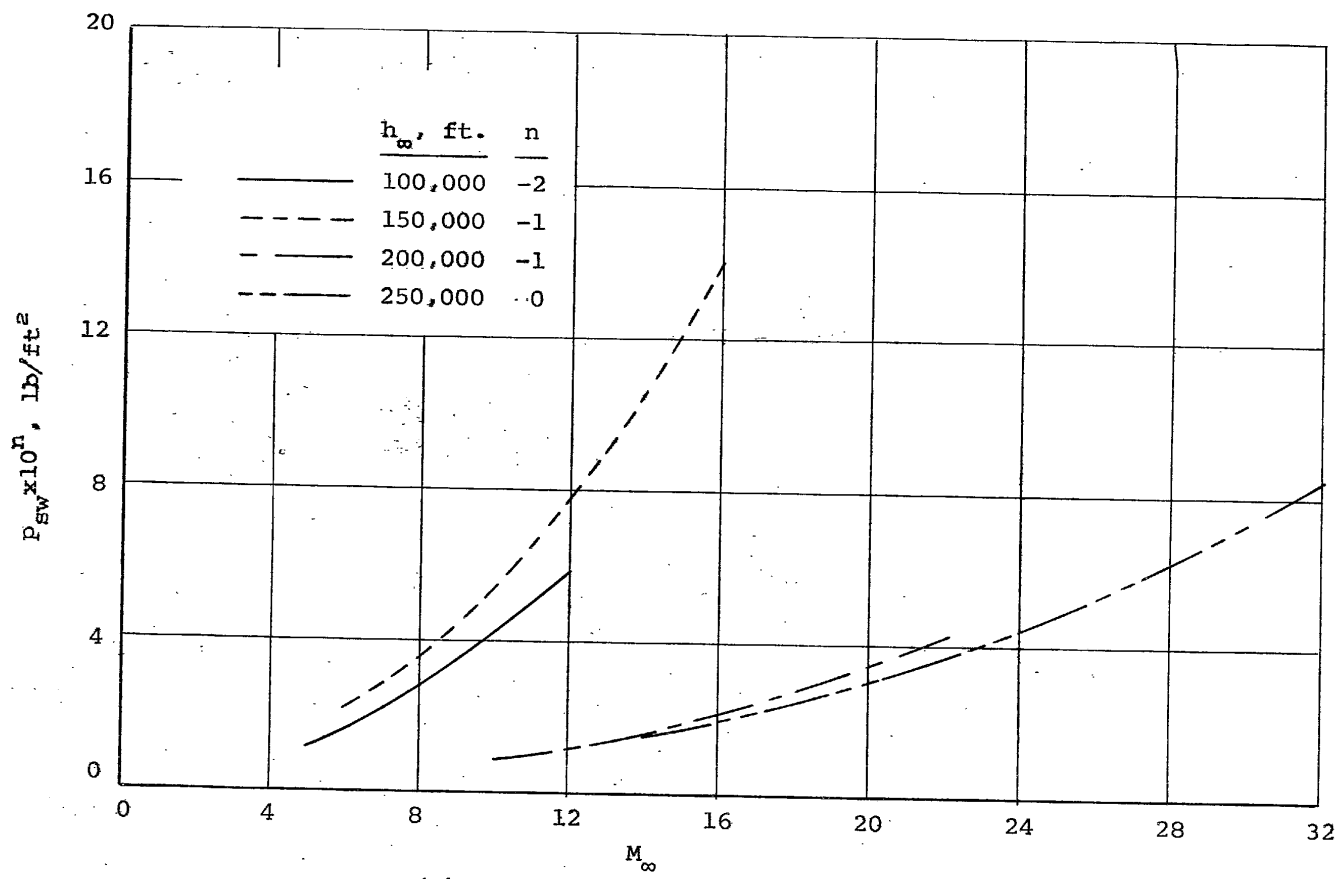


Figure III-13.- Concluded.

Approved For Release 2000/04/12 : CIA-RDP67B00657R000300070001-0

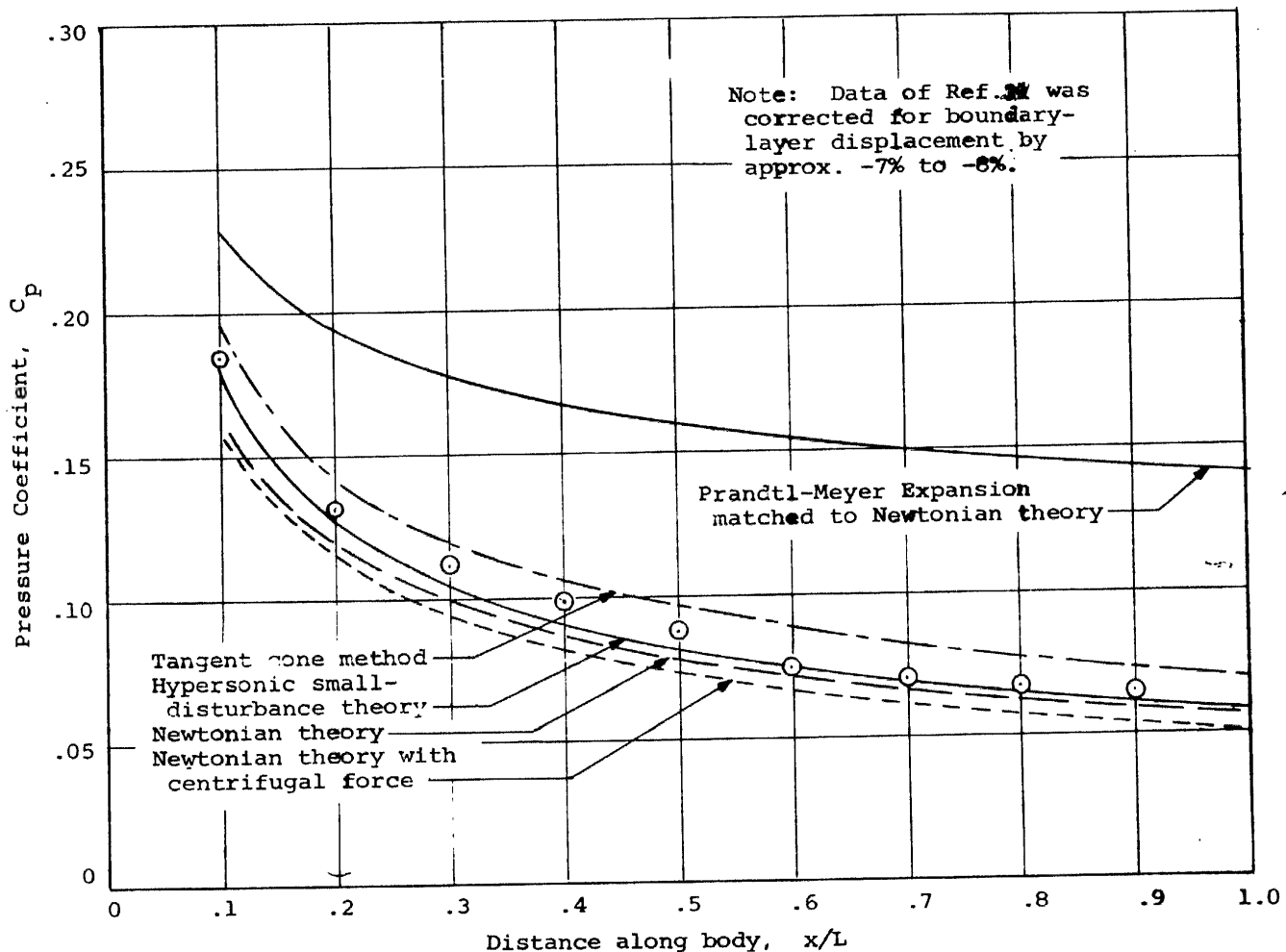


Figure III-14.- Pressure distribution for a 3/4-power body of revolution at $M_\infty = 7.7$, according to data of Reference 21 and several theoretical methods.

Approved For Release 2000/04/12 : CIA-RDP67B00657R000300070001-0

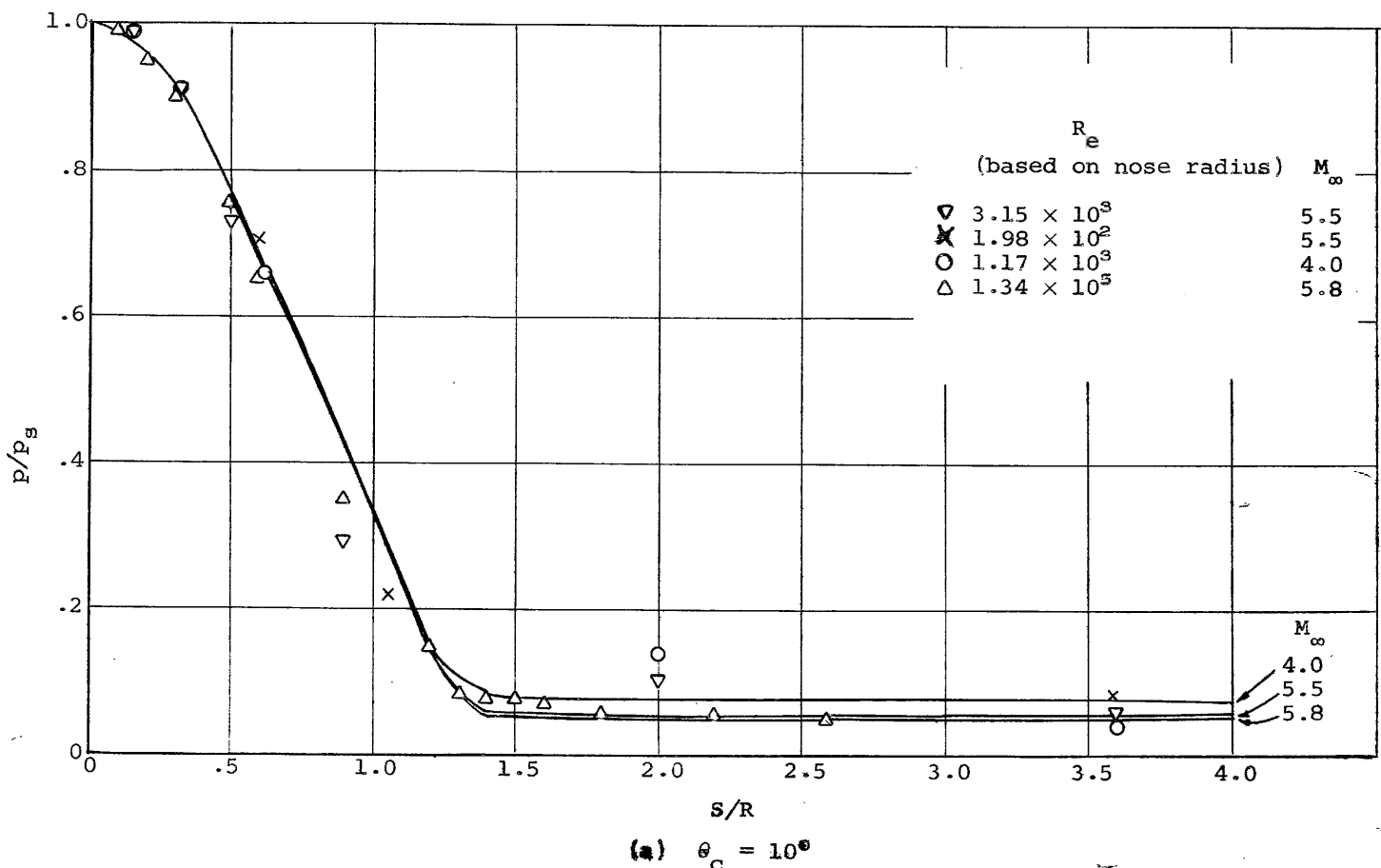


Figure III-13. Comparison of Newtonian impact theory with experimental pressure distributions on blunt cones.

Approved For Release 2000/04/12 : CIA-RDP67B00657R000300070001-0

Approved For Release 2000/04/12 : CIA-RDP67B00657R000300070001-0

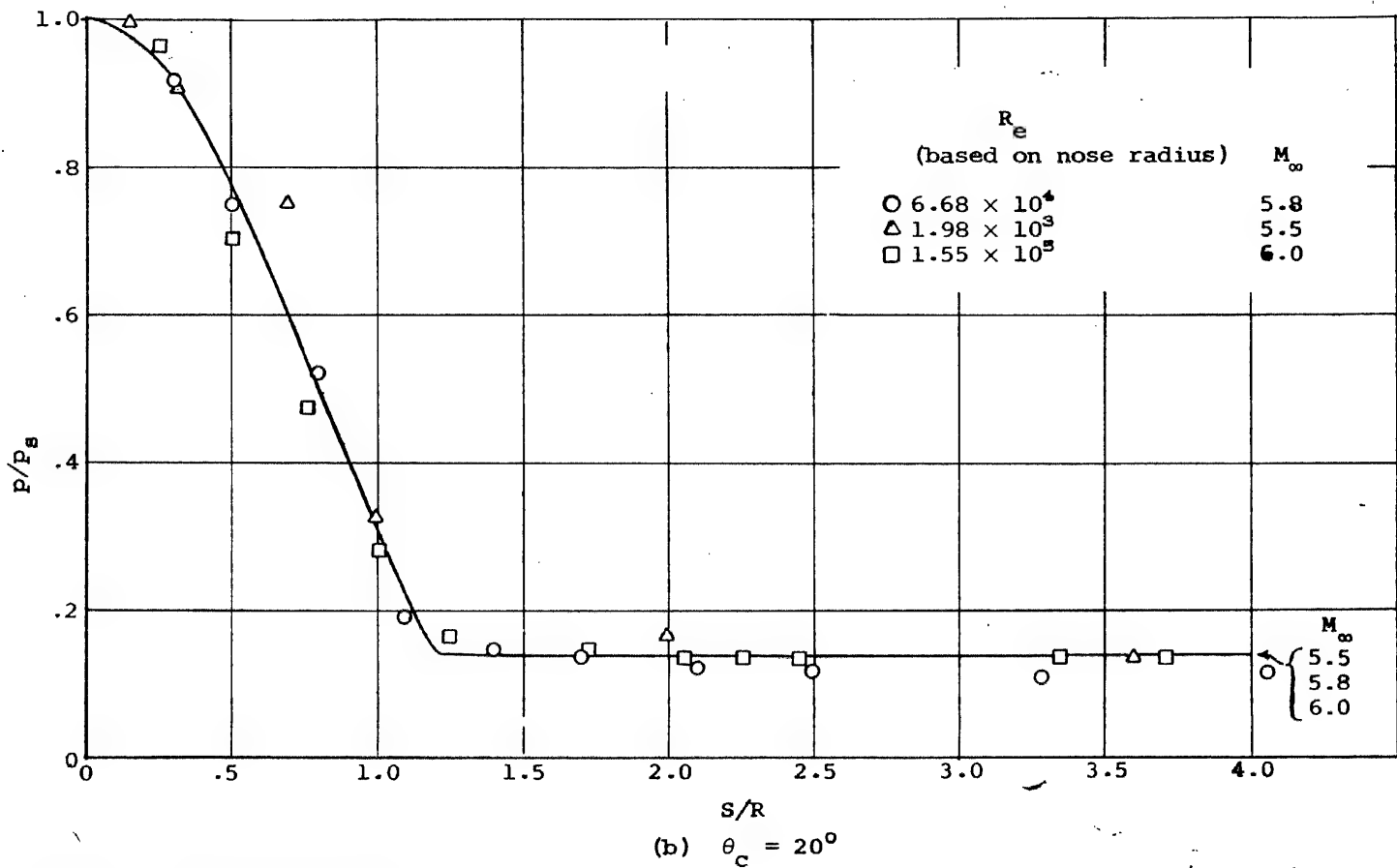


Figure III-15--Concluded.

Approved For Release 2000/04/12 : CIA-RDP67B00657R000300070001-0

Approved For Release 2000/04/12 : CIA-RDP67B00657R000300070001-0

PART IV

Approved For Release 2000/04/12 : CIA-RDP67B00657R000300070001-0

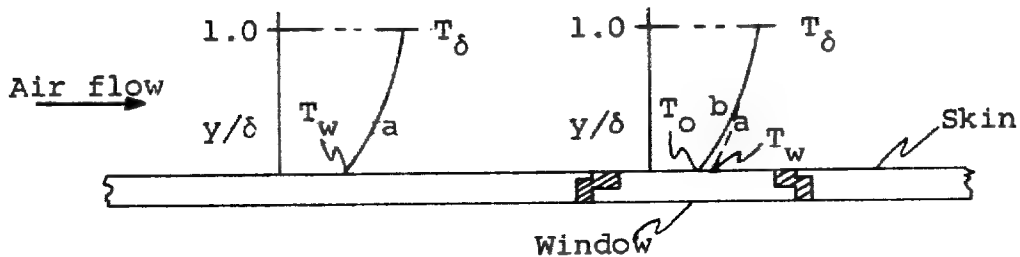
PART IV: DETERMINATION OF BOUNDARY-LAYER CHARACTERISTICS

INTRODUCTION

In the foregoing section, we calculated the shape and location of the shock wave relative to the camera window and determined conditions between the shock wave and at the outer edge of the boundary layer. The purpose of the present section is to determine the details of the flow inside the boundary layer, in particular, the distributions of density and temperature which may be important for the scattering and luminosity calculations, and the boundary layer thickness which we may also need for these calculations. In addition, the details of the boundary layer are required in order to check the assumption made in Part III that the air in the boundary layer came through the normal shock wave.

The boundary-layer characteristics at the location of the camera window depend on the entire history of the boundary layer from the nose to the window. The temperature at the inner edge of the boundary layer is the same as the external skin temperature. This temperature will vary from nose to window because of variation in the aerodynamic heating rate, variations in the ability of the structure to absorb or radiate heat, and so forth. Between the skin in front of the window and the window itself there is, in addition, a material difference which further contributes to the temperature difference.

The implications of this difference between the skin temperature T_w and the window outer temperature T_o can be explained with the aid of the following sketch, which illustrates the highly cooled case.



There will probably be a thermal joint between window and skin which will allow the skin to exist at one general temperature level T_w and the outer window at another temperature level T_o . These temperatures will be different because of the difference in the ability of the skin and window to absorb and radiate heat. By lateral conduction, the window temperatures should be fairly uniform over the outer window surface. At the inner edge of the boundary layer, the air temperature changes abruptly from T_w to T_o in crossing the forward thermal joint. As the flow continues along the window, the boundary-layer profiles change from equilibrium profiles, corresponding to a skin temperature T_w , to those corresponding to T_o . However, for the highly cooled case (i.e., when the stagnation temperatures are much higher than the allowable skin temperature or window temperature), the

change in boundary-layer profile is small. Thus, so long as the window diameter is small compared with the length of boundary layer run ahead of the window, the boundary-layer profiles can be taken to persist over the window. (See Refs. 1 and 2.) Therefore, the boundary-layer thickness at the window δ_w and the temperature and density profiles at the window will be taken as those just ahead of the windows.

The analysis of the present section will be concerned only with determining the character of the boundary layer developed immediately ahead of the camera window and will be independent of the window temperature and any heat transfer through the window, which subjects are treated in Part V. The analysis of this section, however, will rely quite heavily on the analysis of Part V, in particular Appendix VA, for determining the boundary layer growth to the camera window.

SYMBOLS

c_f	skin friction coefficient
f	enthalpy ratio defined by Equation (IV-30)
h_∞	flight altitude, ft
i	enthalpy, ft^2/sec^2
I	total enthalpy, $i + v^2/2$, ft^2/sec^2
m	quantity defined by Equation (IV-17)
M	Mach number
p	static pressure, lb/ft^2
Pr	Prandtl number, taken as 0.72
r_o	parameter to account for boundary layer thinning on three dimensional bodies, ft
R	radius of hemispherical nose, ft
s	distance along surface of vehicle in plane of symmetry measured from stagnation point, ft
T	temperature, $^{\circ}\text{R}$
v	velocity, ft/sec
x	distance measured along flat plate from leading edge, ft
y	coordinate normal to vehicle surface, ft
y	distance defined by Equation (IV-42) and sketch preceding it, ft
Γ	boundary-layer energy thickness, ft
δ	boundary-layer thickness, ft
η	dummy variable introduced by Equation (IV-12), ft
θ	boundary-layer momentum thickness, ft
θ_c	cone semiapex angle, deg

λ coordinate along vehicle surface measure from stagnation point, ft
 μ viscosity, lb-sec/ft²
 ρ air mass density, slugs/ft³
 τ shear stress, lb/ft²

Subscripts

i incompressible
l laminar
t turbulent
w conditions on vehicle surface
b conditions at edge of boundary layer
 ∞ free stream or flight conditions

Superscripts

1 constant in Equation (IV-29), zero for two dimensional flow, one for rotationally symmetric flow
' quantities evaluated at reference enthalpy, Equation (IV-34)

INVESTIGATION

In order to determine the boundary layer characteristics which are required in the present investigation (physical thickness and velocity, temperature and density distributions), an analysis will be developed for determining the physical thickness. All of the other quantities which are required will be obtained in the course of the analysis. Let us first specify certain assumptions which are made in the analysis. These are:

1. The pressure through the boundary layer is constant at the value at the outer edge.
2. The enthalpy through the boundary layer is a linear function of the velocity.
3. Locally, the shapes of the profile (made dimensionless by local thickness and conditions at the edge of the boundary layer) are the same on the configurations being treated as on a flat plate.
4. If the boundary layer is turbulent, it is turbulent from the stagnation point.
5. The transformation used to convert the compressible laminar boundary layer equations to an incompressible layer applies to the turbulent boundary layer also.

The first assumption is that which is usually made in boundary layer work. The second assumption is the usual one when local conditions are to be determined. For a Prandtl

number of unity and zero pressure gradient it can be shown that the enthalpy indeed is a linear function of the velocity. For air at room temperature the Prandtl number is not unity but is 0.72. It has been shown by various investigators, however, that this change in Prandtl number does not change certain boundary layer quantities, such as skin friction, ratio of displacement thickness to momentum thickness, etc., by a large percentage (see for example Refs. 3, 4 and 5). At the higher temperatures encountered in the present work, the Prandtl number does not depart from 0.72 by a large percentage. Hence, the assumption of a Prandtl number of unity should not affect the high temperature results much more significantly than the low temperature results. The third assumption is consistent with the method developed in Part V of this report for determining the surface temperature of the vehicle which will be used in this part. The fourth assumption is made since it simplifies the analysis and gives a conservative estimate of the thickness (a larger thickness than would occur if transition occurred back on the vehicle). Whereas there is not a great deal of information available to justify the fifth assumption, there is some information (Ref. 4 for example) which indicates good agreement between experiment and theories utilizing this approach.

The approach used in determining the boundary layer thickness can be considered in three steps. According to assumption three we are assuming that the ratio of boundary layer momentum thickness to boundary layer thickness for our hypersonic configurations can be simply related to that for a flat plate with a compressible boundary layer and real gas effects. Thus the first step is to derive the flat plate relationships. The second step is to evaluate the boundary layer momentum thickness on the configurations being studied in this report using the method of Part V. Then using the first and second steps we obtain the boundary layer thickness on the example hypersonic configurations as the final step. The boundary layer profiles come out as a by-product of the calculative process.

Derivation of Basic Equations for a Flat Plate

By definition the local skin-friction coefficient for a compressible boundary layer is related to the shearing stress τ as follows:

$$c_f = \frac{\tau}{(1/2)\rho_\delta v_\delta^2} \quad (IV-1)$$

where the subscript δ indicates conditions at the edge of the boundary layer as determined by the methods of Part III. Let us now define an incompressible boundary layer at an undetermined temperature T' and density ρ' which are

uniform through the boundary layer and at the same shearing stress τ , velocity v_δ , and uniform pressure through the boundary layer p_δ as the compressible boundary layer.

$$c_f' = \frac{\tau}{(1/2)\rho' v_\delta^2} \quad (IV-2)$$

These two skin-friction coefficients are, therefore, related by the ratio of the densities.

$$\frac{c_f'}{2} = \frac{\rho'}{\rho_\delta} \frac{c_f'}{2} \quad (IV-3)$$

From Reference 3, the laminar and turbulent skin-friction coefficients on a flat plate with zero pressure gradient in incompressible flow are given by

$$\frac{c_{f_l}'}{2} = 0.332 \left(\frac{\rho_l' v_\delta x}{\mu_l'} \right)^{-1/2} \quad \left. \right\} \quad (IV-4)$$

and

$$\frac{c_{f_t}'}{2} = 0.0289 \left(\frac{\rho_t' v_\delta x}{\mu_t'} \right)^{-1/5} \quad \left. \right\} \quad (IV-4)$$

where the subscripts l and t indicate laminar and turbulent respectively. By combining Equations (IV-3) and (IV-4), the compressible skin friction coefficients are

$$\frac{c_{f_l}'}{2} = 0.332 \left(\frac{\rho_l' \mu_l'}{\rho_\delta \mu_\delta} \right)^{1/2} \left(\frac{\rho_\delta v_\delta x}{\mu_\delta} \right)^{-1/2} \quad \left. \right\} \quad (IV-5)$$

$$\frac{c_{f_t}'}{2} = 0.0289 \left(\frac{\rho_t'}{\rho_\delta} \right) \left(\frac{\mu_t' \rho_\delta}{\mu_\delta \rho_t'} \right)^{1/5} \left(\frac{\rho_\delta v_\delta x}{\mu_\delta} \right)^{-1/5} \quad \left. \right\} \quad (IV-5)$$

The von Karman momentum equation reduces to the following expression for flow on a flat plate with zero pressure gradient

$$\frac{c_f}{2} = \frac{d\theta}{dx} \quad (IV-6)$$

where θ is the momentum thickness. Therefore, by combining Equations (IV-5) and (IV-6) and integrating, the following expressions are obtained for the laminar and turbulent momentum thicknesses on a flat plate of uniform temperature

$$\left. \begin{aligned} \theta_l &= 0.664 \left(\frac{\rho_l' \mu_l'}{\rho_0 \mu_0} \right)^{1/2} \left(\frac{\rho_0 v_0}{\mu_0} \right)^{-1/2} x^{1/2} \\ \theta_t &= 0.0361 \left(\frac{\rho_t'}{\rho_0} \right) \left(\frac{\mu_t' \rho_0}{\mu_0 \rho_t} \right)^{1/5} \left(\frac{\rho_0 v_0}{\mu_0} \right)^{-1/5} x^{4/5} \end{aligned} \right\} \quad (IV-7)$$

The momentum thickness of a laminar incompressible boundary layer on a flat plate at temperature T_0 and density ρ_0 is from Reference 4

$$\theta_{i_l} = 0.664 \left(\frac{\rho_0 v_0}{\mu_0} \right)^{-1/2} x^{1/2} \quad (IV-8)$$

and that for the turbulent layer from the same reference is

$$\theta_{i_t} = 0.0361 \left(\frac{\rho_0 v_0}{\mu_0} \right)^{-1/5} x^{4/5} \quad (IV-9)$$

The compressible boundary layer momentum thickness can, therefore, be expressed in terms of the incompressible thickness.

$$\left. \begin{aligned} \theta_l &= \left(\frac{\rho_l' \mu_l'}{\rho_0 \mu_0} \right)^{1/2} \theta_{i_l} \\ \theta_t &= \left(\frac{\rho_t'}{\rho_0} \right) \left(\frac{\mu_t' \rho_0}{\mu_0 \rho_t'} \right)^{1/5} \theta_{i_t} \end{aligned} \right\} \quad (IV-10)$$

Even though these relationships have been developed for a flat plate, they become more general if assumption three is employed.

By definition the momentum thickness of a compressible boundary layer is given by the following integral expression.

$$\theta = \int_0^{\delta} \frac{\rho v}{\rho_0 v_0} \left(1 - \frac{v}{v_0} \right) dy \quad (IV-11)$$

Let us now make the following substitution

$$\int_0^{\eta_0} d\eta = \eta_0 = \int_0^{\delta} m \frac{\rho}{\rho_0} dy \quad (IV-12)$$

and assume the nondimensional velocity v/v_0 is a function of η/η_0 only. Chapman and Rubesin (Ref. 6) make this assumption for an ideal gas. The quantity η can be considered as a distance normal to the plate which is a distortion of the actual y distance. The distortion is made in such a way that the velocity profile on a nondimensional

basis with the density profile resulting from compressible flow and real gas effects is the same as the velocity profile for a reference incompressible boundary layer. It is convenient to think of η as a simple distortion to the y scale. Therefore

$$\theta = \frac{1}{m} \int_0^{\eta_0} \frac{v}{v_0} \left(1 - \frac{v}{v_0}\right) d\eta \quad (IV-13)$$

The momentum thickness of an incompressible boundary layer of thickness η_0 is defined as

$$\theta_i = \int_0^{\eta_0} \frac{v}{v_0} \left(1 - \frac{v}{v_0}\right) d\eta \quad (IV-14)$$

so that the compressible momentum thickness can be written as

$$\theta = \frac{\theta_i}{m} \quad (IV-15)$$

For the laminar and turbulent boundary layers this expression is

$$\left. \begin{aligned} \theta_l &= \frac{\theta_i l}{m_l} \\ \theta_t &= \frac{\theta_i t}{m_t} \end{aligned} \right\} \quad (IV-16)$$

A comparison of Equations (IV-10) and (IV-16) gives

$$\left. \begin{aligned} \frac{1}{m_l} &= \left(\frac{\rho_l' \mu_l'}{\rho_0 \mu_0} \right)^{1/2} \\ \frac{1}{m_t} &= \left(\frac{\rho_t'}{\rho_0} \right) \left(\frac{\mu_t' \rho_0}{\mu_0 \rho_t'} \right)^{1/5} \end{aligned} \right\} \quad (IV-17)$$

as the values of the constants relating the compressible boundary layer momentum thickness to the incompressible boundary layer momentum thickness which has the same properties as those at the edge of the compressible layer.

Let us now determine the ratio of the incompressible momentum thickness to the incompressible physical thickness on a flat plate, that is, the ratio of θ_i to η_6 . To do this we must treat the laminar and turbulent cases separately.

For the case of the laminar boundary layer we will assume a Blasius velocity profile (Ref. 4). The results of a numerical solution of the Blasius equation for flow on a flat plate are presented on page 107 of Reference 4 and those which we shall require are presented in Table IV-1 at the end of this part of the present report. In the Blasius velocity profile the velocity approaches the velocity at the edge of the boundary layer asymptotically. Consequently, we shall define the physical thickness η_6 as being the distance outward at which the local velocity in the boundary layer has reached 99 percent of the velocity at the edge of the boundary layer. Therefore, from Table IV-1 we find on a flat plate that

$$\eta_{6,1} \approx 5.0 \left(\frac{\rho_6 v_6}{\mu_6} \right)^{-1/2} x^{1/2} \quad (IV-18)$$

and by combining Equation (IV-8) with this result we find

$$\frac{\theta_{i_l}}{\eta_{\delta_l}} = \frac{0.664}{5.0} = 0.133 \quad (IV-19)$$

In the case of the turbulent boundary layer we shall assume that the velocity in the boundary layer varies as some power of the distance outward through the boundary layer. Consistent with the skin friction relationship of Equation (IV-5) this can be written

$$\frac{V}{V_{\delta}} = \left(\frac{\eta}{\eta_{\delta_t}} \right)^{1/7} \quad (IV-20)$$

for the velocity distribution through the boundary layer on a flat plate. An integration of Equation (IV-14) using this distribution gives the following value of the ratio of the momentum thickness to physical thickness (Ref. 4) for a flat plate

$$\frac{\theta_{i_t}}{\eta_{\delta_t}} = \frac{7}{72} = 0.0972 \quad (IV-21)$$

Equation (IV-19) and (IV-21) can now be combined with Equation (IV-16) to give the thicknesses in terms of the momentum thicknesses of the compressible boundary layers

$$\left. \begin{aligned} \eta_{\delta_l} &= \frac{m_l \theta_l}{0.133} \\ \eta_{\delta_t} &= \frac{m_t \theta_t}{0.0972} \end{aligned} \right\} \quad (IV-22)$$

where m_l and m_t are given by Equation (IV-17).

Momentum Thickness on Hypersonic Configurations

To determine the compressible momentum thickness we shall make use of the analysis of Appendix VA of Part V of the present report. The method presented there will allow us to calculate the momentum thickness on the configurations of interest in this study (Part II) whereas Equation (IV-7) of this part is for a flat plate. This implies the assumption that the ratio of θ to η_0 on the three dimensional configurations we are treating is the same as on a flat plate.

Equation (VA-32) defines the following integral expression for the energy thickness of the boundary layer.

$$\Gamma = \int_0^{\delta} \frac{\rho V (I_0 - I)}{\rho_0 V_0 (I_0 - I_w)} dy \quad (IV-23)$$

where I is the total enthalpy.

$$I = i + \frac{V^2}{2} \quad (IV-24)$$

Let us now make the assumption that locally the total enthalpy is a linear function of the velocity.

$$I = i + \frac{V^2}{2} = AV + B \quad (IV-25)$$

Therefore

$$I_0 = i_0 + \frac{V_0^2}{2} = AV_0 + B \quad \left. \right\} \quad (IV-26)$$

and

$$I_w = i_w + \frac{0}{2} = B$$

By substituting Equations (IV-25) and (IV-26) into (IV-23)

$$\Gamma = \int_0^{\delta} \frac{\rho v}{\rho_0 v_0} \frac{(Av_0 + B - Av - B)}{(Av_0 + B - B)} dy = \int_0^{\delta} \frac{\rho v}{\rho_0 v_0} \left(1 - \frac{v}{v_0}\right) dy \quad (IV-27)$$

A comparison of this expression with Equation (IV-11), the definition of momentum thickness, shows that

$$\Gamma = \theta \quad (IV-28)$$

Therefore, Equations (VA-56) and (VA-57) can be used to determine the laminar and turbulent momentum thicknesses.

$$\left. \begin{aligned} \theta_l^2 &= \frac{1}{(r_0 l \rho_0 v_0)^2} \int_0^{\delta} \left[\frac{0.332 (\rho_l' / \rho_0) f_l r_0 l \rho_0 v_0}{(\text{Pr})^{2/3} (\rho_l' v_0 / \mu_l')^{1/2} (1/2)^{1/2}} \right]^2 \frac{dr}{1/2} \\ \theta_t^{5/4} &= \frac{1}{(r_0 l \rho_0 v_0)^{5/4}} \int_0^{\delta} \left[\frac{0.0296 (\rho_t' / \rho_0) f_t r_0 l \rho_0 v_0}{(\text{Pr})^{2/3} (\rho_t' v_0 / \mu_t')^{1/5} (4/5)^{1/5}} \right]^{5/4} \frac{dr}{4/5} \end{aligned} \right\} \quad (IV-29)$$

The functions f_l and f_t are

$$\left. \begin{aligned} f_l &= \frac{i_0 + (\text{Pr})^{1/2} (v_0^2/2) - I_w}{i_0 + (v_0^2/2) - I_w} \\ f_t &= \frac{i_0 + (\text{Pr})^{1/3} (v_0^2/2) - I_w}{i_0 + (v_0^2/2) - I_w} \end{aligned} \right\} \quad (IV-30)$$

Boundary Layer Thickness on Hypersonic Configurations

This determination of the momentum thickness will allow us to evaluate η_{δ_l} and η_{δ_t} given by Equation (IV-22). To determine the actual physical thickness we must go back to

Equation (IV-12), the substitution made earlier. A reversal of this substitution gives

$$\left. \begin{aligned} \delta_l &= \frac{1}{m_l} \int_0^{\eta_{\delta_l}} \frac{\rho_{\delta}}{\rho} d\eta \\ \delta_t &= \frac{1}{m_t} \int_0^{\eta_{\delta_t}} \frac{\rho_{\delta}}{\rho} d\eta \end{aligned} \right\} \quad (IV-31)$$

These expressions are then evaluated taking into account real gas effects by making use of the specified velocity profile and the assumption that the total enthalpy is a linear function of the velocity. This method of evaluation will be described in detail in the next section.

Calculative Method

The preceding section has presented a derivation of the basic equations needed to determine the boundary layer characteristics required in the present study. It is the purpose of this section to outline the calculative method which will produce the desired quantities.

In order to proceed with the calculation we must first specify the configuration (i.e. blunt cone or blunt swept wing), the point on the vehicle at which the boundary layer characteristics are to be determined (the camera window for this investigation), and the flight conditions of the vehicle (i.e. flight altitude and flight Mach number).

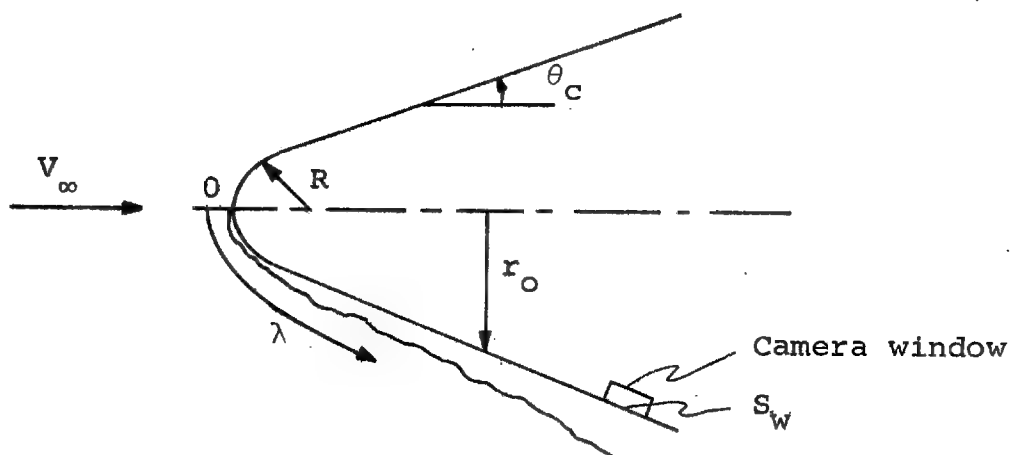
The first step in the calculation is to use the methods presented in Part III to determine the conditions at the edge of the boundary layer (ρ_6 , v_6 , p_6 , and T_6) as a function of distance along the surface of the vehicle, λ , from the stagnation point. Next, the method of Part III is used to determine whether the boundary layer over the camera window is laminar or turbulent.

Calculation of Momentum Thickness.-

This information having been determined allows us to select the correct equation of Equations (IV-29) for the calculation of the boundary layer momentum thickness at the camera window. These equations at this point are

$$\begin{aligned}
 \left(\theta_l^2\right)_{s_w} &= \frac{1}{(r_o^l \rho_6 v_6)_{s_w}^2} \\
 &\int_0^{s_w} \left[\frac{0.332 (\rho_l' / \rho_6) f_l r_o^l \rho_6 v_6}{(Pr)^{2/3} (\rho_l' v_6 / \mu_l')^{1/2} (1/2)^{1/2}} \right]^{1/2} \frac{d\lambda}{1/2} \\
 \left(\theta_t^{5/4}\right)_{s_w} &= \frac{1}{(r_o^l \rho_6 v_6)_{s_w}^{5/4}} \\
 &\int_0^{s_w} \left[\frac{0.0296 (\rho_t' / \rho_6) f_t r_o^l \rho_6 v_6}{(Pr)^{2/3} (\rho_t' v_6 / \mu_t')^{1/5} (4/5)^{1/5}} \right]^{5/4} \frac{d\lambda}{4/5}
 \end{aligned} \tag{IV-32}$$

The quantity ahead of the integral sign is evaluated at the camera window, and the integral itself is integrated graphically from the stagnation point to the window. The parameter r_o^l takes into account the thinning of the boundary layer caused by the expanding body. On the cone the exponent l is 1.0 and on the wing it is zero since in Part V the flow along the centerline of the wing is treated as two dimensional. On the blunt cone r_o is (as can be seen from the following sketch)



$$\begin{aligned}
 r_o &= R \sin \left(\frac{\lambda}{R} \right) & , \lambda \leq R \left(\frac{90^\circ - \theta_c}{57.3} \right) \\
 r_o &= R \cos \theta_c + \left[\lambda - R \left(\frac{90^\circ - \theta_c}{57.3} \right) \right] \sin \theta_c, \lambda \geq R \left(\frac{90^\circ - \theta_c}{57.3} \right)
 \end{aligned} \quad \left. \right\} \text{ (IV-33)}$$

On the blunt swept wing r_o equals 1.0.

The quantities in Equation (IV-32) which remain to be specified are those with a prime for a superscript and the functions f_l and f_t . These require a knowledge of the

variation in surface temperature, T_w , with distance λ . This is determined by the method of Part V. With this temperature and the variation of the local pressure at the edge of the boundary layer, p_δ , with λ , the wall enthalpy variation with λ can be found. The pressure through the boundary layer is assumed constant so that each combination of p_δ and T_w determine a point on a chart of the thermodynamic properties of equilibrium air (Ref. 7 or 8) and the wall enthalpy, i_w , ($I_w = i_w$ since $v_w = 0$) can be read. In a similar manner p_δ and T_δ determine a point and i_δ can be read. Consequently, f_l or f_t (Equation (IV-30)) can be found as a function of λ .

The reference quantities ρ' and μ' can be found, as a function of λ , from the reference enthalpy i' , and the pressure p_δ at the edge of the boundary layer with the help of the thermodynamic chart. The reference enthalpies for the laminar and turbulent cases are (References 9 and 10)

$$i_l' = 0.23 i_\delta + 0.19 \left[i_\delta + \text{Pr}^{1/2} \left(\frac{v_\delta^2}{2} \right) \right] + 0.58 i_w \quad \text{and} \quad \left. \begin{array}{l} i_t' = 0.36 i_\delta + 0.19 \left[i_\delta + \text{Pr}^{1/3} \left(\frac{v_\delta^2}{2} \right) \right] + 0.45 i_w \end{array} \right\} \text{IV-34}$$

The viscosity μ' is a function of the reference temperature T'

$$\mu' = 2.27 \times 10^{-8} \frac{(T')^{3/2}}{(T' + 202)} \quad \text{IV-35}$$

Calculation of η_0 .-

After the graphical integration, θ is known and we are ready to determine η_0 from Equation (IV-22). For this purpose the value of m given by Equation (IV-17) is required. The values of ρ' , μ' , ρ_0 and μ_0 are those at the camera window. All of these quantities were determined in the calculation of the momentum thickness, θ , except for μ_0 . This quantity is

$$\mu_0 = 2.27 \times 10^{-8} \frac{(T_0)^{3/2}}{(T_0 + 202)} \quad (IV-36)$$

Calculation of Boundary Layer Thickness and Boundary Layer Profiles.-

Equation (IV-31) can now be evaluated to determine the actual physical thickness of the boundary layer at the camera window. In the process of doing this, we shall also obtain ρ and T as a function of (η/η_0) . The values of ρ and T will then be known as functions of (y/δ) , in which form they are the density and temperature profiles within the boundary layer at the camera window.

Let us rewrite Equation (IV-31) in the following form to determine the boundary layer thickness

$$\left. \begin{aligned} \delta_l &= \frac{\eta_0 \rho_0}{m_l} \int_0^1 \frac{1}{\rho} d(\eta/\eta_0) \\ \delta_t &= \frac{\eta_0 \rho_0}{m_t} \int_0^1 \frac{1}{\rho} d(\eta/\eta_0) \end{aligned} \right\} \quad (IV-37)$$

The quantities ahead of the integral have been determined previously so that all that remains to be determined is the density profile as a function of η/η_5 . This profile can be found if we can specify two of the gas properties variations through the boundary layer as a function of η/η_5 . Then with the aid of a chart of the thermodynamic properties of air in chemical equilibrium (Ref. 7 or 8), the values of ρ as a function of η/η_5 and also T can be determined. The first gas property which is specified is the pressure. Since we have assumed the pressure through the boundary layer to be constant, we have

$$p = f(\eta/\eta_5) = p_5 \quad (\text{IV-38})$$

The second quantity which is determined as a function of (η/η_5) is the enthalpy, i. The assumption has been made that the total enthalpy is a linear function of the velocity

$$, I = i + \frac{V^2}{2} = AV + B \quad (\text{IV-39})$$

The two boundary conditions are that at the wall

$$\eta = 0, V = 0 \text{ and } I = I_w = i_w$$

and at the edge of the boundary layer

$$\eta = \eta_5, V = V_5 \text{ and } I = I_5 = i_5 + \frac{V_5^2}{2}$$

By imposing these boundary conditions we find that

$$B = i_w$$

and

$$A = \frac{1}{V_0} \left(i_0 - i_w + \frac{V_0^2}{2} \right)$$

Therefore, Equation (IV-39) becomes

$$I = i + \frac{V^2}{2} = \frac{V}{V_0} \left(i_0 - i_w + \frac{V_0^2}{2} \right) + i_w$$

and

$$i = \frac{V}{V_0} (i_0 - i_w) + \frac{V_0^2}{2} \left(\frac{V}{V_0} - \frac{V^2}{V_0^2} \right) + i_w \quad (IV-40)$$

The local enthalpy has now been expressed in terms of known enthalpies, the velocity at the edge of the boundary layer, and the local velocity. When Equation (IV-12) was introduced, it was assumed that the velocity was a function of η/η_0 only. In fact the Blasius distribution of Table (IV-1) was assumed for the laminar boundary layer and the profile of Equation (IV-20) was assumed for the turbulent boundary layer. Hence, V/V_0 is known as a function of η/η_0 and, therefore, the enthalpy variation of Equation (IV-40) is known. Thus, we have the local pressure, p , (Eq. (IV-38)) and the local enthalpy, i , (Eq. (IV-40)) variations and with the aid of Reference 7 or 8 the corresponding variations of density, ρ , and temperature, T , can be found. Equation (IV-37) can now

be integrated graphically to determine the boundary layer thickness, δ .

The density, ρ , temperature, T , and velocity, v , are now known as a function of η/η_δ . They must now be specified as functions of y/δ . Consequently, the relationship between η/η_δ and y/δ must be established. This can be done from Equation (IV-31). From this equation the following expressions can be written

$$dy = \frac{1}{m} \frac{\rho_\delta}{\rho} d\eta$$

Therefore

$$y = \frac{\rho_\delta \eta_\delta}{m} \int_0^{\eta/\eta_\delta} \frac{1}{\rho} d(\eta/\eta_\delta)$$

and

$$\delta = \frac{\rho_\delta \eta_\delta}{m} \int_0^1 \frac{1}{\rho} d(\eta/\eta_\delta)$$

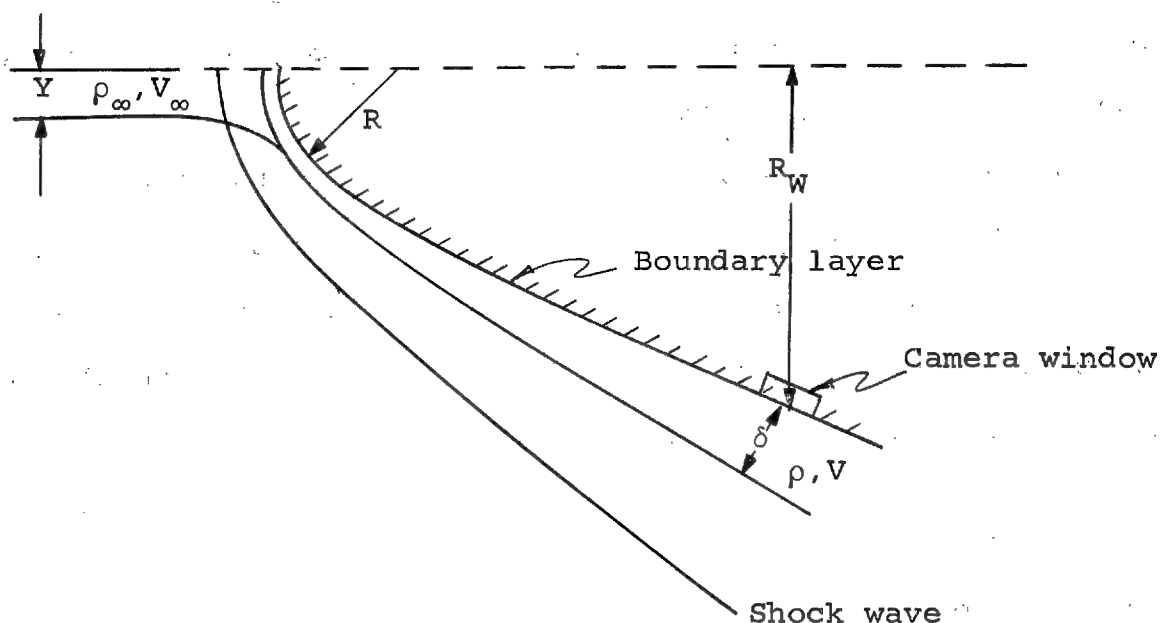
By dividing we find

$$\frac{y}{\delta} = \frac{\int_0^{\eta/\eta_\delta} \frac{1}{\rho} d(\eta/\eta_\delta)}{\int_0^1 \frac{1}{\rho} d(\eta/\eta_\delta)} \quad (IV-41)$$

so that y/δ can be evaluated as a function of η/η_δ . Thus we have ρ , T , and v as functions of y/δ .

Calculation of Boundary Layer Mass Flow.-

One other quantity of interest is the mass flow in the boundary layer. This is of interest in order to check the assumption of Part III that the air in the boundary layer all came through a normal shock wave. Consider the following sketch.



The free stream air ahead of the shock wave is at constant density and velocity and the boundary layer air at the camera window is at varying density and velocity as was just determined. If the mass flow in the boundary layer at the window is equated to the mass flow in a free-stream stream tube of width Y , we obtain the following two relationships.

For the three dimensional cone

$$\pi Y^2 \rho_\infty V_\infty = 2\pi R_W \int_0^\delta \rho V dy \quad (IV-42)$$

and for the two-dimensional wing

$$Y \rho_\infty V_\infty = \int_0^\delta \rho V dy \quad (IV-43)$$

The solution of these equations for Y will give the stream tube size ahead of the shock wave which has the same mass flow as the boundary layer at the camera window.

In order for the assumption to be valid that the air at the edge of the boundary layer undergoes a normal shock, Y must be small compared to the nose radius of the vehicle, R . For a shock wave of the same radius of curvature as the vehicle nose, the shock wave angle at Y is (see Part III)

$$90^\circ - \epsilon = \sin^{-1} \frac{Y}{R}$$

For a value of Y of $0.15 R$ where $R = 1.0$ ft.

$$\epsilon \approx 81.4 \text{ deg.}$$

RESULTS AND DISCUSSION

A method has been presented in this part of the report for determining the following boundary-layer characteristics:

1. Thickness
2. Velocity profile
3. Temperature profile

4. Density profile

5. Mass flow

The luminosity calculations which will be made for Part VI of this report require the thickness and temperature and density profiles in the boundary layer. The optical resolution studies of Part VII will require the density profile and the thickness. The assumption has been made in the analysis of Parts III and V that the air in the boundary layer at the camera window came through the normal part of the shock wave ahead of the vehicle. To check this assumption the mass flow in the boundary layer is required.

Appendix IVA and Figures IV-1 and IV-2 present a sample calculation of the above quantities in order to illustrate the calculative procedure outlined in the preceding section. The results of the calculations made for the two configurations and the flight conditions outlined in Part II are presented in Figures IV-3 through IV-8. All of the calculations have been made assuming the boundary layer to be laminar. In Part III it was found that at all altitudes except 100,000 feet this was certainly the case. Based on the transition criterion used in Part III, the camera window was quite close to the transition point at 100,000 feet.

Figures IV-3 and IV-4 present the density and temperature profiles at the camera window calculated for the hemispherically blunted cone. Figures IV-5 and IV-6 show the results of the

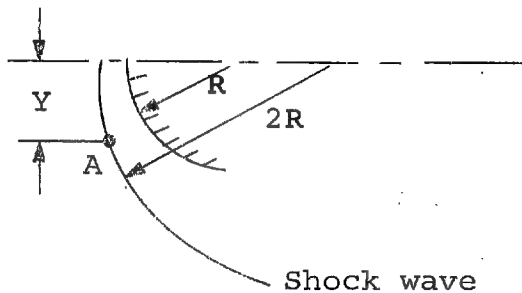
same calculations made for the blunt swept wing configuration. The calculations for both vehicles exhibit the same characteristics. At the lower Mach numbers and altitudes, the density has a minimum and the temperature has a maximum at the middle of the boundary layer. For most of the Mach-number-altitude regime, the boundary layer remains at essentially constant density and temperature for about 80 percent of the distance from the outside of the boundary layer ($y/\delta = 1.0$) to the wall ($y/\delta = 0.0$) with most of the change taking place right near the wall.

The actual density and temperature profiles, rather than the dimensionless ones, can be obtained by using the values of ρ_δ and T_δ calculated in Part III.

Figure IV-7 presents the results of the boundary layer thickness, δ , calculations. In these plots δ has been divided by the shock wave standoff distance, Δ , which was found in Part III. As can be seen, at an altitude of 250,000 feet boundary layer thicknesses occur equal to or greater than the shock wave standoff distances. This indicates that the assumption in Part III that the boundary layer is thin compared to the shock standoff distance is no longer valid. The air at 250,000 feet is so thin that low density effects are important and modification of the methods presented for computing the flow field is indicated. The first modification is that the shock standoff distance should now be measured from the displacement

thickness of the boundary layer rather than from the vehicle surface.

Another assumption made in Part III and in this part of the report is that all of the air in the boundary layer came through a nearly normal shock wave. The calculations shown in Figure IV-8 were made to check this assumption. In this figure the radius, Y , of the free-stream stream tube which has the same mass flow as that in the boundary layer at the camera window is plotted. If Y is compared to the radius of curvature of the shock wave at the nose of the vehicle, the previously mentioned assumption can be checked. Near the stagnation point it does not appear too unreasonable to assume that the shock wave radius of curvature is twice that of the nose as shown in the following sketch



Then at point A the shock wave slope ϵ is

$$\epsilon = - \sin^{-1} \frac{Y}{2R} + 90^\circ$$

For the worst case shown in Figure IV-8, Y is approximately 0.8 feet. Therefore, the shock wave slope corresponding to

this γ is about 66.5° . Hence, at the highest altitude, 250,000 feet, the assumption is beginning to be contradicted. Because of this, the results to be presented for this altitude are probably not as good as for the lower altitudes. The accuracy of the solution can be increased by iterating the present calculation taking into account the obliquity of the bow wave.

CONCLUSIONS

In this part of the present report, a method is developed, which utilizes the analysis presented in Part V, for determining the boundary layer characteristics (thickness; velocity, temperature and density profiles; and mass flow) of the configurations of Part II. A sample calculation is presented in Appendix IVA.

The results of the thickness and mass flow calculations can be used to check some of the assumptions made in the flow field computations of the present report, Parts III, IV, and V, for the configurations and flight conditions of Part II. These results indicate the following:

1. The assumption of a boundary layer which is thin compared to the shock wave standoff distance is quite good to altitudes of 200,000 feet.
2. The assumption that all of the air in the boundary layer came through a nearly normal shock wave is also valid to a 200,000-foot altitude but above this begins to break down.

In summary, it appears that the methods presented in Parts III, IV and V for determining the flow fields surrounding the vehicles of Part II can be used with a fair degree of confidence up to altitudes of 200,000 feet.

APPENDIX IVA

NUMERICAL EXAMPLE OF THE DETERMINATION OF THE
BOUNDARY LAYER CHARACTERISTICS

As a numerical example illustrating the calculative method of this part of the report, let us select the same flight conditions and configuration as were used in the calculative example of Appendix VC. This is done since we will have need for the results of that example. The conditions are:

1. Configuration - blunt cone (Fig. II-1(a))
2. Mach number - $M_\infty = 16$
3. Altitude - $h_\infty = 200,000$ ft
4. Boundary layer type - laminar
5. Free-stream conditions from Reference 11

Temperature - $T_\infty = 449^\circ$ R

Pressure - $p_\infty = 4.7151 \times 10^{-1}$ lb/ft²

Density - $\rho_\infty = 6.1180 \times 10^{-7}$ slugs/ft³

Speed of sound - $a_\infty = 1038.7$ ft/sec

The first quantity to be calculated is the boundary layer momentum thickness at the camera window θ_1 which is given by Equation (IV-32). This involves a numerical integration from the stagnation point ($\lambda = 0$) to the window ($\lambda = S_w$).

$$S_w = R \frac{(90 - \theta_c)}{57.3} + L_w \quad (\text{IVA-1})$$

$$= 7.484 \text{ ft}$$

where L_w is the distance along the surface from the shoulder to the window (6 ft).

Let us now evaluate the quantity ahead of the integral sign. The exponent of r_o is 1.0 for the blunt cone so that at the window Equation (IV-33) gives

$$r_o = 1.52 \text{ ft}$$

By combining this with ρ_δ and v_δ at the window from Figure III-5 of Part III we have

$$(r_o^l \rho_\delta v_\delta)^2 = 8.410 \times 10^{-6} \quad (\text{IVA-2})$$

To evaluate the integral and the δ conditions (those at the edge of the vehicle), the methods of Part III are used. The primed quantities are evaluated by determining the reference enthalpy i_l' , (Eq. (IV-34)), as a function of λ . The T_w variation, shown in Figure V-2, and the pressure at the edge of the boundary layer, p_δ , are used to determine i_w . If T_w and p_δ are known, i_w can be read from a thermodynamic chart for air (Ref. 7 or 8). The viscosity, μ_l' , is calculated as a function of λ using Equation (IV-35). The quantities i_l' and p_δ and either Reference 7 or 8 are used to determine T_l' . The quantities f_l and r_o^l are found using Equations (IV-30) and (IV-33). The evaluation of Equation (IV-32) using these quantities gives the following momentum thickness

$$\theta_l = 0.0688 \text{ ft} \quad (\text{IVA-3})$$

The next quantity to be determined is the thickness η_δ . Equation (IV-22) gives this quantity. The parameter, m_l , is

IV-33-45

found by evaluating Equation (IV-17) at the camera window.

At this point

$$\rho_l = 2.015 \times 10^{-7} \text{ slugs/ft}^3$$

$$\mu_l = 158.63 \times 10^{-8} \text{ lb-sec/ft}^2$$

$$\rho_\delta = 1.610 \times 10^{-7} \text{ slugs/ft}^3$$

$$\mu_\delta = 1.556 \times 10^{-8} \text{ lb-sec/ft}^2$$

and

$$m_l = 0.8842 \quad (\text{IVA-4})$$

Substituting the values of Equations (IVA-3) and (IVA-4) into Equation (IV-22)

$$\eta_{\delta_l} = 0.4574 \text{ ft} \quad (\text{IVA-5})$$

Let us now find the boundary layer thickness δ_l of Equation (IV-37). The quantity ahead of the integral is, from the previously calculated quantities

$$\frac{\eta_{\delta_l} \rho_\delta}{m_l} = 0.8313 \times 10^{-7} \quad (\text{IVA-6})$$

To evaluate the integral, the density profile through the boundary layer is required. This is found by determining two of the gas property profiles as a function of η/η_δ and using the thermodynamic charts (Ref. 7 or 8). The first property, which we know, is the pressure which is constant at p_δ (Fig. III-5)

$$p_\delta = 1.6 \text{ lb/ft}^2$$

The second property is the enthalpy, i , given by Equation (IV-40). Everything in this equation is known. The quantities i_δ , i_w and V_δ have been determined previously. Since we have assumed a Blasius profile for the laminar boundary layer, V/V_δ can be determined as a function of η/η_δ from Table IV-1. Thus, i is found as a function of η/η_δ . From one of the thermodynamic charts (Ref. 7 or 8), ρ and T can be found as a function of η/η_δ . The thickness δ_l can now be determined by integrating $1/\rho$ from $\eta/\eta_\delta = 0$ to $\eta/\eta_\delta = 1$. The value of this integral and Equation (IVA-6) yield δ_l

$$\delta_l = 0.4610 \text{ ft} \quad (\text{IVA-7})$$

For use in the other sections of this report, we need to express the velocity, temperature and density profiles in terms of y/δ not η/η_δ . The relationship between η/η_δ and y/δ is given by Equation (IV-41). The results of this integration are shown in Figure (IV-1). The density, temperature, and velocity profile as functions of y/δ are shown in Figure (IV-2).

The stream tube thickness, Y , is found from Equation (IV-42) by numerically integrating the product of the density and velocity from the wall to the edge of the boundary layer. Doing this we find

$$Y = 0.443 \text{ ft.}$$

REFERENCES

1. Rubesin, M. W.: The Effect of an Arbitrary Surface-Temperature Variation Along a Flat Plate on the Convective Heat Transfer in an Incompressible Turbulent Boundary Layer. NACA TN 2345, 1951.
2. Rubesin, M. W.: An Analytical Investigation of Convective Heat Transfer from a Flat Plate Having a Stepwise Discontinuous Surface Temperature. ASME Paper No. 48-A-43. Presented at the Annual Meeting of ASME in New York, Nov. 28 - Dec. 3, 1948.
3. Rubesin, Morris W.: A Modified Reynolds Analogy for the Compressible Turbulent Boundary Layer on a Flat Plate. NACA TN 2917, March 1953.
4. Schlichting, H.: Boundary Layer Theory. Permagon Press, New York, 1955.
5. Sivells, James C. and Payne, Robert G.: A Method of Calculating Turbulent-Boundary-Layer Growth at Hypersonic Mach Numbers. AEDC-TR-59-3, March 1959.
6. Chapman, D. R. and Rubesin, M. W.: Temperature and Velocity Profiles in the Compressible Laminar Boundary Layer with Arbitrary Distribution of Surface Temperature. Journal of Aeronautical Sciences, Vol. 16, 1949, p. 547.
7. Moeckel, W. E. and Weston, K. C.: Composition and Thermo-dynamic Properties of Air in Chemical Equilibrium. NACA TN 4265, 1958.
8. Feldman, Saul: Hypersonic Gas Dynamic Charts for Equilibrium Air. Avco Research Laboratory, Avco Mfg. Corp., Jan. 1957.
9. Johnson, H. A. and Rubesin, M. W.: Aerodynamic Heating and Convective Heat Transfer. Summary of Literature Survey. Transactions of the A.S.M.E., Vol. 71, No. 5, July 1949.
10. Sommer, Simon C. and Short, Barbara J.: Free-Flight Measurements of Turbulent-Boundary-Layer Skin Friction in the Presence of Severe Aerodynamic Heating at Mach Numbers from 2.8 to 7.0. NACA TN 3391, 1955.
11. Minzner, R. A., Champion, K. S. W., and Pond, H. L.: The ARDC Model Atmosphere, 1959. Air Force Surveys in Geophysics No. 115, A. F. Cambridge Res. Center, TR-59-267, Aug. 1959.

TABLE (IV-1).- BLASIUS LAMINAR BOUNDARY LAYER PROFILE
ALONG A FLAT PLATE AT ZERO INCIDENCE

$\eta \left(\frac{V_0 \rho_0}{\mu_0 x} \right)^{1/2}$	$\frac{\eta}{\eta_0}$	$\frac{V}{V_0}$
0	0	0
0.2	0.04	0.066
0.4	0.08	0.133
0.6	0.12	0.199
0.8	0.16	0.265
1.0	0.20	0.330
1.2	0.24	0.394
1.4	0.28	0.456
1.6	0.32	0.517
1.8	0.36	0.575
2.0	0.40	0.630
2.2	0.44	0.681
2.4	0.48	0.729
2.6	0.52	0.772
2.8	0.56	0.812
3.0	0.60	0.846
3.2	0.64	0.876
3.4	0.68	0.902
3.6	0.72	0.923
3.8	0.76	0.941
4.0	0.80	0.956
4.2	0.84	0.967
4.4	0.88	0.976
4.6	0.92	0.983
4.8	0.96	0.988
5.0	1.00	0.992

Approved For Release 2000/04/12 : CIA-RDP67B00657R000300070001-0

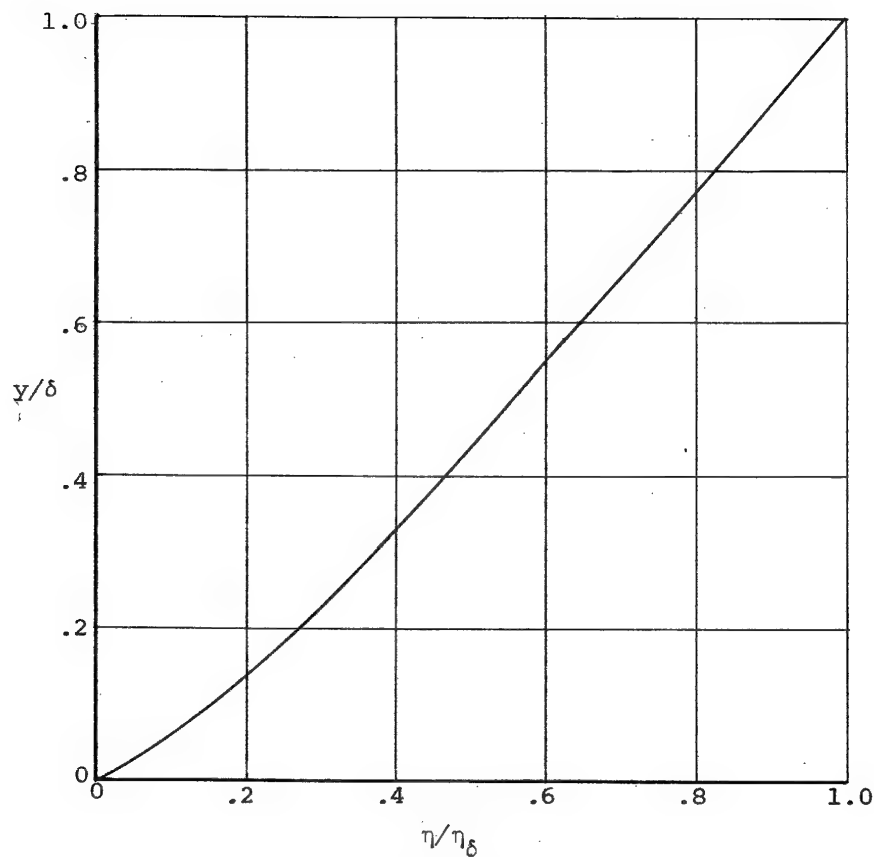


Figure IV-1.- Relationship between y/δ and η/η_δ from Equation (IV-41)
for the numerical example of Appendix IVA.

Approved For Release 2000/04/12 : CIA-RDP67B00657R000300070001-0

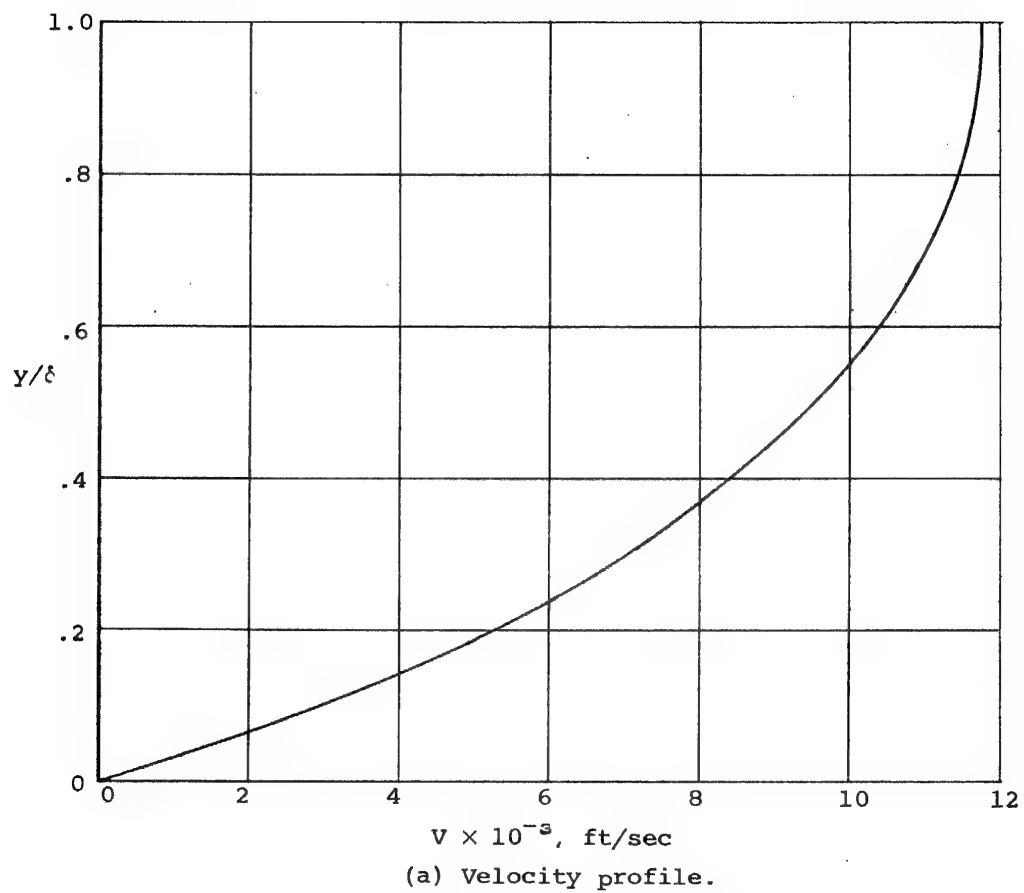
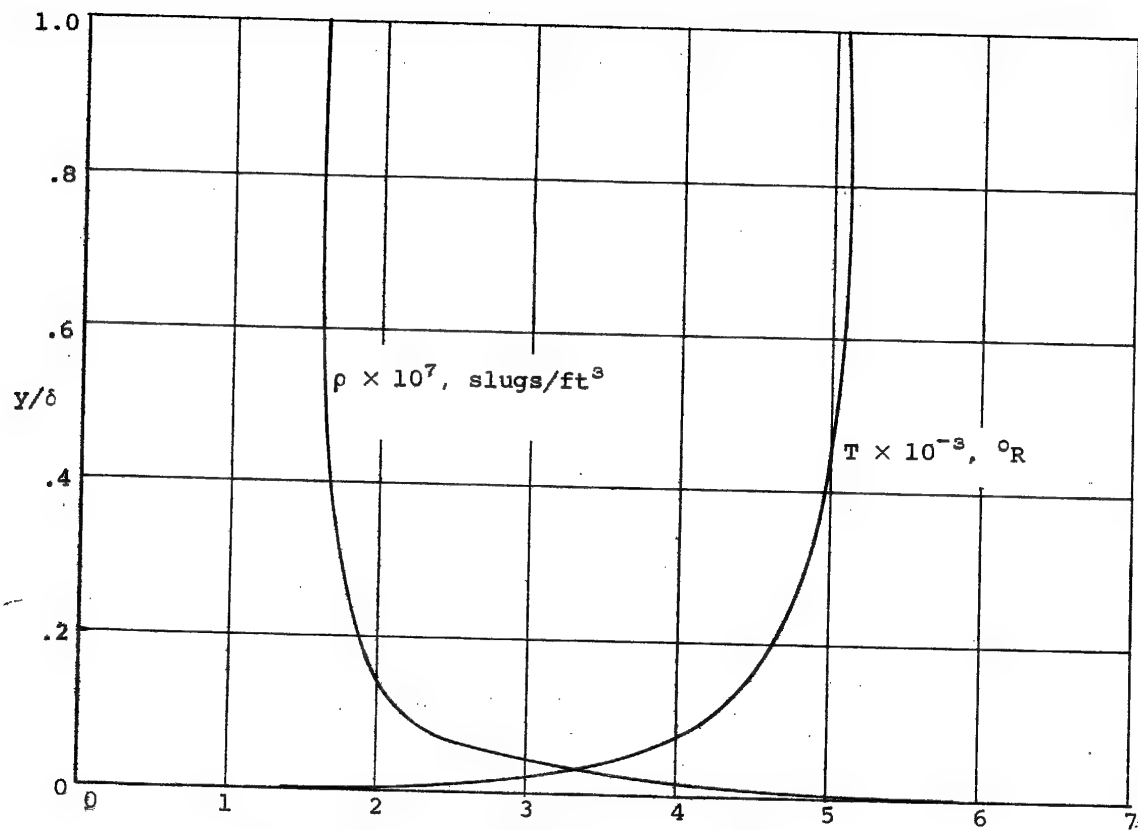


Figure IV-2.- Boundary-layer profiles of numerical example of Appendix IVA.

Approved For Release 2000/04/12 : CIA-RDP67B00657R000300070001-0



(b) Density and temperature profiles.

Figure IV-2.- Concluded.

Approved For Release 2000/04/12 : CIA-RDP67B00657R000300070001-0

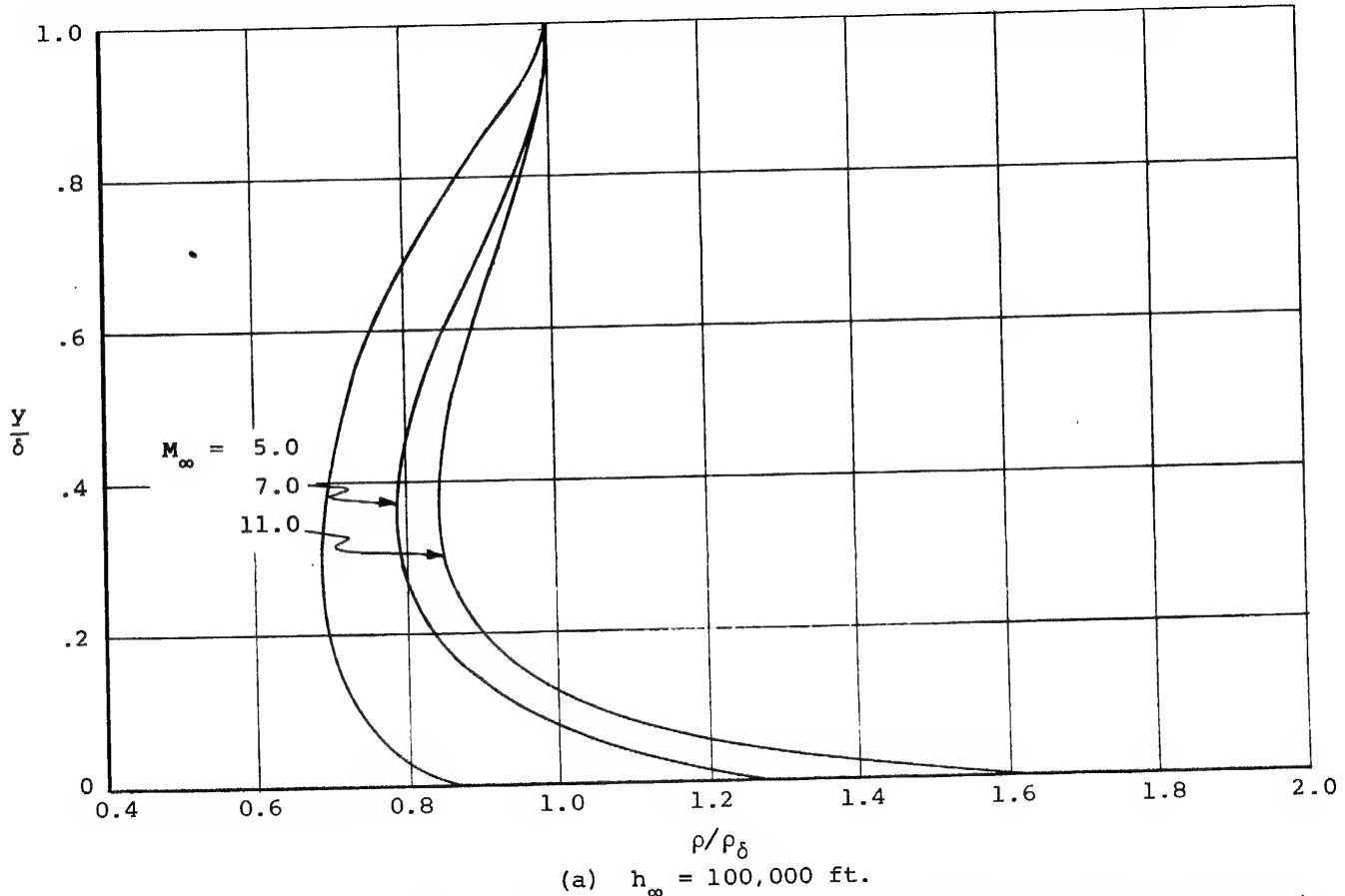
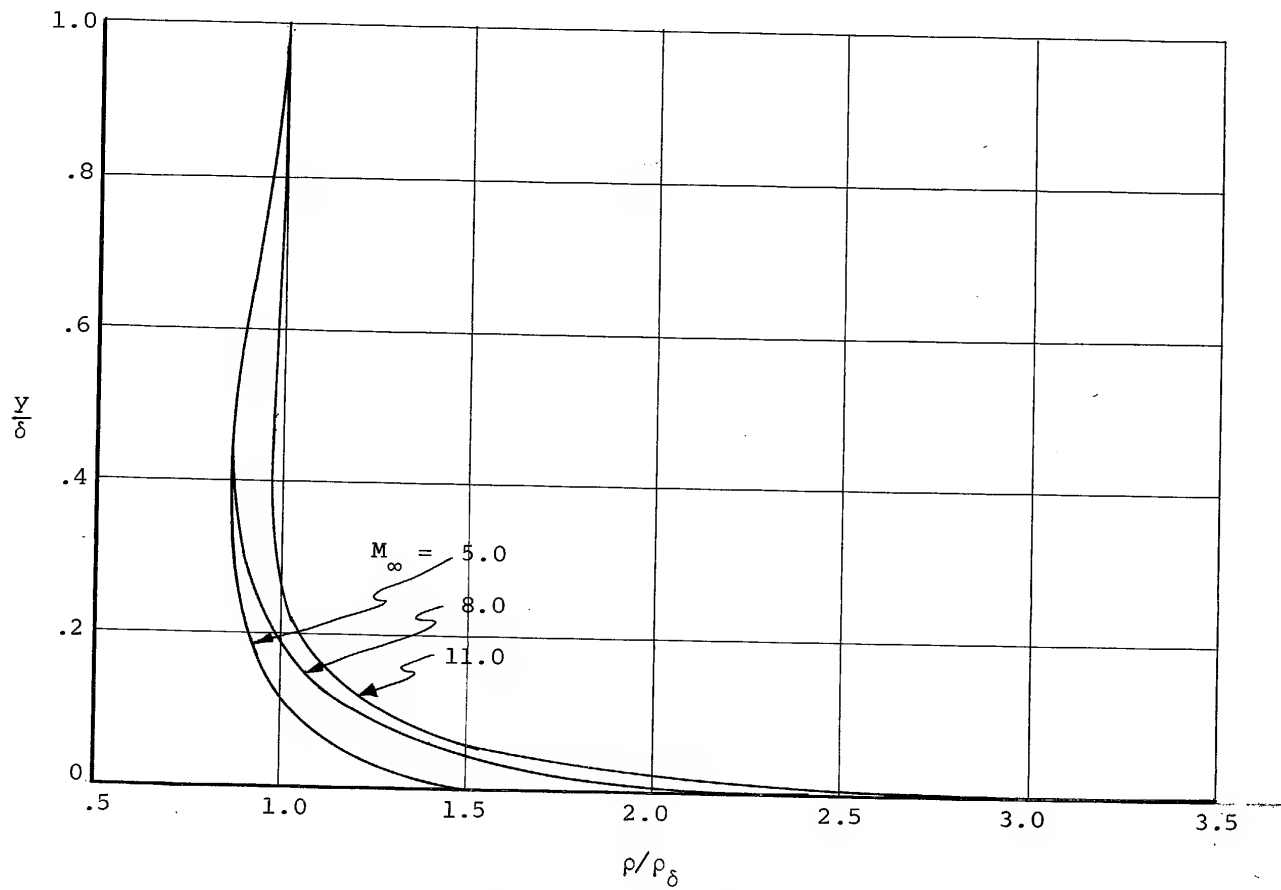


Figure IV-3.- Laminar boundary layer density profiles at the camera window on the hemispherically blunted cone ($L_W = 6.0$ ft., $\theta_C = 5^\circ$, $R = 1.0$ ft.).

Approved For Release 2000/04/12 : CIA-RDP67B00657R000300070001-0



(b) $h_\infty = 150,000$ ft.

Figure IV-3.- Continued.

Approved For Release 2000/04/12 : CIA-RDP67B00657R000300070001-0

Approved For Release 2000/04/12 : CIA-RDP67B00657R000300070001-0

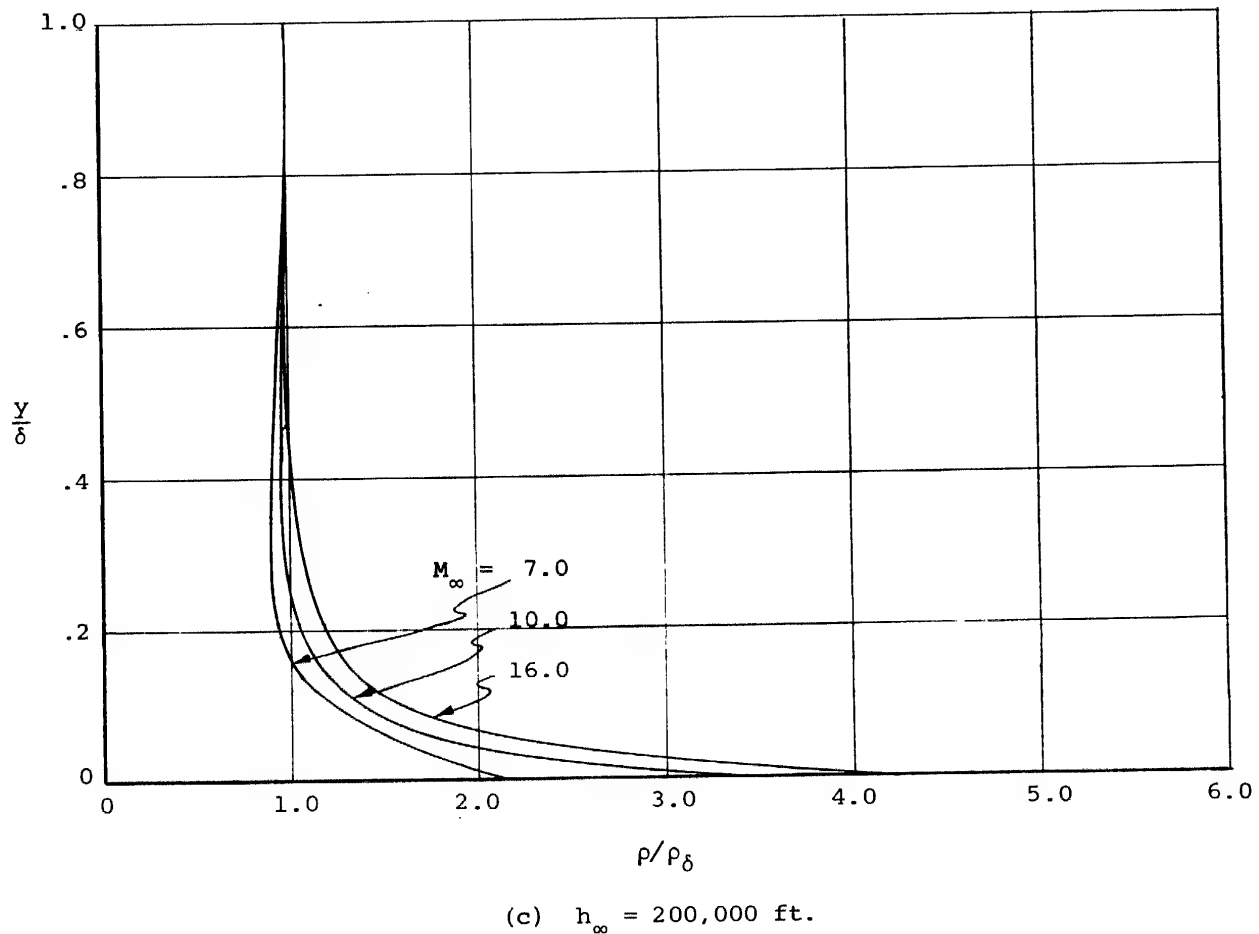
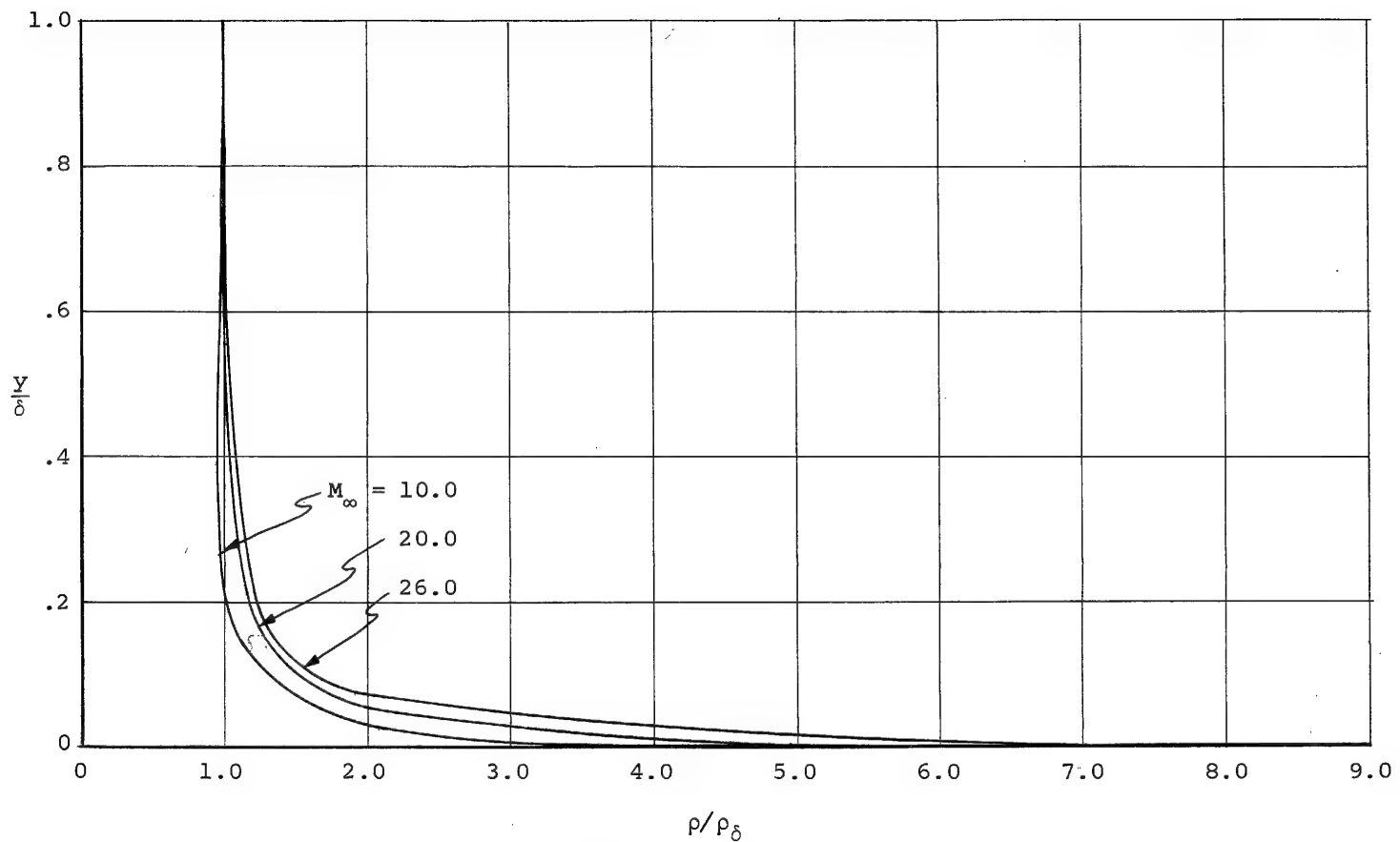


Figure IV-3.- Continued.

Approved For Release 2000/04/12 : CIA-RDP67B00657R000300070001-0

Approved For Release 2000/04/12 : CIA-RDP67B00657R000300070001-0



(d) $h_\infty = 250,000$ ft.

Figure IV-3.- Concluded.

Approved For Release 2000/04/12 : CIA-RDP67B00657R000300070001-0

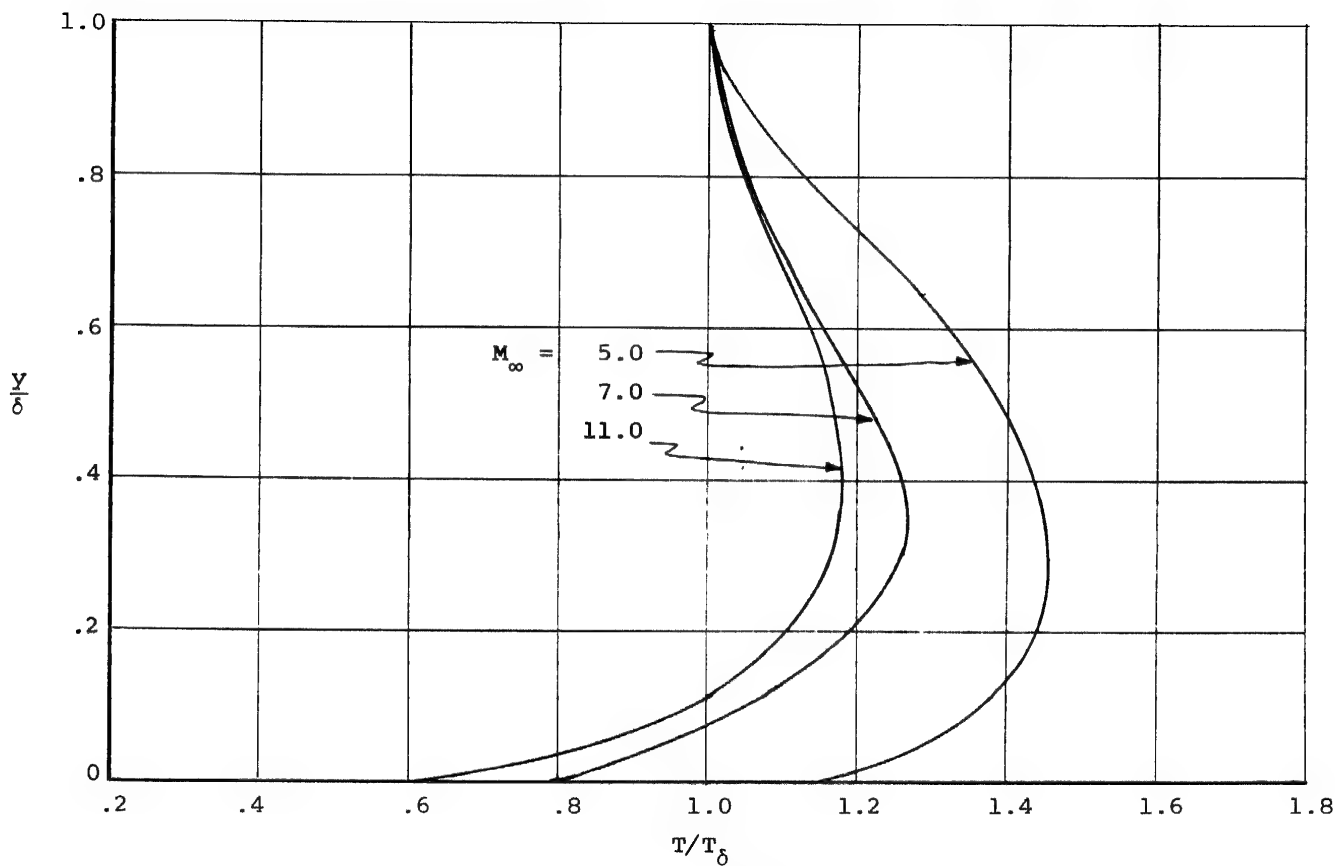


Figure IV-4-- Laminar boundary layer temperature profiles at the camera window on the hemispherically blunted cone ($L_w = 6.0$ ft., $\theta_c = 5^\circ$, $R = 1.0$ ft.).

Approved For Release 2000/04/12 : CIA-RDP67B00657R000300070001-0

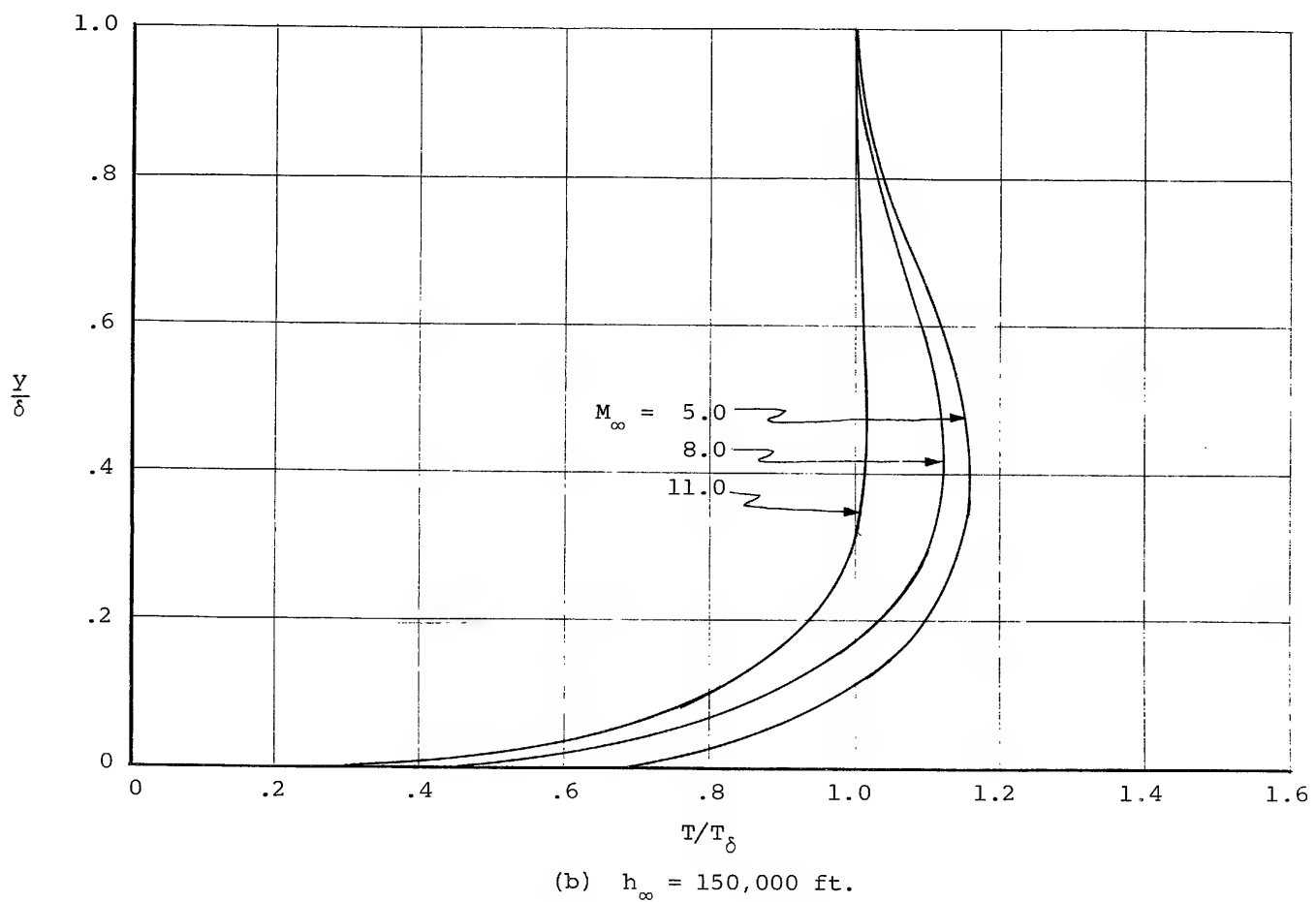


Figure IV-4.- Continued.

Approved For Release 2000/04/12 : CIA-RDP67B00657R000300070001-0

Approved For Release 2000/04/12 : CIA-RDP67B00657R000300070001-0

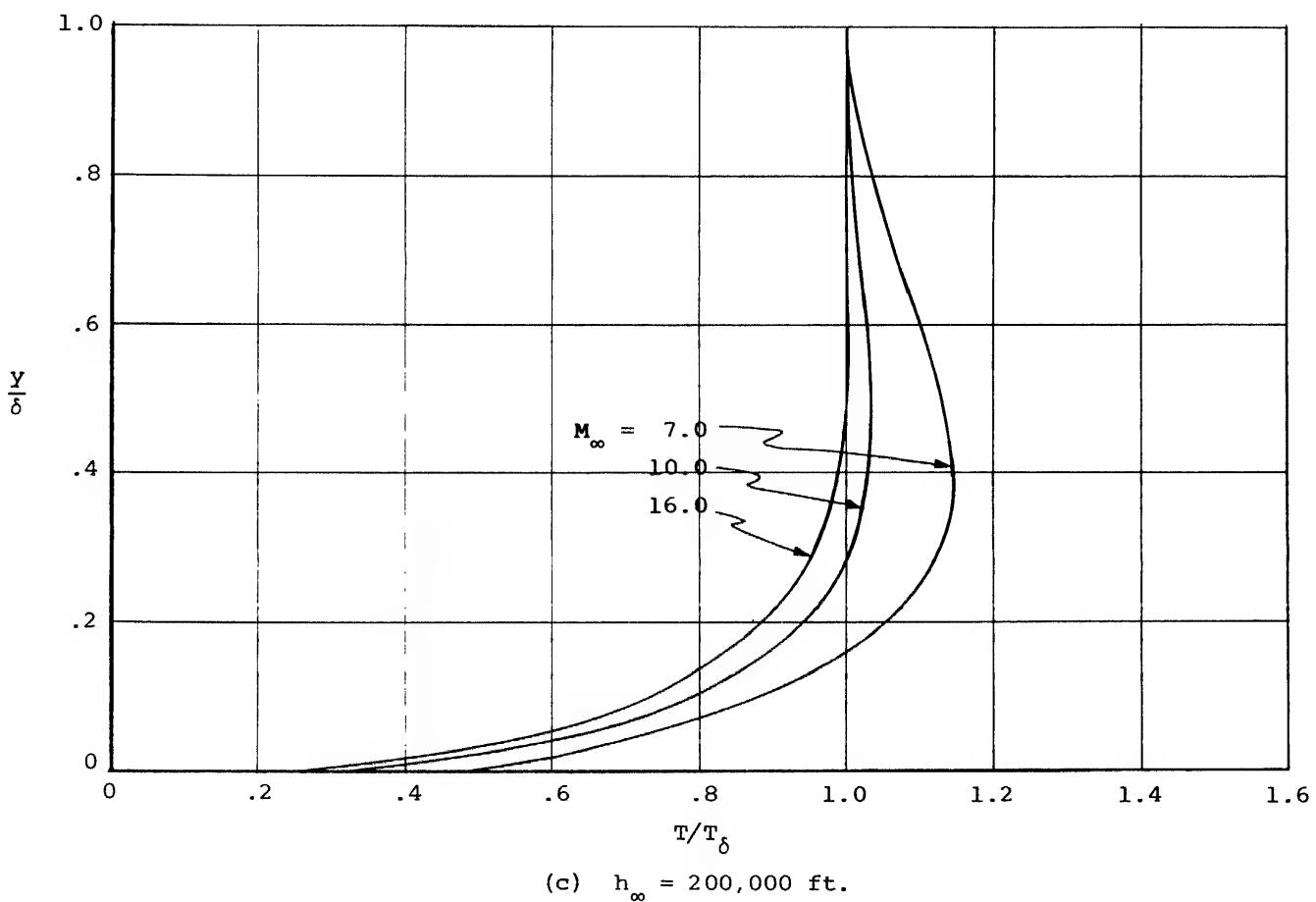
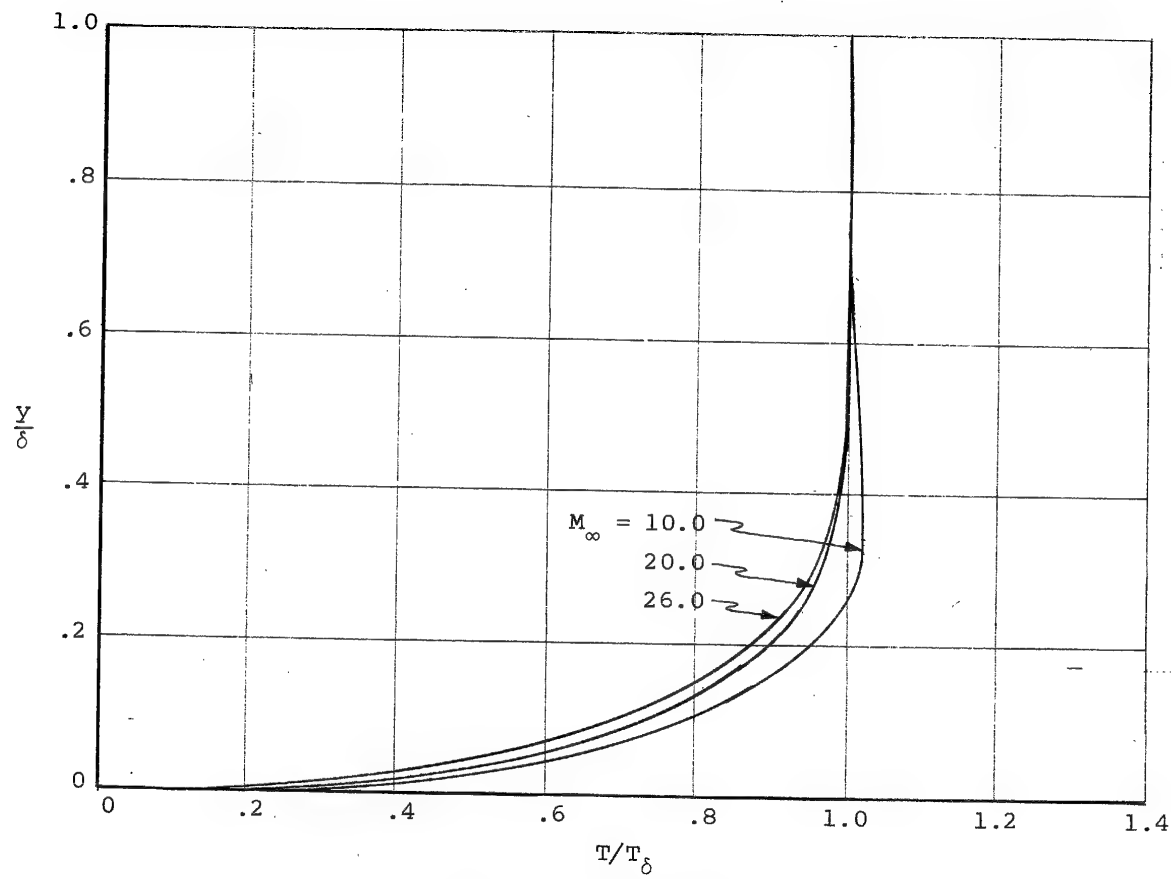


Figure IV-4.- Continued.

Approved For Release 2000/04/12 : CIA-RDP67B00657R000300070001-0

Approved For Release 2000/04/12 : CIA-RDP67B00657R000300070001-0



(d) $h_\infty = 250,000$ ft.

Figure IV-4.- Concluded.

Approved For Release 2000/04/12 : CIA-RDP67B00657R000300070001-0

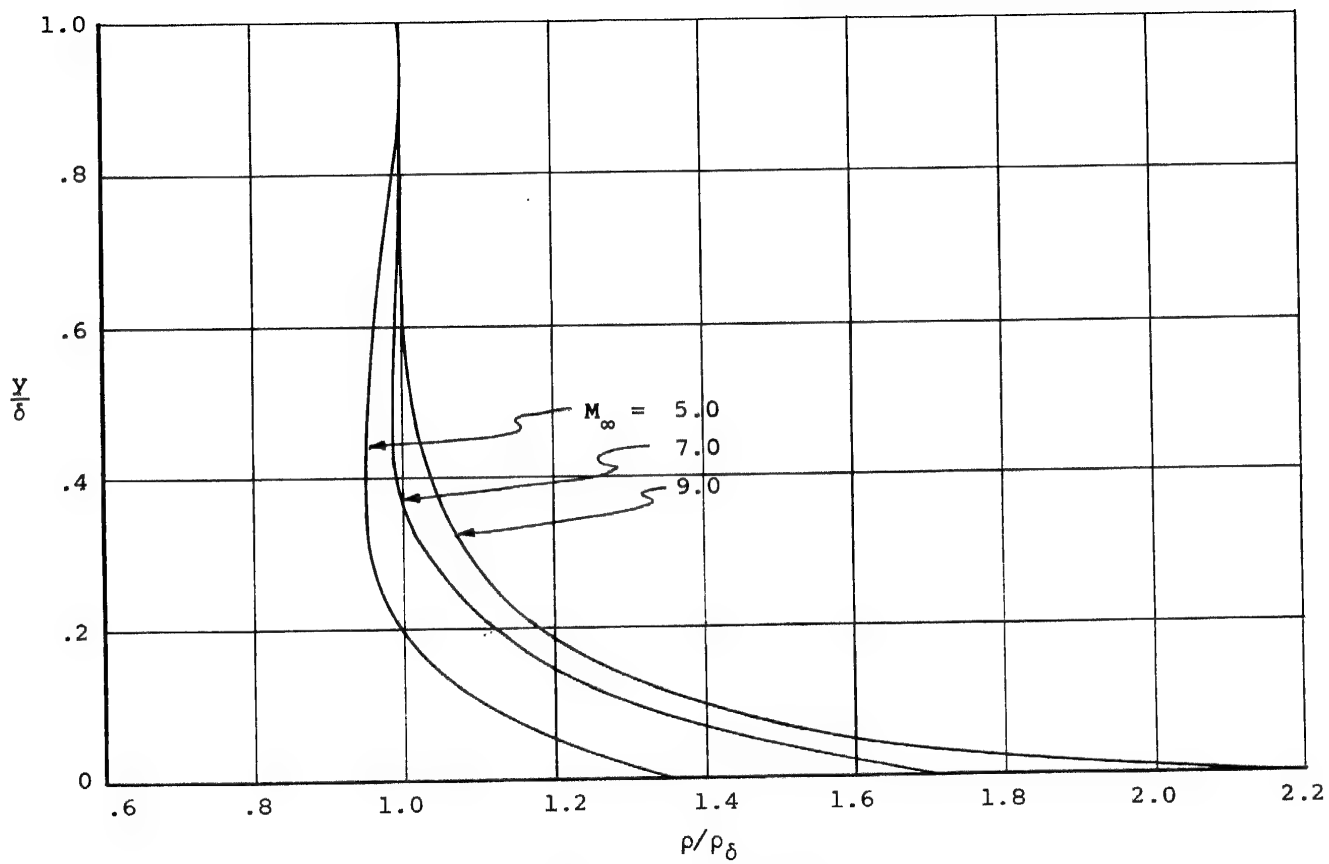


Figure IV-5.- Laminar boundary layer density profiles at the camera window location on the blunt swept wing ($L_w = 6.0$ ft., $\Lambda = 70^\circ$, $\alpha = 20^\circ$, $R = 1.0$ ft.).

Approved For Release 2000/04/12 : CIA-RDP67B00657R000300070001-0

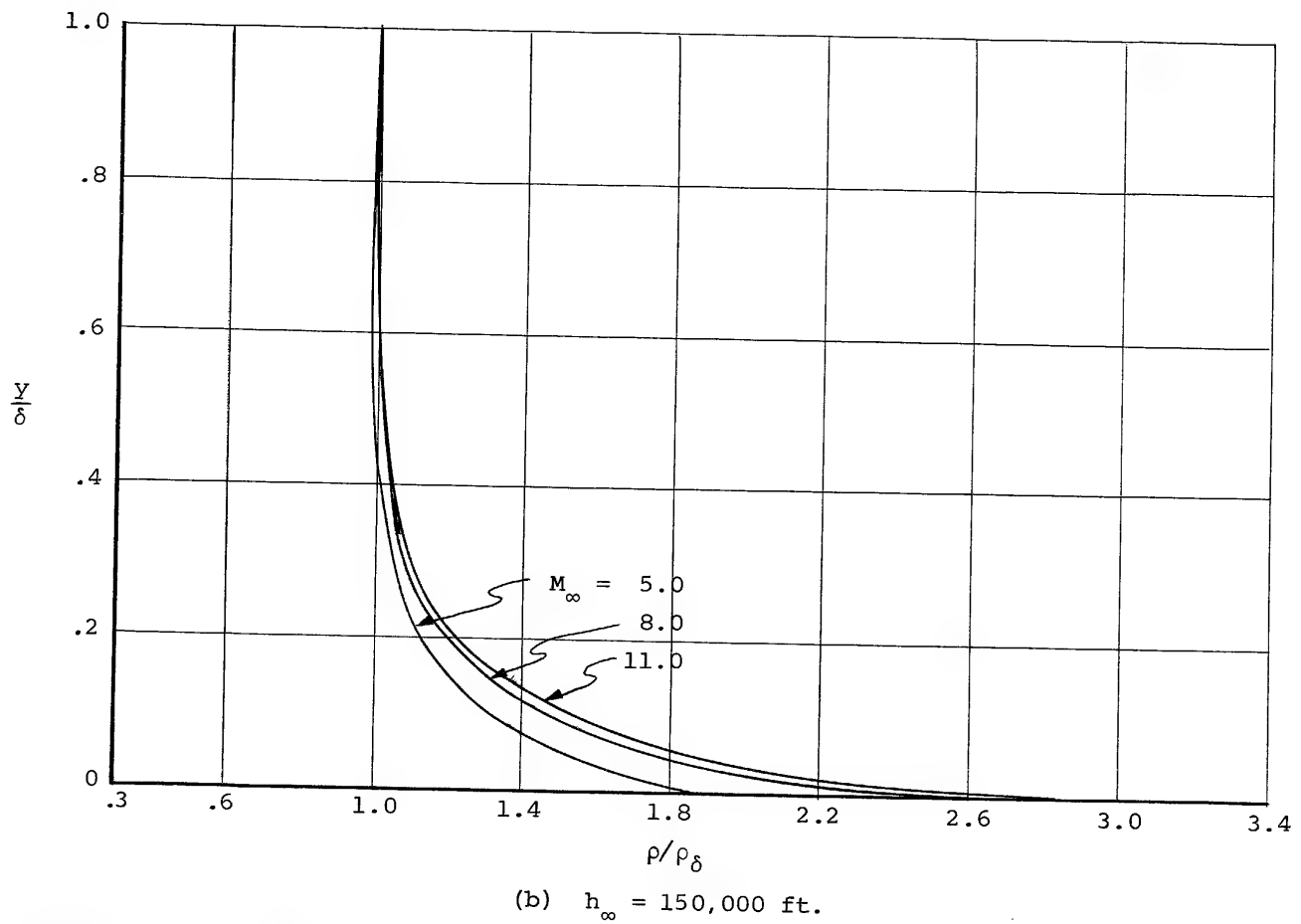


Figure IV-5.- Continued

Approved For Release 2000/04/12 : CIA-RDP67B00657R000300070001-0

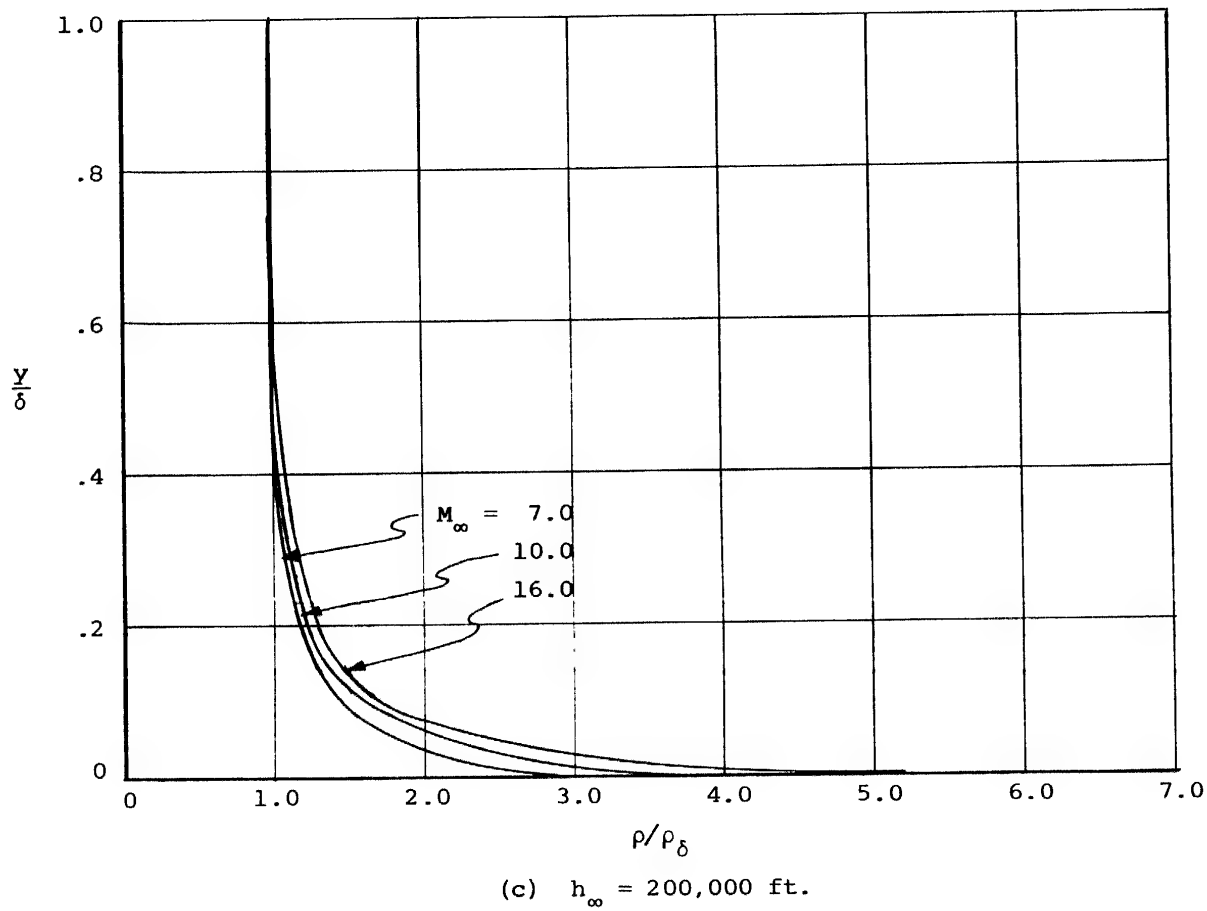


Figure IV-5.- Continued.

Approved For Release 2000/04/12 : CIA-RDP67B00657R000300070001-0

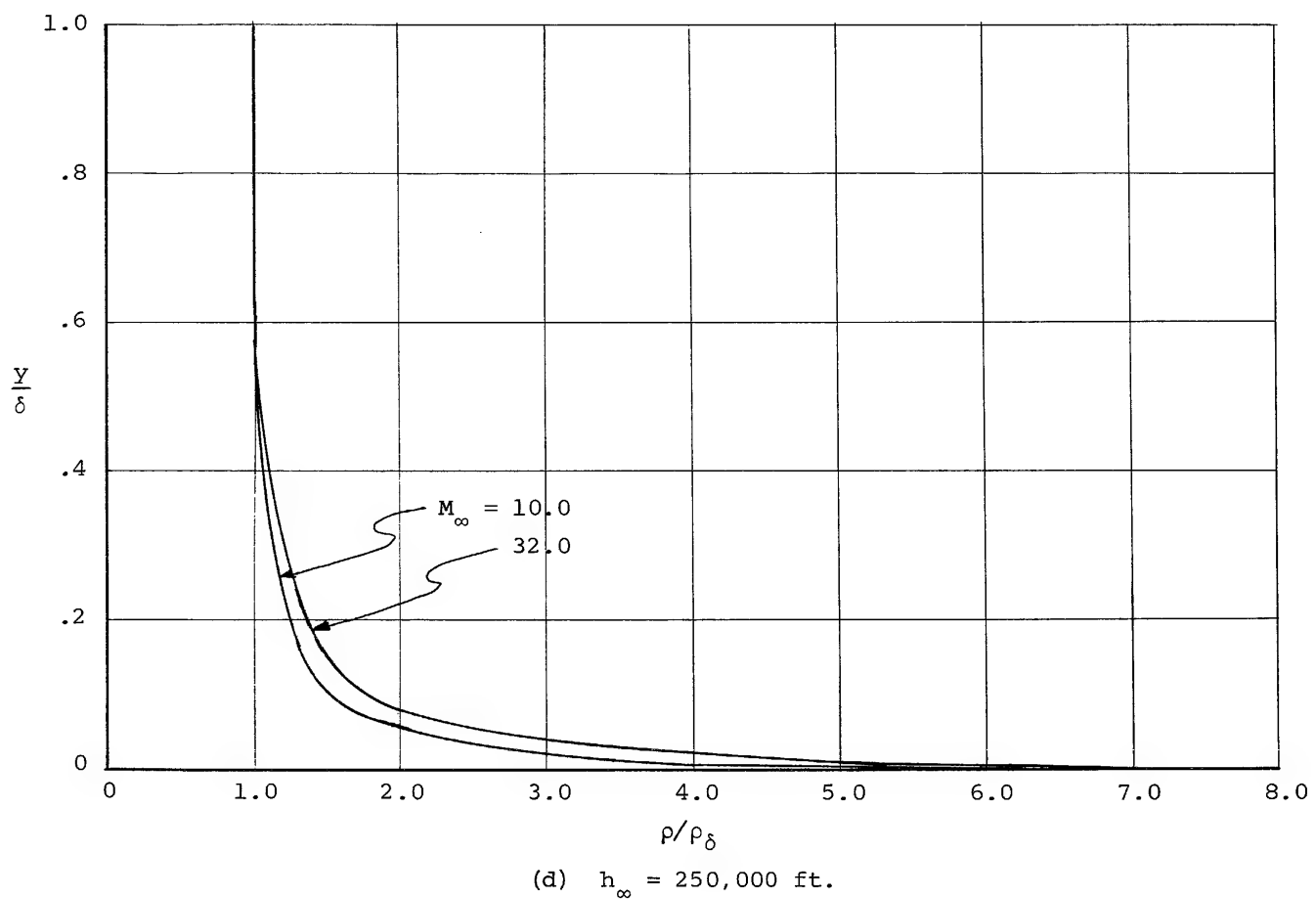


Figure IV-5.-- Concluded.

Approved For Release 2000/04/12 : CIA-RDP67B00657R000300070001-0

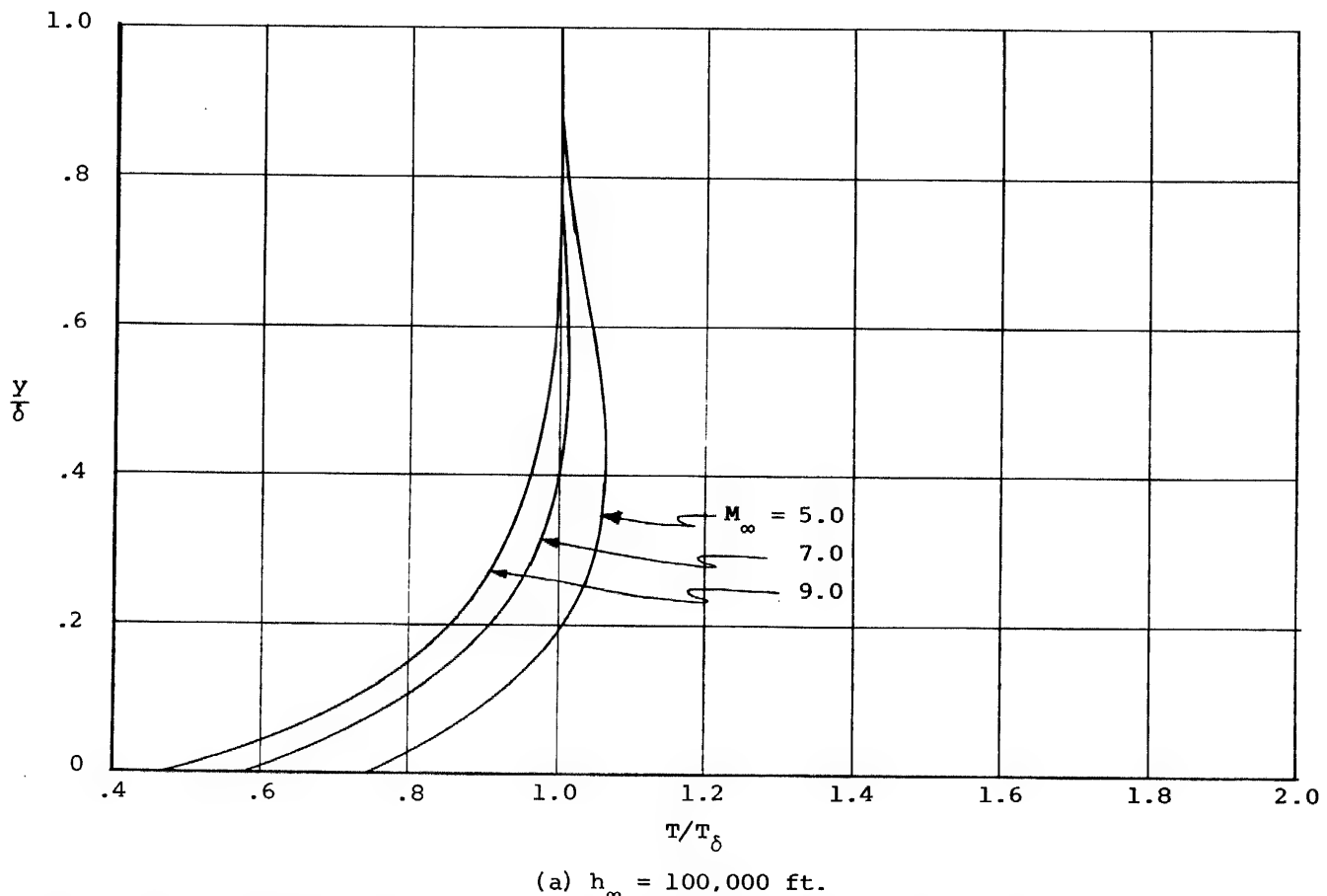
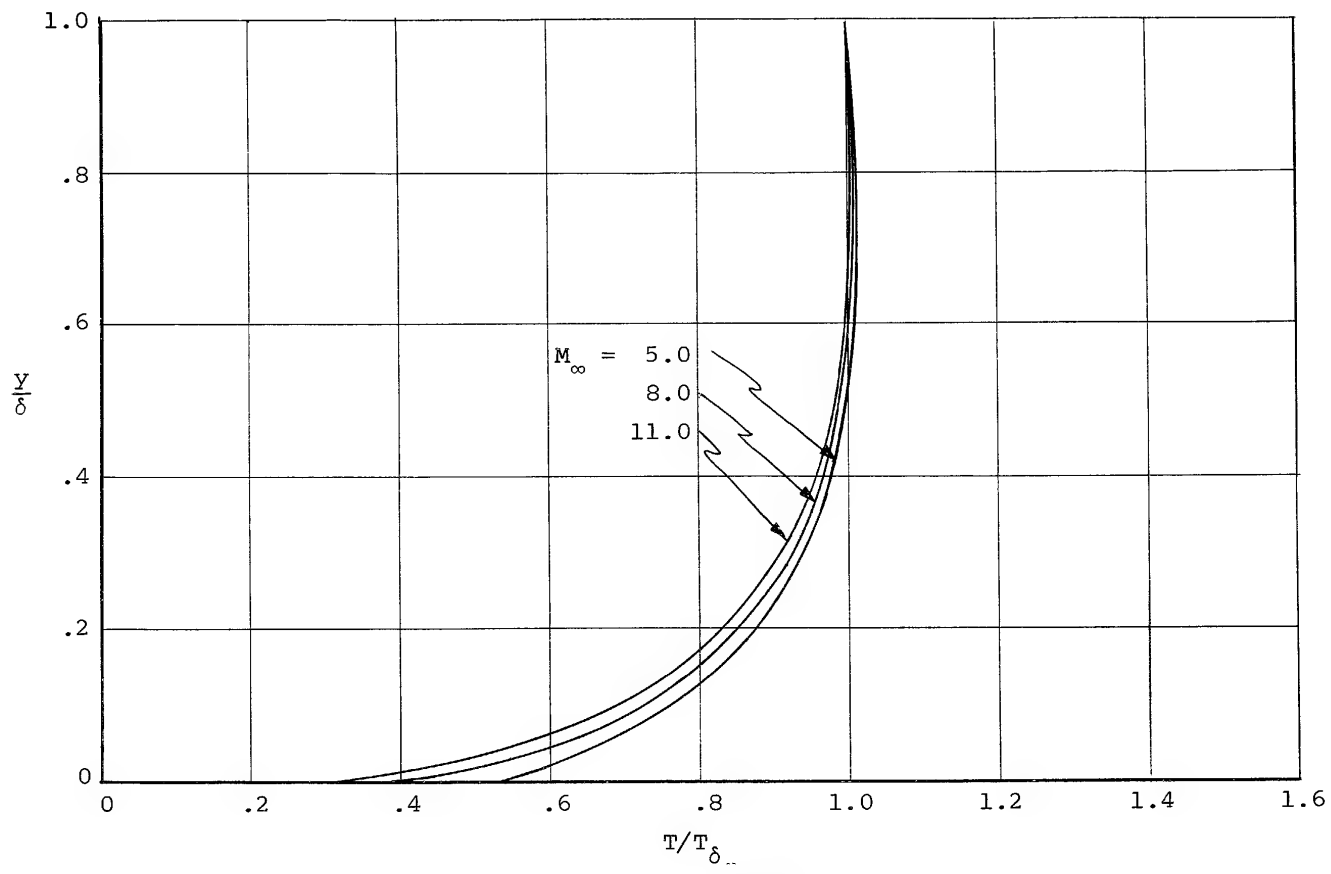


Figure IV-6.- Laminar boundary layer temperature profiles at the camera window location on the blunt swept wing ($L_W = 6.0$ ft., $\Lambda = 70^\circ$, $\alpha = 20^\circ$, $R = 1.0$ ft.).

Approved For Release 2000/04/12 : CIA-RDP67B00657R000300070001-0



(b) $h_{\infty} = 150,000$ ft.

Figure IV-6-- Continued.

Approved For Release 2000/04/12 : CIA-RDP67B00657R000300070001-0

Approved For Release 2000/04/12 : CIA-RDP67B00657R000300070001-0

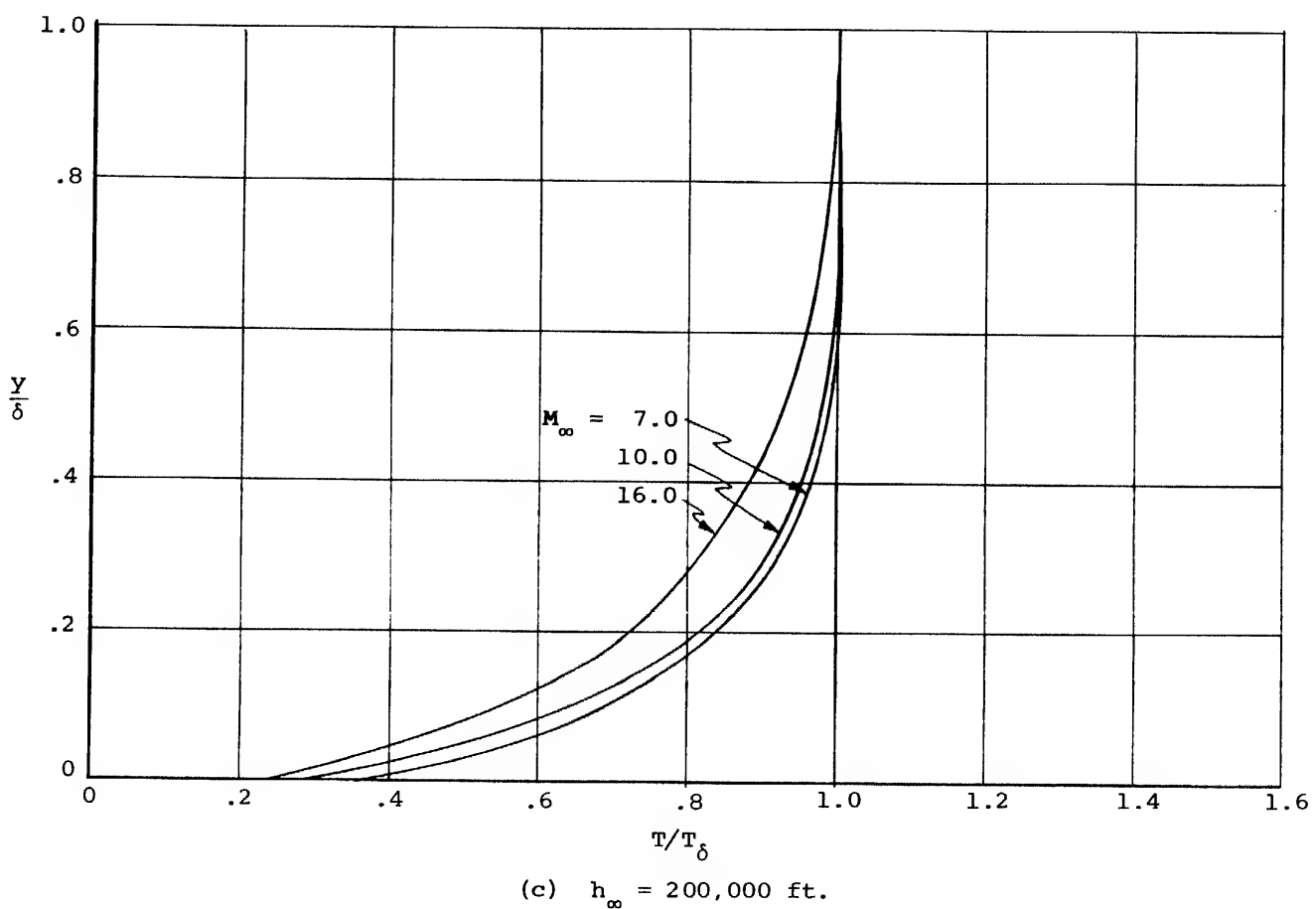


Figure IV-6.- Continued.

Approved For Release 2000/04/12 : CIA-RDP67B00657R000300070001-0

Approved For Release 2000/04/12 : CIA-RDP67B00657R000300070001-0

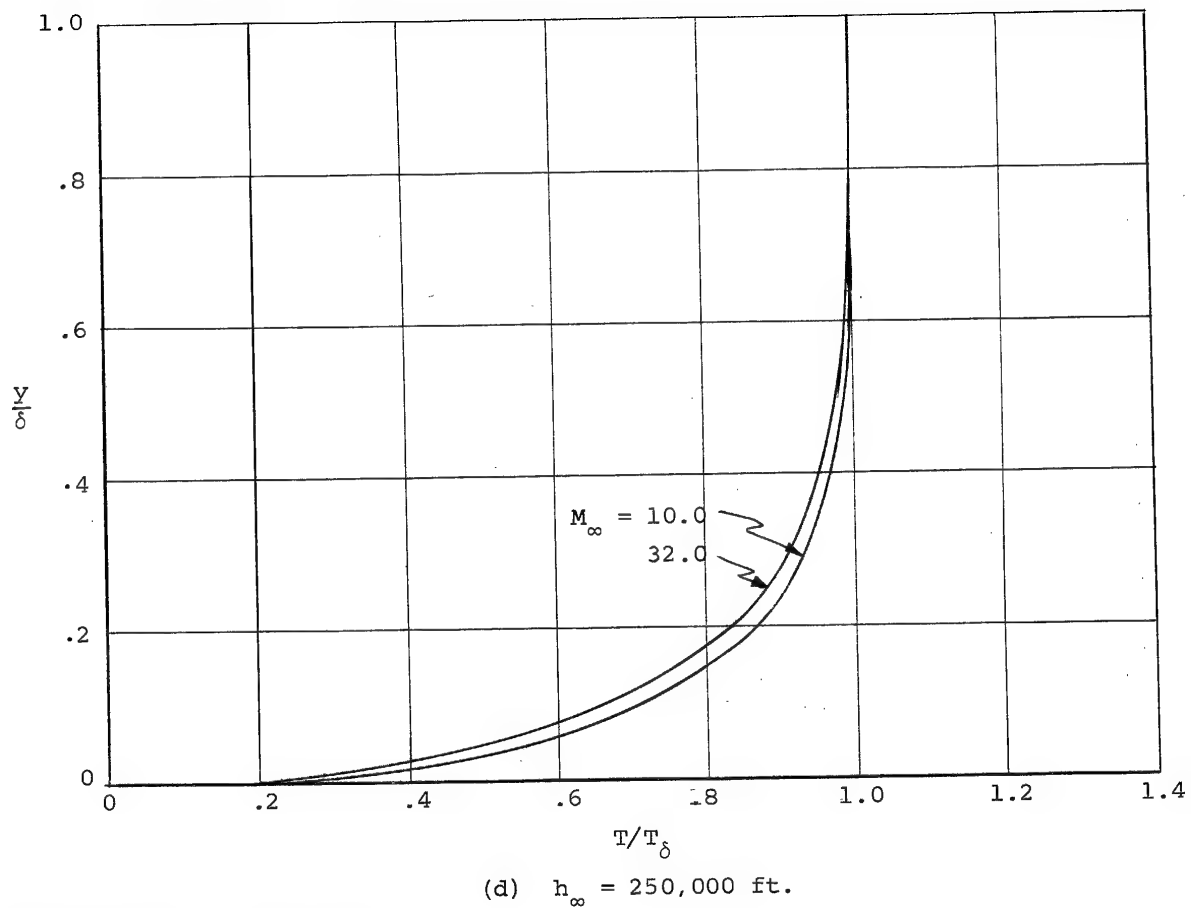
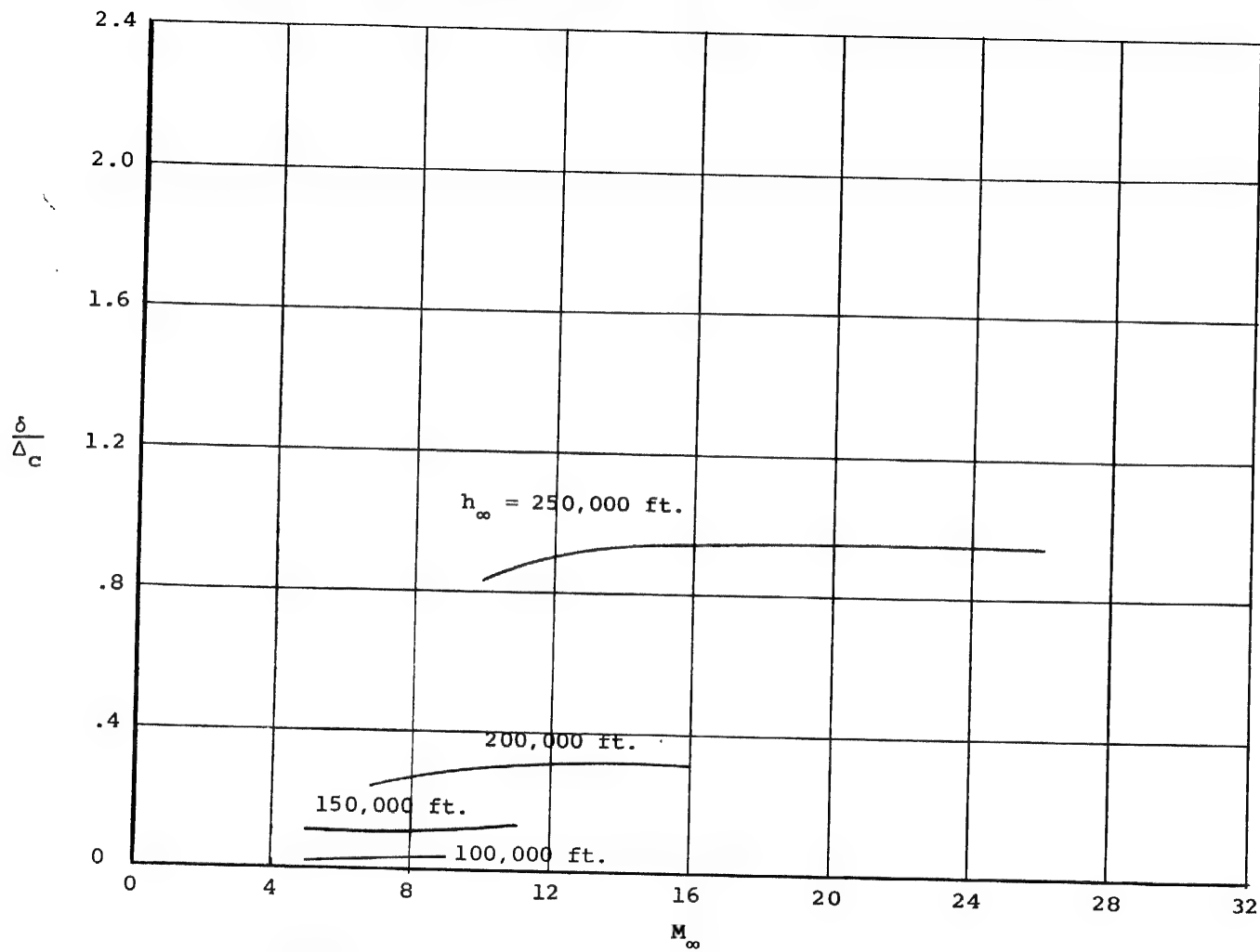


Figure IV-6.- Concluded.

Approved For Release 2000/04/12 : CIA-RDP67B00657R000300070001-0

Approved For Release 2000/04/12 : CIA-RDP67B00657R000300070001-0

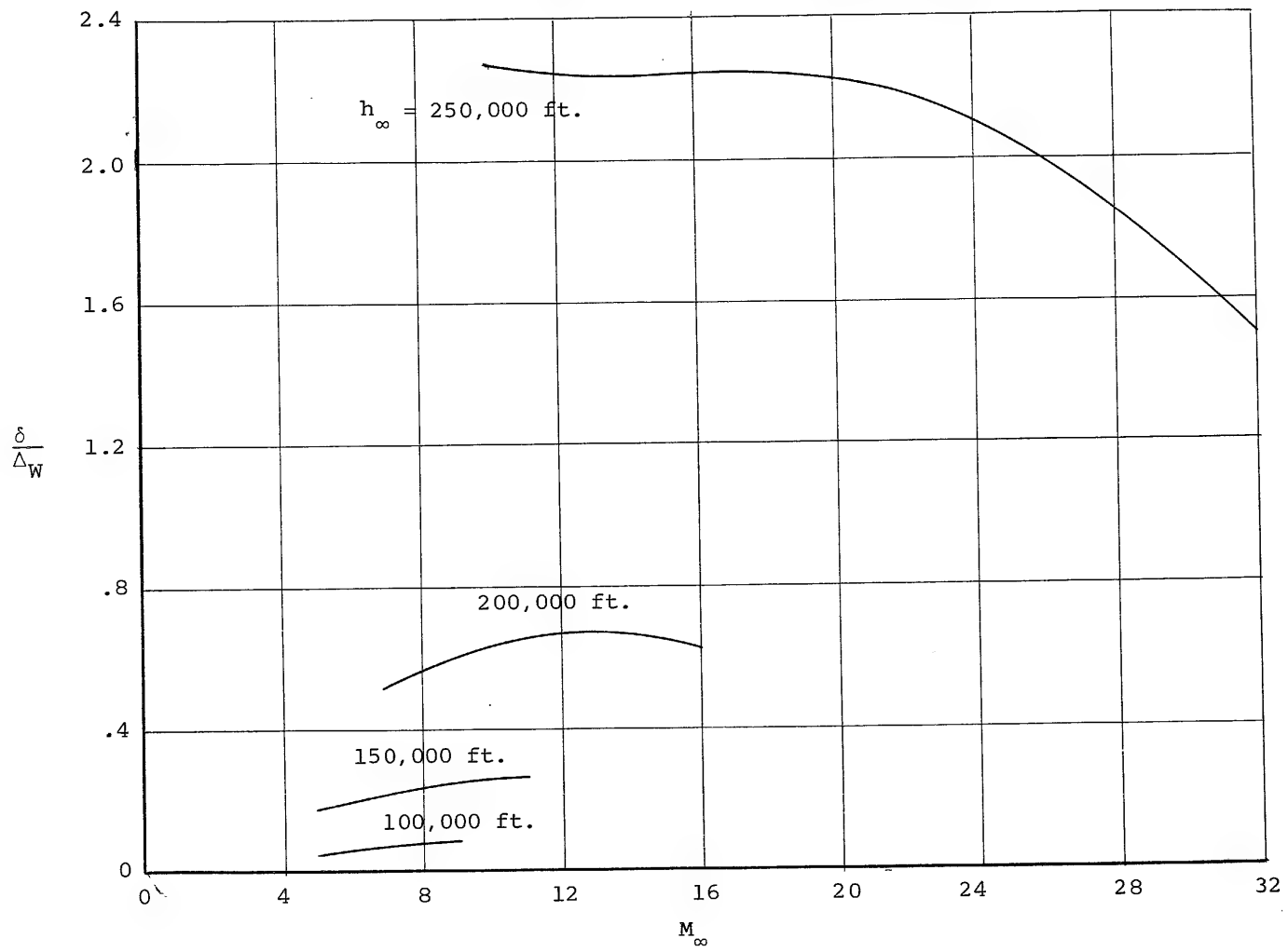


(a) Hemispherically blunted cone ($\theta_c = 5^\circ$, $R = 1.0$ ft., $L_w = 6.0$ ft.).

Figure IV-7.- Ratio of boundary layer thickness to shock wave standoff distance at camera

Approved For Release 2000/04/12 : CIA-RDP67B00657R000300070001-0

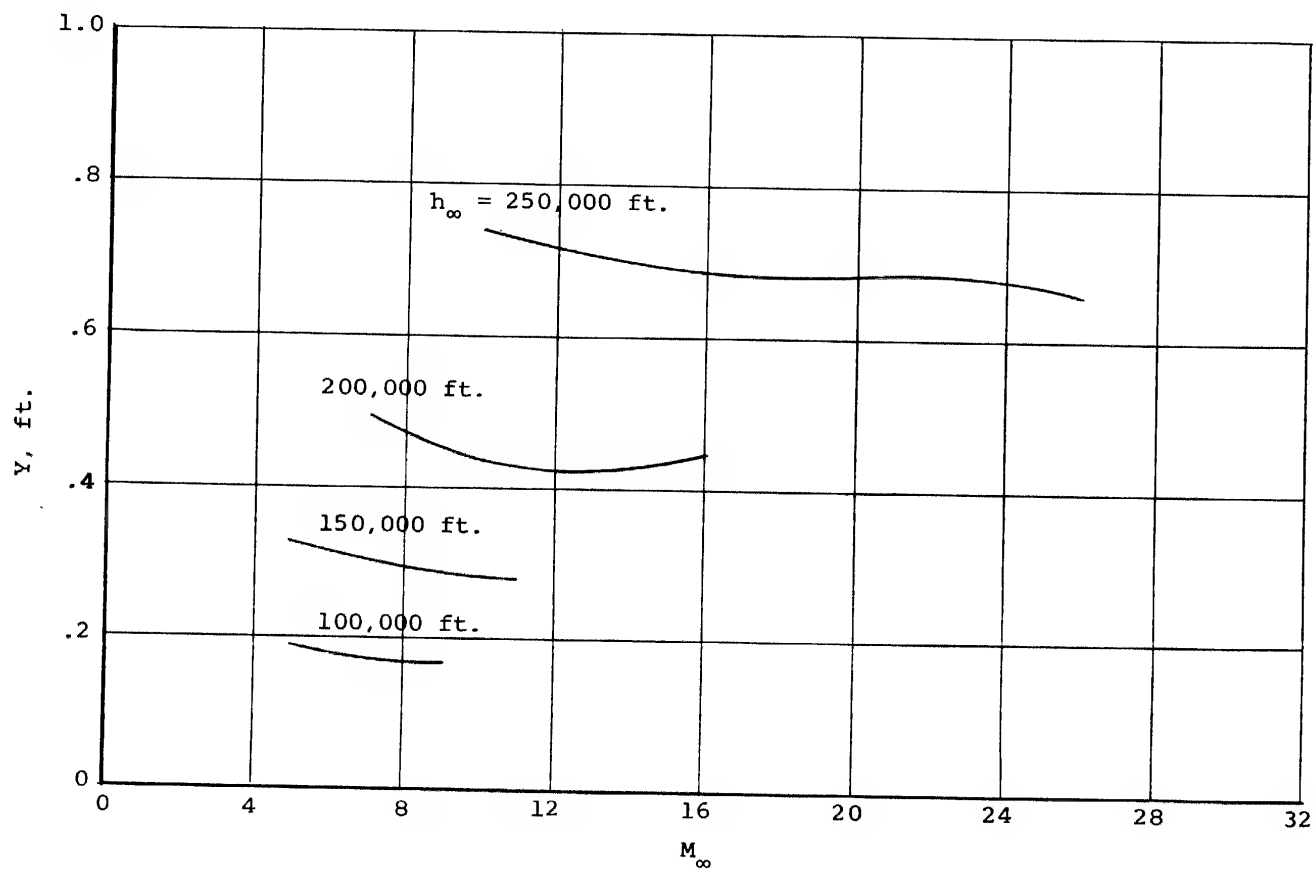
Approved For Release 2000/04/12 : CIA-RDP67B00657R000300070001-0



(b) Blunt swept wing ($\Lambda = 70^\circ$, $\alpha = 20^\circ$, $R = 1.0$ ft., $L_W = 6.0$ ft.).

Figure IV-7.- Concluded

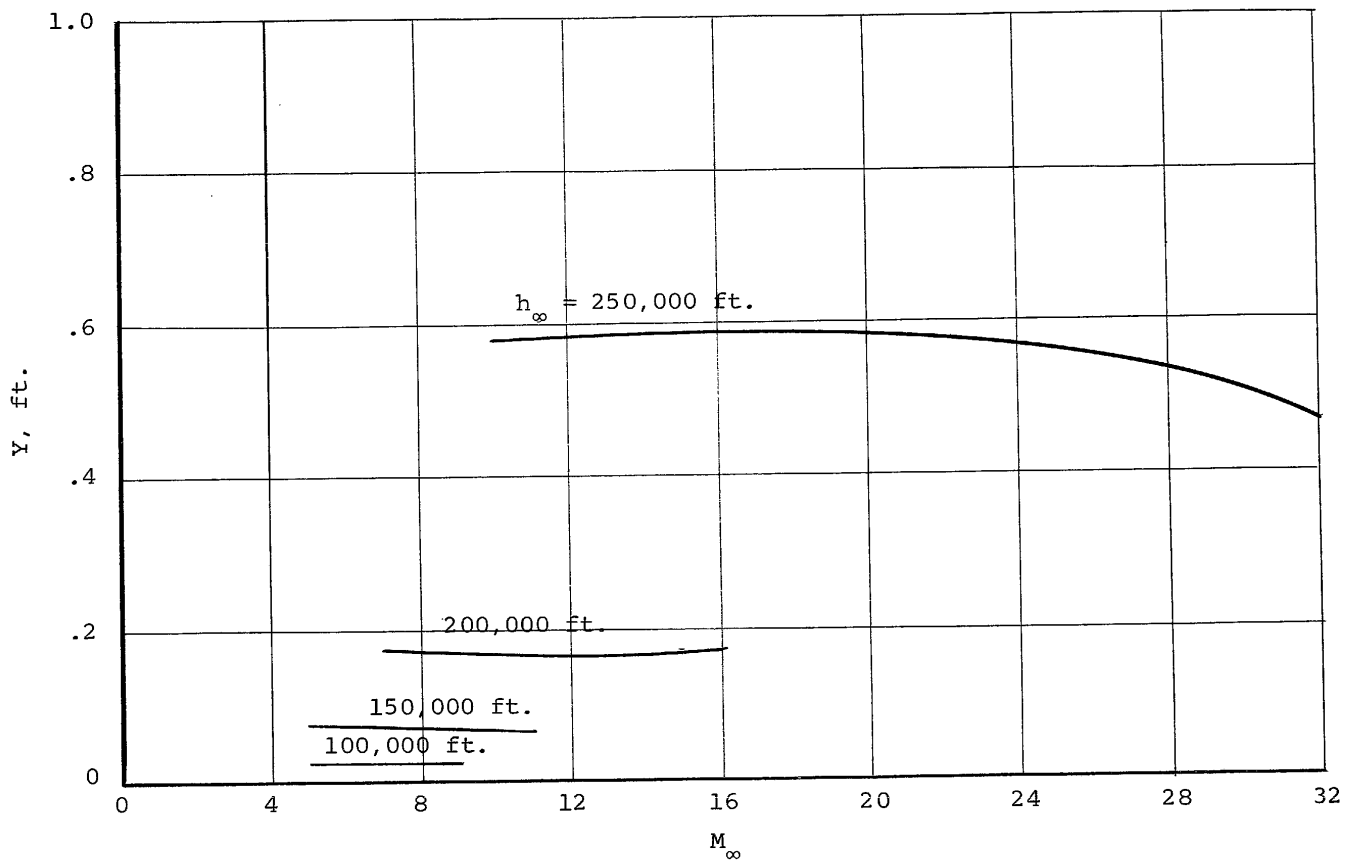
Approved For Release 2000/04/12 : CIA-RDP67B00657R000300070001-0



(a) Hemispherically blunted cone ($\theta_c = 5^\circ$, $R = 1.0$ ft., $L_w = 6.0$ ft.).

Figure IV-8.- Free-stream stream tube radius with the same mass flow as the boundary layer at the camera window.

Approved For Release 2000/04/12 : CIA-RDP67B00657R000300070001-0



(b) Blunt swept wing ($\Lambda = 70^\circ$, $\alpha = 20^\circ$, $R = 1.0$ ft., $L_W = 6.0$ ft.).

Figure IV-8.- Concluded.

Approved For Release 2000/04/12 : CIA-RDP67B00657R000300070001-0

PART V: THERMAL CHARACTERISTICS OF THE CAMERA WINDOW

INTRODUCTION

The thermal conditions of a camera window mounted in the lower portion of a blunt cone or a thick blunt wing at hypersonic speeds will be investigated to determine the effects of aerodynamic heating on aerial photography. There are two main problems concerning aerodynamic heating of the camera window: (1) the temperature level may become high enough to structurally weaken the window material or the temperature differential through the window may create stresses large enough to fracture the material; (2) the thermal stresses cause distortion of the window which results in refraction errors and loss of resolution. The thermal gradients are a result of aerodynamic heating on the outside of the window while much cooler temperatures exist within the camera cavity on the inside of the window. The camera cavity must be maintained within certain temperature limits because of film and camera considerations.

This part of the investigation is concerned with determining the temperatures on the inner and outer surfaces of the camera window for the two configurations at various combinations of altitude and Mach number. In the determination of these temperatures, the heat-transfer rate from the boundary layer air to the outer surface of the window and the heating rate through the window to the camera cavity are both determined. The analysis is developed in such a manner that the heat-transfer rates may be determined for

either a laminar or turbulent boundary layer. A combined laminar-turbulent boundary layer can be treated as well, using the assumption that the energy integral (see Appendix VA) is constant at transition.

The analysis of the convective heating rate from the boundary layer to the wall of blunt-nosed vehicles is considerably more difficult than for sharp-nosed vehicles, such as the sharp cones investigated in Phase I of this program (Ref. 1). In order to determine the thermal characteristics of the camera window for this study, a method was derived by M. W. Rubesin of Vidya whereby the convective heat-transfer rate may be calculated for blunt bodies including real-gas effects by the use of the reference enthalpy method for either laminar or turbulent boundary layers. This derivation is given in Appendix VA. The method applies to blunt bodies of revolution at zero angle of attack or to two-dimensional blunt wings at any angle of attack. It assumes that the enthalpy variation along the surface of the body is small compared to the stagnation enthalpy. The solution of this problem involves an iterative integration process and graphical solutions of simultaneous equations. An illustrative example of a solution by this method is given in Appendix VC.

SYMBOLS

A	point of tangency of nose and straight portion of body
a	speed of sound, ft/sec
a_1	constant defined by Equation (V-7), 0.332 for laminar flow and 0.0296 for turbulent flow
c_p	pressure coefficient, $(p - p_\infty) / (\frac{1}{2} p_\infty V_\infty^2)$
c_p	specific heat at constant pressure
D	point on body at front edge of camera window
f	enthalpy ratio, defined in Equation (V-12)
g	gravitational acceleration, 32.2 ft/sec ²
H	heat-transfer coefficient of camera cavity, BTU/ft ² -hr- ^o R
i	enthalpy, BTU/lb
J	mechanical equivalent of heat, 778 ft-lb/BTU
k	thermal conductivity of camera window material, BTU/hr-ft- ^o F
Pr	Prandtl number, taken as 0.72
p	static pressure, lb/ft ²
q_c	convective heat-transfer rate, BTU/ft ² -hr
q_r	radiation heat-transfer rate, BTU/ft ² -hr
R	radius of hemispherical nose or wing leading edge, ft
r	recovery factor ($Pr^{1/2}$ for laminar flow; $Pr^{1/3}$ for turbulent flow)
r_o	radius of cross section, ft
S	distance measured along surface of wing or body in plane of symmetry from stagnation point, ft
s	location of stagnation point
T	temperature, ^o R
t	thickness of camera window, ft

v velocity, ft/sec
y coordinate normal to window surface
z compressibility factor, $p/\rho RT$
 α local angle of attack of surface, deg
 ϵ emissivity, taken as 0.80 for wall and 0.93 for camera window
 η/η_0 coefficient of viscosity ratio to correct for dissociation of air
 θ_c cone semiaxial angle, deg
 μ viscosity, lb-sec/ft²
 ρ air mass density, slugs/ft³
 σ Stefan-Boltzmann constant, 0.173×10^{-8} BTU/ft²-deg⁴-hr
 τ transmissivity of camera window material (taken as zero)
 ϕ angle between centerline of body and radial line to specified locations on surface of nose, deg

Subscripts

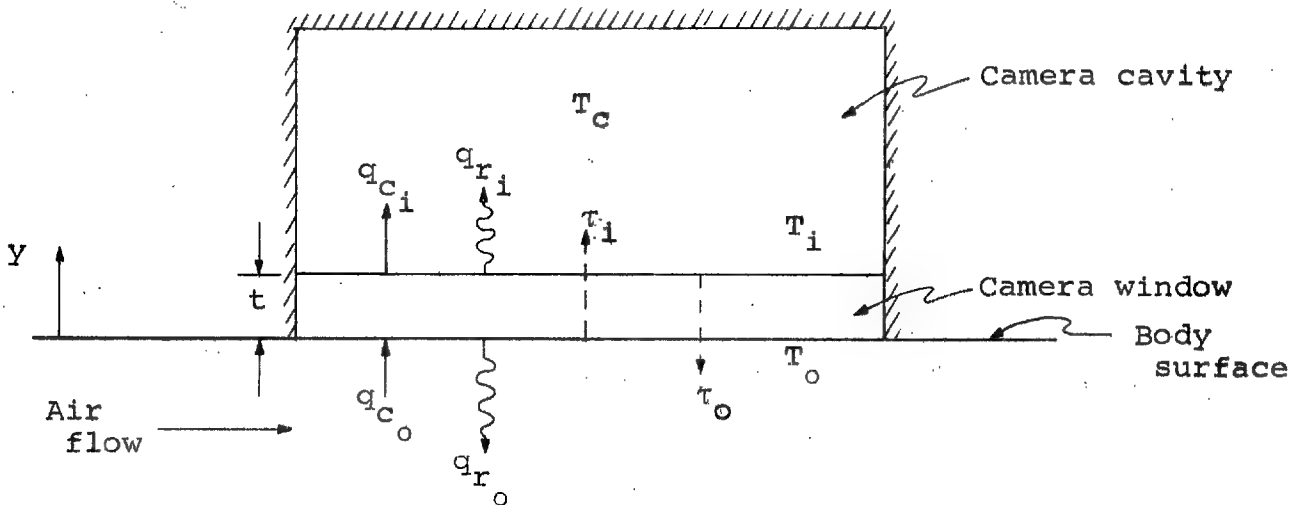
c conditions inside cavity
i inner surface of window
l laminar flow
o outer surface of window
r recovery
s stagnation
t turbulent
w wall condition
 δ outer edge of boundary layer
 ∞ free-stream conditions

Superscripts

- l constant defined by Equation (V-7), (0 for two-dimensional flow, 1 for rotationally symmetric flow)
- m constant defined by Equation (V-7), (0.5 for laminar flow, 0.2 for turbulent flow)
- n constant defined by Equation (V-7), (2 for laminar flow, 1.25 for turbulent flow)
- u constant defined by Equation (V-7), (1 for laminar flow, 0.25 for turbulent flow)
- primed quantities refer to a reference condition

INVESTIGATION

In order to determine the temperatures of the inner and outer surfaces of the camera window, a heat balance will be set up for the regions surrounding the window. A sketch of the camera window and cavity is shown below with a schematic representation of the types of heat transfer involved in this problem.



For the present analysis it will be assumed that the window is opaque to infrared radiation in the wavelengths occurring at the anticipated temperatures so that the transmissivity τ of the heat

through the window is zero. A previous preliminary analysis indicated that the heat transfer through the glass by internal radiation may be neglected for the range of temperatures to be involved in this study. It will also be assumed that the diameter of the window is small compared with its distance from the nose of the body and that the thickness of the window is small compared with the local radius of the body in which the camera is mounted. In addition, tangential conduction is neglected and the camera cavity is assumed to be enclosed by black surfaces, as indicated by the cross hatching in the preceding sketch, and maintained at a uniform temperature. The analysis is thereby reduced to a one-dimensional heat flow problem, and is restricted to the steady case.

A heat balance will be made on each surface by equating the heat conducted to the surface per unit time to the heat leaving the surface by radiation and convection. The heat balance for the inner surface of the window is

$$q_{c_i} + q_{r_i} = -k \frac{dT}{dy} \Big|_{y=t} \quad (V-1)$$

and for the outer surface,

$$q_{c_o} - q_{r_o} = -k \frac{dT}{dy} \Big|_{y=0} \quad (V-2)$$

where k is the thermal conductivity of the window material. Transparent fused silica has been selected as a likely material for this application. The thermal conductivity of transparent fused silica is given as a function of temperature in the following table taken from

unpublished data:

Temperature, $^{\circ}$ F	200	600	1000	1500	2000
k	0.90	1.05	1.53	2.82	5.37

where k is in BTU/hr-ft- $^{\circ}$ F.

The heat conduction through the window may be expressed as
(Ref. 1)

$$k \frac{dT}{dy} = \frac{1}{t} \left[0.674 (T_i - T_o) + 0.347 \times 10^{-3} (T_i^2 - T_o^2) \right. \\ \left. - 0.306 \times 10^{-6} (T_i^3 - T_o^3) + 0.144 \times 10^{-9} (T_i^4 - T_o^4) \right] \quad (V-3)$$

The heat radiated from the outer surface of the camera window is given by

$$q_{r_o} = 0.173 \epsilon_o \left(\frac{T_o}{100} \right)^4 \quad (V-4)$$

The radiation and convective heat transfer from the inner surface of the window are given by

$$q_{r_i} = 0.173 \epsilon_i \left[\left(\frac{T_i}{100} \right)^4 - \left(\frac{T_c}{100} \right)^4 \right] \quad (V-5)$$

and

$$q_{c_i} = H(T_i - T_c) \quad (V-6)$$

Equation (V-5) assumes that the camera cavity has completely black walls. The value of the heat-transfer coefficient H will depend upon the circulation flow within the cavity. If air at atmospheric pressure is convecting freely within the cavity, H can be taken as equal to unity, whereas an H of zero corresponds to vacuum conditions within the cavity.

This heat balance neglects any radiation from the earth, atmosphere, or any other object outside the camera window. The earth radiation is shown to be negligible by the following example:

$$\text{Earthshine} \approx 40 \text{ BTU/hr ft}^2$$

albedo $\approx 175 \text{ BTU/hr ft}^2$ where $\approx 90\%$ passes through glass therefore,

$$\text{Earth } q_r \approx 60 \text{ BTU/hr ft}^2$$

whereas, if the temperature of the outer window surface is approximately 2000° R ,

$$q_{r_o} \approx 10^4 \text{ BTU/hr ft}^2$$

The convective heat-transfer rate from the boundary layer airflow to the camera window for blunt bodies in dissociated air is given by the following equation which is derived in Appendix VA (note symbols which have been changed to keep consistent with symbols and units used in this report):

$$q_c = \frac{3600 a g f^n (r_o)^l v_\delta \rho' (\mu')^u (i_s - i_w)}{(Pr)^{2/3} \left[\int_0^s f^n (r_o)^{nl} v_\delta \rho' (\mu')^u d\lambda \right]^m} \quad (V-7)$$

The primed values refer to a reference condition. That is, there is a reference temperature T' or enthalpy h' for which the convective heat transfer in a compressible flow satisfies the incompressible equation for the same specified conditions (see Ref. 2). The reference enthalpy for a laminar boundary layer is given by

(Refs. 2 and 3):

$$\left. \begin{aligned} i_l' &= 0.23 i_\delta + 0.19 i_r + 0.58 i_w \\ i_t' &= 0.36 i_\delta + 0.19 i_r + 0.45 i_w \end{aligned} \right\} \quad (V-8)$$

and for the turbulent case

$$i_r = i_\delta + r \frac{V_\delta^2}{2gJ} \quad (V-9)$$

The recovery enthalpy i_r is defined as

where the recovery factor r is $(Pr)^{1/2}$ for the laminar case and $(Pr)^{1/3}$ for the turbulent case. The reference viscosity μ' is obtained from the expression (Ref. 4)

$$\mu' = 2.28 \times 10^{-8} (T')^{1/2} \left(1 + \frac{202}{T'} \right) \left(\frac{\eta}{\eta_0} \right) \quad (V-10)$$

and the reference density ρ' is obtained directly from the Mollier diagram of Reference 5 at i' and p_δ or from Reference 6 and the expression

$$\rho' = 39.5 \frac{p_\delta}{Z' T' g} \quad (V-11)$$

where p_δ is in atmospheres and T' in $^{\circ}$ R. The reference temperature T' is found on the Mollier diagram at i' and p_δ . The value of f is determined by the equation

$$f = \frac{i_\delta + r \frac{V_\delta^2}{2gJ} - i_w}{i_\delta + \frac{V_\delta^2}{2gJ} - i_w} \quad (V-12)$$

The method for determining the values of the conditions at the edge of the boundary layer can be found in Part III of this report.

It should be noted that when solving for the local pressure coefficient C_p from the expression

$$C_p = (C_p)_s \sin^2 \alpha \quad (V-13)$$

α is the angle between the normal to the body surface and the free-stream airflow and is equal to θ_c only for points on the conical surface.

The constants in Equation (V-7) depend upon whether the boundary layer is laminar or turbulent; therefore, a table is presented below listing the constants for laminar and turbulent cases.

Table V-1

Constant	Laminar	Turbulent
a_1	0.332	0.0296
m	0.5	0.2
n	2	1.25
u	1	0.25

The method used to obtain the conditions at the edge of the boundary layer and to solve the equation for the convective heat-transfer rate are slightly different for the blunt cone than for the blunt wing. For this reason the two configurations will be considered separately.

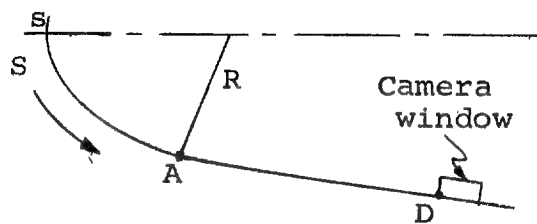
Method of Solution for Blunt Cone

The solution of the convective heat-transfer equation for a blunt cone will be considered first. The value of q_c is determined by an iteration process because q_c is a function of the wall temperature which is initially unknown. The wall temperature is estimated for the first iteration. Upon determining q_c , the radiation equilibrium temperature at that q_c is found from the expression

$$q_c = q_r = 0.173 \epsilon_w \left(\frac{T_w}{100} \right)^4 \quad (V-14)$$

After this value of T_w is known, the wall enthalpy i_w is determined from the Mollier diagram at T_w and p_δ . At this point the calculation of q_c is repeated using the new value of i_w in the equation. This process is continued until the value of T_w becomes essentially constant between computations. This temperature is then used in the calculations to determine the window temperatures.

In order to evaluate the integral in the denominator of Equation (V-7), the integral is broken into two parts, one for the hemispherical nose and the other for the cone, as shown in the following sketch:



the integral is then expressed as

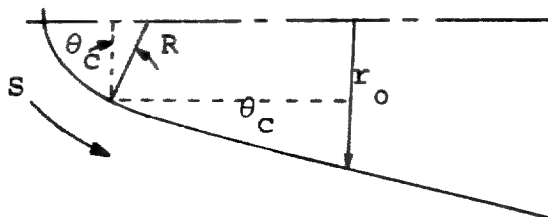
$$\int_0^{S_D} f^n r_o^{nl} v_\delta \rho'(\mu')^u d\lambda = \int_0^{S_A} f^n r_o^{nl} v_\delta \rho'(\mu')^u d\lambda + \int_{S_A}^{S_D} f^n r_o^{nl} v_\delta \rho'(\mu')^u d\lambda \quad (V-15)$$

where the exponent l is equal to unity for the blunt cone.

Because the value of the wall enthalpy must be known to solve for f , ρ' , and μ' , the wall temperature T_w must be known as a function of S . Because each of the terms in the integrand is a function of S over the hemispherical nose, the integration in the region from s to A is done graphically. To do this, the terms in the integrand are determined at several values of S on the nose. The value of the integrand is then plotted as a function of the distance S and integrated graphically. The conical sections may be integrated directly as r_o is the only term taken as a variable in the integrand for this region.

The expression for the radius of cross section for the conical portion of the body as determined from the sketch below is

$$r_o = R \cos \theta_c + \left[S - R \left(\frac{\pi}{2} - \theta_c \right) \right] \sin \theta_c \quad (V-16)$$



The remaining terms in the integrand are assumed to be constant because it is expected that the temperature along the conical section will remain nearly constant.

It is necessary that Equation (V-7) be solved for each point at which the wall temperature is to be calculated by Equation (V-14). The temperature at each point is then used in the second iteration as previously stated. The solution of Equation (V-7) at the stagnation point requires that the equation be solved for its limit as r_0 approaches zero. The convective heat-transfer equation at the stagnation point as derived in Appendix VB becomes

$$(q_c)_s = \frac{2837(p_s - p_\infty)^{1/4}(i_s - i_w)(\rho')^{1/2}(\mu')^{1/2}g}{R^{1/2}(\rho_s)^{1/4}(\Pr)^{2/3}} \quad (V-17)$$

Since it has been assumed that the size of the window is small compared with the distance to the window from the nose of the cone, the convective heat-transfer rate to the wall at the front of the window can be assumed to be representative of the average convective heat transfer to the camera window. It may be expected that a slight discontinuity in the surface temperature will occur between the wall at the edge of the window and the window itself. The effects of this discontinuity on the heat transfer to the window are assumed to be negligible because the change in the wall enthalpy corresponding to the temperature change will be very small compared with the difference between the stagnation enthalpy and the wall enthalpy.

Method of Solution for Blunt Wing

The thermodynamic relationships for determining the convective heat transfer to the camera window in the blunt wing are quite similar to those relationships previously established for the blunt cone. The expression for the convective heating rate

$$q_c = \frac{3600 a f_r^n r_o^l v_\delta \rho' (\mu')^u (i_s - i_w) g}{(Pr)^{2/3} \left[\int_0^S f^n r_o^n l v_\delta \rho' (\mu')^u d\lambda \right]^m} \quad (V-7)$$

is the same for the blunt wing as for the blunt cone with the exception that the exponent l is zero in the case of the blunt wing. The integral in Equation (V-7) is solved by splitting it into parts in the same manner as for the blunt cone. The solution of the integral around the nose is again a graphical integration carried out in the same manner as for the blunt cone. The results of Part II of this report show that the pressure along the straight section of the bottom of the wing is nearly constant; therefore, for the purpose of determining the heat transfer, the pressure along the bottom of the wing will be assumed constant at the value determined at the nose-wing tangency point. The local pressures over the nose are determined by the method described in Part III. The integral in Equation (V-7) can then be solved analytically for the flat section of the wing.

The method of iteration to find the actual wall temperatures along the surface of the wing will be the same as for the blunt

cone and the convective heat-transfer rate on the body at the edge of the window will be assumed to be the same as the average convective heat-transfer rate to the camera window.

Camera Window Temperatures

The steps followed to solve for the inner and outer window temperatures using the heat-transfer relations discussed in this section are listed below. This procedure consists of solving Equations (V-1) and (V-2), which are fourth-degree equations in temperature, simultaneously by graphical methods.

For specified values of camera window thickness, camera cavity temperature, camera cavity heat-transfer coefficient, free-stream Mach number, altitude, semiapex angle of cone or angle of attack of wing, radius of hemispherical nose of cone or leading edge of wing, and distance of camera window from nose, the following steps will yield the inner and outer window temperatures:

1. Calculate q_{c_o} at point D (Equation (V-7)) which is assumed to be the same as the convective heat-transfer at the window q_{c_w} . The value of q_{c_w} is considered to be insensitive to T_o because the driving potential $(i_s - i_w)$ is large so that small changes in T_o , hence small changes in i_w , do not affect the driving potential. Plot q_{c_o} versus T_o .
2. Calculate $q_{r_o} = k \frac{dT}{dy}$ from Equations (V-3) and (V-4) and plot as a function of T_o (one curve for each T_i) on same plot with q_{c_o} .

3. Plot T_o versus T_i as determined from the intersections of curves (1) and (2). This curve represents possible solutions of Equation (V-2).
4. Calculate q_{r_i} from Equation (V-5) and plot as function of T_i (one curve).
5. Calculate $-k \frac{dT}{dy} - q_{c_i}$ from Equations (V-3) and (V-6) and plot as a function of T_i (one curve for each T_o) on same plot as (4).
6. Plot T_o versus T_i as determined from the intersection of curves (4) and (5) on the same plot as (3). This curve represents possible solutions of Equation (V-1), and the intersection with the curve of (3) gives the temperatures T_o and T_i which satisfy Equations (V-1) and (V-2) simultaneously.

RESULTS AND DISCUSSION

Calculations were made to determine the camera window inner and outer surface temperatures and heat-transfer rates to the cavity for the two configurations and the range of Mach numbers and altitudes specified in Part II. The parameters specified for the calculations are:

Window thickness - 1/2 in.

Cavity wall and air temperature - 100° F

Distance of window from nose tangency point - 6 ft

Radius of nose - 1 ft

Semiapex angle of cone - 5°

Angle of attack of wing - 20°

Emissivity of body - 0.80

Emissivity of window - 0.93

Two values for the heat-transfer coefficient H at the inner surface of the window were considered. An H of zero was taken to simulate an evacuated cavity and an H of unity was taken to correspond approximately to the value for free convection from a vertical wall in a room at sea level. The thermal conductivity of the window was varied according to the table on page V-7.

A calculative example for the solution of the convective heat transfer to a blunt cone is given in Appendix VC and Figures V-1 and V-2. This example is for a cone at zero angle of attack at a Mach number of 16 and an altitude of 200,000 feet. The example illustrates that the iterative process does converge

rapidly to a solution whose accuracy is satisfactory to permit the determination of the camera window temperatures.

The results of the aerodynamic heating calculations for the blunt cone are shown in Figures V-3 and V-4 where the window outer surface temperature, the temperature difference across the window, and the heat transfer into the cavity are plotted as functions of Mach number and altitude for $H = 0$ and $H = 1$. The same parameters are plotted for the thick blunt wing in Figures V-5 and V-6. From these curves the following general observations can be made:

1. The effect of increasing Mach number is to increase the outer temperature of the window, the temperature differential through the window and the heat transfer into the cavity.
2. The effect of increasing altitude is to reduce the window outer temperature, the temperature differential through the window and the heat transfer into the cavity.
3. The effect of increasing H from zero to unity is a very small reduction of the outer temperature of the window, approximately 2 percent. The effect is more significant for the temperature differential, increasing approximately 15 percent. This is due to the additional cooling of the inner face of the window by convection at H equal to unity, whereas for H equal zero, the inner face is cooled only by radiation. The effect of increasing H

from zero to unity is to increase the heat transfer to the cavity by an amount as high as approximately 20 percent. Again, this is due to the combined effects of both radiation and convection for the case of H equal to unity.

4. The window outer temperature, the temperature differential through the window, and the heat-transfer rate to the cavity are all considerably greater for the thick blunt wing than for the blunt cone. This is due mainly to the wing surface's being inclined 20° with the free stream while the cone surface is only inclined 5° .

Subsequent to the heat-transfer calculations for which the room-temperature emissivity of quartz glass of 0.93 was used, information on the emissivity as a function of temperature has been obtained (Ref. 9). The effect of the reduction in emissivity with increasing temperature is to raise the calculated temperature of the window. The results of using the information of Reference 9 in place of the constant value of emissivity would be to increase the high end of the window temperature range by approximately 4 percent for the blunt cone and 8.5 percent for the thick blunt wing. The lower window temperatures will, of course, be less affected as their corresponding values of emissivity approach the room-temperature emissivity.

As a result of the findings of Part III of this report, the foregoing calculations were conducted only for the condition of laminar flow. However, at an altitude of 100,000 feet the boundary

layer over the window may be turbulent. In this case the temperature of the outer surface of the window, the temperature difference through the window, and the heat transfer into the cavity are considerably higher than shown for the laminar case. An indication of the magnitude of the temperature increase may be seen from Figure V-1 of Phase I of this contract (Ref. 1).

The values for the heat transfer into the cavity, as presented in the (c) part of Figures V-3 through V-6, are an indication of the cooling system requirements necessary to prevent aerodynamic heating from raising the cavity temperature above 100° F.

CONCLUSIONS

Analytical methods are presented for determining the temperature of a camera window mounted in the bottom surface of a blunt cone or a thick blunt wing which is traveling at hypersonic speeds. A method is derived in Appendixes VA and VB for calculating the convective heat transfer to blunt bodies accounting for real-gas effects. A calculative example of the procedure used to compute the convective heat transfer to the camera window is presented in Appendix VC.

Calculations have been conducted to determine the temperatures of the inner and outer surfaces of the window and the heat transferred from the window into the cavity. These calculations were performed for the configurations and the altitude and Mach

number ranges determined in Part II. These calculations indicate:

1. The maximum temperatures occurring on the outer surface of the window for the range of altitudes and Mach numbers covered is less than 2000° R.
2. Evacuating the cavity decreases the temperature differential through the glass and decreases the heat transfer to the cavity.
3. The window for the winged configurations gets considerably hotter than that for the nonwinged configurations for the flight conditions selected.

APPENDIX VA

DERIVATION OF INTEGRAL TYPE EQUATIONS FOR EVALUATING CONVECTIVE HEAT TRANSFER USING REFERENCE ENTHALPY TECHNIQUES

The equations that represent the flow over a body of revolution can be written as follows¹:

$$(r\rho u)_x + (r\rho v)_y = 0 \quad (VA-1)$$

$$\rho u u_x + \rho v u_y = - p_x + (\mu u_y)_y \quad (VA-2)$$

and

$$\rho u h_x + \rho v h_y = u p_x + (k T_y)_y + \mu (u_y)^2 \quad (VA-3)$$

Equations (VA-1), (VA-2), and (VA-3) represent the continuity, momentum and energy equations respectively. The derivation of the integral equations begins with the establishment of the value of the velocity normal to the surface by integrating (VA-1) with respect to y. There results

$$\int_0^y (r\rho u)_x dy + r\rho v - r\rho_w v_w = 0 \quad (VA-4)$$

In (VA-4), v_w , the normal velocity at the surface is permitted values other than zero to account for any mass transfer at the surface. At the edge of the boundary layer, where temperatures and the velocity parallel to the surface have both approached the free-stream values asymptotically,

Equation (VA-4) becomes

$$\int_0^{\delta} (r\rho u)_x dy + r\rho_{\delta} v_{\delta} - r\rho_w v_w = 0 \quad (VA-5)$$

Now, some methods of solution require use of the momentum

¹Subscript x or y refers to differentiation with respect to x or y.

equation which is first solved, and then the heat transfer rates are found by employing the Reynolds analogy locally. Although in the present approach, the energy equation will be solved directly, the momentum equation will be derived to be used in comparison with the energy equation. If the momentum equation is multiplied by r and the continuity equation by u there results

$$r\rho uu_x + r\rho vu_y = -rp_x + r(\mu u_y)_y \quad (VA-6)$$

$$u(r\rho u)_x + u(r\rho v)_y = 0 \quad (VA-7)$$

Adding (VA-6) and (VA-7) and considering differentiation by parts yields

$$(r\rho uu)_x + (r\rho vu)_y = -rp_x + r(\mu u_y)_y \quad (VA-8)$$

Integrating (VA-8) with respect to y results in

$$\int_0^y (r\rho uu)_x dy + r\rho vu - r\rho_w v_w u_w = -rp_x \delta + r(\tau - \tau_w) \quad (VA-9)$$

It is noted that r , p_x are not functions of y and that $\tau = \mu u_y$. With zero slip, $u_w = 0$. At the edge of the boundary layer, use of (VA-5) permits writing (VA-9) as

$$\int_0^\delta (r\rho uu)_x dy + u_\delta (r\rho_w v_w - \int_0^\delta (r\rho u)_x dy) = -rp_x \delta - r\tau_w \quad (VA-10)$$

From the flow external to the boundary layer it is noted that

$$\rho_\delta u_\delta (u_\delta)_x = -p_x \quad (VA-11)$$

Transposing and regrouping terms in Equation (VA-10)

results in

$$r\tau_w + r\rho_w v_w u_\delta = r\rho_\delta u_\delta (u_\delta)_x^\delta + \int_0^\delta u_\delta (r\rho u)_x dy - \int_0^\delta (r\rho u u)_x dy \quad (VA-12)$$

This equation can be rewritten as

$$\begin{aligned} r\tau_w + r\rho_w v_w u_\delta &= r\rho_\delta u_\delta (u_\delta)_x^\delta + \int_0^\delta (r\rho u u_\delta)_x dy - \int_0^\delta r\rho u (u_\delta)_x dy \\ &\quad - \int_0^\delta (r\rho u u)_x dy \\ &= r(u_\delta)_x \int_0^\delta (\rho_\delta u_\delta - \rho u) dy + \int_0^\delta [r\rho u (u_\delta - u)]_x dy \quad (VA-13) \end{aligned}$$

Because the term in the brackets of the last term of (VA-13) has a zero value at the outer edge of the boundary layer, the equation can be rewritten as

$$r\tau_w + r\rho_w v_w u_\delta = r(u_\delta)_x \int_0^\delta (\rho_\delta u_\delta - \rho u) dy + \frac{d}{dx} \int_0^\delta r\rho u (u_\delta - u) dy \quad (VA-14)$$

The integrals in Equation (VA-14) are related to the momentum thickness θ and the displacement thickness δ^* as shown

$$\theta = \int_0^\delta \frac{\rho u}{\rho_\delta u_\delta} \left(1 - \frac{u}{u_\delta}\right) dy \quad (VA-15)$$

$$\delta^* = \int_0^\delta \left(1 - \frac{\rho u}{\rho_\delta u_\delta}\right) dy \quad (VA-16)$$

Therefore,

$$\rho_\delta u_\delta^2 \theta = \int_0^\delta \rho u (u_\delta - u) dy \quad (VA-17)$$

and

$$\rho_{\delta} u_{\delta} \delta^* = \int_0^{\delta} (\rho_{\delta} u_{\delta} - \rho u) dy \quad (VA-18)$$

Substituting (VA-17) and (VA-18) into (VA-13) results in

$$r\tau_w + r\rho_w v_w u_{\delta} = r(u_{\delta})_x \rho_{\delta} u_{\delta} \delta^* + \frac{d}{dx} (r\rho_{\delta} u_{\delta}^2 \theta) \quad (VA-19)$$

Expanding (VA-19)

$$\begin{aligned} r\tau_w + r\rho_w v_w u_{\delta} &= r(u_{\delta})_x \rho_{\delta} u_{\delta} \delta^* + (r)_x \rho_{\delta} u_{\delta}^2 \theta + r(\rho_{\delta})_x u_{\delta}^2 \theta \\ &\quad + r\rho_{\delta} 2 u_{\delta} (u_{\delta})_x \theta + r\rho_{\delta} u_{\delta}^2 \theta_x \end{aligned} \quad (VA-20)$$

Defining the local skin friction coefficient as

$$\frac{C_f}{2} = \frac{\tau_w}{\rho_{\delta} u_{\delta}^2} \quad (VA-21)$$

and dividing (VA-20) through by $r\rho_{\delta} u_{\delta}^2$ results in

$$\frac{C_f}{2} + \frac{\rho_w v_w}{\rho_{\delta} u_{\delta}} = \frac{d\theta}{dx} + \left[\frac{1}{u_{\delta}} \frac{du_{\delta}}{dx} \left(\frac{\delta^*}{\theta} + 2 \right) + \frac{1}{r} \frac{dr}{dx} + \frac{1}{\rho_{\delta}} \frac{d\rho_{\delta}}{dx} \right] \theta \quad (VA-22)$$

Equation (VA-22) represents the integral form of the momentum equation.

The integral form of the energy equation is obtained in a similar fashion. First, Equation (VA-2) is multiplied through by u to yield

$$\rho u \left(\frac{u^2}{2} \right)_x + \rho v \left(\frac{u^2}{2} \right)_y = - u p_x + u (\mu u_y)_y \quad (VA-23)$$

This is added to Equation (VA-3) to obtain an energy equation

expressed in total enthalpy, namely

$$\rho u \left(h + \frac{u^2}{2} \right)_x + \rho v \left(h + \frac{u^2}{2} \right)_y = (kT_y)_y + (\mu uu_y)_y \quad (\text{VA-24})$$

To account for the effects on a body of revolution Equation (VA-24) is multiplied by r

$$r\rho u \left(h + \frac{u^2}{2} \right)_x + r\rho v \left(h + \frac{u^2}{2} \right)_y = r (kT_y)_y + r (\mu uu_y)_y \quad (\text{VA-25})$$

If Equation (VA-1) is multiplied by the total enthalpy, there results

$$\left(h + \frac{u^2}{2} \right) (r\rho u)_x + \left(h + \frac{u^2}{2} \right) (r\rho v)_y = 0 \quad (\text{VA-26})$$

Adding (VA-25) and (VA-26) results in

$$\left[r\rho u \left(h + \frac{u^2}{2} \right) \right]_x + \left[r\rho v \left(h + \frac{u^2}{2} \right) \right]_y = r (kT_y)_y + r (\mu uu_y)_y \quad (\text{VA-27})$$

Integrating with respect to y to the edge of the boundary layer results in

$$\int_0^{\delta} (r\rho u H)_x + r\rho \delta v \delta H_{\delta} - r\rho_w v_w H_w = - r (kT_y)_w \quad (\text{VA-28})$$

when

$$H = h + \frac{u^2}{2}$$

$$u_y \rightarrow 0 \text{ at } y \rightarrow \delta$$

$$u = 0 \quad y = 0$$

Letting the heat transferred to the body be represented by

$$q_w = (kT_y)_w$$

and introducing Equation (VA-5) results in

$$\int_0^{\delta} (r\rho u H)_x dy + \left[r\rho_w v_w - \int_0^{\delta} (r\rho u)_x dy \right] H_{\delta} - r\rho_w v_w H_w = - r q_w \quad (VA-29)$$

Now $H_{\delta} \neq f(x \text{ or } y)$ so that Equation (VA-29) can be re-written as

$$r q_w + r\rho_w v_w (H_{\delta} - H_w) = \int_0^{\delta} \left[r\rho u (H_{\delta} - H) \right]_x dy \quad (VA-30)$$

Since the term within the braces is equal to zero at the upper limit of integration, Equation (VA-30) can be written as

$$r q_w + r\rho_w v_w (H_{\delta} - H_w) = \frac{d}{dx} r \int_0^{\delta} \rho u (H_{\delta} - H) dy \quad (VA-31)$$

An energy integral can be defined as follows

$$\Gamma = \int_0^{\delta} \frac{\rho u}{\rho_{\delta} u_{\delta}} \frac{(H_{\delta} - H)}{(H_{\delta} - H_w)} dy \quad (VA-32)$$

It is quite similar to the momentum thickness, in fact the two are identical when $H = u$ as in the case of flow on a flat plate and with a Prandtl number of unity. When (VA-32) is substituted into Equation (VA-31), there occurs

$$r q_w + r\rho_w v_w (H_{\delta} - H_w) = \frac{d}{dx} \left[r\rho_{\delta} u_{\delta} (H_{\delta} - H_w) \Gamma \right] \quad (VA-33)$$

For the case where the change in temperature, or $\frac{dH_w}{dx}$, is small compared to the driving potential, $(H_{\delta} - H_w)$,

Equation (VA-33) can be rewritten as

$$\frac{q_w}{\rho_0 u_0 (H_0 - H_w)} + \frac{\rho_w v_w}{\rho_0 u_0} = \frac{d\Gamma}{dx} + \frac{\Gamma}{r \rho_0 u_0} \frac{d}{dx} (r \rho_0 u_0) \quad (\text{VA-34})$$

Equation (VA-34) constitutes the integral form of the energy equation.

Solution of Energy Integral Equation

There are several methods employed for solving for the rate of heat transfer to the surface of a body employing the integral equations. Often the momentum equation is solved first and then the Reynolds analogy is employed locally to evaluate the heat transfer rate. To do this it is necessary to know or to assume values of the ratio of the displacement to momentum thickness. A simpler approach will be employed here. The energy equation will be solved directly using the reference property method and the assumption that the local heat transfer is the same as it is on a flat plate when both are expressed in terms of the energy thickness.

On a flat plate the following relationships are known to exist:

$$St' = \frac{a}{(Pr')^{2/3} (\rho' u_0 x / \mu')^m} \quad (\text{VA-35})$$

where for laminar flow

$$a = 0.332$$

$$m = 0.5$$

and for turbulent flow

$$a = 0.0296$$

$$m = 0.2$$

Also the heat transfer rate to the body is given by

$$q_w = St' \rho' u_\delta \left(h_\delta + R \frac{u_\delta^2}{2} - H_w \right) \quad (VA-36)$$

where for laminar flow

$$R = (Pr')^{1/2}$$

and for turbulent flow

$$R = (Pr')^{1/3}$$

If Equations (VA-35) and (VA-36) are combined there results

$$\begin{aligned} \frac{q_w}{\rho_\delta u_\delta (h_\delta - H_w)} &= \frac{a \rho' u_\delta}{(Pr')^{2/3} (\rho' u_\delta x / \mu')^m} \frac{[h_\delta + R(u_\delta^2/2) - H_w]}{\rho_\delta u_\delta (h_\delta - H_w)} \\ &= \frac{a (\rho')^{1-m} (\mu')^m z}{\rho_\delta u_\delta^m x^m (Pr')^{2/3}} \end{aligned} \quad (VA-37)$$

where

$$z = \frac{h_\delta + R(u_\delta^2/2) - H_w}{h_\delta + (u_\delta^2/2) - H_w} \quad (VA-38)$$

Equation (VA-37) can be substituted into the energy integral equation

$$\frac{q_w}{\rho_\delta u_\delta (h_\delta - H_w)} = \frac{d}{dx} + \frac{1}{r \rho_\delta u_\delta} \frac{d}{dx} (r \rho_\delta u_\delta) \Gamma \quad (VA-39)$$

which simplifies to

$$\frac{q_w}{\rho_\delta u_\delta (h_\delta - H_w)} = \frac{d}{dx} \Gamma \quad (VA-40)$$

on a flat plate whose change in temperature, or $\frac{dH_w}{dx}$, is small compared to the driving potential $(H_0 - H_w)$. Combining Equations (VA-37) and (VA-40) yields

$$\frac{d\Gamma}{dx} = \frac{az(\rho'/\rho_0)}{(Pr')^{2/3}(\rho'u_0/\mu')^m x^m} \quad (VA-41)$$

When it is remembered that each of the terms on the right side of the equation, other than x^m , are independent of x on a flat plate, Equation (VA-41) can be integrated directly to give

$$\Gamma \Big|_{\Gamma_i} = \frac{az(\rho'/\rho_0)}{(Pr')^{2/3}(\rho'u_0/\mu')^m} \frac{x^{1-m}}{1-m} \Big|_{x_i}^x \quad (VA-42)$$

Now (VA-35) only applies when the boundary layers begin at $x = 0$, therefore

$$\Gamma_i = 0 \text{ when } x_i = 0 \quad (VA-43)$$

Thus

$$\Gamma = \frac{az(\rho'/\rho_0)}{(Pr')^{2/3}(\rho'u_0/\mu')^m} \frac{x^{1-m}}{1-m} \quad (VA-44)$$

Equation (VA-44) can be solved for x^m as

$$x^m = \left[\frac{(Pr')^{2/3}(\rho'u_0/\mu')^m(1-m)\Gamma}{az(\rho'/\rho_0)} \right]^{\frac{m}{1-m}} \quad (VA-45)$$

Substituting this into Equation (VA-37) yields

$$\frac{q_w}{\rho_0 u_0 (H_0 - H_w)} = \frac{a(\rho/\rho_0)z}{(Pr')^{2/3}(\rho'u_0/\mu')^m \left[\frac{(Pr')^{2/3}(\rho'u_0/\mu')^m(1-m)\Gamma}{az(\rho'/\rho_0)} \right]^{\frac{m}{1-m}}} \quad (VA-46)$$

This equation simplifies to

$$\begin{aligned}
 \frac{q_w}{\rho_0 u_0 (H_0 - H_w)} &= \frac{a^{\frac{1}{1-m}} (\rho'/\rho_0)^{\frac{1}{1-m}} Z^{\frac{1}{1-m}}}{(Pr')^{2/3} \left(\frac{1}{1-m}\right)^{\frac{m}{1-m}} (\rho' u_0 / \mu')^{\frac{m}{1-m}} (1-m)^{\frac{m}{1-m}} \Gamma^{\frac{m}{1-m}}} \\
 &= \left[\frac{a (\rho'/\rho_0) Z}{(Pr')^{2/3} (\rho' u_0 / \mu')^m (1-m)^m} \right]^{\frac{1}{1-m}} \quad (VA-47)
 \end{aligned}$$

It is now assumed that Equation (VA-47) applies to a body of revolution as well as a plate. Thus, using (VA-47) in (VA-39) yields for the body of revolution.

$$\frac{d\Gamma}{dx} + \frac{1}{r\rho_0 u_0} \frac{d}{dx} (r\rho_0 u_0) \Gamma = \left[\frac{a (\rho'/\rho_0) Z}{(Pr')^{2/3} (\rho' u_0 / \mu')^m (1-m)^m} \right]^{\frac{1}{1-m}} \Gamma^{-\frac{m}{1-m}} \quad (VA-48)$$

This is a Bernouli type of first order equation that is solved by transforming the dependent variable. Let

$$\Gamma = p^{1-m}$$

$$(1-m) p^{-m} \frac{dp}{dx} + \frac{1}{r\rho_0 u_0} \frac{d}{dx} (r\rho_0 u_0) p^{1-m} = g p^{-m} \quad (VA-49)$$

Where g represents the bracketed term in Equation (VA-48), Equation (VA-49) simplifies to

$$\frac{dp}{dx} + \frac{1}{(1-m)(r\rho_0 u_0)} \frac{d}{dx} (r\rho_0 u_0) p = \frac{g}{1-m} \quad (VA-50)$$

The integrating factor for this equation is

$$e^{\int \frac{1}{1-m} \frac{1}{r\rho_0 u_0} \frac{d}{dx} (r\rho_0 u_0) dx} = e^{\frac{1}{1-m} \ln (r\rho_0 u_0)} = (r\rho_0 u_0)^{\frac{1}{1-m}} \quad (\text{VA-51})$$

Therefore (VA-50) becomes

$$\frac{d}{dx} \left[(r\rho_0 u_0)^{\frac{1}{1-m}} p \right] = \frac{g(r\rho_0 u_0)^{\frac{1}{1-m}}}{1-m} \quad (\text{VA-52})$$

This integrates directly to yield

$$(r\rho_0 u_0)^{\frac{1}{1-m}} p \Big|_{x_i}^x = \int_{x_i}^x \frac{g(r\rho_0 u_0)^{\frac{1}{1-m}}}{(1-m)} d\lambda \quad (\text{VA-53})$$

Reintroducing Γ yields

$$\begin{aligned} (r\rho_0 u_0 \Gamma)^{\frac{1}{1-m}} - (r_i \rho_{0i} u_{0i} \Gamma_i)^{\frac{1}{1-m}} \\ = \int_{x_i}^x \left[\frac{a (\rho'/\rho_0) z r\rho_0 u_0}{(Pr')^{2/3} (\rho' u_0 / \mu')^m (1-m)^m} \right]^{\frac{1}{1-m}} \frac{d\lambda}{(1-m)} \end{aligned} \quad (\text{VA-54})$$

Therefore

$$\begin{aligned} \Gamma^{\frac{1}{1-m}} &= \left(\frac{r_i}{r} \frac{\rho_{0i}}{\rho_0} \frac{u_{0i}}{u_0} \Gamma_i \right)^{\frac{1}{1-m}} \\ &+ \frac{1}{(r\rho_0 u_0)^{\frac{1}{1-m}}} \int_{x_i}^x \left[\frac{a (\rho'/\rho_0) z r\rho_0 u_0}{(Pr')^{2/3} (\rho' u_0 / \mu')^m (1-m)^m} \right]^{\frac{1}{1-m}} \frac{d\lambda}{(1-m)} \end{aligned} \quad (\text{VA-55})$$

Combination of Equations (VA-55) and (VA-47) results in the expression for the local heat transfer rate to a point x on the body of revolution.

For the case of the laminar boundary layer which begins at the stagnation point, i.e., $r_i = 0$ and $u_{\delta i} = 0$

$$\Gamma^2 = \frac{1}{(r\rho_{\delta}u_{\delta})^2} \int_0^x \left[\frac{(0.332) (\rho'/\rho_{\delta}) z r\rho_{\delta}u_{\delta}}{(\Pr')^{2/3} (\rho' u_{\delta}/\mu')^{1/2} (1/2)^{1/2}} \right]^2 \frac{d\lambda}{1/2} \quad (\text{VA-56})$$

If the turbulent boundary layer begins at the leading edge

$$\Gamma^{5/4} = \frac{1}{(r\rho_{\delta}u_{\delta})^{5/4}} \int_0^x \left[\frac{0.0296 (\rho'/\rho_{\delta}) z r\rho_{\delta}u_{\delta}}{(\Pr')^{2/3} (\rho' u_{\delta}/\mu')^{1/5} (4/5)^{1/5}} \right]^{5/4} \frac{d\lambda}{4/5} \quad (\text{VA-57})$$

The heat transfer expressions under these conditions from (VA-47) are as follows:

$$\frac{q_w}{\rho_{\delta}u_{\delta}(H_{\delta}-H_w)} = \left[\frac{a (\rho'/\rho_{\delta}) z}{(\Pr')^{2/3} (\rho' u_{\delta}/\mu')^m} \right]^{\frac{1}{1-m}} \frac{1}{\left\{ \frac{(1-m)^{\frac{1}{1-m}}}{(r\rho_{\delta}u_{\delta})^{\frac{1}{1-m}}} \int_0^x \left[\frac{a (\rho'/\rho_{\delta}) z r\rho_{\delta}u_{\delta}}{(\Pr')^{2/3} (\rho' u_{\delta}/\mu')^m (1-m)^m} \right]^{\frac{1}{1-m}} \frac{d\lambda}{1-m} \right\}^m} \quad (\text{VA-58})$$

If $\Pr' \approx \text{constant}$, equation (VA-58) reduces to

$$\frac{q_w}{\rho_{\delta}u_{\delta}(H_{\delta}-H_w)} = \frac{a (\rho'/\rho_{\delta}) z}{(\Pr')^{2/3} (\rho' u_{\delta} x / \mu')^m G^m} \quad (\text{VA-59})$$

where

$$G = \left\{ \left[\frac{(\rho' u_\delta / \mu')^m}{Z r \rho_\delta u_\delta (\rho' / \rho_\delta)} \right]^{\frac{1}{1-m}} \frac{1}{x} \int_0^x \left[\frac{Z r \rho_\delta u_\delta (\rho' / \rho_\delta)}{(\rho' u_\delta / \mu')^m} \right]^{\frac{1}{1-m}} d\lambda \right\} \quad (\text{VA-60})$$

The final forms of these equations can be written as

$$\frac{q_w}{\rho_\delta u_\delta (H_\delta - H_w)} = \frac{a Z (\rho' / \rho_\delta)^{1-m} (\mu' / \mu_\delta)^m}{(Pr')^{2/3} (\rho_\delta u_\delta x / \mu_\delta)^m G^m} \quad (\text{VA-61})$$

where

$$G = \frac{1}{x} \left[\frac{(\rho_\delta u_\delta / \mu_\delta)^m}{Z r \rho_\delta u_\delta (\rho' / \rho_\delta)^{1-m} (\mu' / \mu_\delta)^m} \right]^{\frac{1}{1-m}} \int_0^x \left[\frac{Z r \rho_\delta u_\delta (\rho' / \rho_\delta)^{1-m} (\mu' / \mu_\delta)^m}{(\rho_\delta u_\delta / \mu_\delta)^m} \right]^{\frac{1}{1-m}} d\lambda \quad (\text{VA-62})$$

For laminar boundary layers Equations (VA-61) and (VA-62) become

$$\frac{q_w}{\rho_\delta u_\delta (H_\delta - H_w)} = \frac{0.332 Z (\rho' / \rho_\delta)^{0.5} (\mu' / \mu_\delta)^{0.5}}{(Pr')^{2/3} (\rho_\delta u_\delta x / \mu_\delta)^{0.5} G_l^{0.5}} \quad (\text{VA-63})$$

Where

$$G_l = \frac{1}{x} \left[\frac{(\rho_\delta u_\delta / \mu_\delta)^{0.5}}{Z r \rho_\delta u_\delta (\rho' / \rho_\delta)^{0.5} (\mu' / \mu_\delta)^{0.5}} \right]^2 \int_0^x \left[\frac{Z r \rho_\delta u_\delta (\rho' / \rho_\delta)^{0.5} (\mu' / \mu_\delta)^{0.5}}{(\rho_\delta u_\delta / \mu_\delta)^{0.5}} \right]^2 d\lambda \quad (\text{VA-64})$$

The expression for q_w reduces to

$$q_w = \frac{0.332 Z^2 r u_\delta \rho' \mu' \left[h_\delta + (u_\delta^2 / 2) - h_w \right]}{(Pr')^{2/3} \left(\int_0^x Z^2 r^2 u_\delta \rho' \mu' d\lambda \right)^{0.5}} \quad (\text{VA-65})$$

For turbulent boundary layers Equations (VA-61) and (VA-62) become

$$\frac{q_w}{\rho_0 u_0 (H_0 - H_w)} = \frac{0.0296 Z (\rho'/\rho_0)^{4/5} (\mu'/\mu_0)^{1/5}}{(\Pr')^{2/3} (\rho_0 u_0 x / \mu_0)^{1/5} G_t^{1/5}} \quad (\text{VA-66})$$

where

$$G_t = \frac{1}{x} \left[\frac{(\rho_0 u_0 / \mu_0)^{1/5}}{Z r \rho_0 u_0 (\rho'/\rho_0)^{4/5} (\mu'/\mu_0)^{1/5}} \right]^{5/4}$$

$$\int_0^x \left[\frac{Z r \rho_0 u_0 (\rho'/\rho_0)^{4/5} (\mu'/\mu_0)^{1/5}}{(\rho_0 u_0 / \mu_0)^{1/5}} \right]^{5/4} d\lambda \quad (\text{VA-67})$$

The expression for q_w for turbulent flow may be reduced to

$$q_w = \frac{0.0296 Z^{5/4} r^{1/4} u_0 \rho' (\mu')^{1/4} [h_0 + (u_0^2/2) - h_w]}{(\Pr')^{2/3} \left[\int_0^x (Z r)^{5/4} u_0 \rho' (\mu')^{1/4} d\lambda \right]^{1/5}} \quad (\text{VA-68})$$

This method was compared with the laminar flow solution by Lees (Ref. 7) whose results may be expressed as

$$q_w = \frac{0.354 r_o^n \rho_e \mu_e u_e [h_e + (u_e^2/2)] (\rho'/\rho_e) (\mu'/\mu_e) (1/\rho_o \mu_o)^{1/2} (1/u_\infty)^{1/2}}{(\Pr')^{2/3} \left[\int_0^s (\rho'/\rho_o) (\mu'/\mu_o) (u_e/u_\infty) (r_o)^{2n} ds \right]^{1/2}}$$

This compares to the expanded derivation of this report which becomes

$$q_w = \frac{0.332z^2 r_o \rho_0 u_0 \mu_0 [h_0 + (u_0^2/2) - h_w] (\rho'/\rho_0)(\mu'/\mu_0) (1/\rho_o \mu_o)^{1/2} (1/u_\infty)^{1/2}}{(\Pr')^{2/3} \left[\int_0^x z^2 r_o^2 (u_0/u_\infty) (\rho'/\rho_o) (\mu'/\mu_o) d\lambda \right]^{1/2}}$$

where $e = 5$, $x = s$ and $n = 0$ for two dimensional flow, $n = 1$ for rotationally symmetric flow. It is seen that the methods are comparable with the exception that the method derived herein includes the effects of the enthalpy ratio, z , the wall enthalpy, h_w , and an approximately 6% difference in the constant.

APPENDIX VB

CONVECTIVE HEAT TRANSFER-RATE AT STAGNATION POINT

To obtain the convective heat-transfer rate at the stagnation point, the limit of the expression for q_w is taken as r approaches zero. Near the stagnation point, the following conditions exist:

$$u_\delta = \beta x$$

where β is found from Newtonian theory to be

$$\beta = \frac{1}{R} \left[\frac{2(p_s - p_\infty)}{\rho_s} \right]^{1/2}$$

where R = radius of nose.

ρ' , μ' \cong constant for small values of x

$$r \cong x$$

$$z \cong 1$$

therefore, from Appendix VA,

$$q_w = \frac{0.332 z^2 r u_\delta \rho' \mu' \left(h_\delta + \frac{u_\delta^2}{2} - h_w \right)}{(Pr)^{2/3} \left[\int_0^x z^2 r^2 u_\delta \rho' \mu' d\lambda \right]^{1/2}}$$

which reduces to,

$$(q_w)_s = \frac{0.332 x^2 \beta (\rho') (\mu') (h_s - h_w)}{(Pr)^{2/3} \left[\beta \rho' \mu' \int_0^x x^3 d\lambda \right]^{1/2}}$$

$$(q_w)_s = \frac{0.664 (\beta \rho' \mu')^{1/2} (h_s - h_w)}{(Pr)^{2/3}}$$

APPENDIX VC

CALCULATIVE EXAMPLE FOR CONVECTIVE HEAT TRANSFER RATE
TO CAMERA WINDOW ON BLUNT CONE

A sample calculation to determine the convective heat transfer to the camera window is presented to illustrate the procedures involved in using the method described in the text. The conditions selected for this example are:

1. Mach number 16
2. Altitude 200,000 ft
3. Blunt cone at zero angle of attack with nose radius = 1 ft and semi-apex angle = 5°
4. Window located 6 ft aft of nose-cone tangent point
5. Laminar flow in boundary layer

The free stream conditions are obtained from the atmospheric tables of Reference 8. These are:

$$T_{\infty} = 449^{\circ}\text{R}$$

$$p_{\infty} = 4.7151 \times 10^{-1} \text{ lb/ft}^2$$

$$\rho_{\infty} = 6.1180 \times 10^{-7} \text{ slugs/ft}^3$$

$$a_{\infty} = 1038.7 \text{ ft/sec}$$

then

$$i_{\infty} = c_p T_{\infty} = 0.24 (449) = 107.76, \text{ BTU/lb}$$

and

$$i_s = i_{\infty} + \frac{V_{\infty}^2}{2gJ}$$

where

$$V_{\infty} = a_{\infty} M_{\infty} = 16,619 \text{ ft/sec}$$

therefore,

$$i_s = 5625 = (i_0)_s \text{ BTU/lb}$$

The value of $(c_p)_s$ at M_∞ for the blunt cone is found from Figure III-1 of part III of this report. The stagnation pressure p_s is found from the relation

$$p_s = p_\infty + 1/2 \rho_\infty V_\infty^2 (c_p)_s = (p_0)_s$$

$$(p_0)_s = 155.9 \text{ lb/ft}^2$$

The value of $(\rho_0)_s$ is obtained from the charts of Reference 6 by determining Z and T at $(i_0)_s = 5625$ and $(p_0)_s = 7.364 \times 10^{-2}$ atm. and solving the expression

$$(\rho_0)_s = 39.65 \frac{(p_0)_s}{(Z_0)_s (T_0)_s g}$$

$$= 7.487 \times 10^{-6} \text{ slugs/ft}^3$$

The primed values, ρ' and μ' , are obtained through the use of i' . For laminar flow,

$$i' = 0.23 i_0 + 0.19 i_r + 0.58 i_w$$

where, from Equation (v-9) and the fact that $V_0 = 0$ at the stagnation point,

$$(i_r)_s = (i_0)_s$$

Since the wall temperature is initially unknown, $(T_w)_s$ will be assumed to be 1000°R ; therefore, from Reference 6 at $(p_0)_s$

and $(T_w)_s$

$$(i_w)_s = 235 \text{ BTU/lb}$$

The value of $(i')_s$ is then,

$$\begin{aligned} (i')_s &= 0.23 (i_g)_s + 0.19 (i_g)_s + 0.58 (i_w)_s \\ &= 2499 \text{ BTU/lb} \end{aligned}$$

Then

$$(\rho')_s = 39.65 \frac{(p_0)_s}{(Z')_s (T')_s g}$$

where $(Z')_s$ and $(T')_s$ are found from Reference 6 at $(i')_s$ and $(p_0)_s$. Using these quantities,

$$(\rho')_s = 1.434 \times 10^{-5} \text{ slugs/ft}^3$$

The value of $(\mu')_s$ is found from Equation (V-10),

$$(\mu')_s = 2.28 \times 10^{-8} (T')_s^{1/2} \left[1 + \frac{202}{(T')_s} \right] \left(\frac{\eta}{\eta_0} \right)'$$

where $(\eta/\eta_0)'$ is found from Figure 8 of Reference 4 at $(T')_s$ and $(p_0)_s$ to be

$$\left(\frac{\eta}{\eta_0} \right)' = 1.0$$

Therefore,

$$(\mu')_s = 1.809 \times 10^{-8} \frac{\text{lb-sec}}{\text{ft}^2}$$

The average Prandtl number for the range of anticipated temperatures is taken as 0.72. The convective heat transfer at the stagnation point is then determined from Equation (V-7) using the quantities which have been established for the terms in the equation; therefore,

$$(q_c)_s = 2.106 \times 10^5 \text{ BTU/ft}^2\text{-hr}$$

The radiation equilibrium temperature of the wall will be determined from Equation (V-14) which can be expressed as

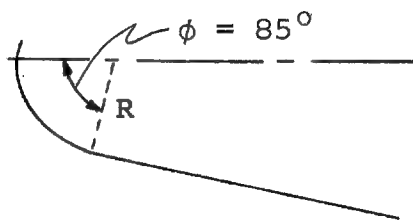
$$(T_w)_s = \left[\frac{(q_c)_s}{0.8(0.173 \times 10^{-8})} \right]^{1/4}$$

thus,

$$(T_w)_s = 3514^{\circ}\text{R}$$

This temperature will be used later to find a new value of i_w to be used in the first iteration of this method.

In order to evaluate the contribution of the hemispherical nose to the integral in the denominator of Equation (V-7), the heat transfer must be determined at several locations along the surface of the nose. To illustrate this procedure a point is selected on the nose corresponding to an angle ϕ of 85° which is the tangency point of the hemisphere and cone as shown in the following sketch



From Equation (V-13) and the expression

$$\alpha = \frac{\pi}{2} - \phi$$

the C_p at angle ϕ is found to be 0.01398. Then

$$\begin{aligned} (p_0)_{s5} &= 1/2 \rho_\infty v_\infty^2 (C_p)_{s5} + p_\infty \\ &= 1.653 \text{ lb/ft}^2 \end{aligned}$$

The value of $(i_0)_{s5}$ is found from the graphs of Reference 6 by locating the point at $(p_0)_s$ and i_s , then following the line of constant entropy to $(p_0)_{s5}$. Taking a constant value of entropy assumes that the flow at the edge of the boundary layer is isentropic. It is thus determined from the graphs that

$$(i_0)_{s5} = 2810 \text{ BTU/lb}$$

The value of $(i_r)_{s5}$ is determined from Equation (V-9) where $r = (Pr)^{1/2}$ for the laminar flow case and where the quantity $(v_0)_{s5}^2/2gJ$ is found from the expression

$$i_s = (i_0)_{s5} + \frac{(v_0)_{s5}^2}{2gJ}$$

thus,

$$\frac{(v_0)_{s5}^2}{2gJ} = 2815 \text{ BTU/lb}$$

From Equation (V-9),

$$(i_r)_{s5} = 5199 \text{ BTU/lb}$$

For the purpose of a first approximation, the wall enthalpy is again assumed to be 235 BTU/lb. The required quantities are now available to solve for $(i')_{85}$ using Equation (V-8) which yields

$$(i')_{85} = 1770 \text{ BTU/lb}$$

The values of $(T')_{85}$ and $(Z')_{85}$ are located on the graphs of Reference 6 at the point corresponding to $(i')_{85}$ and $(p')_{85}$. These values are:

$$(T')_{85} = 4392^{\circ}\text{R}$$

$$(Z')_{85} = 1.070$$

Knowing $(T')_{85}$ and $(Z')_{85}$, the terms $(\mu')_{85}$ and $(\rho')_{85}$ are determined from Equations (V-10) and (V-11). They are found to be

$$(\mu')_{85} = 1.5805 \times 10^{-6} \text{ lb-sec/ft}^2$$

$$(\rho')_{85} = 2.046 \times 10^{-7} \text{ slugs/ft}^3$$

All of the terms in Equation (V-12) are now known, thus

$$(f)_{85} = 0.9210$$

The value of r_o is found from the relation $r_o = \sin \phi$ to be

$$r_o = 0.9962 \text{ ft}$$

The constants n , u and m are taken from Table (V-I) for the laminar case and l is equal to 1 for the blunt cone.

The integrand in the denominator of Equation (V-7) is evaluated using the quantities determined at $\phi = 85^\circ$. The value of the integrand is then plotted as a function of the distance s to the 85° point. This value of $(s)_{85}$ is found from the expression

$$s = \phi R$$

Where

$$\phi = 1.483 \text{ radians}$$

therefore,

$$(s)_{85} = 1.483 \text{ ft}$$

The same procedure is followed for several other angles from 0 to 85 degrees and the integrand at each angle plotted as a function of its distance s . The resulting curve is shown in Figure V-1. Equation (V-7) is solved for each of the points selected on the nose by

1. Graphically integrating the curve of Figure VC-1 from $s = 0$ to s at the point concerned to obtain the integral in the denominator of the equation.
2. Assuming that i_w at the point is 235 BTU/lb.
3. Taking a_1 from Table (V-1) for laminar flow.
4. Solving for v_5 from the value of $(v_5^2)_{\phi} / 2gJ$ previously determined.

For $\phi = 85$ degrees,

$$(v_5)_{85} = 11,871 \text{ ft/sec}$$

From Equations (V-7) and (V-14)

$$(q_c)_{85} = 4987 \text{ BTU/ft}^2\text{-hr}$$

$$(T_w)_{85} = 1379^{\circ}\text{R}$$

The wall temperatures at the other locations on the nose are obtained in the same manner. A curve of T_w vs. S is shown in Figure V-2.

In order to solve for the convective heat transfer rate at point D on the cone, the integral in the denominator of Equation (V-7) is evaluated in two sections, (1) from the stagnation point to $\phi = 85^{\circ}$ (point A) and (2) from point A to point D. From Equations (V-15) and (V-16) the integral becomes

$$\int_0^{1.484} \left[f^n r_o^n v_0 \rho' (\mu')^u d\lambda \right] + f^n v_0 \rho' (\mu')^u \int_{1.484}^{7.484} (0.087s + 0.867)^n d\lambda$$

this expression reduces to

$$2.82 \times 10^{-8} + (f^n)_{85} (v_0)_{85} (\rho')_{85} (\mu')_{85}^u \quad (9.617)$$

The fact that the terms f , v_0 , ρ' and μ' are the same as found at point A is the result of α , and hence p_0 , being constant from A to D. The value of i_w is again taken as 235 BTU/lb. Equation (V-7) then yields

$$(q_c)_D = 5245 \text{ BTU/ft}^2\text{-hr}$$

and from Equation (V-14),

$$(T_w)_D = 1396^{\circ}\text{R}$$

The entire calculative process is now repeated with the assumed value of i_w replaced by the local value of i_w determined from the calculated T_w at each location. The value of i_w is found from the plots of Reference 6 at the point determined by T_w and p_0 .

At the stagnation point, using the calculated T_w ,

$$(i_w)_s = 965$$

Using Equations (V-8), (V-10), (V-11) and the graphs of References 4 and 6,

$$(i')_s = 2922 \text{ BTU/lb}$$

$$(\rho')_s = 1.301 \times 10^{-5} \text{ slugs/ft}^3$$

$$(\mu')_s = 1.835 \times 10^{-8} \text{ lb-sec/ft}^2$$

The revised stagnation point heat transfer (Eq. (V-7)) becomes

$$(q_c)_s = 1.748 \times 10^5 \text{ BTU/ft}^2\text{-hr}$$

and from Equation (V-14),

$$(T_w)_s = 3355^{\circ}\text{R}$$

This substitution of the calculated i_w for the assumed value is carried out at each of the locations previously investigated in the same manner as described for the stagnation

point. The wall temperatures are again calculated and plotted on Figure VC-2. It can be seen by comparing the first and second curves that the fortuitous choice of the initial i_w has permitted only one iteration to yield an accurate wall temperature at point D on the cone. The value of $(q_c)_D$ determined by the second set of calculations will then be used as described in the text for the solution of the heat balance through the camera window.

REFERENCES

1. Nielsen, Jack N., Goodwin, Frederick K., Sacks, Alvin H., Rubesin, Morris W., Ragent, Boris, and Noble, Charles E.: Effects of Supersonic and Hypersonic Aircraft Speed Upon Aerial Photography. Final Technical Report, Phase I, Vidya Report No. 17, March 1960.
2. Johnson, H. A. and Rubesin, M. W.: Aerodynamic Heating and Convective Heat Transfer. Summary of Literature Survey. Transactions of the A.S.M.E., Vol. 71, No. 5, July 1949.
3. Sommer, Simon C. and Short, Barbara J.: Free-Flight Measurements of Turbulent Boundary-Layer Skin Friction in the Presence of Severe Aerodynamic Heating at Mach Numbers from 2.8 to 7.0. NACA TN 3391, 1955.
4. Hansen, C. Frederick: Approximations for the Thermodynamic and Transport Properties of High-Temperature Air. NACA TN 4150, March 1958.
5. Feldman, Saul: Hypersonic Gas Dynamic Charts for Equilibrium Air. Avco Research Laboratories, Jan. 1957.
6. Moeckel, W. E., and Weston, Kenneth C.: Composition and Thermodynamic Properties of Air in Chemical Equilibrium. NACA TN 4265, April 1958.
7. Eckert, E. R. G. and Tewfik, O. E.: Use of Reference Enthalpy in Specifying the Laminar Heat-Transfer Distribution Around Blunt Bodies in Dissociated Air. Journal of the Aero/Space Sciences, Vol. 27, No. 6, June 1960.
8. Minzner, R. A., Champion, K. S. W., and Pond, H. L.: The ARDC Atmosphere, 1959. Air Force Surveys in Geophysics, No. 115. Air Force Cambridge Research Center, TR-59-267, Aug. 1959.
9. Anon.: Materials Handbook, NP-5, New Products Division, Corning Glass Works, Jan. 10, 1958.

Approved For Release 2000/04/12 : CIA-RDP67B00657R000300070001-0

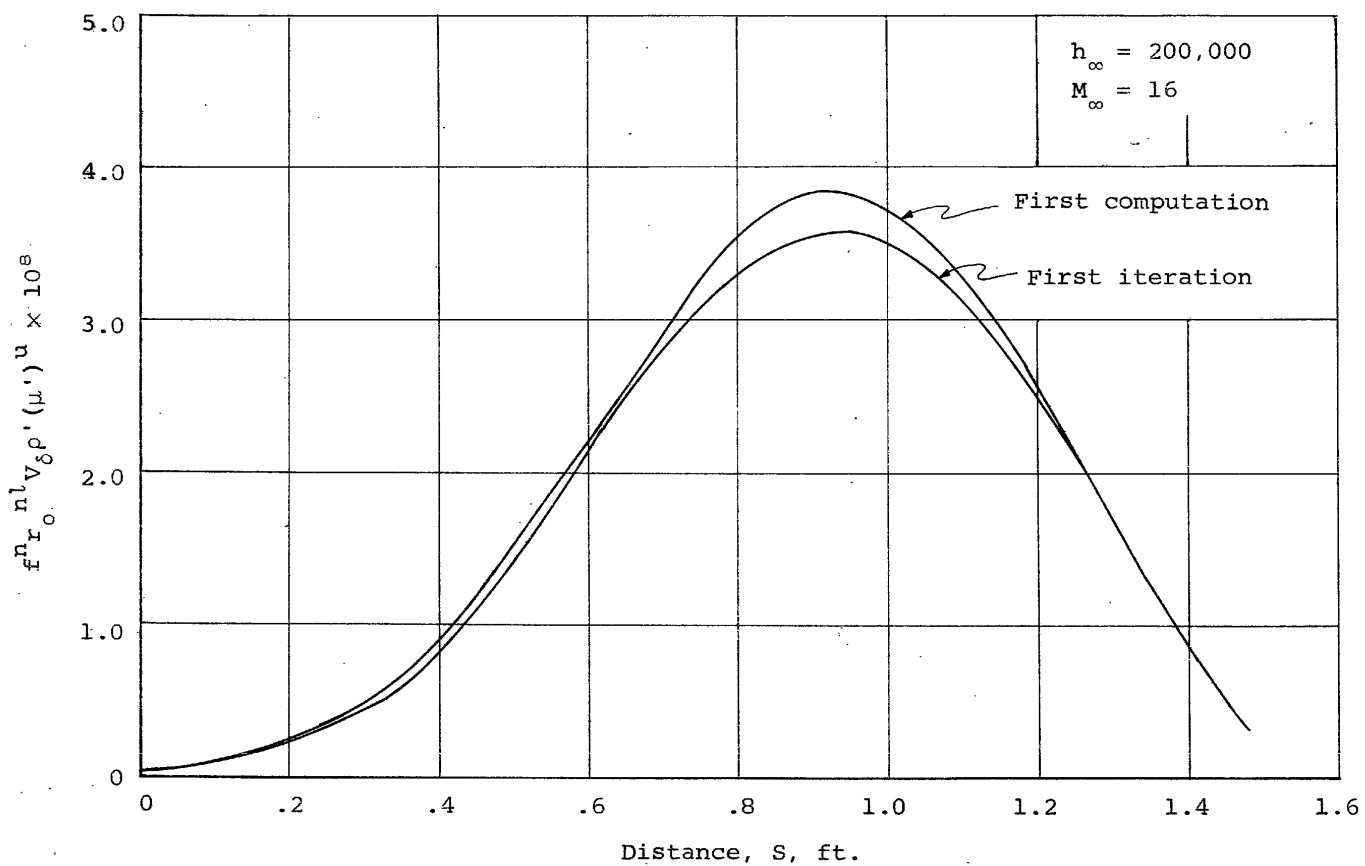


Figure V-1.- Integrand of Equation (V-7) as a function of distance from stagnation point for hemispherical nose.

Approved For Release 2000/04/12 : CIA-RDP67B00657R000300070001-0

Approved For Release 2000/04/12 : CIA-RDP67B00657R000300070001-0

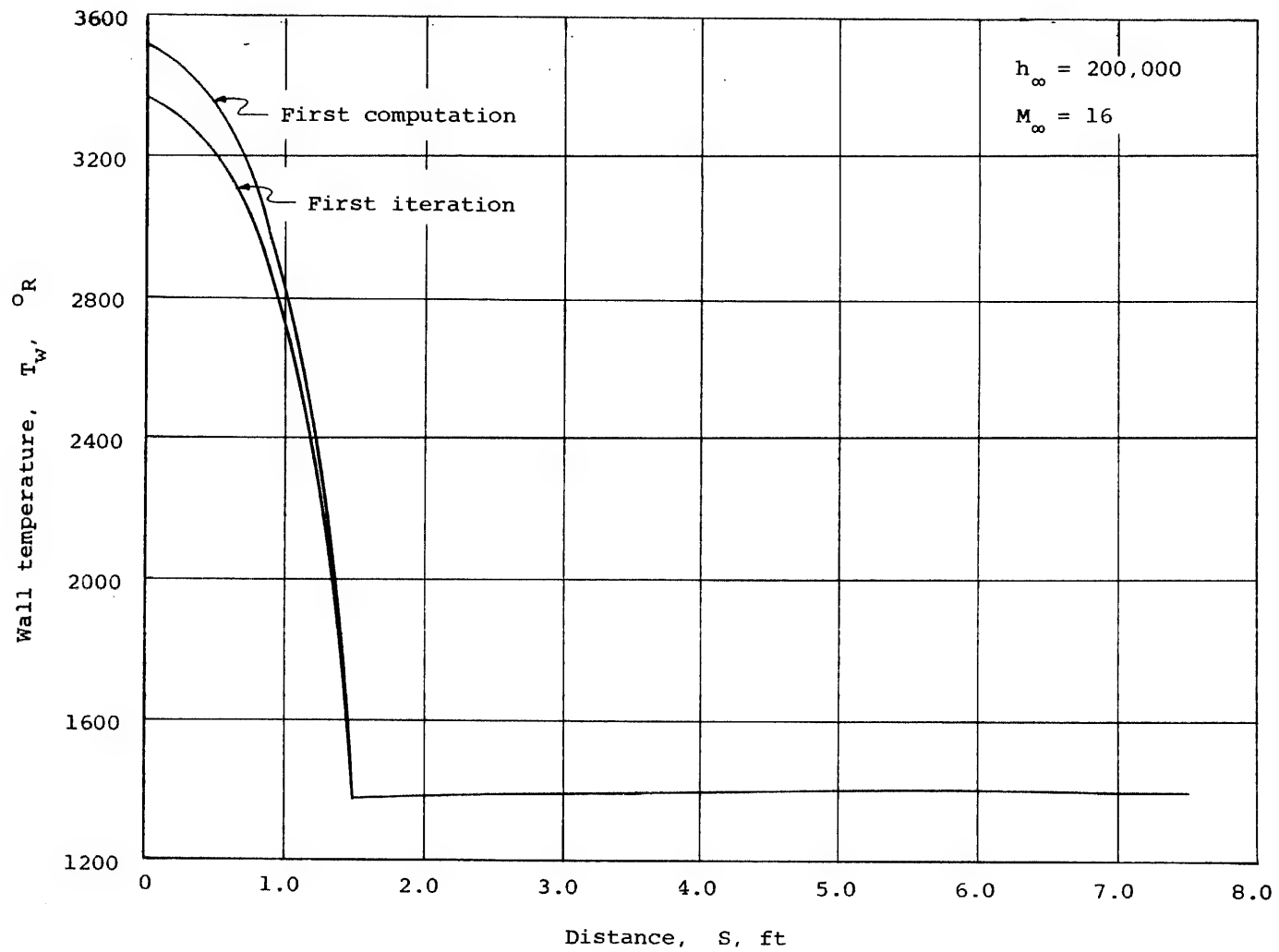
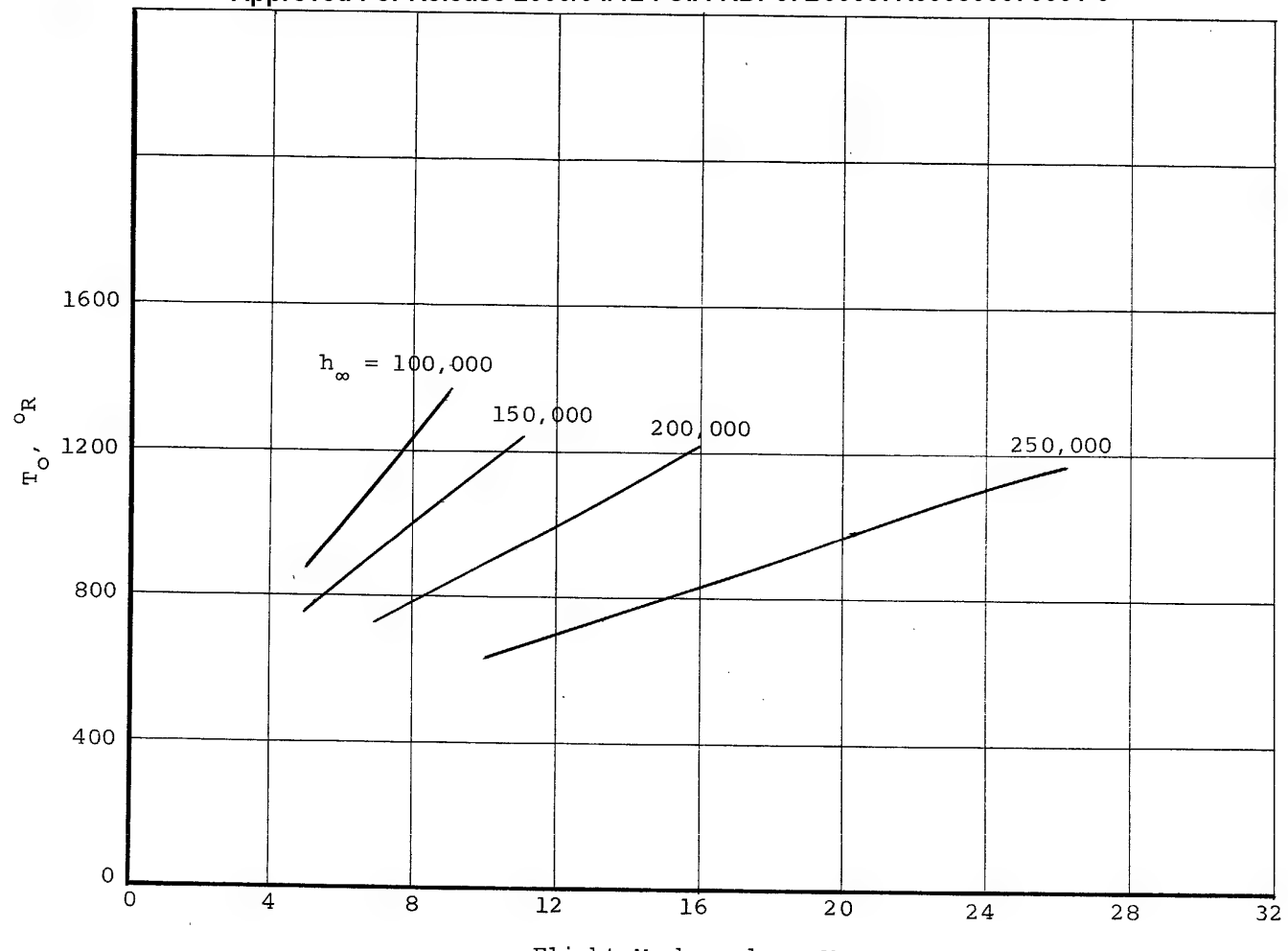


Figure V-2.- Wall temperature distribution along surface of blunt cone.

Approved For Release 2000/04/12 : CIA-RDP67B00657R000300070001-0

Approved For Release 2000/04/12 : CIA-RDP67B00657R000300070001-0

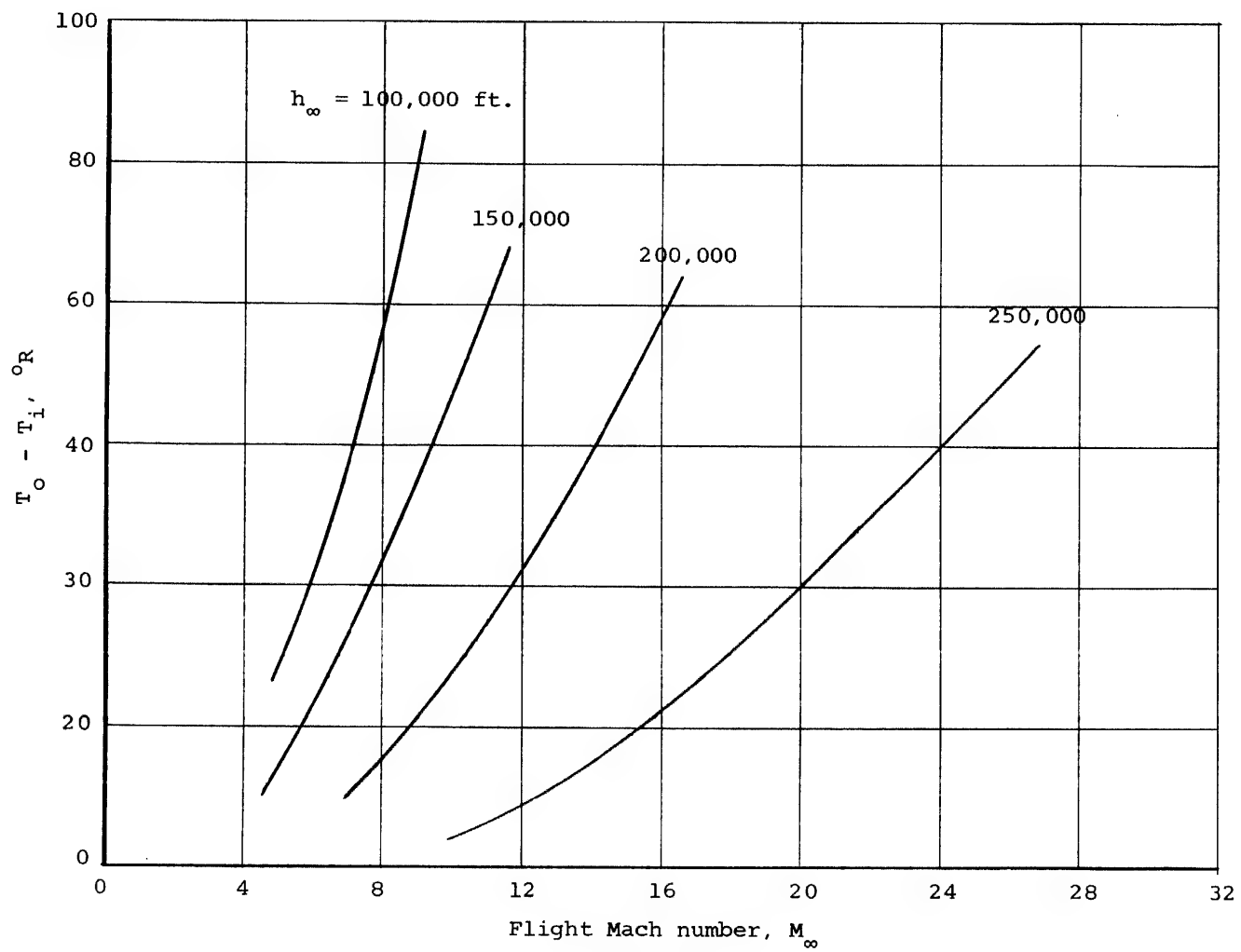


(a) Window outer surface temperature.

Figure V-3.- Aerodynamic heating at camera window for blunt cone with $H = 0$.

Approved For Release 2000/04/12 : CIA-RDP67B00657R000300070001-0

Approved For Release 2000/04/12 : CIA-RDP67B00657R000300070001-0

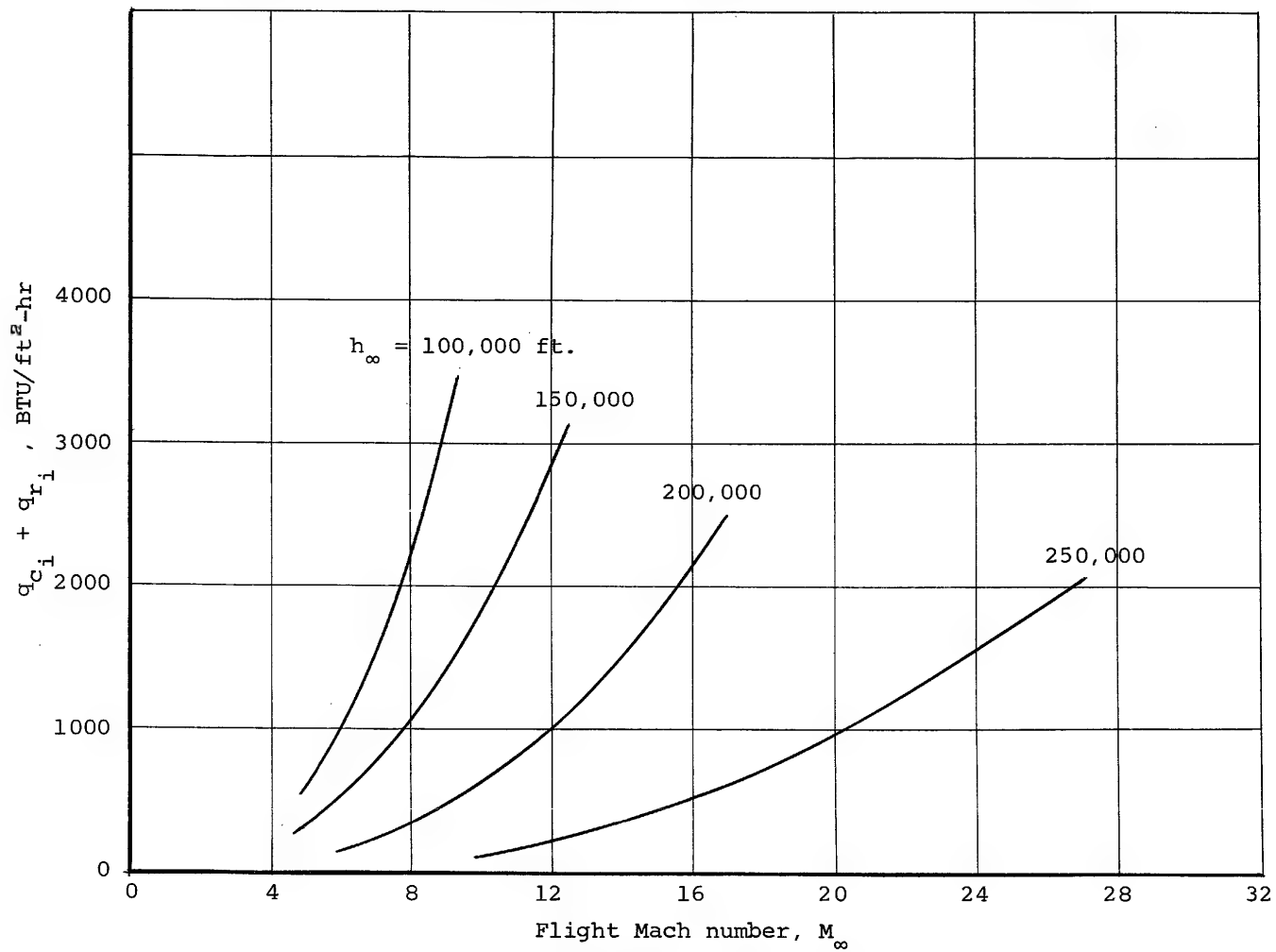


(b) Temperature difference across window

Figure V-3.- Continued

Approved For Release 2000/04/12 : CIA-RDP67B00657R000300070001-0

Approved For Release 2000/04/12 : CIA-RDP67B00657R000300070001-0

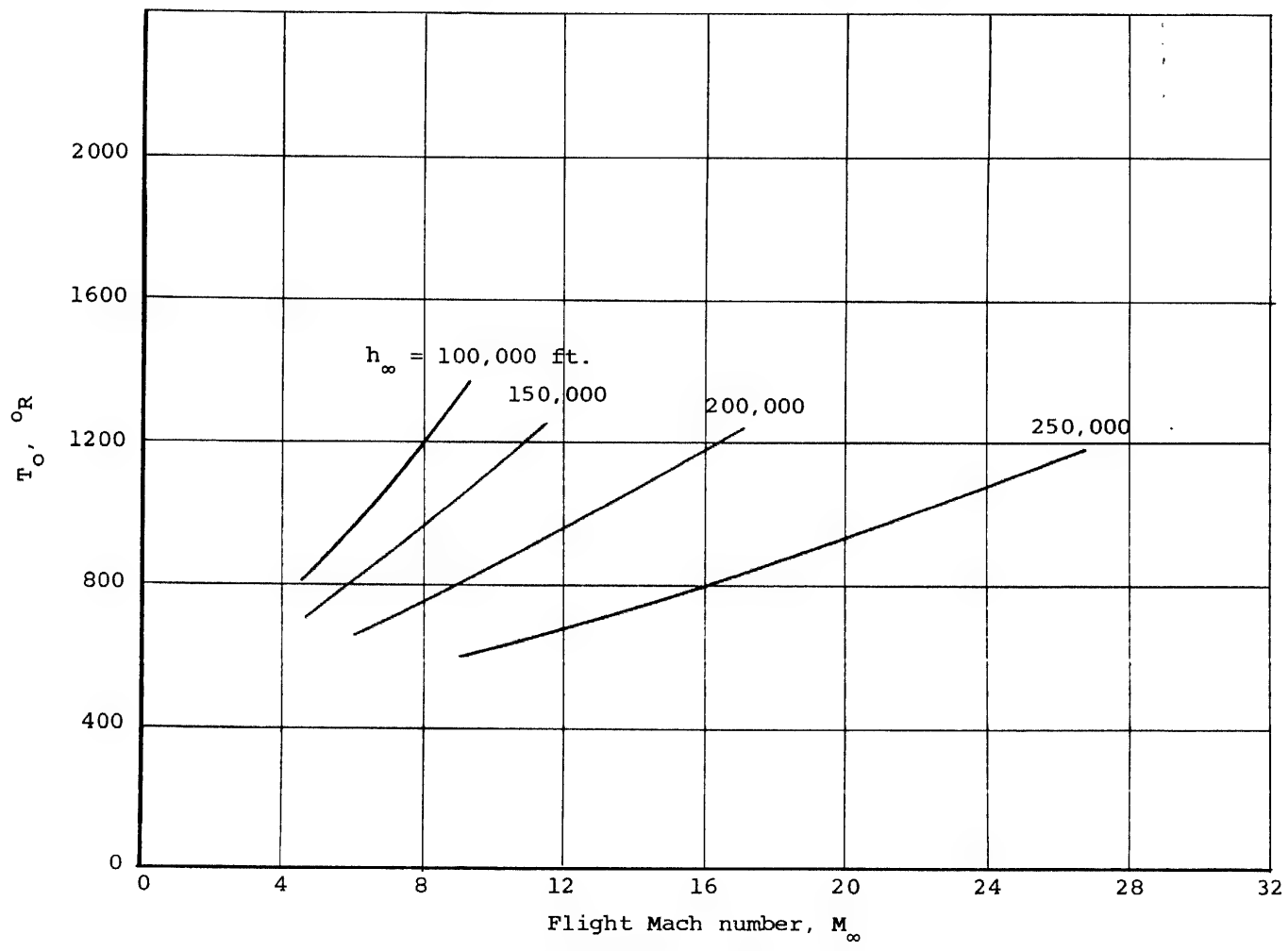


(c) Heat transfer rate to cavity

Figure V-3.- Concluded.

Approved For Release 2000/04/12 : CIA-RDP67B00657R000300070001-0

Approved For Release 2000/04/12 : CIA-RDP67B00657R000300070001-0

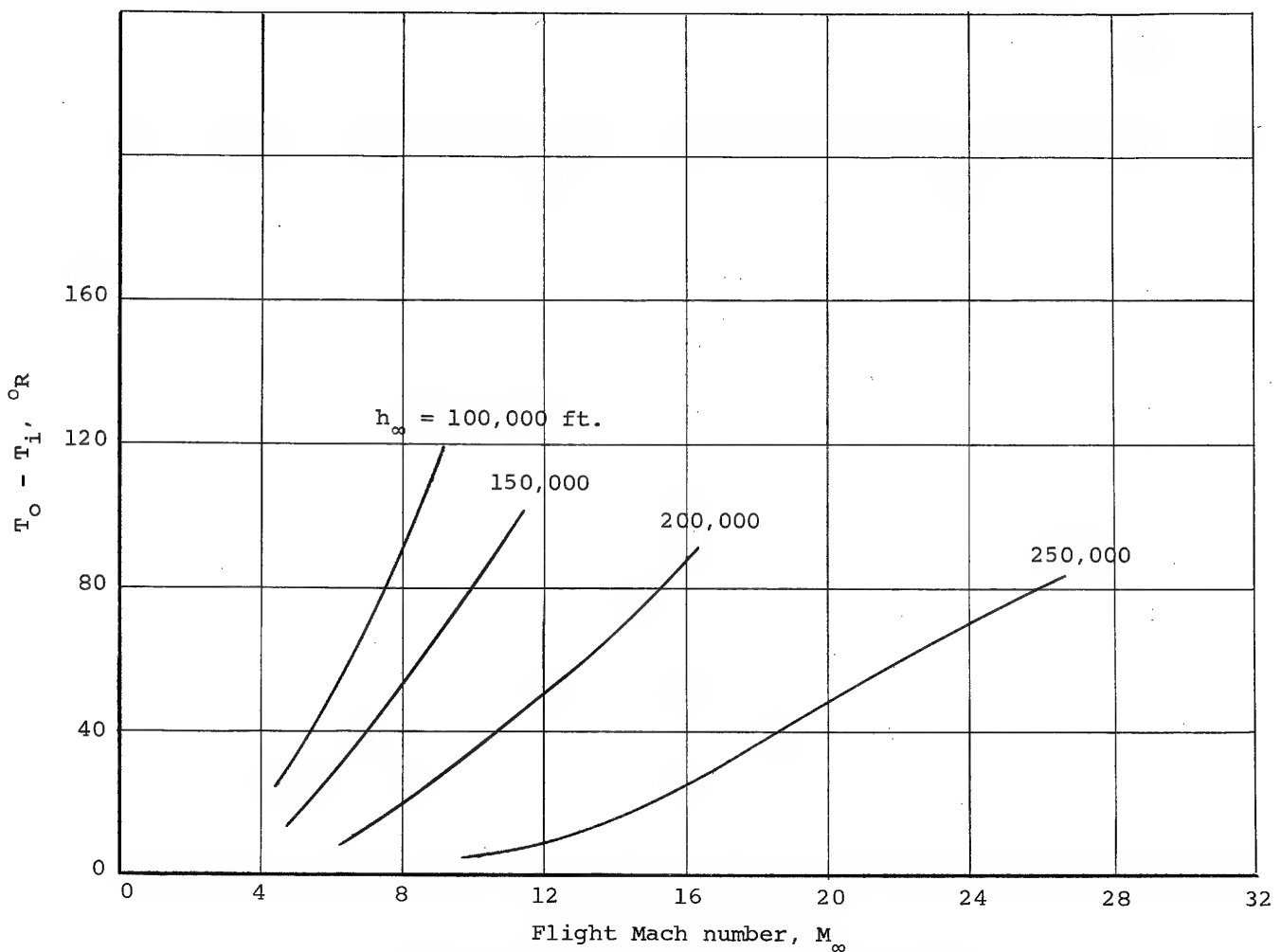


(a) Window outer surface temperature

Figure V-4.- Aerodynamic heating at camera window for blunt cone with $H = 1$

Approved For Release 2000/04/12 : CIA-RDP67B00657R000300070001-0

Approved For Release 2000/04/12 : CIA-RDP67B00657R000300070001-0

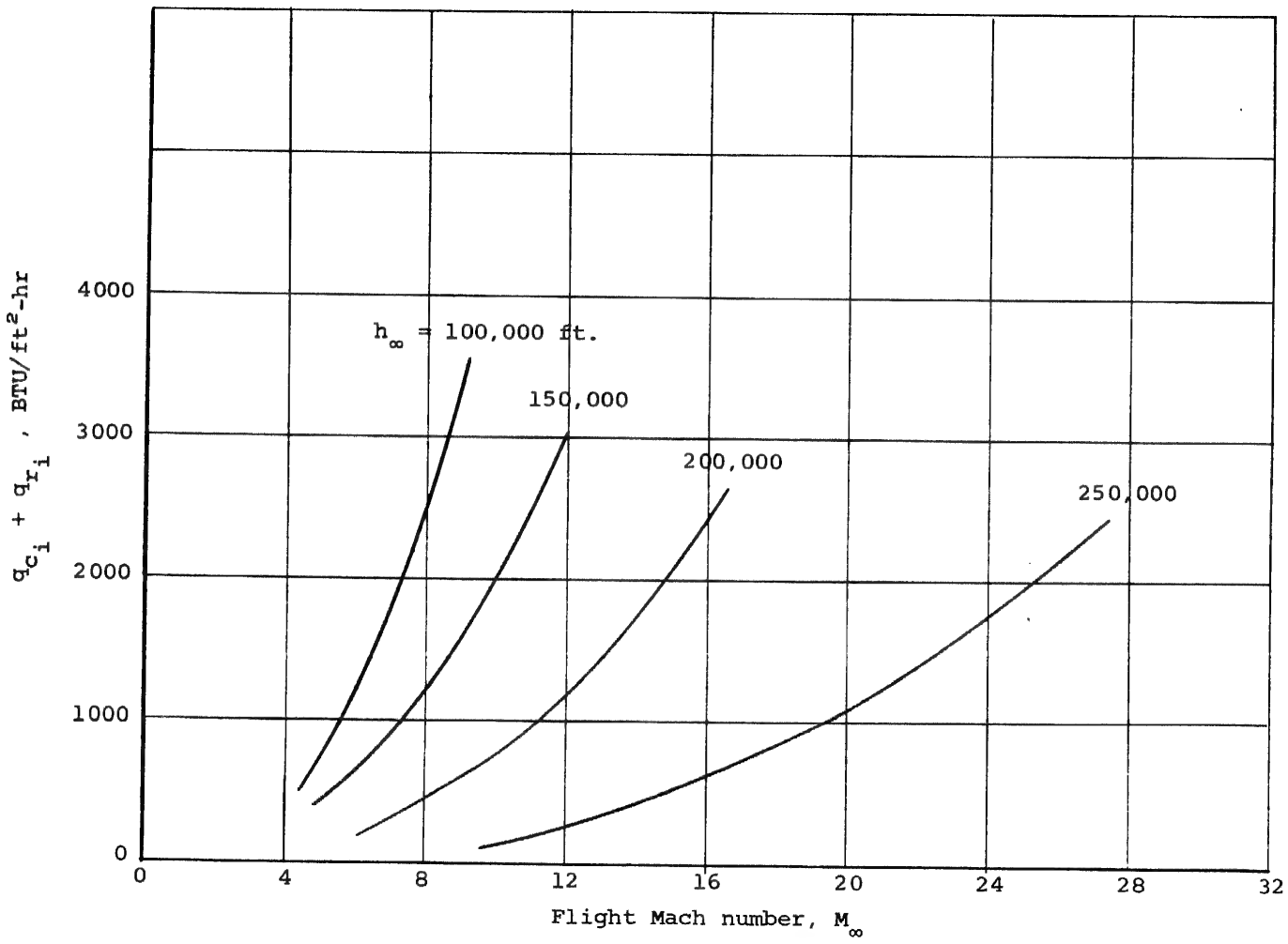


(b) Temperature difference across window

Figure V-4-- Continued.

Approved For Release 2000/04/12 : CIA-RDP67B00657R000300070001-0

Approved For Release 2000/04/12 : CIA-RDP67B00657R000300070001-0

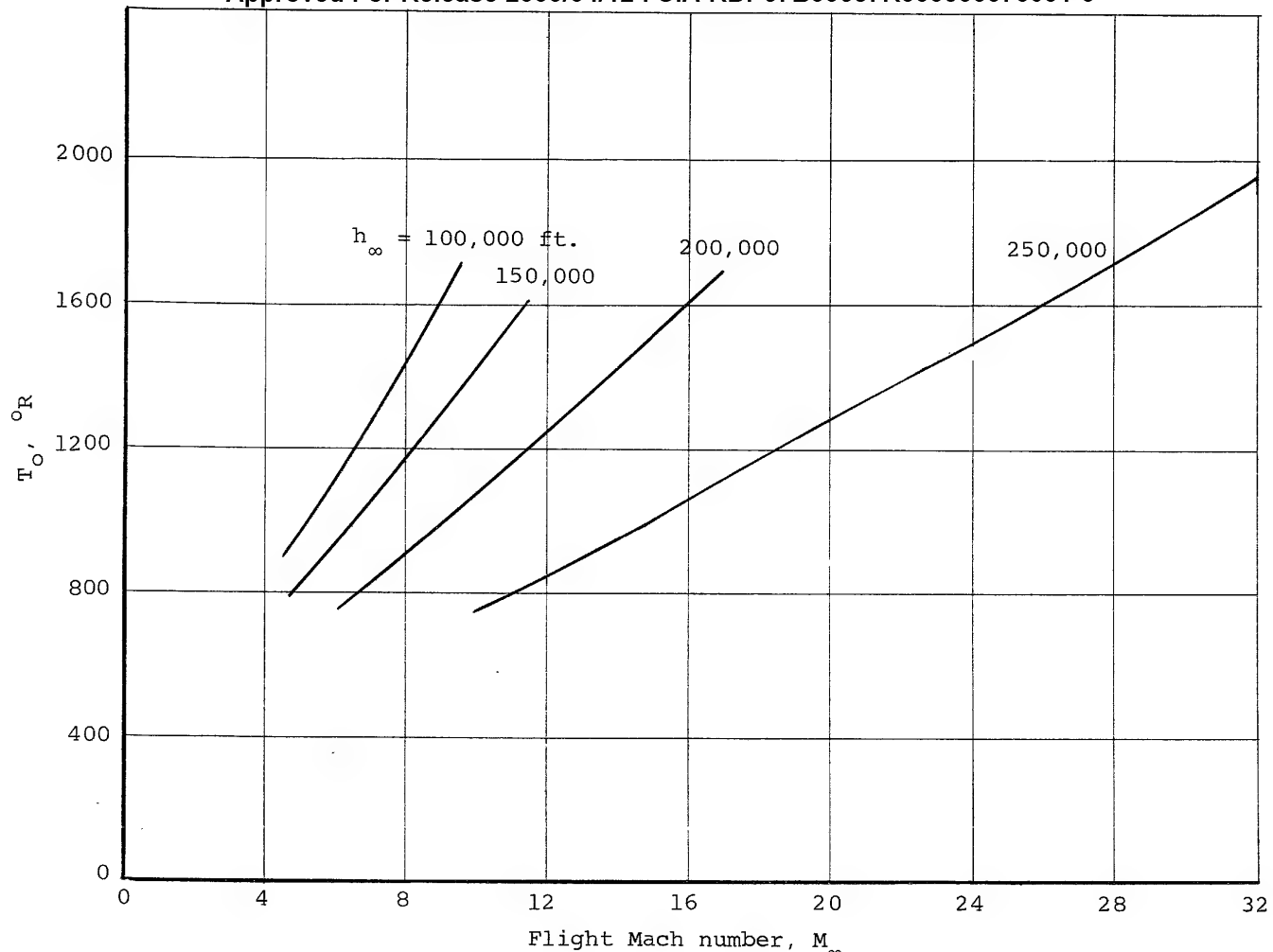


(c) Heat transfer rate to cavity

Figure V-4.- Concluded.

Approved For Release 2000/04/12 : CIA-RDP67B00657R000300070001-0

Approved For Release 2000/04/12 : CIA-RDP67B00657R000300070001-0

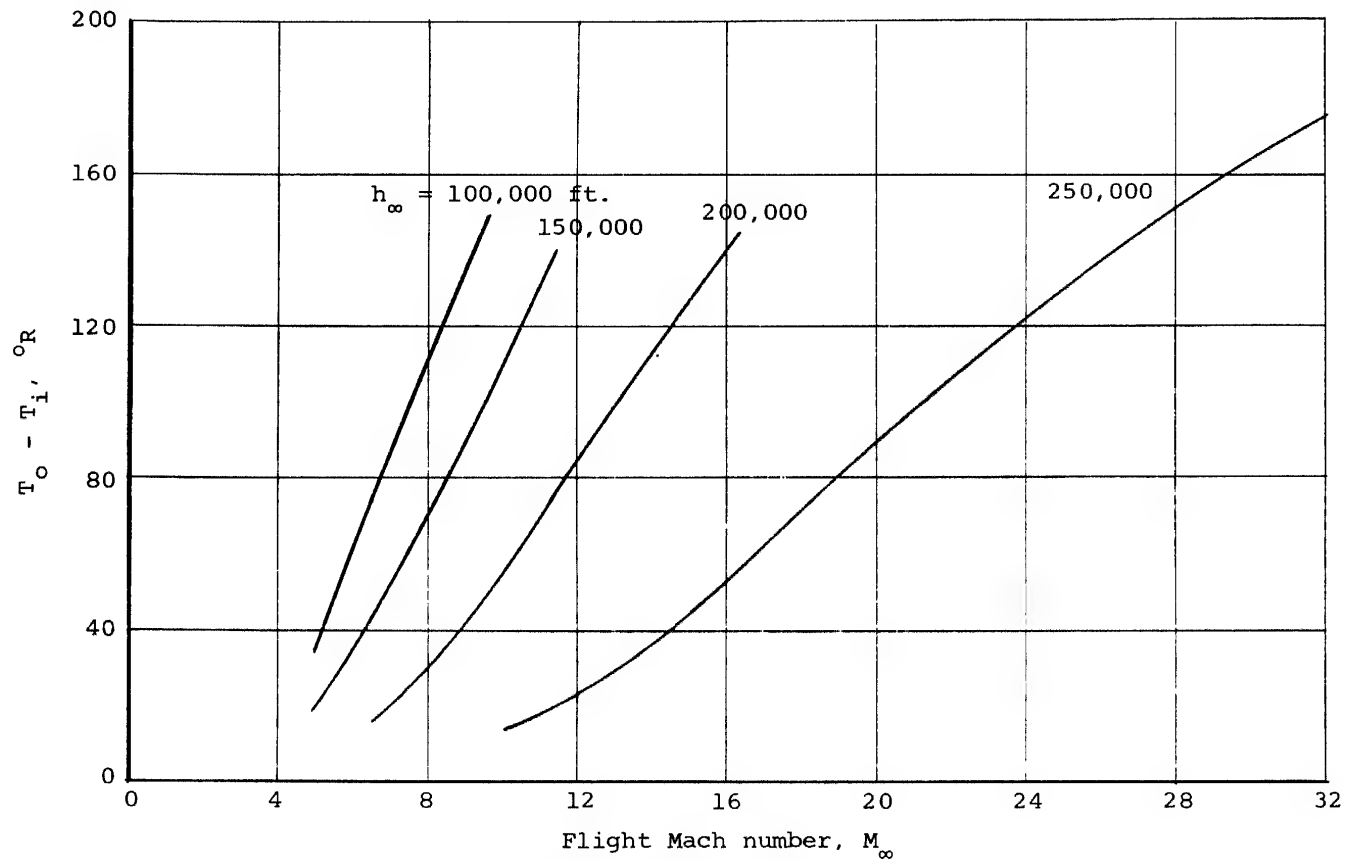


(a) Window outer surface temperature

Figure V-5.- Aerodynamic heating at camera window for thick blunt wing with $H = 0$

Approved For Release 2000/04/12 : CIA-RDP67B00657R000300070001-0

Approved For Release 2000/04/12 : CIA-RDP67B00657R000300070001-0



(b) Temperature difference across window

Figure V-5.- Continued.

Approved For Release 2000/04/12 : CIA-RDP67B00657R000300070001-0

Approved For Release 2000/04/12 : CIA-RDP67B00657R000300070001-0

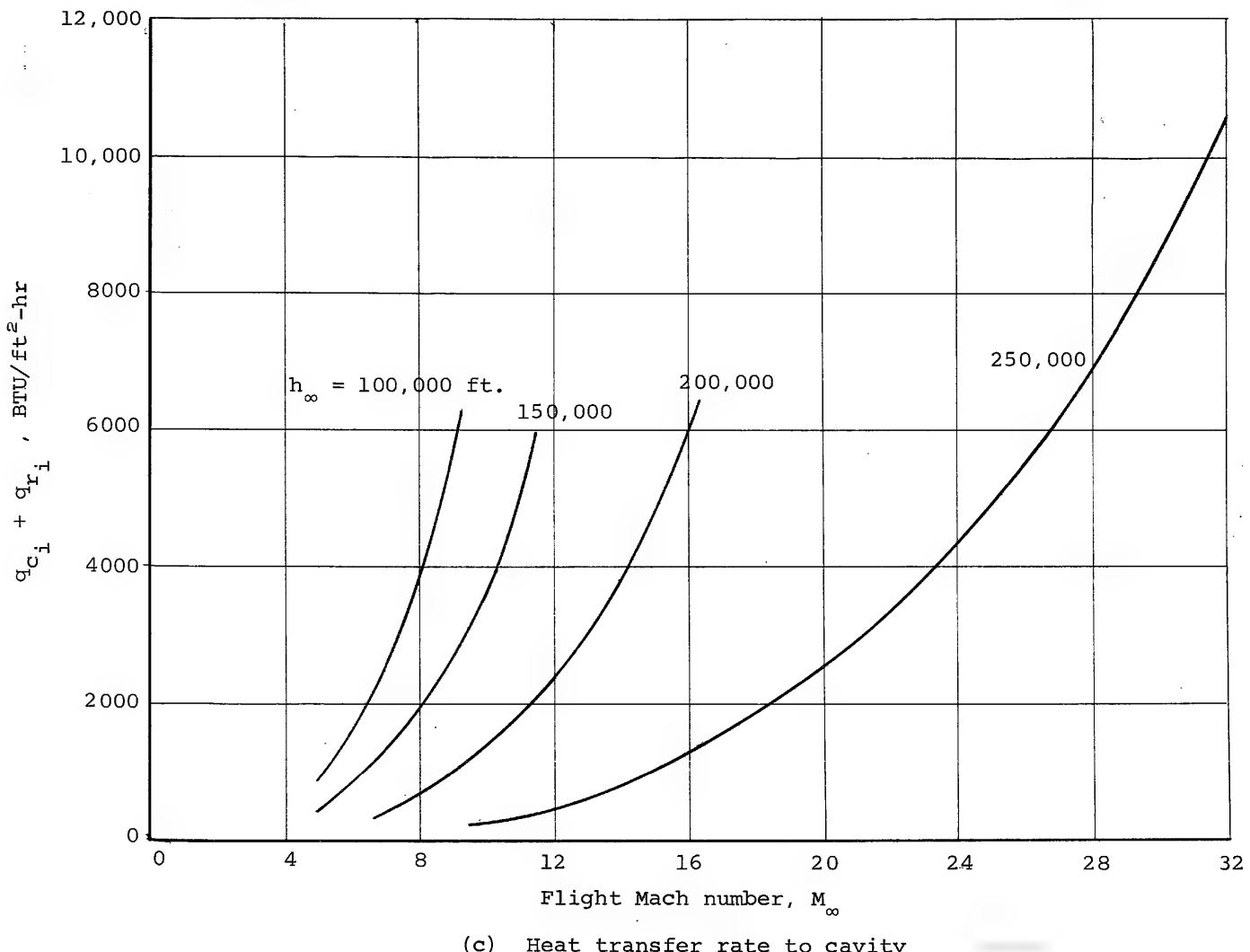
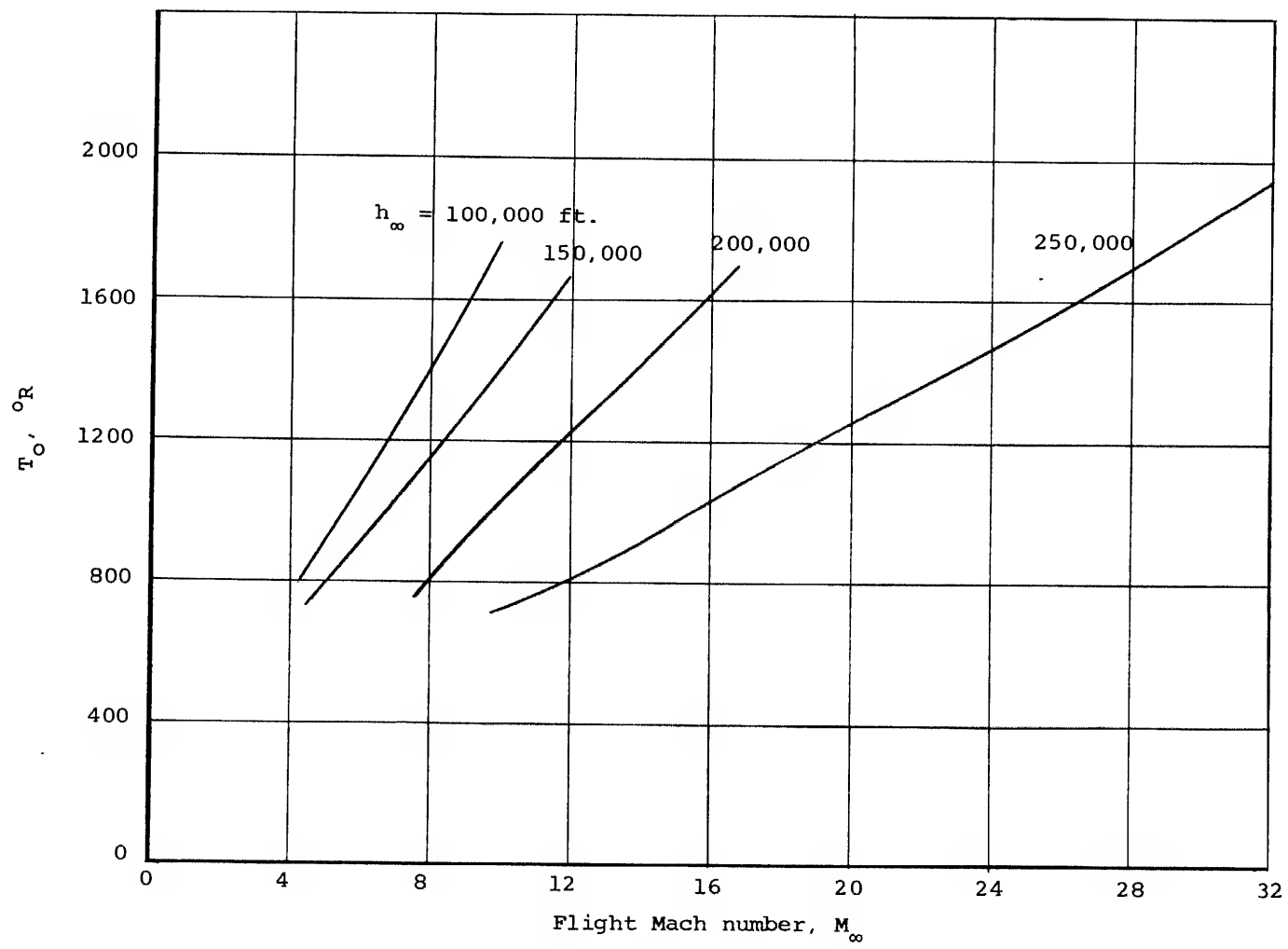


Figure V-5.- Concluded

Approved For Release 2000/04/12 : CIA-RDP67B00657R000300070001-0

Approved For Release 2000/04/12 : CIA-RDP67B00657R000300070001-0

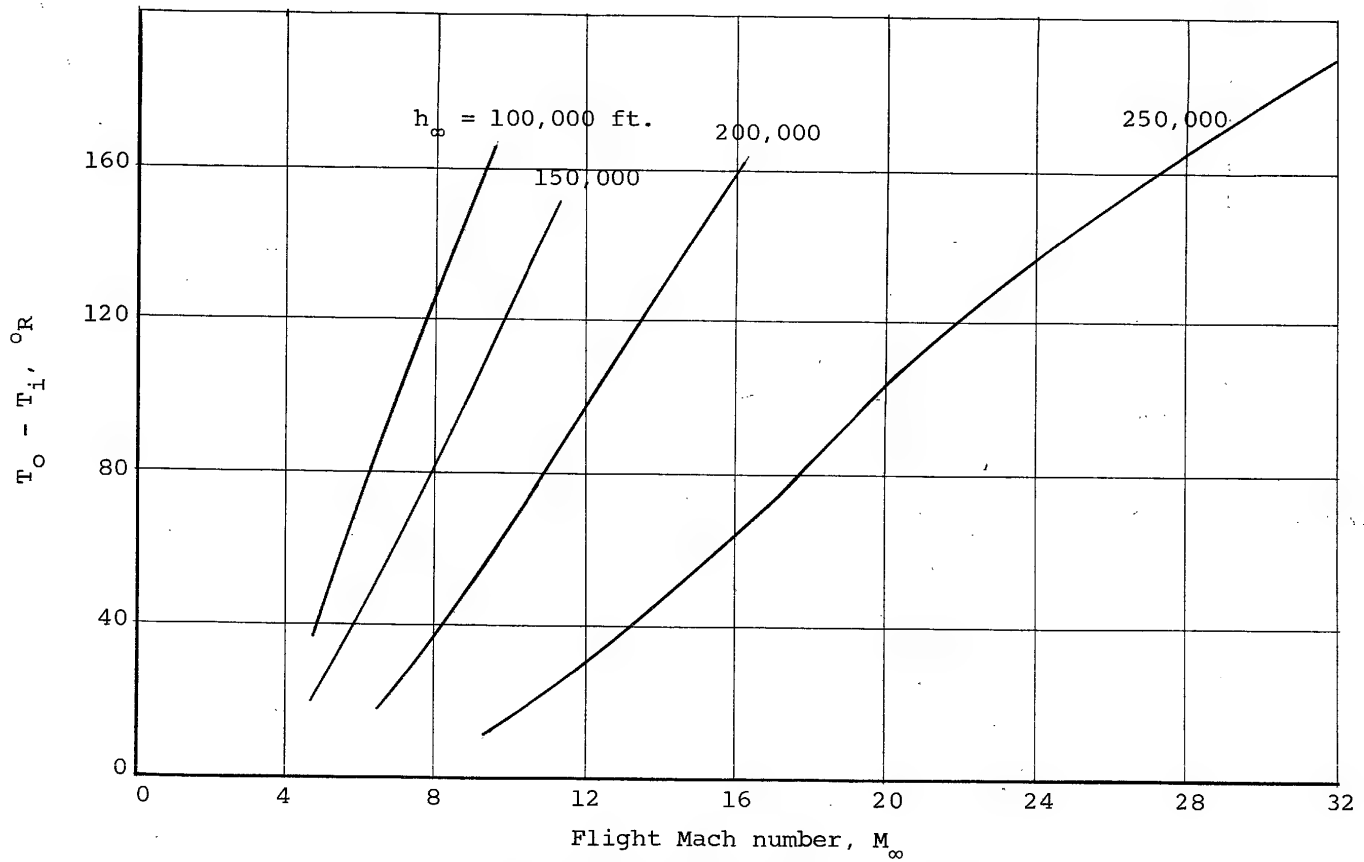


(a) Window outer surface temperature

Figure V-6.- Aerodynamic heating at camera window for thick blunt wing with $H = 1$

Approved For Release 2000/04/12 : CIA-RDP67B00657R000300070001-0

Approved For Release 2000/04/12 : CIA-RDP67B00657R000300070001-0

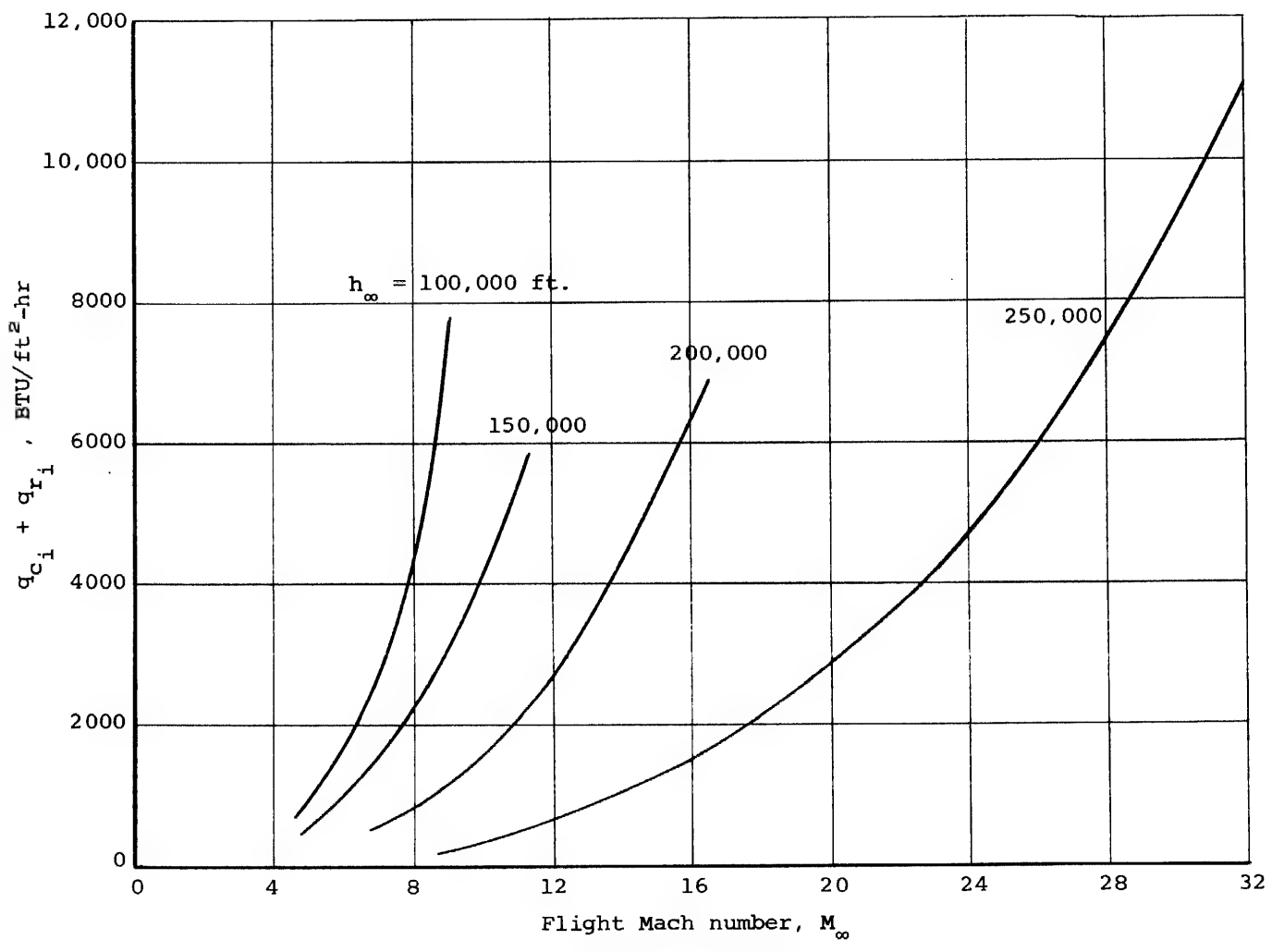


(b) Temperature difference across window

Figure V-6.- Continued.

Approved For Release 2000/04/12 : CIA-RDP67B00657R000300070001-0

Approved For Release 2000/04/12 : CIA-RDP67B00657R000300070001-0



(c) Heat transfer rate to cavity

Figure V-6.- Concluded.

Approved For Release 2000/04/12 : CIA-RDP67B00657R000300070001-0

PART VI: LUMINOSITY AND CONTRAST

INTRODUCTION

At hypersonic speeds, the temperature of the air surrounding the vehicle between the shock wave and the vehicle surface may become high enough so that the air radiates energy in the visible spectrum. In photographing the ground from this vehicle, the optical system will have to look through this luminous layer. This will produce a certain brightness at the camera objective which may cause the contrast between an object on the ground and its background to drop below the value required for satisfactory photography.

One purpose of this part of the present study is to set up a rational analysis for evaluating the effect of air luminosity on aerial photography. A second purpose of the study is to determine for typical hypersonic configurations those regions in the Mach number, altitude diagram wherein the effects of luminosity on aerial photography are deleterious. A third purpose is to discuss schemes which may tend to alleviate these effects. The analysis of this section is concerned with the reduction in contrast due to luminosity. Although luminosity clearly has the effect of degrading resolution, an analysis of this problem has not been attempted.

In part III of the final technical report, Phase I, a study of the effect of luminosity on aerial photography was

made. As a criterion of satisfactory photography, this study assumed that the focal-plane illuminance from air luminosity be less than one-fifth of a typical value which would otherwise exist. This criterion is rough in that it does not account for variations in ground and atmosphere illuminance, but instead uses an average value. Also, it does not take into account the inherent contrast between the object being photographed and its background, nor does it consider any effects of wave length. The criterion developed herein takes all these factors into account.

Since the publication of the Phase I final report, more extensive data have become available on the absorption coefficient of the air as a function of the thermodynamic state of the air. These data, which go to lower densities, are used herein to calculate the luminosity of the air.

The present section is written in three principal parts. The first part concerns the loss of contrast between the ground and the lower side of the luminous air layer and follows the general approach outlined by Middleton in Reference 1. The second part deals with the change in contrast across the luminous air layer. The last part involves luminosity calculations for several hypersonic configurations to establish luminosity boundaries in the Mach number, altitude diagram.

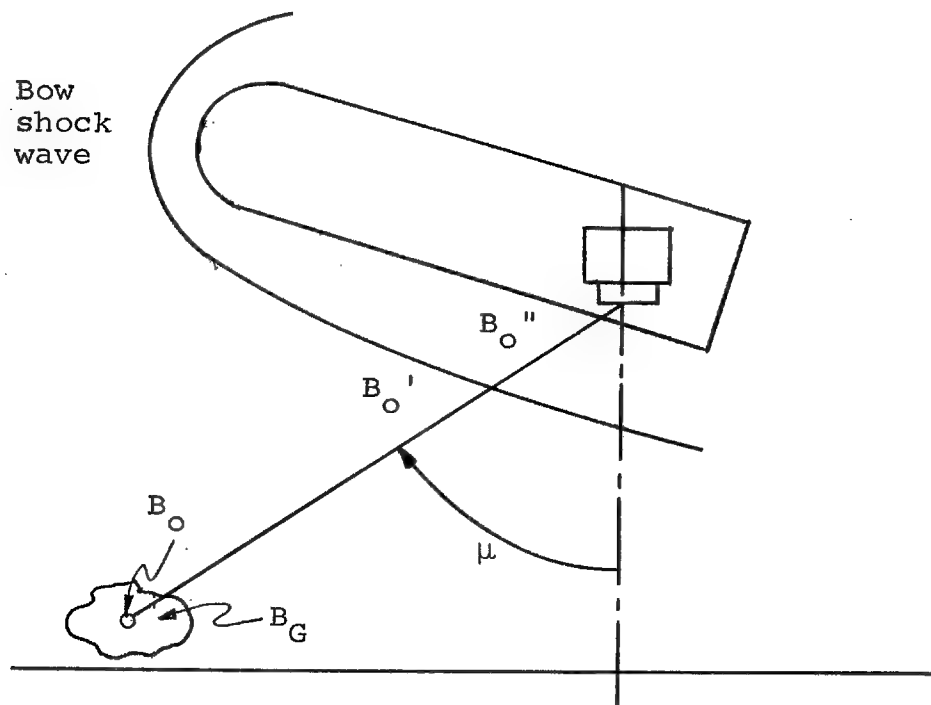
SYMBOLS

B	brightness ¹
B_A	brightness of total air column due to air light
B_a	brightness of air layer of unit thickness
$B_a(0)$	value of B_a at sea level
B_G	intrinsic brightness of object background for nadir angle μ
B_G'	apparent brightness of object background viewed from objective at nadir angle μ , no luminosity
B_G''	apparent brightness of object background viewed from camera objective at nadir angle μ , with luminosity
B_H	brightness of horizon in direction of view from object to camera
B_L	brightness of luminous layer at camera objective
b_L	brightness of a unit volume of luminous gas
B_o	intrinsic brightness of object being photographed at nadir angle μ
B_o'	apparent brightness of object being photographed at nadir angle μ when viewed at camera, no luminosity
B_o''	apparent brightness of object being photographed at nadir angle μ when viewed at camera, with luminosity
B_S	brightness of sky in direction of camera
C	intrinsic contrast at ground between object and background
C'	apparent contrast between object and background just below luminous layer
C''	apparent contrast between object and background just above luminous layer

¹The brightness used herein is not weighted for the response of the eye, but is a pure radiometric quantity. See Appendix VIA for definition of brightness.

$f(r)$	$\frac{\rho}{\rho_0} = e^{-\bar{\alpha}r} \cos \mu$
h	altitude, ft
L	equivalent optical-path length at sea level
M_∞	flight Mach number
R	slant distance along optical path from ground to camera
dS	elementary area of receiving surface
ds	elementary area of radiating surface
$\bar{\alpha}$	$1/23,500$, reciprocal of altitude change for density of ARDC atmosphere to vary by the base e , ft^{-1}
β	Rayleigh scattering parameter, ft^{-1}
β_0	Rayleigh scattering parameter at sea level, ft^{-1}
λ	wavelength, microns, unless specified otherwise
μ	nadir angle, deg
ρ	mass density of air, slugs/ ft^3
ρ_0	value of ρ at sea level, 0.002378 slugs/ ft^3
ρ_0^*	reference value of ρ used in Appendix VIC, 0.002508 slugs/ ft^3
ξ	slant distance along optical path measured from camera objective

GENERAL DESCRIPTION OF PROBLEM



An aerial camera, mounted in a hypersonic vehicle, is taking a picture in a downward direction at some nadir angle, μ , of a ground object of intrinsic brightness B_o , surrounded by a background of intrinsic brightness B_G . The size of the object is large enough so that questions of resolution do not arise. Between the object and the camera, the only source of scattering is Rayleigh scattering due to air molecules. The problem of Mie scattering due to haze is thus precluded. Because of the sources of illumination, such as sun, earth, and sky, the atmosphere between the object and camera scatters some light by molecular scattering into the ray bundle in the direction of the camera. This source of illumination will be

termed air light. Between the head shock wave and the vehicle lower surface there exists a layer of luminous air through which the light ray must pass before reaching the window. Beneath this layer, the apparent brightness of the ground object is B_o' and above it, B_o'' .

In this part of the report, we are concerned with the effect that luminosity of the air has on aerial photography. If sufficient contrast between object and background still persists after passing through the luminous air layers, photography can still be performed despite increased brightness by reducing the exposure time. The effect of the luminosity will thus depend on the intrinsic contrast at the ground, as well as the reduction in contrast due to the pervading atmosphere.

The characteristics of the camera and film can have some bearing on the deleterious effects that luminosity can exert on aerial photography. For instance, in the luminosity section of the final report, Phase I, considerable variation of the light intensity on the film was calculated for the luminous layer, assuming the camera has no antivignetting device. In this section, we will not make such a calculation, and we will assume that the camera is equipped with an antivignetting device. We will thus be concerned solely with the contrast and brightness as functions of nadir angle. The film-camera combination will require a certain threshold contrast below which it cannot produce adequate aerial photography. This

threshold specified in front of the camera objective will, for any combination of nadir angle, wave length, Mach number, altitude, etc., specify a ground contrast below which detail cannot be photographed.

It is of interest to list the assumptions which form the basis for the present study.

1. The size of the object viewed is large enough to avoid questions of resolution.
2. Any light scattering between object and camera is solely due to air molecules (Rayleigh scattering) and not to haze.
3. The intrinsic brightness of a layer of air per unit thickness under a fixed set of atmospheric illumination conditions is proportional to the air density.
4. The atmosphere is an exponential approximation to the ARDC atmosphere given by (see Fig. VI-1):

$$\rho = \rho_0 e^{-\bar{\alpha}h} \quad (\text{VI-1})$$

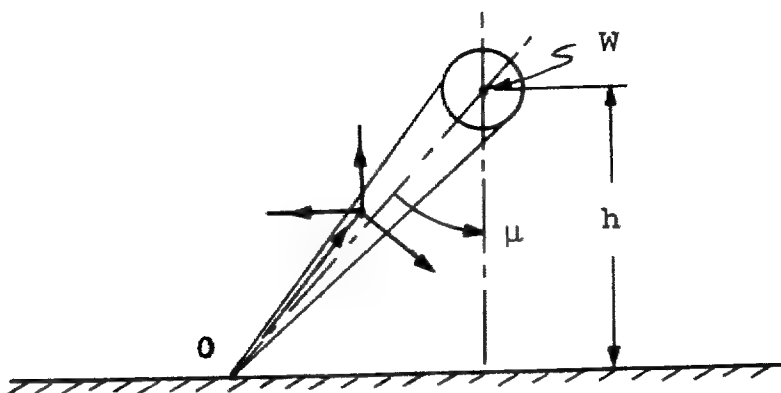
5. The earth is flat.
6. The resolution of the image is not degraded by the luminous air layer below that necessary to resolve the object being viewed.
7. The minimum contrast at the camera for marginal aerial photography is assumed to be 0.02.
8. The absorption of light by the luminous air layer is insignificant.

EFFECT OF ATMOSPHERE ON BRIGHTNESS AND CONTRAST

As previously mentioned, it is first necessary to determine the brightness and contrast of ground objects being aerially photographed without effects induced by the forward motion of the aircraft, if such effects on aerial photography are to be evaluated. As a consequence, the purpose of this section is to determine the contrast and brightness of ground objects viewed from aloft without effects induced by forward motion of an aircraft.

Attenuation of Brightness by Rayleigh Scattering

The basic model being considered is shown in the following sketch:



A bundle of light rays originating at some ground object O are beamed toward the camera window W . Because of air molecules, some of the rays are scattered out of the bundle, and the inherent brightness B_O of the ground object is

diminished to some apparent brightness B_o' , depending on the location of the observer. In Appendix VIB, the following expression was derived for the brightness ratio for monochromatic light of wavelength λ :

$$\frac{B_o'}{B_o} = e^{-\beta_o L} \quad (VI-2)$$

where

β_o Rayleigh scattering coefficient at sea level (ARDC atmosphere) for wavelength λ

L equivalent sea-level length of optical path

$$L = \frac{1}{\bar{\alpha} \cos \mu} (1 - e^{-\bar{\alpha} h}) \quad (VI-3)$$

where

$\bar{\alpha}$ $1/23,500 \text{ ft}^{-1}$

μ nadir angle

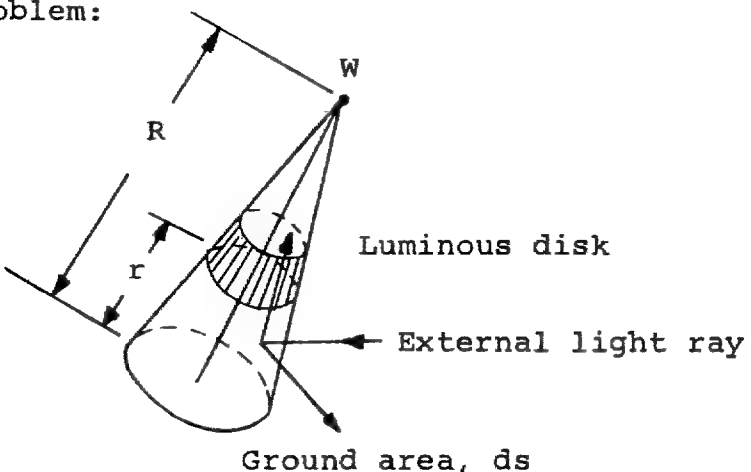
h altitude, ft

It is of interest to obtain a notion of the importance of the attenuation for several altitudes and nadir angles. The ratio of B_o'/B_o is shown versus altitude h in Figure VI-2(a) for vertical viewing, $\mu = 0^\circ$, and oblique viewing, $\mu = 45^\circ$, for $\lambda = 4000 \text{ \AA}$. (For $\lambda = 7600 \text{ \AA}$, the attenuation is 7.7 percent of that for $\lambda = 4000 \text{ \AA}$.) It is seen that the maximum loss of brightness due to the atmosphere is about 20 percent for $\lambda = 4000 \text{ \AA}$ and $\mu = 45^\circ$. An increase in λ from 4000 \AA to 7600 \AA reduces the loss to a much lesser amount; about 2 percent. An increase in nadir angle, μ , increases

the loss of brightness. Generally speaking, the effect of loss of brightness due to Rayleigh scattering has a lesser effect on contrast than the presence of air light, as will now be shown. Since B_o'/B_o is only a function of $\beta_o L$, Figure VI-2 (b) has been prepared which, if $\beta_o L$ is determined, allows the brightness ratio to be found.

Increase in Brightness Due to Air Light

A column of air in the atmosphere is illuminated by sun, sky, and earth so that the column viewed along its axis will have brightness due to Rayleigh scattering from these sources of illumination. Consider the following sketch which illustrates the problem:



The light ray from the sky enters the cone of view of the ground object being photographed. Molecules in the cone of view scatter the light ray, and some of the light is scattered in the direction of the camera. The increased brightness at the camera will be calculated. Such brightness tends to reduce the apparent contrast of the ground object against its background.

An elementary area of the ground object ds subtends a certain solid angle at the camera objective. To obtain the brightness at the objective due to the air light, focus attention on a disk of the air column which has inherent brightness B_a per unit thickness. This brightness depends, among other things, on sun elevation, amount of cloud cover, etc. It is assumed that the brightness of a disk of unit thickness is proportional to the density of the air in the disk. The apparent brightness at the camera objective of a disk of thickness dr is

$$dB_a = B_a dr e^{-\int_r^R \beta dr} \quad (VI-4)$$

where the exponential function represents the attenuation due to Rayleigh scattering. The Rayleigh scattering coefficient (Appendix VIB) varies directly with the air density as follows:

$$\beta = \beta_0 \frac{\rho}{\rho_0} = \beta_0 e^{-\bar{\alpha}h} = \beta_0 e^{-\bar{\alpha}r \cos \mu} = \beta_0 f(r) \quad (VI-5)$$

so that

$$dB_A = B_a dr e^{-\beta_0 \int_r^R f(r) dr} \quad (VI-6)$$

Let us assume that the brightness of a layer of air of unit thickness is proportional to the density so that

$$B_a = B_a(0) f(r) \quad (VI-6)$$

where $B_a(0)$ is the brightness at sea level. The brightness of the entire air column at the camera objective is found by integration

$$B_A = B_a(0) \int_0^R f(r) e^{-\beta_0 \int_r^R f(r) dr} dr \quad (VI-7)$$

or

$$B_A = \frac{B_a(0)}{\rho_0} \left(1 - e^{-\beta_0 L} \right) \quad (VI-8)$$

where

$$L = \int_0^R e^{-\bar{\alpha}r \cos \mu} dr = \frac{1 - e^{-\bar{\alpha}R \cos \mu}}{\bar{\alpha} \cos \mu} \quad (VI-9)$$

The quantity L is the equivalent sea-level length of the optical path.

The brightness of the air column at the camera objective, as given by Equation (VI-8), contains two basic parameters, β_0 and $B_a(0)$. The value of the Rayleigh scattering coefficient β_0 is well-known, and its inverse quadratic dependence on wavelength is given in Appendix VIB. The quantity $B_a(0)$ is not so well-known, depending as it does on any factor which can influence the intensity of the light falling on the air column. We will replace it, as a parameter, with the sky brightness.

For a good observer looking up at the sky, the apparent sky brightness B_S can be calculated by rewriting Equation (VI-7) as

$$B_S = B_a(0) \int_0^\infty f(r) e^{-\beta_0 \int_0^r f(\xi) d\xi} dr \quad (VI-10)$$

integration yields

$$B_s = \frac{B_a(0)}{\beta_o} \left(1 - e^{-\frac{\beta_o}{\bar{\alpha} \cos \mu}} \right) \quad (VI-11)$$

If we now let μ approach 90° , so that we are looking at the horizon, the brightness of the horizon is

$$B_H = \frac{B_a(0)}{\beta_o} \quad (VI-12)$$

This relationship will be used to replace $B_a(0)$ with the horizon brightness as a parameter in the following section. The relationship holds for each wave length in the luminous spectrum.

Contrast for Downward Viewing from Camera

Objective; Brightness

The contrast of the ground object against its background will now be determined, together with the brightness of the background as a result of attenuation by Rayleigh scattering and augmentation by air light. The following analysis, like that preceding it, applies strictly to monochromatic light. By integration, the total effect for either object or background can be obtained for the spectrum of interest.

The intrinsic brightness of the object at the ground is B_o , and the intrinsic brightness of the background is B_G . The comparable values after passing through the atmosphere, but before passing through the luminous layer are B_o' and

B_G' . The intrinsic contrast is defined to be

$$C = \frac{B_O - B_G}{B_G} \quad (VI-13)$$

If the object brightness is zero, C is -1; if the object is infinitely bright, $C = \infty$. At the camera objective, B_O and B_G have been attenuated by Rayleigh scattering in accordance with Equation (VI-2), but have been augmented by air light in accordance with Equation (VI-11). Accordingly, we have

$$B_O' = B_O e^{-\beta_O L} + B_H (1 - e^{-\beta_O L}) \quad (VI-14)$$

$$B_G' = B_G e^{-\beta_O L} + B_H (1 - e^{-\beta_O L}) \quad (VI-15)$$

The contrast at the camera is now

$$C' = \frac{B_O' - B_G'}{B_G'} = \frac{(B_O - B_G) e^{-\beta_O L}}{B_G'} \quad (VI-16)$$

From Equations (VI-13), (VI-14), and (VI-15), it is easy to show that

$$\frac{C'}{C} = \frac{1}{1 + \frac{B_S}{B_G} \left(\frac{e^{\beta_O L} - 1}{1 - e^{-\beta_O/\bar{a} \cos \mu}} \right)} = \frac{1}{1 + \frac{B_H}{B_G} (e^{\beta_O L} - 1)} \quad (VI-17)$$

The contrast-reduction ratio C'/C is thus a function of $\beta_O L$ and B_H/B_G . This latter parameter, the sky-ground ratio, varies with the sky condition and the background condition on

the earth. It can vary through several orders of magnitude. Typical values are included in the following table:

Sky Condition	Background	B_H/B_G
Clear	Fresh snow	0.2
Clear	Desert	0.4
Clear	Forest	4
Overcast	Fresh snow	1
Overcast	Desert	7
Overcast	Forest	25

The above values are approximate across the visible spectrum. For an overcast sky where most of the ground illuminance is due to scattered light, the ratio B_H/B_G is approximately equal to the reciprocal of the ground reflectance. Under a clear sky where much of the illuminance is due to direct light, the ratio is lower. The values of B_G correspond to the local background against which the contrast is being assessed. The values of B_H/B_G can range through several orders of magnitude and can have a similar range of effects on contrast-reduction ratio.

The parameter $\beta_o L$ depends on the wave length (because of β_o), nadir angle, and altitude for a clear atmosphere with Rayleigh scattering

$$\beta_o L \cos \mu = \frac{\beta_o}{\bar{\alpha}} \left(1 - e^{-\bar{\alpha}h} \right) \quad (VI-18)$$

The value of $\beta_o L \cos \mu$ is plotted versus wave length with altitudes as parameters in Figure VI-3. It is noted that by

the time h has reached 40,000 feet, the value of $\beta_o L$ has reached about 85 percent of its value for $h = \infty$. An increase in wavelength from 4000 Å to 7600 Å causes about a 13-fold decrease in $\beta_o L$. This figure establishes the range of $\beta_o L$ values for Rayleigh scattering. For haze, the values can easily increase by an order of magnitude.

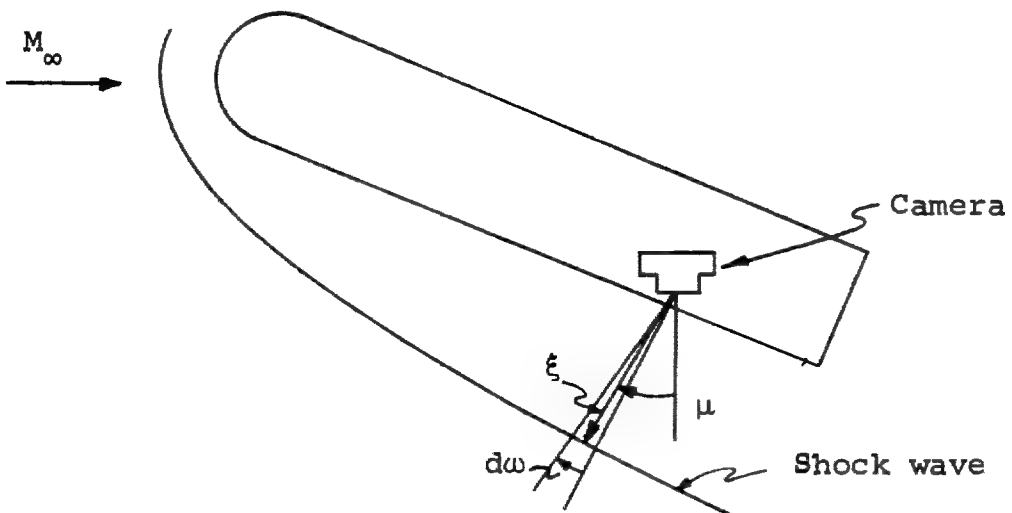
To illustrate the effect of $\beta_o L$ and B_H/B_G on the contrast-reduction ratio C'/C , Figure VI-4 has been prepared. Here the ratio C'/C is plotted versus B_H/B_G for constant values of $\beta_o L$ for the ranges of these values established earlier. Since $\beta_o L \cos \mu$ varies from 0 to 0.277, $\beta_o L$ will range from 0 to 0.391 if $\mu \leq 45^\circ$. It is clear that increasing sky-ground ratio B_H/B_G has an important effect on the reduction of contrast. For large values of this parameter, it is clear that much air light is scattered into the beam incident on the objective, reducing the contrast by increasing the brightness of the background. An increase in the parameter $\beta_o L$ decreases the contrast by attenuating the original light and by increasing the air light. A combination of Figures VI-3 and VI-4 gives a relatively rapid means for evaluating the contrast-reduction ratio C'/C as a function of wavelength, altitude, nadir angle, and sky-ground ratio. It is to be remembered that the assumptions listed previously have been made. Haze can have such a powerful effect on contrast that it overrides that due to Rayleigh scattering.

EFFECT OF LUMINOUS LAYER ON
BRIGHTNESS AND CONTRAST

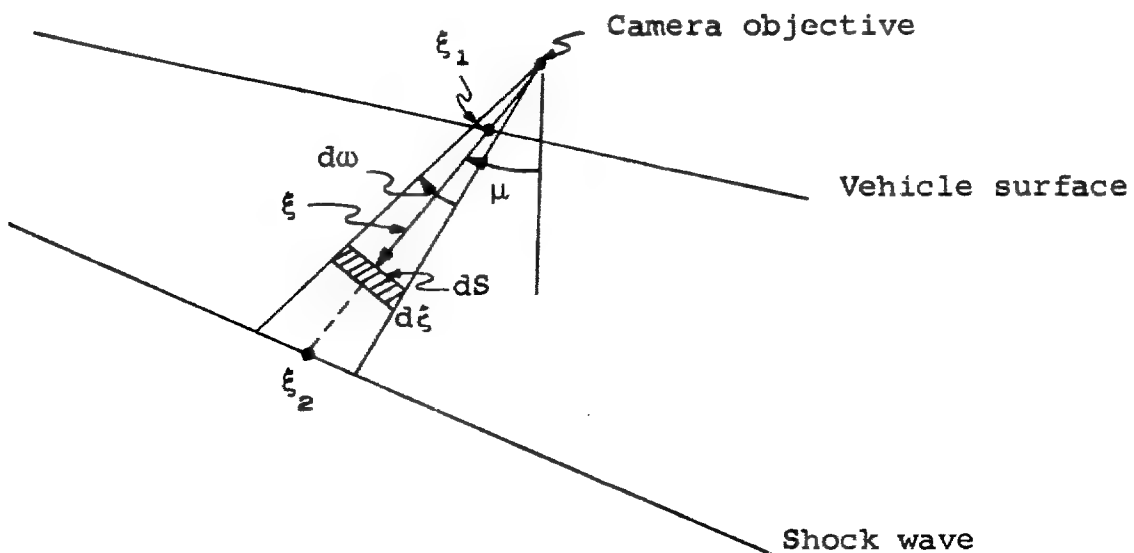
The effect of the atmosphere on the brightness and contrast of a ground object and its background as seen at the camera objective has been examined in the preceding section of this part of the report. In addition to the atmospheric-induced effects, an increase in the brightness level of both the object and the background and, hence, a reduction in contrast may result at hypersonic Mach numbers because of the luminous layer of air surrounding the vehicle between the vehicle surface and the shock wave. It is therefore the purpose of this section to determine the increase in brightness at the camera objective due to the luminous layer and, also, the contrast of ground objects viewed from the camera objective, including effects induced by both the atmosphere and the luminous layer.

Increase in Brightness Due to
the Luminous Layer

As the flight Mach number increases, the temperature of the air in the region between the shock wave and the vehicle surface increases until it radiates energy in the visible spectrum. In attempting to photograph the ground from this vehicle, the optical system will have to look through a volume of this luminous gas which will produce a certain brightness at the camera objective. Consider the following sketch:



In the sketch, we have a vehicle flying at an altitude, h_{∞} , above sea level at a Mach number, M_{∞} . Let the ground object which is being photographed lie at some nadir angle, μ , with respect to the vertical and subtend a solid angle, $d\omega$. Consequently, in viewing this ground object, the camera must look through the volume of luminous air between the vehicle surface and the shock wave which is determined by the solid angle, $d\omega$. This volume will produce a certain brightness at the camera objective which will now be determined. For this purpose let us look at the next sketch.



Let the element of volume, $dSd\xi$, of the gas between the vehicle surface and the shock wave have a brightness, b_L .

Then the brightness at the camera objective of this disk of thickness $d\xi$ is

$$dB_L = b_L d\xi \quad (VI-19)$$

By integrating along the length of the path from ξ_1 to ξ_2 , the brightness at the camera objective of the volume of luminous gas determined by the solid angle, $d\omega$, is obtained

$$B_L = \int_{\xi_1}^{\xi_2} b_L d\xi \quad (VI-20)$$

The limits of integration, ξ_1 and ξ_2 , can be obtained from the geometry of the vehicle, the camera objective location, and the shock-wave stand-off distance, which is determined in Part III of this report.

The last quantity to be determined is the brightness of an element of volume of the luminous gas. Recently, data have been published (Ref. 2) which tabulate the absorption coefficient of air as a function of wavelength for various densities and temperatures. In Appendix VIC, the method of converting these absorption coefficients to brightnesses is presented, and the results of this conversion are presented in Figures VI-5 through VI-7. It should be pointed out that the results

presented in Reference 2 are purely theoretical and have not been verified by extensive experimental results. These results are based on calculations of the chemical composition of air in thermodynamic equilibrium by Gilmore (Ref. 3).

Let us return to Equation (VI-20). If the temperature and density in the region between the vehicle surface and the shock wave were constant, b_L would be a constant and could be taken outside the integral sign and the equation integrated analytically. However, Parts III and IV of this report have shown that large changes in temperature and density occur in this region. The methods of Parts III and IV, therefore, must be used to find the temperature, T , and the density, ρ , as functions of ξ and these variations then used to find the b_L variation. This curve can then be integrated graphically from ξ_1 to ξ_2 to obtain B_L .

We have neglected absorption in the calculations. For a luminous layer of air at $10,000^{\circ}$ F and a density of 0.01 atmosphere, it is estimated that the radiating gas layer must be 10^3 centimeters thick before it produces a radiation intensity equal to that of a black body at the same temperature. For temperatures and densities which will generally exist in the luminous layer occurring within the scope of the present work, the thicknesses required will be larger since they vary directly with the fourth power of the temperature and inversely with the density. Absorption is therefore

negligible, provided the actual path length is small compared with 10^3 centimeters. For the present configuration, such will be the case.

Contrast for Downward Viewing from Camera Objective

Including Effect of Luminous Layer

Let us now determine the brightnesses and the contrast of the ground object against its background, including the effects of Rayleigh scattering, augmentation by air light, and augmentation by the luminous layer. Equations (VI-14) and (VI-15) give the brightnesses of the object and background at the camera objective, respectively, including the attenuation by Rayleigh scattering and augmentation by air light. Since both of these brightnesses are increased by the brightness of the luminous layer, the following expressions can be written for the brightnesses of the object and the background at the camera objective, including the three effects:

$$B_O'' = B_O' + B_L = B_O e^{-\beta_O L} + B_H \left(1 - e^{-\beta_O L}\right) + B_L \quad (\text{VI-21})$$

$$B_G'' = B_G' + B_L = B_G e^{-\beta_O L} + B_H \left(1 - e^{-\beta_O L}\right) + B_L \quad (\text{VI-22})$$

The resulting apparent contrast is defined in the same manner as in Equation (VI-13) so that at the camera objective it is

$$C'' = \frac{B_O'' - B_G''}{B_G''} \quad (\text{VI-23})$$

and if Equations (VI-21) and (VI-22) are used,

$$C'' = \frac{B_O - B_G}{B_G''} e^{-\beta_O L} \quad (VI-24)$$

The reduction in contrast by the luminous layer is the ratio of C'' to C' , where C' is the apparent contrast between the object and the background just below the luminous layer. From Equations (VI-14) through (VI-16), (VI-22), and (VI-24), this ratio is

$$\begin{aligned} \frac{C''}{C'} &= \frac{B_G'}{B_G''} = \frac{B_G e^{-\beta_O L} + B_H (1 - e^{-\beta_O L})}{B_G e^{-\beta_O L} + B_H (1 - e^{-\beta_O L}) + B_L} \\ &= \frac{1}{1 + B_L / [B_G e^{-\beta_O L} + B_H (1 - e^{-\beta_O L})]} \quad (VI-25) \end{aligned}$$

This equation can be rewritten in the following form:

$$\frac{C''}{C'} = \frac{1}{1 + \left(B_L e^{\beta_O L} / B_G \right) \left[\frac{1}{1 + (B_H / B_G) (e^{\beta_O L} - 1)} \right]}$$

and

$$\frac{C''}{C} = \frac{1}{\frac{C'}{C} + \left(B_L e^{\beta_O L} / B_G \right)} \quad (VI-26)$$

Therefore, in addition to the parameters occurring in Equation (VI-17), the loss of contrast due to the luminous layer also depends on the ratio of the brightness of the luminous layer to the brightness of the background. It is to be noted that the brightness of the luminous layer depends on wavelength as well as nadir angle.

The brightness of the background depends on the solar irradiance and the spectral reflectance of the object as shown in Appendix VID. The solar irradiance is the amount of radiant energy from the sun incident per unit area on a plane perpendicular to the sun's rays. This quantity is dependent on the thickness of the air layer through which the rays pass. When the sun is at its zenith, the light rays are passing through one air mass. As the zenith angle increases, the air mass through which the rays pass increases. Representative values of solar irradiance taken from Reference 5 are given in the following table:

Solar Irradiance, watts/cm ² -micron		
Wave length	Zenith Angle	Solar Irradiance
.4 μ	0°	8×10^{-2}
.7 μ	0°	1.3×10^{-1}
.4 μ	60°	5×10^{-2}
.7 μ	60°	1.1×10^{-1}

The spectral reflectance of an object is the percentage of the incident energy of a given wave length which is reflected by the object. Reference 6 presents quite an extensive tabulation of spectral reflectances for various types of terrain. The tables for three of these types are reproduced here in Table VI-1.

The brightness of the background is the product of the solar irradiance and the spectral reflectance of the terrain being viewed. The range of values which this quantity, B_G , can take on is from about 10^{-3} to 10^{-1} . The value of 10^{-3} corresponds to viewing a forest in the afternoon with light of wave length 0.4 microns. The value of 10^{-1} is for the same wave length but for viewing fresh snow when the sun is at its zenith.

To show the effect of the various parameters in Equation (VI-26) on the final contrast ratio Figure VI-8 has been prepared. Figure VI-8(a) has C''/C plotted against B_L/B_G for the entire range of the latter parameter while Figure VI-8(b) is an enlarged plot of the right-hand end of the curves.

RESULTS AND DISCUSSION

The preceding section of this part of the report described a number of sources of reduction in contrast between an object on the ground and its background when observed from a vehicle operating at a high altitude and Mach number. The possible sources of reduction in contrast studied were:

1. Rayleigh scattering
2. Air light
3. Luminosity

The reduction in contrast due to the combined effects of air light and Rayleigh scattering is shown in Figure VI-4. In this figure the ratio of the contrast after these effects have been taken into account to the intrinsic contrast at the ground is plotted against the ratio of the horizon brightness to the background brightness. Representative values of this latter ratio are tabulated on page VI-15. This figure clearly shows that the greatest contrast reduction results for large values of $\beta_o L$ and dark backgrounds. The parameter $\beta_o L$ is a function of altitude, nadir angle and wave length as is shown by Figure VI-3. Since in the present study we are interested in high altitudes, we can direct our attention to the infinite altitude curve. Figures VI-3 and VI-4 show that the contrast reduction due to air light and Rayleigh scattering can be minimized by using the longer wave lengths of light and small nadir angles.

The reduction in contrast due to the luminous layer of air surrounding a high speed vehicle is shown in Figure VI-8. In this figure the ratio of the contrast after accounting for Rayleigh scattering, air light, and luminosity to the contrast before these are taken into account is plotted against the ratio of the brightness of the luminous layer to the brightness of the background. In order for C''/C to differ from C'/C by a significant amount, B_L/B_G must be greater than 10^{-1} to 10^{-2} . From the discussion in the preceding section, B_G can have values as low as 10^{-3} so that B_L must be greater than 10^{-4} or 10^{-5} in order for the luminous layer to cause a noticeable reduction in contrast.

Values of the brightness of the luminous layer for the flight conditions and configurations of Part II of this report have been determined. Except at the highest Mach numbers at the 250,000 foot altitude, the temperatures in the flow field (see Parts III and IV) were well below the temperatures required for the gas to radiate significantly in the visible spectrum. The data of Reference 2 indicates that for temperatures below about 2500° K air does not radiate in the visible spectrum. Consequently, the Mach number range of Part II was extended for the purpose of making the luminosity calculations. The results of the calculations are presented in Figures VI-9 and VI-10 for the two configurations and three nadir angles (-45° , 0° , 45°)

and two wave lengths of light (.4 and .7 microns). An examination of these figures allows the following observations to be made about the brightness of the luminous layer:

1. It is greater on the wing than on the cone for the same flight conditions since the surface of the wing is inclined at a greater angle with the flight direction therefore causing higher temperatures.
2. It is greater for a nadir angle of 45 degrees since this is the case for which the ray path length through the luminous layer is the longest.
3. It is greater for the shorter wave length, 0.4 microns.

It is of interest now to point out how Figures VI-3, VI-4 and VI-8 through VI-10 can be used to determine the required ground contrast in order to have a specified contrast at the camera objective. To do this let us consider an example. The desired contrast at the camera objective, C' , is 0.02. The wave length under consideration is 0.4 microns and the photography is being taken from a cone flying at 150,000 feet at a Mach number of 20. The nadir angle is 0° . From Figure VI-3 the value of $\beta_o L$ is 0.28. If the background being observed is a forest, then for a clear sky B_H/B_G (see table on page VI-15) is 4.0. Figure VI-4 enables us to find the contrast ratio after accounting for Rayleigh scattering and air light. This is

found to be approximately 0.43. If the pictures are being taken at noon, the ground brightness is obtained from the value of the solar irradiance (p. VI-23) and the spectral reflectance (Table VI-1). This is (from Eq. VID-4)

$$\begin{aligned} B_G &= (8 \times 10^{-2}) (0.033) \left(\frac{1}{\pi} \right) \\ &= 0.84 \times 10^{-3} \end{aligned}$$

The brightness of the luminous layer from VI-9(b) is

$$B_L = 6.3 \times 10^{-4}$$

Therefore

$$\frac{B_L}{B_G} = 0.75$$

and from Figure VI-8(a) the final contrast ratio is

$$\frac{C''}{C} = 0.30$$

Since we have said that the minimum acceptable contrast at the camera objective is 0.02 ($C'' = 0.02$), the intrinsic contrast between the object and its background must be

$$\begin{aligned} C &= \frac{0.02}{0.30} \\ &= 0.067 \end{aligned}$$

CONCLUSIONS

The following conclusions can be drawn from the work presented in this section of the report.

1. A rational criterion has been developed for assessing the importance of air luminosity on aerial photography. The method first determines the loss of contrast due to air light and Rayleigh scattering and then determines the further reduction due to luminosity.

2. The loss of contrast due to light scattered out of the cone of view in a Rayleigh atmosphere is generally less than that due to external light scattered into the cone of view.

3. In order for the luminous air in the flow field surrounding the vehicle to reduce the contrast further at the camera objective, the brightness of the luminous layer at this point must be greater than 10^{-4} or 10^{-5} watts per square centimeter per steradian per micron.

4. The contrast at the camera objective for photography taken from the blunt cone configuration at a wavelength of 0.4 microns at the flight conditions outlined in Part II will not be reduced by luminosity. Luminosity does affect that taken from the swept wing at this wavelength at the high Mach numbers and the 200,000 and 250,000-foot altitudes. At the longer wavelengths this effect disappears.

RECOMMENDATIONS

As a result of the investigation carried out in this part of the report, the following recommendations for minimizing the loss of contrast are made:

1. The camera window should be mounted as far forward on the nose of the vehicle as possible in order to minimize the distance which the light ray must travel through the luminous layer.

2. For the same reason as above, the viewing direction should be as close to vertical as possible.

3. The loss of contrast due to air light and Rayleigh scattering can be minimized by using film sensitive to the longer wave lengths of light.

The following recommendations are made with regard to areas of possible future study:

1. Various film and filter combinations should be examined with the aim of determining the combination which minimizes the loss of contrast.

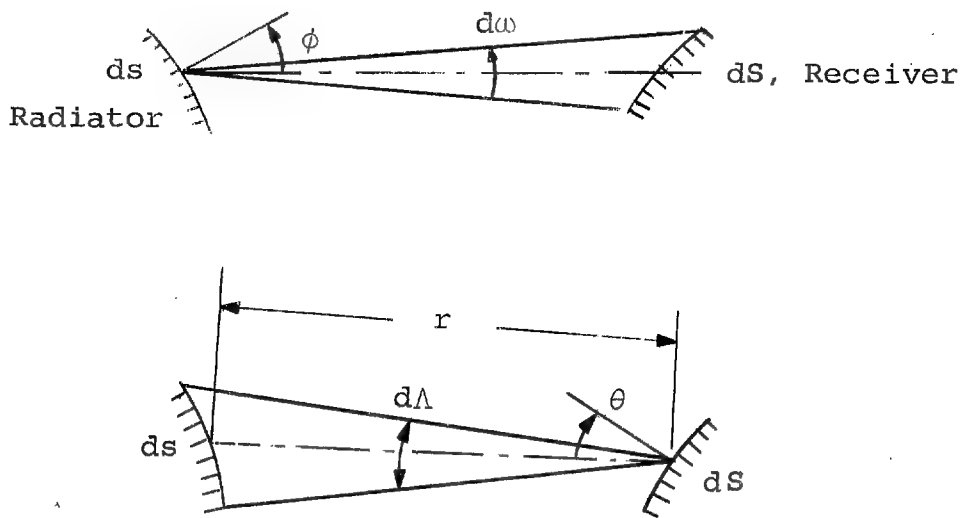
2. The effect of angle of attack of the swept wing glider should be investigated.

3. A similar study should be made for the infrared and microwave wavelength bands.

4. Upward viewing should also be studied so as to determine the region on the Mach number, altitude diagram where guidance systems utilizing celestial navigation may be expected to operate satisfactorily.

APPENDIX VIA
 RELATIONSHIPS BETWEEN FLUX, INTENSITY,
 AND BRIGHTNESS

The following sketch will be used to define the various physical quantities:



Let the total energy radiated by the receiver be E ergs. The total flux is defined as the energy per unit time.

$$\frac{dE}{dt} = \text{total flux, ergs/sec}$$

Consider now the monochromatic flux, that is, the flux per unit wavelength (microns)

$$\frac{d^2E}{dt d\lambda} = \text{monochromatic flux, ergs/sec-micron}$$

The emittance is the flux per unit area of the source

$$\frac{d^2E}{dt ds} = \text{emittance, ergs/sec-cm}^2$$

The foregoing quantities are properties of the source that are independent of direction. However, such properties of the source as intensity and brightness are directional.

The intensity of the source for a particular direction is the flux per steradian.

$$\frac{d^2E}{dtd\omega} = \text{intensity, ergs/sec-steradian}$$

Intensity is a property of the source which is independent of distance.

The brightness of the source in a given direction is the flux per steradian per area of the source normal to the direction of view (ds_n).

$$\frac{d^3E}{dtd\omega ds_n} = \text{brightness, ergs/sec-steradian-cm}^2$$

The area ds_n is simply

$$ds_n = ds \cos \phi$$

Brightness, as defined, is independent of the size of the source and the distance from it for no absorption or scattering. The property of brightness is of particular significance in this study because of its close relationship to contrast.

The physical quantities of emittance, intensity, and brightness have been defined independent of wave length. It is clear that they can also be defined monochromatically and we shall use them principally in this connection.

The property of brightness, which depends intrinsically on the source and the viewing direction, can be related to the energy being received at a receiver such as ds . In fact, it can be shown that the flux per unit receiver area normal to the line of sight per steradian subtended by the source is numerically equal to the brightness. By its source definition,

$$B = \frac{d^3E}{dt d\omega ds_n}$$

At the receiver, the flux is

$$\frac{d^3E}{dt} = (B d\omega) ds \cos \phi$$

We have

$$d\omega = \frac{ds \cos \theta}{r^2} \quad d\Lambda = \frac{ds \cos \phi}{r^2}$$

so that

$$\begin{aligned} \frac{d^3E}{dt} &= B \left(\frac{ds \cos \theta}{r^2} \right) ds \cos \phi \\ &= B ds_n d\Lambda \end{aligned}$$

$$B = \frac{d^3E}{dt d\Lambda ds_n}$$

Thus, the brightness is equal to the flux per unit receiver area normal to the line of sight per steradian subtended by the source at the receiver.

APPENDIX VIB

ATTENUATION OF IMAGE BRIGHTNESS BY
RAYLEIGH SCATTERING

The molecular scattering of light through a uniform medium is described mathematically by the Rayleigh scattering coefficient. If the brightness of a light beam at its source is B_0 , the brightness is decreased by molecular scattering in a manner depending exponentially on path length as follows:

$$B = B_0 e^{-\beta_0 L} \quad (\text{VIB-1})$$

where

L path length at sea level

β_0 Rayleigh scattering coefficient at sea level

The reciprocal of the Rayleigh scattering coefficient is the length of the optical path at sea level necessary to reduce the brightness by a factor $1/e$.

The coefficient β_0 is given by

$$\beta_0 = \frac{32\pi^3(n - 1)^2}{3N\lambda^4} \quad (\text{VIB-2})$$

where

N molecules per cm^3

λ wave length, cm

n index of refraction

$n-1$ 0.116 ρ

ρ density, slugs/ ft^3

At sea level in the ARDC atmosphere (Ref. 4),

$$N = 2.54 \times 10^{19} \text{ molecules/cm}^3$$

$$\rho = 0.002378 \text{ slugs/ft}^3$$

For a wavelength of 0.4 microns; that is, 4×10^{-5} centimeters, we find

$$\beta_0 = \frac{(32)(\pi^3)(0.116)^2(0.002378)^2}{3(2.54) 10^{19} (4)^4 10^{-20}} \text{ cm}^{-1}$$

$$\beta_0 = \frac{1}{25.7} \text{ km}^{-1}$$

For nonhorizontal viewing, the density is not uniform, and Equation (VIB-1) must be expressed in differential form and integrated along the path. In differential form,

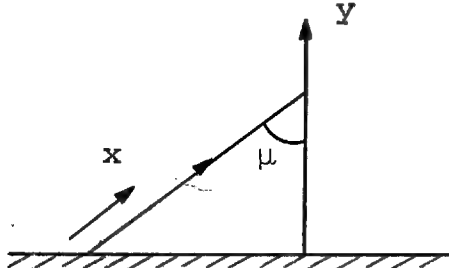
$$dB = -B_0 e^{-\beta L} \beta dx$$

$$\frac{dB}{B} = -\beta dx \quad (\text{VIB-3})$$

For a fixed wavelength, β varies directly with the density so that, from Equation (VI-1),

$$\beta = \beta_0 (\rho/\rho_0) = \beta_0 e^{-\bar{\alpha} y} \quad (\text{VIB-4})$$

Consider a light path from the ground upward at some zenith angle μ .



$$\frac{dB}{B} = -\beta_o e^{-\bar{\alpha}x} \cos \mu \, dx = \frac{-\beta_o e^{-\bar{\alpha}y}}{\cos \mu} \, dy$$

$$\log \frac{B}{B_o} = \frac{\beta_o}{\bar{\alpha} \cos \mu} e^{-\bar{\alpha}y} \Big|_0^h$$

$$\log \frac{B}{B_o} = - \frac{\beta_o}{\bar{\alpha} \cos \mu} \left(1 - e^{-\bar{\alpha}h} \right)$$

Let us define the equivalent sea-level path length as L
so that

$$L = \frac{1}{\bar{\alpha} \cos \mu} \left(1 - e^{-\bar{\alpha}h} \right) \quad (\text{VIB-5})$$

then

$$B = B_o e^{-\beta_o L} \quad (\text{VIB-6})$$

APPENDIX VIC

CONVERSION OF ABSORPTION COEFFICIENT
DATA TO BRIGHTNESS

Reference 2 contains a series of tables of absorption coefficients as a function of wavelength, density, and temperature. These coefficients have been calculated using the tables of Reference 3 to obtain the chemical composition of air in thermodynamic equilibrium at the various temperatures and densities. In order to utilize this information in the present work, it is necessary to convert the absorption coefficients to brightnesses. This can be done in the following way.

For a slab of gas of thickness, r , in thermodynamic equilibrium at a temperature, T , the brightness (see Appendix VIA) for monochromatic light is given by

$$B_L = \frac{d^4 E}{dtd\omega d\lambda ds_n} = \left(1 - e^{-\mu' \lambda r}\right) \frac{d^4 E_B}{dtd\omega d\lambda ds_n} \quad (\text{VIC-1})$$

where

$$\frac{d^4 E_B}{dtd\omega d\lambda ds_n} = \frac{2hc^2}{\lambda^5 \left(e^{-hc/kT\lambda} - 1\right)} \quad (\text{VIC-2})$$

is the brightness of a black body, and

$$\mu' \lambda = \mu_\lambda \left(1 - e^{-hc/kT\lambda}\right) \quad (\text{VIC-3})$$

is the apparent absorption coefficient. The factor in parentheses corrects the true absorption coefficient for induced emission.

For the special case of an optically thin gas layer,

$$\mu'_{\lambda} r \ll 1.0$$

we find

$$B_L \approx \mu_{\lambda} r \left(\frac{2hc^2}{\lambda^5} e^{-hc/kT\lambda} \right) \quad (\text{VIC-4})$$

or

$$b_L = \frac{dB_L}{dr} \approx \mu_{\lambda} \left(\frac{2hc^2}{\lambda^5} e^{-hc/kT\lambda} \right) \quad (\text{VIC-5})$$

where

b_L brightness of a unit volume of luminous gas,
watts/cm³-steradian-micron

h Planck's constant, 6.6253×10^{-27} erg sec

k Boltzmann's constant, 1.3804×10^{-16} erg/°K

c velocity of light, 2.9979×10^{10} cm/sec

T temperature, °K

λ wave length, Å

μ_{λ} absorption coefficient, cm⁻¹

If the above constants are substituted in Equation (VIC-5), the following expression is obtained for converting the absorption coefficient for a specific wave length and temperature to brightness:

$$b_L \approx 119.090 \times 10^{22} \lambda^{-5} \mu_{\lambda} e^{-\frac{1.43885 \times 10^8}{\lambda T}} \quad (\text{VIC-6})$$

This conversion has been made for the following cases and the results are presented in Figures (VI-5) through (VI-7):

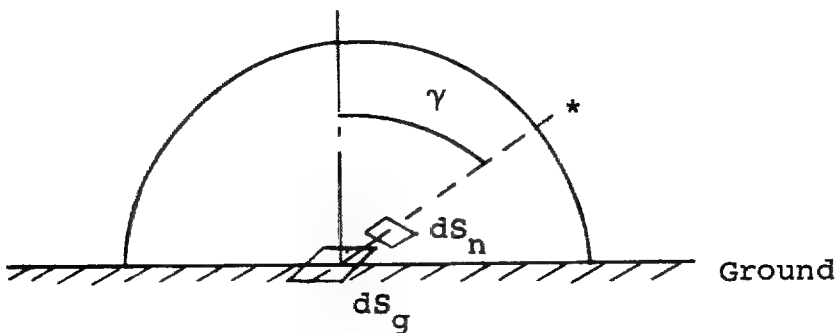
<u>T, °K</u>	<u>ρ/ρ_0^*</u>
3000	$10^{-1}, 10^{-2}, 10^{-3}, 10^{-4}, 10^{-5}, 10^{-6}$
4000	ditto
6000	ditto

The quantity ρ_0^* is the value of the standard density used in Reference 3

$$\begin{aligned}\rho_0^* &= 1.2931 \times 10^{-3} \text{ gm/cm}^3 \\ &= 2.508 \times 10^{-3} \text{ slugs/ft}^3\end{aligned}$$

APPENDIX VI-D
DETERMINATION OF GROUND BRIGHTNESS

In determining the contrast loss due to the luminous layer, the important parameter is the ratio of the ground brightness to the brightness of the luminous layer. It is the purpose of this appendix to explain how intrinsic ground brightness has been determined. Consider the sun at zenith angle γ with a unit area normal to the sun's rays



Let I_n be watts per cm^2 per micron incident on area ds_n normal to the sun's rays. Let I_g be the watts per cm^2 per micron on the ground area ds_g due to the sun and sky. Then we have

$$I_g = I_n \cos \gamma \quad (\text{VID-1})$$

The values of I_n are given for several wave lengths and zenith angles on page VI-23.

Let us now suppose the ground is a diffuse reflector of reflectivity r_λ for a given wave length. We can then imagine the ground to be a source of emittance $I_g r_\lambda$. In the

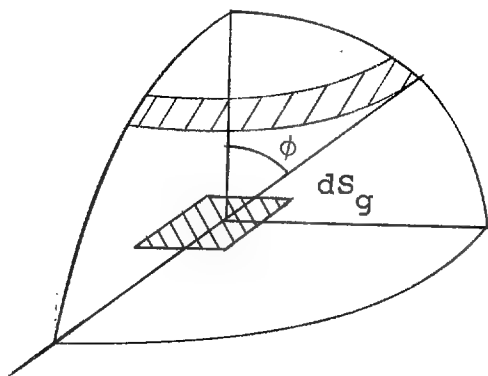
terminology and symbols of Appendix VIA, page VI-31, we have

$$\text{Emittance} = \frac{d^3 E}{dtds_g d\lambda} = I_n \cos \gamma r_\lambda \quad (\text{VID-2})$$

Since we have assumed the ground to be a diffuse source following Lambert's law, its brightness does not depend on the viewing angle and has the value B_g

$$B_g = \frac{I_n \cos \gamma r_\lambda}{\pi} \quad (\text{VID-3})$$

To derive this result consider the following configuration:



The ground brightness by definition is on a monochromatic basis

$$B_g = \frac{d^4 E}{dtd\omega(ds_g \cos \phi) d\lambda}$$

where $ds_g \cos \phi$ is the area of the source normal to the viewing direction and $d\omega$ is the solid angle that the receiver subtends at the source. Consider circular elements of the hemisphere as shown above as the receiver. Then

$$d\omega = \frac{2\pi r \sin \phi r d\phi}{r^2} = 2\pi \sin \phi d\phi$$

Since the brightness is independent of ϕ for a diffuse source, we have

$$\frac{d^4E}{dtds_g d\lambda d\omega} = B_g \cos \phi$$

Performing an integration over a hemisphere, we have

$$\begin{aligned} \frac{d^3E}{dtds_g d\lambda} &= B_g \int \cos \phi \, d\omega = 2\pi B_g \int_0^{\pi/2} \sin \phi \cos \phi \, d\phi \\ &= \pi B_g \end{aligned}$$

Thus we have

$$B_g = \frac{1}{\pi} \frac{d^3E}{dtds_g d\lambda} = \frac{I_n \cos \phi r_\lambda}{\pi} \quad (\text{VID-4})$$

REFERENCES

1. Middleton, W. E. K.: *Vision Through the Atmosphere*. University of Toronto Press, reprinted 1958.
2. Meyerott, R. E., Sokoloff, J., and Nicholls, R. A.: *Absorption Coefficients of Air*, Advance courtesy copy of a forthcoming Geophysics Research Paper of the Geophysics Research Directorate, Air Force Cambridge Research Center, Bedford, Mass.
3. Gilmore, R. R.: *Equilibrium Composition and Thermodynamic Properties of Air to 24,000° K.* Rand Corporation RM-1543. August 24, 1955.
4. Minzner, R. A. and Ripley, W. S.: *The ARDC Model Atmosphere*. AF Survey in Geophysics, No. 86, A. F. Cambridge Research Center, TN 56-204, December 1956.
5. Jones, Loyd A. and Condit, H. R.: *Sunlight and Skylight as Determinants of Photographic Exposure. I Luminous Density as Determined by Solar Altitude and Atmospheric Conditions*. Journal of the Optical Society of America, vol. 38, no. 2, February 1948.
6. United States Air Force, Geophysics Research Directorate: *Handbook of Geophysics*. The Macmillan Company, New York, 1960.

TABLE VI-1. SPECTRAL REFLECTANCE OF NATURAL OBJECTS

<u>λ</u> <u>(A)</u>	<u>Fresh Snow</u>	<u>Desert</u>	<u>Forest</u>
4000	0.830	0.118	0.033
4200	0.825	0.122	0.036
4400	0.821	0.142	0.040
4600	0.815	0.158	0.042
4800	0.806	0.172	0.046
5000	0.798	0.186	0.050
5200	0.790	0.202	0.063
5400	0.780	0.221	0.083
5600	0.770	0.242	0.088
5800	0.760	0.262	0.080
6000	0.756	0.273	0.078
6200	0.748	0.279	0.079
6400	0.740	0.282	0.078
6600	0.730	0.283	0.077
6800	0.720	0.286	0.099
7000	0.710	0.290	0.140
7200	0.700	0.295	0.189
7400	0.690	0.302	0.225
7600	0.680	0.309	0.251

Approved For Release 2000/04/12 : CIA-RDP67B00657R000300070001-0

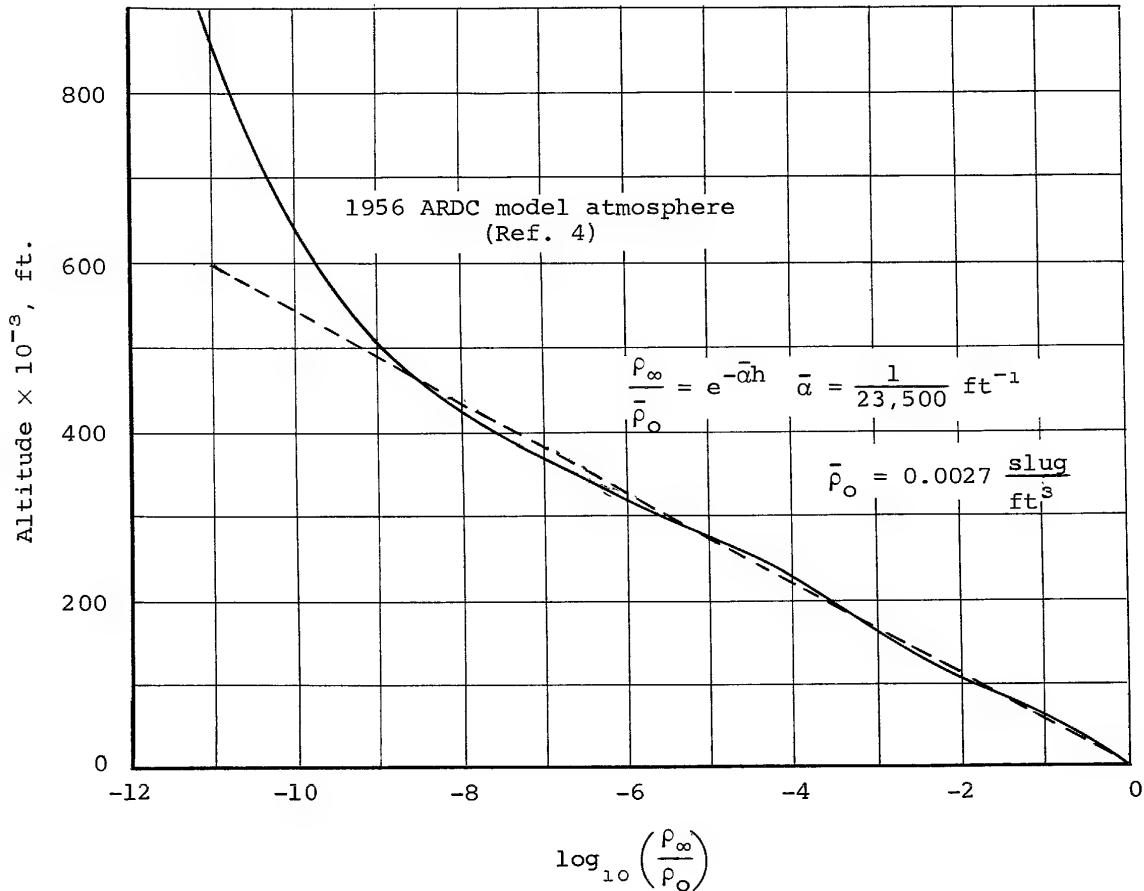


Figure VI-1.- Comparison of exponential approximation with ARDC model of earth atmosphere.

Approved For Release 2000/04/12 : CIA-RDP67B00657R000300070001-0

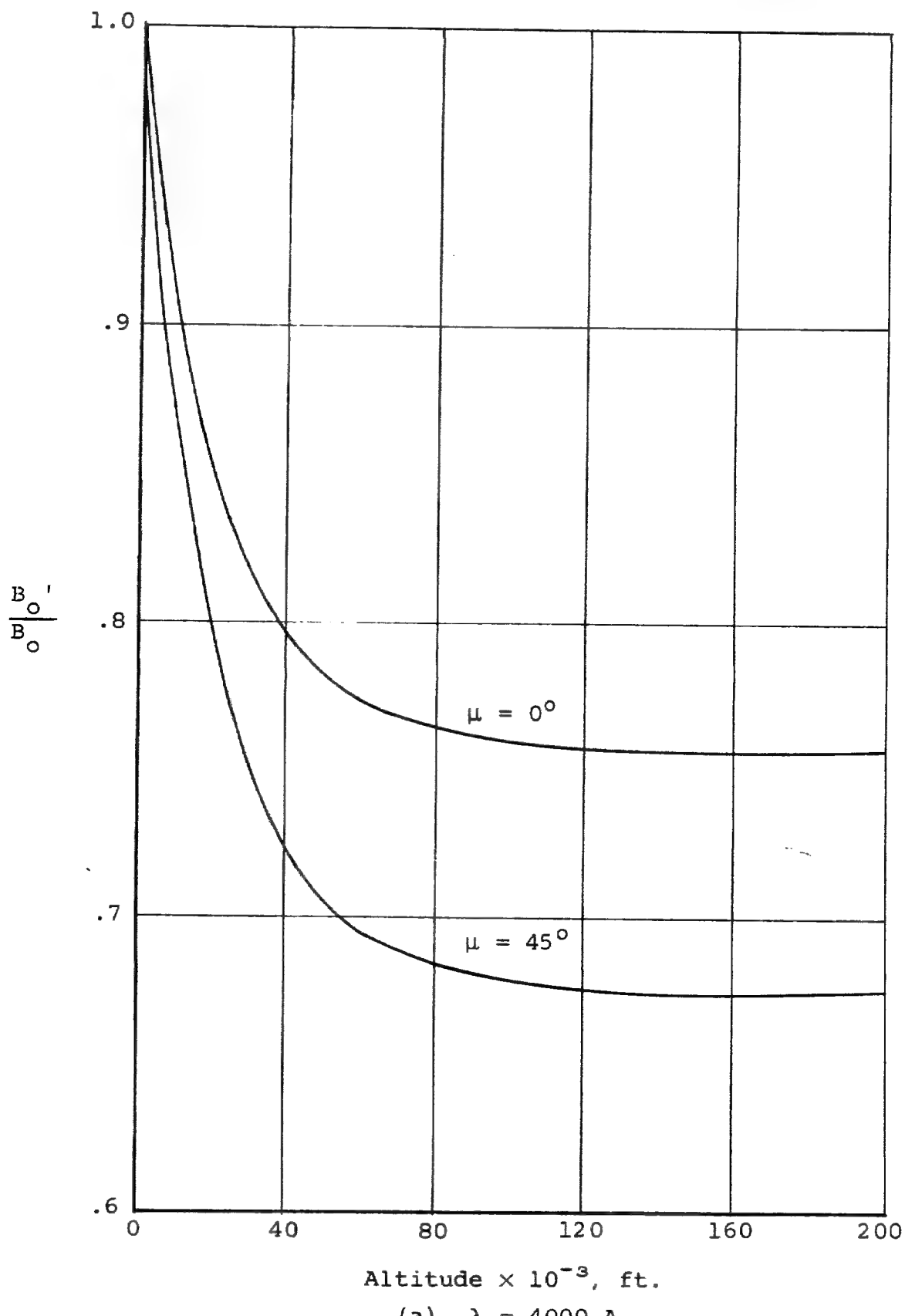
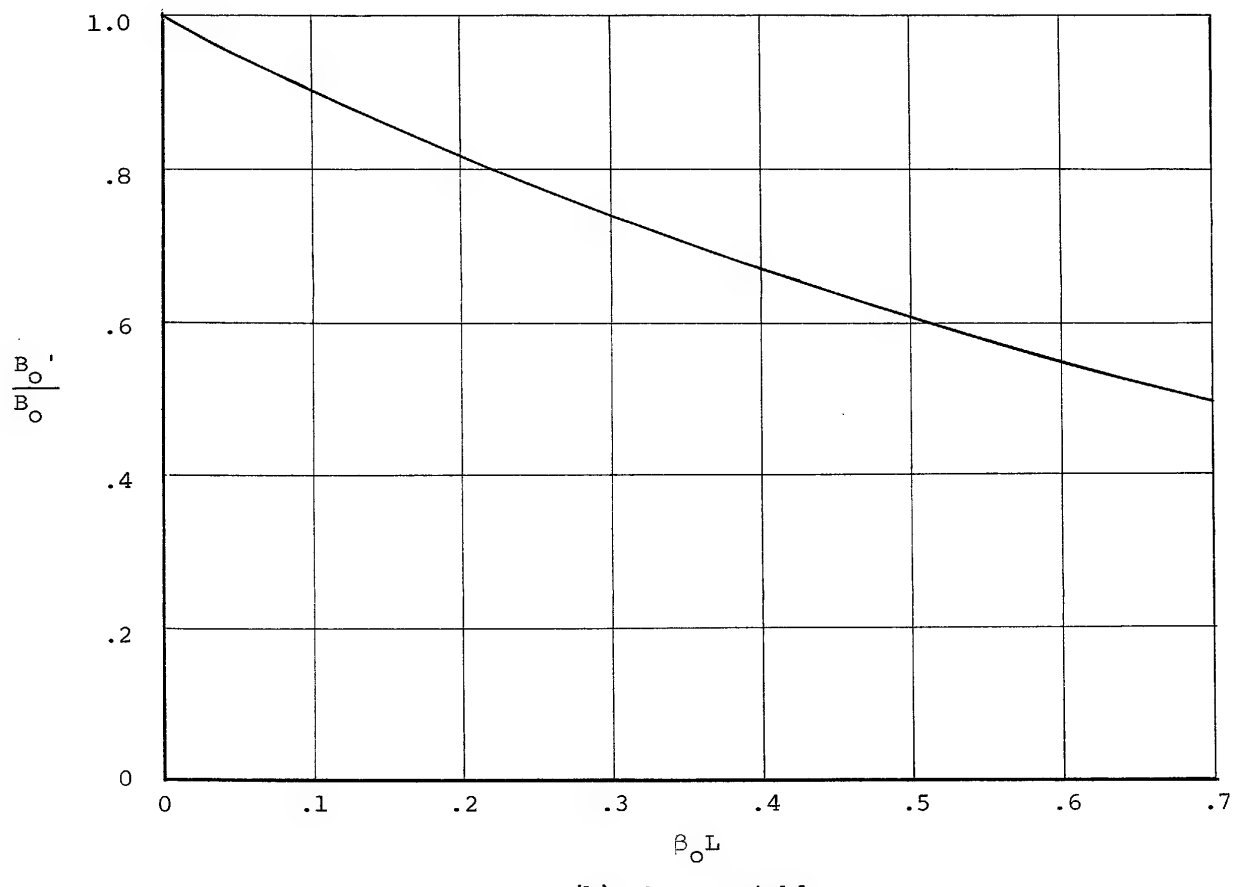


Figure VI-2.- Effect of Rayleigh scattering on object brightness with no air light.

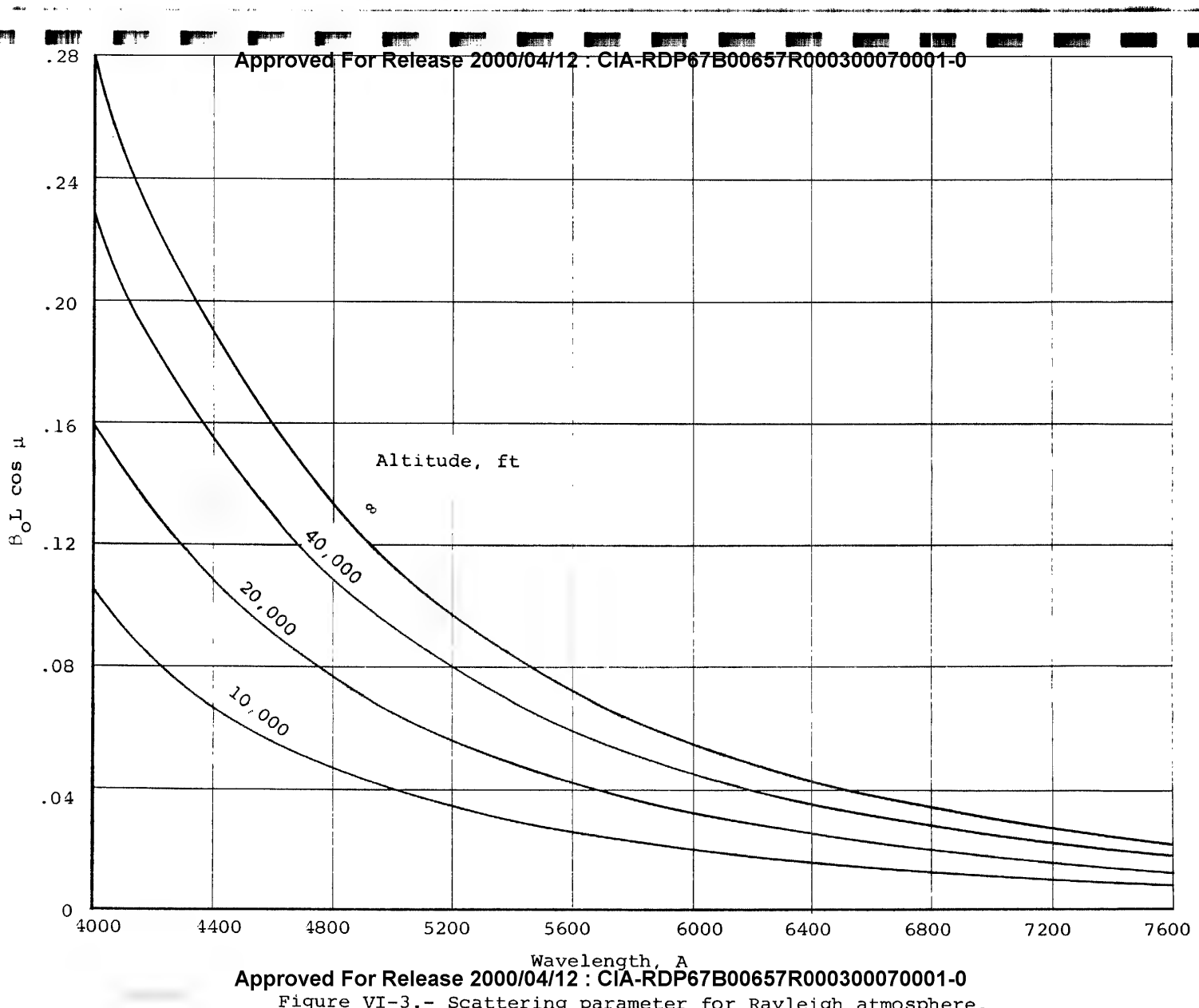
Approved For Release 2000/04/12 : CIA-RDP67B00657R000300070001-0



(b) λ = Variable

Figure VI-2.- Concluded.

Approved For Release 2000/04/12 : CIA-RDP67B00657R000300070001-0



Approved For Release 2000/04/12 : CIA-RDP67B00657R000300070001-0

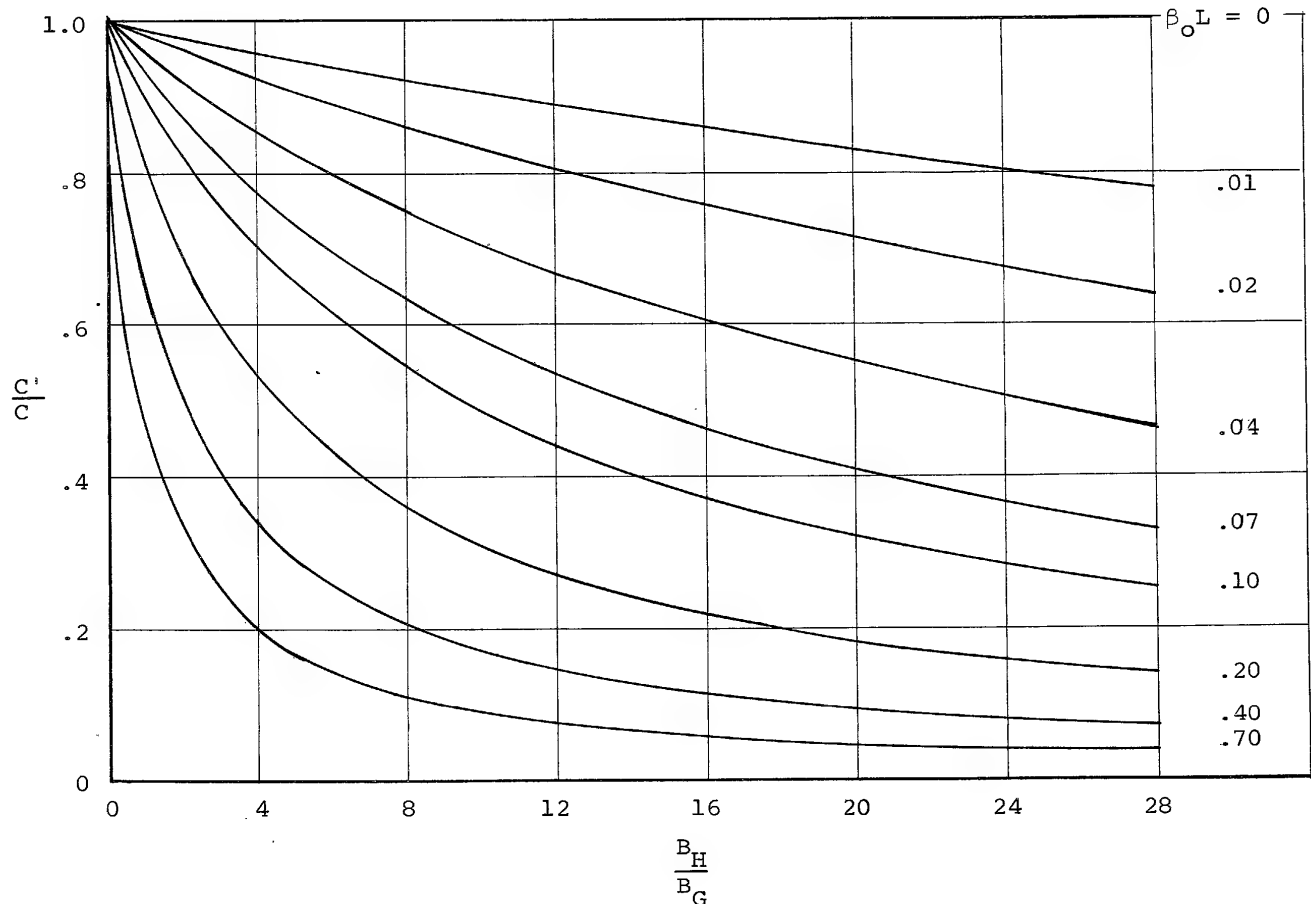


Figure VI-4.- Contrast-reduction ratio due to air light and Rayleigh scattering for a clear atmosphere.

Approved For Release 2000/04/12 : CIA-RDP67B00657R000300070001-0

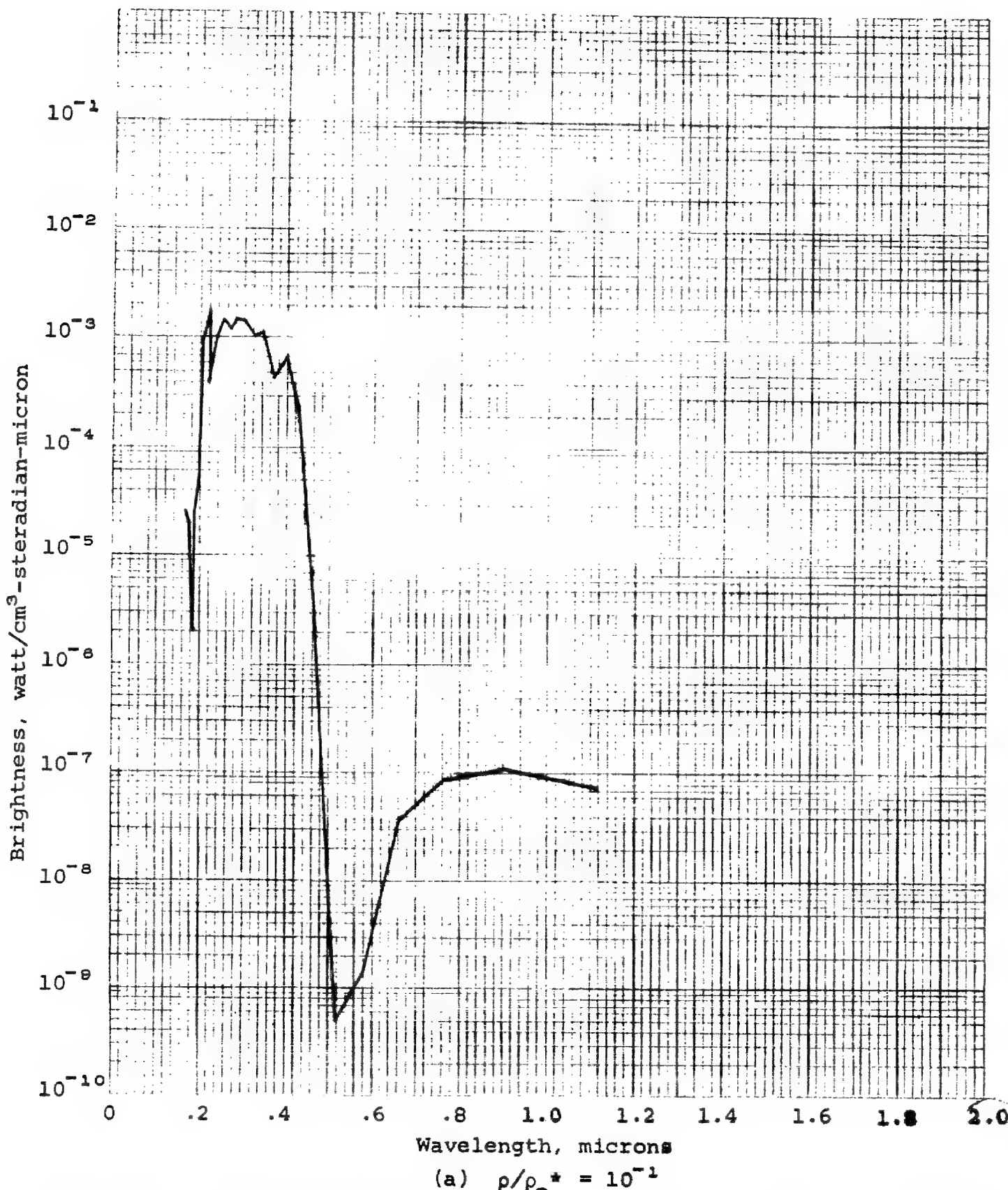


Figure VI-5.- Brightness of a unit volume of air, at a temperature of 3000° K, as a function of wavelength for various density ratios.

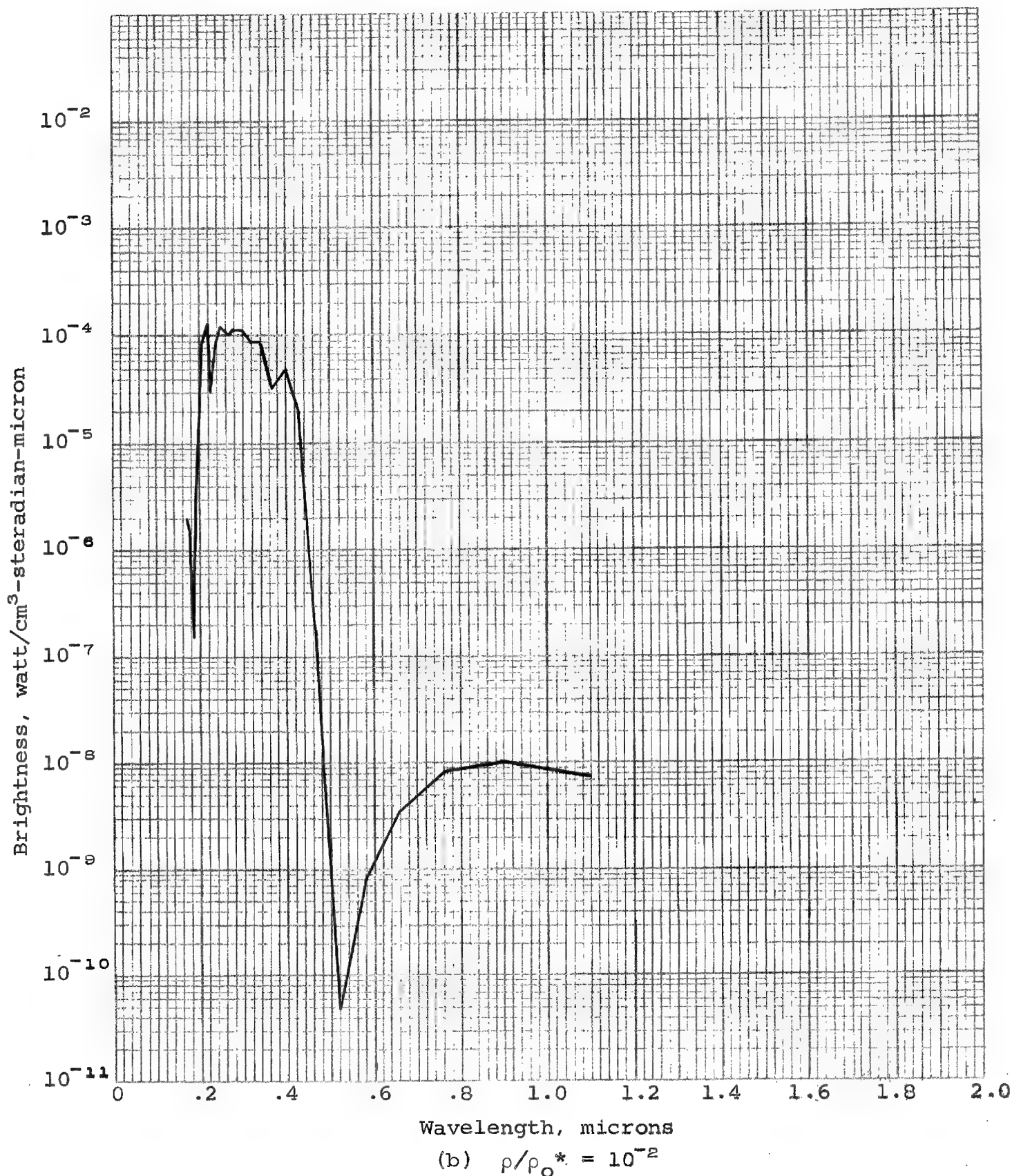


Figure VI-5.- Continued.

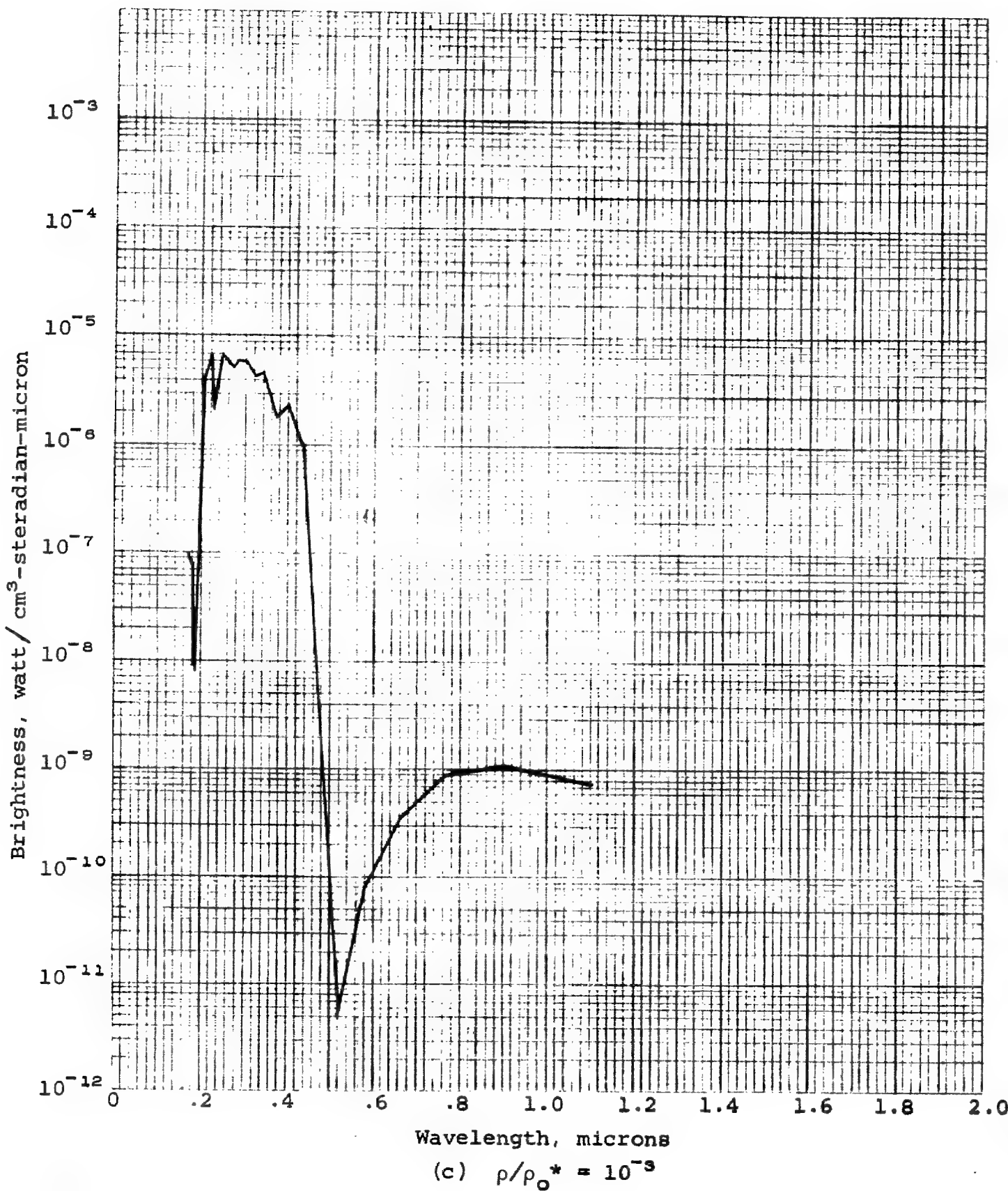


Figure VI-5.- Continued.

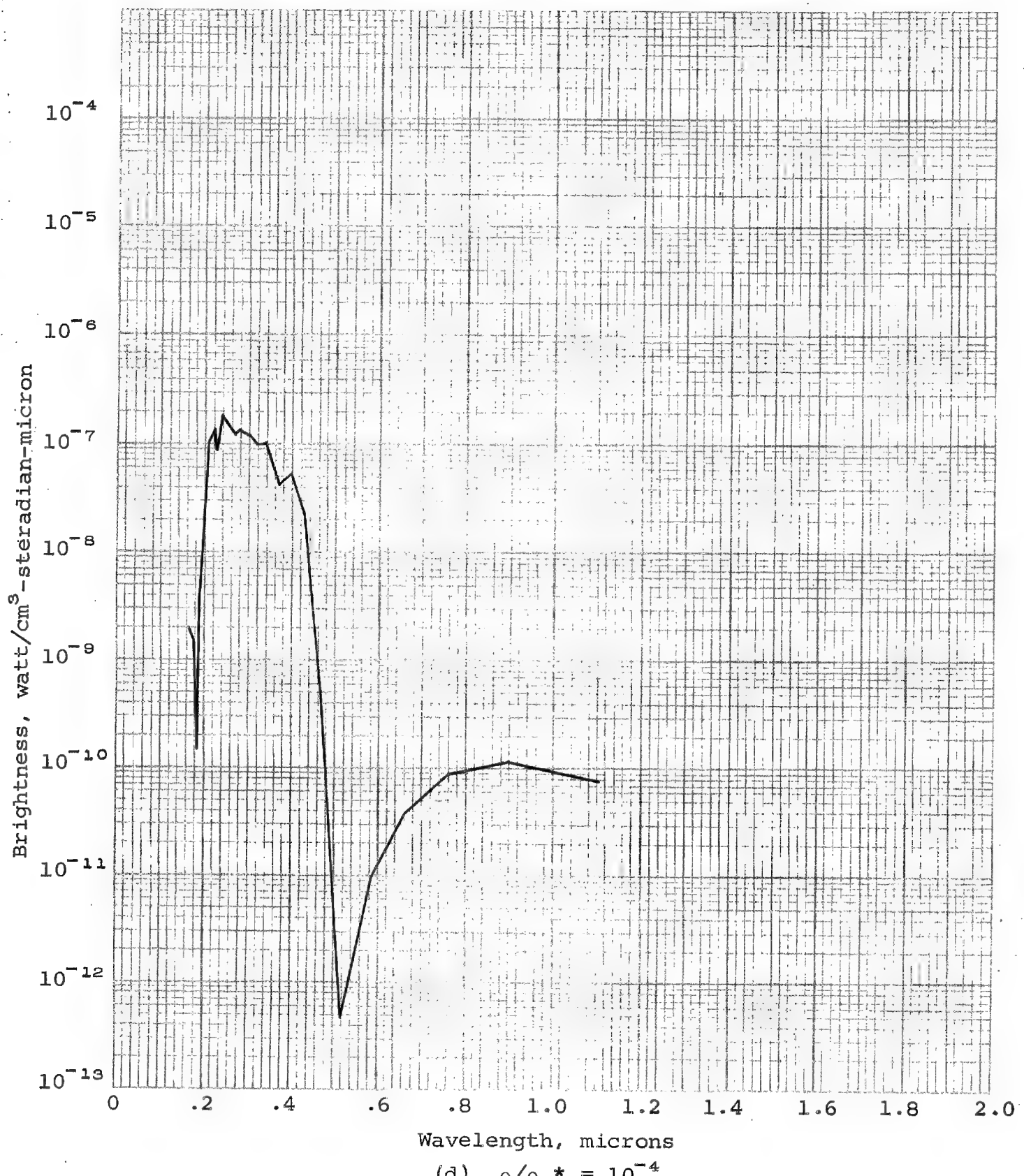


Figure VI-5.- Continued.

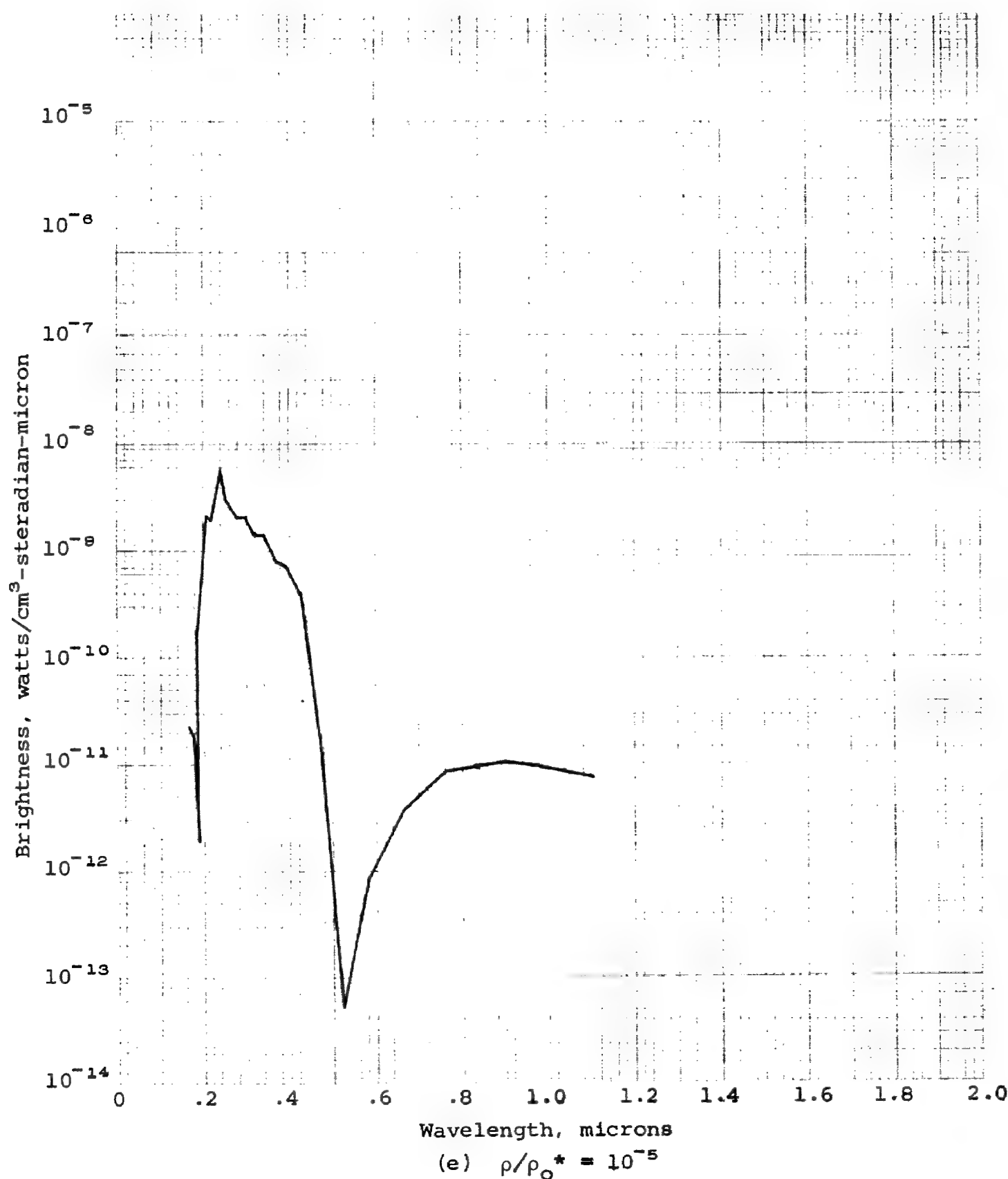


Figure VI-5.- Continued.

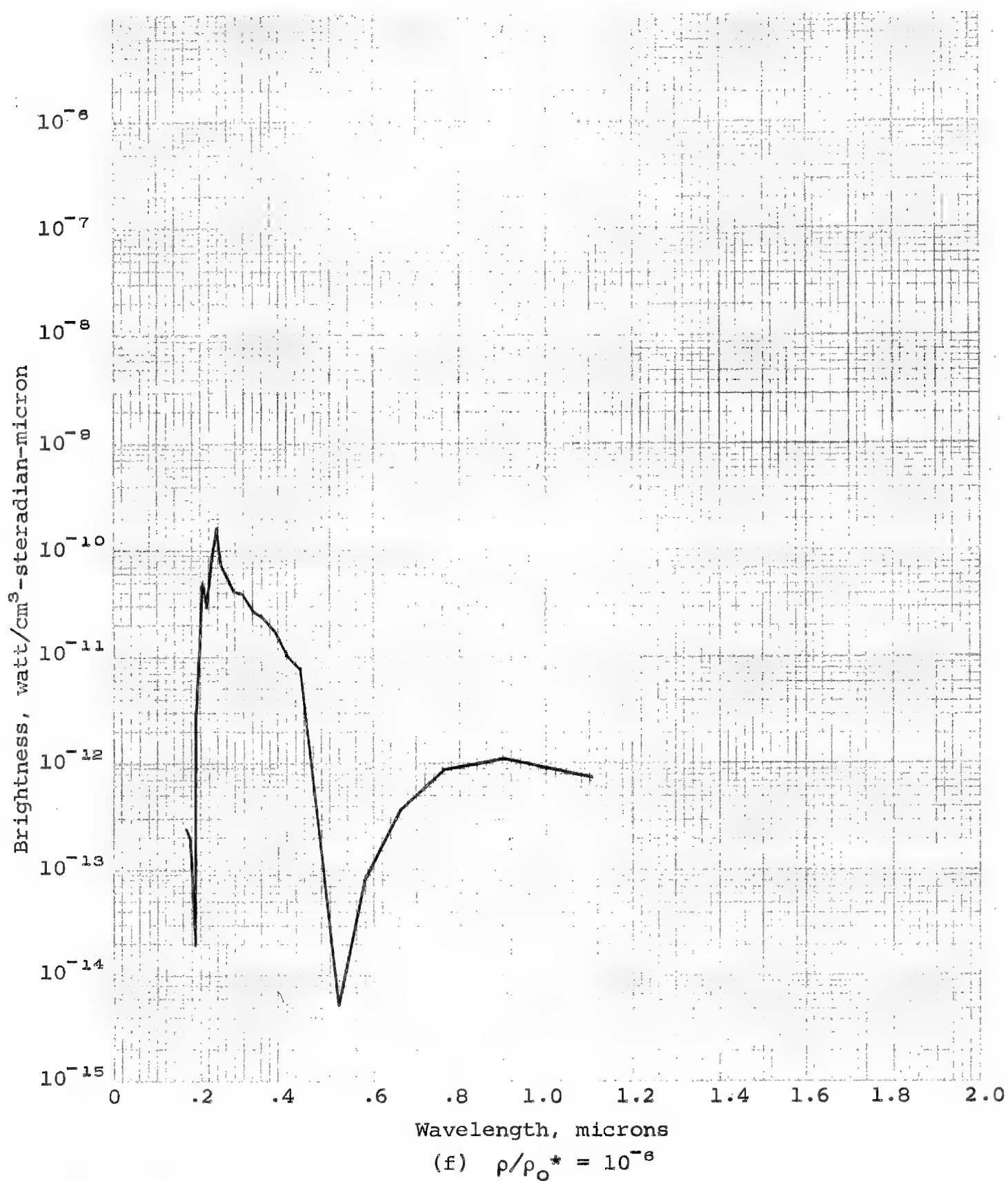


Figure VI-5.- Concluded.

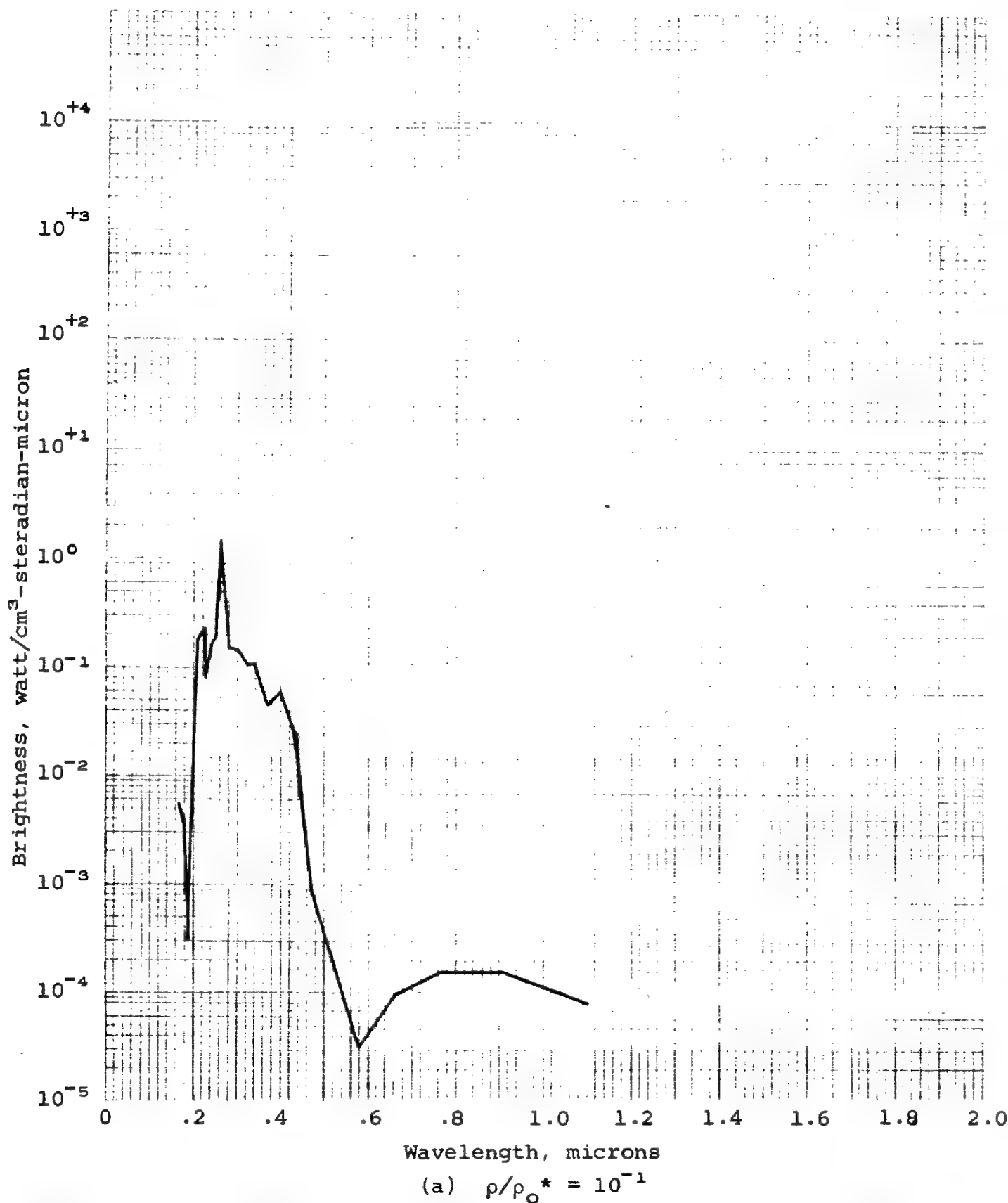


Figure VI-6.- Brightness of a unit volume of air, at a temperature of 4000° K , as a function of wavelength for various density ratios.

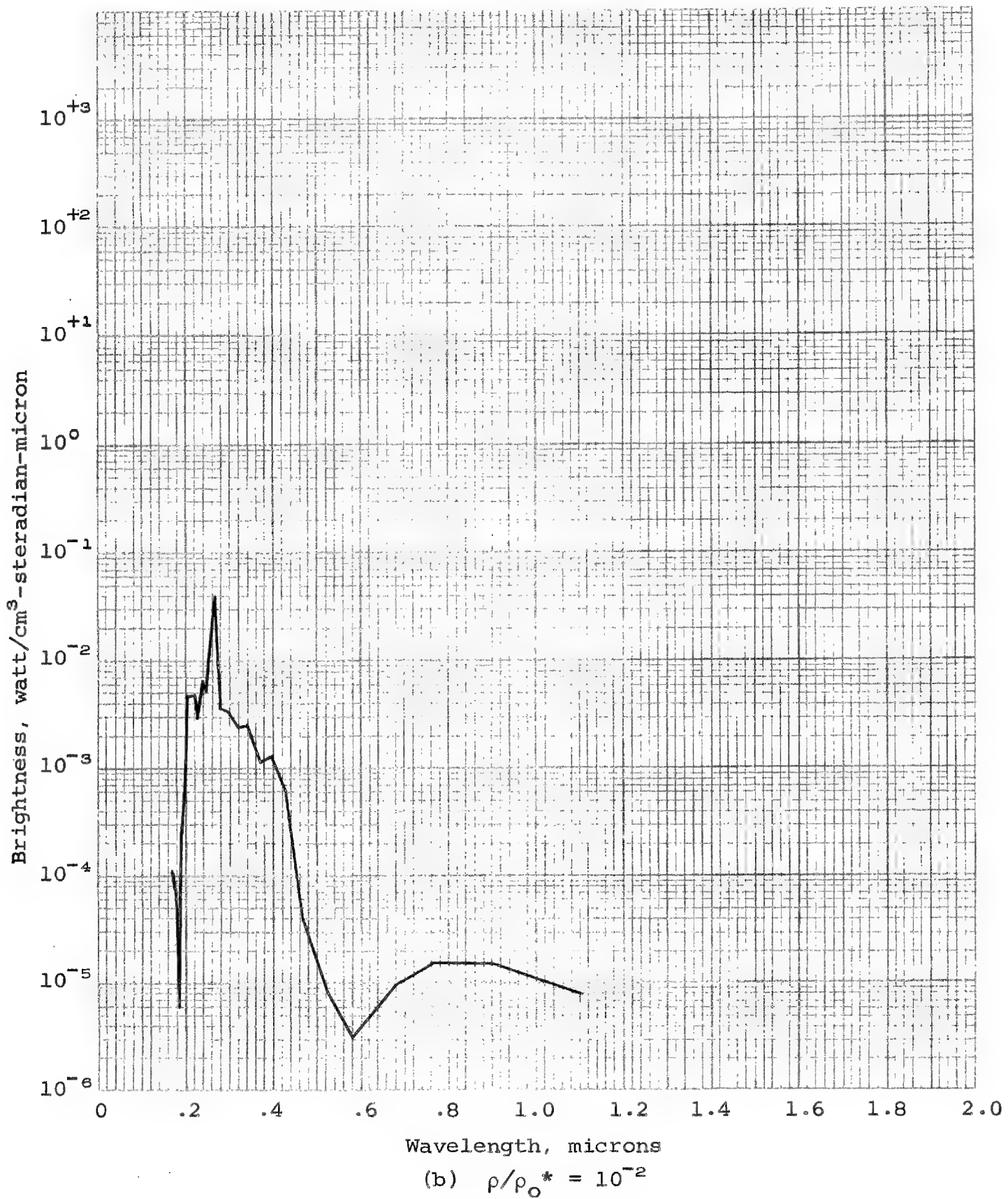


Figure VI-6.- Continued.

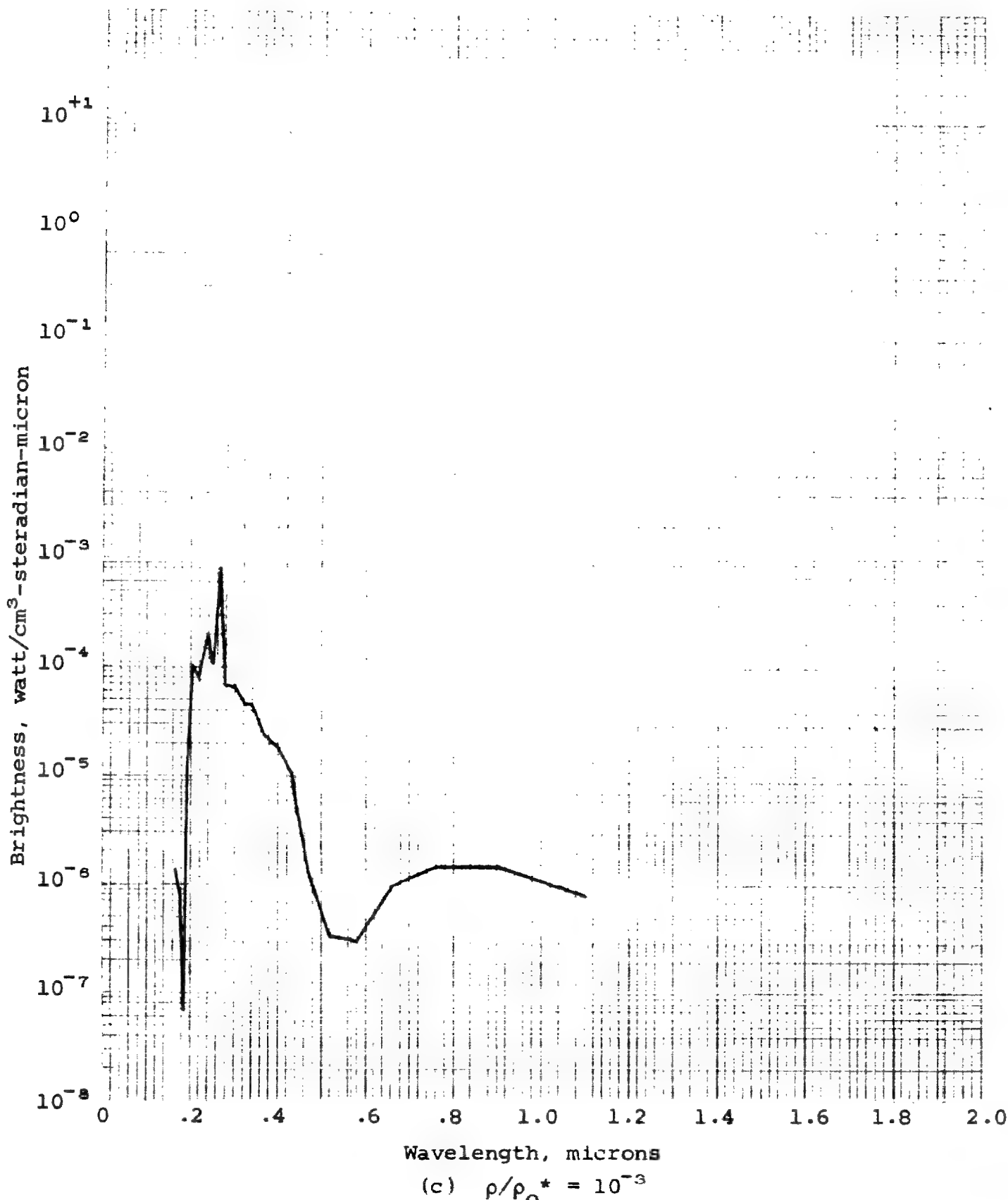


Figure VI-6.- Continued.

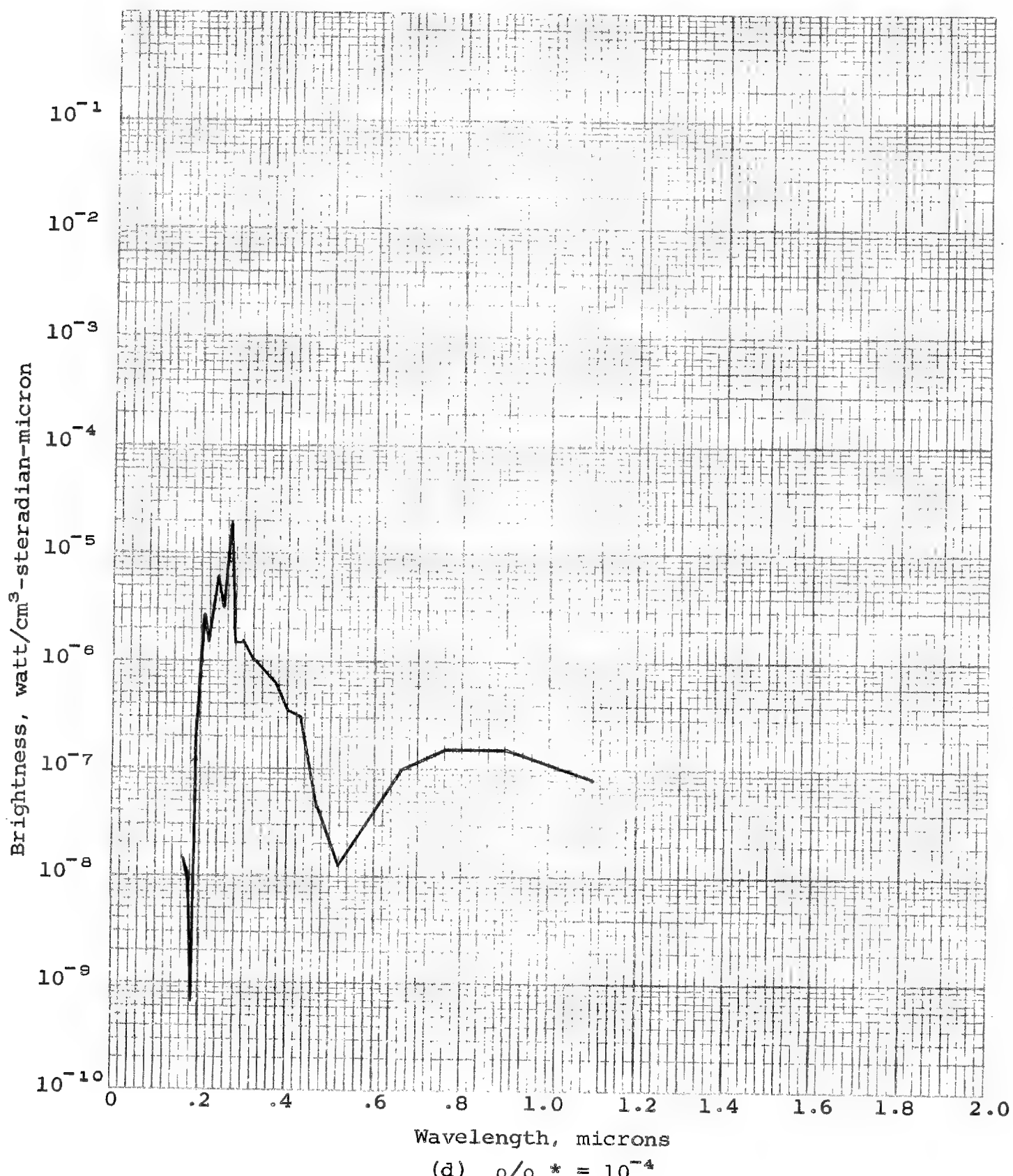


Figure VI-6.- Continued.

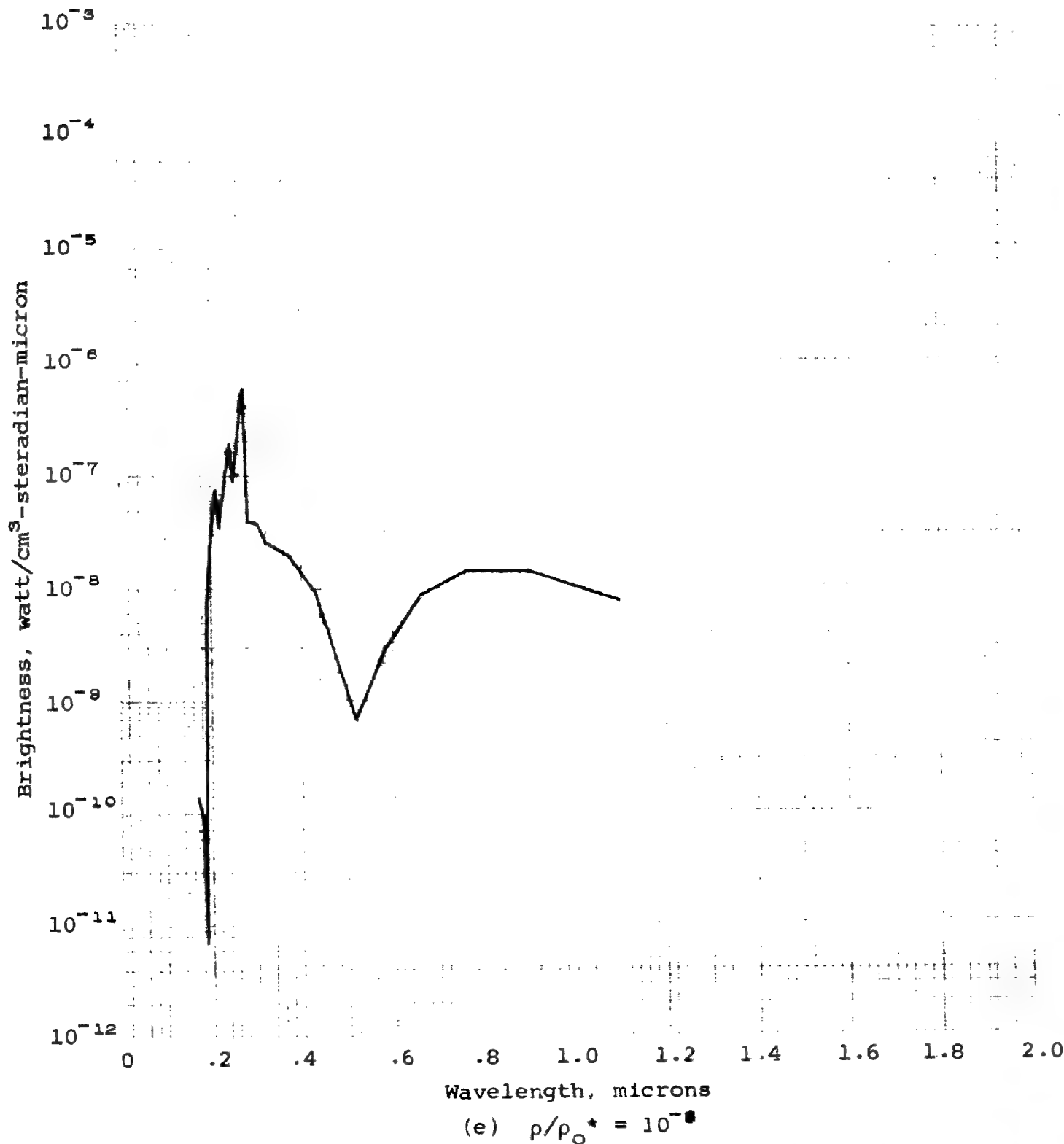


Figure VI-6.- Continued.

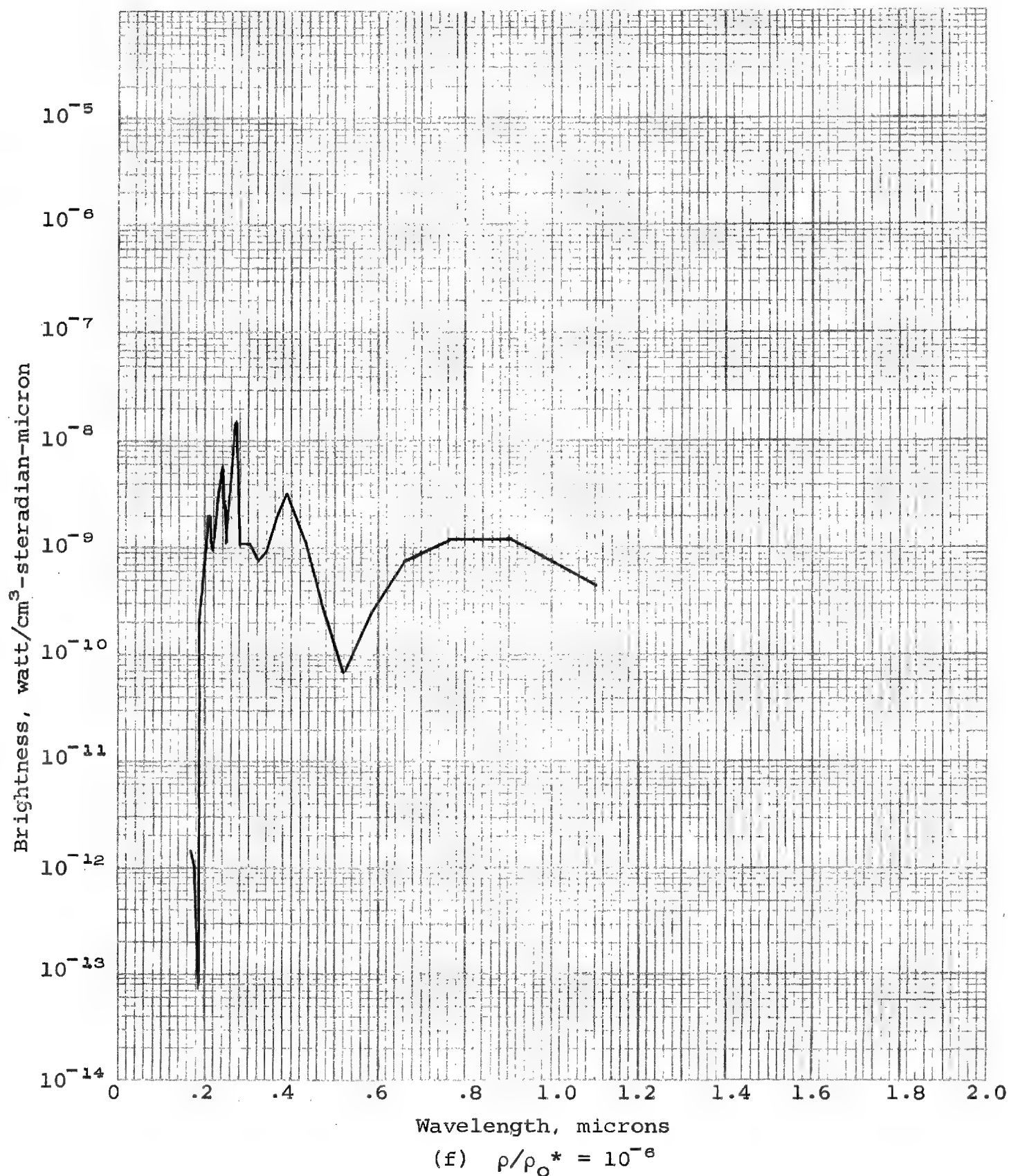


Figure VI-6.- Concluded.

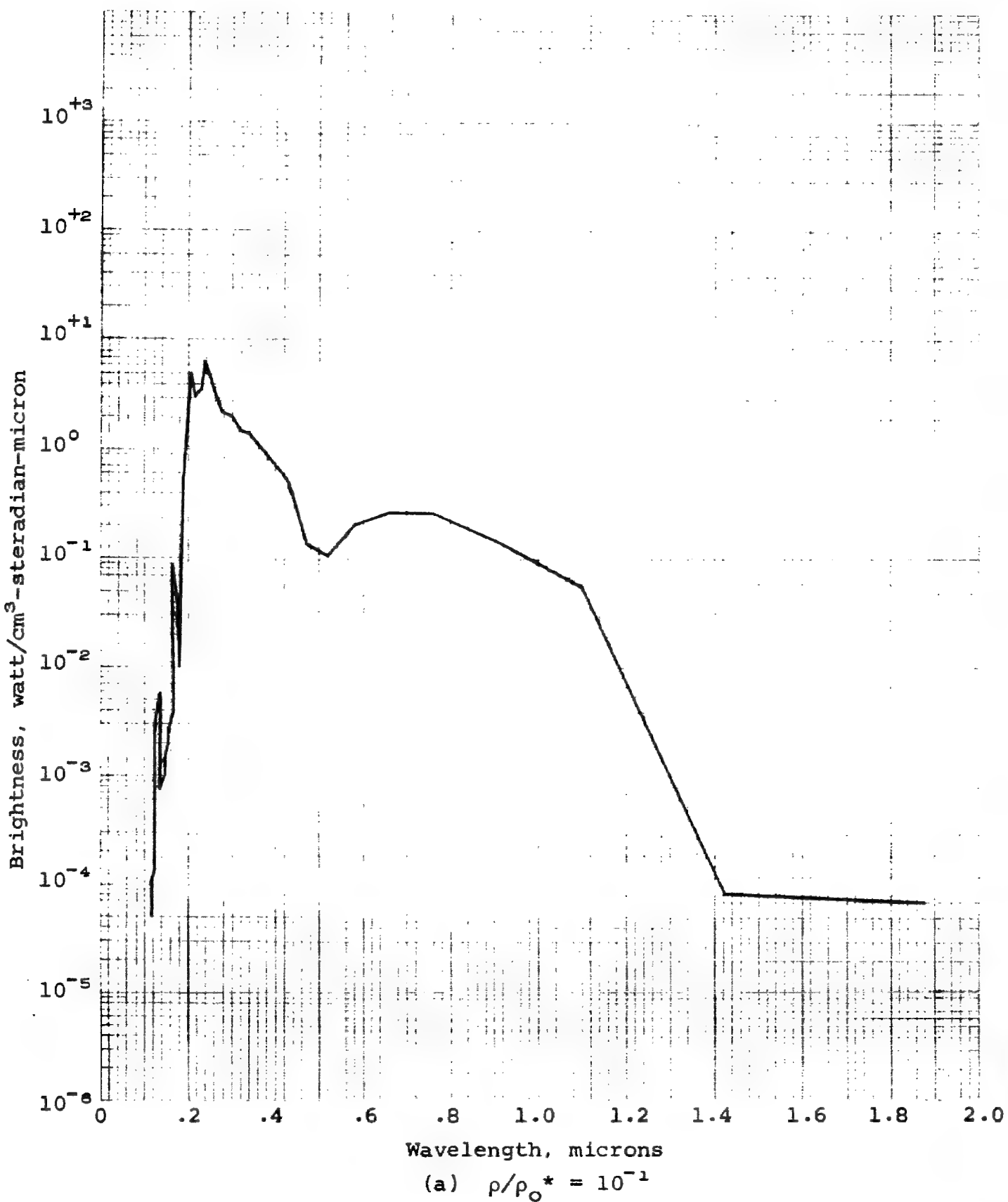


Figure VI-7.- Brightness of a unit volume of air, at a temperature of 6000° K, as a function of wavelength for various density ratios.

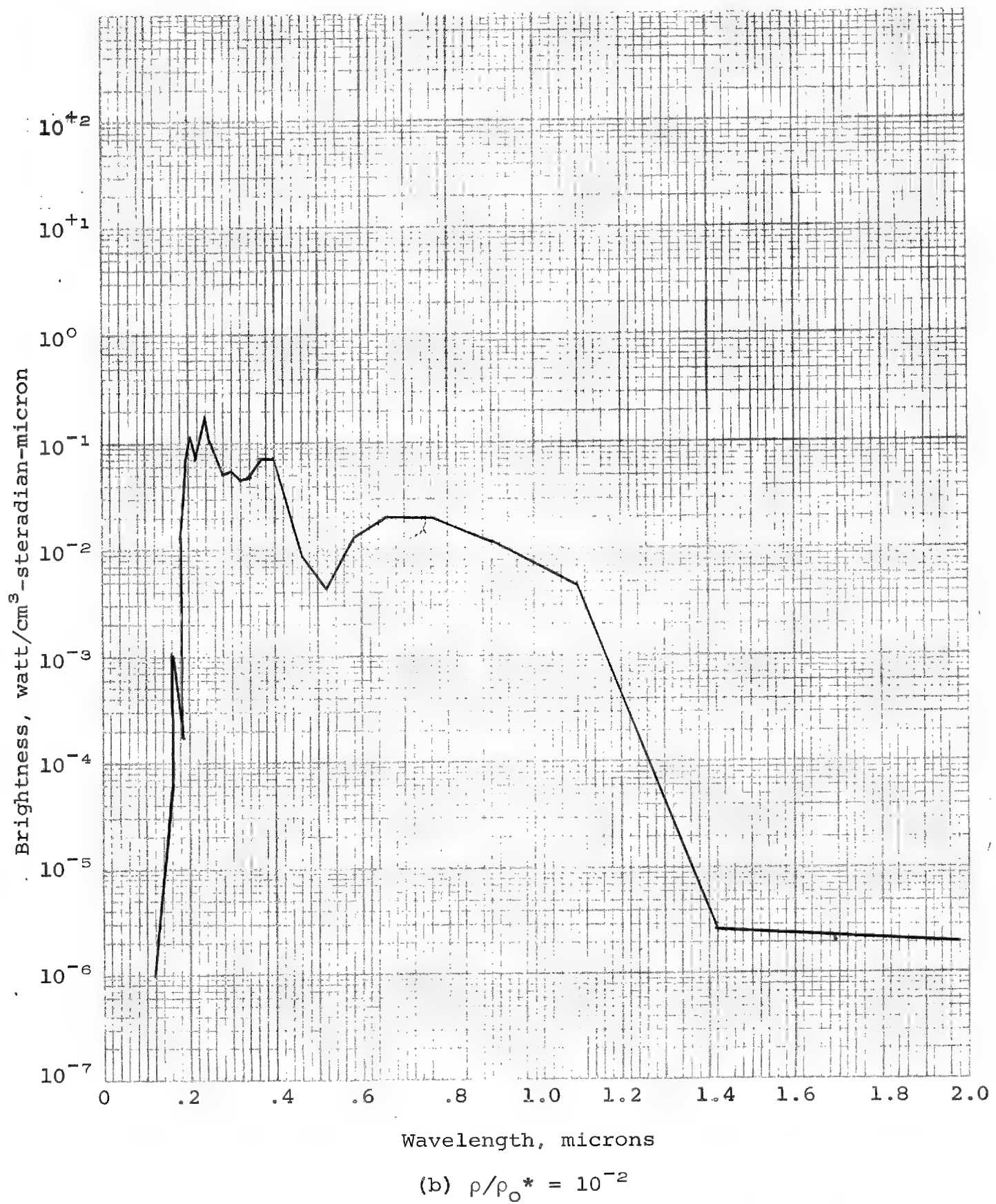


Figure VI-7.- Continued.

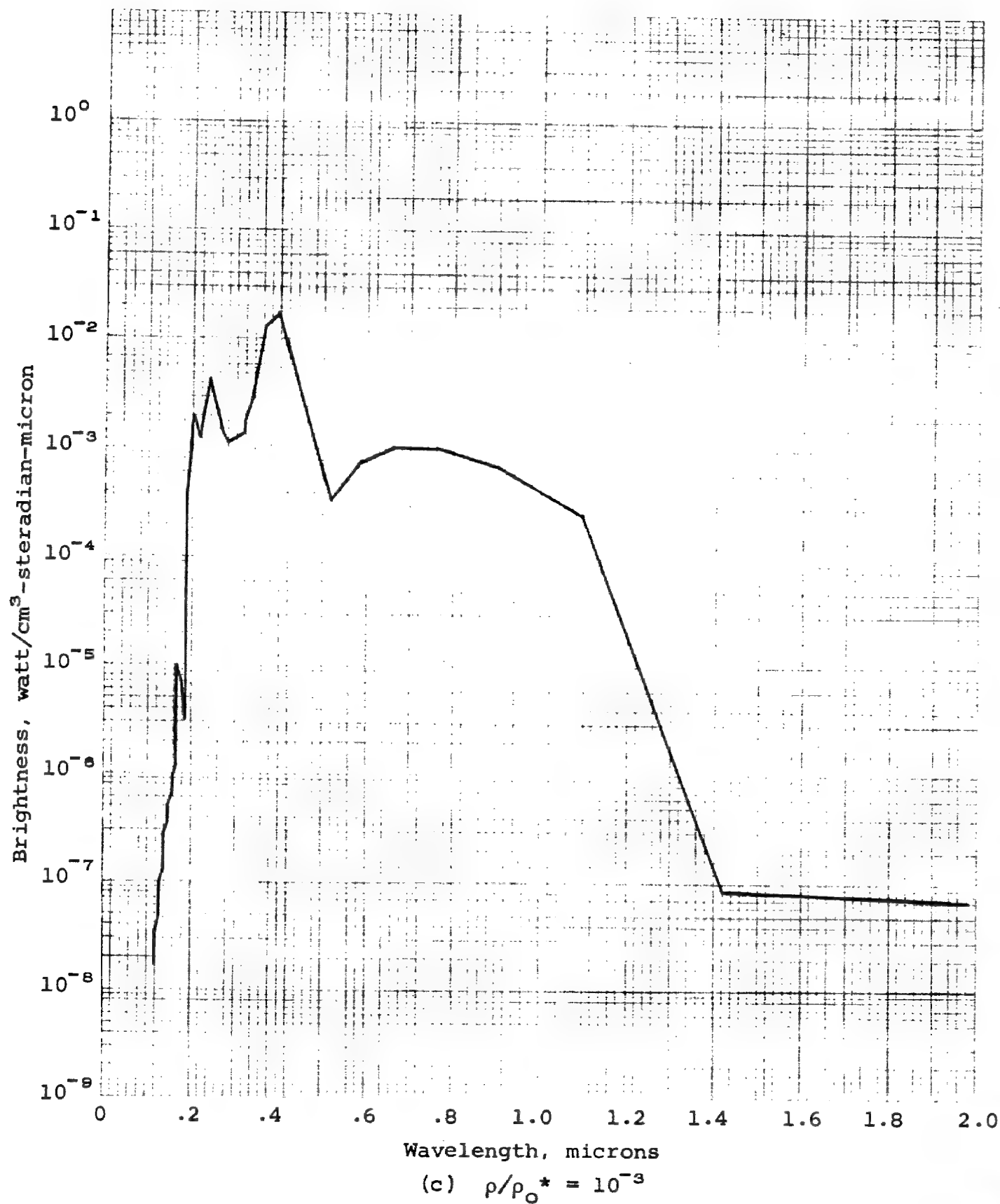


Figure VI-7.- Continued.

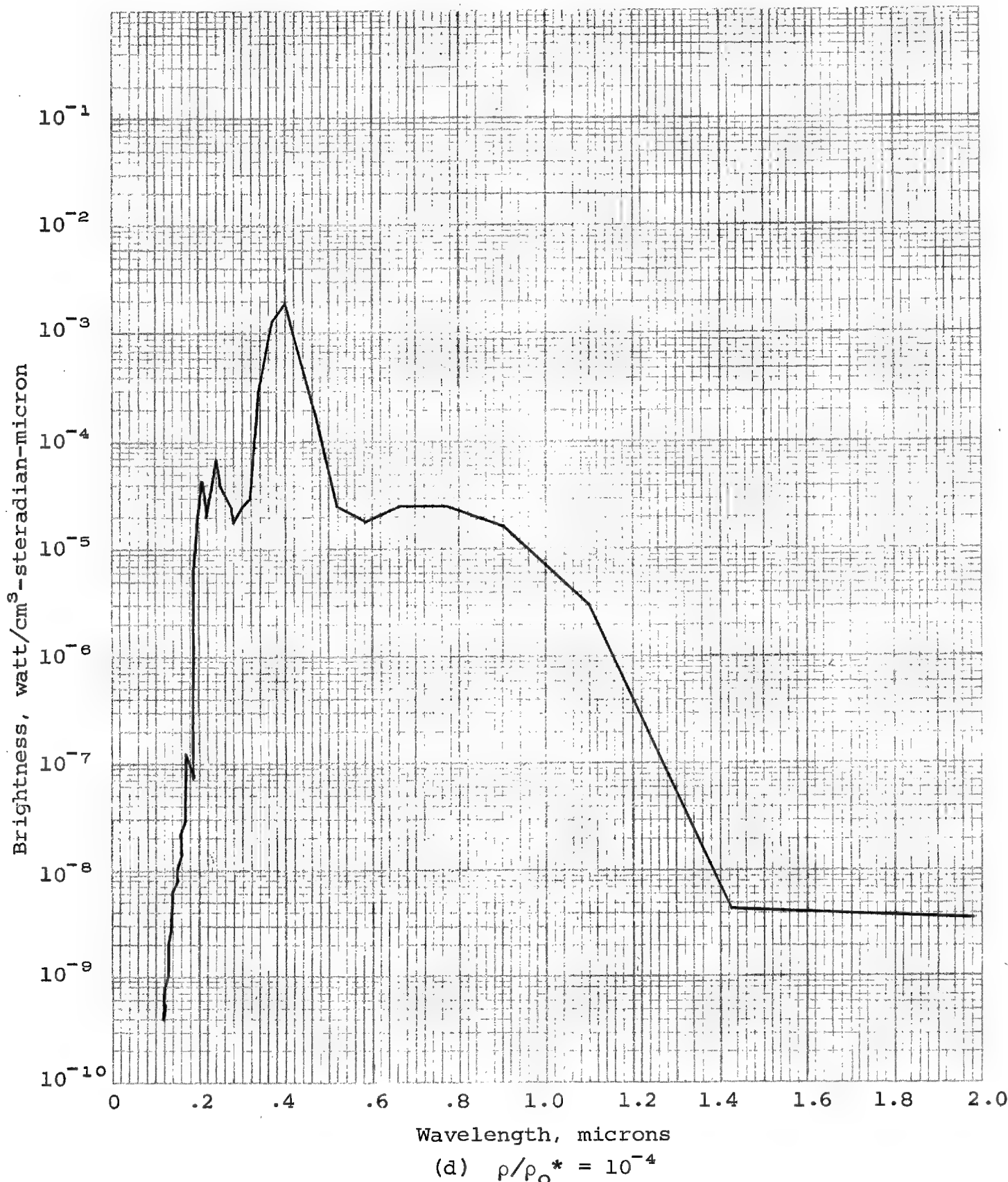


Figure VI-7.- Continued.

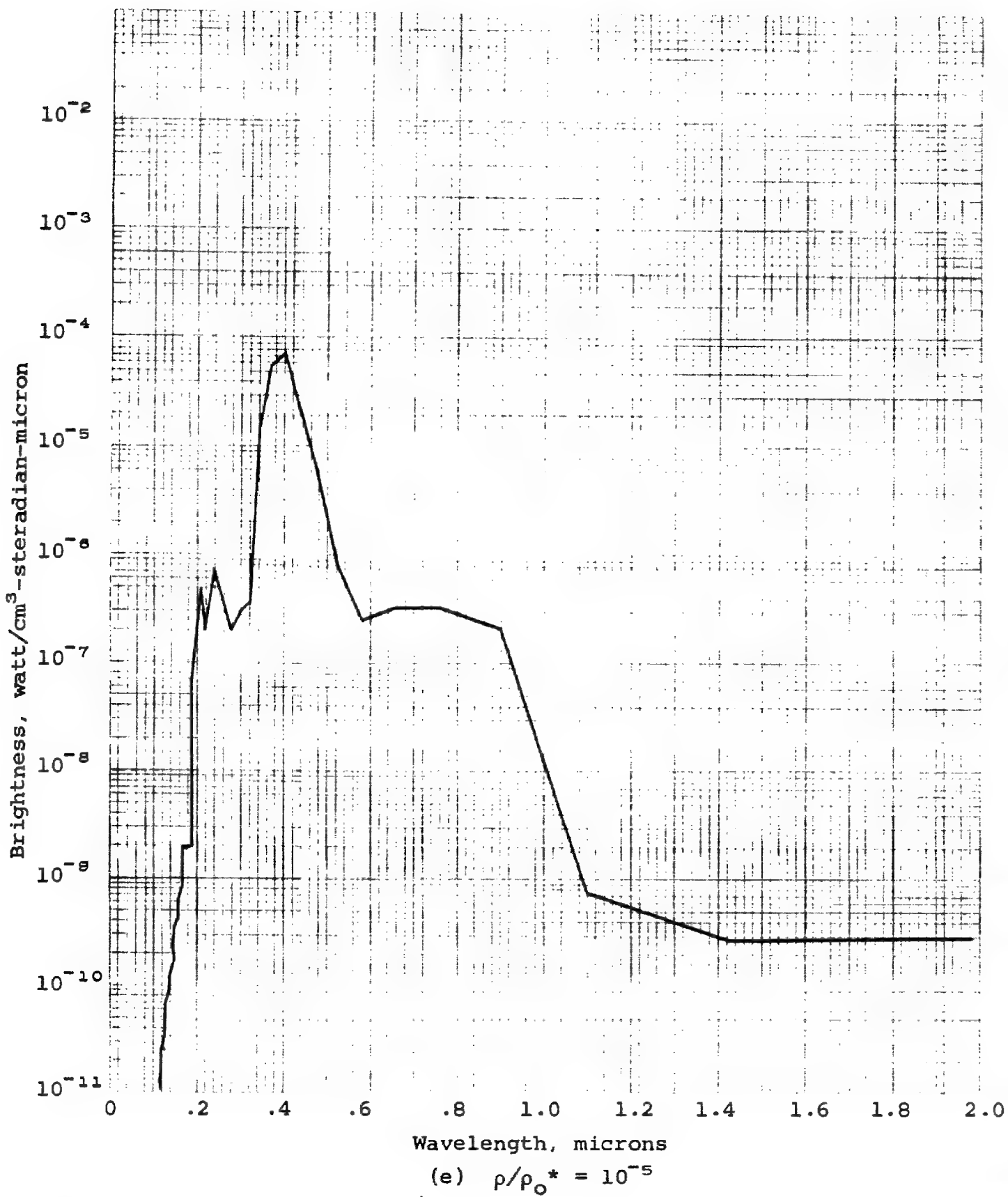


Figure VI-7.- Continued.

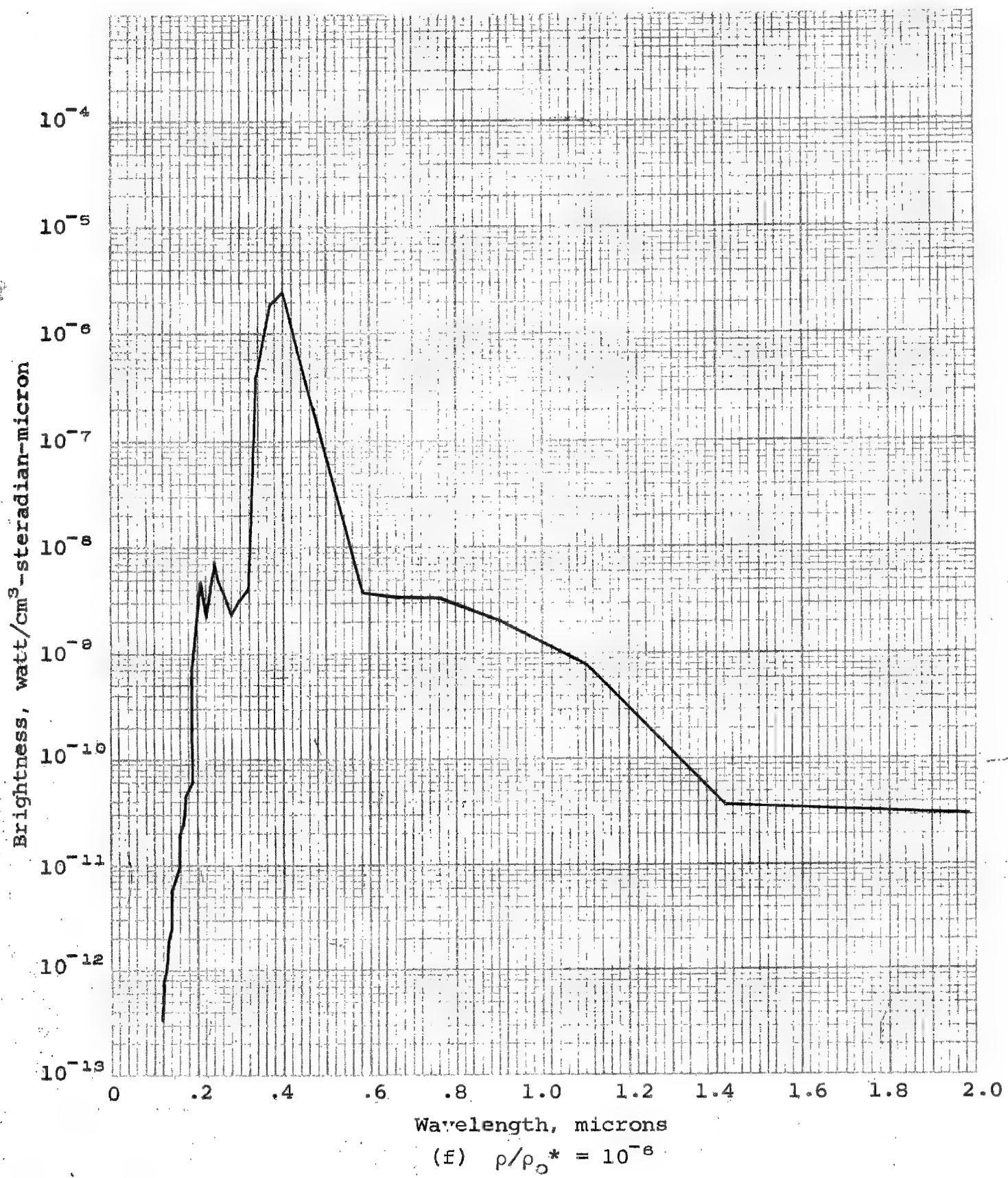


Figure VI-7.- Concluded.

Approved For Release 2000/04/12 : CIA-RDP67B00657R000300070001-0

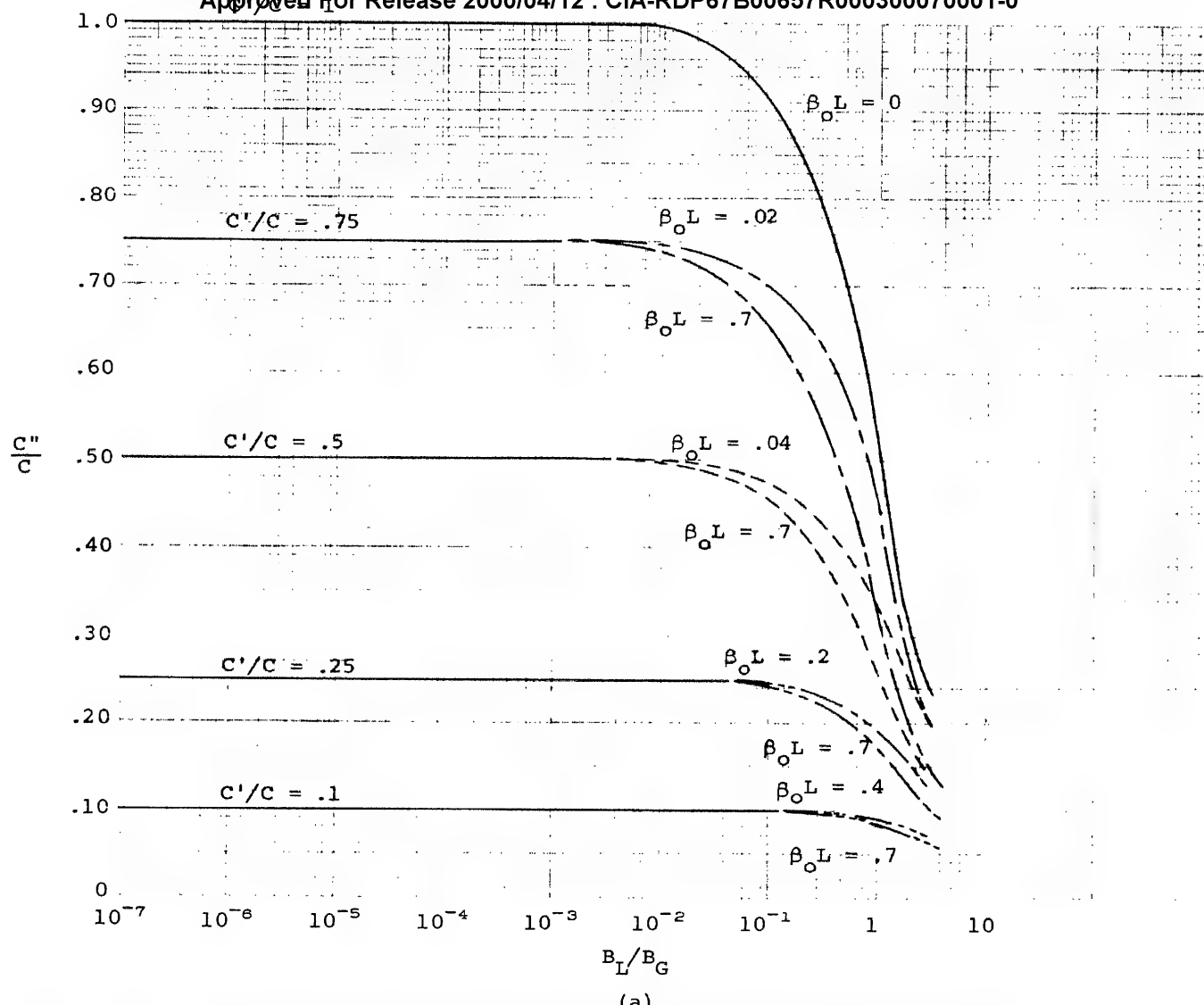


Figure VI-8. - Approved For Release 2000/04/12 : CIA-RDP67B00657R000300070001-0

Approved For Release 2000/04/12 : CIA-RDP67B00657R000300070001-0

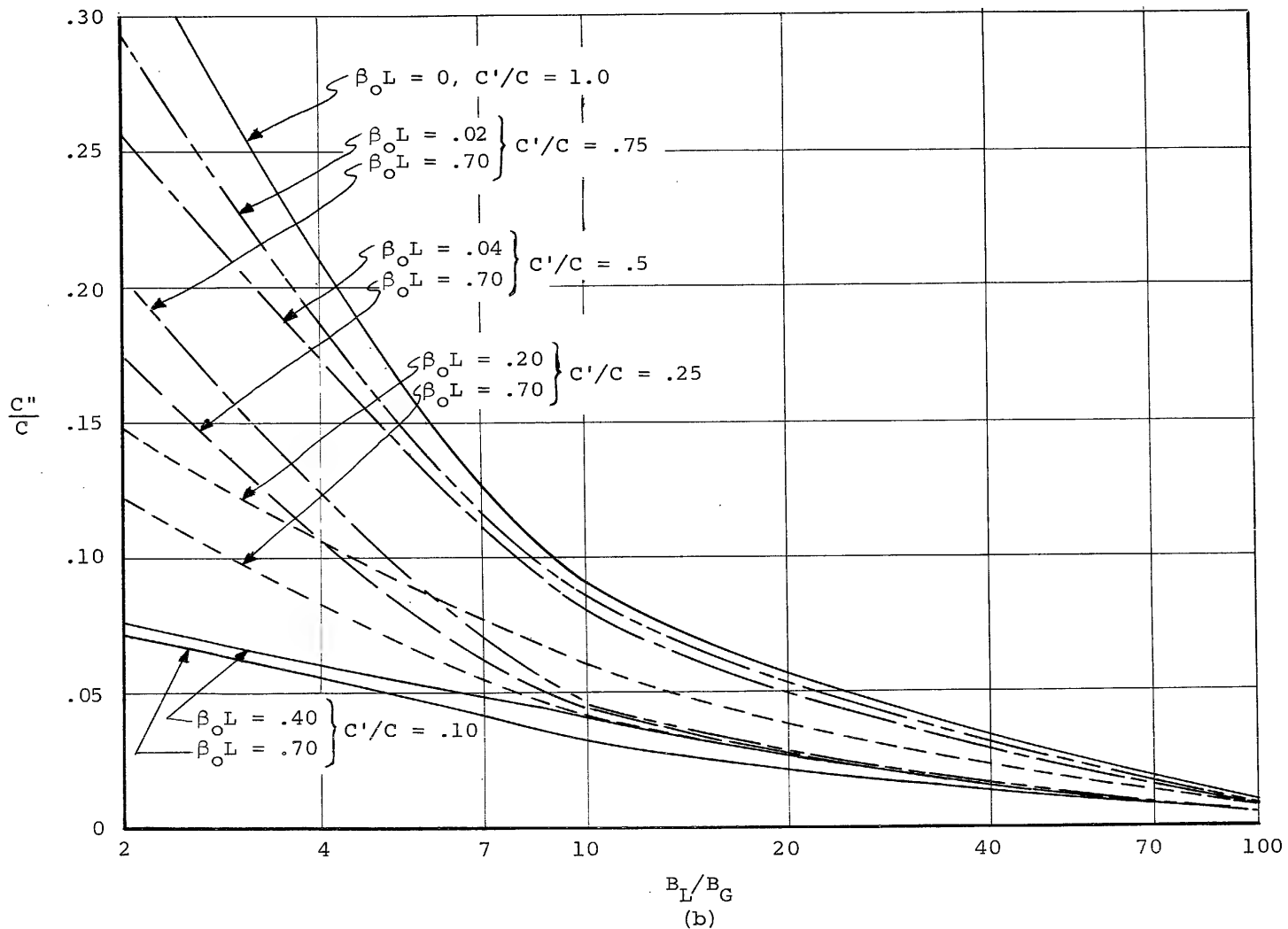


Figure VI-8.- Concluded.

Approved For Release 2000/04/12 : CIA-RDP67B00657R000300070001-0

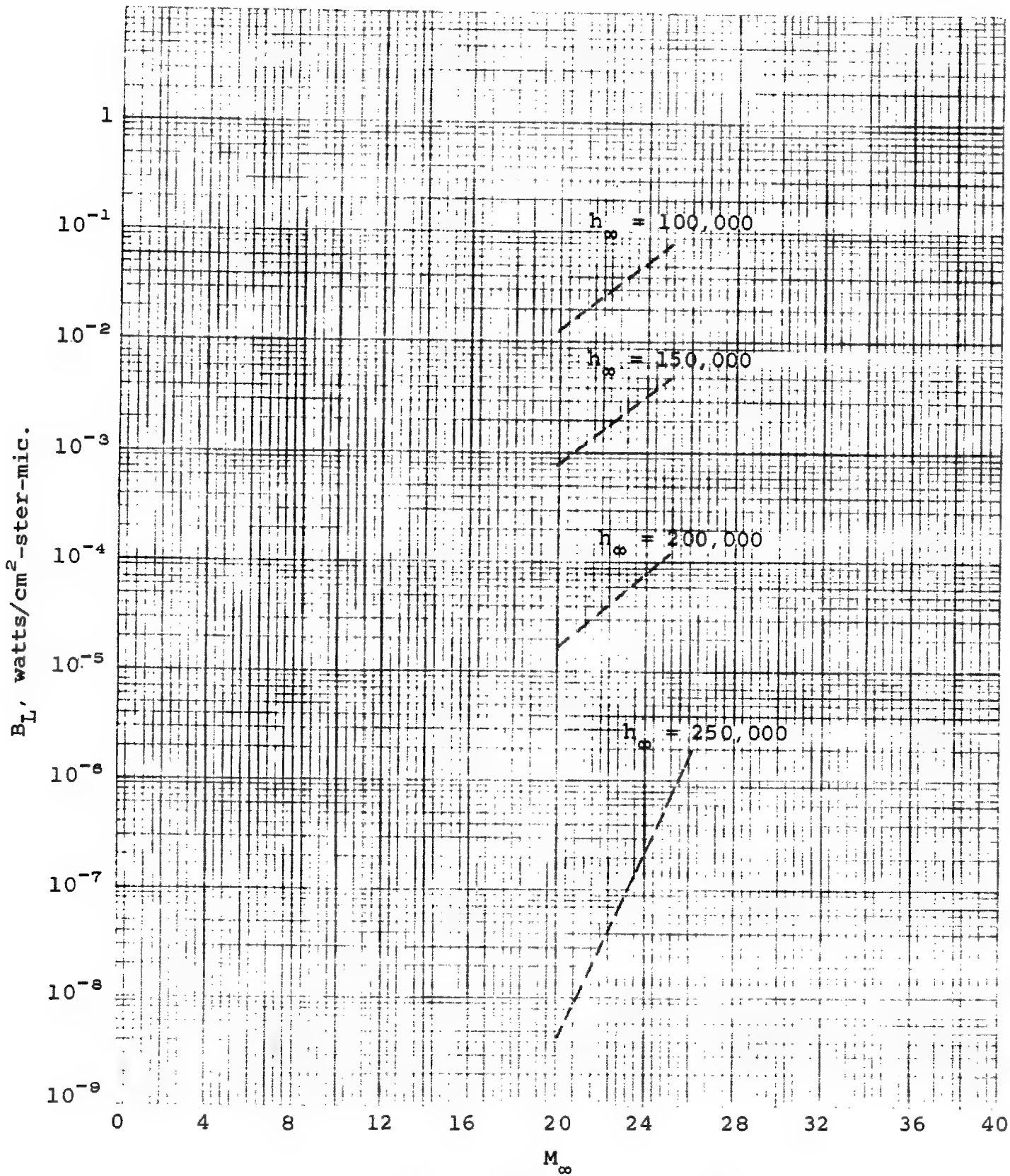
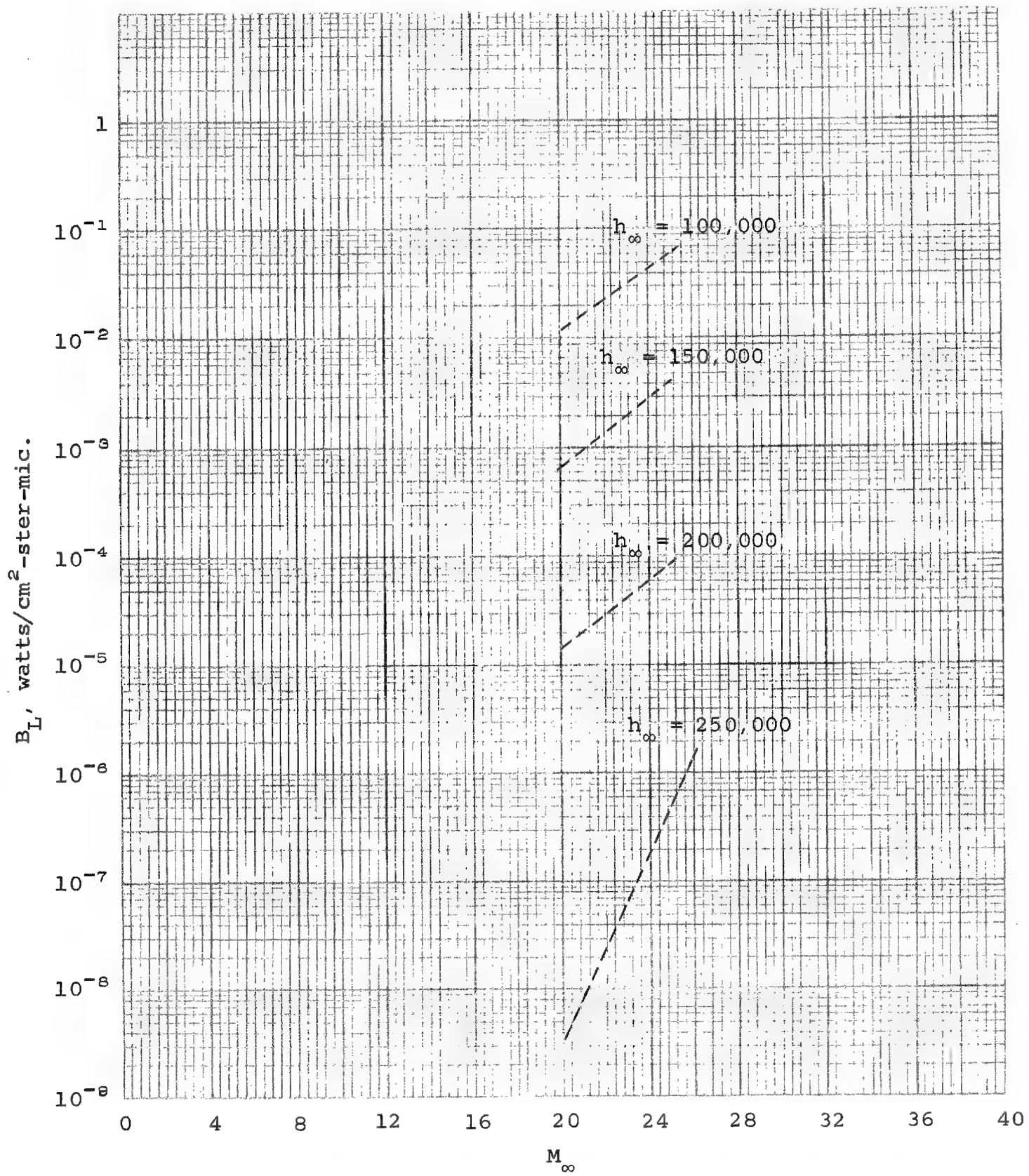
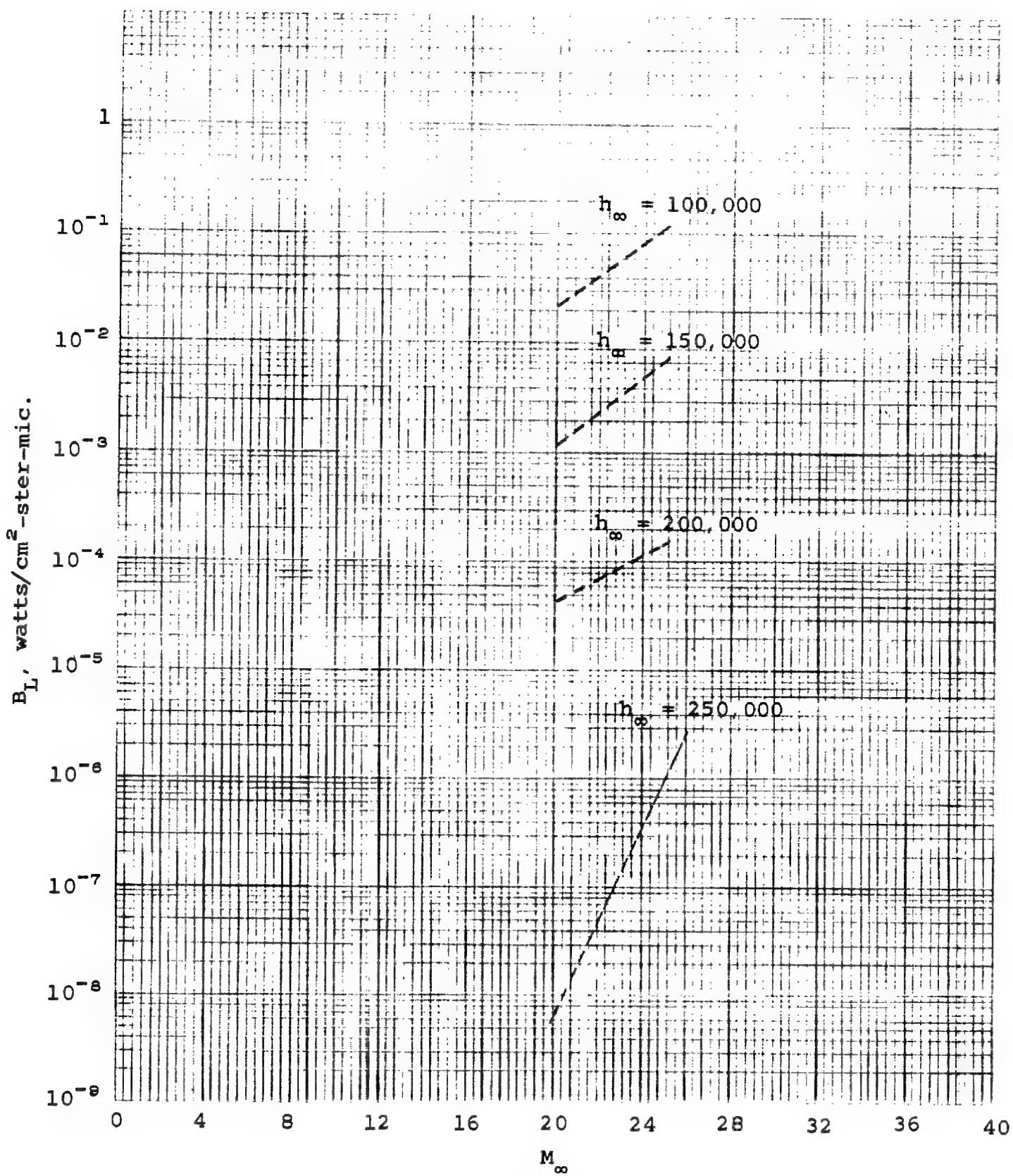
(a) $\mu = -45$ deg., $\lambda = 0.4$ mic.

Figure VI-9.- Brightness of the luminous layer surrounding a hemispherically blunted cone as seen at the camera objective ($\theta_c = 5^\circ$, $R = 1.0$ ft., $L_w = 6.0$ ft.)



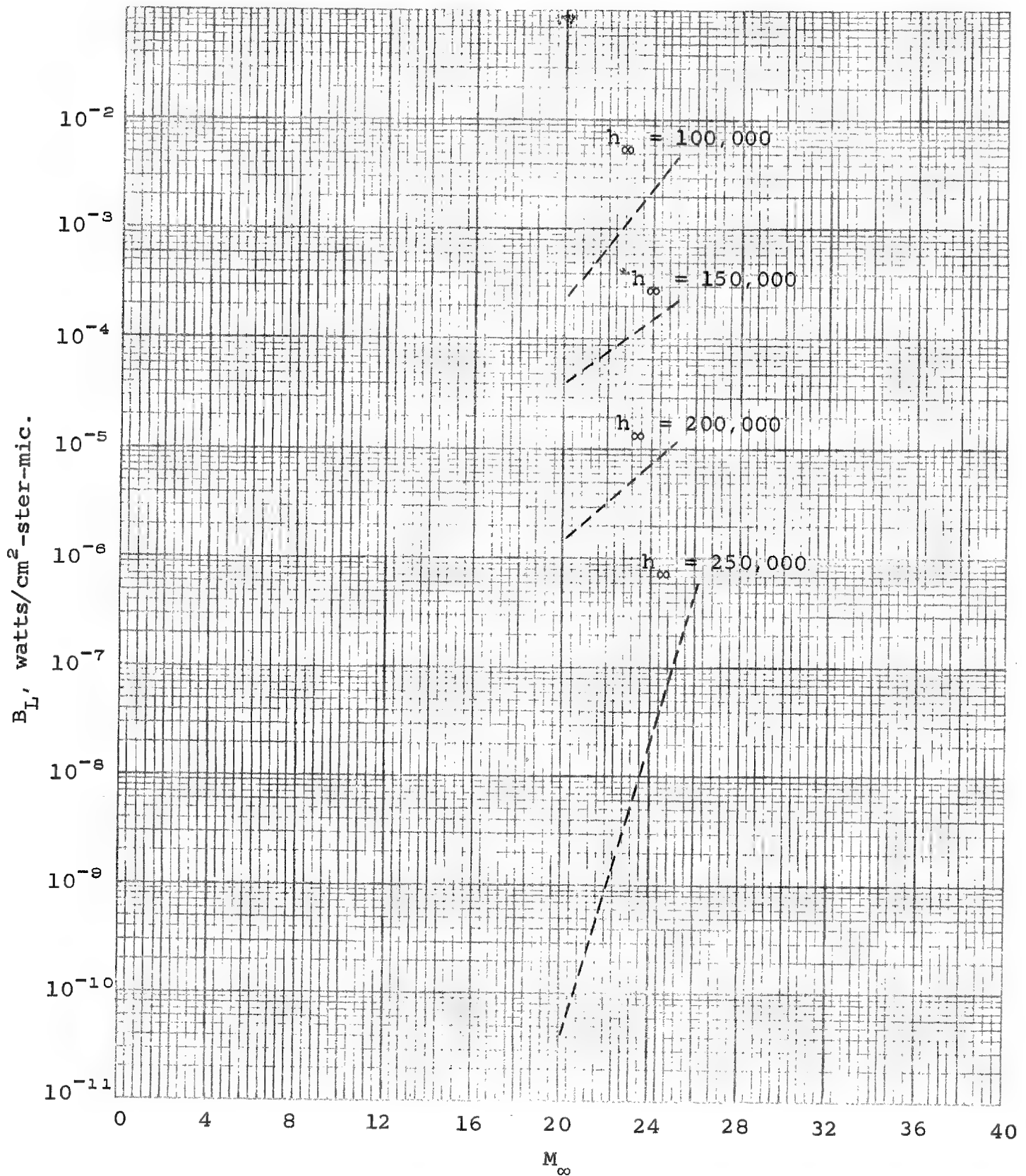
(b) $\mu = 0$ deg., $\lambda = 0.4$ mic.

Figure VI-9.- Continued.



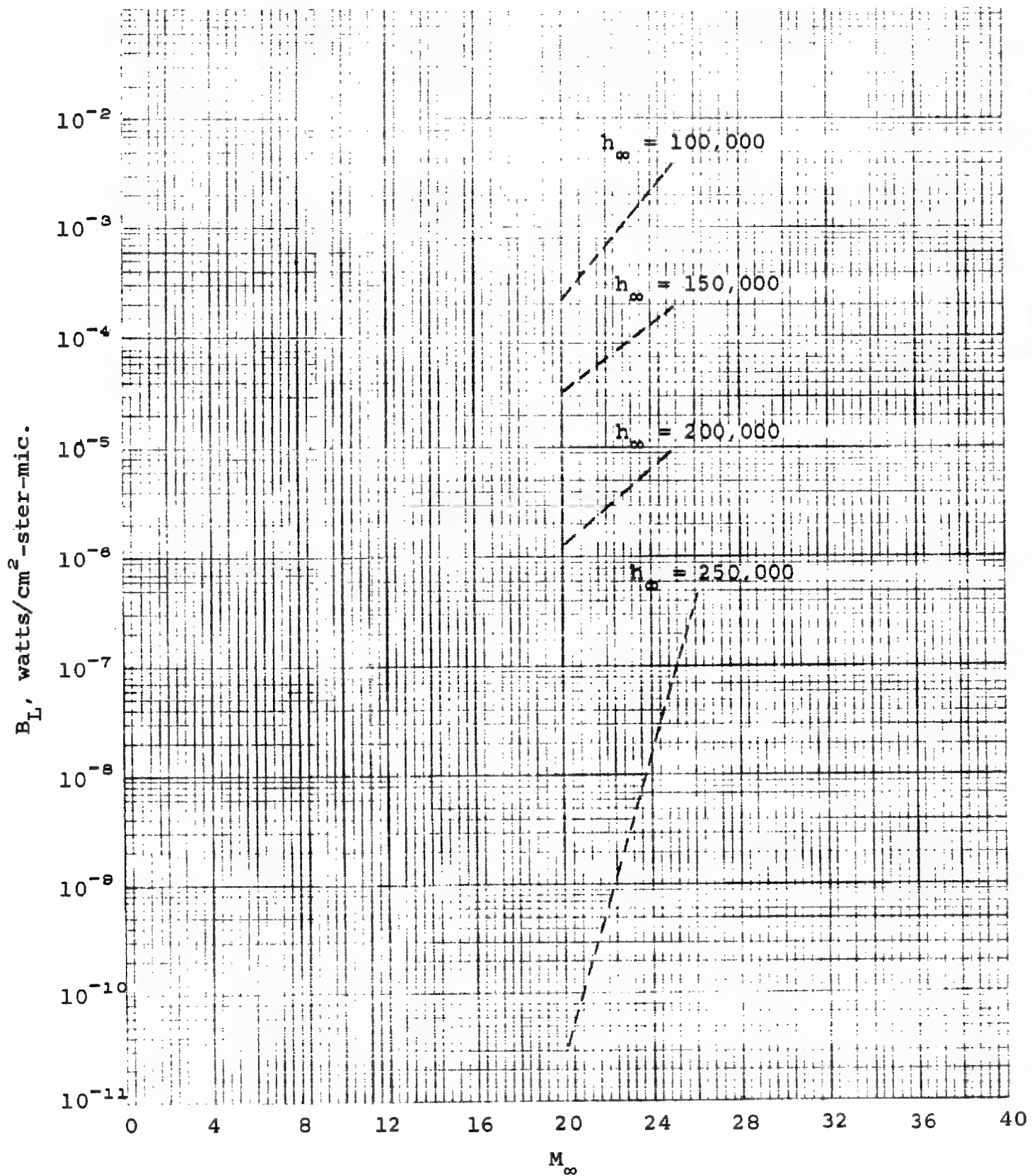
(c) $\mu = 45$ deg., $\lambda = 0.4$ mic.

Figure VI-9.- Continued.



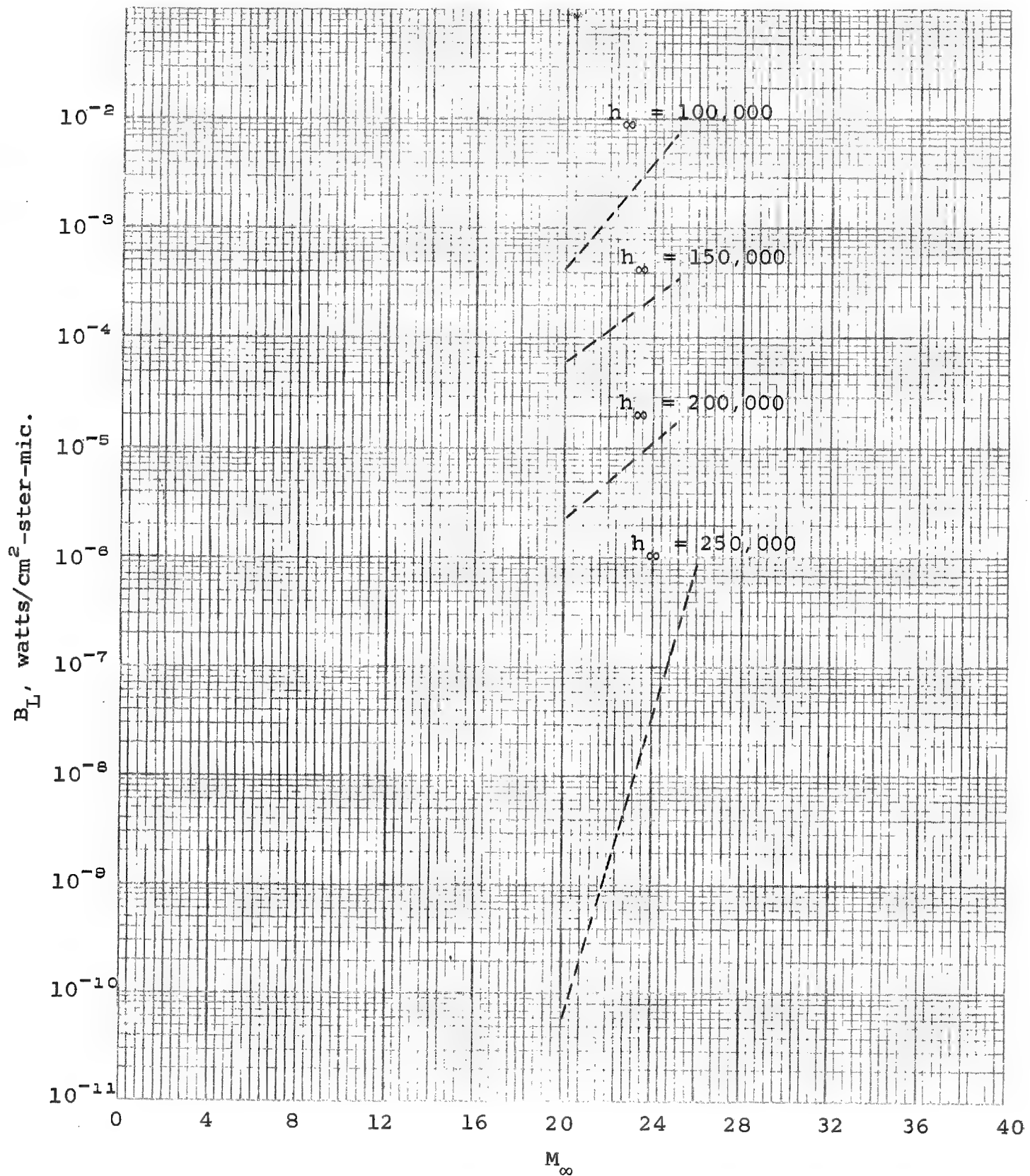
(d) $\mu = -45$ deg., $\lambda = 0.7$ mic.

Figure VI-9.- Continued.



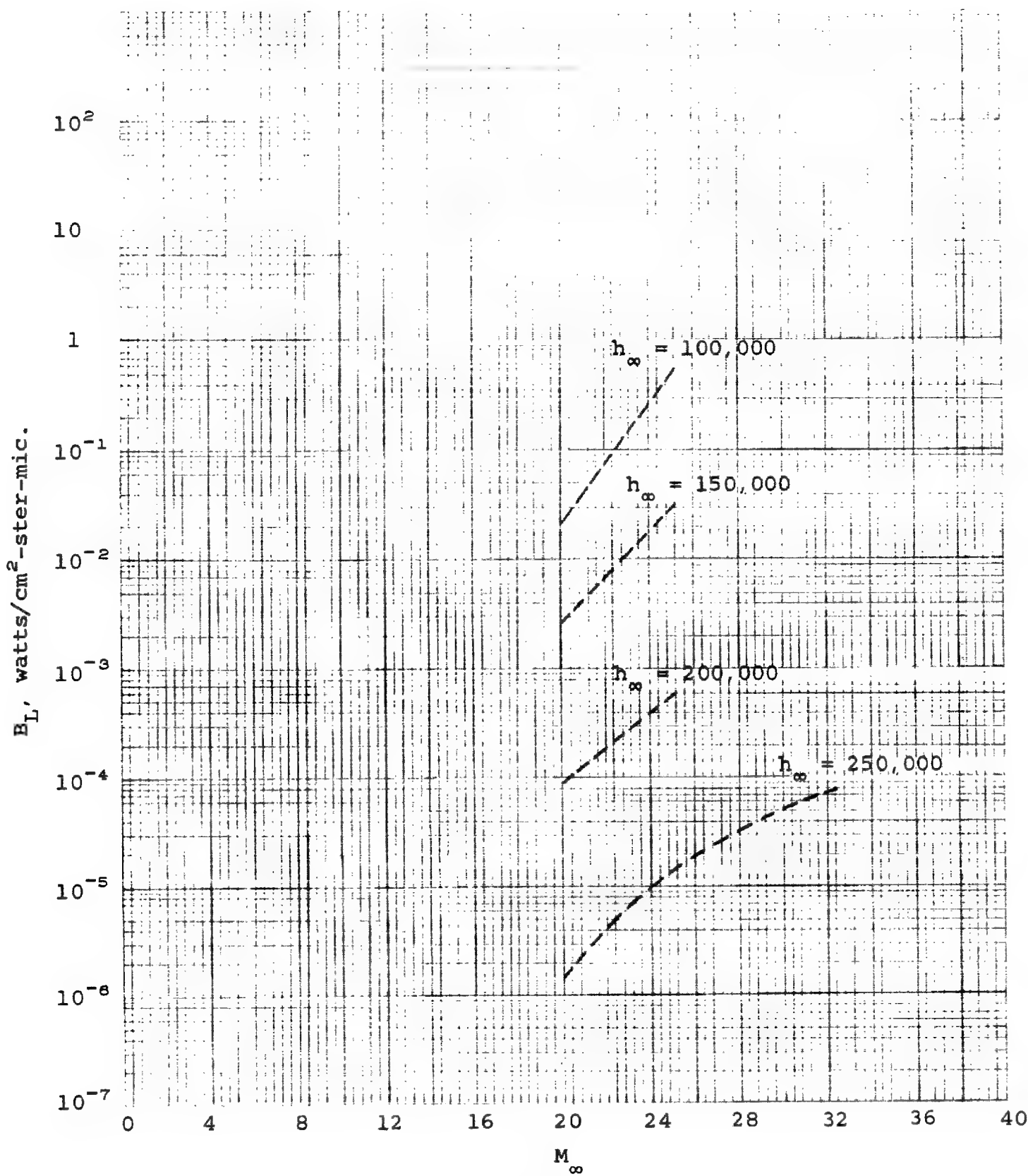
(e) $\mu = 0$ deg., $\lambda = 0.7$ mic.

Figure VI-9.- Continued.



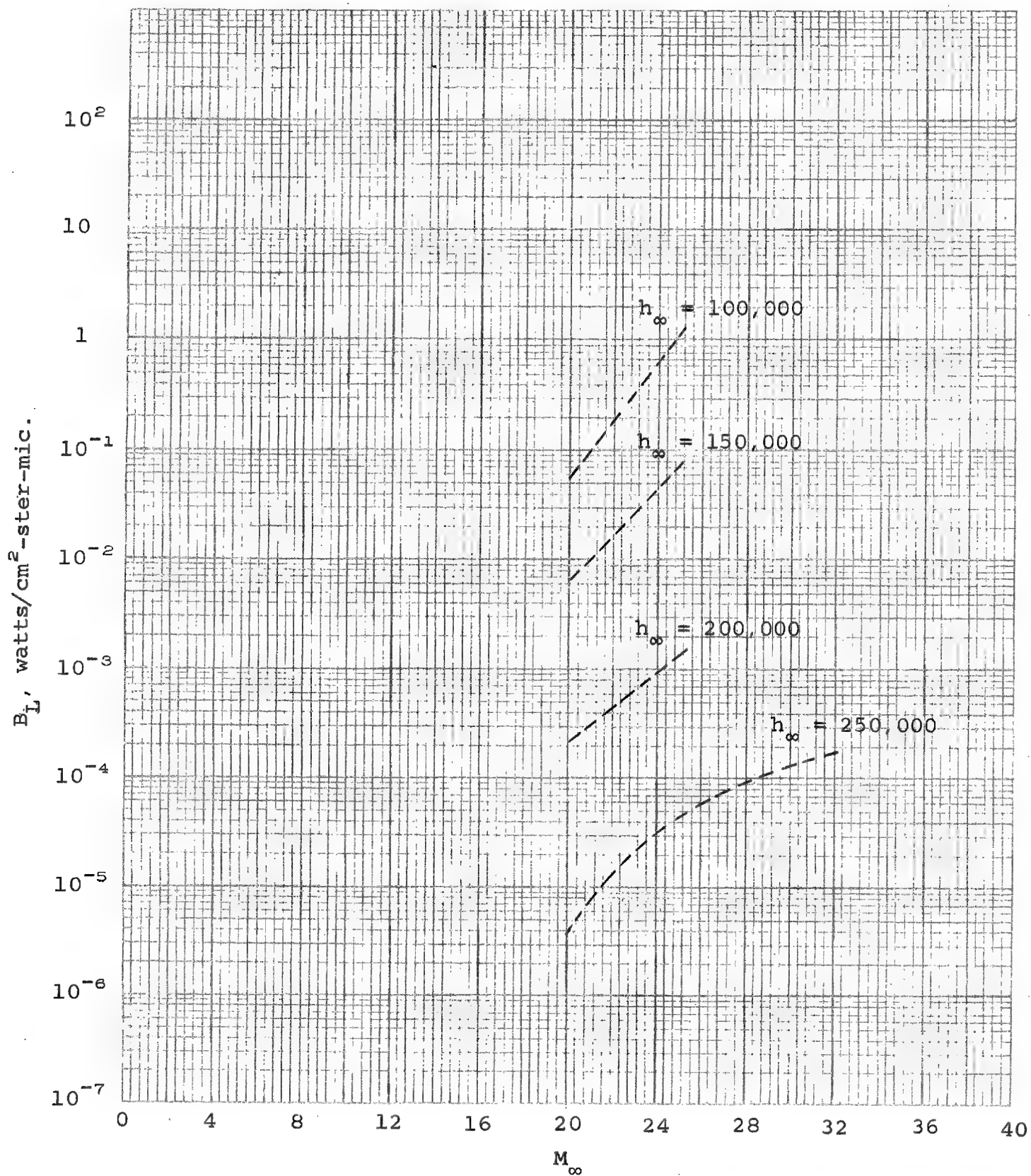
(f) $\mu = 45$ deg., $\lambda = 0.7$ mic.

Figure VI-9.- Concluded.



(e) $\mu = 0$ deg., $\lambda = 0.7$ mic.

Figure VI-10.- Continued.



(f) $\mu = 45$ deg., $\lambda = 0.7$ mic.

Figure VI-10.- Concluded.

PART VII: OPTICAL RESOLUTION

INTRODUCTION

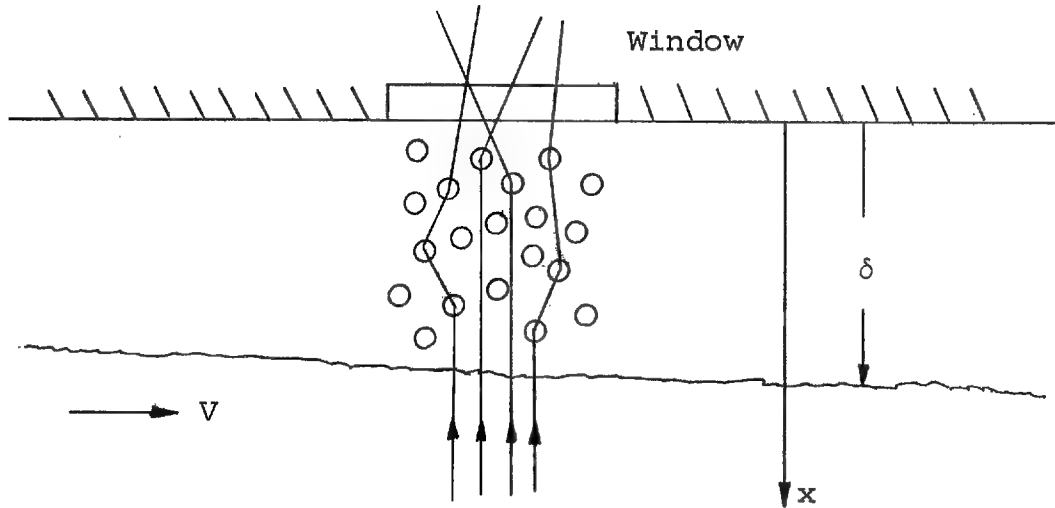
In Phase I certain wind-tunnel data were applied to the prediction of the loss of resolution caused by turbulent boundary layers in flight up to altitudes of 100,000 feet and Mach numbers up to 5. In Phase II of the present study the emphasis has been placed on the Mach number range above 5 and on altitudes above 100,000 feet. It turns out that for the example configurations studied herein the boundary layers are almost always laminar over the windows. With respect to Figure III-6, if we choose the transition Reynolds number to be 0.5×10^6 in accordance with Part III, then the flow is always laminar over the window for the blunt cone. With respect to Figure III-11, the flow over the window mounted in the blunt swept wing will probably be turbulent at about 100,000 feet altitude, but is laminar at slightly greater altitudes. Accordingly there will be no loss of resolution due to turbulence except possibly for the swept wing at the lowest altitude. As a result no turbulent boundary layer calculations were made in Phase II. Also no systematic calculation of resolution boundaries in the Mach number, altitude diagram were made.

In the course of the present investigation, several points in connection with the application of the wind-tunnel data of Reference 3 to hypersonic flight have arisen. The

correlation of these wind-tunnel data for the loss of resolution due to a turbulent boundary layer is semi-empirical. Furthermore, it is based on data taken in a supersonic wind tunnel where the air at the outer edge of the boundary layer is cooler than the outer surface of the window. In flight just the opposite case prevails; the air at the outer edge of the boundary layer in hypersonic flight is much hotter than the outer window surface temperature as shown, for instance, in Figures III-9 and III-10. As a result the boundary layer condition in flight is quite different than in the wind tunnel. A modification of the method of Liepmann, Reference 4, is now suggested which might help in the study of the foregoing problem. The modified method may also be useful in the study of real gas effects.

INVESTIGATION

In viewing through a turbulent boundary layer a parallel bundle of light rays is scattered due to density inhomogeneities in the boundary layer.



If the distribution and magnitude of these density inhomogeneities is known, it is possible to trace the "scattering" of a ray. They are, however, statistically random in space and time. The analysis of scattering by turbulent boundary layers is thus highly dependent on the fluid mechanics of turbulent flow. Liepmann in Reference 4 has made a rational analysis based on the mechanics of turbulent flow to indicate the controlling parameters in scattering.

The density in the boundary layer at any point is the sum of a time average ρ_0 plus a fluctuating component, ρ' .

$$\rho = \rho_0 + \rho' \quad (\text{VII-1})$$

Now a general relationship for the index of refraction in terms of density is

$$\begin{aligned} n - 1 &= K \rho \\ K &= 0.116 \text{ ft}^3/\text{slug} \\ \rho &= \text{slugs}/\text{ft}^3 \end{aligned} \quad (\text{VII-2})$$

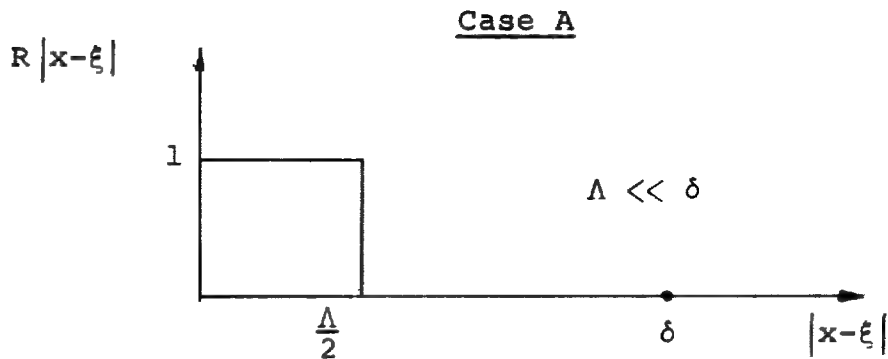
Let $n_o(x)$ be the index of refraction corresponding to the average value of ρ and let $v(x)$ be a small quantity denoting the fluctuation of n

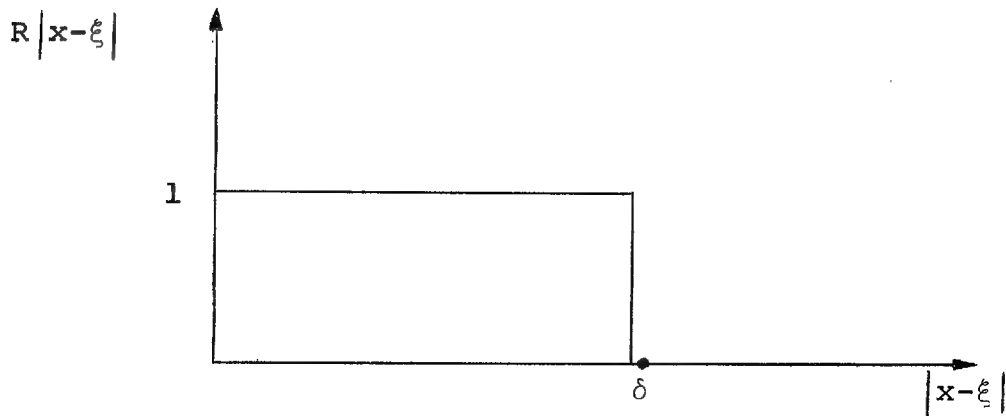
$$n = n_o(x) (1 + v) \quad (\text{VII-3})$$

Liepmann introduces the correlation function which is a measure of how fluctuations in v are correlated at two points as a function of the distance between them.

$$R |x-\xi| = \frac{\overline{(\frac{\partial v}{\partial y})_x} (\overline{\frac{\partial v}{\partial y}})_\xi}{\overline{(\frac{\partial v}{\partial y})^2}} \quad (\text{VII-4})$$

where the bars denote time averages. If $|x-\xi| = 0$, then $R = 1$. Liepmann then assumes two forms of the correlation



Case B

The mean square angular deviation of the light ray at the window is

$$\overline{\epsilon_w^2} = \frac{2}{n_o^2(\delta)} \int_0^\delta \int_0^\delta n_o(x) n_o(\xi) \overline{\left(\frac{\partial v}{\partial y}\right)^2} R |x-\xi| dx d\xi \quad (\text{VII-5})$$

In case A, we have

$$\begin{aligned} \overline{\epsilon_w^2} &= \frac{2}{n_o^2(\delta)} \int_0^\delta n_o(x) dx \int_{x-\Lambda/2}^{x+\Lambda/2} n_o(\xi) \overline{\left(\frac{\partial v}{\partial y}\right)^2} d\xi \\ \overline{\epsilon_w^2} &= \frac{2 \Lambda}{n_o^2(\delta)} \int_0^\delta n_o^2(x) \overline{\left(\frac{\partial v}{\partial y}\right)^2} dx \\ \overline{\epsilon_w^2} &= \frac{2 \Lambda \delta}{n_o^2(\delta)} \left[\frac{1}{\delta} \int_0^\delta n_o^2(x) \overline{\left(\frac{\partial v}{\partial y}\right)^2} dx \right] \end{aligned} \quad (\text{VII-6})$$

In case B, we have

$$\overline{\epsilon_w^2} = \frac{2 \delta^2}{n_o^2(\delta)} \left[\frac{1}{\delta^2} \int_0^\delta \int_0^\delta n_o(x) n_o(\xi) \overline{\left(\frac{\partial v}{\partial y} \right)^2} dx d\xi \right] \quad (\text{VII-7})$$

Case B refers to turbulent fluctuations which are perfectly correlated across the boundary layer, while case A refers to turbulence fluctuations whose scale Λ is small with respect to the boundary layer thickness. Since this latter case appears more plausible, let us confine our attentions to it henceforth.

In evaluating the integral of Equation (VII-6), we note that the index of refraction varies from 1.00028 for a density corresponding to normal condition at sea level to 1.0000 for zero density. We can then take it out of the integral and set it to unity. Thus

$$\overline{\epsilon_w^2} = 2 \Lambda \delta \left[\frac{1}{\delta} \int_0^\delta \overline{\left(\frac{\partial v}{\partial y} \right)^2} dx \right] \quad (\text{VII-8})$$

The next assumption is that the mean square fluctuation $\overline{v^2}$ divided by the length over which the fluctuation takes place squared (Λ^2) yields the mean square gradient

$$\overline{\left(\frac{\partial v}{\partial y} \right)^2} = \frac{\overline{v^2}}{\Lambda^2} \quad (\text{VII-9})$$

We can now relate the mean square fluctuation in index of refraction $\overline{n^2}$ to the density fluctuation.

$$n^2 = n_0^2 (1 + 2 \nu + \nu^2)$$

$$n^2 = 1 + 2 \kappa (\rho_0 + \rho') + \kappa^2 (\rho_0^2 + 2 \rho_0 \rho' + \rho'^2)$$

Taking time averages

$$\overline{n^2} = n_0^2 \left(\overline{\nu^2} + 1 \right)$$

$$\overline{n^2} = \kappa^2 \overline{(\rho')^2} + n_0^2$$

so that

$$\sqrt{\overline{\nu^2}} = \kappa \sqrt{\overline{(\rho')^2}} \quad (\text{VII-10})$$

We must now make an assumption to estimate the magnitude of the density fluctuations. In this respect we depart from Liepmann by making a local similarity argument. We assume that if ρ and u are the local values in the boundary layer and ρ_w and $u_w = 0$ are the values at the window, then

$$\frac{\sqrt{\overline{(\rho')^2}}}{|\rho - \rho_w|} = \frac{\sqrt{\overline{(u')^2}}}{u} \quad (\text{VII-11})$$

where u' is the axial velocity fluctuation. With this assumption,

$$\left(\frac{\partial \nu}{\partial y} \right)^2 = \frac{\kappa^2 \overline{(\rho')^2}}{\Lambda^2} = \frac{\kappa^2}{\Lambda^2} \frac{\overline{(u')^2}}{u^2} |\rho - \rho_w|^2 \quad (\text{VII-12})$$

Equation (VII-6) now becomes

$$\overline{\epsilon_w^2} = 2 \Lambda \delta \cdot \frac{K^2}{\Lambda^2} \left(\overline{\left(\frac{u'}{u} \right)^2} \right) \left(\frac{1}{\delta} \int_0^\delta \left| \rho - \rho_w \right|^2 dx \right) \quad (VII-13)$$

$$\overline{\epsilon_w^2} = \frac{2\delta}{\Lambda} (n_w - 1)^2 \left(\overline{\left(\frac{u'}{u} \right)^2} \right) \left(\frac{1}{\delta} \int_0^\delta \left| \frac{\rho - \rho_w}{\rho_w} \right|^2 dx \right)$$

This result is based on the further assumption that

the turbulence $\left(\overline{\left(u'/u \right)^2} \right)^{1/2}$ is sensibly constant across the boundary layer. We see that the mean angular scattering $\left(\overline{\epsilon_w^2} \right)^{1/2}$ of a light ray, which is a measure of the loss of resolution, is thus

1. Proportional to the percent turbulence
2. Inversely proportional to $\sqrt{\Lambda}$
3. Proportional to $\sqrt{\delta}$ and $(n_w - 1)$

Another important parameter is the dependence of the integral on the density distribution through the boundary layer.

This distribution depends on Mach number at the edge of the boundary layer, temperature at the edge of the boundary layer, and window temperature. In fact a method for obtaining the density distribution is given in Part IV for a 1/7-power turbulent velocity profile and a real gas.

DISCUSSION AND CONCLUSIONS

The foregoing derivation is meant as an approximate method for investigating the effects of boundary layer scattering when boundary layer density profiles differ from those under which experimental measurements have been made. At hypersonic flight speeds such density profiles are quite different from those obtained in supersonic wind tunnels.

The foregoing analysis is quasi-rational, containing as it does several assumptions which cannot be justified because of the lack of understanding of the mechanics of turbulent flow. It is, however, sufficiently rational to contain the elements of its own verification or modification as the mechanics of turbulent flow becomes better understood. Calculations based on the method might lead to insight into the question of whether resolution loss is increased by going from the wind tunnel to flight. It may be useful in the study of real gas effects.

While we have concluded that turbulent boundary layers for the present configurations are not important above a 100,000-foot altitude, it would be a mistake to assume that this result is general. The blunt swept wing in this study is always at 20 degrees angle of attack and the window is only 6 feet behind the nose. For reentry gliders at high angles of attack with windows mounted far behind the nose, turbulent flow can be important at much higher altitudes

than 100,000 feet. Ablation may also cause the boundary layer to be turbulent.

RECOMMENDATIONS

While the foregoing analysis is quasi-rational, it might form a successful basis for the correlation of the data of Reference 3. In fact it is recommended that the data of Reference 3 be correlated if possible on the basis of the present theory or a modification thereof.

It is recommended that Liepmann's analysis be extended to infrared and microwave radiations to obtain a knowledge of how turbulence influences these radiations.

There is a definite need for flight test information on the loss of resolution due to turbulent boundary layers at supersonic speeds. Such tests are hard to carry out and must be carefully designed and executed if they are to produce meaningful results. Such tests should be designed to produce data comparable with the wind-tunnel data of Stine and Winovich.

REFERENCES

1. Nielsen, Jack N., et al: Effects of Supersonic and Hypersonic Aircraft Speed Upon Aerial Photography. Second Interim Report, Phase II. Vidya Report No. 28, Oct. 28, 1960.
2. Nielsen, Jack N., et al: Effects of Supersonic and Hypersonic Aircraft Speed on Aerial Photography. Final Technical Report, Phase I. Vidya Report No. 17, Apr. 28, 1960.
3. Stine, H. A. and Winovich, W.: Light Diffusion Through High-Speed Turbulent Boundary Layers. NACA RM A56 B21, May, 1956.
4. Liepmann, H. W.: Deflection and Diffusion of a Light Ray Passing Through a Turbulent Boundary Layer. Report No. SM-14397. Douglas Aircraft Company, May 1952.

PART VIII: REFRACTION AND METRIC DISTORTION

INTRODUCTION

The purpose of this part of the present report is to extend the refraction and metric distortion studies reported in the final report issued under Phase I of this contract (Ref. 1) to higher Mach numbers and altitudes. In the Phase I study, the investigation was limited to Mach numbers of 5.0 or less and altitudes not exceeding 100,000 feet. The previous study used a sharp cone as a typical configuration. Since this is not a representative shape for a configuration which will operate at Mach numbers above 5.0, the calculations of this part of the present report will be made for a cone with a hemispherically blunted nose and for a highly swept blunt wing with a cylindrical leading edge. Both of these configurations and the flight conditions for which the calculations will be made are described in detail in Part II.

The following sources of refractions, and the associated metric distortions, will be considered:

1. Window curvature caused by aerodynamic heating
2. Boundary layer on the vehicle surface
3. Flow field between the boundary layer and the bow shock wave
4. Bow shock wave
5. Atmosphere

These are the same sources as were considered in Phase I (Ref. 1). Consequently, the equations of this reference for determining the refractions and the resulting ground displacements could be used in the present study if the correct flow field surrounding the vehicle was used. The flow-field determination of the Phase I study is not suitable for the present study for two reasons. First, the method presented there is for a sharp cone, and second, the method is for an ideal gas. At the Mach numbers considered in the present study, the temperatures in the flow field surrounding the vehicle become high enough so as to cause real-gas effects, such as dissociation and ionization, to become important. These real-gas properties may affect the refractions in at least two ways:

1. By changing the specific refractivity of the gas (the constant relating the index of refraction to the density)
2. By causing a considerable change in the density variation in the near flow field over what would be found for an ideal gas

It is, therefore, the purpose of this part of the report to present the necessary equations for performing systematic refraction calculations for a specified vehicle and its known flow field. Specific calculations will be presented for the vehicles and flight conditions outlined in Part II of this study. The flow fields calculated and presented in Parts III

and IV will be used as will the camera window temperatures found by the method of Part V.

The effect of temperature on the specific refractivity of air will also be investigated and the results presented in Appendix VIIIA.

SYMBOLS

h	altitude, feet
K	specific refractivity, feet ³ /slug
M	Mach number
n	index of refraction of gas
n_o	index of refraction of fused quartz, taken as 1.5
p	pressure, lb/ft ²
T	temperature, °R unless indicated otherwise
T_i	temperature of inner surface of window, °R
α	angle of attack, deg.
$\bar{\alpha}$	coefficient of thermal expansion, taken as 0.278×10^{-6} per °R
β	atmospheric constant defined by Equation (VIII-13), ft ⁻¹
Δx	ground displacement, positive rearward, ft.
ϵ	shock wave slope, deg.
θ_c	blunt cone, cone angle, deg.
μ	nadir angle, angle between plumb line from the origin of ray and light ray direction, deg.
ρ	density, slugs/ft ³
ϕ	angle of incidence, deg.

Subscripts

A	due to atmosphere
BL	due to or at boundary layer
FF	due to flow field between boundary layer and bow shock wave
G	at ground

SW due to or at shock wave
T due to temperature induced window curvature
W at window
 δ at edge of boundary layer
o at outer surface of window
 ∞ free stream or flight conditions

INVESTIGATION

In the present investigation, the magnitude and direction of the ground displacements caused by the following sources will be determined:

1. Window curvature caused by aerodynamic heating
2. Boundary layer over the camera window
3. Flow field between the boundary layer and the bow shock wave
4. Bow shock wave
5. Atmosphere

Since the displacements caused by the near flow field (i.e. 2, 3, and 4 above) are very small at the altitudes under consideration (the results of the calculations will show this to be true), equations will be presented for determining the displacements only in the vertical plane of symmetry.

Ground Displacements Caused by

Camera Window Curvature

The analysis presented in Part VI of Reference 1 can again be used to determine the ground displacements caused by camera window curvature brought about by aerodynamic heating. Let us again assume that the camera window is a simply supported plate, and that a temperature difference across the glass causes the window to distort into a segment of a sphere. For an arbitrary nadir angle the expression

for the ground displacement taken from Reference 1 is

$$\Delta x_T = \frac{\bar{\alpha} h_\infty}{\cos^2 \mu} (T_o - T_i) \left(\frac{\sin \phi_W}{\sqrt{n_o^2 - \sin^2 \phi_W}} - \tan \phi_W \right) \quad (\text{VIII-1})$$

The angle ϕ_W is the angle of incidence that the light ray makes with the window surface. Let us now look at Figure VIII-1. For the two configurations being considered here this angle is, on the blunt cone

$$\phi_W = \mu + \theta_c \quad (\text{VIII-2})$$

and on the swept wing

$$\phi_W = \mu + \alpha \quad (\text{VIII-3})$$

Substitution of these two expressions into Equation (VIII-1) results in the following expressions for the ground displacements caused by camera window curvature due to a temperature difference across the glass. For the blunt cone

$$\Delta x_T = \frac{\bar{\alpha} h_\infty}{\cos^2 \mu} (T_o - T_i) \left[\frac{\sin (\mu + \theta_c)}{\sqrt{n_o^2 - \sin^2 (\mu + \theta_c)}} - \tan (\mu + \theta_c) \right] \quad (\text{VIII-4})$$

and for the swept wing

$$\Delta x_T = \frac{\bar{\alpha} h_\infty}{\cos^2 \mu} (T_o - T_i) \left[\frac{\sin (\alpha + \mu)}{\sqrt{n_o^2 - \sin^2 (\alpha + \mu)}} - \tan (\alpha + \mu) \right] \quad (\text{VIII-5})$$

For the present calculations fused quartz will be taken as the window material. Therefore,

$$\bar{\alpha} = .278 \times 10^{-6} \text{ } 1/\text{ } ^\circ\text{R}$$

$$n_o = 1.5$$

The temperature differences across the glass for the two configurations and the flight conditions of Part II have been calculated in Part V.

Ground Displacement Caused by
Refraction by the Boundary Layer

In Reference 1 the general expressions were derived for the refractions of a light ray passing through the boundary layer in an arbitrary direction. For the special case where the ray is in the vertical plane of symmetry of the vehicle (azimuth angle of 0° or 180°), the expressions reduce to the following:

$$\Delta x_{BL} = - K \frac{h_\infty}{\cos^2 \mu} (\tan \phi_{BL}) (\rho_\delta - \rho_o) \quad (\text{VIII-6})$$

The boundary layer lies on the window surface (see Fig. VIII-1) so that ϕ_{BL} is equal to ϕ_W . Therefore, Equations (VIII-2) and (VIII-3) specify the incident angle that the light ray traveling at an arbitrary nadir angle makes with the boundary layer. The boundary layer is treated as a surface with a density change across it since it is quite thin and the two edges are nearly parallel. Thus, the two densities needed

are the density at the outer edge of the boundary layer, ρ_δ , and that at the outer surface of the camera window, ρ_o . The first of these has been calculated in Part III for the configurations and flight conditions of Part II. The second of these densities can be found with the aid of either Reference 2 or 3 since we know the pressure at the edge of the boundary layer, p_δ , (the pressure is assumed constant through the boundary layer) and the temperature at the outer surface of the camera window, T_o . The pressure is calculated in Part III and the temperature in Part V.

One other quantity remains to be specified. This is the value of the specific refractivity of the gas in the boundary layer. At high temperatures air dissociates and ionizes so that the chemical composition changes. The specific refractivity depends on the individual values for the various species of molecules and atoms which make up the gas, so as the gas dissociates it can change from the low temperature value for air ($K = 0.116$). In Appendix VIIIA the specific refractivity has been calculated as a function of temperature. The results are shown in Figure VIII-2. For the flight conditions of the present study, the temperature and density profiles through the boundary layer have been calculated in Part IV. Using these results in conjunction with the results of Part III and Figure VIII-2, it can be seen that for these flight conditions the low temperature value of the specific refractivity can be used.

The final expressions for the ground displacements caused by the boundary layer refraction are, for the blunt cone

$$\Delta x_{BL} = -0.116 \frac{h_\infty}{\cos^2 \mu} \left[\tan (\mu + \theta_c) \right] (\rho_\delta - \rho_\infty) \quad (\text{VIII-7})$$

and for the swept wing

$$\Delta x_{BL} = -0.116 \frac{h_\infty}{\cos^2 \mu} \left[\tan (\mu + \alpha) \right] (\rho_\delta - \rho_\infty) \quad (\text{VIII-8})$$

Ground Displacement Caused by
Refraction by the Flow Field Between the Boundary Layer
and the Bow Shock Wave

Reference 1 determined the ground displacement caused by the flow field between the boundary layer and the bow shock wave by integrating along the path of the ray from the edge of the boundary layer to just inside the shock wave. This could be done in this case since the flow field surrounding a sharp cone at low Mach numbers (where real-gas effects are not important) could be determined quite precisely. As was discussed in Part III of the present report, the precise determination of the flow fields surrounding vehicles of the type of the present study is impossible at the present state of the art. Density and temperature distributions were specified in Part III, however, the slopes of the lines of constant density were not. Hence, a method such as was used

in Reference 1 can not be employed here. Fortunately, it does not appear that a method which is so exact is needed. It can be seen from the calculations of the shock wave slope in Part III that they do not differ by more than 15° from the vehicle surface slope. An average value of the vehicle surface slope and the shock wave slope will probably give accurate enough results. In Reference 1, where Mach numbers as low as 1.2 were considered, these slopes could differ by 45 or 50 degrees. By using the densities just behind the shock wave, ρ_{SW} , and at the outer edge of the boundary layer, ρ_δ , the following expressions can be used to determine the ground displacements caused by the flow field between the shock wave and the boundary layer. On the blunt cone

$$\Delta x_{FF} = -0.116 \frac{h_\infty}{\cos^2 \mu} \left[\tan \left(\mu + \frac{\theta_c + \epsilon}{2} \right) \right] (\rho_{SW} - \rho_\delta) \quad (\text{VIII-9})$$

and on the wing

$$\Delta x_{FF} = -0.116 \frac{h_\infty}{\cos^2 \mu} \left[\tan \left(\mu + \frac{\alpha + \epsilon}{2} \right) \right] (\rho_{SW} - \rho_\delta) \quad (\text{VIII-10})$$

The quantities, ρ_{SW} , ρ_δ , and ϵ , have been calculated and are presented in Part III.

Ground Displacement Caused by
Refraction by the Shock Wave

The shock wave is treated as a surface with a density change across it, and the incident angle is the sum of the nadir angle and the shock wave slope. Hence for both configurations the ground displacement is given by

$$\Delta x_{SW} = -0.116 \frac{h_{\infty}}{\cos^2 \mu} \left[\tan (\mu + \epsilon) \right] (\rho_{\infty} - \rho_{SW}) \quad (\text{VIII-11})$$

Ground Displacement Caused by
Refraction by the Atmosphere

Since the density of the atmosphere decreases as the altitude increases, it may be expected that an altitude will be reached above which there is no measurable increase in the angular refraction of a light ray caused by the atmosphere or in the resulting ground displacement. The angular refraction is proportional to the density change, so that this altitude will be the point at which the density has become negligible compared to the density at the ground.

That is,

$$\rho_G - \rho_{\infty} \approx \rho_G \quad (\text{VIII-12})$$

Calculations have been performed by two different methods in order to determine this altitude. The first method is

that presented in Part II of Reference 1, where the density is assumed to vary exponentially with altitude. That is,

$$\rho_{\infty} = \rho_G e^{-\beta h_{\infty}} \quad (\text{VIII-13})$$

From this reference, the equation for the ground displacement due to the atmosphere is

$$\Delta x_A = - \frac{\tan \mu}{\beta \cos^2 \mu} \left[K (\rho_G - \rho_{\infty}) - K \rho_{\infty} \log \left(\frac{\rho_G}{\rho_{\infty}} \right) \right] \quad (\text{VIII-14})$$

If Equation (VIII-13) is solved for β and the resulting expression substituted in Equation (VIII-14), the expression for Δx_A becomes

$$\Delta x_A = - K \rho_{\infty} h_{\infty} \frac{\tan \mu}{\cos^2 \mu} \left[\frac{(\rho_G / \rho_{\infty}) - 1}{\log(\rho_G / \rho_{\infty})} - 1 \right] \quad (\text{VIII-15})$$

or

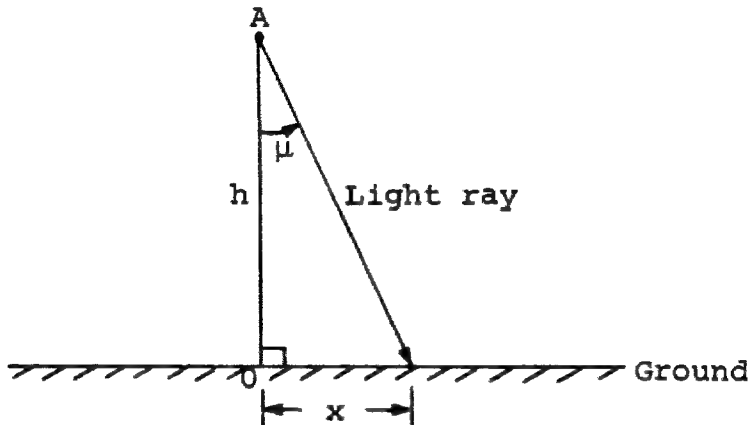
$$\frac{\cos^2 \mu}{\tan \mu} \Delta x_A = - K \rho_{\infty} h_{\infty} \left[\frac{(\rho_G / \rho_{\infty}) - 1}{\log(\rho_G / \rho_{\infty})} - 1 \right]$$

The second method for determining the variation in Δx_A with altitude is that of numerical integration. Let us write the expression for the angular refraction in differential form

$$d\mu = - \frac{K}{n} \tan \mu d\rho = - K \tan \mu d\rho \quad (\text{VIII-16})$$

since $n \approx 1.0$.

Now consider the following sketch:



A light ray of nadir angle μ originating at point A strikes the ground a distance x from point O. Therefore,

$$x = h \tan \mu \quad (\text{VIII-17})$$

Differentiation of this expression gives

$$dx = \frac{h}{\cos^2 \mu} d\mu$$

and substitution of Equation (VIII-16) into this expression results in the following expressions for Δx_A :

$$dx = - \frac{h}{\cos^2 \mu} K \tan \mu d\rho$$

$$\frac{\cos^2 \mu}{\tan \mu} dx = - K h d\rho \quad (\text{VIII-18})$$

$$\frac{\cos^2 \mu}{\tan \mu} \Delta x_A = - K \int_0^h h \frac{d\rho}{dh} dh$$

It should be noted that both Equations (VIII-15) and (VIII-18) assume that the angular refraction as the ray travels through the atmosphere is small, so that the tangent and cosine of the incident angle remain constant along the ray.

RESULTS AND DISCUSSION

Calculations have been made for the two configurations of Part II and all of the flight conditions outlined therein. Three nadir angles have been considered, -45, 0, and 45 degrees, in these calculations. The results are presented in Figures VIII-3 through VIII-11.

Figures VIII-3 and VIII-4 show the ground displacements caused by the window curvature induced by the temperature difference across the glass. Only the case of the heat transfer coefficient to the cavity of unity ($H = 1.0$) is plotted. The ground displacements for a nadir angle of 45 degrees are much larger than are those for the other nadir angles. This is to be expected since the light ray when looking rearward is incident on the glass at an angle which is the sum of the nadir angle and the vehicle surface slope (5 degrees on the cone and 20 degrees on the wing). Also, the displacements encountered in photography from the wing at μ equal to 45° are larger than those from the cone since in Part V the temperature differences were found to be larger and also the slope of the surface is larger.

All of the calculations of the ground displacements caused by window curvature have been made for a fused quartz glass window. This material has a relatively low coefficient of thermal expansion so for nearly all other types of windows the ground displacements will be larger. Hence, it is certainly desirable to use fused quartz.

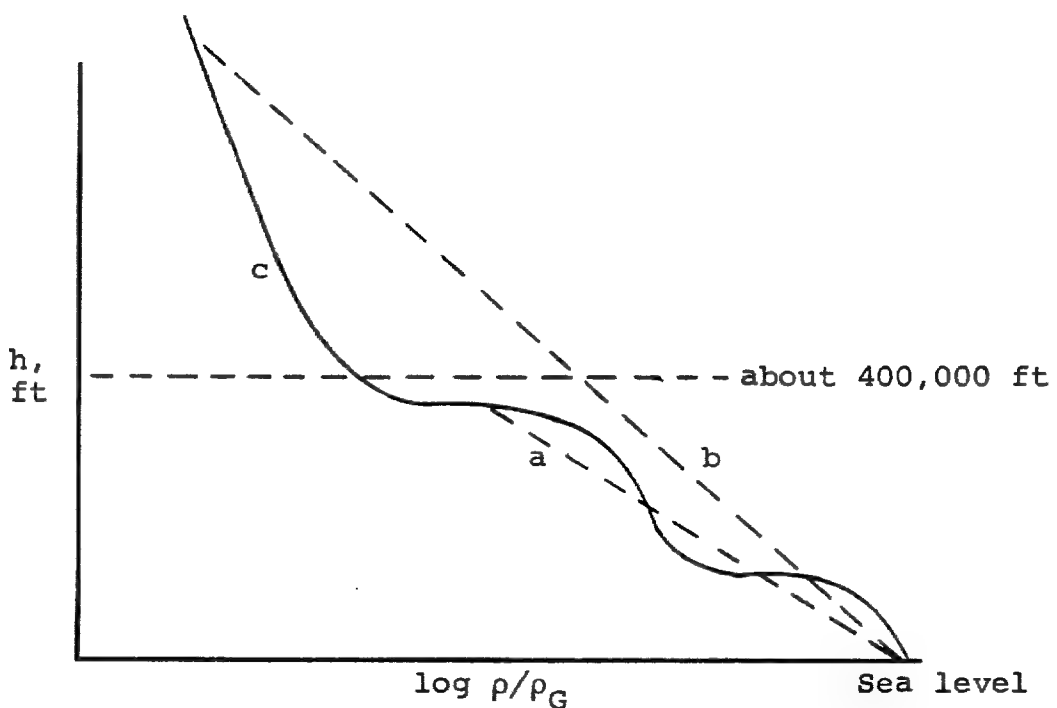
Figures VIII-5 through VIII-10 present the results of the calculations of the ground displacements caused by the three parts of the near flow field. For all of the altitudes except 100,000 feet, these displacements are negligible. At 100,000 feet they could possibly have some importance since they do become the same order of magnitude as the displacements caused by the window curvature. However, on the basis of these calculations, it is apparent that if corrections for metric distortion are to be made to photographs taken from an altitude greater than 100,000, they need not be made for the refractions caused by the near flow field.

Ground displacements caused by atmospheric refraction have been calculated in accordance with Equations (VIII-15) and (VIII-18), and the results are presented in Figure VIII-11 as a function of altitude h_{∞} . The first equation is solved by choosing an altitude, h_{∞} , and obtaining the corresponding density, ρ_{∞} , from Reference 4. (The quantity ρ_G is the sea-level or ground density.) Equation (VIII-18) is solved

by choosing a variation in h from $h = 0$ to $h = h_{\infty}$ and, the slope of the density, altitude curve at each of these altitudes is determined from Reference 4. The product of h and $d\rho/dh$ is then integrated numerically from $h = 0$ to $h = h_{\infty}$ to determine Δx_A .

An examination of Figure VIII-11 shows that the curve obtained from Equation (VIII-18) reaches a maximum at an altitude of about 200,000 feet. Further increases in flight altitude will, therefore, not increase the ground displacement due to atmospheric refraction. Equation (VIII-15), however, behaves quite differently. The value of Δx_A given by this curve increases up to an altitude of about 200,000 feet and then begins to decrease. At about 400,000 feet it begins to increase again and is still increasing at 800,000 feet. Another feature of interest is that the curve determined by Equation (VIII-15) is lower than that of Equation (VIII-18) for altitudes below 600,000 feet.

The fact that Equation (VIII-15) does not approach a constant value can be explained by the following sketch, which shows the variation of the logarithm of the density with altitude (Ref. 4):



The method used for the exponential atmosphere (Eq. (VIII-15)) assumes a linear variation of altitude with the logarithm of the density ratio, as shown by the straight lines a and b. The slopes of these curves determine the constant β in Equation (VIII-13). Since these are determined by the flight altitude of interest, h_{∞} , and sea level, it is apparent that as we move up curve c (taken from Ref. 4) the slope will continually change. If we examine Equation (VIII-14), we see that even after the quantity in brackets reaches a constant (ρ_{∞} becomes very small compared to ρ_G) this variation in β will cause a variation in the calculated displacement Δx_A .

CONCLUSIONS

On the basis of the calculations presented in this part of the report, the following conclusions can be drawn with regard to correcting photographs for metric distortion:

1. At altitudes above 100,000 feet corrections should be made for displacements caused by window curvature due to aerodynamic heating but are probably not necessary for displacements caused by the near flow field except in extremely high resolution photography.
2. Corrections should be made for atmospheric refraction.
3. A numerical integration indicates that the angular refraction of a light ray by the atmosphere and the resulting ground displacement do not increase if the flight altitude is increasing above 200,000 feet.
4. The method presented in Part II of the Phase I final report, Reference 1, will yield fairly good results for the ground displacement due to atmospheric refraction to altitudes of about 600,000 feet. The results of this method, however, are lower than those obtained by numerical integration and do not approach a constant value as the altitude increases.
5. Rearward viewing through a flush window on the lower surface of the blunt swept wing will cause extremely large refraction errors at high angles of attack. For instance,

for an angle of attack of 45° and a nadir angle of 40°, the angle of incidence is 85°.

RECOMMENDATIONS

To minimize the metric distortion to photography taken from altitudes above 100,000 feet caused by aerodynamic effects, that is, the near flow field and aerodynamic heating, photography should be taken looking through the window as nearly perpendicular as possible. This will minimize the displacement due to window curvature which is by far the largest. Any atmospheric refraction introduced this way can be corrected for quite easily.

Since the window curvature is the most important source of metric distortion, methods should be investigated for supporting the window in order to minimize the curvature caused by a temperature difference across the glass.

APPENDIX VIIIA

EFFECT OF TEMPERATURE ON THE
SPECIFIC REFRACTIVITY OF AIR

For low temperature air the following relationship exists between the index of refraction and density

$$n - 1 = K\rho \quad (\text{VIIIA-1})$$

where K is the specific refractivity. This quantity for air at low temperatures is

$$K = 0.116 \text{ ft}^3/\text{slug}$$

More generally, however, Equation (VIIIA-1) can be written in the following way for a mixture of gases

$$n - 1 = \sum_i K_i \rho_i \quad (\text{VIIIA-2})$$

where the subscript i indicates the i^{th} species. Thus, K_i is the specific refractivity of this species and ρ_i is the partial density of this species.

As air is heated, the molecules of oxygen and nitrogen dissociate and form atomic oxygen and nitrogen and nitric oxide. Hence, instead of the air being made up of three species (argon is also present in a significant amount), it is now made up of six species. Accounting only for dissociation the specific refractivity, K , can be written

$$K = \frac{1.991}{28.966} \left(K_{O_2}^W Y_{O_2} + K_{N_2}^W Y_{N_2} + K_O^W Y_O \right. \\ \left. + K_N^W Y_N + K_{NO}^W Y_{NO} + K_A^W Y_A \right) \quad (\text{VIIIA-3})$$

The specific refractivities of the various species can be obtained from Reference 5 except for K_N and K_O . These are given in Reference 6. The following table lists the values of K_i and w_i , the molecular or atomic weights, of the six species

Species	K_i , ft ³ /slug	w_i
O ₂	.0985	32.000
N ₂	.1243	28.016
O	.0933	16.000
N	.1599	14.008
NO	.1167	30.008
A	.0814	39.944

One other quantity is needed. This is y_i , the number of particles per atom of each species. Reference 2 presents this information as a function of temperature and density.

Figure VIII-2 was calculated using these values. The calculations were carried to the temperature where ionization became significant. This figure shows that the specific refractivity is quite a strong function of temperature and density once the nitrogen molecules have begun to dissociate.

REFERENCES

1. Nielsen, Jack N., Goodwin, Frederick K., Sacks, Alvin H., Rubesin, Morris W., Ragent, Boris, and Noble, Charles E.: Effects of Supersonic and Hypersonic Aircraft Speed Upon Aerial Photography. Final Technical Report, Phase I, Vidya Report No. 17, March 1960.
2. Moeckel, W. E., and Weston, Kenneth C.: Composition and Thermodynamic Properties of Air in Chemical Equilibrium. NACA TN 4265, April 1958.
3. Feldman, Saul: Hypersonic Gas Dynamic Charts for Equilibrium Air. Avco Research Laboratories, January 1957.
4. Minzner, R. A., Champion, K. S. W., and Pond, H. L.: The ARDC Atmosphere, 1959. Air Force Surveys in Geophysics, No. 115. Air Force Cambridge Research Center, TR-59-267, August 1959.
5. Handbook of Chemistry and Physics: Thirty-First Edition, Chemical Rubber Publishing Company, Cleveland, Ohio, 1949.
6. Alpher, R. A., and White, D. A.: Optical Refractivity of High-Temperature Gases, I. Effects Resulting from Dissociation of Diatomic Gases. General Electric Research Laboratory, General Electric Company. December 5, 1958.

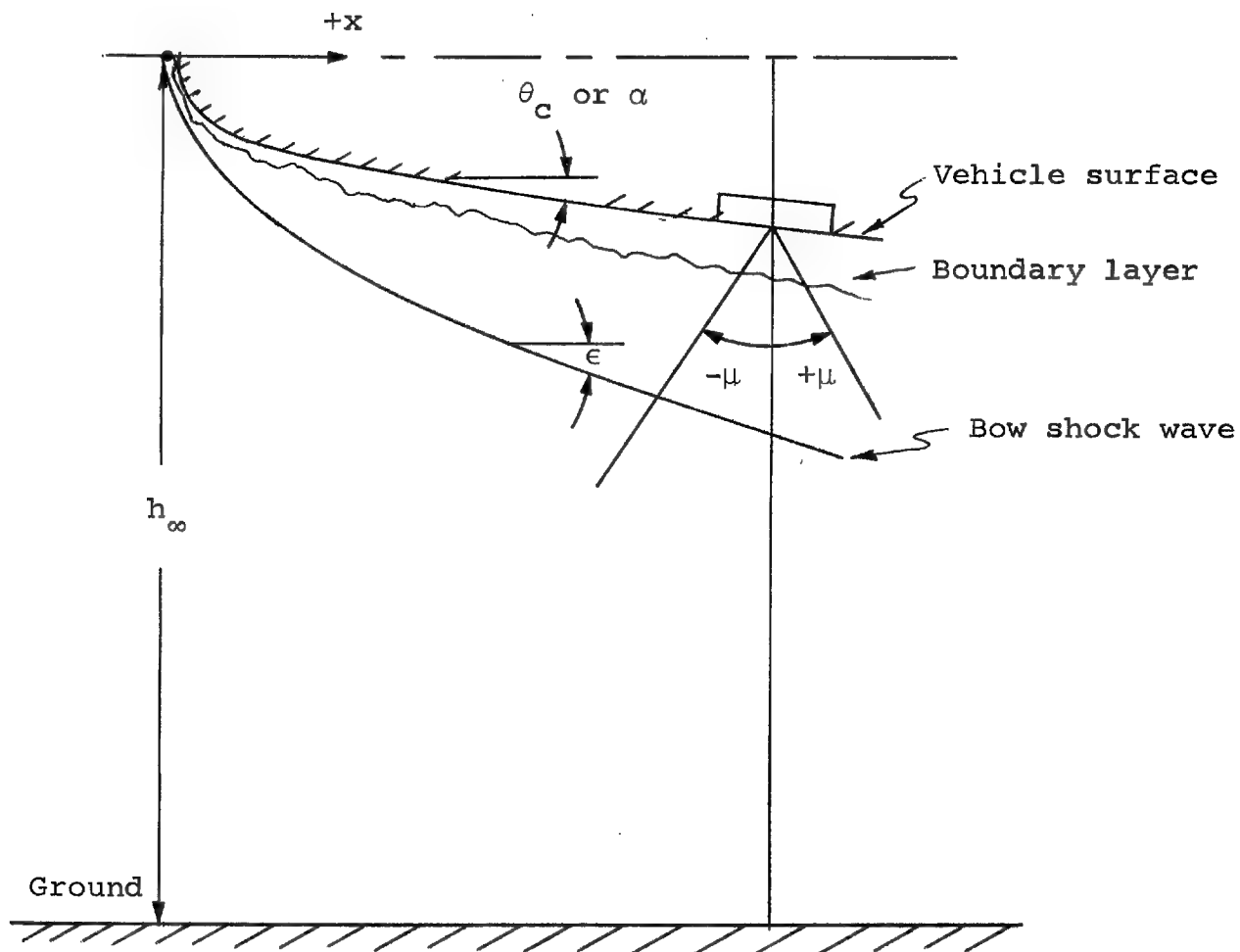


Figure VIII-1.- Near flow field and notation.

Approved For Release 2000/04/12 : CIA-RDP67B00657R000300070001-0

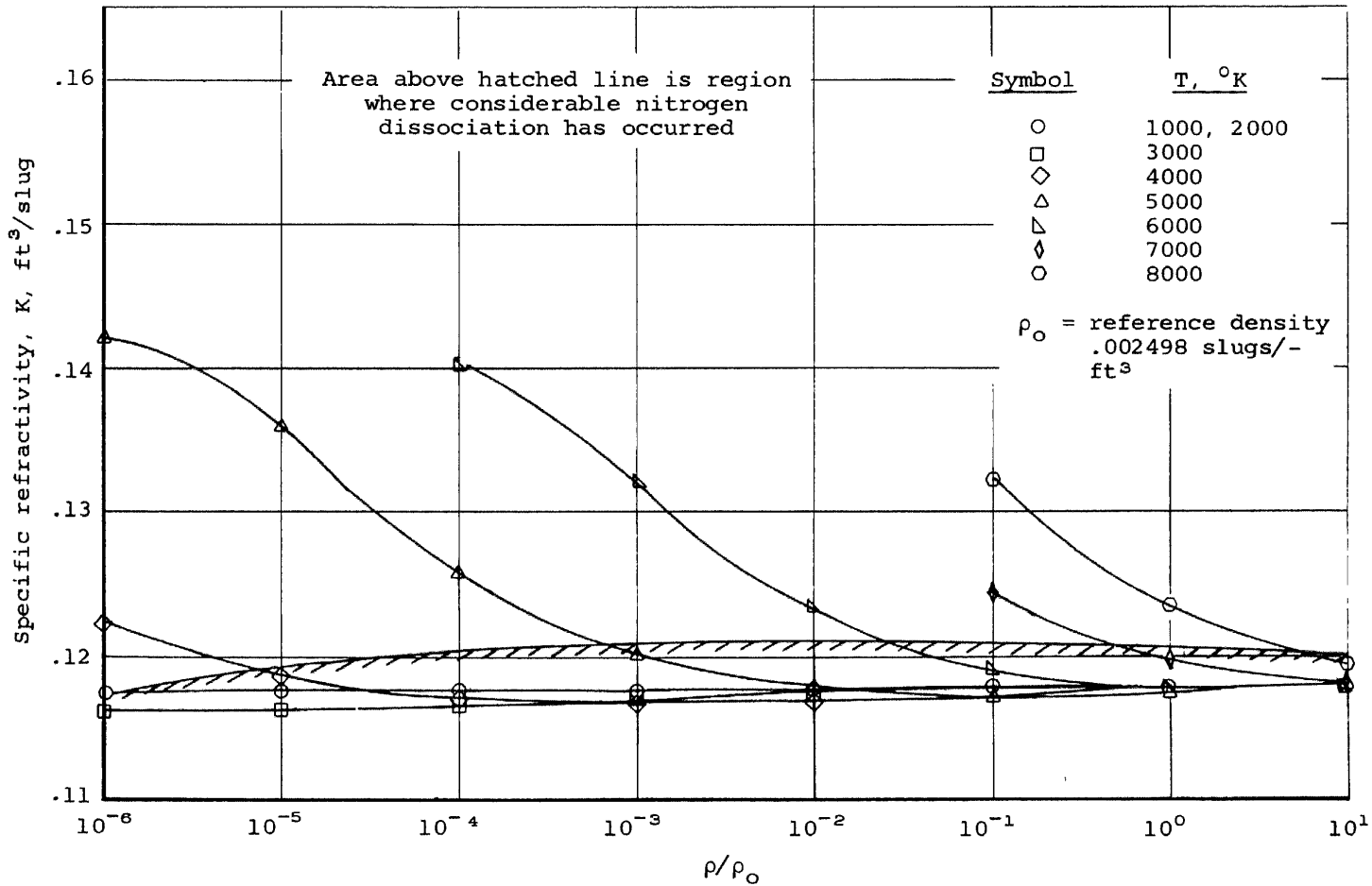


Figure VIII-2-- Specific refractivity of air as a function of temperature and density.

Approved For Release 2000/04/12 : CIA-RDP67B00657R000300070001-0

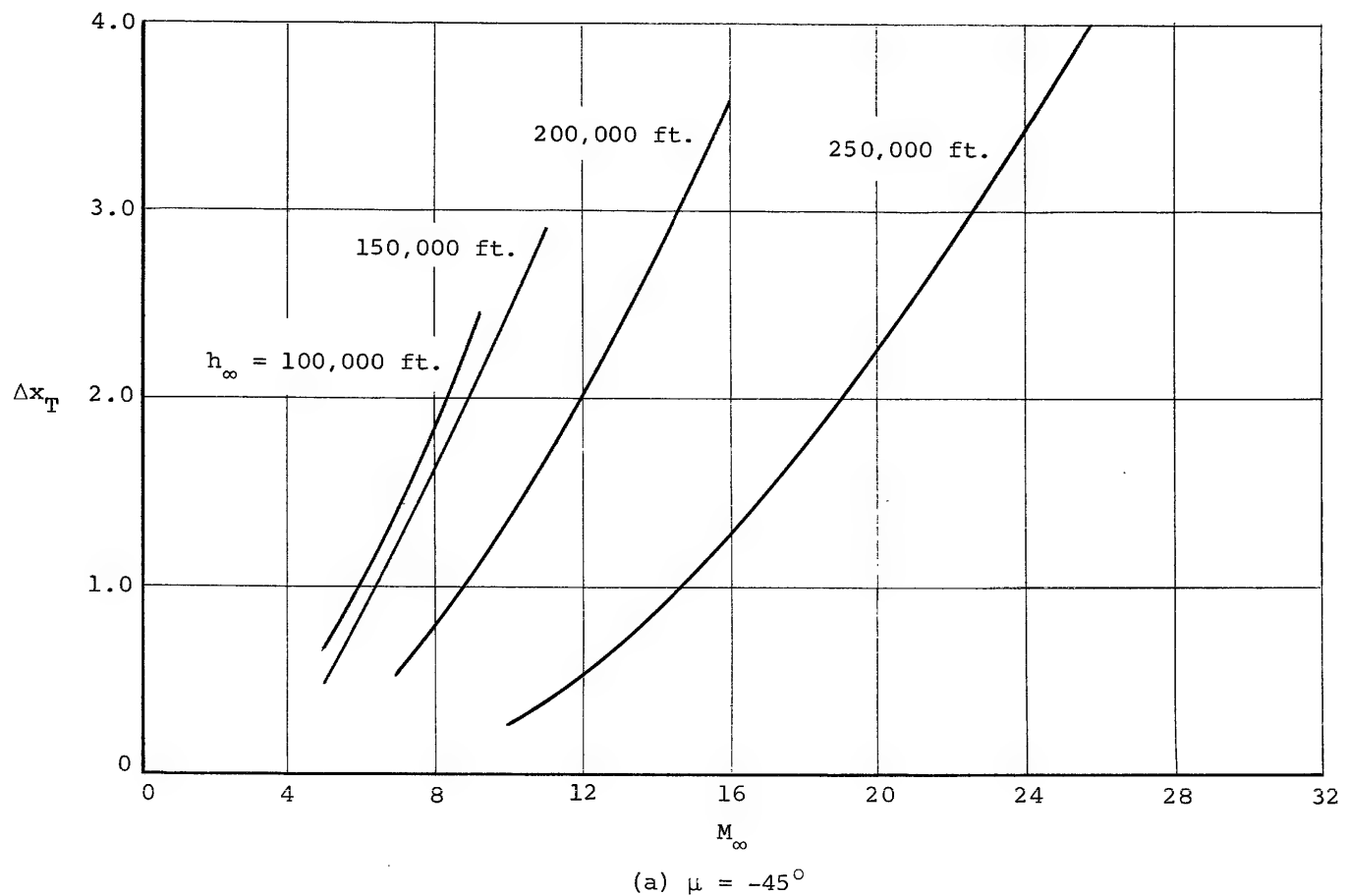


Figure VIII-3.- Ground displacements caused by camera window curvature. Blunt cone, $\theta_c = 5^\circ$, $H = 1.0$.

Approved For Release 2000/04/12 : CIA-RDP67B00657R000300070001-0

Approved For Release 2000/04/12 : CIA-RDP67B00657R000300070001-0

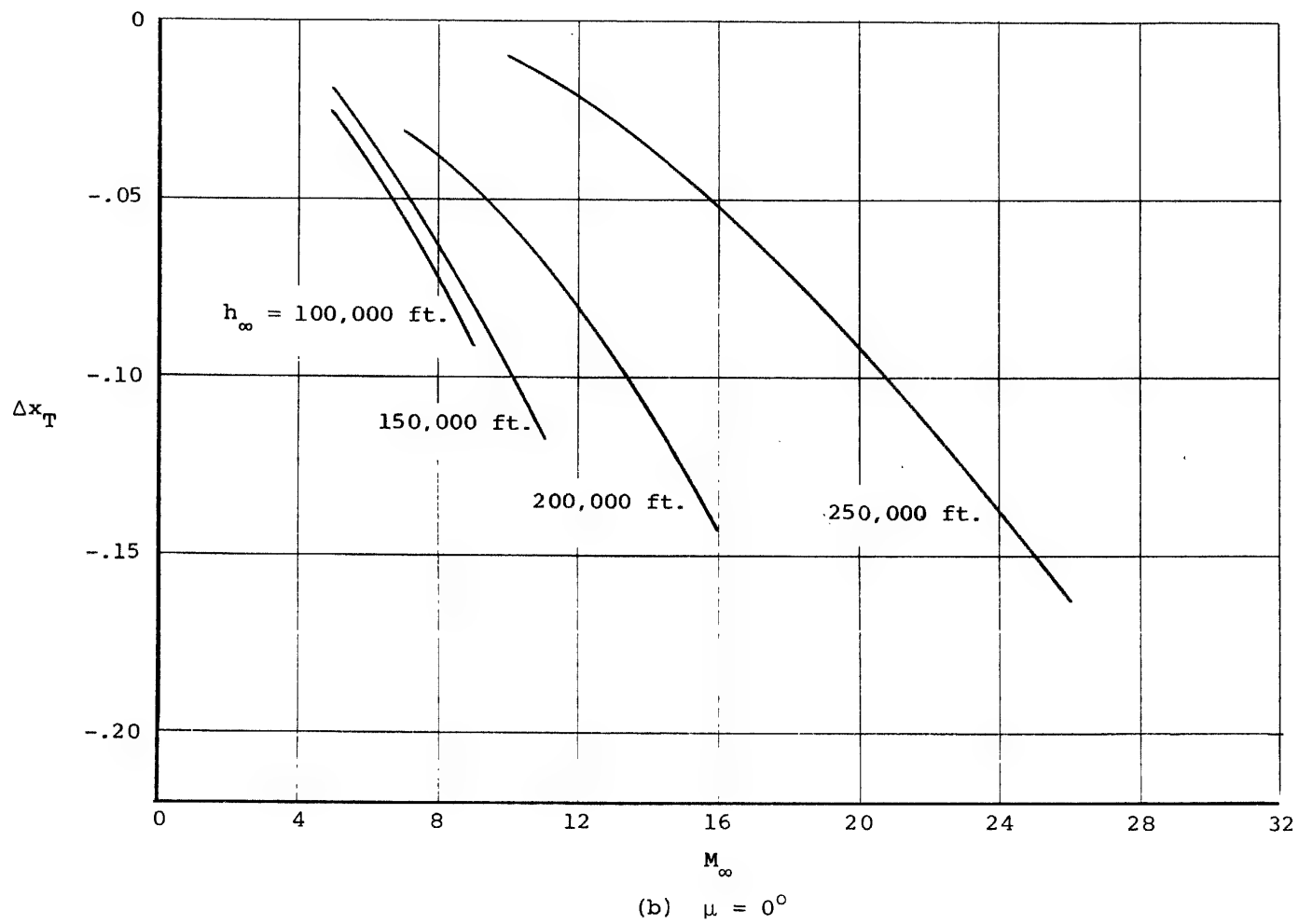


Figure VIII-3.- Continued.

Approved For Release 2000/04/12 : CIA-RDP67B00657R000300070001-0

Approved For Release 2000/04/12 : CIA-RDP67B00657R000300070001-0

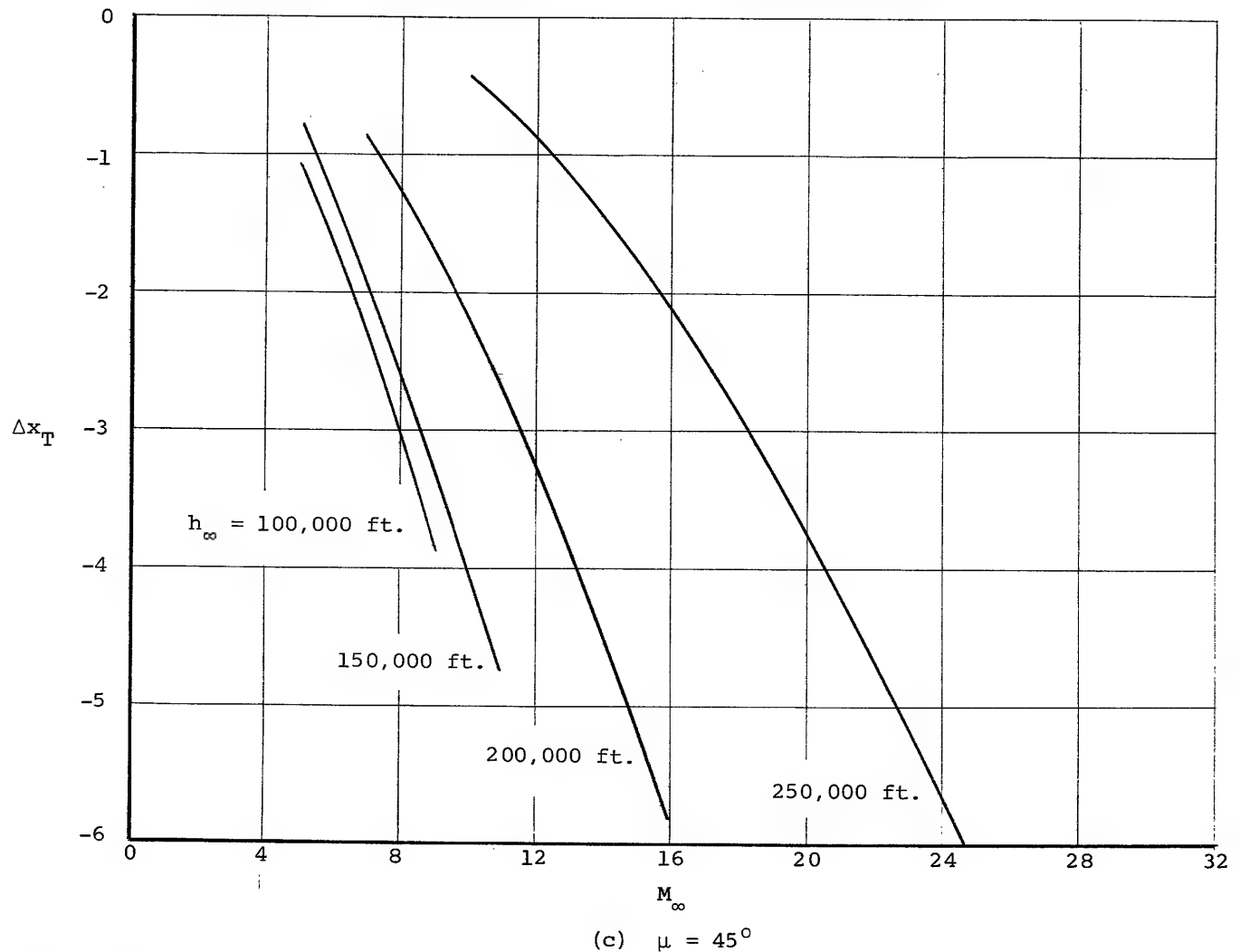


Figure VIII-3.- Concluded.

Approved For Release 2000/04/12 : CIA-RDP67B00657R000300070001-0

Approved For Release 2000/04/12 : CIA-RDP67B00657R000300070001-0

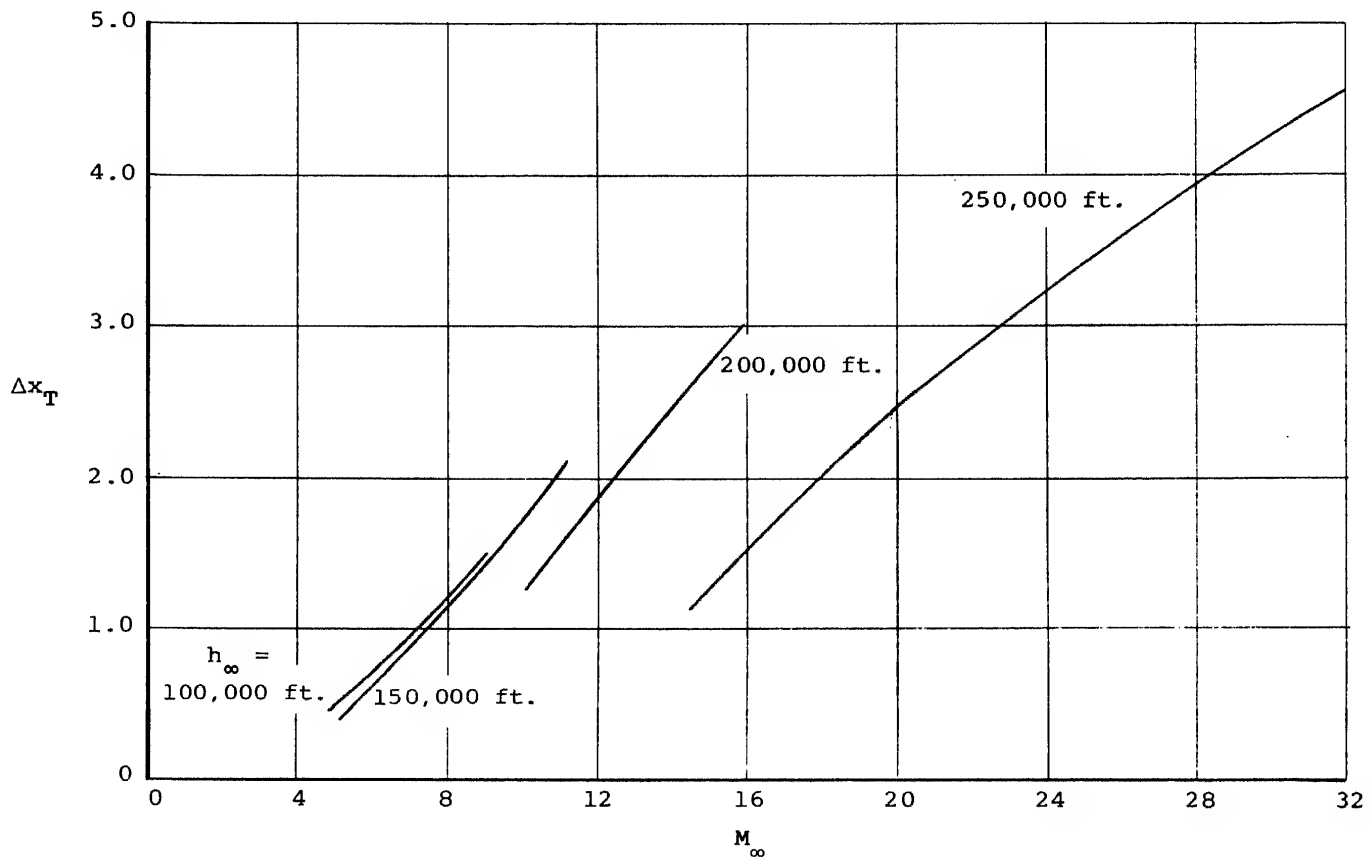


Figure VIII-4.- Ground displacements caused by camera window curvature. Swept wing,
 $\alpha = 20^\circ$, $H = 1.0$.

Approved For Release 2000/04/12 : CIA-RDP67B00657R000300070001-0

Approved For Release 2000/04/12 : CIA-RDP67B00657R000300070001-0

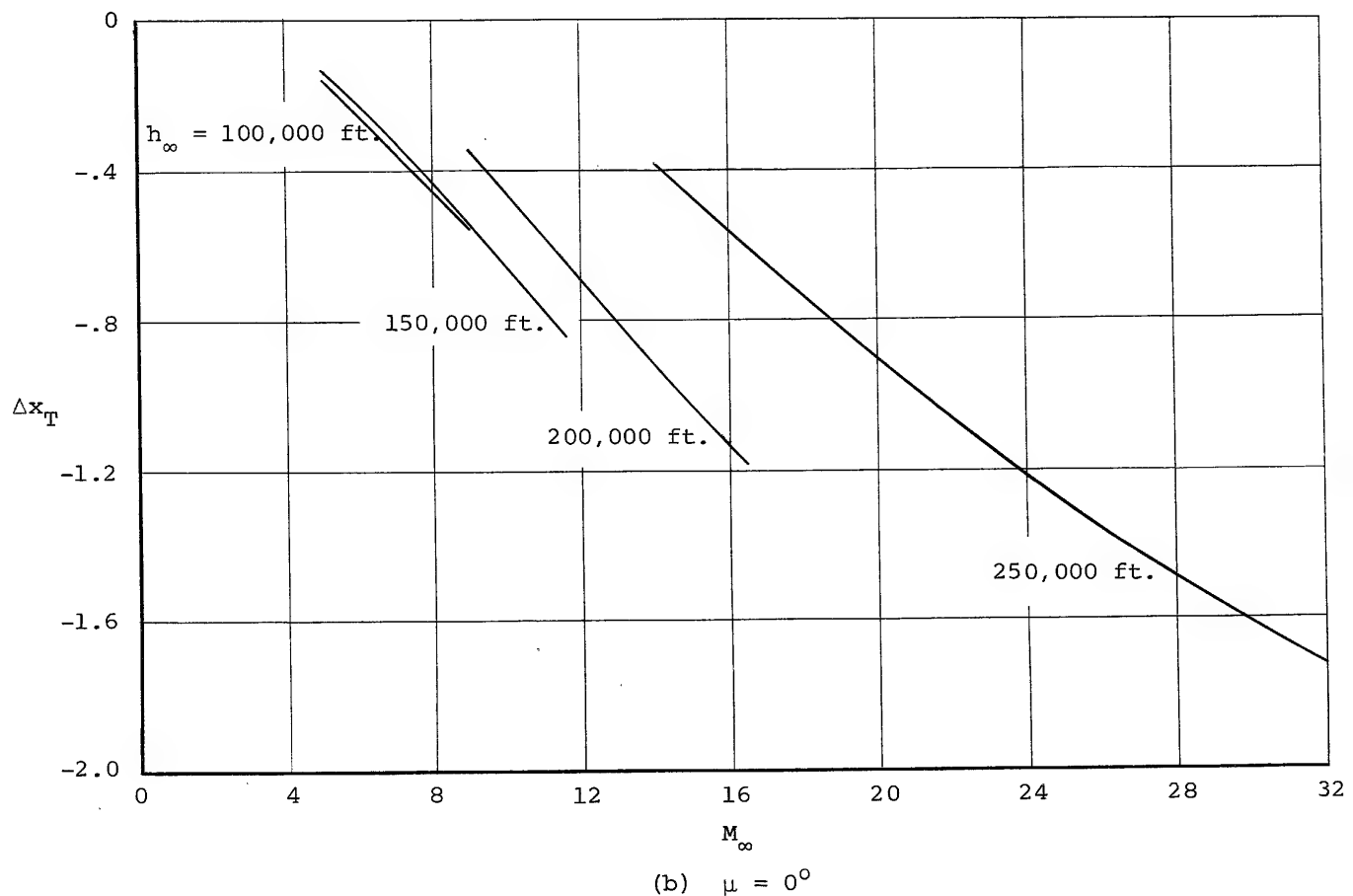


Figure VIII-4.- Continued.

Approved For Release 2000/04/12 : CIA-RDP67B00657R000300070001-0

Approved For Release 2000/04/12 : CIA-RDP67B00657R000300070001-0

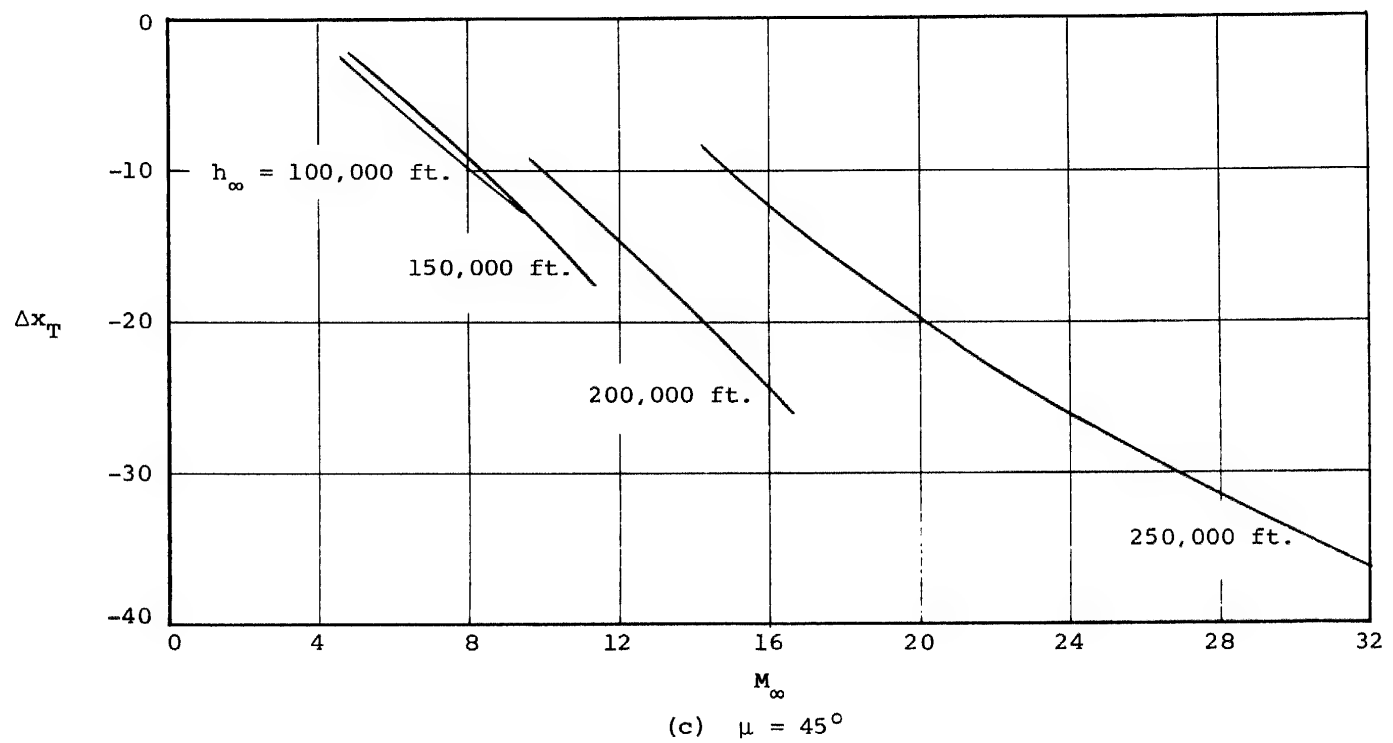


Figure VIII-4.- Concluded.

Approved For Release 2000/04/12 : CIA-RDP67B00657R000300070001-0

Approved For Release 2000/04/12 : CIA-RDP67B00657R000300070001-0

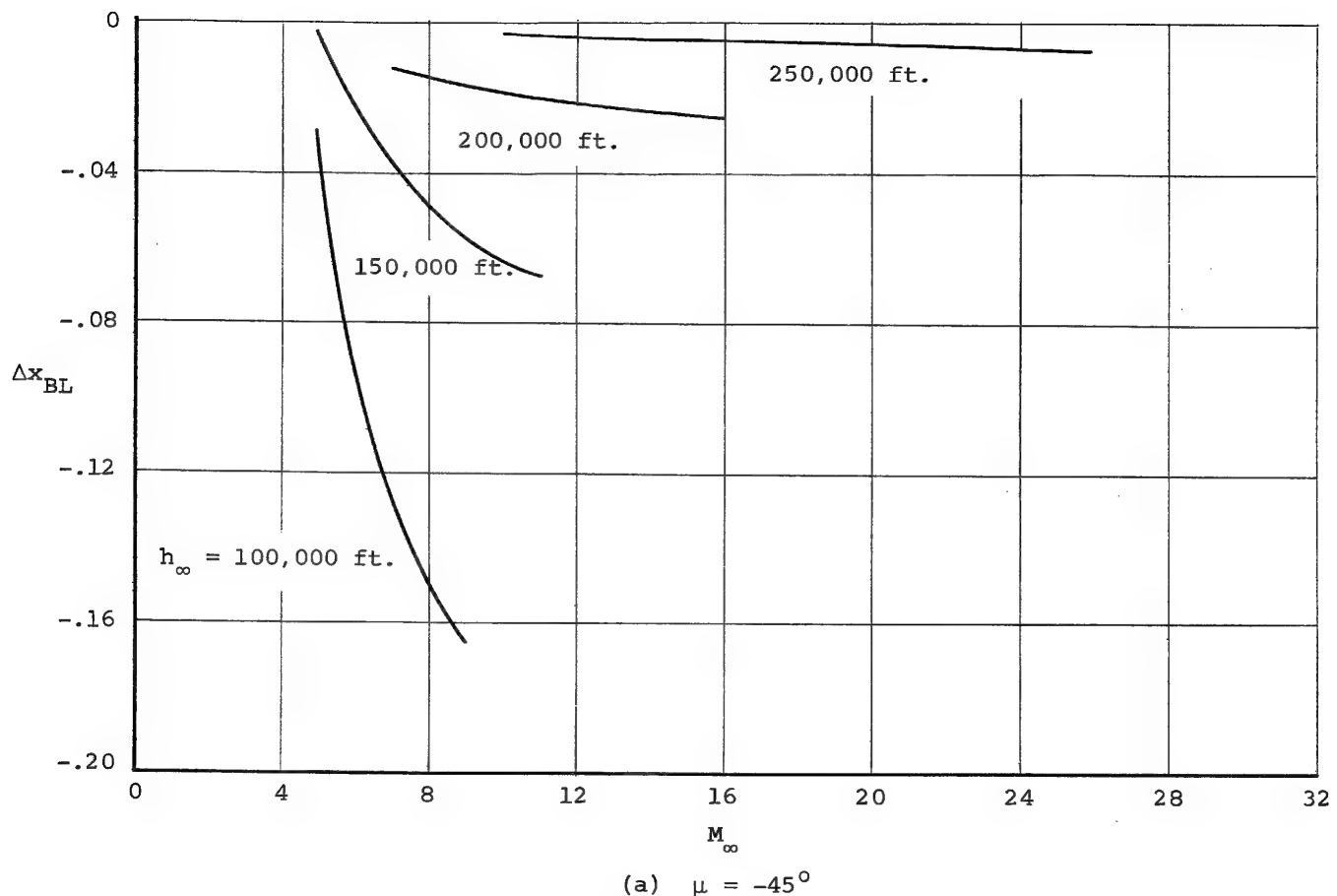


Figure VIII-5.- Ground displacements caused by boundary layer refraction. Blunt cone, $\theta_c = 5^\circ$, $H = 1.0$.

Approved For Release 2000/04/12 : CIA-RDP67B00657R000300070001-0

Approved For Release 2000/04/12 : CIA-RDP67B00657R000300070001-0

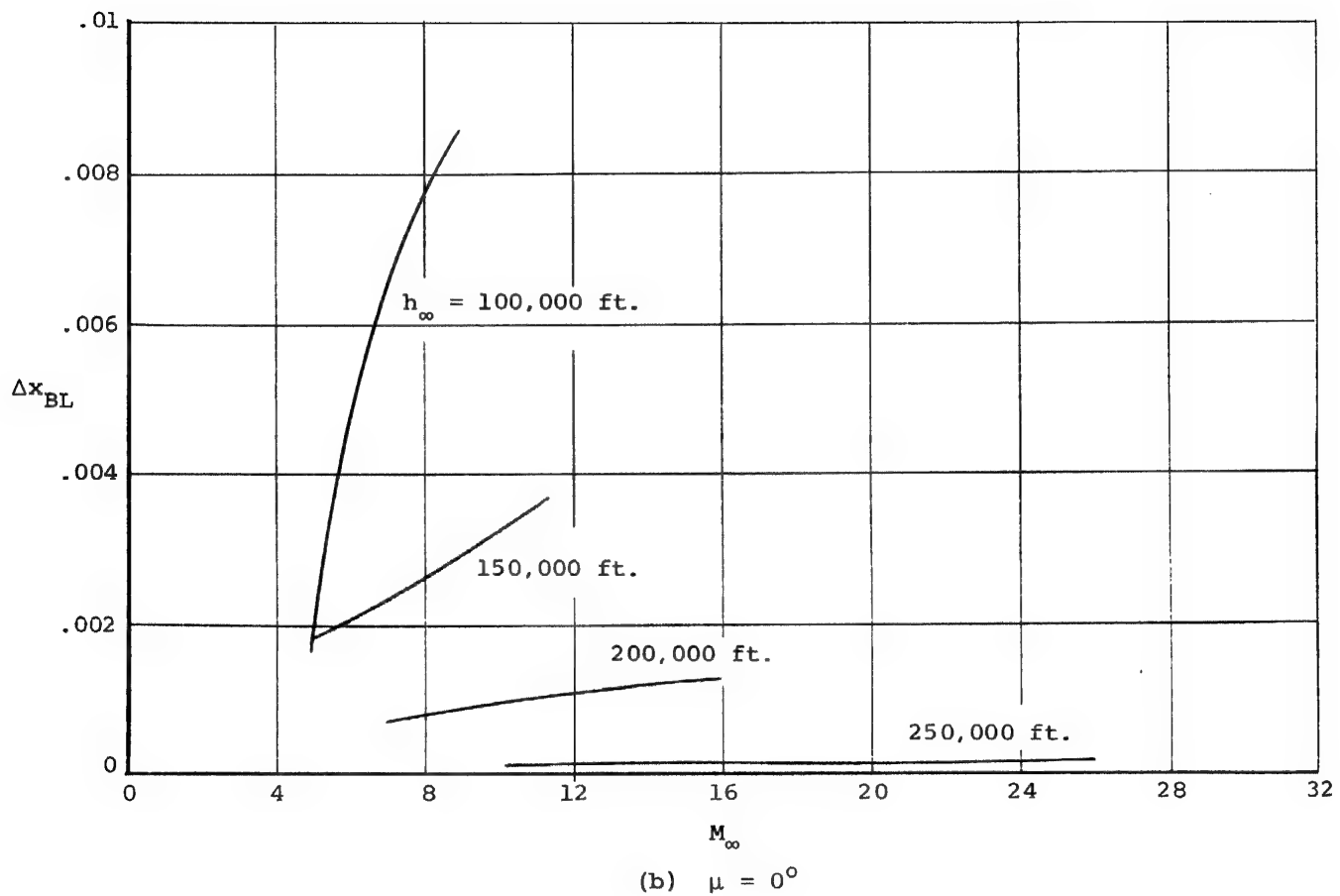


Figure VIII-5.- Continued.

Approved For Release 2000/04/12 : CIA-RDP67B00657R000300070001-0

Approved For Release 2000/04/12 : CIA-RDP67B00657R000300070001-0

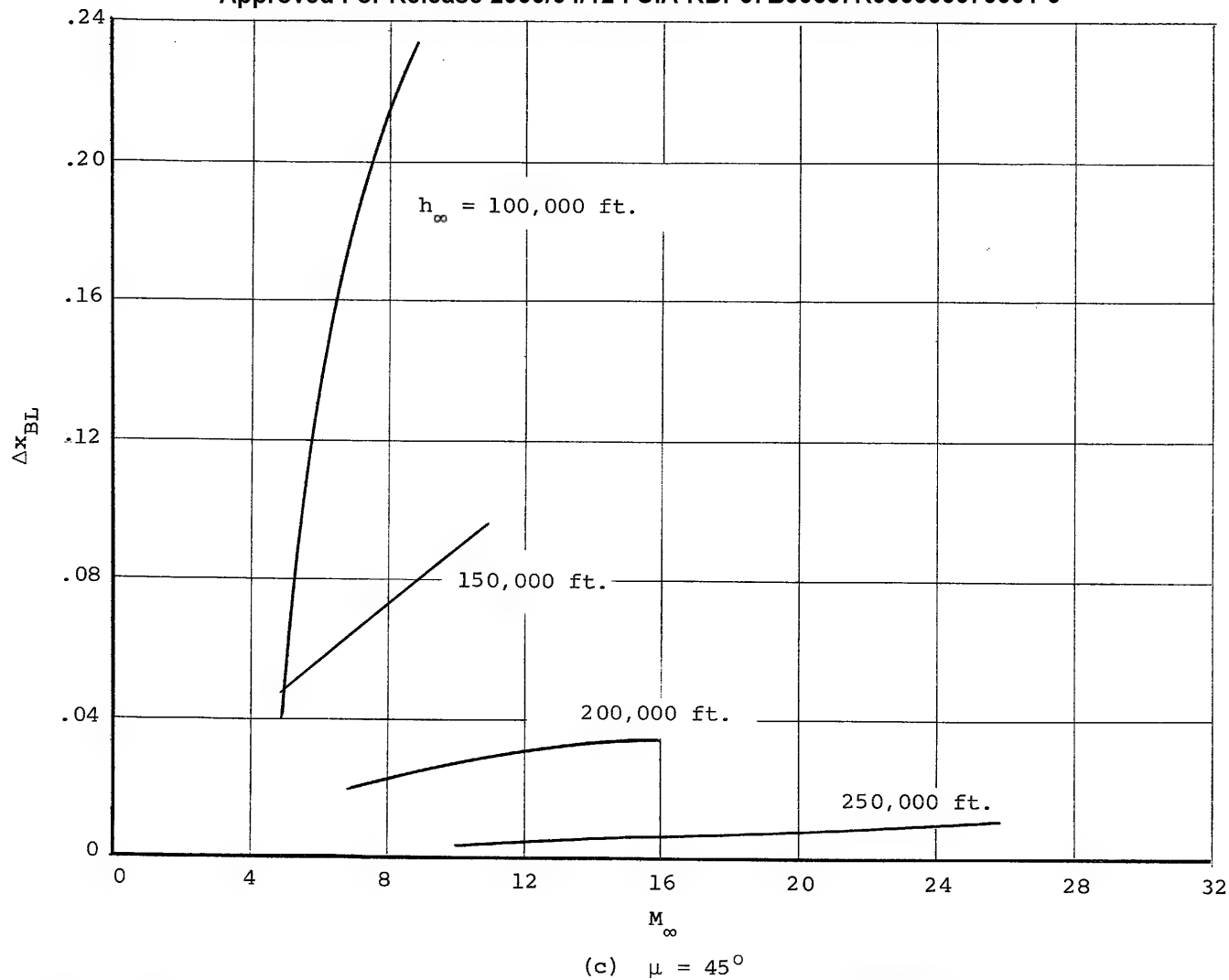
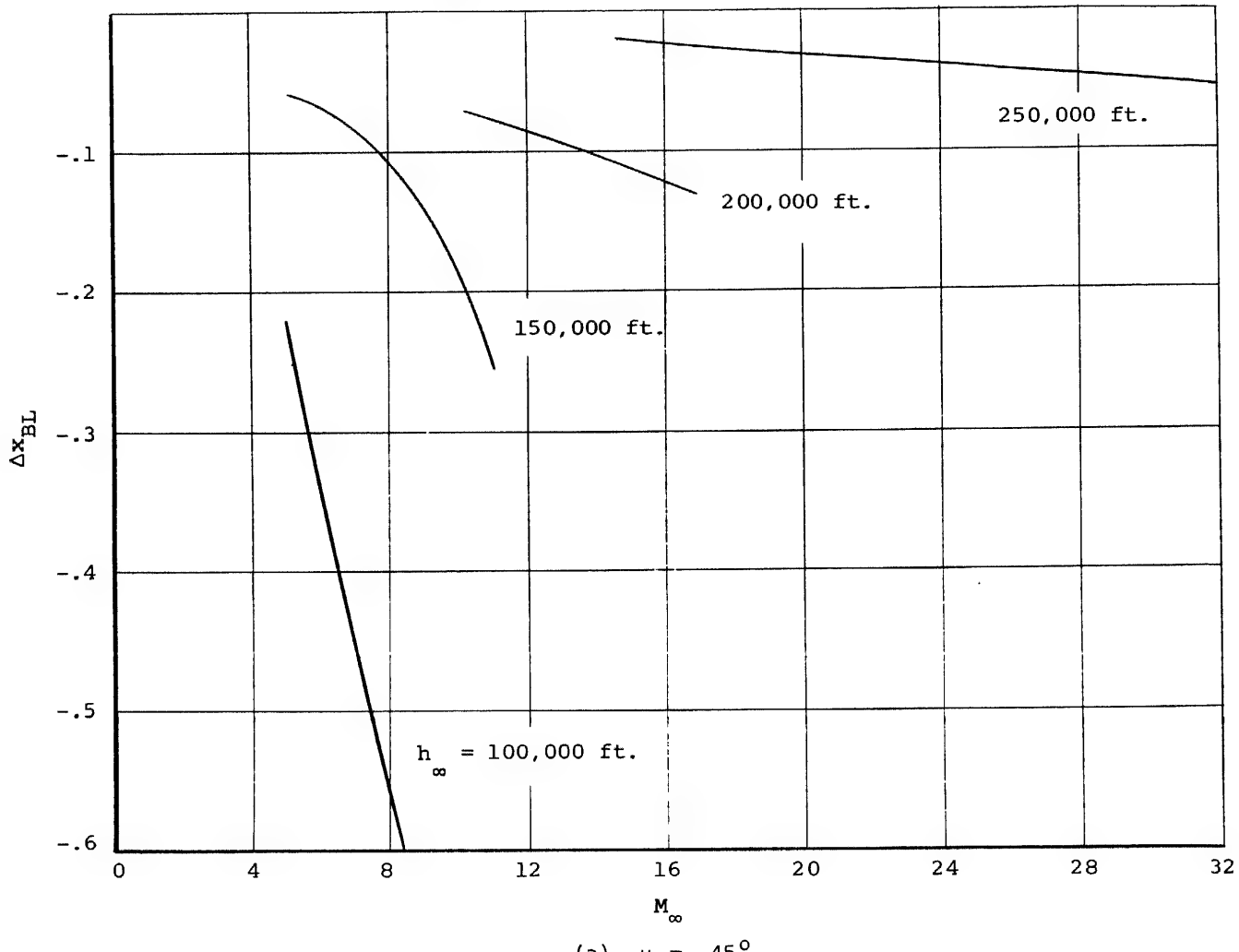


Figure VIII-5.- Concluded.

Approved For Release 2000/04/12 : CIA-RDP67B00657R000300070001-0

Approved For Release 2000/04/12 : CIA-RDP67B00657R000300070001-0



(a) $\mu = -45^\circ$

Figure VIII-6.- Ground displacements caused by boundary layer refraction. Swept wing,
 $\alpha = 20^\circ$, $H = 1.0$.

Approved For Release 2000/04/12 : CIA-RDP67B00657R000300070001-0

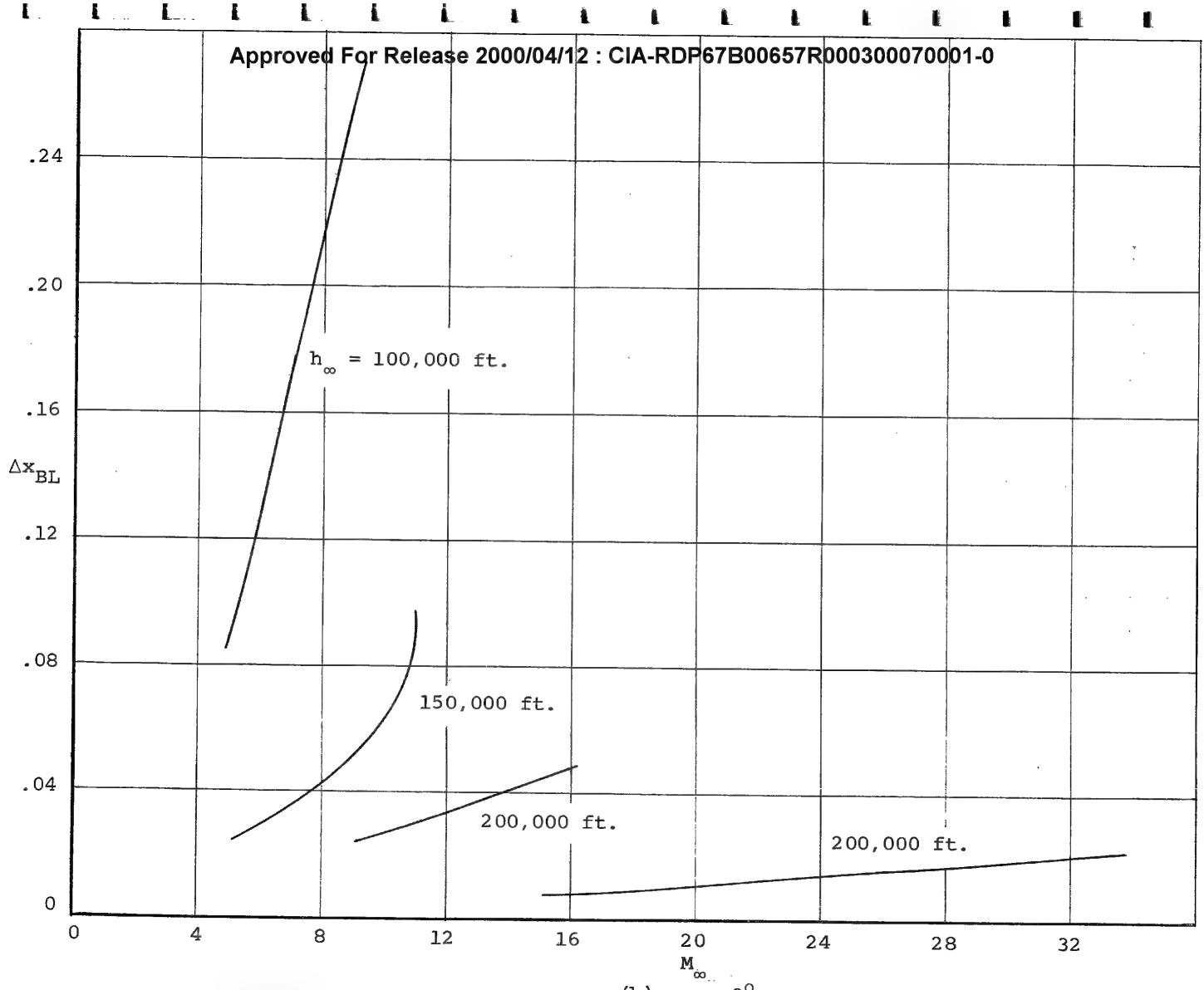


Figure VIII-6.- Continued

Approved For Release 2000/04/12 : CIA-RDP67B00657R000300070001-0

Approved For Release 2000/04/12 : CIA-RDP67B00657R000300070001-0

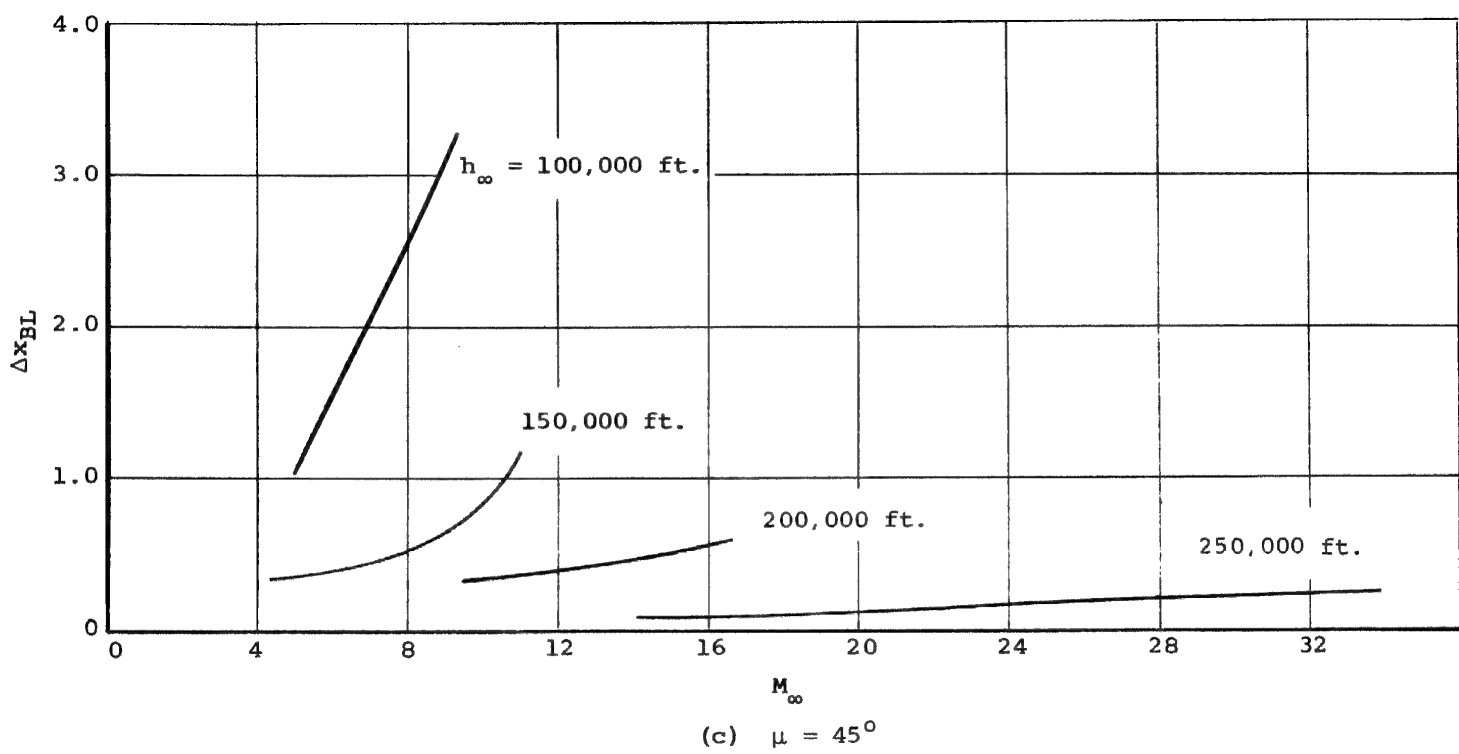
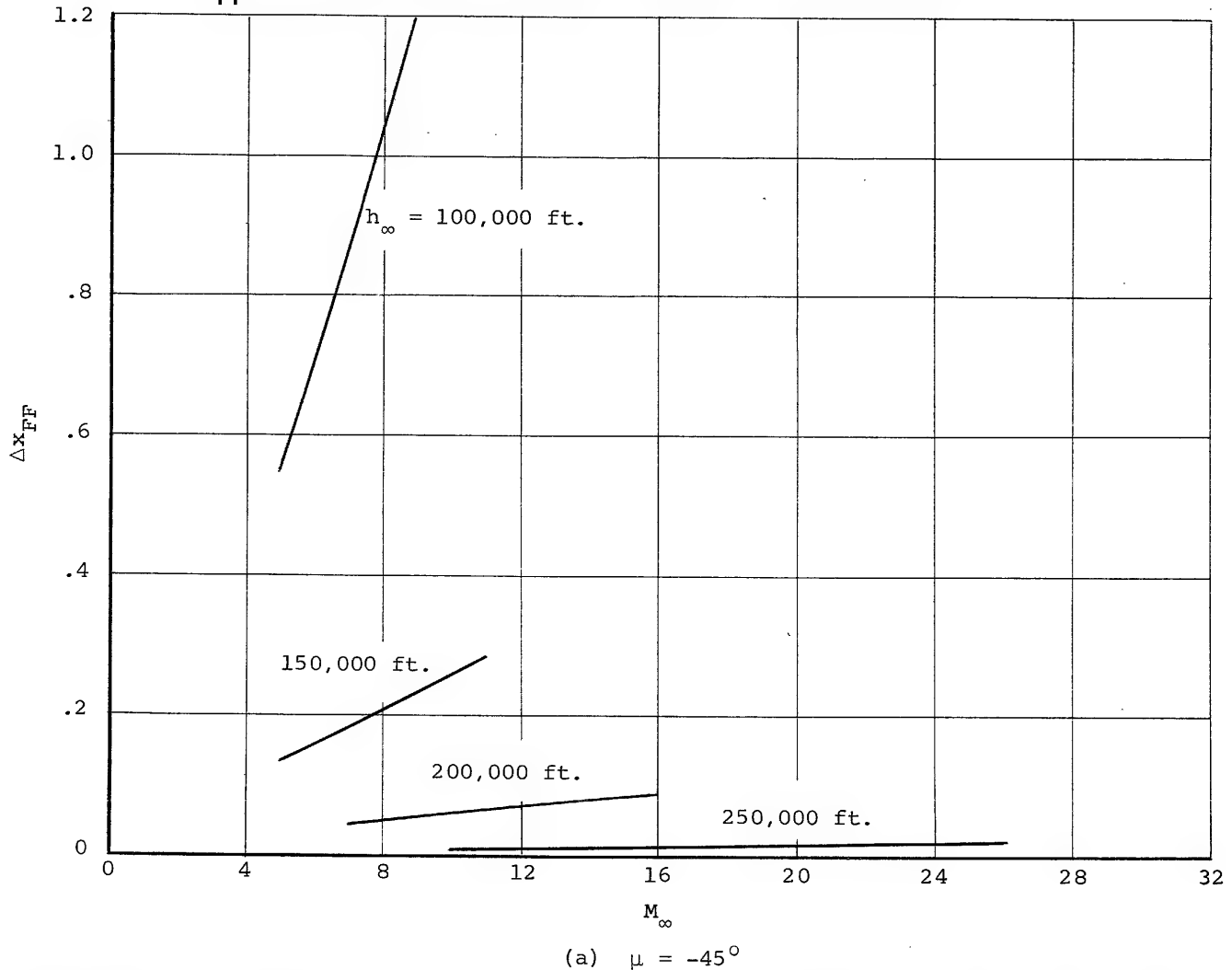


Figure VIII-6.- Concluded.

Approved For Release 2000/04/12 : CIA-RDP67B00657R000300070001-0

Approved For Release 2000/04/12 : CIA-RDP67B00657R000300070001-0



(a) $\mu = -45^\circ$

Figure VIII-7.- Ground displacements caused by flow field between boundary layer and bow shock wave, blunt cone, $\theta_c = 5^\circ$.

Approved For Release 2000/04/12 : CIA-RDP67B00657R000300070001-0

Approved For Release 2000/04/12 : CIA-RDP67B00657R000300070001-0

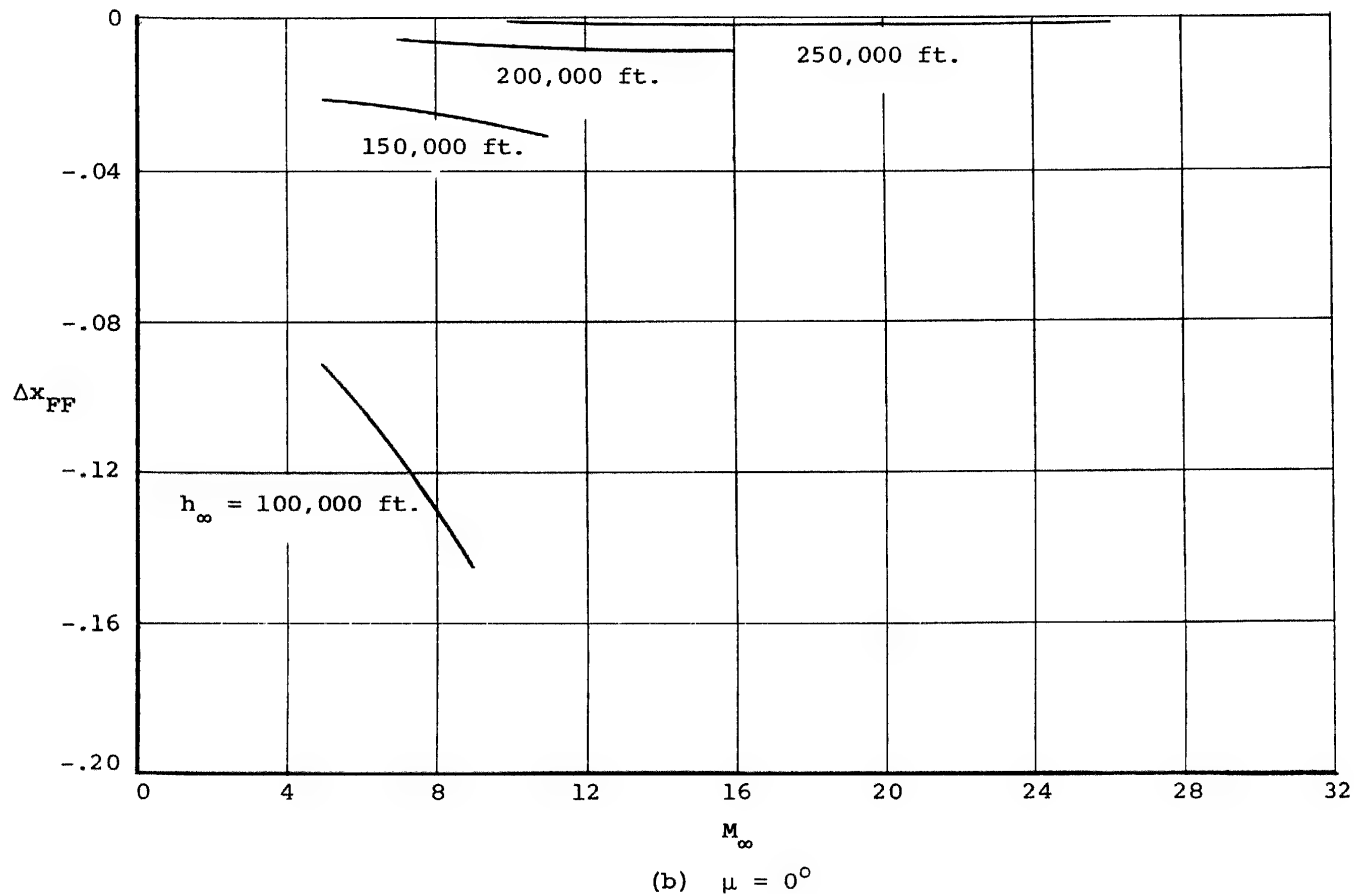


Figure VIII-7.- Continued.

Approved For Release 2000/04/12 : CIA-RDP67B00657R000300070001-0

Approved For Release 2000/04/12 : CIA-RDP67B00657R000300070001-0

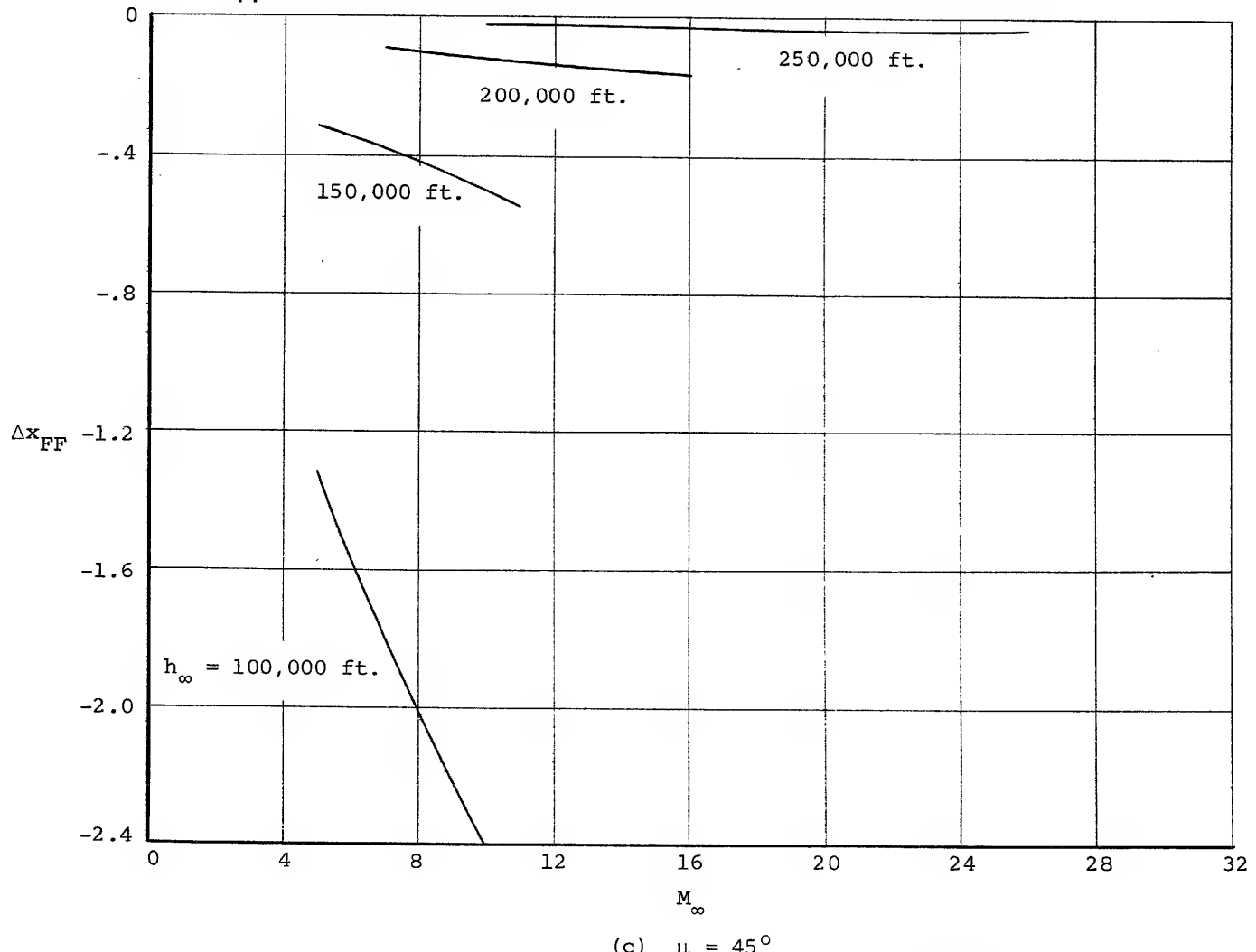


Figure VIII-7.- Concluded.

Approved For Release 2000/04/12 : CIA-RDP67B00657R000300070001-0

Approved For Release 2000/04/12 : CIA-RDP67B00657R000300070001-0

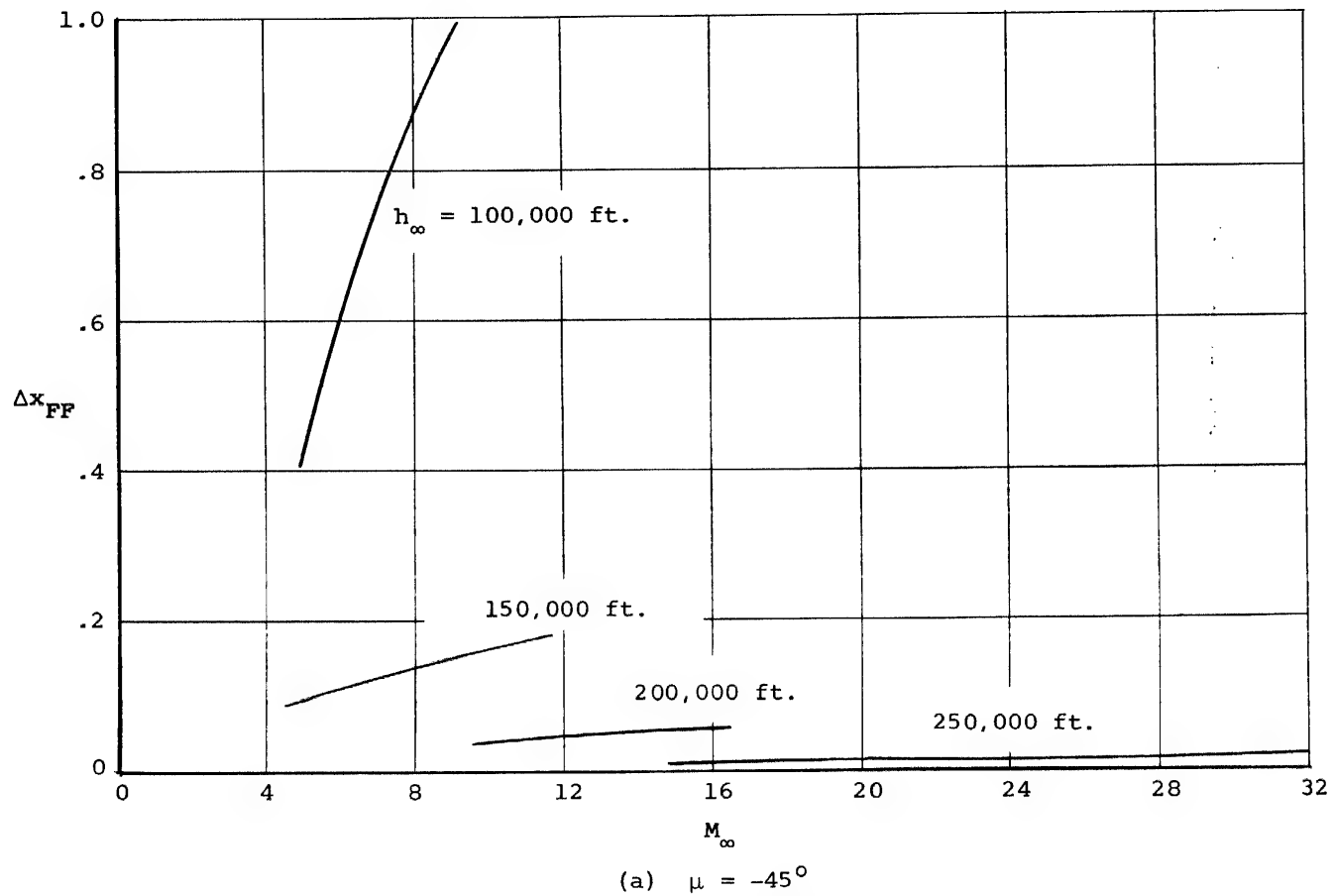


Figure VIII-8.- Ground displacements caused by flow field between boundary layer and bow shock wave. Swept wing, $\alpha = 20^\circ$.

Approved For Release 2000/04/12 : CIA-RDP67B00657R000300070001-0

Approved For Release 2000/04/12 : CIA-RDP67B00657R000300070001-0

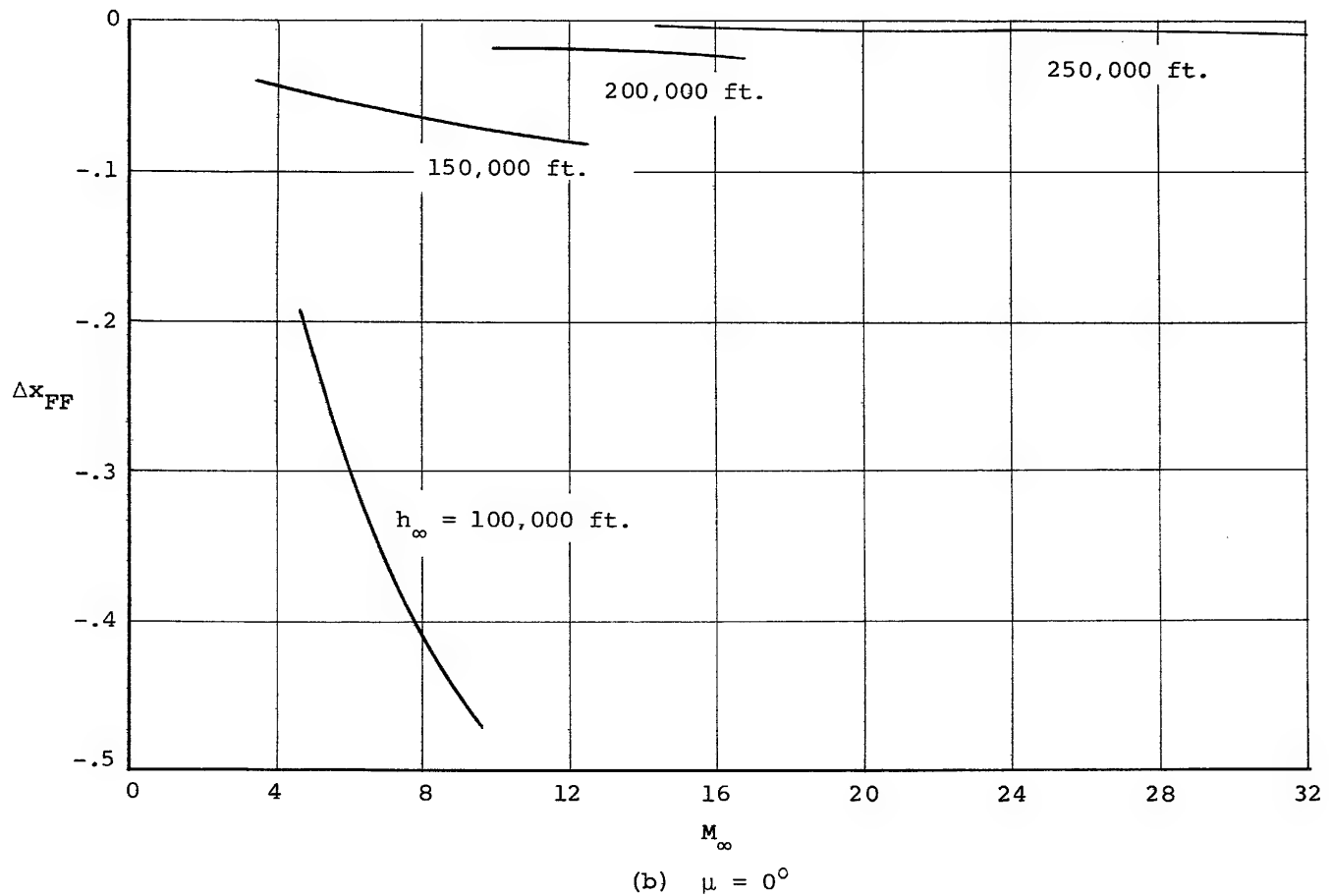


Figure VIII-8.- Continued.

Approved For Release 2000/04/12 : CIA-RDP67B00657R000300070001-0

Approved For Release 2000/04/12 : CIA-RDP67B00657R000300070001-0

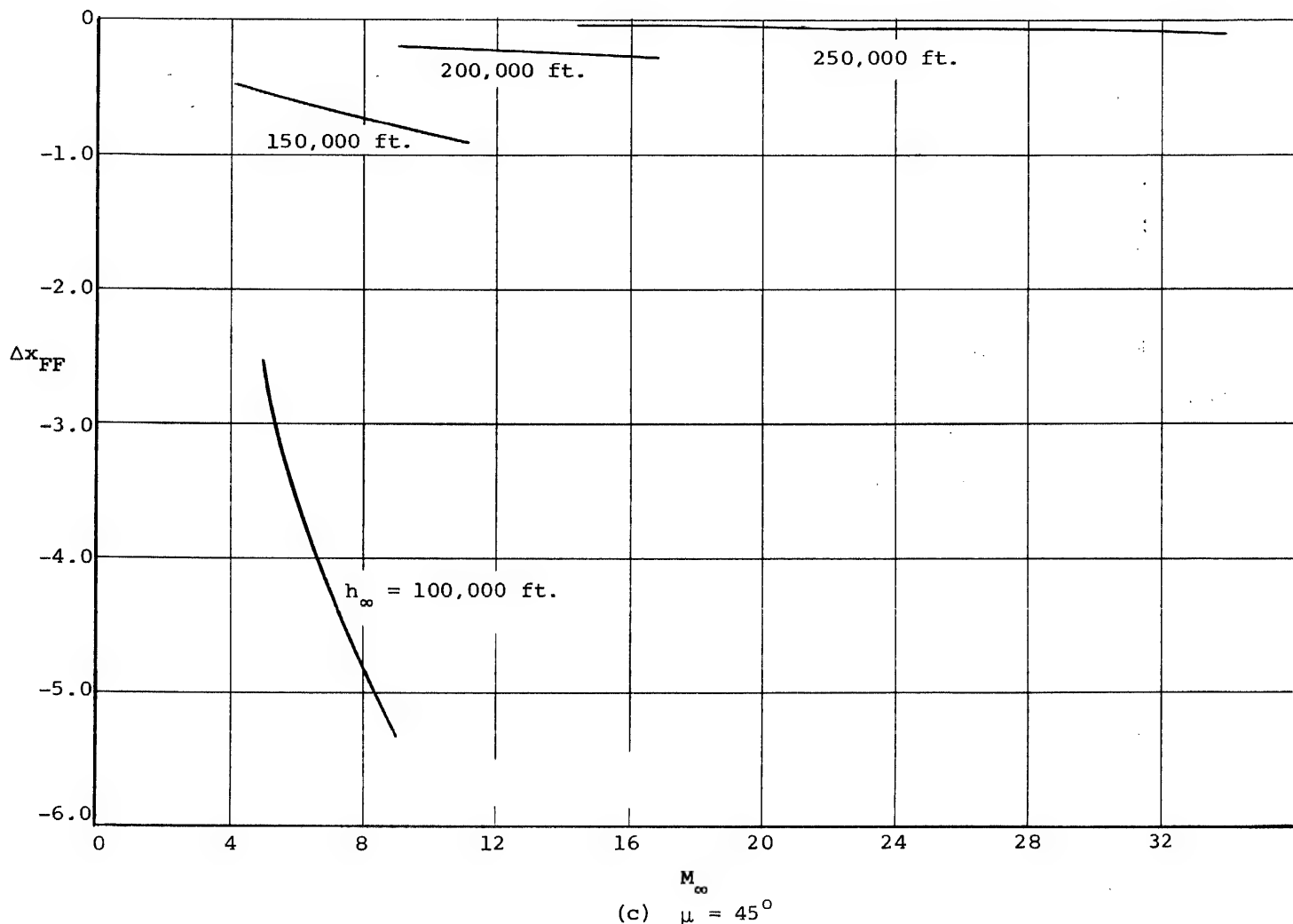


Figure VIII-8.- Concluded.

Approved For Release 2000/04/12 : CIA-RDP67B00657R000300070001-0

Approved For Release 2000/04/12 : CIA-RDP67B00657R000300070001-0

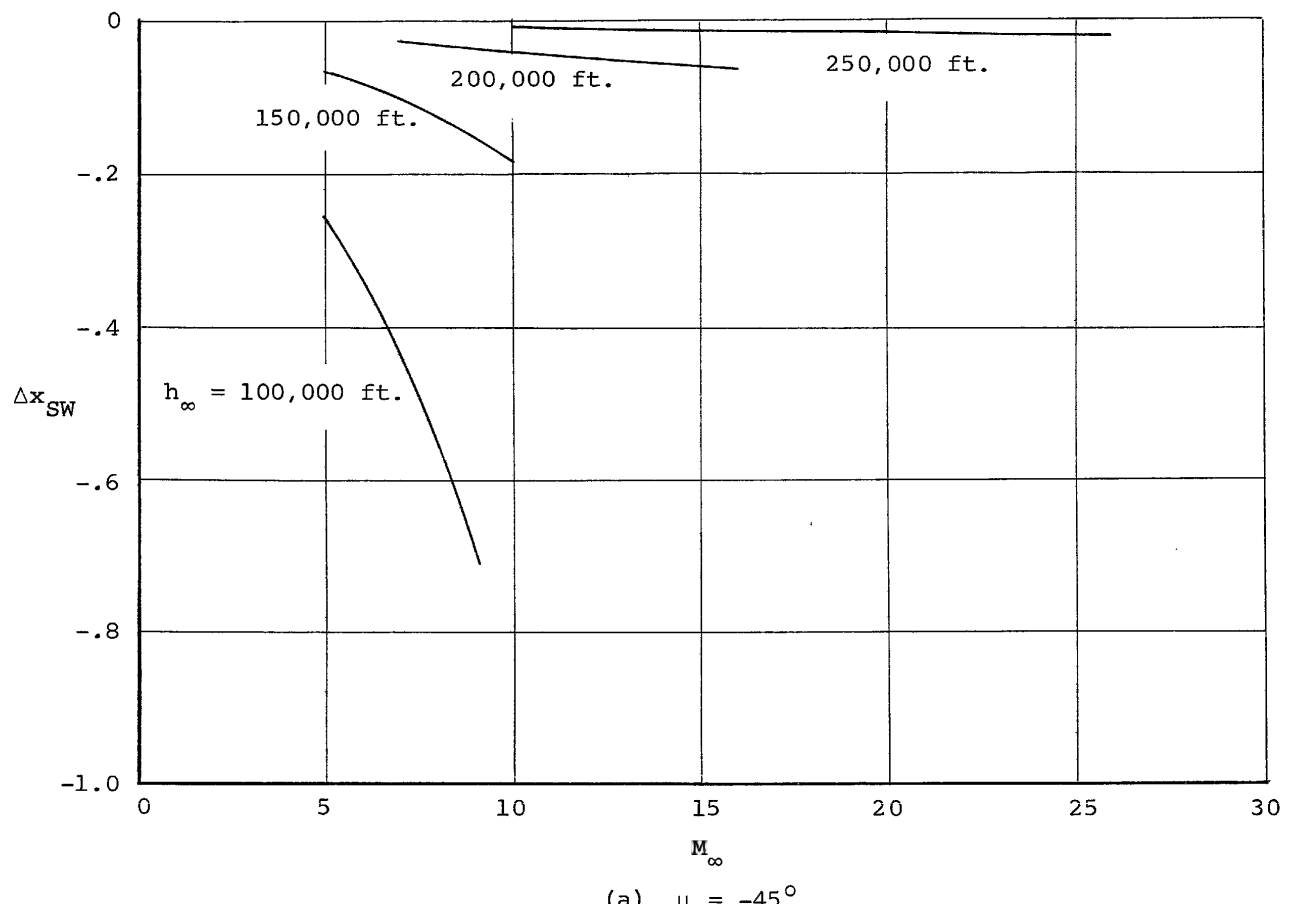


Figure VIII-9.- Ground displacements caused by shock wave. Blunt cone, $\theta_c = 5^\circ$.

Approved For Release 2000/04/12 : CIA-RDP67B00657R000300070001-0

Approved For Release 2000/04/12 : CIA-RDP67B00657R000300070001-0

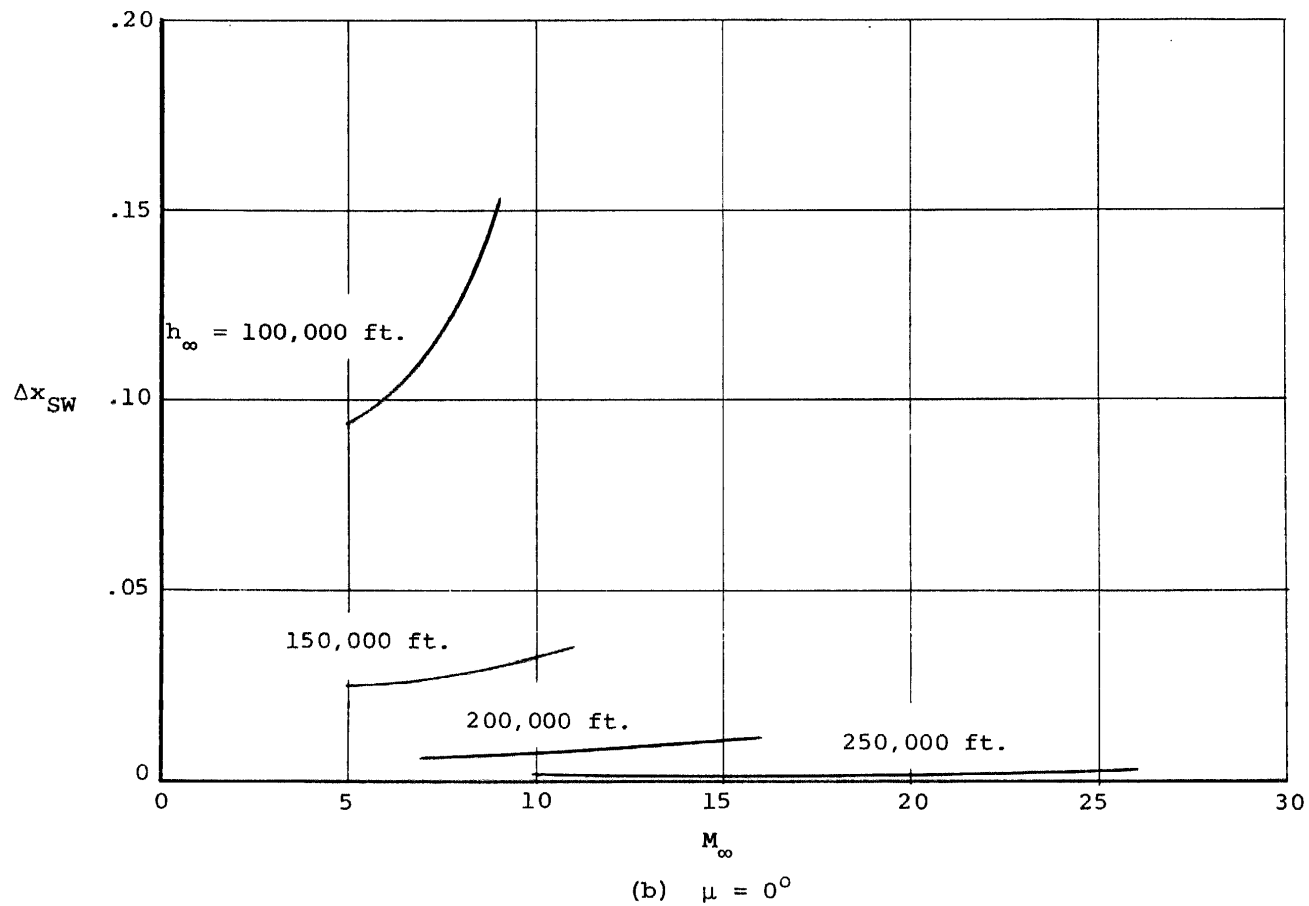


Figure VIII-9.- Continued.

Approved For Release 2000/04/12 : CIA-RDP67B00657R000300070001-0

Approved For Release 2000/04/12 : CIA-RDP67B00657R000300070001-0

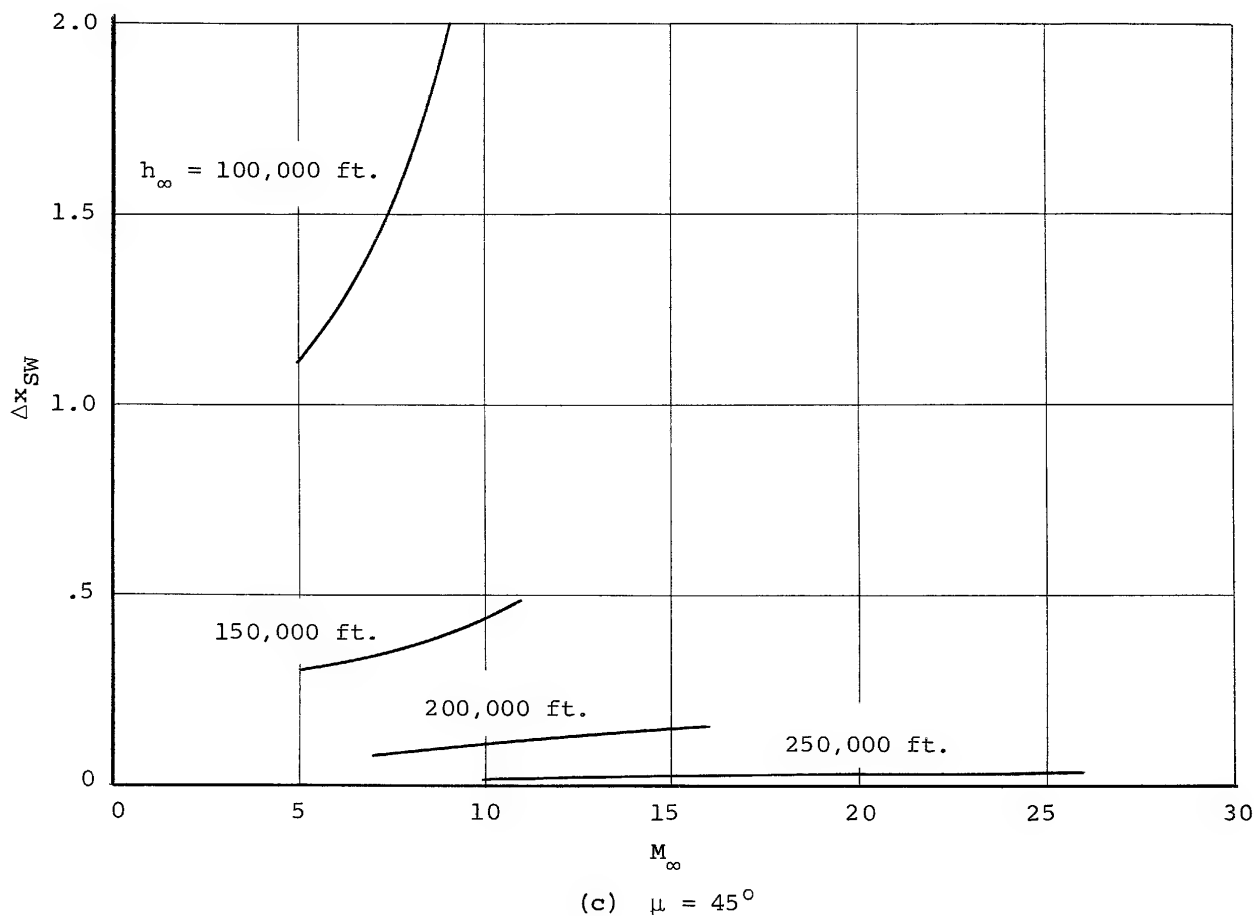


Figure VIII-9.- Concluded.

Approved For Release 2000/04/12 : CIA-RDP67B00657R000300070001-0

Approved For Release 2000/04/12 : CIA-RDP67B00657R000300070001-0

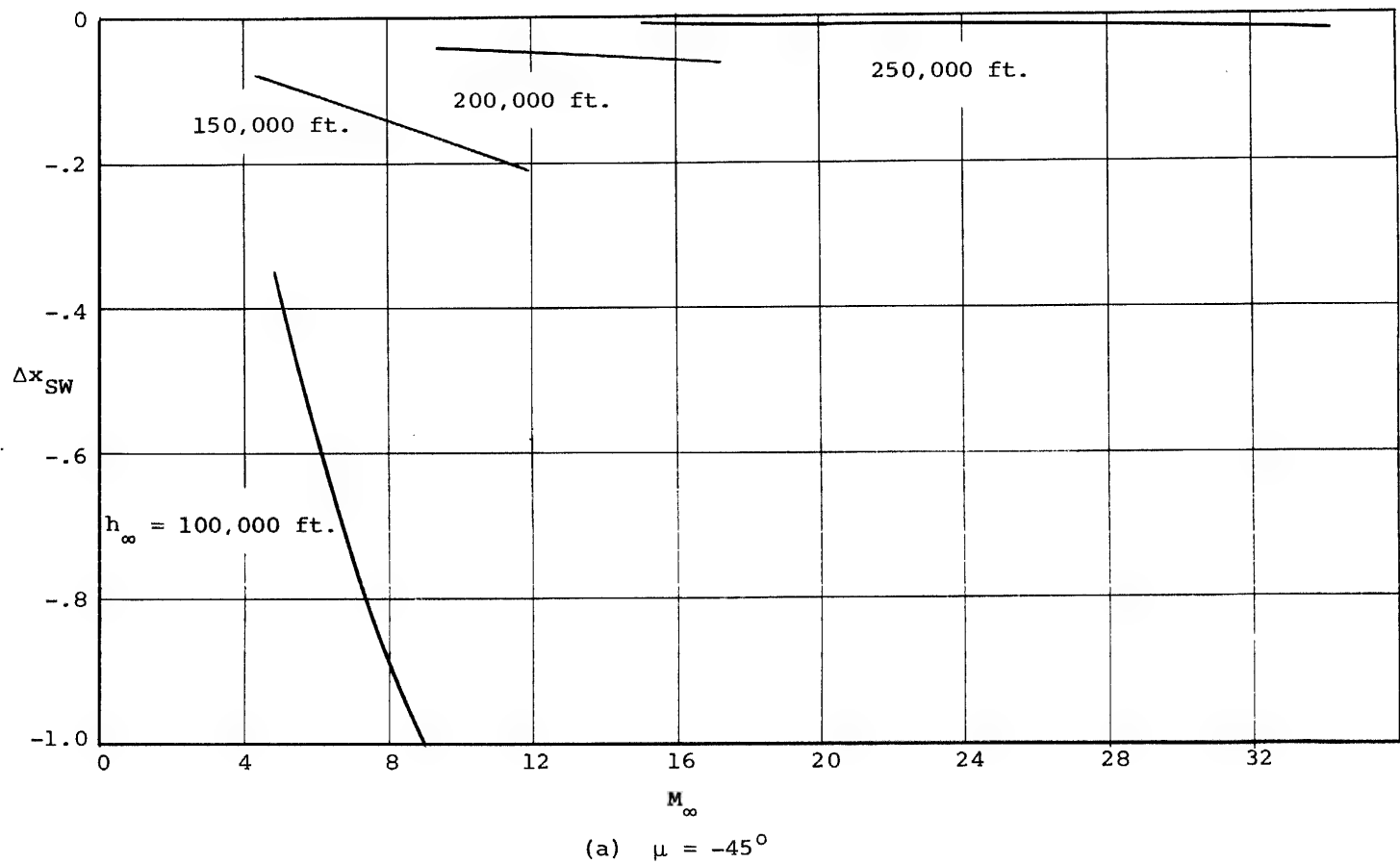


Figure VIII-10.- Ground displacements caused by shock wave. Swept wing, $\alpha = 20^\circ$.

Approved For Release 2000/04/12 : CIA-RDP67B00657R000300070001-0

Approved For Release 2000/04/12 : CIA-RDP67B00657R000300070001-0

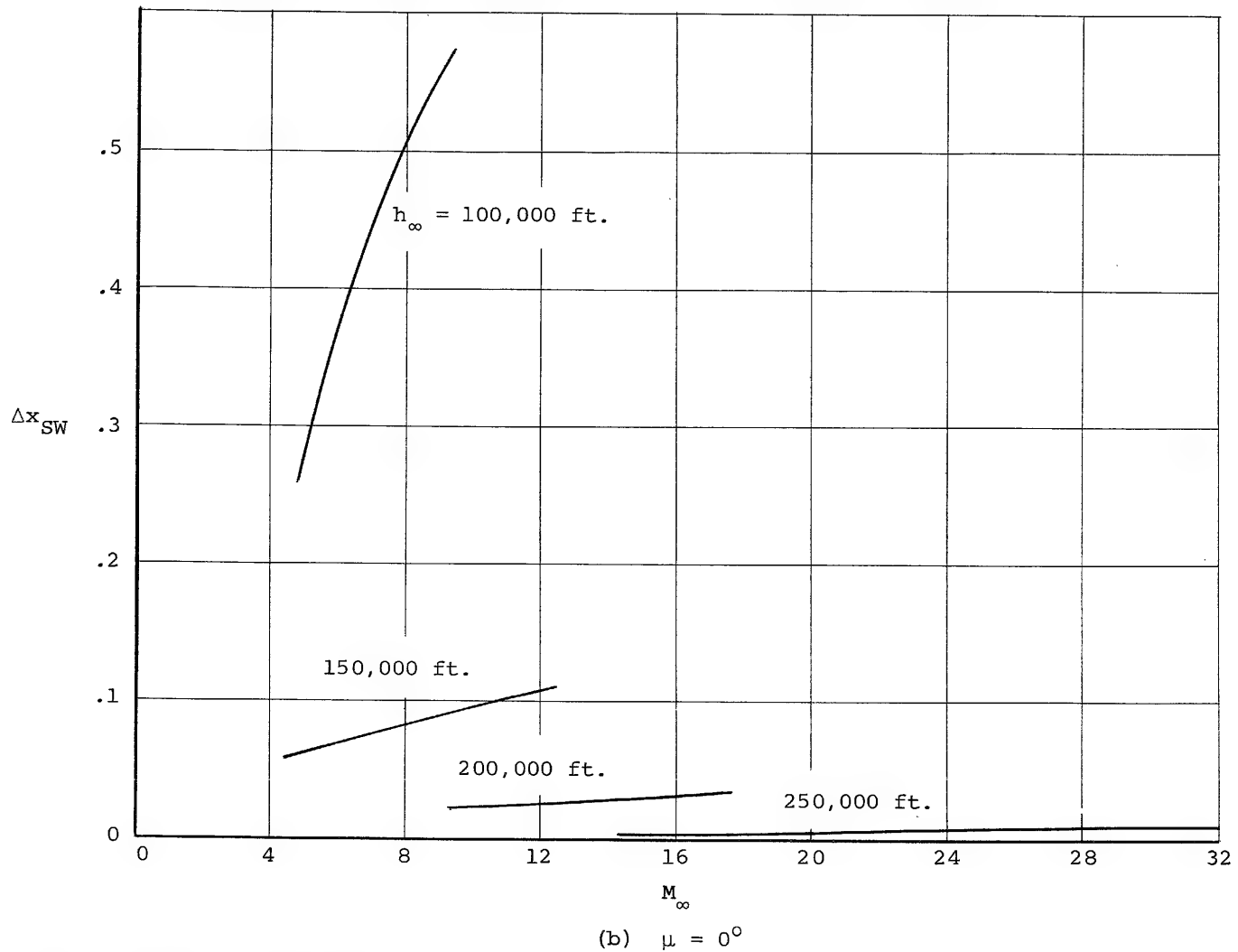
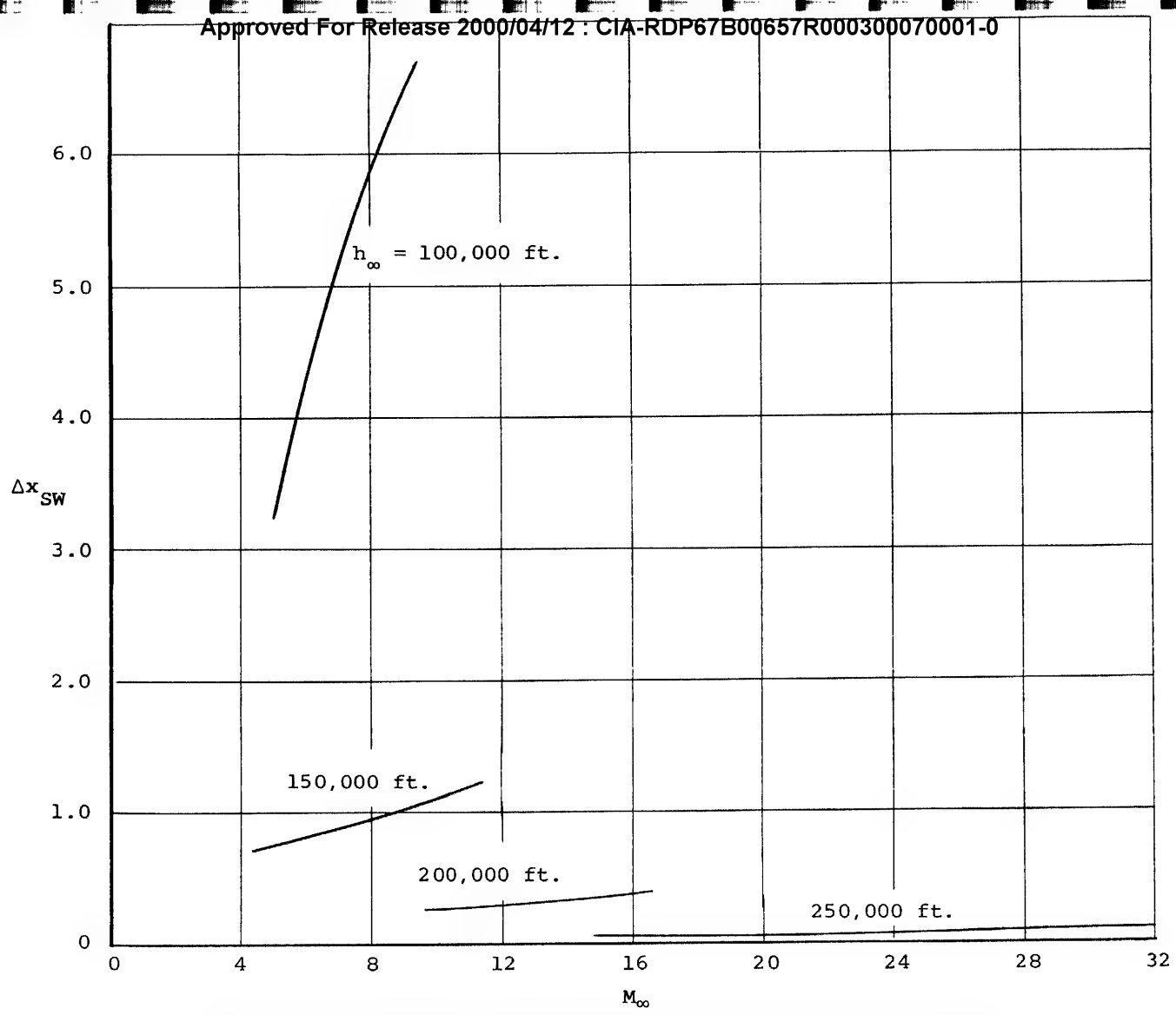


Figure VIII-10.- Continued.

Approved For Release 2000/04/12 : CIA-RDP67B00657R000300070001-0



Approved For Release 2000/04/12 : CIA-RDP67B00657R000300070001-0

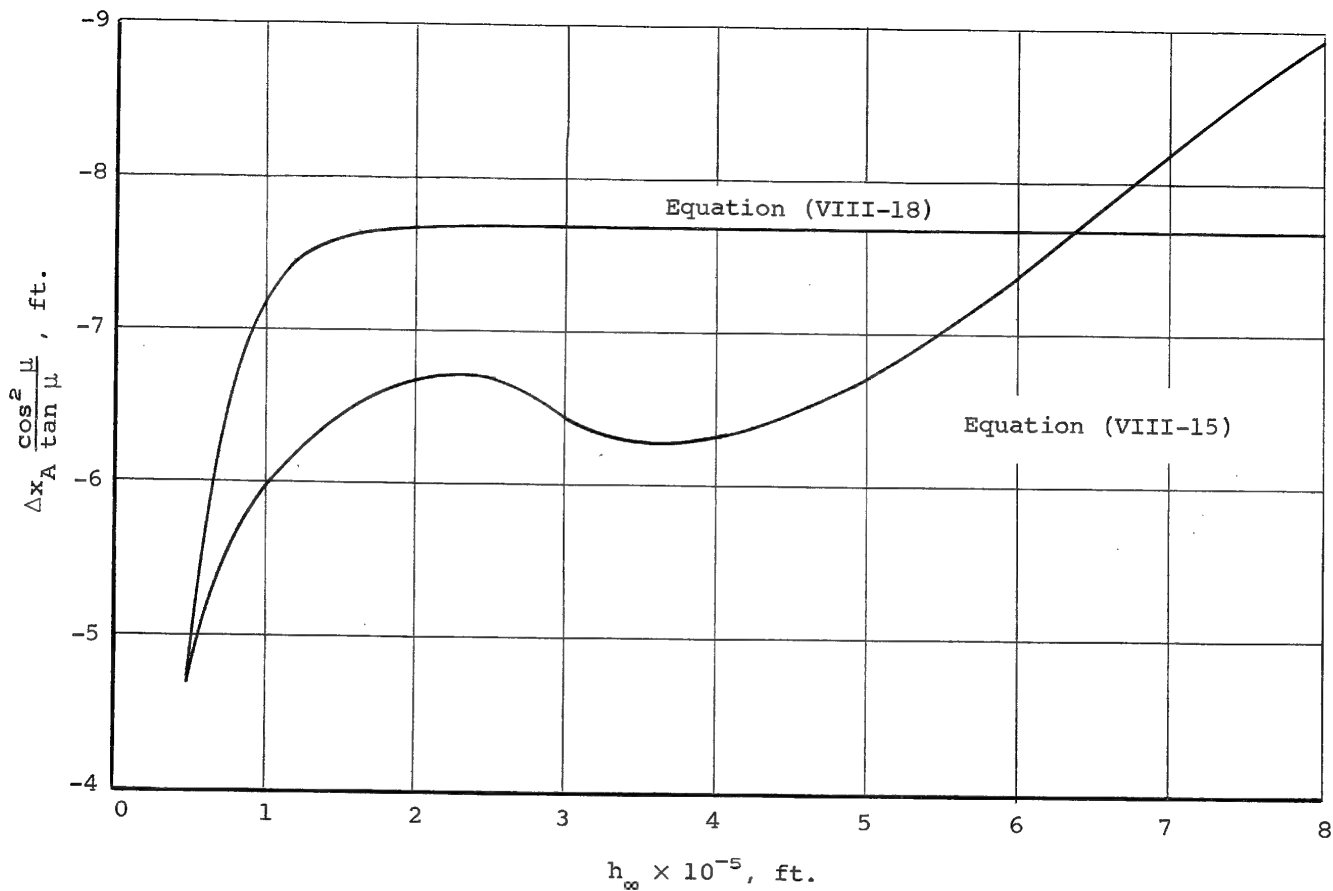


Figure VIII-11.- Comparison of methods for determining ground displacement due to atmospheric refraction.

Approved For Release 2000/04/12 : CIA-RDP67B00657R000300070001-0

PART IX: MAPPING AND RECONNAISSANCE FROM HYPERSONIC VEHICLES

INTRODUCTION

The purpose of this part is to consider collectively the various environmental effects which have been treated in the preceding parts to see how they influence the suitability of various regions in the Mach number, altitude diagram for mapping or reconnaissance. Systematic calculations have been made of various effects for various combinations of Mach numbers and altitudes which span the corridors of continuous flight for the winged and nonwinged hypersonic vehicles considered herein. These corridors of continuous flight are the approximate regions in the $M - h$ diagram¹ where the vehicles must operate if they are to be able to generate enough lift to sustain flight and withstand the structural temperatures due to aerodynamic heating. From the standpoint of mapping and reconnaissance, we are interested in knowing what limiting lines appear on the $M - h$ diagram with respect to the following items:

- (1) Window temperatures
- (2) Window temperature difference
- (3) Contrast reduction due to luminosity
- (4) Refraction errors
- (5) Resolution losses induced by turbulent boundary layers

¹The Mach number, altitude diagram is henceforth termed the $M - h$ diagram

We will consider these items in order to assess their importance in limiting the usefulness of various regions of the corridor of continuous flight for mapping and reconnaissance purposes. The prospects will be examined for alleviating any deleterious effects encountered. In particular, configurational changes which might alleviate such effects will be of interest.

While the results of the present study are necessarily for specific configurations, both winged and nonwinged types have been considered in the interests of generality. What general conclusions can be drawn from these specific configurations will be made.

We will be concerned exclusively with downward viewing.

SYMBOLS

A reference area for drag, ft^2
 B_H brightness of horizon, watts/cm^2 - steradian-micron
 B_G brightness of ground, watts/cm^2 - steradian-micron
 B_L brightness of luminous layer, watts/cm^2 - steradian-micron
C inherent ground contrast
 C' ground contrast at window, no luminosity
 C'' ground contrast at window, luminosity
 C_D drag coefficient
h altitude, ft
 M_∞ flight Mach number
 T_s stagnation temperature
 T_o outer window temperature
 T_i inner window temperature
 ΔT $(T_o - T_i)$
 Δx apparent ground displacement due to refraction
W vehicle weight, lbs
 α angle of attack, deg
 β_o^L see Part VI
 μ nadir angle, deg, or wavelength, microns
 γ sun zenith angle, deg

DISCUSSION

Corridors of Continuous Flight

As reference regions we will be concerned with corridors of continuous flight in the $M - h$ diagram. These corridors will be regions with respect to which the various deleterious or beneficial phenomena may be referenced. Consider the corridor of continuous flight described by Figure IX-1(a) for the nonwinged vehicle, the blunt cone. The actual corridor chosen is somewhat arbitrary. For instance, the lower boundary is taken from Figure II-2 as that for a stagnation temperature of 3000°F . We could have chosen a lower value, but we then would have practically no corridor at certain Mach numbers. This value is probably beyond the present state of the art with radiation cooling techniques, but is within the capability of ablation cooling. Also, increasing the nose radius will decrease the stagnation temperature for a given altitude and Mach number. The upper boundary is also taken from Figure II-2 for a $W/C_D A$ of 3.22, a low value of this parameter. Our reference corridor for the blunt cone will correspond to the foregoing boundaries throughout this part of the report.

The reference corridor for the winged vehicle; namely, the blunt swept wing, is shown in Figure IX-1(b), as taken from Figure II-3. The lower boundary corresponds to a leading-edge temperature of 3000°F . This value is somewhat beyond the present state of the art for radiation materials but is within that for

ablation materials. The upper boundary is an equilibrium glide trajectory for a wing loading of 20 lbs/ft² and an angle of attack of 20 degrees. All calculations for the winged vehicle are for this angle of attack. The upper boundary can be raised by increasing the angle of attack or decreasing the wing loading.

It is emphasized that these reference corridors are arbitrary, and precise corridors are not needed for the present purposes. The corridors are somewhat broader than presently feasible at the present state of the art for continuous flight. It is possible to operate outside of the corridors for short periods of time.

External Window Temperature

One of the critical questions in hypersonic flight is that of external window temperature. If the temperature exceeds certain values, depending on the glass, it can induce the following effects:

- (1) Cause softening of the glass
- (2) Cause breaking of the glass by temperature gradients
- (3) Radiate sufficiently to interfere with vision through it or with photography through it

The outer window temperatures are shown in Figure IX-2(a) for the nonwinged vehicle, and in Figure IX-2(b) for the winged vehicle as taken from the results of Part V. For the nonwinged vehicle, it is seen that the window temperature is about 1200°R

at the lower boundary of the corridor of continuous flight. It is clear that quartz glass and other high-temperature glass can withstand this temperature level for sustained periods. The window temperature which is lower than the stagnation-point temperature is due to the smaller inclination of the window to the airstream, a geometric effect which reduces the air density at the window location. Moving the window downstream would cool it further as long as the boundary layer remains laminar.

The results for the winged vehicle in Figure IX-2(b) show values of the window temperature over 2000° R. This temperature can be withstood by quartz glass. Whether or not radiation from the glass itself would seriously interfere with optical viewing at these glass temperatures has not been determined herein. If the winged vehicle were to operate at still higher angles of attack, the density on the lower surface would be increased and the glass temperature would be correspondingly increased. It thus appears that special glass will be required in the winged vehicle.

Window Temperature Differences

The temperature difference across the present $\frac{1}{2}$ -inch thick window is of importance for several reasons. First, it is directly proportional to the heat being conducted into the camera cavity per unit time from unit window area. Secondly, the refraction errors due to the lens effect of the window induced by temperature gradients are directly proportional to

the temperature differences, as shown by Equation (VI-8) of the Phase I final report. Little can be done to minimize these errors unlike those due to the pressure difference across the window which can be minimized by venting to the outside. Thirdly, temperature differences may cause failure of the window through excessive stresses.

The actual temperature differences encountered by the present nonwinged and winged vehicles are shown in Figure IX-3. For the nonwinged vehicle, a temperature difference of 80° F near the lower boundary of the corridor of continuous flight can be withstood by many types of glass. For the winged vehicle, considerably larger temperature differences exist. Such is to be expected as a consequence of the greater densities on the lower surface of the winged vehicle. Larger temperature differences might be anticipated for larger angles of attack.

If it is necessary to cover the window to avoid excessive peak temperatures and then to uncover it for viewing, the additional problem of thermal shock arises. Much larger temperature gradients will be induced in the window than the present ones which are for the state of thermal equilibrium. The possibility thus arises of breakage of windows by thermal shock.

Luminosity and Contrast

The way in which luminosity of the air influences apparent contrast of ground objects viewed through the luminous air layer

is a complicated problem from the physical point of view. An attempt has been made in Part VI to put this question on a rational basis. In this part we will examine the question of what the ground contrast C must be to obtain a certain contrast C'' at the window. A number of parameters affect this result, as the following list demonstrates:

- (a) Terrain: forest, desert, snow, etc.
- (b) Sky conditions: clear or overcast
- (c) Wavelength: 0.4μ to 0.7μ
- (d) Altitude: $h > 100,000$ ft
- (e) Configuration: blunt cone or blunt swept wing
- (f) Nadir angle: $\mu = -45^\circ, 0, -45^\circ$
- (g) Sun zenith angle: $\gamma = 0^\circ, 60^\circ$
- (h) Mach number: variable
- (i) Angle of attack: $\alpha = 0^\circ$ (blunt cone)
 $\alpha = 20^\circ$ (blunt swept wing)

Following the calculative example of Part VI, the required ground contrast C has been calculated to produce a contrast $C'' = 0.02$ at the window for various Mach numbers and altitudes for the nonwinged and winged vehicles. The following parameters have been chosen for the calculations:

Terrain: Forest

Sky: Clear

Wavelength: 0.4 microns

Nadir angle: 0°

Sun zenith angle: 0°

Angle of attack: 0° (cone), 20° (wing)

The calculated values of C at the various points are shown in Figure IX-4 for both the nonwinged and winged vehicles.

The results for the nonwinged vehicle show that the reduction in contrast from the ground to the vehicle is approximately 57 percent for all altitudes above about 50,000 feet without including the effects of luminosity. This means that the ground contrast would have to be 0.047 on the ground to be 0.02 at the window without any effects of luminosity. Increases in required ground contrast above 0.047 are due to air luminosity. It is quite interesting that the nonwinged vehicle does not suffer from contrast reduction as a result of air luminosity anywhere in its corridor of continuous flight.

The results for the winged vehicle indicate results quite different from those for the nonwinged vehicle. In the first place, quite high ground contrasts are required in the corridor of continuous flight near Mach numbers of 20. By flying close to the upper boundary, the required ground contrast can be minimized. The required values of C are larger for the winged vehicle than for the nonwinged vehicle because of the higher densities, as well as high temperatures, of the luminous air under the vehicle. Aerodynamically, the increase is due principally to the larger angle of attack (20°) of the surface in which the window of the winged vehicle is mounted.

The angle of attack of the surface in which the window of the nonwinged vehicle is mounted is 5° . Higher angles of attack than 20° will probably cause further increases in the deleterious effects of luminosity as it decreases the ability to take aerial photography.

One point of interest is whether the required contrast C is strongly dependent on wavelength. To investigate this fact the calculations were redone for the winged vehicle with a wavelength of 0.7 microns. The results are shown in Figure IX-5. The contrast reduction without luminosity C'/C is 0.89 for this case because of the lower scattering coefficient for the longer wavelength. The required ground contrast to produce $C'' = 0.02$ at the window is 0.023. The figure shows that the effect of luminosity in increasing the required ground contrast is negligible for this case. This favorable result is due to the following causes:

- (a) The solar irradiance has increased more than 50 percent in going from 0.4 microns to 0.7 microns so that the ground is brighter.
- (b) The spectral reflectivity for a forest has increased from 0.033 to 0.140 for this change in wavelength, further increasing the ground brightness.
- (c) The scattering coefficient is much lower for the high wavelength so that there is less contrast reduction as a result of the atmosphere.

(d) The brightness of the luminous layer at $M = 20$ and $h = 100,000$ feet has changed from 3.2×10^{-1} watts/cm 2 - steradian-micron to 2.3×10^{-2} watts/cm 2 - steradian-micron at 0.7 microns so that the luminous layer is not so bright.

It is interesting to determine which case requires the greatest ground contrast to produce a given contrast at the window. Anything which increases the atmospheric scattering reduces the ground brightness. Also, increasing the brightness of the luminous air layer will increase the required ground contrast. Reductions in C'/C are greatest for large values of $\beta_o L$ and B_H/B_G . The value of $\beta_o L$ is nearly constant at a maximum value of 0.28 for 0.4 microns above an altitude of about 50,000 feet. The value of B_H/B_G is maximum for a forest with an overcast sky. The value of C''/C is lowest for the largest $\beta_o L$ and B_L/B_G . Changes in B_L and B_G are both important in this respect. The value of B_L is increased by using a winged rather than a nonwinged vehicle, looking backwards at $\mu = 45^\circ$ through a greater length of luminous layer, using a wavelength of 0.4 microns instead of 0.7 microns for which the air is less luminous, and using low altitudes and high Mach numbers. The value of B_G is a minimum at a large zenith angle, that is, when the sun is low in the sky. The solar irradiance

is also less for the smaller wavelengths. The spectral reflectivity is least for a forest at the lower wavelength. These factors all add up to produce the greatest required ground contrast for the following set of conditions:

- (a) Terrain: Forest
- (b) Sky: Overcast
- (c) Wavelength: 0.4 micron
- (d) Altitude: $h > 50,000$ ft
- (e) Configuration: Winged vehicle
- (f) Nadir angle: $\mu = 45^\circ$ rearward
- (g) Zenith angle: $\gamma = 60^\circ$ (sun low in sky)
- (h) Mach number: Large
- (i) Angle of attack: Large

The contrast 'C'' used herein refers to that existing at the outer face of the window. There is a further reduction in contrast due to passage of the light through the window, particularly at high window temperatures. This problem has not been analyzed herein.

Refraction Errors

The principal sources of refraction error are lens effects of the window due to temperature gradient or pressure gradient, the flow field about the vehicle, and, finally, the atmosphere. Another source of refraction error can be the difference in air density between the inner surface of the camera window and its outer surface. This component is readily calculated and

will not be included herein. The refraction error being considered is the apparent displacement of a ground point due to refraction by the above sources. We will confine our attention to the vertical plane of symmetry and look backwards at a nadir angle of $+45^{\circ}$. This condition yields the largest ground displacements Δx for the conditions considered in Part VIII.

In Figure IX-6, the ground displacements due to the window temperature differences (shown in Figure IX-3) are shown on the $M - h$ diagram for both nonwinged and winged vehicles. The values of Δx are negative since the rearward looking rays are bent forward and because the positive x -axis is rearward against the flight direction. For the winged vehicle a ground displacement of about 6 feet seems to be the maximum within the corridor of continuous flight. It is interesting to note that the lines of constant displacements are nearly parallel to the lines of constant temperature difference in Figure IX-3. Furthermore, the displacements should be proportional to the temperature difference to the extent that the coefficient of expansion of the window material is not variable with temperature (i.e., Equation VI-5 of Phase I final report). Reference to Figures IX-2 and IX-3 also shows that the temperature differences are nearly constant for constant external window temperatures. Thus problems of window maximum temperature and problems of metric distortion due to window temperature effects are closely related.

In Figure IX-6(b), much larger apparent ground displacements occur for the winged vehicle than for the nonwinged vehicle. This is again the result of higher window temperatures and temperature differences and a larger incident angle for rearward viewing for the winged vehicle.

Generally speaking, at altitudes above 100,000 feet, the effect of the vehicle flow field including boundary layer and shock waves has a negligibly small effect on ground displacements compared to window temperature differences or atmospheric refraction. At 100,000 feet the window temperature effects and the flow field effects are about equal as the following table shows for the winged vehicle:

Mach number	6	8
Δx due to window temperature difference, Ft	-5.5	-10
Δx due to aerodynamic flow field, Ft	+2.3	+ 4

However, the flow field effects decrease as the density decreases for constant Mach number and become less significant at high altitudes. The atmospheric refraction contributes a ground displacement dependent on altitude and nadir angle only. From Figure VIII-11 for $\mu = 45^\circ$ we find that Δx is about 15 feet maximum and is constant above altitudes of about 150,000 feet.

Loss of Resolution Due to Turbulent Boundary Layers

Except for the winged vehicle at a 100,000-foot altitude, the boundary layers are all laminar for the present study. Hence, calculations of loss of resolution due to turbulent boundary layers were not made.

CONCLUSIONS

A systematic study has been made of the following factors, important for mapping and reconnaissance, from a nonwinged and a winged hypersonic configuration:

- (a) External window temperatures
- (b) Window temperature differences
- (c) Luminosity and contrast
- (d) Refractive errors (metric distortion)
- (e) Resolution loss due to turbulent boundary layers

With respect to the specific nonwinged configuration, it appears that mapping and reconnaissance are feasible from the standpoint of all of the above factors. However, the vehicle in question is designed for a low value of $W/C_D A$; namely, 3.2 with a stagnation temperature of about 3000°F maximum. Such a vehicle has a fairly narrow corridor of continuous flight, but mapping and reconnaissance should both be possible within the corridor. The best position within the corridor appears to be near its upper boundary on the basis of all the above

factors. Effects of window radiation, however, have not been studied.

For the specific winged vehicle studied herein, all of the factors listed above were more severe than for the non-winged vehicle. This result is principally due to mounting the window on an impact surface with a local angle of attack of 20°. For this angle of attack and the winged configuration it appears possible to perform successful reconnaissance in most of the corridor of continuous flight. One possible exception to this conclusion is the severe loss of contrast due to the luminous air layer for short wavelengths. At long wavelengths, 0.7 microns, these losses are small. If the present vehicle were to operate at higher angles of attack, it is anticipated that the deleterious effects of the environment would be intensified with respect to mapping. Satisfactory mapping is probably possible; however, the refraction errors will be fairly large because of the temperature-induced lens effect in the window.

It is stressed that these conclusions are based only on the environment effects included in the present study. For the winged vehicle deleterious effects of window radiation may occur since window temperatures exceed 2000°R. This possibility was not evaluated. Also, the present study includes no deleterious effects of ablation materials which may be used for heat protection. No unsteady heat-transfer effects have

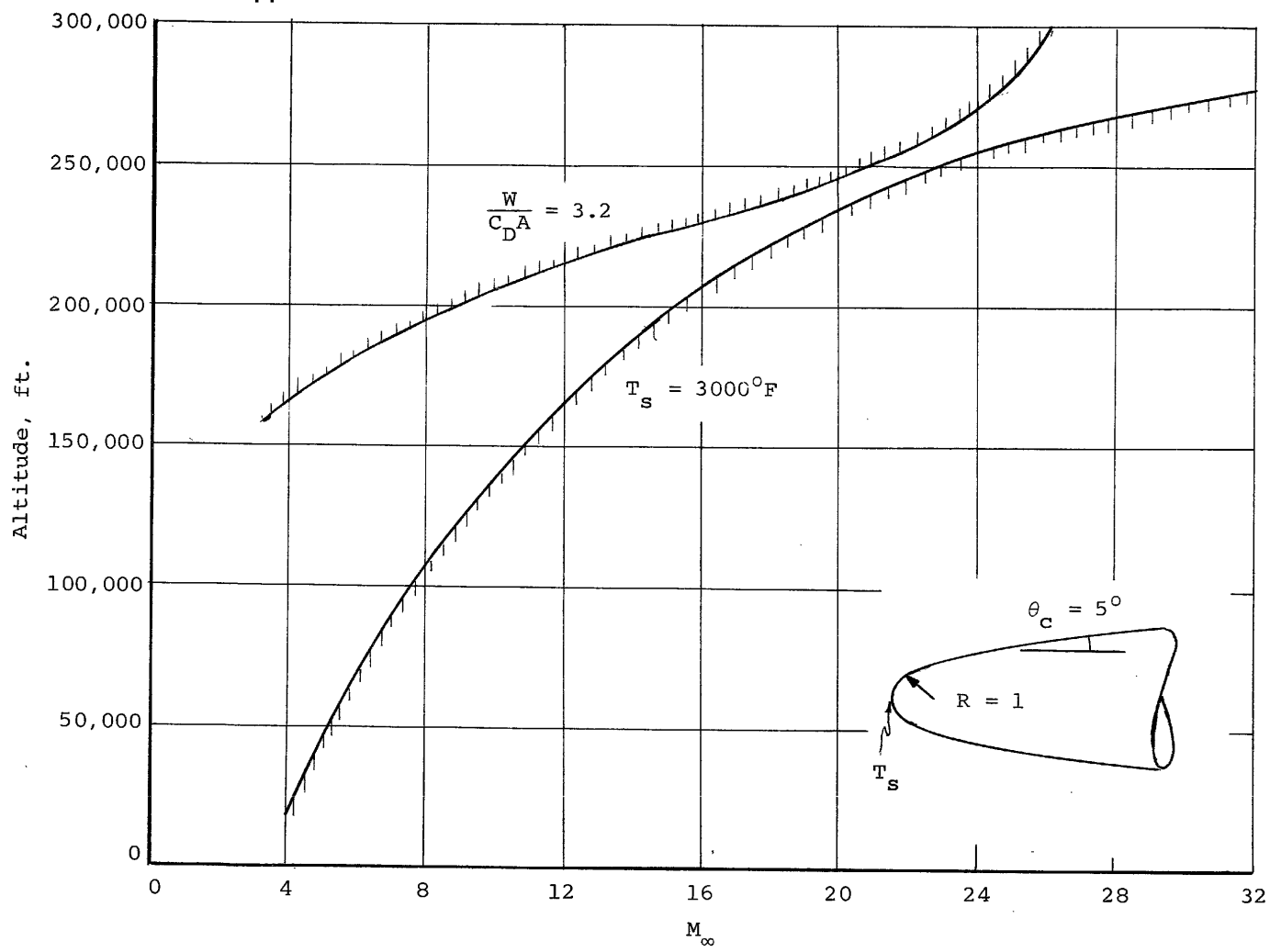
been considered. Such effects might include thermal shock induced by jettisoning a window heat protective cover.

RECOMMENDATIONS

The present study is not exhaustive and has raised a number of points which bear further investigation.

1. The present configurations should be studied over an angle-of-attack range to determine the importance of this parameter. Since it appears to be particularly important for a winged vehicle, at least this configuration should be studied.
2. Additional work needs to be done for "hot" windows.
The following problems should be examined:
 - (a) Contrast reduction caused by radiation from the window itself
 - (b) Thermal stresses in the glass, in particular thermal shock
3. The luminosity calculations presented in this report are only fragmentary and need extending.
4. The problems of upward viewing encountered by navigation systems utilizing star tracking need investigation.
5. Generally speaking, a study similar to the present should be made to assess the importance of the environment on infra-red and radar photography.

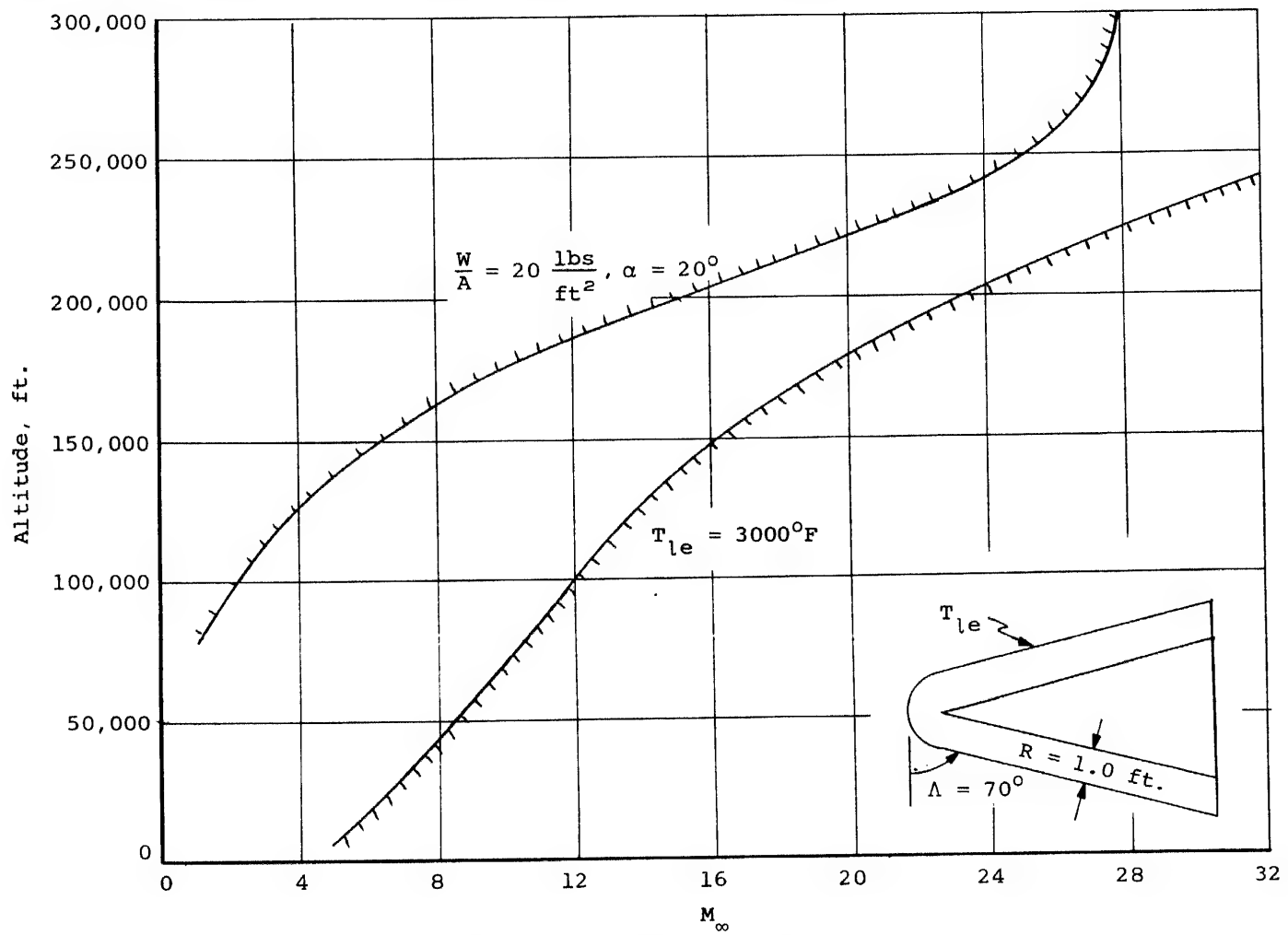
Approved For Release 2000/04/12 : CIA-RDP67B00657R000300070001-0



(a) Nonwinged vehicle, blunt cone

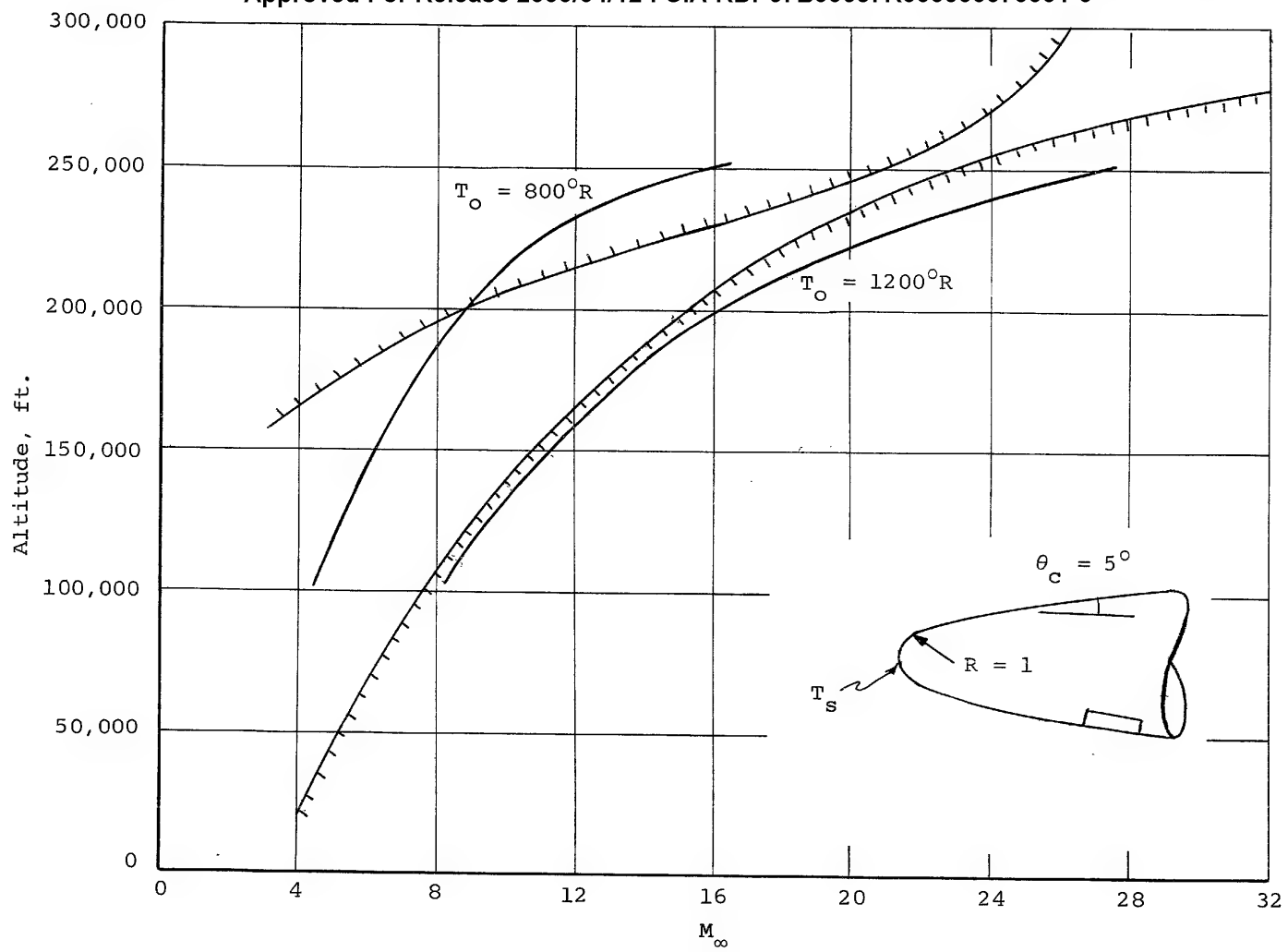
Figure IX-1.- Reference corridors of continuous flight.

Approved For Release 2000/04/12 : CIA-RDP67B00657R000300070001-0



(b) Winged vehicle, blunt swept wing

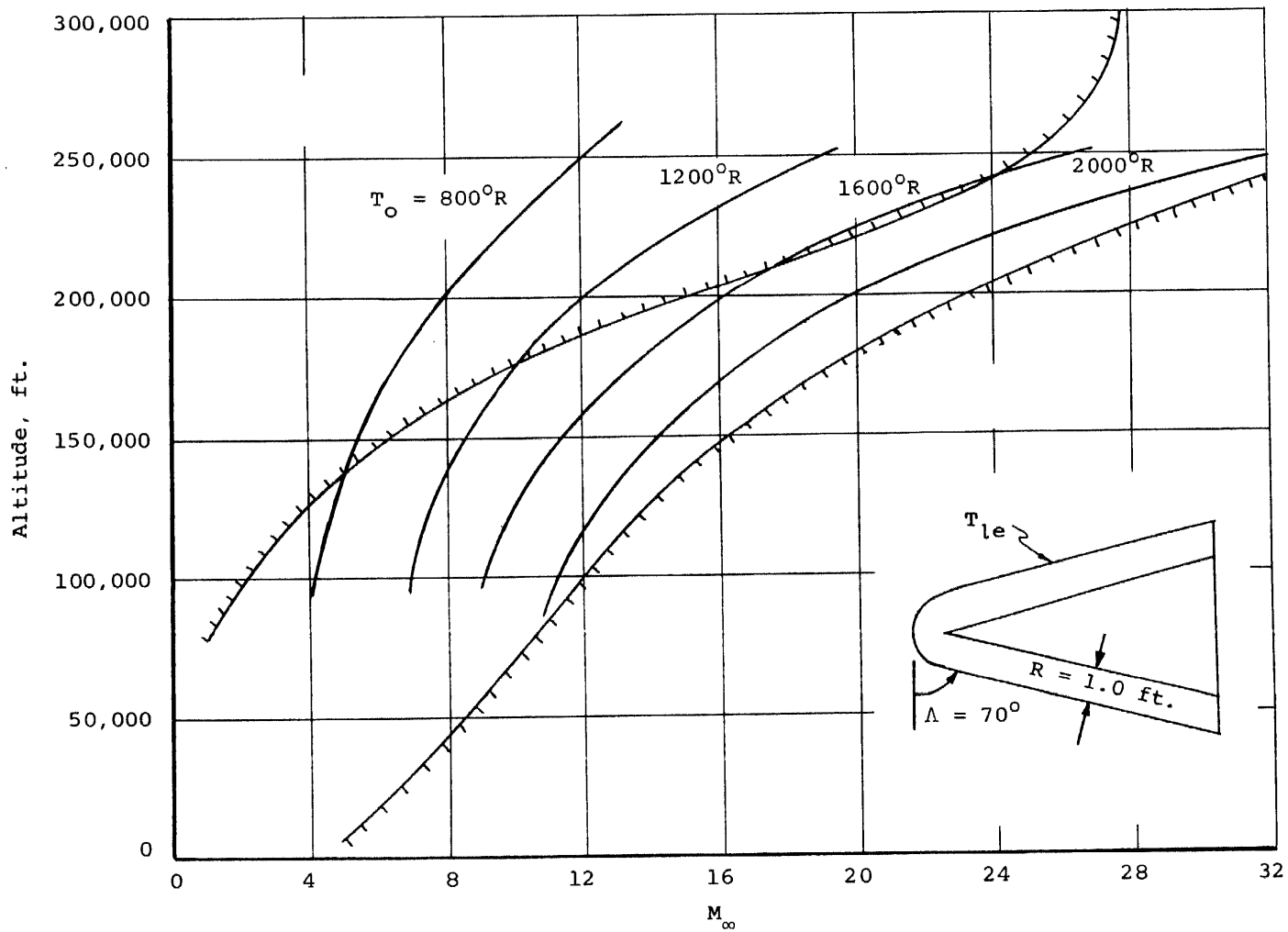
Approved For Release 2000/04/12 : CIA-RDP67B00657R000300070001-0



(a) Nonwinged vehicle

Figure IX-2.- External window temperature, T_s

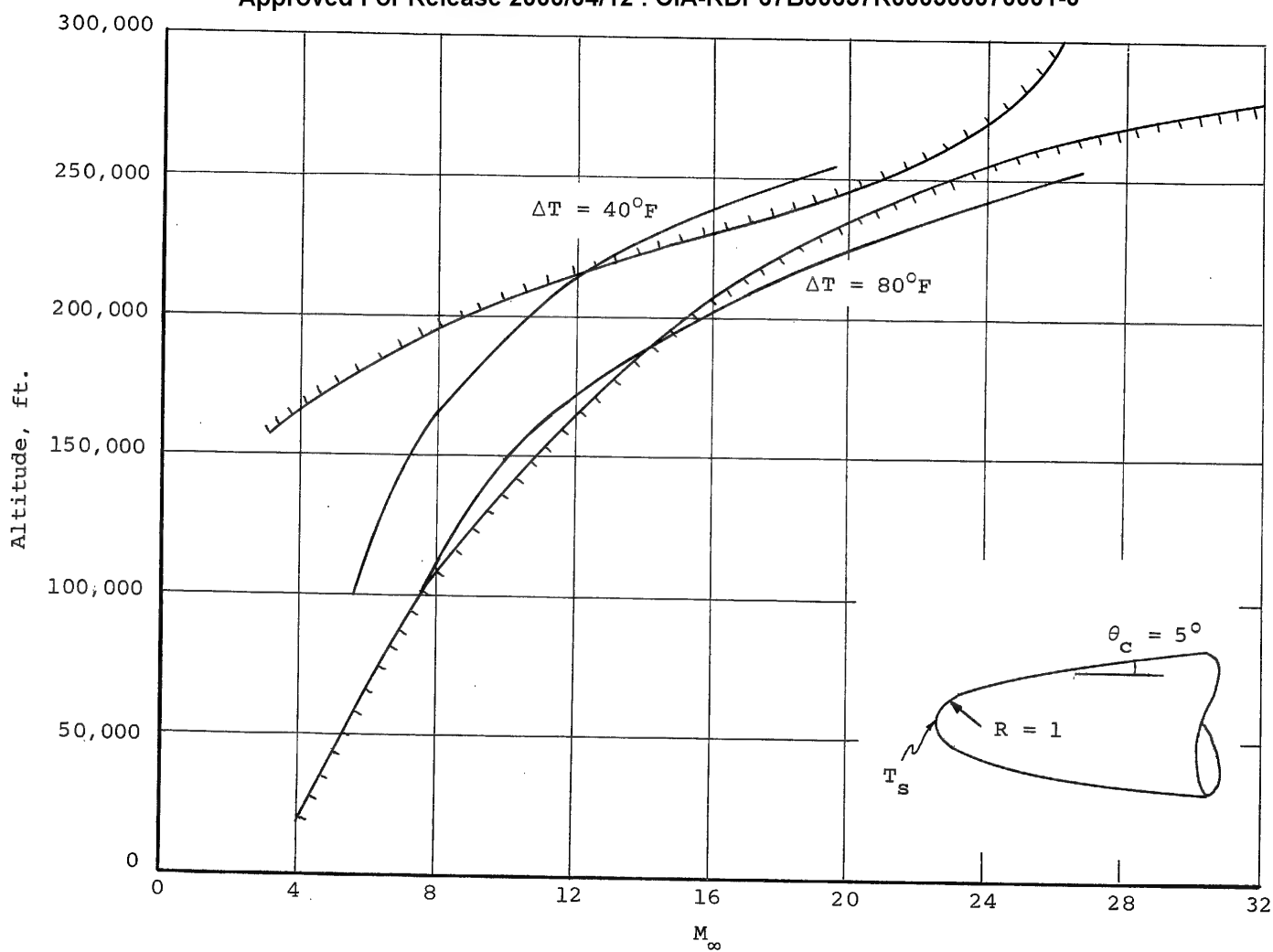
Approved For Release 2000/04/12 : CIA-RDP67B00657R000300070001-0



(b) Winged vehicle, $\alpha = 20^{\circ}$

Figure IX-2.- Concluded.

Approved For Release 2000/04/12 : CIA-RDP67B00657R000300070001-0



(a) Nonwinged vehicle

Figure IX-3.- Window temperature differences.

Approved For Release 2000/04/12 : CIA-RDP67B00657R000300070001-0

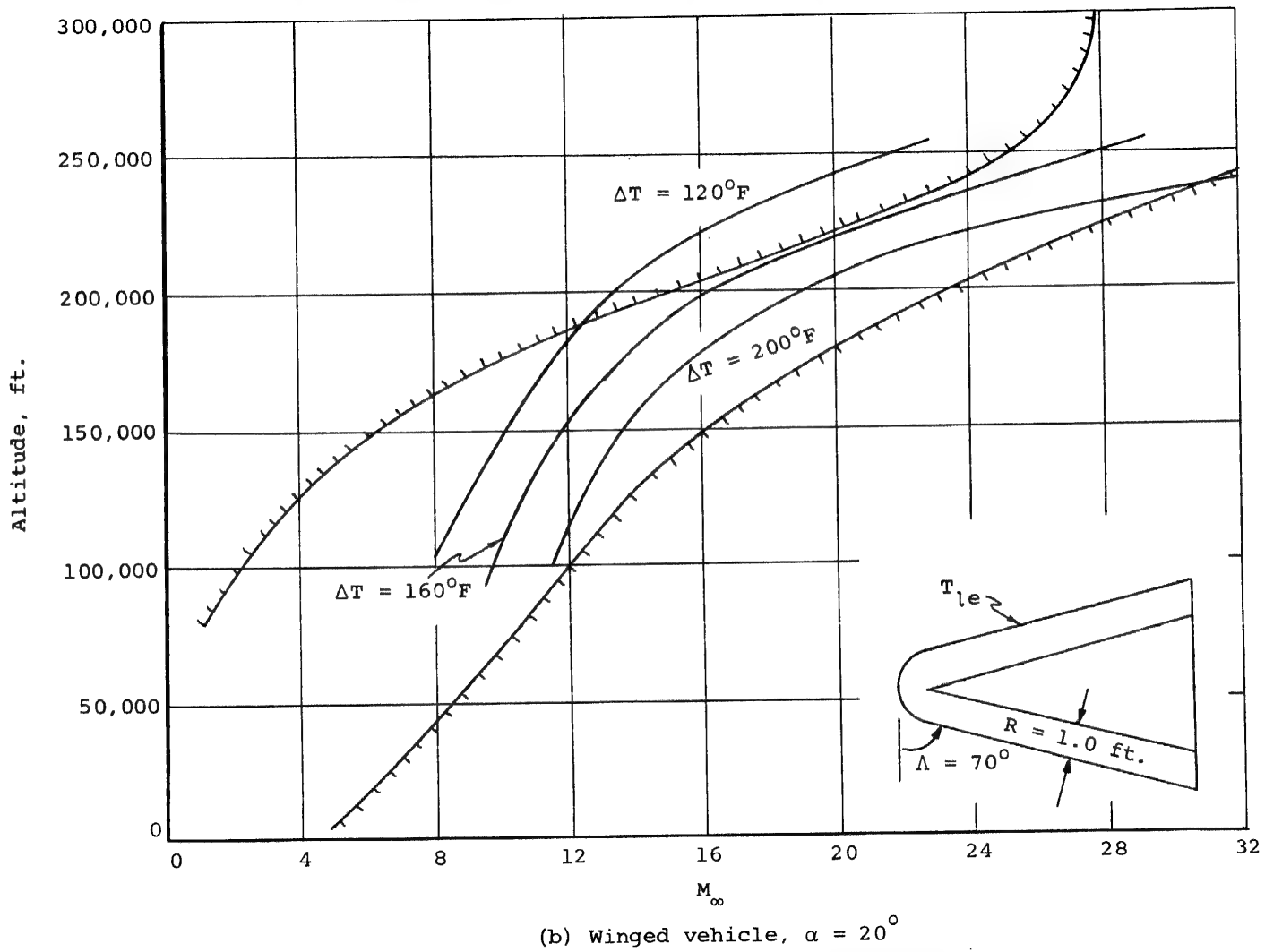
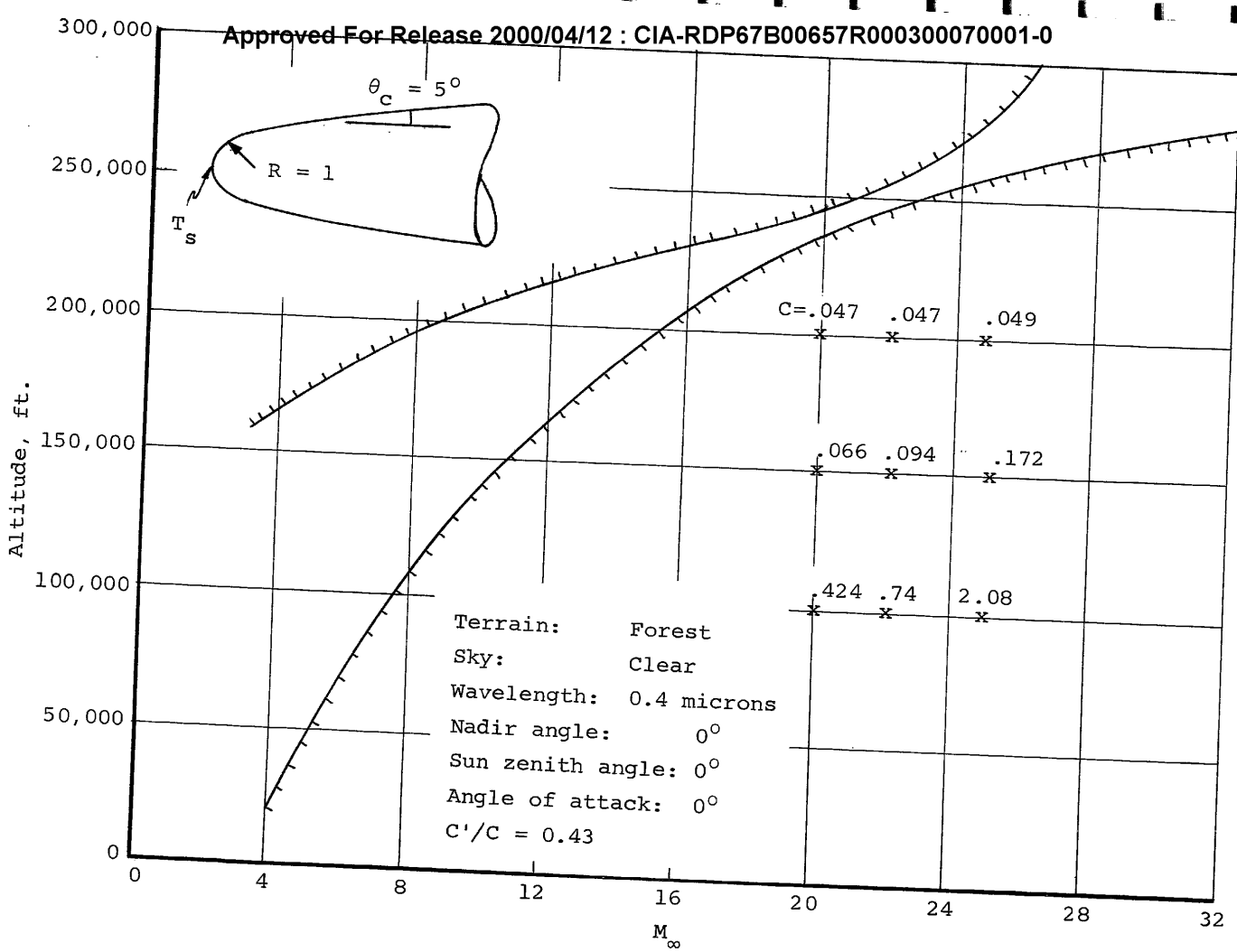
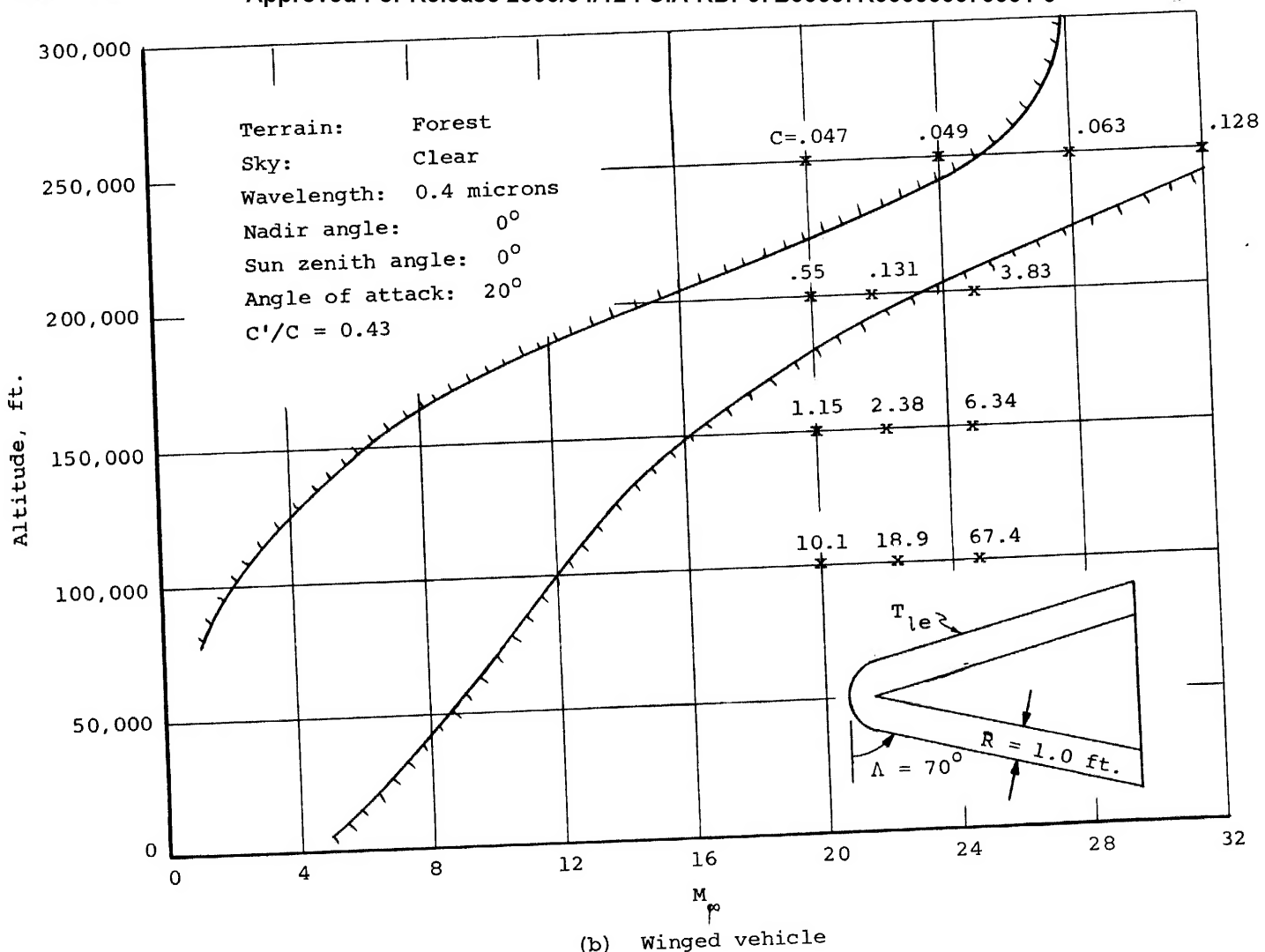


Figure IX-3.- Concluded



(a) Nonwinged vehicle

Figure IX-4.- Required ground contrast to produce $C'' = 0.02$ at window at 0.4 microns wavelength.



Approved For Release 2000/04/12 : CIA-RDP67B00657R000300070001-0

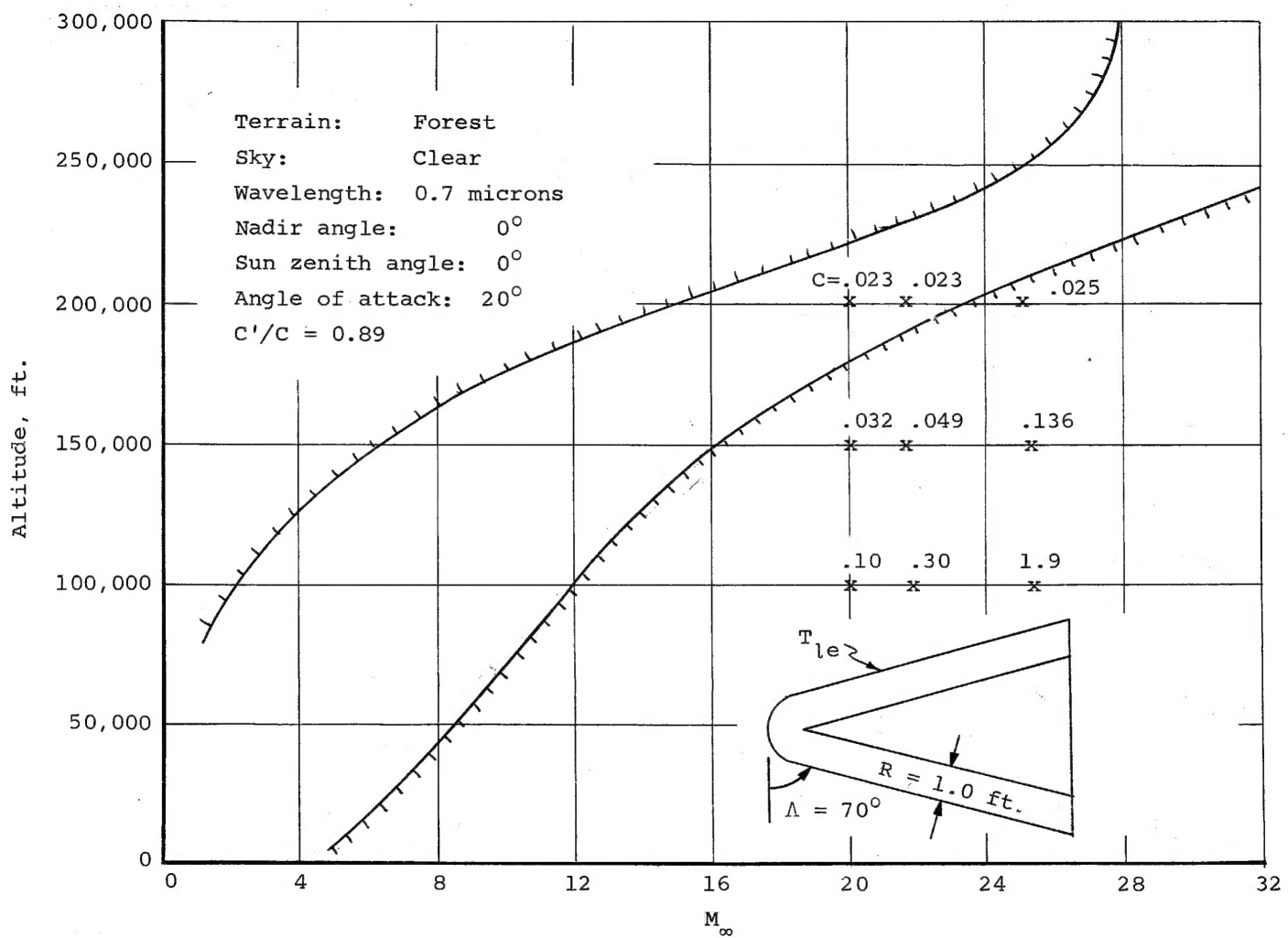
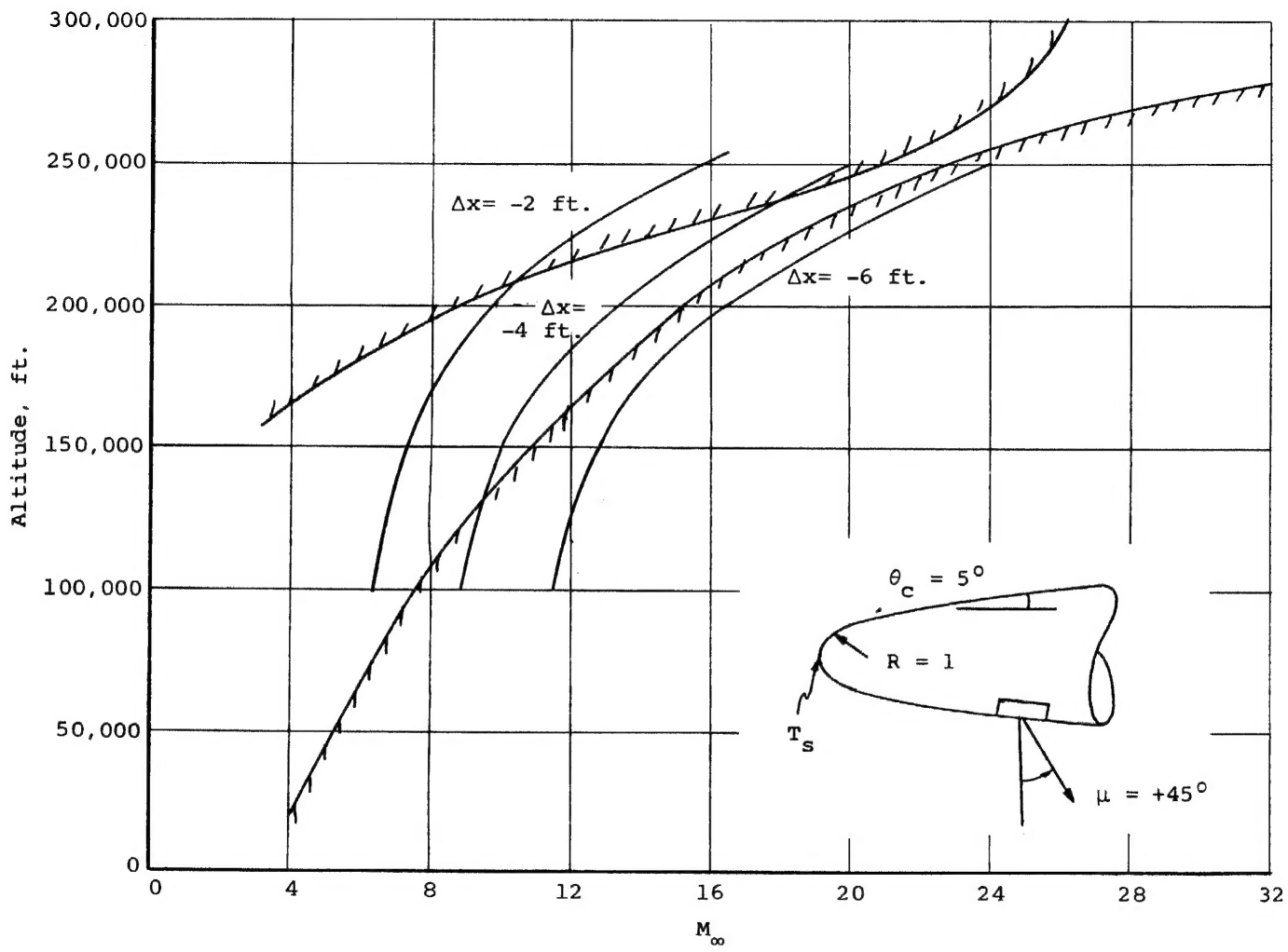


Figure IX-5.- Required ground contrast to produce $C'' = 0.02$ at window at 0.7 microns wavelength.

Approved For Release 2000/04/12 : CIA-RDP67B00657R000300070001-0

Approved For Release 2000/04/12 : CIA-RDP67B00657R000300070001-0

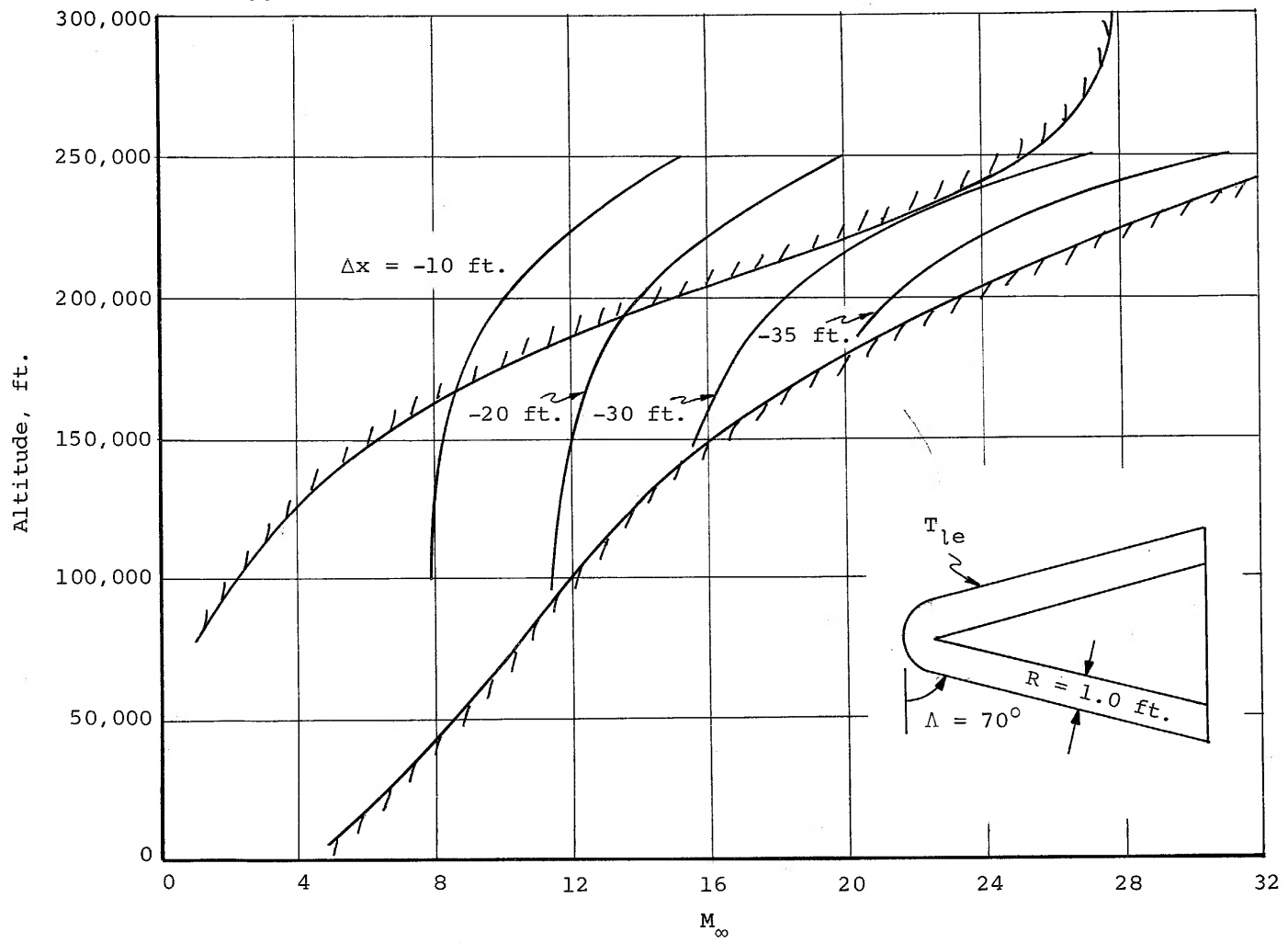


(a) Nonwinged vehicle

Figure IX-6.- Refractive ground displacements in vertical plane of symmetry due to window

Approved For Release 2000/04/12 : CIA-RDP67B00657R000300070001-0

Approved For Release 2000/04/12 : CIA-RDP67B00657R000300070001-0



(b) Winged vehicle, $\alpha = 20^\circ$

Figure IX-6-- Concluded.

Approved For Release 2000/04/12 : CIA-RDP67B00657R000300070001-0